

**AEROSOL COMPOSITION AND HYGROSCOPICITY STUDIES:  
INSTRUMENT DEVELOPMENT/CHARACTERIZATION, AMBIENT AND  
LABORATORY MEASUREMENTS, AND MODELING**

Thesis by  
Armin Sorooshian

In Partial Fulfillment of the Requirements for the  
Degree of Doctor of Philosophy



California Institute of Technology  
Pasadena, California

2008  
(Defended May 5, 2008)

© 2008

Armin Sorooshian

All Rights Reserved

*To Shirin, Soroosh, and Jamshid*

## Acknowledgements

Because of two people I came to Caltech for graduate school. My father inspired me to pursue a career in academia. From Jost O. L. Wendt, my undergraduate research advisor at the University of Arizona, I first heard the names John Seinfeld and Rick Flagan.

John and Rick have been two amazing advisors. They provided me with abundant resources and opportunities, including flying in the back of a research aircraft to navigate pilots and be responsible for keeping a payload of instruments functional. I appreciate them for trusting me with this duty; this experience stands out as one of the most exciting and educational parts of my research at Caltech. John has been a role model because of his ability to effectively manage time, advise students, and be organized in all aspects of the academic profession. He usually responded to emails within minutes, was always available for meetings, edited papers immediately, and provided excellent advice. Rick was a constant source of creativity. He helped me with instrumentation, provided ideas for experiments, and would sit with me in his office, with great patience, providing advice and teaching me how to be a better technical writer.

I worked most closely with Fred Brechtel. He has helped me in a countless number of ways, including teaching me about instrumentation. I thank him for his calm demeanor and patience in training me. Not only is he a gifted engineer and terrific colleague, but a genuinely warm friend. I also thank Andy Corless at BMI for his help with learning how to use various instruments.

I have worked with many wonderful people in the Seinfeld/Flagan research group. I want to thank Tracey and Tomtor, who brought me under their wings in the field. I have



shared some of my most memorable moments with these two wonderful people. Harmony was very helpful during our first year, as we both tried to maintain a strong sense of humor during some tough times. Shane and I spent a great amount of time together in various field studies. I want to thank him for asking insightful questions and providing excellent feedback whenever I had questions. Maybe someday we will both be able to go back to the Barking Spider together. I was very delighted to be able to work closely with Scott in the last year and a half. We overlapped on a project together and I am grateful for his maturity, assistance, and ideas. He is not only a very intelligent person, but also a great friend. He was the one person that could keep up with me in the buffet lines at the Ath. Some of my most memorable moments were working in the laboratory at very late hours across from Jason. I also thank Andrew M., whom I have been absolutely delighted to get to know and spend time with in the field. I want to thank Sally, Jesse, and Arthur for their help with chamber experiments, and for being awesome people. It was a fantastic experience mentoring Rebecca Simpson as part of a summer MURF project; I thank her for having been so motivated and pleasurable to interact with. Others I wish to thank include Roya, Puneet, Xerxes, Bill, Daven, Julia, Havala, Anne, Song, Amir, Adam, Dean, Andreas, Philip, Candy, and Andrea.

I want to thank Patrick Chuang and Thanos Nenes who I have had the pleasure of interacting with in various field studies and conferences. Both have provided me with valuable support. I also had the pleasure of collaborating closely with both Graham Feingold and Barbara Ervens. They were both very energetic during our interactions. Graham's passion about the science of clouds has certainly rubbed off on me. I give thanks to Michael Hoffmann, who I have had memorable discussions with in my last year

at Caltech. Nathan Dalleska provided valuable technical support whenever I experienced problems in the lab. I extend thanks to staff members who have helped me along the way: Ann Hilgenfeldt, Marcy Fowler, Yvette Grant, and Kathy Bubash.

I want to thank everyone at CIRPAS: Haf Jonsson, Roy Woods, Mike Hubbell, Chris Maguire, Greg Cooper, Gintas Buzorius, Nava Roy, Bob Bluth, Richard Boyd, Dennis Hamaker, Reggie Burch, and Sara Moore. Haf has not only been a team player in the field, but also a wonderful person to interact with on a personal level. Our time together in the field and on the Quintescence allowed for meaningful discussions about science, family, and life. Roy was always willing to help and I am still in awe at how he could fasten down that double rack in the Twin Otter. As flight scientist, I was able to spend many hours on the Twin Otter with Mike and Chris. I am in deep admiration of their talent as pilots (and Roy, although I never had the pleasure of flying with him), and their ability to carry out the glorious Charlie Bravo Flight. I also thank them for not beating me up after the infamous Cow Flight.

I would like to thank the Betty and Gordon Moore Foundation for providing funding for my first four years at Caltech. I thank the funding agencies that supported my research: the Office of Naval Research, the National Science Foundation, and the National Oceanic and Atmospheric Administration.

I want to thank my following friends: Andrew B. for six stitches and being a loyal friend and roommate for four years; Arian and Parvin for unique support and lengthy discussions about Arizona basketball; Win for making me laugh; Ubaldo for his vision and Magic Time; Marc for always being solid; Edgardo for his spirit; Stephanie for her good taste in wine and music; Ali for allowing me to practice my Farsi with someone;

BOB for our legendary tailgating parties, kicking field goals late at night, and being solid; Danielle for laughter; Chip for his trust in me; and BUND for meaningful conversations.

The glowing light in my life during the last half of my time at Caltech has been an angel named Atria. She has had an unmeasurable effect on me. Thank you.

Finally, I wish to thank my family. My brother, Jamshid, has always been a great role model and I have followed his footsteps in several ways. He has made sacrifices that have directly resulted in my well-being and I am always thankful for that. I am appreciative for him trying to make me not take life and work so seriously and to relax and take a deep breath sometimes. I am grateful for the constant love and support from my parents, Shirin and Soroosh. Amongst so many other things, I thank them for teaching me the value of family, education, working hard, and enjoying life.

## **Abstract**

Aerosols influence climate by altering the global energy balance via scattering and absorbing solar radiation (direct effects), and by their effect on the reflectance of clouds and occurrence of precipitation (indirect effects). Aerosols also influence biogeochemical cycles, lead to diminished environmental visibility, and harm human health. This thesis focuses on advancing knowledge of critical properties, specifically composition and hygroscopicity, which govern the role of aerosols in climatic and environmental change. The methods used in this work include a combination of instrument development/characterization, ambient and laboratory measurements, and modeling.

An instrument was developed to quantify the water-soluble composition of aerosols. The particle-into-liquid sampler (PILS) grows ambient particles into droplets that grow sufficiently large to be collected by inertial impaction. After being collected in vials, the liquid sample can be analyzed with a variety of analytical methods including ion chromatography. Results from characterization tests are presented, which summarize instrument accuracy, precision, size and time resolution, and uncertainties. An instrument model was developed to simulate operation of the PILS; the model considers plumbing transmission efficiencies, droplet growth, mixing effects, and volatilization losses. Model predictions and measurements are compared and are shown to exhibit good agreement.

A second instrument, termed the differential aerosol sizing and hygroscopicity spectrometer probe (DASH-SP), was developed to quantify aerosol hygroscopic growth and refractive index. This technique employs size classification of dry aerosol particles, equilibrates the classified particles to multiple relative humidities, and then measures the

sizes of the grown particles using optical particle counters. Similar to the PILS, results from an extensive set of characterization test are presented. DASH-SP measurements of growth factor for various inorganic and organic acid salts are reported and compared to thermodynamic predictions.

Airborne aerosol measurements from four separate field campaigns are presented. The main topics of investigation from the ambient experiments include the following: (1) in-cloud production of secondary organic aerosol; (2) a characterization of the sources and character of water-soluble aerosol composition during the 2006 Gulf of Mexico Atmospheric Composition and Climate Study (GoMACCS); and (3) a comprehensive airborne characterization of aerosol from a massive bovine source.

# Table of Contents

<b>Dedication</b>	<b>iii</b>
<b>Acknowledgements</b>	<b>iv</b>
<b>Abstract</b>	<b>viii</b>
<b>List of Tables</b>	<b>xviii</b>
<b>List of Figures</b>	<b>xx</b>
<b>1 Introduction</b>	<b>1</b>
1.1 Background and Motivation.....	2
1.2 Organization of Thesis.....	3
1.3 References.....	5
<b>2 Modeling and Characterization of a Particle-into-liquid Sampler (PILS)</b>	<b>8</b>
2.1 Abstract.....	9
2.2 Introduction.....	10
2.3 Modified PILS.....	11
2.4 PILS Model .....	15
2.4.1 Model Equations.....	16
2.4.2 Model Predictions.....	17
2.5 PILS-IC Detection Levels.....	19
2.5.1 Ion Chromatography (IC) System.....	19
2.5.2 PILS-IC Technique Background Levels.....	20
2.6 Evaluation of Model With Laboratory Data.....	22
2.6.1 PILS Collection Efficiency for Different Aerosol Seeds.....	25

2.6.2 Tip Temperature Sensitivity Tests.....	27
2.7 Field Data.....	30
2.8 Future Work.....	30
2.9 Conclusions.....	31
2.10 Acknowledgements.....	34
2.11 References.....	34
<b>3 Rapid Size-resolved Aerosol Hygroscopic Growth Measurements: Differential Aerosol Sizing and Hygroscopicity Spectrometer Probe (DASH-SP)</b>	<b>53</b>
3.1 Abstract.....	54
3.2 Introduction.....	55
3.3 DASH-SP Description.....	58
3.4 Experimental Methods.....	63
3.5 Instrument Characterization.....	64
3.5.1 Size Limits of OPC Detection.....	64
3.5.2 Time Resolution.....	64
3.5.3 DASH-SP Accuracy, Precision, and Uncertainties.....	66
3.5.4 Stability.....	69
3.6 Data Analysis.....	69
3.7 Growth Factor Measurements.....	73
3.7.1 Inorganic Salts.....	73
3.7.2 Organic Acids.....	74
3.8 Validation of Iterative Data Processing Code.....	77
3.9 Field Implementation of DASH-SP.....	79

3.10 Conclusions.....	81
3.11 Acknowledgements.....	83
3.12 References.....	84
<b>4 Oxalic Acid in Clear and Cloudy Atmospheres: Analysis of Data from International Consortium for Atmospheric Research on Transport and Transformation 2004</b>	<b>104</b>
4.1 Abstract.....	105
4.2. Introduction.....	106
4.3. Twin Otter (TO) Research Aircraft.....	108
4.4. PILS-IC Measurements.....	110
4.5. Field Measurements.....	112
4.5.1. Field Data Summary.....	112
4.5.2. Case Study: Power Plant Plume in Cloud (Flight 5 on 9 August 2004).....	116
4.6. Cloud Parcel Model.....	119
4.6.1. Description and Modifications.....	119
4.6.2. Sensitivity Analysis.....	123
4.7. Comparison of Model Predictions to Field Measurements.....	126
4.7.1. Case Study: Power Plant Plume in Cloud.....	127
4.7.2. Case Study: Clouds Uninfluenced by Local Pollution Sources....	131
4.7.3. Comparison of Predictions From Both Cases to all In-Cloud Field Measurements.....	132



4.7.4. Contribution of Different Aqueous-Phase Pathways to Production of Oxalic Acid.....	134
4.8. Conclusions.....	136
4.9. Acknowledgments.....	137
4.10. References.....	137
<b>5 On the Source of Organic Acid Aerosol Layers Above Clouds</b>	<b>159</b>
5.1 Abstract.....	160
5.2 Introduction.....	160
5.3 Aircraft Measurements.....	162
5.4 Sources of Oxalate above Cloud.....	165
5.5 Physical Processes at the Cloudtop Interface (Large Eddy Simulations).....	167
5.6 Oxalic Acid Chemistry.....	170
5.7 Methanesulfonate.....	173
5.8 Acknowledgements.....	174
5.9 References.....	174
<b>6 Particulate Organic Acids and Overall Water-soluble Aerosol Composition Measurements from the 2006 Gulf of Mexico Atmospheric Composition and Climate Study (GoMACCS)</b>	<b>188</b>
6.1 Abstract.....	189
6.2 Introduction.....	190
6.3 Twin Otter (TO) Research Aircraft.....	193
6.4 Water-soluble Chemical Characterization of Southeastern Texas Aerosol...	194
6.5 Sources and Character of Organic Acids.....	198

6.5.1 Saturated Dicarboxylic Acids.....	198
6.5.2 Unsaturated and Hydroxylated Dicarboxylic Acids.....	201
6.5.3 Saturated Monocarboxylic Acids.....	202
6.5.4 Unsaturated Monocarboxylic Acids.....	204
6.6 Role of Organic Acids in Cloud Droplet Chemistry.....	206
6.6.1 Oxalic Acid as a Reaction Product in Clouds.....	206
6.6.2 High Nitrate Episodes: Methacrylic Acid in Cloud Droplets and Suppressed Organic Acid Formation.....	210
6.7 Organic Acids Downwind of the Houston Ship Channel.....	212
6.8 Evaluation of Ambient Data Relative to Laboratory Chamber Experiments of <i>m</i> -xylene Photooxidation.....	214
6.9 Conclusions.....	216
6.10 Acknowledgements.....	218
6.11 References.....	218
<b>7 Comprehensive Airborne Characterization of Aerosol From a Major Bovine Source</b>	<b>238</b>
7.1 Abstract.....	239
7.2 Introduction.....	240
7.3 Experimental Methods.....	243
7.3.1 Aerosol Chemical Composition (PILS).....	243
7.3.2 Aerosol Chemical Composition (Aerodyne cToF-AMS).....	245
7.3.3 Aerosol Hygroscopicity and Refractive Index (DASH-SP).....	247
7.3.4 Cloud Condensation Nuclei Counter (CCNc).....	248

7.3.5 Size Distributions and Particle Number Concentration.....	248
7.3.6 Flight Strategy.....	249
7.4 Results.....	250
7.4.1 Meteorology.....	250
7.4.2 Particle Number Concentrations and Size Distributions.....	251
7.4.3 Submicrometer Aerosol Chemical Composition.....	252
7.4.3.1 Total Aerosol Mass and Major Components.....	253
7.4.3.2 Inorganic Aerosol.....	254
7.4.3.3 Organic Aerosol.....	254
7.4.4 Aerosol Mixing State.....	256
7.4.5 Refractive Index.....	257
7.4.6 Hygroscopic Properties of the Aerosol.....	258
7.4.6.1 Subsaturated Water Uptake.....	258
7.4.6.2 CCN.....	259
7.5 Discussion.....	261
7.5.1 Enhancements in Mass Production and Water Uptake in the Plume Aerosol.....	261
7.5.2 Amines as an Atmospheric Base.....	262
7.5.2.1 Is Nitric Acid or Ammonia the Limiting Reactant?.....	262
7.5.2.2 Sources and Character of Amines.....	264
7.5.2.3 Total Amine Mass Calculations.....	266
7.5.3 Degree of Oxidation and Volatility in the Aerosol.....	267
7.5.4 Factors Influencing Aerosol Number/Mass Concentrations.....	268

7.5.5 Estimated Subsaturated Hygroscopic Growth Factors for the Organic Fraction.....	269
7.5.6 Relationship Between Sub- and Supersaturated Water Uptake.....	272
7.5.7 Parameterization for Sub- and Supersaturated Water Uptake.....	273
7.6. Conclusions.....	275
7.7 Acknowledgements.....	277
7.8 References.....	277
<b>8 Conclusions</b>	<b>311</b>
<b>Appendices</b>	<b>316</b>
<b>Appendix A Chemical Composition of Secondary Organic Aerosol Formed from the Photooxidation of Isoprene</b>	<b>317</b>
<b>Appendix B Evidence for Organosulfates in Secondary Organic Aerosol</b>	<b>344</b>
<b>Appendix C Characterization of 2-Methylglyceric Acid Oligomers in Secondary Organic Aerosol Formed from the Photooxidation of Isoprene Using Trimethylsilylation and Gas Chromatography/Ion Trap Mass Spectrometry</b>	<b>356</b>
<b>Appendix D Aerosol-Cloud Drop Concentration Closure for Clouds Sampled During the International Consortium for Atmospheric Research on Transport and Transformation 2004 Campaign</b>	<b>373</b>
<b>Appendix E Secondary Aerosol Formation from Atmospheric Reactions of Aliphatic Amines</b>	<b>386</b>
<b>Appendix F Regional Variation of Organic Functional Groups in Aerosol Particles on Four U.S. East Coast Platforms during ICARTT 2004</b>	<b>412</b>

<b>Appendix G</b>	<b>Effect of NO<sub>x</sub> Level on Secondary Organic Aerosol (SOA) Formation from the Photooxidation of Terpenes</b>	<b>424</b>
<b>Appendix H</b>	<b>Secondary Organic Aerosol (SOA) Formation from Reaction of Isoprene with Nitrate Radicals (NO<sub>3</sub>)</b>	<b>441</b>
<b>Appendix I</b>	<b>Molar Mass, Surface Tension, and Droplet Growth Kinetics of Marine Organics from Measurements of CCN Activity</b>	<b>515</b>

## List of Tables

Table 2.1 Equations for Droplet Growth and Transmission Efficiency in Different Stages of the PILS.....	37
Table 2.2 Filter Mode Background Levels.....	39
Table 2.3 Effect of Using $(\text{NH}_4)_2\text{SO}_4$ and $\text{NH}_4\text{NO}_3$ Independently as Wash-flow Solutions.....	40
Table 2.4 Minimum Time Response to Step Changes in Concentration for the Original and Modified PILS Designs as a Function of the Debubbler Residence Time....	41
Table 2.5 PILS Collection Efficiency for Anions and Cations Compared to the DMA..	42
Table 2.6 Molar Ratios for Different Aerosols Tested by the PILS.....	43
Table 3.1. Aerosol Hygroscopicity Measurement Techniques.....	93
Table 4.1. Twin Otter Payload Description.....	143
Table 4.2. Comparison of PILS Original (Old) and Re-Analyzed (New) Vials from Flight 5 on 9 August 2004.....	144
Table 4.3. Molar Ratio of Oxalate Relative to Sulfate, Nitrate, and Ammonium.....	145
Table 4.4. Initial Conditions for Two Simulations.....	146
Table 5.1. Summary of Lagrangian Trajectory Results.....	182
Table 6.1. Selected Organic Acid Measurements in Urban Atmospheres.....	226
Table 6.2. Chemical Formulas and Structures for the Organic Acids Studied.....	227
Table 6.3. Organic Acid Product Distribution for a Series of <i>m</i> -xylene Laboratory Chamber Photooxidation Experiments.....	228

Table 7.1. Summary of In-plume and Out-of-plume Measurements of Composition and Particle Number and Mass Concentration.....	288
Table 7.2. DASH-SP Hygroscopicity and Dry Particle Refractive Index Data Categorized by the Time of Flight as Shown in Figure 1. Data at RH = 85% are not available for Flight A.....	289
Table 7.3. Summary of CCN Data for Flights A and B.....	290
Table 7.4. Summary of $\kappa$ Values ( <i>Petters and Kreidenweis, 2007</i> ) Derived from Subsaturated Hygroscopic Growth Factor Data at RHs of 85%, and 92%. Data at RH = 85% are not available for Flight A.....	291

## List of Figures

Figure 1.1. Earth's annual global mean energy budget (Kiehl and Trenberth, 1997).....	7
Figure 1.2. Global mean radiative forcings (RF) and their 90% confidence interval (IPCC, 2007).....	8
Figure 2.1. Schematic diagram of the modified PILS.....	44
Figure 2.2. Modeled stages of the modified PILS.....	45
Figure 2.3. Temperature dependence of the equilibrium constants for three reactions....	46
Figure 2.4. Transmission efficiency in the PILS as a function of particle diameter for all plumbing prior to droplet growth in the condensation chamber, and the relative contribution of diffusion and inertial deposition to the total losses.....	47
Figure 2.5. Final droplet diameters after growth in the condensation chamber ( $\tau = 1$ s) as a function of the initial particle diameters for different (a) accommodation coefficients (b) and tip temperatures.....	48
Figure 2.6. Percentage of $\text{NH}_4^+$ remaining in the particle phase after the 1 s residence time in the condensation chamber as a function of particle surface temperature, acidity, and the amount of water (which is related to the dilution factor).....	49
Figure 2.7. Comparison of experimental and theoretical mass concentrations in the modified PILS.....	50
Figure 2.8. Tip temperature sensitivity results for a test where the modified PILS sampled $(\text{NH}_4)_2\text{SO}_4$ aerosol.....	51



Figure 2.9. (a) Flight tracks; (b) Time series of the mass concentrations of various inorganic and organic acid ions measured during one ICARTT flight that was marked by the presence of clouds.....	52
Figure 3.1. Schematic of DASH-SP.....	94
Figure 3.2. Time required as a function of particle number concentration to obtain sufficient pulses for the modal pulse height to be within 1% of the mode that would be obtained when counting at least 10,000 particles at constant particle composition. Also shown is the time needed for the standard deviation to be within 1%, 5%, and 10% of the standard deviation that would be obtained when counting at least 10,000 particles at constant particle composition.....	95
Figure 3.3. Stability statistics for different species and sizes over a time span of four months.....	96
Figure 3.4. OPC response as a function of dry particle size for salts of different refractive index.....	97
Figure 3.5. Data processing procedure from DASH-SP raw pulse height data to growth ( <i>GFs</i> ) for both laboratory-generated aerosol, for which the composition and refractive index ( <i>n</i> ) of the dry particles are known, and for ambient aerosol, where the composition and refractive index of the dry particles are unknown.....	98
Figure 3.6. Experimentally determined growth factor curves for inorganic and organic acid species.....	99

Figure 3.7. Comparison between two thermodynamic models and DASH-SP data for ammonium sulfate particles.....	100
Figure 3.8. Size distributions from wet ammonium sulfate and dry PSL aerosol laboratory tests.....	101
Figure 3.9. Panel A) Flight tracks during a MASE II flight (July 16, 2007) during which the Twin Otter aircraft sampled emissions from a large cargo ship off the central coast of California.....	102
Figure 4.1. Twin Otter flight tracks during the ICARTT field study.....	147
Figure 4.2. Simplified illustration of how the Twin Otter flew when it encountered two specific atmospheric conditions: (a) Power plant plume in cloud; (b) Power plant plume in cloud-free air with precipitation from scattered clouds overhead.....	148
Figure 4.3. Vertical distribution of ions measured by the PILS during ICARTT.....	149
Figure 4.4. Oxalate and $\text{SO}_4^{2-}$ molar concentrations for each atmospheric condition encountered.....	150
Figure 4.5. Flight 5 (9 August 2004): (a) Flight tracks; (b) Time series of altitude, LWC, and aerosol number concentration; (c) Time series of $\text{SO}_4^{2-}$ , organic ions, and the aerosol volume concentration.....	151
Figure 4.6. Evolution of the DACAD aerosol size distribution (dry: < 20%) for Flight 5 on 9 August 2004.....	152
Figure 4.7. Multiphase organic chemistry.....	153
Figure 4.8. Model predictions for the power plant plume in cloud case (simulation of Flight 5 on 9 August 2004).....	154

Figure 4.9. Comparison of Flight 5 (9 August 2004) field data and model predictions for $\text{SO}_4^{2-}$ and oxalate growth.....	155
Figure 4.10. Model predictions for the case of clouds uninfluenced by local pollution sources.....	156
Figure 4.11. Comparison of oxalate and $\text{SO}_4^{2-}$ molar concentrations between model predictions and field data for clouds with and without power plant plume influence.....	157
Figure 4.12. Contribution of different aqueous-phase pathways to production of oxalic acid.....	158
Figure 5.1. Schematic of physical processes leading to an organic acid aerosol layer above clouds.....	183
Figure 5.2. Particulate oxalate concentrations below and above 14 different cloud fields probed during MASE.....	184
Figure 5.3. Particulate organic acid concentrations below and above 22 different cloud systems probed during GoMACCS.....	185
Figure 5.4. A-C: Example of the temporal evolution of trajectories from a 2D slice of the 3D LES simulation. D: Temporal evolution of cloudtop from the LES simulation of the stratocumulus cloud observed July 5, 2005, which was influenced by ship emissions corresponds to 7/5 in Figure 5.2).....	186
Figure 5.5. Droplet residual particle data from two different GoMACCS cloud profiling events.....	187
Figure 6.1. Spatial distribution of the PILS water-soluble mass concentration during GoMACCS.....	229

Figure 6.2. Total water-soluble charge balance for all samples collected during GoMACCS.....	230
Figure 6.3. Comparison between the water-soluble mass concentration and DMA volume concentration in different regions of the lower troposphere.....	231
Figure 6.4. Vertical distribution of the total water-soluble mass and different ionic components.....	232
Figure 6.5. Vertical distribution of the different organic acids and diethylamine.....	233
Figure 6.6. Contribution of individual organic acids to the total organic acid mass in different regions of the lower troposphere.....	234
Figure 6.7. Comparison of the oxalate:glyoxylate mass ratio between ambient measurements of cloud droplet residual particles and model predictions for clouds influenced by pollution sources ("polluted") and those that are not ("clean")...	235
Figure 6.8. Flight tracks during a study aimed at analyzing the evolution of aerosol properties in three major plumes originating in the Houston Ship Channel.....	236
Figure 6.9. Organic acid product evolution from a photooxidation experiment with the following conditions: 75 ppb <i>m</i> -xylene/low NO <sub>x</sub> /non-acid ammonium sulfate seed aerosol.....	237
Figure 7.1. A) Complete flight tracks for the two flights in the San Joaquin Valley of California. The shaded mountain areas are meant to provide a relative view of how the San Joaquin Valley is bordered by major topographical features. B/C) Detailed tracks for flights A (12 July 2007) and B (30 July 2007) with a step-by-step description of the aircraft maneuvers.....	292

Figure 7.2. Upper panel) Time series of particle number concentration and meteorological data for flight A. Lower panel) Time series of aerosol size distribution.....	293
Figure 7.3. Upper panel) Time series of particle number concentration and meteorological data for flight B. Lower panel) Time series of aerosol size distribution.....	294
Figure 7.4. Vertical profiles of particle number concentration and meteorological data for flights A (upper panel) and B (lower panel).....	295
Figure 7.5. HYSPLIT five-day backward trajectory analysis for flights A (panel A) and B (panel B).....	296
Figure 7.6. Time series of PILS water-soluble aerosol composition and cToF-AMS composition for flights A (upper panel) and B (lower panel).....	297
Figure 7.7. Spatial distribution of various aerosol species during flight A. A) Nitrate and diethylamine; B) <i>Excess nitrate</i> remaining after both sulfate and nitrate have been neutralized by ammonium (see Section 7.3.2 for further explanation); C) ammonium; D) organics.....	298
Figure 7.8. Spatial distribution of various aerosol species during flight B. A) Nitrate and diethylamine; B) <i>Excess nitrate</i> remaining after both sulfate and nitrate have been neutralized by ammonium (see Section 7.3.2 for further explanation); C) ammonium; D) organics.....	299
Figure 7.9. Vertical distribution of total submicrometer particulate mass and species concentrations from both the PILS and cTOF-AMS, for flights A (upper panel) and B (lower panel).....	300

Figure 7.10. Aerosol mass spectra from the cToF-AMS in the background aerosol and in the plume at various downwind distances from the feedlot for flight B.....	301
Figure 7.11. A comparison of the plume organic mass spectra versus the background aerosol organic mass spectra for flights A (upper panel) and B (lower panel)...	302
Figure 7.12. Speciated size distributions as determined by the cToF-AMS for flights A (panel A) and B (panel B).....	303
Figure 7.13. Growth factor data from flight A at RHs of 74% (upper panel) and 92% (lower panel).....	304
Figure 7.14. Growth factor data from flight B at RHs of 74% (A), 85% (B), and 92% (C).....	305
Figure 7.15. Relationship between the hygroscopic growth factor at 92% RH and mass fractions of nitrate and organics during flight B.....	306
Figure 7.16. Time series of activated fraction of aerosol (CCN/CN), and total CCN concentration during flights A (upper panel) and B (lower panel).....	307
Figure 7.17. Normalized CCN activation ratio, $(\text{CCN/CN})_{\text{measured}}:(\text{CCN/CN})_{\text{ammonium sulfate}}$ , as a function of hygroscopic growth factors for flight B.....	308
Figure 7.18. The relationship between the $m/z$ 57:44 ratio, the organic mass fraction, the CCN fraction with less droplet growth than ammonium sulfate ( $D_i < D_{AS}$ ), and the hygroscopic growth factor at RH = 92%.....	309
Figure 7.19. Spatial distribution of the calculated organic growth factors, using the ZSR mixing rule, for flights A (upper panel) and B (lower panel).....	310

# **Chapter 1**

## **Introduction**

## 1.1 Background and Motivation

Aerosols, defined here as suspended particulate matter, influence climate by altering the global radiative balance (Figure 1.1). The climatic effects associated with aerosols include their ability to scatter and absorb solar radiation (direct effects) and their effect on the reflectance of clouds and occurrence of precipitation (indirect effects) (IPCC, 2007). It is understood that aerosols exhibit a negative net anthropogenic radiative forcing globally, but the current level of scientific understanding of the forcing magnitude is low (Figure 1.2; IPCC, 2007). This poses a major obstacle when trying to predict future climate change. Of particular interest are aerosol-cloud interactions because the uncertainty associated with these interactions is the highest of all forcings. Aerosols also influence biogeochemical cycles, lead to diminished environmental visibility, and harm human health (EPA, 2004).

To understand the relationship between aerosols and climate, it is necessary to perform measurements of key aerosol properties, which include the following: size distribution, number concentration, composition, hygroscopicity, and refractive index. When the former four measurements are combined with knowledge of key cloud properties, such as liquid water content, drop number concentration, and drop size, it is possible to investigate aerosol–cloud interactions. One way to reduce uncertainties in the radiative forcing associated with aerosol effects is to perform ambient in-situ measurements of atmospheric aerosols. Instrumentation needs to be designed to make rapid measurements suitable for aircraft deployment, such that short time-scale events can be resolved. Airborne aerosol measurements can then be used to validate and improve atmospheric models.



## 1.2 Organization of Thesis

This thesis is devoted to the development and characterization of aerosol instrumentation, the application of these instruments in field and laboratory studies, and evaluating models with measurements. Chapters 2 and 3 focus on the development and characterization of two novel aerosol instruments, which were designed for aircraft deployment. Chapter 2 introduces the particle-into-liquid sampler (PILS), which when coupled to ion chromatography, can quantify water-soluble aerosol composition. Chapter 3 introduces the differential aerosol sizing and hygroscopicity spectrometer probe (DASH-SP), which employs differential mobility analysis in-concert with multiple humidification and optical sizing steps to determine dry optical size and hygroscopic growth factors for size-selected aerosols.

Chapters 4-7 discuss measurements carried out on the Center for Interdisciplinary Remotely-Piloted Aircraft Studies (CIRPAS) Twin Otter in the following four different field studies: International Consortium for Atmospheric Research on Transport and Transformation (ICARTT 2004), Marine Stratus/Stratocumulus Experiment I and II (MASE 2005, 2007), Gulf of Mexico Atmospheric Composition and Climate Study (GoMACCS 2006). The aircraft payload consisted of a suite of aerosol instruments, but specific attention is given to PILS and DASH-SP measurements.

Chapters 4-5 specifically focus on the production of secondary organic aerosol in clouds. Owing to the low volatility and water-soluble nature of organic acids, these species constitute a significant fraction of SOA mass. Chapter 4 explores the production of oxalic acid in clouds during the 2004 ICARTT study. ICARTT measurements of

sulfate, oxalate, and oxalate's aqueous-phase precursors are presented in both clear air and clouds. Predictions from a state-of-the-art chemical/microphysical cloud parcel model show good agreement with ambient data for the relative magnitude of sulfate and organic acid growth in clouds. Clear evidence is presented for aqueous-phase oxalic acid production as the primary mechanism for oxalic acid formation in ambient aerosols.

Chapter 5 explores the sources of enhanced organic acid aerosol layers that were observed directly above cloudtops in measurements from MASE I and GoMACCS. As derived from large eddy simulations of stratocumulus under the conditions of MASE, both Lagrangian trajectory analysis and diurnal cloudtop evolution provide evidence that a significant fraction of the aerosol mass concentration above cloud can be accounted for by evaporated droplet residual particles. In addition, entrainment of free tropospheric aerosol is also argued to lead to enhanced organic acid levels above clouds.

Chapter 6 presents a thorough characterization of the water-soluble aerosol composition during the 2006 GoMACCS study in southeastern Texas. Special attention is given to the sources and character of organic acids ( $C_2$ – $C_9$ ). The organic acid mass composition in the Houston Ship Channel, an area emitting large amounts of aromatic hydrocarbons, is compared to measurements from laboratory studies of *m*-xylene photooxidation. Chapter 7 reports an extensive airborne characterization of aerosol downwind of a massive bovine source in the San Joaquin Valley (California) on two flights during the MASE II study. Measurements are presented for chemical composition, particle size distribution, mixing state, sub- and supersaturated water uptake behavior, light scattering properties, and the interrelationship between these parameters and meteorology.

Chapter 8 presents the main conclusions of this thesis. Appendices A-I present results from studies devoted to aerosol composition, aerosol formation, and aerosol-cloud interactions.

### **1.3 References**

1. Intergovernmental Panel on Climate Change (IPCC) (2007). *Climate Change 2007*, Cambridge, UK: Cambridge Univ. Press, Cambridge and New York.
2. U.S. Environmental Protection Agency (2004). *Air Quality Criteria for Particulate Matter*, EPA 600/P-99/002aF-bF, Washington, DC: EPA.
3. Kiehl, J. T., and Trenberth, K. E. (1997). Earth's Annual Global Mean Energy Budget, *Bull. Amer. Meteor. Soc.*, 78, 197-208.

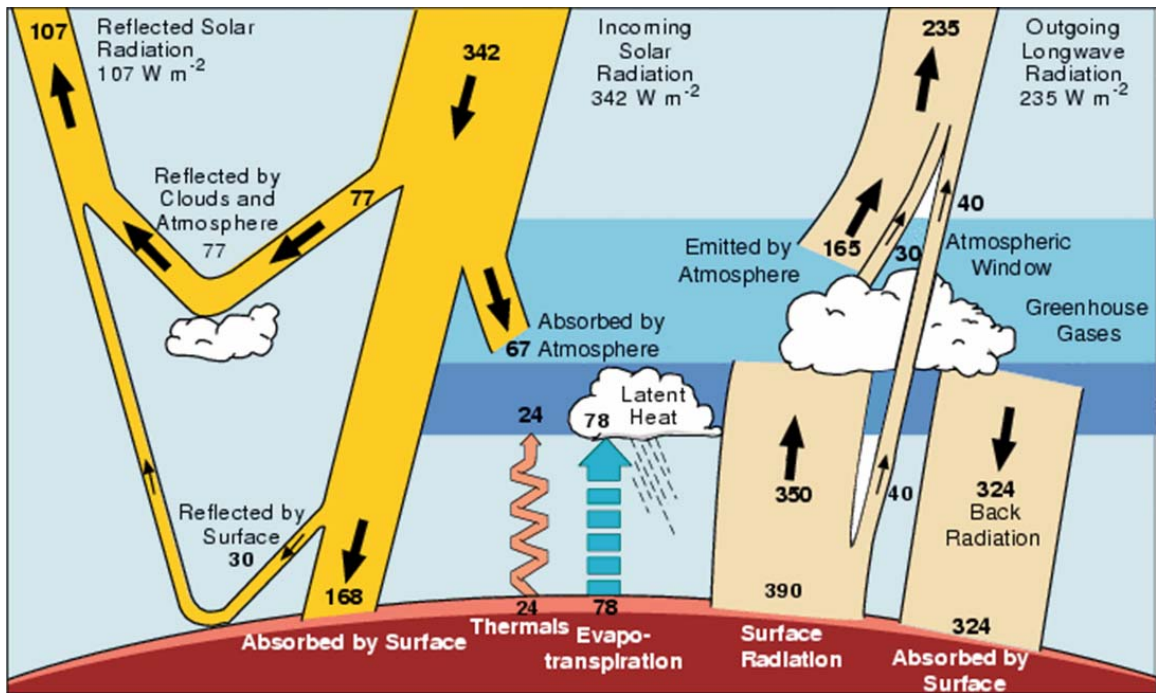


Figure 1.1. Earth's annual global mean energy budget (Kiehl and Trenberth, 1997).

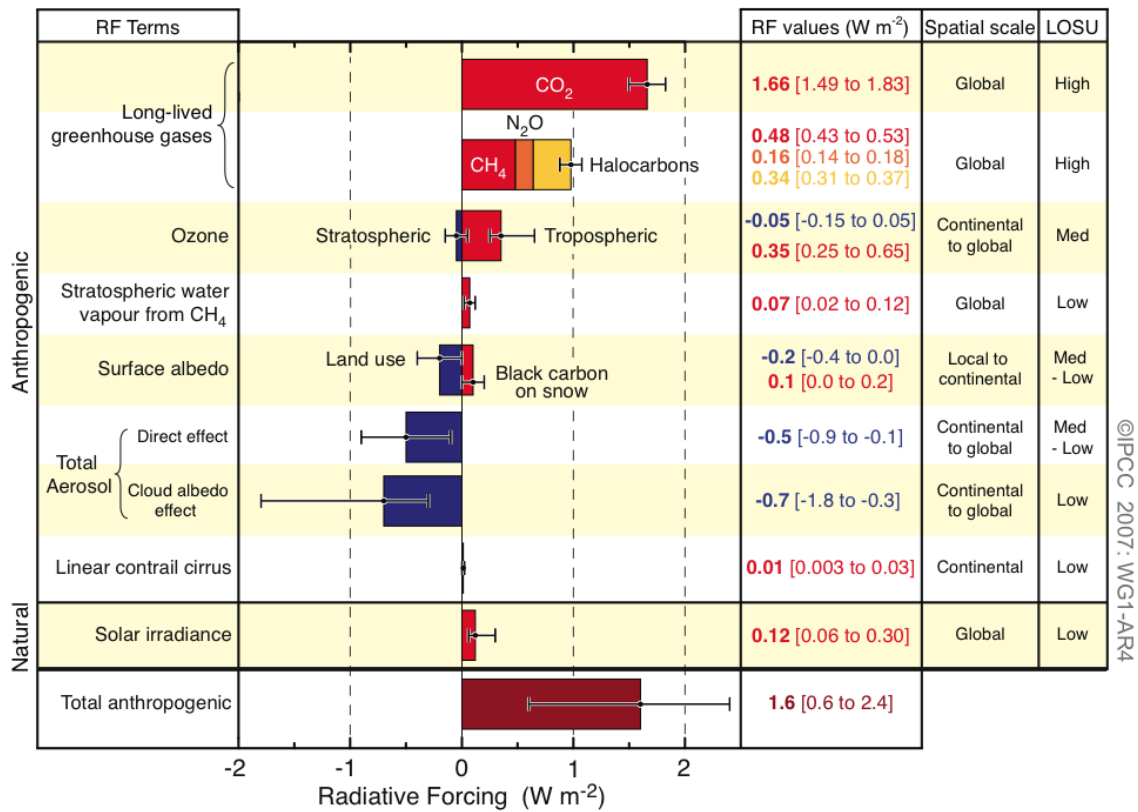


Figure 1.2. Global mean radiative forcings (RF) and their 90% confidence intervals (IPCC, 2007). Columns on the right-hand side specify best estimates and confidence intervals (RF values), typical geographical extent of the forcing (Spatial scale), and level of scientific understanding (LOSU).

## **Chapter 2**

# **Modeling and Characterization of a Particle-Into-Liquid Sampler (PILS)\***

---

\*This chapter is reproduced by permission from “Modeling and Characterization of a Particle-Into-Liquid Sampler (PILS)” by A. Sorooshian, F. J. Brechtel, Y. L. Ma, R. J. Weber, A. Corless, R. C. Flagan, and J. H. Seinfeld, *Aerosol Sci. Tech.*, 40, 396-409, 2006. Copyright 2006. American Association for Aerosol Research.

## 2.1 Abstract

A modified particle-into-liquid sampler (PILS), based on the original design of Weber et al. (2001), is presented. The principal modification in this design is that collected liquid sample is delivered to vials held on a rotating carousel as opposed to an on-line analytical detector. A model is developed to predict aerosol mass concentrations measured by a PILS based on operating parameters and characteristics of the sampled aerosol. A backward model predicts the concentrations of the sampled aerosol based on operating parameters and concentrations measured by the PILS. Both models, which consider plumbing transmission efficiencies, droplet growth, mixing effects, and volatilization losses, predict mass concentrations that are consistent with laboratory tests for step changes in concentration. The average collection efficiency for species ( $\text{Na}^+$ ,  $\text{K}^+$ ,  $\text{SO}_4^{2-}$ ,  $\text{Cl}^-$ ,  $\text{NO}_3^-$ ) from a variety of aerosols compared to simultaneous measurements with a differential mobility analyzer (DMA) exceeded 96% except for  $\text{NH}_4^+$  (88%);  $\text{NH}_4^+$  is theoretically shown to be the most vulnerable to volatilization, followed by  $\text{Cl}^-$  and then  $\text{NO}_3^-$ , with greater losses caused by increasing droplet pH and temperature. The characterization tests highlight the importance of reducing  $\text{NH}_4^+$  volatilization by keeping a stable tip temperature of  $100^\circ\text{C}$  at the point where steam and ambient air mix in the condensation chamber. Maintaining a stable tip temperature also avoids fluctuations in supersaturations that lead to increased deposition losses of larger droplets. Sample data from the 2004 International Consortium for Atmospheric Research on Transport and Transformation (ICARTT) field campaign are presented.

## 2.2 Introduction

Instrumental methods for quantifying atmospheric aerosol chemical composition have evolved from filter-based sampling to devices that provide real-time measurements (Buhr et al., 1995; Simon and Dasgupta, 1995; Zellweger et al., 1999; Stolzenburg and Hering, 2000; Slanina et al., 2001; Weber et al., 2001; Orsini et al., 2003). Real-time measurements avoid both the potential sampling artifacts and long turn-around time for processed results associated with filter sampling. Weber et al. (2001) developed the original particle-into-liquid sampler (PILS), which grows particles in supersaturated water vapor, thereby creating droplets sufficiently large to be collected by inertial impaction and then chemically analyzed in real-time. The liquid sample can be partitioned into fractions and analyzed by different analytical techniques, such as ion chromatography (IC) and total organic carbon (TOC) analysis.

We report here on a PILS, developed by Brechtel Manufacturing Inc. ([www.brechtel.com](http://www.brechtel.com)), which is based on a modification of the original design of Weber et al. (2001). The principal modification in this design is that two syringe pumps drive the liquid sample from the impaction plate at the end of the condensation chamber to vials held on a rotating carousel; in the original PILS design, liquid sample is driven directly from the impaction plate to an analytical detector with either a peristaltic pump or two syringe pumps downstream of the analytical device. Benefits of syringe pumps over peristaltic pumps include steadier flow rates and less degradation in pump tubing over time. The sampling rate of this modified PILS is not limited by the duty cycle time of any on-line analytical detector, which is advantageous for airborne sampling.



A model is needed to predict sample behavior in both the original and modified PILS in order to quantify effects such as volatilization losses and mixing. We present here a mathematical model to simulate the major processes affecting the aerosol sample within the PILS. A model of the instrument is developed that, given the input aerosol concentration, predicts the mass concentration in successive vials collected; the model incorporates plumbing efficiencies, droplet growth, evaporation of semi-volatile species, and the residence time distribution in the debubbler and two syringes that drive the liquid sample to vials. These same processes are considered in a backward model, intended to predict the aerosol mass concentration entering the inlet based on observed concentrations within vials. The two models are used to simulate operation of both the modified and the original PILS, where the step involving the syringes is eliminated when considering the original PILS. Model predictions are compared to data obtained from characterization tests with the original and modified PILS, which include evaluation of the PILS collection efficiency using a differential mobility analyzer (DMA) while sampling a variety of different laboratory aerosols. Sample data from the 2004 International Consortium for Atmospheric Research on Transport and Transformation (ICARTT) field campaign are presented to show that the modified PILS can successfully quantify ambient concentrations of inorganic and organic acid ions with time resolution appropriate for aircraft sampling.

### **2.3 Modified PILS**

The basic principle of the PILS instrument is to grow aerosol particles into droplets sufficiently large to be collected by inertial impaction for subsequent chemical

analysis (Weber et al., 2001). Many of the instrumental features of the modified PILS design presented here are the same as those described by Orsini et al. (2003). As shown in Figure 2.1, the modified PILS samples ambient air at approximately  $12.5 \text{ L min}^{-1}$ , with a critical orifice maintaining a constant volumetric flow rate. A single-stage pre-impactor ( $D_{50} = 1 \text{ }\mu\text{m}$ ) removes super-micrometer sized particles. An automated three-way valve (Swagelok) either directs flow through (filter mode) or bypasses (sample mode) a high-efficiency particulate air (HEPA) filter to allow for background level testing during experiments. A series of three denuders remove gases that can bias aerosol measurements; inorganic vapors are removed by two denuders with annular glass surfaces (URG-2000-30x242-3CSS), and a third denuder (Sunset Laboratory Inc.), composed of 15 thin carbon filter paper sheets ( $3.15 \text{ cm} \times 20.32 \text{ cm} \times 0.04 \text{ cm}$  thick) with  $0.2 \text{ cm}$  gaps between them, removes organic gases. The glass denuders are placed upstream of the carbon denuder so that detailed extraction tests can be carried out following operation.

The ambient air mixes with steam that is introduced through a tube ( $0.04 \text{ cm ID}$ ), the tip of which has a thermocouple attached to provide accurate steam injection tip temperature readings. An algorithm is used to account for pressure fluctuations (specifically for airborne operation) and air flow over the tip, to provide real-time control of the steam injection tip temperature at  $100 \pm 2^\circ\text{C}$ . Rapid adiabatic mixing of the steam and the cooler ambient air produces a high supersaturation of water vapor that allows droplets to grow large enough ( $D_p > 1 \text{ }\mu\text{m}$ ) to be collected by inertial impaction onto a wettable quartz or polycarbonate impactor plate. The condensation chamber is kept at a slight angle ( $15^\circ$ ) to allow wall condensate to be removed by a drain line at the end of the

chamber's main body. Those particles too small ( $< 1 \mu\text{m}$ ) to be collected by inertial impaction leave the system with the exhausted air flow.

Impacted droplets are transported down the impactor by a wash-flow (0.15 to 0.20  $\text{mL min}^{-1}$ ) supplied by two syringe pumps with 250  $\mu\text{L}$  syringes (Kloehn Ltd. Model V3), which work together using a “handshaking” technique. Using this technique, one syringe aspirates sample from a wash-flow stock bottle in a downward stroke, while the other is dispensing already-collected wash-flow to the top of the impactor plate in an upward stroke. A stainless steel mesh wick on the perimeter aids in drawing the liquid down the impactor plate. Two syringes use the “handshaking” technique to extract the liquid sample from the bottom of the impactor plate (0.13  $\text{mL min}^{-1}$ ) and deliver it to a debubbler; volumes of 250 and 50  $\mu\text{L}$  were used for these syringes (these syringes, regardless of volume, are operated at the same speed,  $2.17 \mu\text{L s}^{-1}$ ), with the lower volume reducing the mean liquid residence time in the PILS. The liquid flow rates are controlled by the programmed syringe pump speeds. After air bubbles are removed by the debubbler, the liquid sample is drawn into one of two syringes (at any one time, one syringe aspirates liquid from the debubbler and the other dispenses liquid to the vials); the debubbler and each syringe behave like two continuously stirred tank reactors (CSTRs) in series. These types of vessels are characterized by perfect mixing, such that the concentration is uniform throughout the vessel. The sample then travels to a computer-controlled injection needle that is inserted into individual vials, the caps of which have septa to minimize contamination. Seventy-two vials are held on a rotating carousel; typically 0.65 mL of sample was collected over a 5-min period in each vial for results presented here. The sample volume and filling time for each vial can be adjusted

to optimize the level of dilution and time resolution needed. The addition of syringe pumps and the vial collection technique are beneficial for aircraft sampling since the liquid sample in each vial can be partitioned into fractions for different analytical tests after each flight. Furthermore, the use of a vial collection system avoids the space, power, weight, and down-time of an analytical device while promoting autonomous operation.

Dilution occurs when the impacted droplets are washed from the impactor plate. In addition to the wash-flow, dilution takes place as a result of water vapor condensation on the impactor wall. The dilution factor is determined by spiking the wash-flow of Milli-Q water with non-interfering ions (LiF and LiBr were used for this study); this factor, which typically ranges from 1.1 to 1.4 during airborne flights, is calculated by taking the ratio of the  $\text{Li}^+$  concentration in the wash-flow supply bottle to the  $\text{Li}^+$  concentration in each vial. The pressure changes that occur during aircraft flights have been shown to have no influence on the dilution factor since the syringe pumps allow for precise liquid sample flow control.

To make meaningful intercomparisons with other instruments sampling the same air stream simultaneously, it is necessary to know the residence time of an air parcel and liquid sample inside the PILS system (Figure 2.2). The debubbler and the syringes complicate this measurement since they act as CSTRs and mix each incoming liquid parcel with their entire liquid volume. An estimate of the residence time in the mixing vessels is made by observing the time needed to empty them when they are completely filled with liquid. All other plumbing residence times are calculated using measured tube volumes and flow rates. The time elapsed from the moment a parcel of air enters the inlet

until it impacts onto the droplet impactor plate is estimated to be 3.6 s; this time will vary between different designs based on the plumbing length between the inlet and the droplet impactor (combined 3 m in this design with tube IDs varying between 0.35 and 1.65 cm). The time for each syringe to complete a full round-trip (downward stroke followed by an upward stroke) is measured to be 46 and 230 s using 50 and 250  $\mu\text{L}$  syringes, respectively. The last liquid parcel to enter a syringe at the end of a downward stroke exits the syringe at the beginning of the next upward stroke, which results in very little time spent in the syringe. As will be shown later, model predictions show that there is a minimum time delay of 301 s and 304-313 s to overcome a step change in concentration for the original and modified PILS (assuming a 66 s debubbler liquid residence time), respectively; the time delays for the modified PILS are used here as a time-offset to intercompare with DMA measurements. The time-offset can be reduced by lowering the debubbler residence time; this involves optimizing the ratio between the flow rate of the wash-flow at the top of the droplet impactor and the speed of the syringes aspirating liquid from the debubbler.

## **2.4 PILS Model**

A model is developed that predicts the mass of solutes in the PILS vials. The model accounts for plumbing transmission efficiencies, droplet growth, loss processes in the condensation chamber including volatilization and droplet deposition, mixing behavior in the debubbler and the syringes, and the “handshaking” behavior of the syringes. This model also predicts the transition time resulting from a step change in concentration for different operating parameters, such as vial-filling time, mixing vessel volumes, and the round-trip time for the syringes. The inverse model starts from

measurements of concentration in vials to back-calculate the actual mass concentrations in the sampled aerosol and to properly adjust the PILS measurements for instrument time response. Both models are also used to simulate sample behavior in the original PILS, with the only difference being that the syringes were not considered.

The important flow elements of the modified PILS are the impactors, the plumbing leading to the condensation chamber, the condensation chamber itself, and the plumbing leading from the droplet impactor to the dispensing needle, which includes the debubbler and two syringes (Figure 2.2). During sample transport within the instrument, plumbing-related particle losses can occur by gravitational settling, diffusional deposition, turbulent inertial deposition, and inertial deposition at bends and flow constrictions. The model considers these processes as a function of particle size for all stages up to the droplet impactor, at which point the masses in each particle size bin are added into a cumulative liquid parcel. Predictions can be used to assess the sensitivity of the droplet size distribution to different initial conditions for the air and water vapor streams.

#### **2.4.1 Model Equations**

The basic equations of the PILS model are given in Table 2.1 (Figure 2.2 indicates which equations are applied when modeling specific stages of the instrument). Semi-volatile species in the sampled particles can evaporate as a result of the release of latent heat of condensation and convective heating of the air sample. Ma (2004) reports a 13 to 16% loss (by mass) of  $\text{NH}_4^+$  based on PILS (original design) intercomparisons with filter samples obtained during four selected ground-based and airborne studies. For the

range of particle surface temperatures examined (25–130°C),  $\text{NH}_4^+$  is the most volatile, followed by  $\text{Cl}^-$ , and then  $\text{NO}_3^-$  (Figure 2.3). To estimate the volatilization of these three species during PILS operation, we calculate the quantity of particle-phase  $\text{NH}_4^+$ ,  $\text{Cl}^-$ , and  $\text{NO}_3^-$  that will be converted to the gas phase in the condensation chamber. It is assumed that before the sampled aerosol reaches the condensation chamber, the denuders remove all of the gas-phase species ( $\text{NH}_3$ ,  $\text{HCl}$ ,  $\text{HNO}_3$ ). The general assumption is made for the equilibria represented in Figure 2.3 that ambient volatile species are in equilibrium between the gas and particle phase, which has been argued to be especially valid for sub-micrometer particles (Pilinis and Seinfeld, 1987; Zhang et al., 2002); however, this assumption has been shown not to hold under all ambient conditions (Hildemann et al., 1984; Quinn et al., 1992; Parmar et al., 2001; Trebs et al., 2005).

After the condensation chamber and the droplet impactor, the liquid sample travels through the debubbler, syringes, and 0.5 mm ID PEEK tubing prior to reaching the dispensing needle. Although no aerosol mass is expected to be lost in these final flow components, mixing occurs in the debubbler and syringes. It is assumed that each liquid parcel drawn into a mixing vessel immediately mixes with the bulk liquid volume and that the mass concentration of the effluent is equal to the uniform concentration inside the vessel.

#### **2.4.2 Model Predictions**

Since the PILS operates with an upstream impactor to remove super-micrometer particles, we examine theoretical losses for sub-micrometer particles in the plumbing up to the condensation chamber (Figure 2.4). Losses are predicted to decrease from 2.21 to

0.42% for particles with diameters ranging from 0.01 to 0.08  $\mu\text{m}$ , respectively. Losses subsequently increase from 0.42 to 8.58% for diameters increasing from 0.08 to 1.0  $\mu\text{m}$ , respectively. Diffusional losses dominate the total losses for the smaller particle range, ranging from 95 to 57% of the total losses, whereas inertial deposition dominates for the larger particle range, ranging from 43 to 98% of the total losses. Inertial deposition at bends, of which 12 are present in this modified PILS design, dominate the inertial losses.

Losses in the condensation chamber are predicted as a function of particle size entering the chamber (Figure 2.5). As the steam temperature increases, the supersaturation increases, resulting in larger final droplet diameters in the condensation chamber. The final droplet size is more sensitive to the supersaturation ratio achieved by having higher tip temperatures than to the initial particle size entering the condensation chamber. The value of the water condensation mass accommodation coefficient ( $\alpha$ ) is shown to have a significant impact on the predicted final size of the droplets; as this value increases, water vapor is more effectively scavenged during condensational growth. There is considerable scatter in experimental measurements for this parameter; values ranging from 0.04 to 1 are applied in current cloud model studies (Kreidenweis et al., 2003). Weber et al. (2001) report that particles in the condenser reach final diameters of nominally 2 to 3  $\mu\text{m}$ , while Orsini et al. (2003) measured a typical droplet size distribution from sampling room air and observed the range of droplet diameters to be between 1 and 5  $\mu\text{m}$  (with the majority of the droplets between 2 and 3  $\mu\text{m}$ ). Sullivan et al. (2004) report that droplet diameters within the PILS can reach up to between 3 and 5  $\mu\text{m}$ , which is consistent with previous studies. The droplet diameters reported in the three aforementioned studies, the two most recent of which used the same steam



condensation chamber as our PILS, are consistent with model predictions assuming an accommodation coefficient between 0.01 and 0.05 and a tip temperature of 100°C (Figure 2.5a).

Losses during the droplet growth stage are dominated by gravitational settling and inertial deposition in the main body of the condensation chamber and in the conical section at the end of the chamber (these regions are defined in Figure 2.2). The losses exceed 1 and 10% when droplets reach sizes of 3 and 8  $\mu\text{m}$ , respectively (Figure 2.5a). Figure 2.5b shows that losses in the conical section exceed those in the main body when droplets grow larger than 2  $\mu\text{m}$ . These results emphasize the importance of keeping the PILS tip temperature close to 100°C to minimize the growth of larger droplets that are more effectively lost by deposition prior to reaching the droplet impactor.

Calculations indicate that volatilization effects are most sensitive to temperature and the acidity of the sampled particles. Figure 2.6 shows the amount of  $\text{NH}_4^+$  expected to remain in the particle phase at the end of the condensation chamber as a function of temperature and acidity. Ammonium is the sole ion vulnerable to volatilization over the span of temperatures, acidity, and dilution factors shown, whereas  $\text{Cl}^-$  and  $\text{NO}_3^-$  losses are predicted to be less than 1%. Ammonium losses are higher as the temperature increases and as the droplet acidity decreases.

## **2.5 PILS-IC Detection Levels**

### **2.5.1 Ion Chromatography (IC) System**

The technique of choice for analyzing the liquid sample is IC. Two Dionex ICS-2000 systems (25  $\mu\text{L}$  sample loops) are used for performing off-line quantitative

speciated inorganic and organic analysis. A Dionex AS-40 Autosampler feeds samples, which are in 0.5 mL vials with filter-caps, to the anion system (AS-11 column 2 x 250 mm, ASRS Ultra II 2-mm suppressor, potassium hydroxide eluent) first, which is equipped with a de-gas unit to rid the injected sample of any air bubbles that can amplify baseline noise. The anion unit has a 6-port injection valve that splits off part of the sample to the cation system (CS12A column 2 x 250 mm, CSRS Ultra II 2-mm suppressor, methanesulfonic acid eluent).

### 2.5.2 PILS-IC Technique Background Levels

The additional steps required in the off-line analysis of samples in this design require background-level testing to check for contamination; sources of contamination include the Milli-Q water used in the wash-flow, plumbing in the PILS, the PILS and IC vials, including sample transfer between them, and the IC system itself. The background levels of individual species concentrations for analyzed filter samples ( $n > 300$ ), presented as the average concentration plus three times the standard deviation ( $\sigma$ ), are between 0.02 and 0.28  $\mu\text{g m}^{-3}$  (Table 2.2). It should be noted that the contribution from the IC alone to these background levels (calculated as the average concentration plus three times  $\sigma$  of the smallest detectable peak for each ion in the IC baseline noise and then converted to air-equivalent units) is less than 0.05  $\mu\text{g m}^{-3}$  for all major inorganic ions ( $\text{NH}_4^+$ ,  $\text{K}^+$ ,  $\text{Mg}^{2+}$ ,  $\text{SO}_4^{2-}$ ,  $\text{Cl}^-$ ,  $\text{NO}_2^-$ ,  $\text{NO}_3^-$ ) except  $\text{Na}^+$  and  $\text{Ca}^{2+}$ , which have IC background levels of 0.10  $\mu\text{g m}^{-3}$ . To minimize background levels, the droplet impactor plate must be continuously cleaned (between each use of the system), the denuders

should be frequently recoated, and the plumbing between the droplet impactor and dispensing needle should be periodically replaced.

Tests were performed to examine if any sinks or sources exist for different species ( $\text{NH}_4^+$ ,  $\text{SO}_4^{2-}$ , or  $\text{NO}_3^-$ ) in the plumbing between the impactor plate and the dispensing needle. A wash-flow solution with known concentrations of either  $(\text{NH}_4)_2\text{SO}_4$  or  $\text{NH}_4\text{NO}_3$  in water was used in place of the standard Milli-Q water solution spiked with LiBr or LiF. For each solution, several vials were collected while no steam was being generated (no droplets made) followed by steam generation. The tip temperature was controlled between  $100 \pm 2^\circ\text{C}$  during steam production. This test would also reveal if heating of the impactor plate due to deposition of warm droplets and convective heating leads to volatility losses for any of the species in the wash-flow solutions. The collection efficiency in these tests is defined as the ratio of ion concentrations in liquid collected into vials to those in the wash-flow stock solution. The results in Table 2.3 show that neither  $\text{NH}_4^+$ ,  $\text{SO}_4^{2-}$ , or  $\text{NO}_3^-$  is preferentially lost on the impactor plate, within the debubbler and syringes, or in the liquid lines before steam production, as the collection efficiency of each ion is approximately unity. During steam generation, volatility losses from the heated impactor plate are negligible since the molar ratios are within the measurement uncertainty (one  $\sigma$ ) of the expected values of two and one for  $(\text{NH}_4)_2\text{SO}_4$  and  $\text{NH}_4\text{NO}_3$ , respectively. However, the one hour duration of these tests leaves open the possibility that higher tip temperatures and longer periods of heating may lead to increased volatilization losses due to heating of the impactor plate.

## 2.6 Evaluation of Model With Laboratory Data

Figure 2.7 compares observed and model-predicted normalized mass concentrations from tests in which the PILS was cycled between sample and filter mode, thereby inducing a step change in mass concentration in the sampled air. The sampled particles were composed of  $\text{Na}_2\text{SO}_4$  with a unimodal size distribution (number concentration mode at 70 nm with a geometric  $\sigma$  of 1.6). Losses due to volatility were not expected since  $\text{SO}_4^{2-}$  and  $\text{Na}^+$  represent relatively non-volatile species. The forward model simulated the operation of the modified PILS for 50 and 250  $\mu\text{L}$  syringes, in addition to the original PILS, which does not employ syringes. For a specific debubbler residence time, the predicted time delay between when a step change is made and when the modified PILS reaches stable concentrations (defined as less than a 1% change by mass between two successive vials) varies according to the syringe round-trip time; for a debubbler residence time of 66 s, the minimum time delays for 50 and 250  $\mu\text{L}$  syringes are predicted to be 304 and 313 s, respectively (Table 2.4). Variations in the minimum time delays predicted are seen for single simulations considering successive step changes due to the position of the two syringes when one of them draws in the first liquid parcel following the step change in concentration; variations ranged between 10 and 60 s for simulations with the 50 and 250  $\mu\text{L}$  syringes, respectively. Data and predictions indicate that it usually takes two “transition vials” (at 5 min each with a debubbler residence time of 66 s) using 50 and 250  $\mu\text{L}$  syringes, during which the concentration gradually increases or decreases depending on the direction of the step change, before stable mass concentrations are reached (Figure 2.7); however, predictions and observations occasionally show that only one transition vial is needed for 50  $\mu\text{L}$  syringes. The

minimum time delay for the original PILS, assuming the same characteristic residence time in the debubbler, is predicted to be 301 s (Table 2.4). The minimum time delays predicted for the original and modified PILS designs are within 12 s of each other, indicating that mixing in the debubbler has a dominant effect on the time response of each design to a step change in concentration. Thus, the addition of syringes in the liquid flow path of the modified design does not significantly increase the minimum time response to concentration changes; however, the syringes have a broadening effect on the range of the time delay during each successive step change in concentration. To decrease the time response, the residence time needs to be minimized in the mixing vessels. Table 2.4 shows that as the debubbler mixing volume is reduced, resulting in lower residence times, the minimum time response also drops substantially. Figure 2.7 also shows modified PILS observations and predictions from a step change test where 1-min vials were collected and the debubbler residence time was reduced to 15 s (using 50  $\mu\text{L}$  syringes with a 15 s round-trip time); one or two 1-min vials are needed prior to stabilization with good agreement between observations and predictions. Predictions for the original PILS show that for an assumed 1-min duty cycle time for an on-line analytical detector and a debubbler residence time of 15 s, one transition vial is needed prior to stabilization during step changes.

After a step increase in concentration, the normalized PILS levels observed indicate that mass losses are less than 1%. This is consistent with mass losses predicted by the forward model for droplet diameters up to 3  $\mu\text{m}$ . Mass losses of less than 3.5% are predicted for droplets with diameters between 3 and 5  $\mu\text{m}$ . Orsini et al. (2003) report that the overall collection efficiency for operation at 15  $\text{L min}^{-1}$  is better than 95% for

particles with diameters between 0.03 and 6.0  $\mu\text{m}$ , which is consistent with our model predictions.

The experimental PILS mass measurements from the step change tests are now used as inputs to the inversion model to back-calculate the time-adjusted mass concentrations of the sampled aerosol (predicted mass measurements from the forward model are used as the input for the original PILS). The goal of the inverse model is to accurately predict the maximum and minimum concentrations attained during the step changes and to minimize the transition time during step changes by effectively deconvoluting mixing effects. The results of the inverse model are reported either as 1 or 4-min scans, where these times represent a broad range of representative DMA scanning times. This allows model predictions to be compared to DMA mass concentrations for experiments where the aerosol density is known. For 50 and 250  $\mu\text{L}$  syringes (assuming a debubbler residence time of 66 s), between two and four 4-min transition scans are needed before the PILS-measured concentrations stabilize and match the step function concentration change. Fewer scans are usually needed prior to stabilization for the 50  $\mu\text{L}$  syringes compared to 250  $\mu\text{L}$  syringes because fewer experimental transition vials are considered, and the mixing time is significantly shorter in the 50  $\mu\text{L}$  syringes (46 s round-trip versus 230 s for 50 and 250  $\mu\text{L}$  syringes, respectively). For the modified PILS test with 1-min vials and the shorter debubbler residence time (15 s), predictions showed that two or three 1-min scans are needed prior to stabilization. It is predicted that only one 1-min scan is needed for the original PILS to reach stable concentrations with a 15 s debubbler residence time and a 1-min duty cycle time. After the period of transition, the

model accurately predicts the minimum and maximum concentrations associated with the step changes to within 1% for both the modified and original PILS.

### **2.6.1 PILS Collection Efficiency for Different Aerosol Seeds**

To determine the PILS collection efficiency for aerosols of different composition and to compare the model with experimental results, the modified PILS sampled a variety of laboratory aerosols in parallel with a DMA. The aerosols studied include  $(\text{NH}_4)_2\text{SO}_4$ ,  $\text{NH}_4\text{NO}_3$ ,  $\text{NaCl}$ ,  $\text{Na}_2\text{SO}_4$ ,  $\text{K}_2\text{SO}_4$ , and  $\text{KNO}_3$ . A constant rate atomizer generated particles that were dried before reaching two  $^{210}\text{Po}$  neutralizers and then injected into a 28 m<sup>3</sup> teflon chamber. A source of constant concentration aerosol allowed for direct comparison between the PILS, DMA, and model predictions. The relative humidity (RH) inside the chamber was maintained at less than 6% and the temperature was kept at 20°C (Vaisala HMP230 series transmitters). The PILS tip temperature was maintained at 100 ± 2°C for these tests. Complete number distributions (10-800 nm) were provided with 4-min frequency by a cylindrical scanning electrical mobility spectrometer, connected to a TSI model 3760 condensation nuclei counter. On average, the size distribution of the atomized seed aerosol particles was unimodal, with a number concentration mode centered between 70 and 100 nm and a geometric  $\sigma$  between 1.5 and 1.7. Using appropriate corrections for particle charging, DMA transfer function, and other scanning voltage correction factors, data from the DMA can be used to calculate a total aerosol volume concentration in the aerosol flow. Because the RH was less than 6% for all tests, the pure seed aerosol densities could be used to convert from volume to mass concentration. The DMA-derived masses were used to determine the relative

contributions of cations and anions present based on the measured anion-to-cation ratios in the atomized solutions. The aerosols listed above were used to study the volatilization effects for  $\text{NH}_4^+$ ,  $\text{Cl}^-$ , and  $\text{NO}_3^-$ . The collection efficiency of two of the aerosols tested,  $(\text{NH}_4)_2\text{SO}_4$  and  $\text{Na}_2\text{SO}_4$ , were also measured by Ma (2004) in a laboratory setting using a similar approach with the original PILS.

The collection efficiency of the PILS compared to the DMA and the molar ratios measured in the PILS vials, as total averages, are shown in Tables 2.5 and 2.6, respectively. The total aerosol mass loadings for these tests ranged between 1 and  $140 \mu\text{g m}^{-3}$ , with no significant variation in the collection efficiency as a function of mass loading for all ions studied. The PILS measurements are within 4% of the DMA-derived mass concentrations for  $\text{K}^+$ ,  $\text{Na}^+$ ,  $\text{SO}_4^{2-}$ ,  $\text{Cl}^-$ , and  $\text{NO}_3^-$ . The collection efficiency of  $\text{NH}_4^+$ , however, is approximately 88% for the two ammonium-containing aerosols studied. The measured molar ratios are near the expected values for each seed aerosol tested, with the exception of ammonium-containing aerosols, where the ratio is lower than expected, confirming that  $\text{NH}_4^+$  is vulnerable to volatilization loss within the PILS system. Measured collection efficiencies of  $\text{Cl}^-$  and  $\text{NO}_3^-$  were on the order of 96 to 97%, suggesting that they are less susceptible to volatilization losses as compared to  $\text{NH}_4^+$ . These results are consistent with thermodynamic data shown earlier (Figure 2.3), indicating that over the temperature span of PILS operation,  $\text{NH}_4^+$  is the ion most susceptible to volatilization.

Ma (2004) reports that when  $(\text{NH}_4)_2\text{SO}_4$  was generated and sampled by a PILS in laboratory tests, the mean  $\text{NH}_4^+:\text{SO}_4^{2-}$  molar ratio showed that  $\text{NH}_4^+$  was undermeasured by approximately  $10 \pm 10\%$ . When  $\text{Na}_2\text{SO}_4$ , a relatively non-volatile compound, was



tested, the mean  $\text{Na}^+:\text{SO}_4^{2-}$  ratio was  $2.03 \pm 0.06$ . A comparison of the results from these two tests provides further evidence that  $\text{NH}_4^+$  volatilization occurs in the PILS. Furthermore, the observed molar ratios from the  $\text{Na}_2\text{SO}_4$  and  $(\text{NH}_4)_2\text{SO}_4$  laboratory tests show agreement between this study and that of Ma (2004).

Theoretical calculations for  $\text{NH}_4^+$  losses in the PILS in Figure 2.6 show consistency with the experimental observations. Ma (2004) showed that the pH for PILS-collected liquid with dissolved particle sample can be 5.6, which is consistent with measurements obtained with the current PILS. Assuming a pH of 5.6 as an average for droplets composed of ammonium-containing aerosol particles, calculations predict that 5 to 15% and 7 to 20% of the total  $\text{NH}_4^+$  is lost by volatilization for particle surface temperatures between 30 and 40°C, respectively, for a range of dilution factors between 1.1 and 1.4 (this range is representative of field and laboratory test conditions). These two particle surface temperatures represent a range of values predicted by the PILS model for the operating conditions in these tests. Therefore, the bars shown in Figure 2.6 should be used as a range for the predicted  $\text{NH}_4^+$  loss. The experimentally determined 12% loss of  $\text{NH}_4^+$  is in the range of the predicted values for the expected operating conditions in the condensation chamber.

### 2.6.2 Tip Temperature Sensitivity Tests

Several tests were performed to determine the influence of the tip temperature on the sampling efficiency of aerosols composed of  $(\text{NH}_4)_2\text{SO}_4$ ,  $\text{NH}_4\text{NO}_3$ ,  $\text{NaCl}$ ,  $\text{Na}_2\text{SO}_4$ ,  $\text{K}_2\text{SO}_4$ , and  $\text{KNO}_3$ . Vials were collected while the tip temperature was maintained at  $100 \pm 2^\circ\text{C}$ . The tip temperature was then allowed to increase to between 120 and 150°C for at

least 20 min before decreasing and restabilizing at  $100 \pm 2^\circ\text{C}$ , during which time vials were continuously being collected.

Figure 2.8 shows results from a representative test performed using  $(\text{NH}_4)_2\text{SO}_4$  aerosol. Prior to the intense heating, the collection efficiency of  $\text{NH}_4^+$  and  $\text{SO}_4^{2-}$  are 90 and 100%, respectively. When the tip temperature was increased to  $147^\circ\text{C}$ , the collection efficiency for both species dropped to between 30 and 35% before returning to their original values when the tip temperature was reduced to  $100^\circ\text{C}$ . During the period after the tip returned to  $100 \pm 2^\circ\text{C}$ ,  $\text{NH}_4^+$  initially exhibited a collection efficiency between 86 and 91% (between 0 and 35 min after the tip returned to  $100 \pm 2^\circ\text{C}$ ), but stabilized at 91% for the last two vials collected 70 and 75 min after the tip returned to  $100 \pm 2^\circ\text{C}$ . The collection efficiency of  $\text{SO}_4^{2-}$  was consistently between 98 and 101% after the intense heating. The increased sensitivity of  $\text{NH}_4^+$  to the intense heating immediately after the tip temperature was lowered to  $100 \pm 2^\circ\text{C}$  is due to the heated condensation chamber and impactor plate, leading to additional volatilization losses before the temperature decreased. The general response of  $\text{NH}_4^+$  to the excessive heating shown in Figure 2.8 is consistent with that observed for the other five aerosols listed above.

These results show that as the tip temperature is increased, particles grow to a sufficiently large size that deposition results in substantial droplet losses in the condensation chamber, specifically in the conical reduction region leading to the impactor jet. The initial decrease in species concentrations may, to a lesser extent, be partly associated with increased condensation of water vapor onto the droplet impactor and resultant dilution, since the temperature difference between the impactor plate and the mixed flow of steam and air is higher just after the tip temperature increases. During

the intense heating, the increased deposition losses explain the observed decreases in collection efficiency of non-volatile species such as  $\text{Na}^+$ ,  $\text{K}^+$ , and  $\text{SO}_4^{2-}$ . Also, intense heating in the condensation chamber was shown to lead to additional volatilization losses for  $\text{NH}_4^+$  (exceeding those shown in Table 2.5) even when the tip temperature was allowed to return to normal operating values, since the chamber and the impactor plate remained at elevated temperatures over one hour after the intense heating tests were completed. These results emphasize the importance of maintaining the tip temperature at  $100^\circ\text{C}$  to minimize volatilization and deposition in the condensation chamber.

The PILS model developed here underestimates losses in the condensation chamber if deposition is primarily responsible for increased losses during the intense heating periods. The model predicts collection efficiencies of 84 and 66% for droplet diameters of 10 and 15  $\mu\text{m}$ , respectively. The droplet diameters predicted for tip temperatures ranging from  $93$  to  $150^\circ\text{C}$  in Figure 2.5b are all less than 6  $\mu\text{m}$ , assuming an accommodation coefficient of 0.01. Larger droplet sizes would be predicted with larger values of the accommodation coefficient, yielding better agreement between measurements and predictions for particle losses; droplets are predicted to grow to 11  $\mu\text{m}$  at a tip temperature of  $150^\circ\text{C}$  and assuming an accommodation coefficient of 1. If the accommodation coefficient has a temperature dependence, this could explain both the increased droplet growth at higher tip temperatures and the significant droplet losses predicted. The equations used to predict droplet losses in the PILS, particularly the conical reduction section, are likely underpredicting the losses for the larger droplets.

## 2.7 Field Data

A modified PILS has been successfully deployed in two field missions and the reader is referred to Sorooshian et al. (2006) for an in-depth analysis of data collected during the 2004 ICARTT field campaign. Flight tracks and data from one flight during ICARTT are shown in Figure 2.9 where the Center for Interdisciplinary Remotely-Piloted Aircraft Studies (CIRPAS) Twin Otter research aircraft flew transect legs downwind of the Conesville Power Plant (Coshocton County, Ohio) in clouds. There was significant  $\text{SO}_4^{2-}$  growth with increasing distance downwind of the plant due to conversion of  $\text{SO}_2$  to  $\text{SO}_4^{2-}$ . The ammonium-to-sulfate molar ratio was between 1.1 and 1.6 for most of the flight downwind of the plant, indicating that there was insufficient ammonia to neutralize the relatively high level of sulfuric acid. The high level of acidity can also explain why virtually no  $\text{NO}_3^-$  was detected ( $< 0.3 \mu\text{g}/\text{m}^3$ ). Oxalate and  $\text{SO}_4^{2-}$  are strongly correlated and aqueous-phase precursors to oxalic acid, including glyoxylate, were detected indicating that aqueous-phase processing in cloud led to the elevated levels of oxalate measured during this flight. The results show that the modified PILS design is effective at quantifying ambient mass concentrations of both inorganic and organic acid ions with 5-min time resolution.

## 2.8 Future Work

There are several ways to improve the design of the PILS. The time response of the instrument to concentration changes can be improved by minimizing the liquid residence time in mixing vessels, primarily the debubbler and the syringes (only used in the modified design). With the modified PILS, syringe volumes can be reduced and they

can be driven at higher speeds to minimize both the unpumped liquid volume in the debubbler and the residence time in the syringes. PILS users can correct for volatilization losses with correction factors (error bars) based on experimental results, such as those presented here for  $\text{NH}_4^+$ . The instrument can also be optimized with respect to sampling organic aerosol both in laboratory tests and ambient field studies. Longer IC programs can be used to improve resolution of organic peaks by storing liquid samples in vials for subsequent off-line chemical analysis vs. the limited time for chromatographic separations of the on-line systems (Weber et al., 2001). It should be noted that the original PILS can perform longer IC programs as well, however, this is only practical for ground-based sampling since users must sacrifice time resolution during airborne flights. The PILS can also be coupled to other analytical detectors to quantify organics other than the organic acids that the IC can detect. A new technique described by Sullivan et al. (2004) couples the PILS to a TOC analyzer in order to quantify water-soluble organic carbon (WSOC). Techniques such as this increase the fraction of the total particulate organic mass that the PILS can speciate and quantify.

## **2.9 Conclusions**

This study has introduced a modified PILS, as well as a model of the PILS sampling behavior. The main modification in this PILS is the implementation of syringe pumps to drive the liquid sample flow from the impactor to vials held on a rotating carousel. The instrument's time resolution is not limited by the duty cycle time of any on-line analytical technique, which is advantageous for airborne studies; this allows for a variety of analytical tests to be performed on an individual liquid sample, including

longer IC gradient programs to resolve more organic peaks. This design of the PILS is also well-suited for remote ground-based operation as it requires less monitoring compared to a PILS connected to an analytical instrument.

An instrument model is developed that takes into account mixing effects, plumbing efficiencies, droplet growth, evaporation of semi-volatile species, and the “handshaking” technique of the syringes. When considering multiple step changes in the aerosol sample, the model accurately predicts experimentally measured concentrations in PILS vials. It was shown that for the modified PILS configurations used in this study (50 and 250  $\mu\text{L}$  syringes with a debubbler residence time of 66 s) that one or two 5-min transition vials are needed before stable concentrations ( $\pm 1\%$  by mass) are reached in successive vials. However, when the debubbler residence time is reduced to 15 s and 1-min vials are collected using 50  $\mu\text{L}$  syringes, only one transition vial is needed. The minimum predicted time delay prior to reaching stabilization after a step change is between 301 and 313 s for two modified PILS configurations and the original PILS (assuming a debubbler residence time of 66 s), suggesting that mixing in the debubbler is mainly responsible for the time delay. An inverse model is also developed to back-calculate the actual time-history of aerosol concentrations entering the PILS based on the measured concentrations. The predictions show intermediate agreement with experimental data from the modified PILS, with the main issue being that the model cannot completely deconvolute the mixing effects within the PILS during the transition between step changes. However, after the transition period in the forward and inversion models, predictions and experimental data for the aerosol mass concentrations agree within 1%.

Results from laboratory characterization tests of the sampling efficiency and volatilization losses within the PILS have been compared to model predictions and good agreement has been found. Characterization tests show that the average modified PILS mass collection efficiency, as compared to the DMA-derived mass for a variety of aerosols exceeds 96% with the exception of  $\text{NH}_4^+$ , which exhibits a collection efficiency of 88% ( $n = 369$ ) for  $(\text{NH}_4)_2\text{SO}_4$  and  $\text{NH}_4\text{NO}_3$ . Results from similar tests conducted with an original PILS for  $(\text{NH}_4)_2\text{SO}_4$  and  $\text{Na}_2\text{SO}_4$  aerosols agree with those observed with the modified PILS. When considering the operating conditions in the condensation chamber, it is predicted that between 5 and 20% of the particle-phase  $\text{NH}_4^+$  is converted to gas-phase  $\text{NH}_3$ , which is consistent with experimental results. The temperature at the point where steam and the aerosol sample mix is an important parameter that must be properly controlled to prevent significant particle losses. If the tip temperature is too high, the increase in supersaturation produces larger droplets that are more effectively lost by deposition in the condensation chamber. Volatilization losses of  $\text{NH}_4^+$  are also increased under high tip temperature conditions. Data from 369 samples of laboratory-generated  $(\text{NH}_4)_2\text{SO}_4$  at different mass loadings suggest that PILS users should apply a correction factor of 1.14 ( $1/0.88$ ) to their  $\text{NH}_4^+$  results to account for volatility losses (when the tip is in the operating range of  $100 \pm 2^\circ\text{C}$ ). However, this factor should be used with caution since  $\text{NH}_4^+$  volatilization is theoretically shown to be sensitive to droplet pH and ambient samples do not necessarily behave like laboratory-generated  $(\text{NH}_4)_2\text{SO}_4$  samples. Field data from ICARTT 2004 show that the modified PILS is successful at quantifying ambient concentrations of inorganic and organic acid ions with 5-min time resolution.

## 2.10 Acknowledgements

This work was supported by the National Science Foundation grant ATM-0340832 and the Office of Naval Research.

## 2.11 References

- Buhr, S. M., Buhr, M. P., Fehsenfeld, F. C., Holloway, J. S., Karst, U., Norton, R. B., Parrish, D. D., and Sievers, R. E. (1995). Development of a Semicontinuous Method for the Measurement of Nitric-Acid Vapor and Particulate Nitrate and Sulfate, *Atmos. Environ.*, 29(19): 2609-2624.
- Crane, R. L., and Evans, R. L. (1977). Inertial Deposition of Particles in a Bent Pipe, *J. Aerosol Sci.*, 8: 161-170.
- Fuchs, N. A. (1964). *The Mechanics of Aerosols*, Pergamon, Oxford.
- Gormley, P. G., and Kennedy, M. (1949). Diffusion from a Stream Flowing Through a Cylindrical Tube. *Proc. R. Irish Acad.*, 52A: 163-169.
- Hameri, K., Laaksonen, A., Vakeva, M., and Suni, T. (2001). Hygroscopic Growth of Ultrafine Sodium Chloride Particles, *J. Geophys. Res.*, 106(D18): 20749-20757.
- Hangal, S., and Willeke, K. (1990). Overall Efficiency of Tubular Inlets Sampling at 0-90 Degrees from Horizontal Aerosol Flows, *Atmos. Environ.*, 24A: 2379-2386.
- Hildemann, L. M., Russell, A. G., and Cass, G. R. (1984). Ammonia and Nitric-Acid Concentrations in Equilibrium with Atmospheric Aerosols - Experiment Vs Theory, *Atmos. Environ.*, 18(9): 1737-1750.
- Kreidenweis, S. M., Walcek, C. J., Feingold, G., Gong, W., Jacobson, M. Z., Kim, C.-H., Liu, X., Penner, J. E., Nenes, A., and Seinfeld, J. H. (2003). Modification of Aerosol Mass and Size Distribution due to Aqueous-phase SO<sub>2</sub> Oxidation in Clouds: Comparison of Several Models, *J. Geophys. Res.*, 108 (D7), 4213, doi:10.1029/2002JD002697.
- Ma, Y. (2004). *Developments and Improvements to the Particle-Into-Liquid Sampler (PILS) and its Application to Asian Outflow Studies*, Ph.D. Dissertation, Georgia Institute of Technology, Atlanta, GA.
- Muyshondt, A., McFarland, A. R., and Anand, N. K. (1996). Deposition of Aerosol Particles in Contraction Fittings, *Aerosol Sci. Technol.*, 24: 205-216.



- Orsini, D. A., Ma, Y., Sullivan, A., Sierau, B., Baumann, K., and Weber, R. J. (2003). Refinements to the Particle-Into-Liquid Sampler (PILS) for Ground and Airborne Measurements of Water Soluble Aerosol Composition, *Atmos. Environ.*, 37: 1243-1259.
- Parmar, R. S., Satsangi, G. S., Lakhani, A., Srivastava, S. S., and Prakash, S. (2001). Simultaneous Measurements of Ammonia and Nitric Acid in Ambient Air at Agra (27 degrees 10' N and 78 degrees 05' E) (India), *Atmos. Environ.*, 35(34): 5979-5988.
- Pilinis, C., and Seinfeld, J. H. (1987). Continued Development of a General Equilibrium-Model for Inorganic Multicomponent Atmospheric Aerosols, *Atmos. Environ.*, 21: 2453-2466.
- Pui, D. Y. H, Romay-Novas, F., and Liu, B. Y. H. (1987). Experimental Study of Particle Deposition in Bends of Circular Cross Section, *Aerosol Sci. Technol.*, 7: 301-315.
- Quinn, P. K., Asher, W. E., and Charlson, R. J. (1992). Equilibria of the Marine Multiphase Ammonia System, *J. Atmos. Chem.*, 14(1-4): 11-30.
- Schwendiman, L. C., Stegen, G. E., and Glissmeyer, J. A. (1975). *Report BNWL-SA-5138*, Battelle Pacific Northwest Laboratory, Richland, Washington.
- Seinfeld, J. H., and Pandis, S. N. (1998). *Atmospheric Chemistry and Physics*, Wiley-Interscience, New York.
- Simon, P. K. and Dasgupta, P. K. (1995). Continuous Automated Measurement of the Soluble Fraction of Atmospheric Particulate Matter, *Anal Chem.*, 67(1): 71-78.
- Slanina, J., ten Brink, H. M., Otjes, R. P., Even, A., Jongejan, P., Khlystov, A., Waijers-Ijpelaar, A., and Hu, M. (2001). The Continuous Analysis of Nitrate and Ammonium in Aerosols by the Steam Jet Aerosol Collector (SJAC): Extension and Validation of the Methodology, *Atmos. Environ.*, 35(13): 2319-2330.
- Sorooshian, A., Varutbangkul, V., Brechtel, F. J., Ervens, B., Feingold, G., Bahreini, R., Murphy, S. M., Holloway, J. S., Atlas, E. L., Buzorius, G., Jonsson, H., Flagan, R. C., and Seinfeld, J. H. (2006). Oxalic Acid in Clear and Cloudy Atmospheres: Analysis of Data from ICARTT 2004, *J. Geophys. Res.*, 111, D23S45, doi:10.1029/2005JD006880.
- Stolzenburg, M. R. and Hering, S. V. (2000). Method for the Automated Measurement of Fine Particle Nitrate in the Atmosphere, *Environ. Sci. Technol.*, 34(5): 907-914.
- Sullivan, A. P., Weber, R. J., Clements, A. L., Turner, J. R., Bae, M. S., and Schauer, J. J. (2004). A Method for On-Line Measurement of Water-Soluble Organic Carbon in Ambient Aerosol Particles: Results from an Urban Site, *Geophys. Res. Lett.*, 31:L13105.
- Thomas, J. W. (1958). *J. Air Pollut. Control Assoc.*, 8:32.

Trebs, I., Metzger, S., Meixner, F. X., Helas, G. N., Hoffer, A., Rudich, Y., Falkovich, A. H., Moura, M. A. L., da Silva, R. S., Artaxo, P., Slanina, J., and Andreae, M. O. (2005). The  $\text{NH}_4^+$ - $\text{NO}_3^-$ -Cl $^-$ - $\text{SO}_4^{2-}$ - $\text{H}_2\text{O}$  Aerosol System and its Gas Phase Precursors at a Pasture Site in the Amazon Basin: How relevant are Mineral Cations and Soluble Organic Acids?, *J. Geophys. Res.*, 110(D7), doi:10.1029/2004JD005478.

Wang, J., McNeill, V. F., Collins, D. R., and Flagan, R. C. (2002). Fast Mixing Condensation Nucleus Counter: Application to Rapid Scanning Differential Mobility Analyzer Measurements, *Aerosol Sci. Technol.*, 36: 678-689.

Weber, R. J., Orsini, D., Daun, Y., Lee, Y. N., Klotz, P. J., and Brechtel, F. J. (2001). A Particle-Into-Liquid Collector for Rapid Measurement of Aerosol Bulk Chemical Composition, *Aerosol Sci. Technol.*, 35:718-727.

Willeke, K., and Baron, P. A. (2001). *Aerosol Measurement: Principles, Techniques, and Applications*, Wiley-Interscience, New York.

Zellweger, C., Ammann, M., Hofer, P., and Baltensperger, U. (1999).  $\text{NO}_y$  Speciation with a Combined Wet Effluent Diffusion Denuder-aerosol Collector Coupled to Ion Chromatography, *Atmos. Environ.*, 33(7): 1131-1140.

Zhang, J., Chameides, W. L., Weber, R. J., Cass, G., Orsini, D., Edgerton, E., Jongejan, P., and Slanina, J. (2002). An Evaluation of the Thermodynamic Equilibrium Assumption for Fine Particulate Composition: Nitrate and Ammonium During the 1999 Atlanta Supersite Experiment, *J. Geophys. Res.*, 108(D7), 8414, doi:10.1029/2001JD001592.

Table 2.1. Equations for Droplet Growth and Transmission Efficiency in Different Stages of the PILS<sup>a</sup>

Notes	Figure 2.2 Label	Equation (with variables defined)	Reference
Transmission Efficiency: Gravitational settling (Laminar)	P1	$\eta_{nbs,grav,lam} = 1 - \frac{2}{\pi} \left[ 2\epsilon \sqrt{1 - \epsilon^{2/3}} - \epsilon^{1/3} \sqrt{1 - \epsilon^{2/3}} + \arcsin(\epsilon^{1/3}) \right],$ $\text{where } \epsilon = \frac{3LV_g}{4dU}, V_g = \frac{D_p^2 \rho_p g C_c}{18\eta}, L = \text{length}, C_c = \text{slip correction factor}, \eta = \text{viscosity}, d = \text{tubing dimension}, \rho_p = \text{particle density}$	Fuchs 1964; Thomas 1958
Transmission Efficiency: Gravitational settling (Turbulent)	P1	$\eta_{nbs,grav,turb} = \exp\left[-\frac{dLV_g}{Q}\right], \text{ where } Q = \text{flow rate}$	Schwendiman et al. 1975
Transmission Efficiency: Diffusion	P2	$\eta_{nbs,diff} = 1 - 2.56 \xi^{2/3} + 1.2\xi + 0.177 \xi^{4/3}, \text{ for } \xi = \frac{\pi DL}{Q} < 0.02,$ $\text{where } D = \text{particle diffusion coefficient}$ $\eta_{nbs,diff} = 0.819 \exp(-3.657 \xi) + 0.097 \exp(-22.3 \xi) + 0.032 \exp(-57 \xi),$ $\text{for } \xi > 0.02$	Gormley and Kennedy 1949
Transmission Efficiency: Turbulent inertial deposition	P3	$\eta_{nbs,turb inert} = \exp\left[-\frac{\pi dLV_t}{Q}\right], \text{ where } V_t = \text{turbulent inertial deposition velocity}$	Willeke and Baron 2001
Transmission Efficiency: Bend deposition (turbulent)	P4	$\eta_{b,nd,turb} = \exp[-2.823 Stk \phi], \text{ where } \phi = \text{bend angle in radians}$	Pui et al. 1987
Transmission Efficiency: Bend deposition (laminar)	P4	$\eta_{b,nd,lam} = 1 - Stk \phi, \text{ where } \phi = \text{bend angle in radians}$	Crane and Evans 1977
Transmission Efficiency: Contraction deposition	P5	$\eta_{c,nd,inert} = 1 - \frac{1}{1 + \left[ \frac{Stk \left[ 1 - \left( \frac{A_o}{A_i} \right) \right]}{3.14 \exp(-0.0185 \phi)} \right]^{-1.24}}, \text{ where } A_o \text{ and } A_i \text{ are the outlet and inlet areas, respectively, } \phi = \text{contraction angle (degrees)}$	Muyshondt et al. 1996
Particles will activate and start growing if they are larger than a critical diameter $D_p^*$	D1	$D_p^* = \frac{4\sigma v_i}{RT \ln S}, \text{ where } \sigma \text{ and } v_i \text{ are the surface tension and molar volume of the condensed liquid, respectively, } S = \text{saturation ratio}$	Seinfeld and Pandis 1998
Particle growth rate in the presence of a supersaturated vapor; effective vapor diffusivity, $D'_v$ , corrects for non-continuum transport conditions and the binary diffusivity of the gas, where $b$ is a correction factor that depends on an accommodation coefficient, $\alpha$ (probability that a water molecule will stick to a particle surface upon contact ( $0 < \alpha < 1$ ))	D2	$\frac{dD_p}{dt} = 2\pi D'_v D'_v (c_{v,ss} - c_{v,s}), \text{ where } D'_v = D_v / \beta, S = p_v / p_{sat},$ $c_{v,ss} = \frac{p_{sat}(T_{\infty})S}{RT}, \text{ and } c_{v,s} = \frac{p_{sat}(T_s)}{RT} \exp\left(\frac{4\sigma v_i}{RTD_p}\right)$	Seinfeld and Pandis 1998
Linearized equation to determine the particle surface temperature (needs to be solved numerically)	D3	$\Delta_T = \frac{\Delta H_v D'_v p_{sat}(T_{\infty})}{k_T T_{\infty}} \times \left[ S - \exp\left(\frac{\Delta H_v \Delta_T}{RT_{\infty}(1 + \Delta_T)} + \frac{4\sigma v_i}{RTD_p}\right) \right],$ $\text{where } \Delta_T = \frac{T_s - T_{\infty}}{T_{\infty}}$	Wang et al. 2002

<sup>a</sup>Laminar and turbulent flow are distinguished by calculating the Reynolds number ( $Re = \rho_g g U d / \eta$ ), where  $\rho_g$ ,  $\eta$ ,  $U$ , and  $d$  are the density and viscosity of the gas, characteristic gas velocity, and tubing dimension, respectively. The transmission efficiency of the two impactors, which are obtained from theoretical impactor efficiency curves, depend on the jet Reynolds number, the ratio of the jet-to-plate distance and the nozzle diameter (values are given in Figure 2.1), and the Stokes number,  $Stk = \rho_p C_c D_p^2 U / 9 \eta W$ , where  $\rho_p$  and  $D_p$

are the particle density and diameter, respectively. The slip correction factor,  $C_c$ , accounts for noncontinuum effects,  $\eta$  is the air viscosity,  $W$  is the nozzle diameter, and  $U$  is the average air velocity at the nozzle exiting point. It is assumed that the droplets that do impact on the second impactor are collected. Hangal and Willeke (1990) argue that there are no inertial transmission losses for sub-isokinetic isoaxial sampling; no losses are assumed to occur in the conical expansion at the beginning of the condensation chamber.

<sup>b</sup>The labels under this column are shown as markers on Figure 2.2 to indicate which equations are applied when modeling specific stages of the PILS. “P” denotes a plumbing transmission efficiency equation and “D” denotes a droplet growth equation.

Table 2.2. Filter Mode Background Levels ( $n > 300$ )

Air-equivalent concentration ( $\mu\text{g m}^{-3}$ )					
	$\text{Na}^+$	$\text{NH}_4^+$	$\text{K}^+$	$\text{Mg}^{2+}$	$\text{Ca}^{2+}$
Average + 3 * $\sigma$	0.11	0.27	0.17	0.19	0.28
	$\text{Cl}^-$	$\text{NO}_2^-$	$\text{NO}_3^-$	$\text{SO}_4^{2-}$	Oxalate
Average + 3 * $\sigma$	0.09	0.10	0.11	0.10	0.02

Table 2.3. Effect of Using  $(\text{NH}_4)_2\text{SO}_4$  and  $\text{NH}_4\text{NO}_3$  Independently as Wash-flow Solutions ( $\text{NH}_4^+$  Collection Efficiency is the Total Average of Both Wash Solution Tests)

Collection efficiency with no steam production			
	$\text{SO}_4^{2-} (n = 25)$	$\text{NH}_4^+ (n = 45)$	$\text{NO}_3^- (n = 20)$
Average	0.99	1.01	0.99
$\sigma$	0.02	0.04	0.02
Before steam production			
	$[\text{NH}_4^+]:[\text{SO}_4^{2-}] (n = 25)$	$[\text{NH}_4^+]:[\text{NO}_3^-] (n = 20)$	
Average	1.97	0.99	
$\sigma$	0.04	0.04	
During steam production			
	$[\text{NH}_4^+]:[\text{SO}_4^{2-}] (n = 39)$	$[\text{NH}_4^+]:[\text{NO}_3^-] (n = 23)$	
Average	1.98	0.98	
$\sigma$	0.03	0.04	

Table 2.4. Minimum Time Response (Defined as the Minimum Time Before Successive Mass Concentrations Vary by Less than 1%) to Step Changes in Concentration for the Original and Modified PILS Designs as a Function of the Debubbler Residence Time

		Minimum Time Response (s)			
		Debubbler Residence Time <sup>a</sup> (s)			
	Syringe Volume (μL)/Round-trip Time (s)	66	50	33	10
Original PILS	NA	301	227	149	43
Modified PILS	50 / 46	304	229	155	45
	250 / 230	313	233	158	48

<sup>a</sup>The debubbler residence time is taken to be the time required to empty it when it is completely filled with liquid during normal operation.

Table 2.5. PILS Collection Efficiency for Anions and Cations Compared to the DMA; a Shape Factor of 1.08 was Applied to the DMA Data for NaCl (Hameri et al. 2001)

Anion Seed aerosol	$\text{SO}_4^{2-}$			$\text{NO}_3^-$		$\text{Cl}^-$
	$(\text{NH}_4)_2\text{SO}_4$ ( $n = 283$ )	$\text{K}_2\text{SO}_4$ ( $n = 11$ )	$\text{Na}_2\text{SO}_4$ ( $n = 19$ )	$\text{NH}_4\text{NO}_3$ ( $n = 86$ )	$\text{KNO}_3$ ( $n = 5$ )	$\text{NaCl}$ ( $n = 16$ )
PILS [x]/DMA [x]	0.99	0.99	0.97	0.97	0.96	0.96
$\sigma$	0.06	0.07	0.05	0.11	0.04	0.04
Cation Seed aerosol	$\text{NH}_4^+$		$\text{Na}^+$		$\text{K}^+$	
	$(\text{NH}_4)_2\text{SO}_4$ ( $n = 283$ )	$\text{NH}_4\text{NO}_3$ ( $n = 86$ )	$\text{NaCl}$ ( $n = 16$ )	$\text{Na}_2\text{SO}_4$ ( $n = 19$ )	$\text{KNO}_3$ ( $n = 5$ )	$\text{K}_2\text{SO}_4$ ( $n = 11$ )
PILS [x]/DMA [x]	0.88	0.88	1.01	0.99	0.99	0.98
$\sigma$	0.08	0.11	0.07	0.06	0.02	0.05



Table 2.6. Molar Ratios for Different Aerosols Tested by the PILS

	$\frac{[\text{NH}_4^+]}{[\text{SO}_4^{2-}]}$ ( $n = 476$ )	$\frac{[\text{NH}_4^+]}{[\text{NO}_3^-]}$ ( $n = 91$ )	$\frac{[\text{Na}^+]}{[\text{Cl}^-]}$ ( $n = 16$ )	$\frac{[\text{Na}^+]}{[\text{SO}_4^{2-}]}$ ( $n = 22$ )	$\frac{[\text{K}^+]}{[\text{SO}_4^{2-}]}$ ( $n = 11$ )	$\frac{[\text{K}^+]}{[\text{NO}_3^-]}$ ( $n = 5$ )
Average	1.82	0.92	1.04	2.02	1.97	1.03
$\sigma$	0.13	0.09	0.07	0.06	0.10	0.04

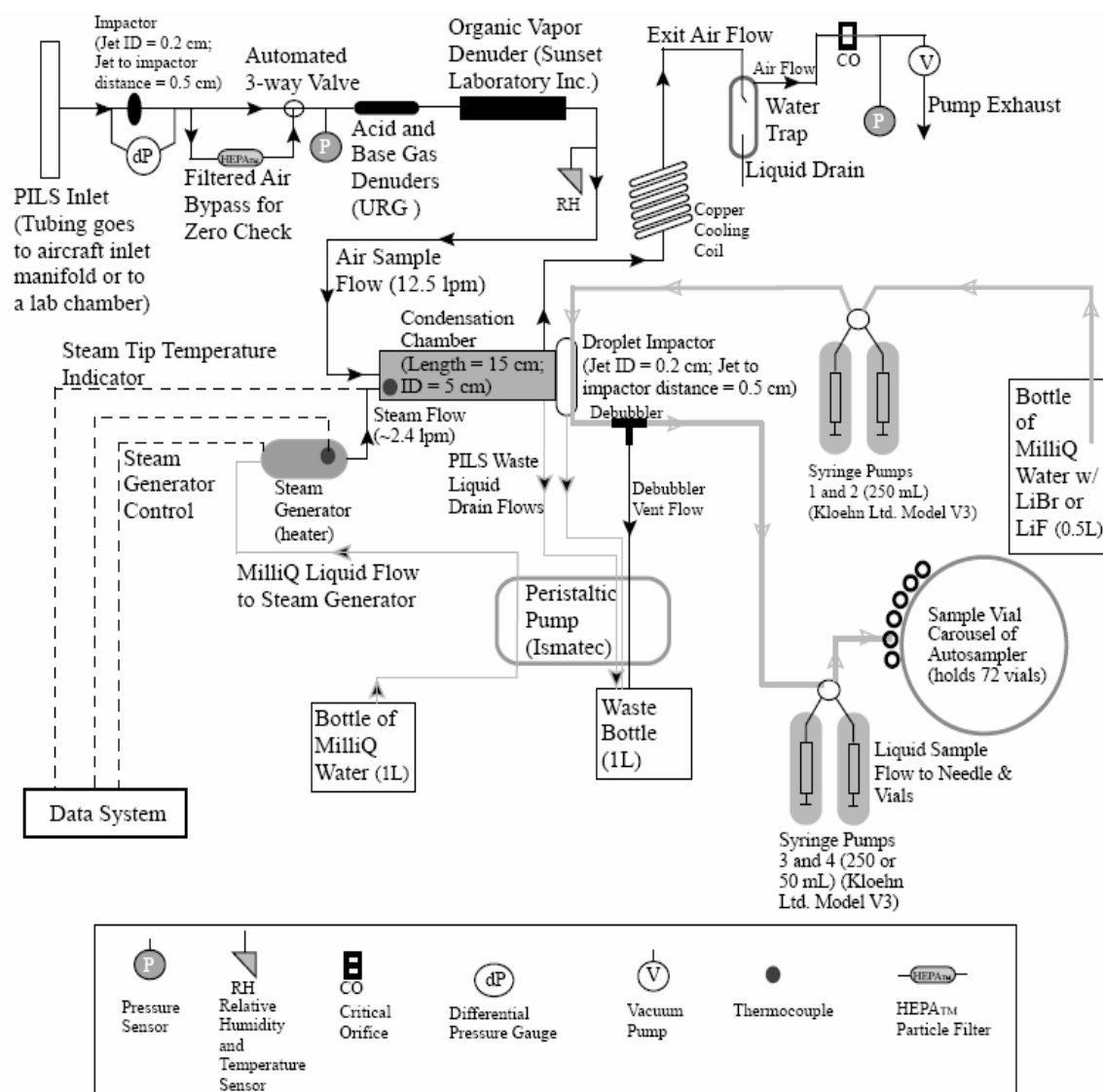


Figure 2.1. Schematic diagram of the modified PILS.

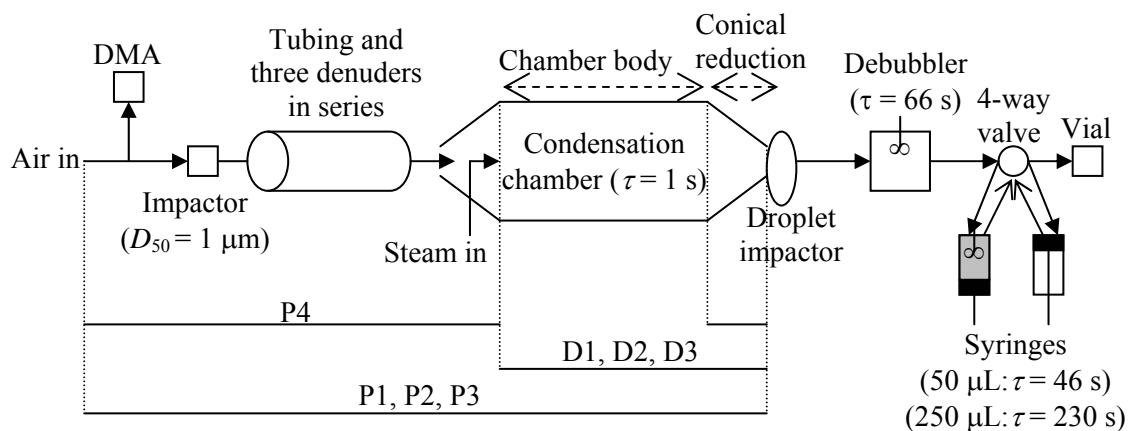


Figure 2.2. Modeled stages of the modified PILS. The “P” and “D” markers indicate which equations from Table 2.1 are applied in the designated stages of the PILS. At any one time, only one of the syringes is dispensing sample to a vial in an upward stroke (the right syringe just finished an upward stroke, and will now begin a downward stroke) while the other aspirates sample from the debubbler in a downward stroke. The value of  $\tau$  reported for the debubbler represents the time required to empty it when it is completely filled with liquid, while  $\tau$  for the syringes represents the cumulative time for a downward and upward stroke. The original PILS sends liquid sample from the debubbler immediately to an analytical detector, such as an IC system, with the liquid driven by a pump downstream of the analytical device.

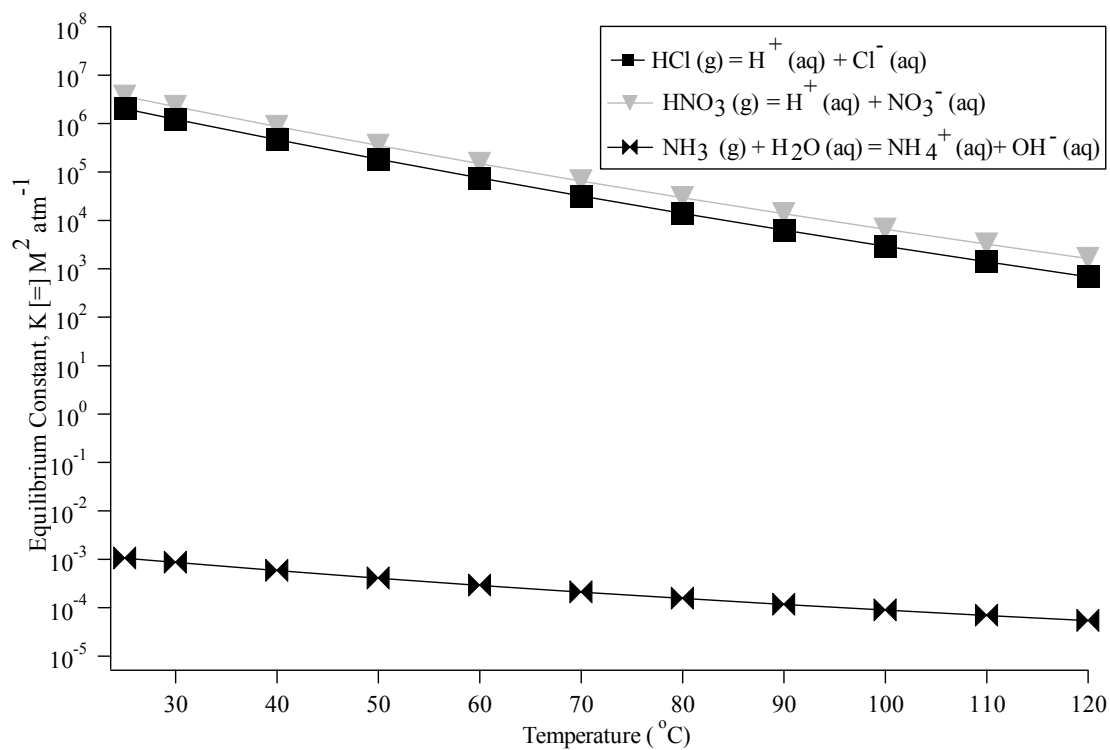
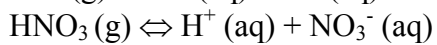
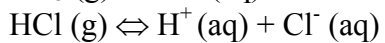
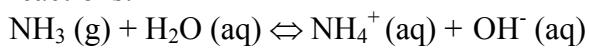


Figure 2.3. Temperature dependence of the equilibrium constants for these three reactions:



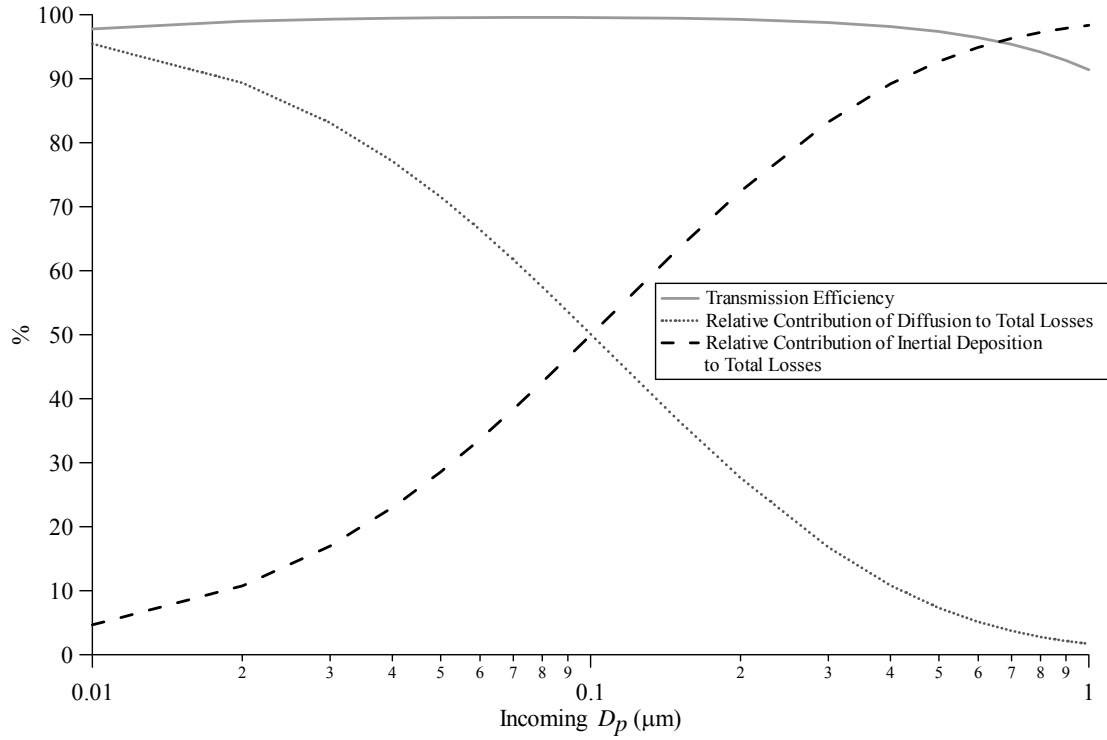


Figure 2.4. Transmission efficiency in the PILS as a function of particle diameter for all plumbing prior to droplet growth in the condensation chamber, and the relative contribution of diffusion and inertial deposition to the total losses.

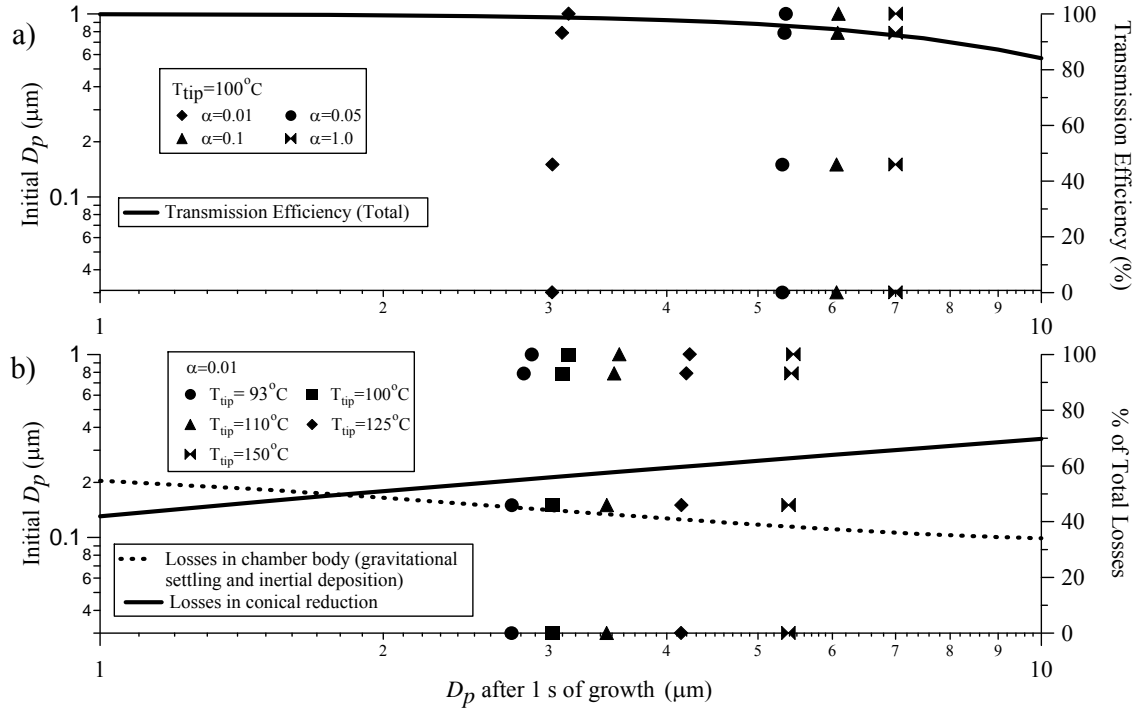


Figure 2.5. Final droplet diameters after growth in the condensation chamber ( $\tau = 1$  s) as a function of the initial particle diameters for different (a) accommodation coefficients (b) and tip temperatures. The (a) total transmission efficiency in the chamber is shown in addition to the (b) relative contribution of different parts of the chamber to the total losses. The final droplet size is more sensitive to both the tip temperature and accommodation coefficient compared to the initial particle size entering the condensation chamber.

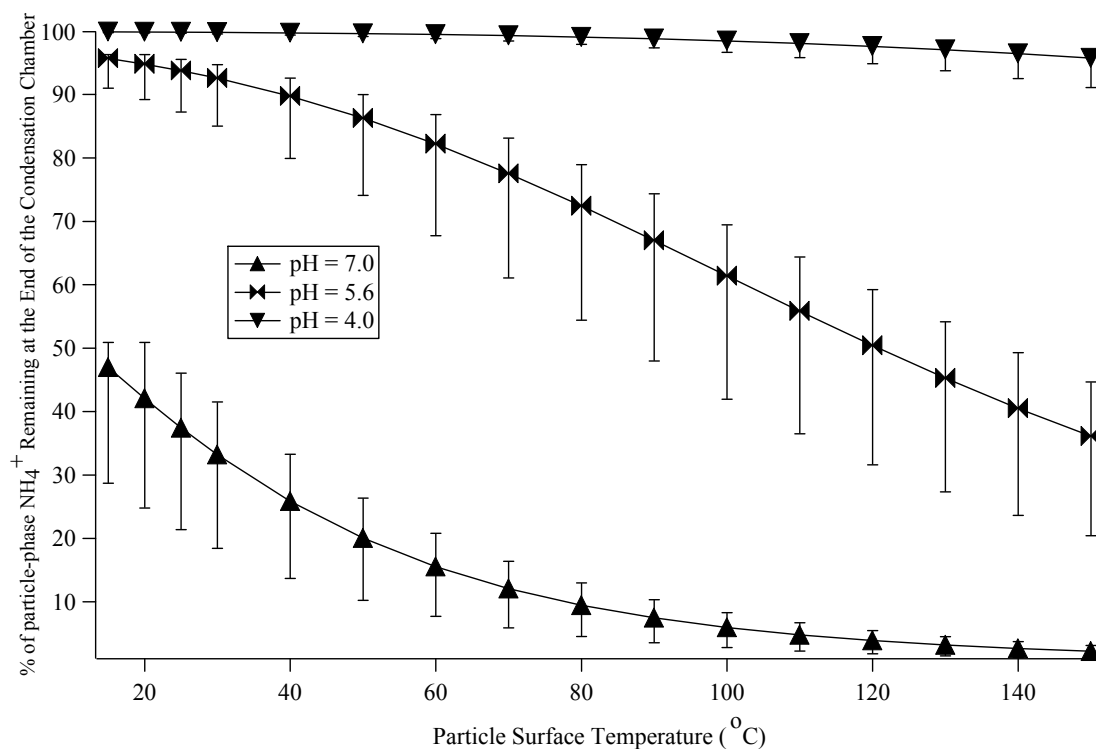


Figure 2.6. Percentage of  $\text{NH}_4^+$  remaining in the particle phase after the 1 s residence time in the condensation chamber as a function of particle surface temperature, acidity, and the amount of water (which is related to the dilution factor). Each marker reflects a dilution factor of 1.25 where the upper and lower bounds reflect dilution factors of 1.4 and 1.1, respectively. Nitrate and chloride results are not shown since they are predicted to stay completely (100%) in the particle phase for all temperatures, acidities, and dilution factors considered here.

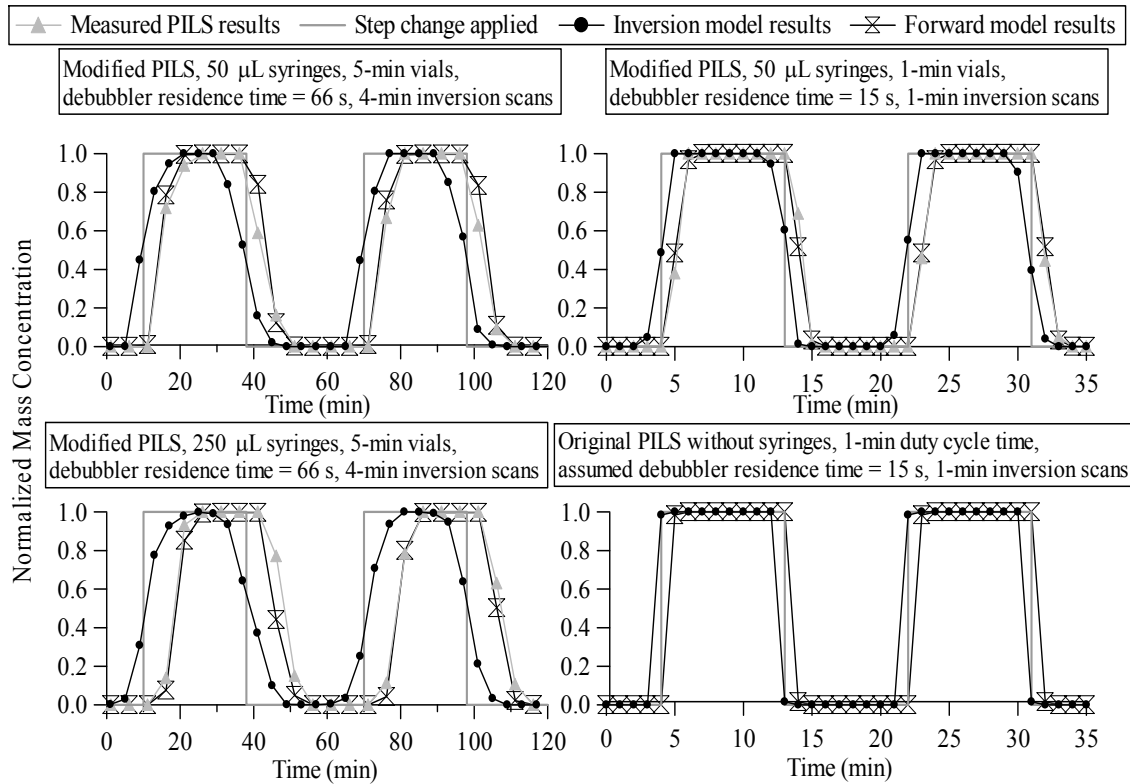


Figure 2.7. Comparison of experimental and theoretical mass concentrations in the modified PILS. Model predictions are also shown for the original PILS, which does not include syringes in the liquid sample's path from the debubbler to the analytical detector. All concentrations have been normalized to the maximum concentration applied during the step changes. The time response is shown to be dramatically improved with shorter debubbler residence times (top right), where the residence time is taken to be the time required to empty the vessel when it is completely filled with liquid during normal operation; the 50  $\mu\text{L}$  syringes were set to operate at three times their usual speed (15 s round-trip) and the flow rate ratio between the wash-flow at the top of the droplet impactor and the liquid being aspirated into the syringes from the debubbler was reduced to 1.01, resulting in less liquid volume being held in the debubbler.



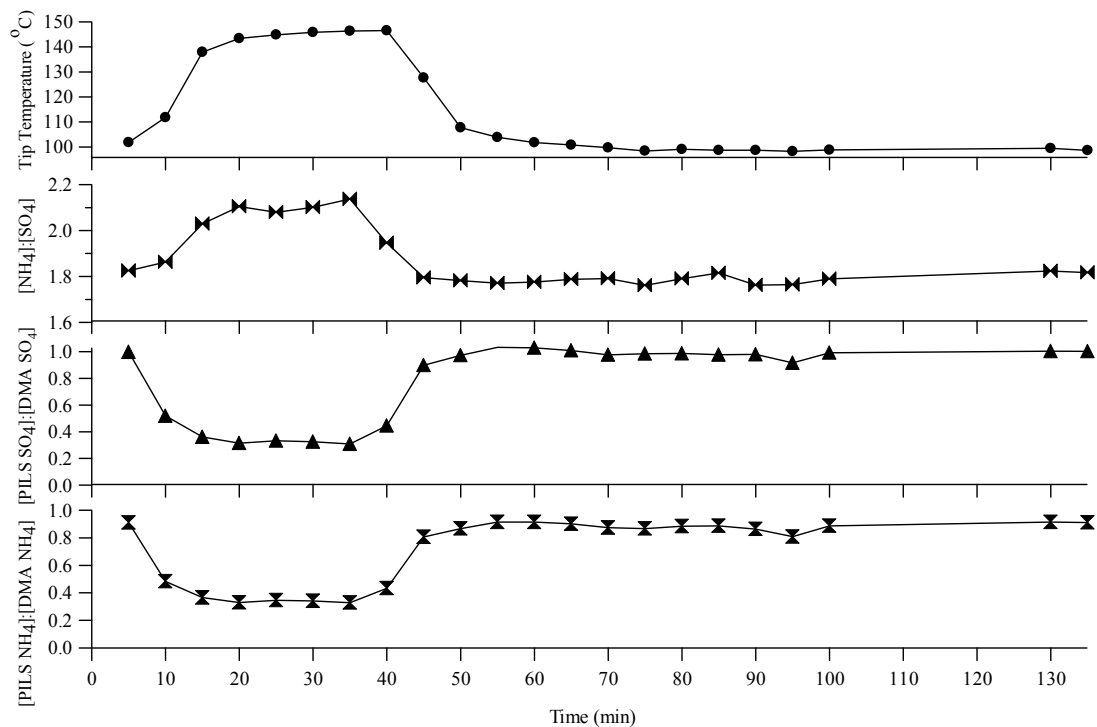


Figure 2.8. Tip temperature sensitivity results for a test where the modified PILS sampled  $(\text{NH}_4)_2\text{SO}_4$  aerosol. During the intense heating (from 10 to 45 min), the tip reaches up to  $147^{\circ}\text{C}$  and the  $\text{NH}_4^+$  and  $\text{SO}_4^{2-}$  mass collection efficiency levels drop significantly. The molar ratio is slightly less than two whenever the tip temperature is held at  $100 \pm 2^{\circ}\text{C}$ , mainly due to  $\text{NH}_4^+$  volatilization.

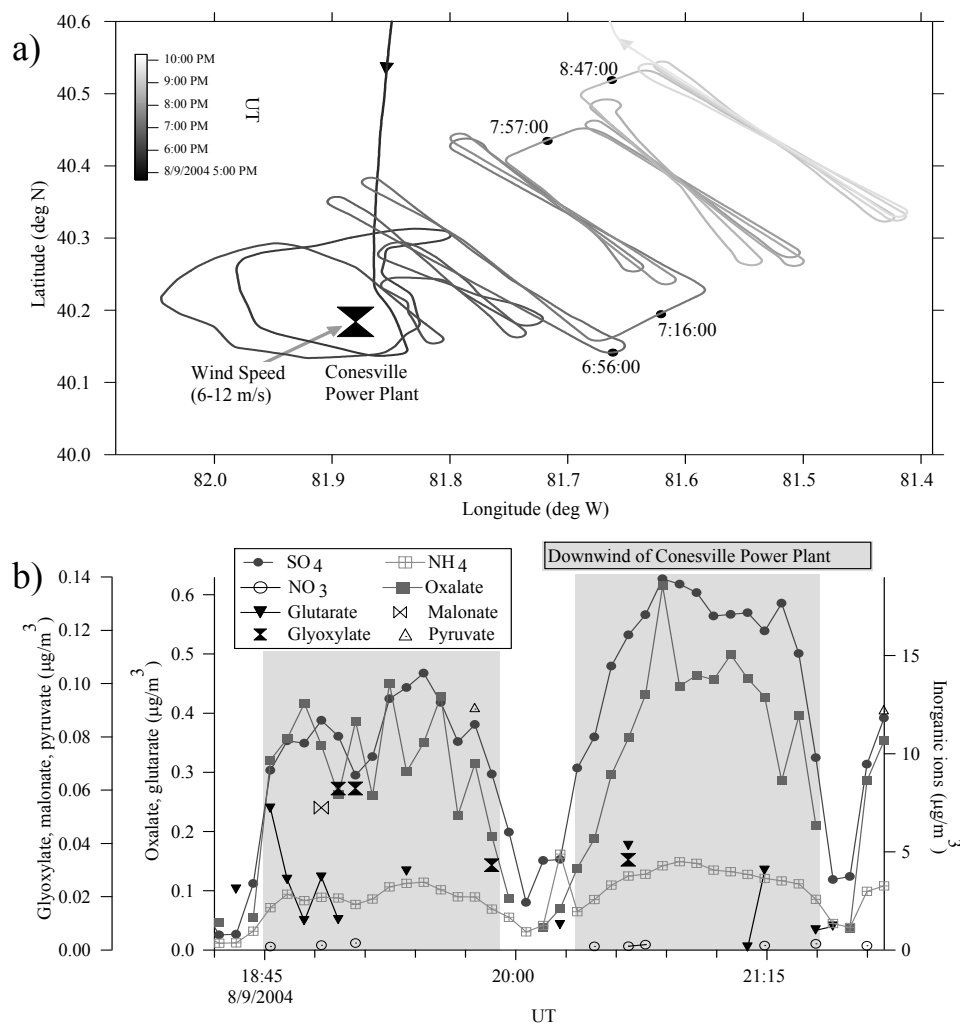


Figure 2.9. (a) Flight tracks; (b) Time series of the mass concentrations of various inorganic and organic acid ions measured during one ICARTT flight that was marked by the presence of clouds. The shaded areas denote when the Twin Otter aircraft was flying downwind of the Conesville Power Plant. The aircraft flew transect legs perpendicular to the studied plume, with increasing distance downwind of the power plant with time.

## **Chapter 3**

# **Rapid Size-Resolved Aerosol Hygroscopic Growth Measurements: Differential Aerosol Sizing and Hygroscopicity Spectrometer Probe (DASH-SP)\***

---

\*This chapter is reproduced by permission from “Rapid Size-Resolved Aerosol Hygroscopic Growth Measurements: Differential Aerosol Sizing and Hygroscopicity Spectrometer Probe (DASH-SP)” by A. Sorooshian, S. Hersey, F. J. Brechtel, A. Corless, R. C. Flagan, and J. H. Seinfeld, *Aerosol Sci. Tech.*, 2008. Copyright 2008. American Association for Aerosol Research.

### 3.1 Abstract

We report on a new instrument developed to perform rapid, size-resolved aerosol hygroscopicity measurements. The differential aerosol sizing and hygroscopicity spectrometer probe (DASH-SP) employs differential mobility analysis in-concert with multiple humidification and optical sizing steps to determine dry optical size and hygroscopic growth factors for size-selected aerosols simultaneously at three elevated relative humidities. The DASH-SP has been designed especially for aircraft-based measurements, with time resolution as short as a few seconds. The minimum particle diameter detected with 50% efficiency in the optical particle counters (OPCs) is  $135 \pm 8$  nm, while the maximum detectable particle diameter is in excess of 1  $\mu\text{m}$ . An iterative data processing algorithm quantifies growth factors and “effective” refractive indices for humidified particles using an empirically-derived three-dimensional surface (OPC pulse height - refractive index – particle size), based on a calculated value of the “effective” dry particle refractive index. Excellent agreement is obtained between DASH-SP laboratory data and thermodynamic model predictions for growth factor dependence on relative humidity for various inorganic salts. Growth factor data are also presented for several organic acids. Oxalic, malonic, glutaric, and glyoxylic acids grow gradually with increasing relative humidity up to 94%, while succinic and adipic acids show no growth. Airborne measurements of hygroscopic growth factors of ship exhaust aerosol during the 2007 Marine Stratus/Stratocumulus Experiment (MASE II) field campaign off the central coast of California are presented as the first report of the aircraft integration of the DASH-SP.

### 3.2 Introduction

Uptake of water by atmospheric aerosols is important in a variety of phenomena: light scattering, ability to act as cloud condensation nuclei, and deposition within the human respiratory system. Aerosol hygroscopicity measurements have been made with a variety of systems (Table 3.1). The parameter normally quantified is the diameter growth factor ( $GF = D_{p,wet}/D_{p,dry}$ ). Laboratory growth factor measurements are commonly performed by levitating a particle in an electrodynamic balance (Cohen et al., 1987a, 1987b; Tang and Munkelwitz, 1993, 1994a, 1994b; Chan et al., 1997; Peng et al., 2001; Peng and Chan, 2001). This method probes single, laboratory-generated particles, directly measuring the mass change in response to humidity variation. The need to directly measure the growth factor of ambient aerosols led to the development of the hygroscopicity tandem differential mobility analyzer (HTDMA) (Liu et al., 1978; Sekigawa, 1983; Rader and McMurry, 1986), in which dry particles of a selected size are exposed to a specific relative humidity (RH), after which the wet size is measured by classifying the grown particles with a second DMA, and counting with a condensation particle counter (CPC). Owing to the long duration of time required to measure the size distribution of the grown particles using a DMA, the HTDMA technique is relatively slow. However, both techniques above enable high-precision measurements of the growth factor.

While these methods have produced important insights into the hygroscopic behavior of atmospheric aerosols, the long time required to determine growth factors for different particle sizes and RHs makes them impractical in a number of important measurement scenarios in which the properties of sampled particles vary rapidly,

especially during airborne measurements. A number of alternate methods, which are described in detail in Table 3.1, have been employed to probe the hygroscopic properties of the atmospheric aerosol more rapidly than is possible with the HTDMA. Several of these methods probe the entire aerosol as measured at different humidities, using nephelometers to probe ensemble light scattering (Rood et al., 1985; Dougle et al., 1998; Carrico et al., 1998, 2000; Sheridan et al., 2002; Magi and Hobbs, 2003; Kim et al., 2006), or measuring aerosol size distributions with optical particle sizing instruments in parallel (Kotchenruther and Hobbs, 1998; Hegg et al., 2006, 2007; Snider and Petters, 2007), or multiple DMAs operated in parallel (Wang et al., 2003). The use of an optical particle counter (OPC) in place of a DMA detector is not new, as several investigators (Covert et al. 1990; Hering and McMurry 1991; Brand et al. 1992) used OPC detection of mobility-classified particles to gain insight into the mixing state of atmospheric aerosol and to determine their optical properties. One approach that attempts to provide the resolution of the HTDMA without the response time limitations is to classify particles with a DMA operated at one RH, equilibrate the classified particles at a second RH, and then measure the resulting size distribution using a fast particle sizer such as an OPC. Kreisberg et al. (2001) classified particles at a high RH, dried the classified particles, and measured the dry particle size using an OPC in an instrument they called the relative humidity-moderated differential mobility optical particle size spectrometer (RH-DMOPSS). The RH-DMOPSS, which is an extension of the DMOPSS design of Stolzenburg et al. (1998), measures shrinkage by drying rather than growth upon humidification like most other hygroscopic growth instruments. The RH-DMOPSS is an improvement upon the HTDMA in that it is faster and can measure a larger range of

particle sizes ( $0.1 - 1.1 \mu\text{m}$ ). However, this instrument provides a growth factor at only one RH at any given time.

In this paper, we describe a new instrument that enables simultaneous determination of growth factors at several RHs, and that overcomes the challenges of determining the size of dry particles with unknown composition. The instrument has been designed especially for aircraft-based measurements. The differential aerosol sizing and hygroscopicity spectrometer probe (DASH-SP), developed by Brechtel Manufacturing Inc. (<http://www.brechtel.com/>), employs DMA classification of dry aerosol particles, equilibrates the classified particles to a new RH, and then measures the sizes of the grown particles using an OPC. An iterative data processing algorithm quantifies growth factors and “effective” refractive indices ( $n$ ) for wet particles based on a calculated “effective” dry particle refractive index; iterations are performed on a three-dimensional surface (pulse height –  $n$  –  $D_p$ ) based on dry particle calibration data from several salts with known refractive indices. By operating four controlled-RH channels in parallel and equipping each of the humidified channels with a separate OPC, hygroscopic growth factors can rapidly be determined at a number of particle sizes without having to incur the time delays required to stabilize a humidification column to a new RH. Depending upon the concentration and size distribution of the aerosol sampled, the growth factors of particles at any selected size within the size resolution of the instrument can be determined in as little as a few seconds.

We present first an overview of the design of the DASH-SP instrument. Results from laboratory characterization tests illustrate the performance of the instrument, including size detection limits, time resolution, stability, accuracy, and inherent

uncertainties. The data processing algorithm is subsequently described, which is used to convert pulse height data to growth factors. Hygroscopicity measurements for various inorganic salts and organic acids are compared to theoretical predictions for growth factor dependence on RH. Finally, airborne field measurements establish that the DASH-SP is capable of measuring growth factors at multiple sizes and RHs with a time resolution as much as two orders of magnitude shorter than that of the HTDMA.

### 3.3 DASH-SP Description

The DASH-SP, illustrated in Figure 3.1, couples a single classification DMA system with a set of growth factor measurement systems that are operated in parallel. The modules that comprise the instrument are, in the order in which the aerosol experiences them: (1) an aerosol drier; (2) an aerosol neutralizer; (3) a classification DMA that selects the dry mobility size range for which growth factor measurements are made; (4) a set of parallel aerosol conditioning modules in which the aerosol is brought to equilibrium at controlled RHs; and (5) a detector at the outlet end that determines the total particle concentration leaving the DMA, and the size distributions of the particles after RH equilibration. The aerosol path through the instrument will now be described in detail.

A 0.5 LPM aerosol sample flow first passes through a Nafion drier (described below), and then passes through a  $^{210}\text{Po}$  neutralizer that brings the dried particles to a stable, steady-state charge distribution. The aerosol then enters a cylindrical DMA with a 33.9-cm-long classification column, and inner and outer radii of 62.4 mm and 72.3 mm, respectively. The DMA sheath flow rate is 5 LPM. The DMA selects particles in a narrow interval of mobility-equivalent diameters in the 0.1 to 1.0  $\mu\text{m}$  range. The



minimum voltage at which particles are classified is 281 V (to select 150 nm diameter particles), so Brownian diffusion does not significantly broaden the DMA transfer function (Flagan 1999), and the transmission characteristics of the DMA closely approach the ideal, nondiffusion transfer function of Knutson and Whitby (1974). Particles larger than 1  $\mu\text{m}$  can be classified by operating the DMA at lower flowrates, although the fraction of particles that carry multiple charges will become significant, making data analysis more difficult. For the present purposes, we shall limit discussion to measurement of growth factors of particles with dry diameters of 1  $\mu\text{m}$  or smaller. The classified aerosol leaving the DMA is split into five separate flows. The total concentration of classified particles is determined, without further conditioning of one of the five flows, by measuring the dry, classified particles using an integral TSI Model 3781 water-based condensation particle counter (CPC). The CPC serves as a redundant particle number concentration measurement against which data from the OPCs, to be described below, can be compared.

The remaining four classified aerosol flows are used to measure growth factors. They first pass through a Perma Pure, LLP, Nafion humidifier (Model MD-070-24FS-4) that consists of a Nafion membrane tube that is enclosed in a coaxial tube. The Nafion efficiently transmits water through the membrane, enabling the small aerosol flow through the center tube to equilibrate with the RH of the larger flow between the membrane and the outer shell. The RH of that larger flow is adjusted by mixing of dry air with air that has been saturated with water vapor by passage through a Nafion tube coil that is immersed in a warm water bath. Feedback control using an RH sensor (Model HMP50YCC1A2X, Vaisala) ensures that a constant, predetermined RH is achieved in

both the conditioned aerosol flow, and the outer flow. One humidifier is kept dry ( $< 8\%$  RH), while the other three are operated at higher and different RHs. The maximum RH is typically below 94% in order to prevent condensation within the instrument, although higher RH can be used for short periods of time.

The aerosol growth factor is measured as a surrogate for particle growth in response to humidity changes in the atmosphere where sufficient time is generally available for the droplets to fully equilibrate with atmospheric water vapor. To simulate the atmospheric response effectively, the time in the conditioning columns must be sufficient to ensure full equilibration. The characteristic time for a droplet to reach thermodynamic equilibrium with water vapor in unsaturated conditions ( $\text{RH} < 100\%$ ) is estimated to be on the order of microseconds (Pilinis et al., 1989). The  $\sim 4$  s residence time within each conditioning column is sufficient to ensure equilibration. Moreover, as described below, the outer flow from the Nafion humidifier is used as a sheath flow within the OPC to ensure that the equilibrium is maintained to the point of measurement.

The four conditioned aerosol flows pass directly to dedicated, custom-built OPCs, designed to detect particles in the 100 nm to 3  $\mu\text{m}$  diameter size range. To ensure that particles pass through the  $1.4 \times 10^{-3} \text{ mm}^3$  view volume of the collection optics, the aerosol (0.06 LPM) and a coaxial sheath flow (4 LPM) are focused by acceleration through a nozzle. Laboratory tests have shown that the sheath and aerosol streams do not mix. The view volume of the OPCs is determined by calculating the intersection volume of the cylindrical particle beam and the laser light sheet through which particles pass. The design of the laser light sheet is such that all particles that enter the OPC optical cavity pass through the light. The thickness of the laser light sheet is measured in two ways: 1)

projecting the laser against a distant surface and then measuring the projected width with a vernier caliper while using a light meter to define the edges of the light; and 2) by using an oscilloscope to measure the pulse width and, therefore, the transit time of individual particles through the light sheet. The particle velocity is calculated using the known flow rate through the accelerating nozzle. By multiplying the velocity by the transit time, the thickness of the laser light sheet is determined. The two methods for measuring the light sheet thickness agree to within 15% and found a thickness of 0.015 mm. However, the light sheet does not have perfect edges. Therefore, larger particles are observed above the comparator threshold for slightly longer pulse widths.

To minimize size changes during measurements, the OPCs measure scattering of light from single particles as they pass through the laser light sheet originating from the diode laser ( $\lambda = 532$  nm, World Star Technologies, Model TECGL-30). Scattered light is collected using an elliptical mirror from a wide angle ( $+64^\circ/-50^\circ$  in vertical plane and  $\pm 74^\circ$  in horizontal plane) in the near forward direction to integrate over the Mie resonances, thereby minimizing intensity oscillations that might otherwise lead to ambiguity in size determination. A cone of scattered light ( $\pm 22^\circ$ ) emanating from the view volume along the axis of the laser is not collected due to a pass-thru hole in the elliptical mirror that is needed to allow the laser to exit the optical cavity. The mirror focuses the scattered light onto a photomultiplier tube (PMT, Hamamatsu Model H6779-02). RH, temperature ( $T$ ), flow, and pressure ( $P$ ) sensors monitor conditions of all flows, both upstream and downstream (except flow) of each OPC.

The DASH-SP employs two data acquisition systems: a high-speed system to acquire the pulse data produced by the photomultipliers, and a second system to monitor

signals from the slower sensors used to record  $T$ , RH, DMA size selection, DMA voltage, OPC gain settings, etc. The signal from the PMT is processed through two gain stages, low gain for measurement of particles larger than about 450 nm, and high gain for particles in the  $135 < D_p < 450$  nm size range. The instrument automatically selects the appropriate gain stage according to the size expected for that channel. A four-channel high-speed digitizer (National Instruments™, Model PCI-6132) accumulates the logarithmically amplified, detected peak PMT signals from individual particles for count rates up to  $2.5 \times 10^6 \text{ s}^{-1}$ , corresponding to a concentration of  $2.5 \times 10^6 \text{ cm}^{-3}$ . Particle coincidence, which occurs when multiple particles are simultaneously in the OPC view volume, is a function of particle number concentration, view volume, and particle size. The coincidence performance of the OPC was validated by simultaneously sampling the same DMA-selected particles with two CPCs and the OPC. One CPC sampled upstream of the OPC, while the second CPC sampled downstream of the OPC. The maximum coincidence error associated with the laboratory and field measurements during this study is 3%, while the 1% particle coincidence concentration limit is approximately  $5000 \text{ cm}^{-3}$  and  $350 \text{ cm}^{-3}$  for the smallest ( $\sim 135$  nm for high gain) and largest ( $\sim 450$  nm for high gain) detectable particles, respectively, in the OPCs.

The DASH-SP can be operated manually or autonomously. In manual operation, the user specifies the RH for each humidifier, the size of particles to be selected by the DMA, and the number of particles to be sized by the OPC for each RH channel. The autonomous mode can step through a number of particle sizes and RHs, measuring a specified number of particles for each  $D_p$ /RH combination. Changing the RH on any conditioning column slows the measurements due to the time required for the RH to

stabilize after such a change. The typical RH equilibration time needed after a step change in RH from  $< 10\%$  to be within  $\pm 1\%$  of 74%, 85%, and 92% was determined to be  $236 \pm 61$  s,  $372 \pm 106$  s, and  $569 \pm 97$  s, respectively ( $n = 11$ ); these equilibration times represent an upper limit since smaller changes in RH within these broad ranges would ideally be carried out during experiments.

### 3.4 Experimental Methods

A series of laboratory experiments were conducted to characterize the DASH-SP while it operated in the manual mode. For all characterization tests described below, test salt aerosols were employed. Salt solutions were prepared by mixing a known amount of salt with Milli-Q water, usually resulting in 0.2% (by mass) solutions. A compressed air source, with a downstream high-efficiency particulate air (HEPA) filter to remove particulate contaminants, supplied flow to a stainless steel, constant-rate atomizer (Liu and Lee 1975) and sheath air flows for the DMA and OPCs. A dilution flow system was used to maintain atomizer output particle number concentrations below  $1000 \text{ cm}^{-3}$  at a DMA-selected size.

The DASH-SP was also deployed on the Center for Interdisciplinary Remotely-Piloted Aircraft Studies (CIRPAS) Twin Otter aircraft in the July 2007 Marine Stratus/Stratocumulus Experiment (MASE II) campaign, in which airborne aerosol and cloud measurements were carried out off the central coast of California. For the duration of the field study, the instrument operated in the autonomous mode where the scan sizes and minimum OPC pulse count quantities were pre-programmed. We briefly present data from one particular flight to report the first airborne deployment of the DASH-SP; a

more comprehensive analysis of data from this entire campaign will be presented in subsequent work.

### **3.5 Instrument Characterization**

#### **3.5.1 Size Limits of OPC Detection**

The range of particle sizes in which characterization experiments are carried out depends on the OPC size detection limits. The optical properties of salts vary, so the size detection limit of the OPCs is a function of the composition of an aerosol sample. By sampling a set of 16 different species (10 inorganic, 6 organic), the minimum particle diameters detected with 50% efficiency in the OPCs were found to be  $135 \pm 8$  nm and  $234 \pm 16$  nm for high- and low-gain settings, respectively. The variation in OPC response as a function of refractive index is contained within the standard deviations, which reflect the variability among the ensemble of salts tested. The maximum size that can be detected accurately by the OPC is approximately  $450 \pm 30$  nm with the high-gain setting, and beyond 1  $\mu$ m with the low-gain setting. However, uncertainties associated with multiply charged particles are enhanced when detecting particles of increasing size, especially near 1  $\mu$ m. Also, electrical saturation of the OPCs results in enhanced uncertainties starting at  $D_p > 450$  nm (high gain) and  $D_p > 700$  nm (low gain).

#### **3.5.2 Time Resolution**

The time resolution of the instrument is determined by three factors: 1) the transport delays between the point where particles enter the DASH-SP or, for a steady aerosol, where they enter the DMA, and the OPC detectors; 2) delays associated with programmed changes in the sampled particle size; and 3) the time required to obtain

statistically significant counts in each OPC channel. A maximum transition time of 17 s is needed when switching between different DMA-selected sizes for normal operating conditions in order to ensure particles of the previous size have exited the system; this addresses the first two factors governing time resolution. The tubing length of each stream from the 5-way splitter (see Figure 3.1) to each humidification chamber and OPC is equivalent, which results in the same particle transit time in each channel. Tests were performed to estimate the minimum number of particles at a given size required to obtain a response with varying degrees of statistical significance. These tests indicate the length of time the instrument should sample at a given set of operating conditions to obtain representative growth factors. Sample sets of over 10,000 pulses were obtained for a selected particle size for different salts ( $D_p = 150 - 404$  nm). Pulses were randomly removed from each data file in a way to determine the variation of the modal pulse height and standard deviation as a function of decreasing counts at a fixed particle size. The ratio of standard deviation to modal pulse height is usually within 10% for pulse numbers ranging from 50 to 10,000. The variation of the modal pulse height is  $\pm 1\%$  when comparing pulse counts of over 10,000 to any number of counts down to 50, below which the difference increases relatively quickly. In order for the standard deviation of observed pulse heights to be within 10%, 5%, and 1% of the original standard deviation calculated for a population of over 10,000 particles, an average of 60, 220, and 530 pulses are required, respectively. Figure 3.2 displays the time required to satisfy these different limits of the original modal pulse height and standard deviation for a wide range of particle number concentrations at a selected dry diameter. For example, for 10 particles  $\text{cm}^{-3}$  at a DMA-selected size, a minimum of 5 s is needed to be within 1% of the

modal pulse height had over 10,000 particles of the same composition been sampled. An additional order of magnitude of time is required to be within 1% of the original standard deviation as compared to 1% of the original mode. As will be shown subsequently, the mode is the critical parameter in quantifying growth factors via the iterative data processing technique. Assuming a pulse height distribution with a distinct and dominant mode (there are often less dominant modes due to multiply-charged particles), the data processing algorithm will determine the correct pulse height distribution mode regardless of the variance in the distribution. Thus, sampling time at a given  $D_p$ /RH combination should be reduced to improve time resolution at the expense of variance, which ultimately has no effect on the accuracy of quantified growth factors.

### **3.5.3 DASH-SP Accuracy, Precision, and Uncertainties**

The uncertainty of the DASH-SP measurement of growth factor depends on the uncertainties in the RH and sizing (DMA and OPC) measurements. Critical to the accuracy of the RH measurements is the calibration procedure. One “reference” RH sensor (Model HMP50YCC1A2X, Vaisala) was initially calibrated over six saturated salt solutions within the 8 – 97% RH range. The remaining 12 RH sensors were then calibrated as an ensemble against the “reference” sensor in a temperature-controlled chamber through which a controlled mixture of dry and humid air was circulated. The accuracy of the RH measurements was evaluated by comparing theoretical deliquescence RH (DRH) for multiple salts with measurements. The DRHs of ammonium sulfate, sodium sulfate, and potassium chloride aerosols agreed with literature values (Seinfeld and Pandis 2006) to within  $\pm 1.0\%$ , while sodium chloride aerosols agreed to within  $\pm$



1.6%. The overall RH measurement uncertainty was calculated by taking the summed root mean square errors of the measured OPC sample and sheath flow RHs, and combining this with the uncertainty associated with the RH sensors. The overall uncertainty was usually  $\pm 1.5\%$ , while the RH sensor precision was  $\pm 0.7\%$ .

Temperature fluctuations and gradients within each of the four humidification chamber-OPC units can lead to uncertainties due to the RH changing. Temperature sensors monitoring the sheath, sample, and exit flows of each OPC exhibited no significant change ( $\Delta T < 1^\circ \text{C}$ ) during laboratory scans that lasted as long as  $\sim 10$  min, but temperatures did show a systematic increase ( $\Delta T > 1^\circ \text{C}$ ) over longer periods of time. During aircraft flights lasting 5 h in which the DASH-SP was deployed, the twelve temperature sensors recorded the same level of variation. For example, the twelve sensors during one representative flight exhibited averages between  $24.0 - 25.0^\circ \text{C}$  and standard deviations between  $3.0 - 3.5^\circ \text{C}$ . However, the RH sensors exhibited significantly less variation due to the feedback control of the humidification by the instrument software: the RH standard deviation ranged between  $0.1 - 1.8\%$  for OPCs with upstream humidification chambers equilibrated at RHs of 74%, 85%, and 92%. Therefore, the RH variation resulting from temperature fluctuations in the humidification chamber-OPC units is normally within the uncertainty of the RH sensor measurements.

The instrument software calculates the DMA voltage required to classify a selected dry size for the specific geometry and operating parameters ( $T$ ,  $P$ , flow rates) of the DMA. Since the DMA sheath flow rate is usually 10 times larger than the aerosol flow rate and relatively large particles are studied, the width of the sampled electrical mobility window is  $\pm 10\%$ . DMA performance was frequently evaluated with calibrated

PSL particles ranging in diameter between 152 - 1101 nm. Accurate DMA operation is exhibited when the maximum particle concentration is observed at the DMA-selected size that matches the actual size of the PSL particles, rather than a smaller or larger size. The maximum particle concentration was observed to occur at DMA-selected sizes within  $\pm 3\%$  of the actual size of the PSL particles tested. It should be noted that the PSL particles studied have a reported size uncertainty ranging from  $\pm 1 - 3\%$ . The average uncertainty associated with growth factor measurements is calculated to be  $\pm 4.3\%$ , with an uncertainty as high as 8% at a dry size of 150 nm at lower RHs ( $< 80\%$ ).

Tests were done to check for contamination both in the form of leaks and in the source of Milli-Q water used in atomizing solutions. When feeding filtered air into the DASH-SP frequently over a period longer than 30 days, no particles were detected by the CPC and fewer than  $1 \text{ cm}^{-3}$  were detected by the OPC (high gain). Particles detected by the OPC corresponded to sizes below the 50% detection limit of the OPC ( $D_p < 135 \text{ nm}$ ). Pure Milli-Q water was atomized into the DASH-SP system; no particles were detected by the CPC beyond 135 nm, and  $< 1 \text{ cm}^{-3}$  were detected by the OPC (high gain). Below 135 nm, background particle concentrations measured by the CPC reached a value as high as  $30 \text{ cm}^{-3}$  at 5 nm; the OPC response at these lower sizes remained at  $< 1 \text{ cm}^{-3}$ . No background particle signals were observed using the low-gain OPC configuration for these tests. Since the experiments conducted with salts usually involved OPC number concentrations between  $100 - 1000 \text{ cm}^{-3}$  at a specific size, any background particles from the water source and inside the system itself are deemed negligible. Moreover, since no particles larger than 135 nm were observed by the OPC for these tests, contamination is

negligible for ambient sampling, as the system is designed to sample at minimum dry  $D_p$  exceeding 135 nm (150 nm for this study).

### 3.5.4 Stability

The stability in dry and wet particle data was studied. For dry data, stability was quantified over a time span of four months by calculating pulse height standard deviation relative to pulse height average ( $\sigma/\bar{x}$ ) for both gain settings and different particle sizes (Figure 3.3). Above 200 nm, at the high-gain OPC setting,  $\sigma/\bar{x}$  is  $< 10\%$ , with the species of greatest atmospheric relevance (ammonium sulfate, ammonium nitrate, sodium chloride) being  $< 3\%$ . For the low-gain setting,  $\sigma/\bar{x}$  is  $< 10\%$  at 350 nm and  $\leq 5\%$  beyond 350 nm for all species studied. For wet studies, the stability in growth factor at different initial dry sizes and RHs between 30 – 92% was quantified for several species, where  $\sigma/\bar{x}$  was usually  $< 3\%$  for all species studied. In summary, the stability of the DASH-SP improves for both dry and wet particles with increasing size above the 50% detection limit of the OPC.

### 3.6 Data Analysis

Data resulting from the collection of scattered light from individual particles are returned by the OPCs as pulse heights, the amplitudes of which depend on particle size, shape, and refractive index, the latter depending on particle composition. For the purposes of pulse height data interpretation, the following assumptions are made: (1) purely scattering, spherical particles (one exception to the sphericity assumption for growth factor calculations is that a shape factor of 1.08 was assumed for dry sodium

chloride particles, thought to be cubic, prior to humidification (Hinds, 1999; Hameri et al., 2001)); (2) the DMA-selected particle size corresponds to the mode of the true particle size distribution, and therefore, the mode of the OPC pulse height distribution; and (3) for particles that undergo humidification, the mode of the OPC pulse height distribution represents the true wet particle size. The first assumption is an approximation for ambient particles, but has been commonly made in previous DMA-OPC studies (Stolzenburg et al., 1998; Hand et al., 2000; Ames et al., 2000; Kreisberg et al., 2001; Hand and Kreidenweis, 2002). Growth factors are calculated using the volume-equivalent diameter ( $D_p$ ), while the DMA classifies particles based on their mobility-equivalent diameter ( $D_{p,mob}$ ), the two diameters of which are only equivalent for spherical particles. Following the methodology of Gysel et al. (2002), employing a shape factor of 1.08 for dry sodium chloride particles results in a value of 0.96 for the ratio  $D_p:D_{p,mob}$ . This provides a representative indication of the sensitivity of growth factor measurements to particles with one type of shape effect (cubic rather than spherical); without the shape factor correction, growth factors for sodium chloride particles would be underestimated by 4%. The volume of water in particles after humidification is often substantial; the assumption that particles are spherical and scatter, but do not absorb, light is generally valid for those particles for which growth is significant.

Before the pulse height distribution modes can be used to determine the particle size and refractive index, dry particle calibrations must be performed to accumulate sufficient data relating pulse height, particle size, and refractive index. OPC calibrations were carried out for a set of six salts of known refractive index (1.39, 1.47, 1.50, 1.52, 1.54, and 1.60; salts listed in Figure 3.4) (Weast, 1987; Lide, 2005) by measuring OPC

pulse height response to a range of DMA-selected diameters (150, 175, 200, 225, 250, 300, 350, 375, 404, and 415 nm) without humidification. Figure 3.4 summarizes the OPC response as a function of dry particle size for salts of different refractive index from one set of calibrations. For each OPC, high-order polynomial equations accurately represent the relationship between OPC pulse height and particle dry diameter for different refractive indices ( $R^2 > 0.995$ ), allowing calculation of size from a given refractive index and OPC pulse height:

$$D_{p,dry} = a_5 x^5 + a_4 x^4 + a_3 x^3 + a_2 x^2 + a_1 x + a_0 \quad [1]$$

where  $x$  = OPC pulse height and constants  $a_0 - a_5$  are determined using calibration data. The relationship between OPC pulse height and refractive index for specific particle dry diameters can be modeled as a cubic polynomial ( $R^2 > 0.996$ ), allowing calculation of refractive index from OPC pulse height at a given dry particle size:

$$\text{Refractive index} = b_3 x^3 + b_2 x^2 + b_1 x + b_0 \quad [2]$$

where  $x$  = OPC pulse height and constants  $b_0 - b_3$  are determined using calibration data. Using equation 2, OPC response curves for different dry particle sizes were extrapolated to calculate pulse heights for refractive indices between 1.33 and 1.39 for which calibration salts were not tested (water has a refractive index of 1.33). A three-dimensional surface can now be generated with the following equation, which is derived from multiple regression analysis:

$$\text{Pulse height} = c_5 + c_4 D_p + c_3 n + c_2 D_p^2 + c_1 n^2 + c_0 D_p n \quad [3]$$

where  $n$  is refractive index and  $D_p$  corresponds to particles in their dry or wet state.

Figure 3.5 summarizes the algorithm used to calculate “effective” refractive index and growth factor from the dry and wet pulse height distribution modes. Initially, the dry

pulse height distribution mode is used to iterate on a two-dimensional surface ( $n$  vs pulse height, fixed  $D_p$ ) to determine the dry particle “effective” refractive index. After guessing a value for the wet particle diameter, a volume-weighted refractive index is calculated to account for the refractive index of both water and the dry particle. Using the wet particle pulse height data, iterations are carried out on the three-dimensional surface to converge on a value for the humidified particle’s “effective” refractive index, which is subsequently used to determine the wet particle diameter and growth factor. This iterative process is not possible without a priori knowledge of the dry particle refractive index, which requires one of the four humidification chambers to be operated in the dry state. This algorithm assumes that particles are internally mixed and that particulate matter is completely dissolved in humidified particles.

One exception to the iterative procedure for humidified particles is when testing laboratory-generated aerosols with known dry-particle refractive indices; a thermodynamic model of particle water uptake (Brechtel and Kreidenweis, 2000a, 2000b) can predict the refractive index for a specific salt at a given RH. Only one step is then needed to interpolate on the three-dimensional surface ( $D_p$  vs. pulse height, fixed  $n$ ) to determine the true wet particle size. The modified Köhler model used includes a parameterization for the solution osmotic coefficient that approaches the correct thermodynamic limit as the solution becomes infinitely dilute (Brechtel and Kreidenweis, 2000a, 2000b). Predictions from both this model and the Aerosol Inorganics Model (AIM) (Clegg et al., 1998; <http://www.aim.env.uea.ac.uk/aim/aim.html>) are used below for comparison with laboratory data for a number of salts.

### 3.7 Growth Factor Measurements

#### 3.7.1 Inorganic Salts

Experiments were carried out to determine growth factor values as a function of RH, from 10% to 94%, for different inorganic species (ammonium nitrate, ammonium sulfate, ammonium nitrate, sodium chloride, potassium chloride, and sodium sulfate) and organic acid species (oxalic, glyoxylic, malonic, succinic, glutaric, and adipic acids). The growth factors for these species are either known or can be calculated theoretically to assess the accuracy of the DASH-SP measurements. However, only the inorganics provide a firm comparison between theory and/or laboratory measurements with those of the DASH-SP since growth factors for organic acids are not as well established as those for inorganic salts.

Figure 3.6 shows the measured hygroscopic growth curves for various inorganic and organic acid species. With the exception of the organic acids and ammonium nitrate, a sharp increase in growth factor is observed at the DRH, providing evidence for the homogeneity of the humidity field experienced by the particles. The measured growth factors of the inorganic species agree well with thermodynamic theory for RH values above the DRH ( $\pm 1\%$ ). For ammonium sulfate at an RH of 92% the discrepancy is  $\pm 4\%$  based on the Brechtel and Kreidenweis (2000a, 2000b) model, and  $\pm 1\%$  based on the Clegg et al. (1998) model. Growth factor measurements at RH values above the DRH show the following levels of agreement with thermodynamic theory: sodium chloride (1.0% above theory,  $\sigma = 2.3\%$ ,  $n > 50$ ), ammonium sulfate (1.5% above theory,  $\sigma = 1.7\%$ ,  $n > 50$ ), sodium sulfate (2.0% below theory,  $\sigma = 2.4\%$ ,  $n > 50$ ). Ammonium nitrate particles have been shown to remain “wet” at RHs as low as 8% (Dougle et al.,

1998; Lightstone et al., 2000), which explains why the observed growth factors exceed unity for RHs below the DRH. Multiple growth factor curves are reported for ammonium nitrate in Figure 3.6 to show that at sizes near 250 nm, the growth factors increase with higher dry particle sizes.

### 3.7.2 Organic Acids

In contrast to inorganic species, the hygroscopic properties of organic aerosol species are not as well known. Organic acids are an important component of atmospheric aerosols (Kawamura and Ikushima, 1993; Khwaja, 1995; Chebbi and Carlier, 1996; Saxena and Hildemann, 1996; Kawamura and Sakaguchi, 1999; Kerminen et al., 2000; Yao et al., 2004; Huang et al., 2005; Fisseha et al., 2006; Sorooshian et al., 2007a), the presence of which can affect the hygroscopicity of ambient particles (Saxena et al., 1995; Hansson et al., 1998; Li et al., 1998; Ansari and Pandis, 2000; Cruz and Pandis, 2000; Peng et al., 2001; Peng and Chan, 2001; Prenni et al., 2001, 2003; Wise et al., 2003). Two- to six-carbon dicarboxylic acids are investigated here, in addition to glyoxylic acid, which is a direct precursor to oxalic acid, the most abundant particulate dicarboxylic acid in the atmosphere (Kawamura and Ikushima, 1993; Kawamura and Sakaguchi, 1999; Kerminen et al., 2000; Poore, 2000; Yao et al., 2004; Crahan et al., 2004; Yu et al., 2005; Huang et al., 2005, 2006; Sorooshian et al., 2006a, 2007a, 2007b).

Oxalic ( $C_2$ ), malonic ( $C_3$ ), glyoxylic ( $C_2$ ), and glutaric ( $C_5$ ) acids do not exhibit a DRH, but rather grow gradually with increasing RH (Figure 3.6). This result is consistent with previous studies which showed that organic acids absorb water at all RHs (Saxena and Hildemann, 1997; Dougle et al., 1998). Unlike the other organic acids



studied, succinic ( $C_4$ ) and adipic ( $C_6$ ) acids exhibited no hygroscopic growth over the RH range studied, which is consistent with the HTDMA results of Prenni et al. (2001). With the exception of glyoxylic acid, previous studies have either measured or calculated DRHs for these organic acids; only malonic (DRH = 74 - 91%) and glutaric (DRH = 84 - 99%) acids exhibit DRHs in the range of RHs tested in this study, while the rest of the organic acids exhibit DRHs exceeding 97% (Saxena and Hildemann 1997; Peng et al. 2001).

Excluding oxalic and glyoxylic acids, the experimental data in Figure 3.6 indicate a clear odd-even carbon number effect, where the odd-carbon number organic acids (malonic and glutaric acids) exhibit relatively more hygroscopic growth as compared to the even-carbon number acids (succinic and adipic acids). This behavior is consistent with the literature (Saxena and Hildemann 1996; Prenni et al. 2001); solubility alternates with the number of carbon atoms in the organic acid molecule up to  $C_{10}$ . Oxalic acid is significantly more hygroscopic than succinic and adipic acids, the other two even carbon-number dicarboxylic acids.

Growth factor values for dicarboxylic acids measured in this study tend to be lower than those predicted by the Brechtel and Kreidenweis model (2000a, 2000b). The growth factors for malonic acid showed the best agreement with predictions as compared to the other organic acids, with a growth factor that is at most 6% below that predicted. The measured growth factor for glutaric acid was at most 17% below predictions. Malonic and oxalic acids exhibited relatively similar growth factors up to an RH of 92% ( $1.53 \pm 0.07$ , 8% below theory, and  $1.58 \pm 0.07$ , 26% below theory, respectively), while glutaric acid showed less growth ( $1.27 \pm 0.05$ , 19% below theory). Because

thermodynamic parameters are not available for glyoxylic acid, only experimental results are shown; glyoxylic acid exhibits similar hygroscopic behavior when compared to oxalic, malonic, and glutaric acids. Glyoxylic acid has a measured growth factor of  $1.44 \pm 0.06$  at an RH of 92%.

Five potential explanations for the disagreement between measurements and predictions for the dicarboxylic acid growth factors include: (1) uncertainties in the model parameters used for each dicarboxylic acid (osmotic coefficient, surface tension, solution density); (2) particles did not crystallize during drying prior to size-selection by the DMA and, therefore, do not properly reflect the quantity of solute; (3) particles were non-spherical; (4) volatilization of the organic acids occurred; and (5) the dicarboxylic acid particles exhibit slower water uptake than the inorganic species studied and did not have enough time to reach equilibrium at a given wet RH. The extent to which each of the five aforementioned explanations leads to the discrepancy between predictions and measurements is not known. It is noted that the second, third, and fifth explanations would ideally lead to an underestimate of the growth factor. In particular, there is less known about the morphology of organics as compared to inorganic species, therefore, if the organic acid particles were not spherical or compact, then the experimentally determined growth factors are less than their actual values from a morphology standpoint. The measurements do provide evidence that ambient particles that contain organic acids, specifically oxalic, malonic, glutaric, and glyoxylic acids, experience growth at low RHs ( $< 65\%$ ).

### 3.8 Validation of Iterative Data Processing Code

In order to assess the validity of the data processing technique for interpreting ambient data, the iterative procedure outlined in Figure 3.5 was applied to data collected from wet ammonium sulfate experiments to quantify “effective” refractive index and growth factor as a function of RH. The three wet RHs used in the field study subsequently discussed, 74%, 85%, and 92%, were also applied in these wet ammonium sulfate tests ( $n > 15$  at each RH). The measurements that have been processed with the iterative code are compared to predictions of the Brechtel and Kreidenweis (2000a, 2000b) and Clegg et al. (1998) models. Figure 3.7 shows that, although the calculated “effective” refractive index at an RH of 74% agrees perfectly with the literature (Weast 1987), the DASH-derived average growth factors exceed theory at this RH by as much as 8%. The measured growth factors at RHs of 85% and 92% lie within one standard deviation of the model predictions, whereas the “effective” refractive indices agree to within 1%. This is a result of the fact that the calculation of growth factor in the iterative data processing code is more sensitive to DMA, OPC, and RH uncertainties as compared to calculation of refractive indices.

Figure 3.8 (A-C) shows examples of the dry and wet size distributions from wet ammonium sulfate data processed with the iterative code. Size distribution data are presented at four RHs (one dry, and three wet RHs) for each of three initial dry sizes (150, 175, and 200 nm). The size distributions for dry particles and those at an RH value of 74% should be identical since ammonium sulfate particles deliquesce at an RH of  $79.9 \pm 0.5\%$  (Seinfeld and Pandis 2006). However, the mode diameters of the size distributions at RH = 74% slightly exceed those of the dry size distributions. The dry and

RH = 74% size distributions are broader at a dry size of 150 nm than at the two larger sizes; this broadening behavior is normally observed when the particle size is close to the minimum OPC detection limit. There is variation in the growth factors at constant RH, as the range in values at RHs of 74%, 85%, and 92% is 0.04 (average  $GF = 1.06$ ), 0.08 (average  $GF = 1.59$ ), and 0.16 (average  $GF = 1.80$ ), respectively. The differences in growth factor at constant RH for various dry sizes is attributable to uncertainties in the measurements and the iterative data processing procedure, particularly the cubic and high-order polynomial equations. However, all of the growth factors reported in Figure 3.8 are within 10% of predictions from the Brechtel and Kreidenweis (2000a, 2000b) and Clegg et al. (1998) models.

One would expect narrower size distributions for the dry ammonium sulfate results in Figure 3.8 since the DMA is selecting one size. To determine whether the broadness of the dry ammonium sulfate size distributions is caused by an instrument issue or by impurities and morphology issues associated with ammonium sulfate particles, dry PSL size distributions were also computed since PSL particles are spherical (Figure 3.8D). The PSL size distributions are considerably narrower than those of dry ammonium sulfate particles, suggesting that the latter aerosol likely consisted of non-spherical particles that affect the final optical sizing; particle shape variations can significantly influence their scattering and absorption properties (Chylek et al., 1984; Videen et al., 1997). The PSL size distributions for particle diameters of 152 nm and 404 nm were slightly broader than distributions at diameters of 199 nm and 300 nm, providing further evidence that the OPCs have somewhat lower size resolution near their minimum and maximum size detection limits. It is unlikely that particle coincidence

plays a role in the broadening behavior apparent in Figure 3.8. If this were the case, the same shape would be observed in the dry PSL distributions for all sizes shown. It is possible, however, that some of the broadening is also due to the particles experiencing a range of RHs.

These results suggest that the iterative procedure is capable of accurately determining refractive indices and providing dry and wet size distributions. Although the distributions may be broader close to the OPC size detection limits, the modes of these distributions can still be used to accurately calculate growth factors.

### **3.9 Field Implementation of DASH-SP**

On July 16, 2007, by prior arrangement, the Twin Otter intercepted and repeatedly sampled the exhaust plume of a large PANAMAX container ship with a 55 MW main engine operating on heavy fuel oil. Figure 3.9A shows the flight tracks during the ship experiment. The aircraft first flew up the plume toward the ship, which was steaming directly into the wind, at an altitude of 30 m; this procedure was repeated three more times. The aircraft also performed several cross-wind transects of the plume at various altitudes in the marine boundary layer ( $< 250$  m), which was clear on this day. Inside the plume, submicrometer particle number concentrations reached as high as  $365,000 \text{ cm}^{-3}$ , as determined with a differential mobility analyzer with a time resolution of  $\sim 73$  s, whereas the background aerosol concentration outside of the plume was  $< 500 \text{ cm}^{-3}$ . The plume was  $\sim 0.4$  km wide during the first downwind transect at an altitude of 30 m and it was 2 km wide during the second to last transect at an altitude of 150 m (the plume was not detected in the last transect at 210 m).

Figure 3.9B displays the water-soluble aerosol composition inside the plume as measured every 4.5 min (equivalent to a flown distance of  $\sim 13.5$  km) by a particle-into-liquid sampler (PILS; Brechtel Manufacturing Inc.) (Sorooshian et al., 2006b). The water-soluble aerosol mass, which reached values as high  $93 \mu\text{g m}^{-3}$  just behind the ship, was composed mainly of sulfate ( $96.2\% \pm 4.0\%$  of water-soluble mass;  $n = 15$ ). Other water-soluble components of the aerosol included  $\text{Na}^+$  ( $1.0\% \pm 2.4\%$ ),  $\text{NO}_3^-$  ( $1.0\% \pm 0.6\%$ ), organic acids ( $0.6\% \pm 0.3\%$ ),  $\text{Cl}^-$  ( $0.6\% \pm 0.9\%$ ), and  $\text{NH}_4^+$  ( $0.5\% \pm 0.4\%$ ). The aerosol was highly acidic, as the ammonium-to-sulfate molar ratio was, on average, 0.03. The ratio of water-soluble mass to the DMA-observed volume concentration of the aerosol was  $1.13 \text{ g cm}^{-3} \pm 0.30 \text{ g cm}^{-3}$ , suggesting that a significant fraction of the aerosol was accounted for by the PILS data, assuming that the ambient aerosol density was close to that of sulfuric acid ( $1.84 \text{ g cm}^{-3}$ ). As observed by an Aerodyne time-of-flight aerosol mass spectrometer, the aerosol contained a large proportion of hydrophobic organic species that were not detected by the PILS. It is likely that some of the hydrophobic species were light-absorbing, like soot, which introduces error in the iterative data processing algorithm because of non-zero imaginary components of the refractive index.

DASH-SP data are presented for the following dry diameters: 150, 175, 200, and 250 nm. The instrument was pre-programmed to detect a minimum of 300 pulses in each OPC channel for this flight. For 150 and 175 nm particles, 1 s and 10 s were usually required before all OPCs detected at least 300 pulses inside and outside of the ship plume, respectively. For 200 and 250 nm particles, 10 - 30 s and 10 - 60 s were required inside and outside of the plume, respectively.

The average dry “effective” refractive index of aerosol in the ship plume was determined to be  $1.53 \pm 0.04$ , while the “effective” refractive index in the background aerosol outside of the plume was  $1.49 \pm 0.04$ . It should be noted that the refractive indices of sulfuric acid, ammonium bisulfate, and ammonium sulfate are 1.41, 1.48, and 1.52, respectively (Weast, 1987; Ames et al., 2000). The time resolution of the DASH-SP is evident in Figure 3.9C, which shows the spatial distribution of growth factors at an RH of 92%. In the ship plume, the average growth factors at RHs of 74%, 85%, and 92% were  $1.11 \pm 0.04$ ,  $1.46 \pm 0.09$ , and  $1.53 \pm 0.10$ , respectively. The corresponding growth factors in the background aerosol were  $1.19 \pm 0.09$  (RH = 74%),  $1.54 \pm 0.05$  (RH = 85%), and  $1.63 \pm 0.08$  (RH = 92%). Therefore, the overall averages suggest that there was a decrease in hygroscopicity inside the ship plume as compared to the background marine aerosol at RHs  $\geq 74\%$ . There was no significant difference in growth factor as the plane flew closer to the ship in its plume from a downwind distance greater than 30 km. We hypothesize that this occurred because the relative mass fractions of acidic sulfate and hydrocarbon-like organic species did not vary appreciably over the range of timescales of transport between the ship and aircraft. The observed growth factors in the plume are lower than what would be expected for pure sulfuric acid, and this is likely a result of the presence of other species, such as hydrophobic organics, in the particles that reduced the hygroscopicity.

### 3.10 Conclusions

This study introduces a new instrument, termed the differential aerosol sizing and hygroscopicity spectrometer probe (DASH-SP). In the instrument, a DMA-selected

monodisperse aerosol flow is split into five flows, one to each of four OPCs with its own upstream humidification column, and one to a CPC. The DASH-SP has been designed for aircraft operation and other applications where hygroscopic growth observations are required at multiple sizes and RHs with high time resolution. An iterative data processing algorithm calculates growth factors and “effective” refractive indices for humidified particles based on a calculated value of the “effective” dry particle refractive index; iterations are performed on a three-dimensional surface (pulse height – refractive index –  $D_p$ ) based on dry particle calibration data from several salts with known refractive indices.

Laboratory tests were performed to characterize the instrument’s performance. The minimum particle diameter detected with 50% efficiency in the OPCs is  $135 \pm 8$  nm; particles with diameters  $> 1 \mu\text{m}$  are detected by the OPCs using the low-gain setting, subject to increasing uncertainty as a function of growing size due to multiply charged particles and electrical saturation of the OPCs. Estimates for the time required to obtain statistically significant counts in each OPC channel were reported for a wide range of particle number concentrations. The RH uncertainty is  $\pm 1.5\%$  with an average uncertainty of  $\pm 4.3\%$  for growth factor measurements. Measured DRHs of ammonium sulfate, sodium sulfate, and potassium chloride aerosols agree with literature values to within  $\pm 1\%$ , while that for sodium chloride aerosols agrees to within  $\pm 1.6\%$ . A high level of stability exists in the dry salt calibrations and growth factors for various salts at RHs up to 92%, especially at particle diameters larger than the 50% detection limit of the OPCs.



Excellent agreement exists between growth factor data for several inorganic salts and predictions from a thermodynamic model. Growth factor data for organic acids show that, with the exception of oxalic and glyoxylic acids (both C<sub>2</sub> acids), the organic acids with an odd number of carbons (malonic and glutaric acids) exhibit greater hygroscopic growth than those with an even number (succinic and adipic acids). Succinic and adipic acids exhibit no hygroscopic growth up to an RH of 94%, while the other organic acids show gradual growth starting at low RHs (< 65%). Oxalic acid, the most abundant organic acid in ambient aerosols, exhibits the greatest hygroscopic growth among all of the organic acids studied.

The DASH-SP was successfully deployed in the 2007 Marine Stratus/Stratocumulus Experiment (MASE II) campaign on board the CIRPAS Twin Otter aircraft. Results are presented here for one flight during this study in which the plume from a large container ship was sampled. Growth factors of the exhaust plume aerosol downwind of this ship at RHs of 74%, 85%, and 92% were  $1.11 \pm 0.04$ ,  $1.46 \pm 0.09$ , and  $1.53 \pm 0.10$ , respectively. The field data demonstrate that the DASH-SP is capable of providing first-of-a-kind, rapid, simultaneous, size-resolved aerosol hygroscopic growth measurements at multiple RHs. Future work will address the instrument response to non-spherical and light-absorbing particles.

### 3.11 Acknowledgements

Brechtel Manufacturing Inc. acknowledges the support of Dr. Ronald Ferek and the ONR SBIR Program under grant N00014-05-C-0016. This work was also supported

by the Office of Naval Research grant N00014-04-1-0118. We appreciate valuable comments and suggestions by Jeff Snider.

### 3.12 References

Aklilu, Y., Mozurkewich, M., Prenni, A. J., Kreidenweis, S. M., Alfarra, M. R., Allan, J. D., Anlauf, K., Brook, J., Leaitch, W. R., Sharma, S., Boudries, H., and Worsnop, D. R. (2006). Hygroscopicity of Particles at Two Rural, Urban Influenced Sites During Pacific 2001: Comparison with Estimates of Water Uptake from Particle Composition, *Atmos. Environ.*, 40:2650-2661.

Ames, R. B., Hand, J. L., Kreidenweis, S. M., Day, D. E., and Malm, W. C. (2000). Optical Measurements of Aerosol Size Distributions in Great Smoky Mountains National Park: Dry Aerosol Characterization, *J. Air Waste Manage.*, 50:665-676.

Ansari, A. S., and Pandis, S. N. (2000). Water Absorption by Secondary Organic Aerosol and its Effect on Inorganic Aerosol Behavior, *Environ. Sci. Technol.*, 34:71-77.

Baltensperger, U., Streit, N., Weingartner, E., Nyeki, S., Prevot, A. S. H., Van Dingenen, R., Virkkula, A., Putaud, J. P., Even, A., ten Brink, H., Blatter, A., Neftel, A., and Gaggeler, H. W. (2002). Urban and Rural Aerosol Characterization of Summer Smog Events During the PIPAPO Field Campaign in Milan, Italy, *J. Geophys. Res.*, 107(D22), doi:10.1029/2001JD001292.

Berg, O. H., Swietlicki, E., and Krejci, R. (1998). Hygroscopic Growth of Aerosol Particles in the Marine Boundary Layer Over the Pacific and Southern Oceans During the First Aerosol Characterization Experiment (ACE 1), *J. Geophys. Res.*, 103(D13):16535-16545.

Brand, P., Ruoss, K., and Gebhart, J. (1992). Performance of a Mobile Aerosol Spectrometer for an In situ Characterization of Environmental Aerosols in Frankfurt City, *Atmos. Environ.*, 26:2451-2457.

Brechtel, F. J., and Kreidenweis, S. M. (2000a). Predicting Particle Critical Supersaturation from Hygroscopic Growth Measurements in the Humidified TDMA. Part I: Theory and Sensitivity Studies, *J. Atmos. Sci.*, 57:1854-1871.

Brechtel, F. J., and Kreidenweis, S. M. (2000b). Predicting Particle Critical Supersaturation from Hygroscopic Growth Measurements in the Humidified TDMA. Part II: Laboratory and Ambient Studies, *J. Atmos. Sci.*, 57:1872-1887.

Busch, B., Kandler, K., Schutz, L., and Neususs, C. (2002). Hygroscopic Properties and Water-Soluble Volume Fraction of Atmospheric Particles in the Diameter Range from 50

nm to 3.8  $\mu\text{m}$  During LACE 98, *J. Geophys. Res.*, 107(D21), doi:10.1029/2000JD000228.

Carrico, C. M., Rood, M. J., and Ogren, J. A. (1998). Aerosol Light Scattering Properties at Cape Grim, Tasmania, During the First Aerosol Characterization Experiment (ACE 1), *J. Geophys. Res.*, 103(D13):16565-16574.

Carrico, C. M., Rood, M. J., Ogren, J. A., Neususs, C., Wiedensohler, A., and Heintzenberg, J. (2000). Aerosol Optical Properties at Sagres, Portugal During ACE-2, *Tellus B.*, 52:694-715.

Carrico, C. M., Kreidenweis, S. M., Malm, W. C., Day, D. E., Lee, T., Carrillo, J., McMeeking, G. R., and Collett, J. L. (2005). Hygroscopic Growth Behavior of a Carbon-Dominated Aerosol in Yosemite National Park, *Atmos. Environ.*, 39:1393-1404.

Chan, C. K., Kwok, C. S., and Chow, A. H. L. (1997). Study of Hygroscopic Properties of Aqueous Mixtures of Disodium Fluorescein and Sodium Chloride Using an Electrodynamic Balance, *Pharmaceut. Res.*, 14:1171-1175.

Chebbi, A., and Carlier, P. (1996). Carboxylic Acids in the Troposphere, Occurrence, Sources, and Sinks: A Review, *Atmos. Environ.*, 30:4233-4249.

Chylek, P., Ramaswamy, V., and Cheng, R. J. (1984). Effect of Graphitic Carbon on the Albedo of Clouds, *J. Atmos. Sci.*, 41:3076-3084.

Clegg, S. L., Brimblecombe, P., and Wexler, A. S. (1998). A Thermodynamic Model of the System  $\text{H}^+$  -  $\text{NH}_4^+$  -  $\text{Na}^+$  -  $\text{SO}_4^{2-}$  -  $\text{NO}_3^-$  -  $\text{Cl}^-$  -  $\text{H}_2\text{O}$  at 298.15 K, *J. Phys. Chem. A.*, 102:2155-2171.

Cocker, D. R., Whitlock, N. E., Flagan, R. C., and Seinfeld, J. H. (2001). Hygroscopic Properties of Pasadena, California Aerosol, *Aerosol Sci. Tech.*, 35:637-647.

Cohen, M. D., Flagan, R. C., and Seinfeld, J. H. (1987a). Studies of Concentrated Electrolyte-Solutions Using the Electrodynamic Balance .1. Water Activities for Single-Electrolyte Solutions, *J. Phys. Chem.*, 91:4563-4574.

Cohen, M. D., Flagan, R. C., and Seinfeld, J. H. (1987b). Studies of Concentrated Electrolyte-Solutions Using the Electrodynamic Balance .2. Water Activities for Mixed-Electrolyte Solutions, *J. Phys. Chem.*, 91:4575-4582.

Covert, D. S., Heintzenberg, J., and Hansson, H. C. (1990). Electrooptical Detection of External Mixtures in Aerosols, *Aerosol Sci. Tech.*, 12:446-456.

Covert, D. S., Hansson, H.-C., Winkler, P., and Heintzenberg, J. (1991). The Degree of Mixing of Hygroscopic Properties in Source and Receptor Locations in Northern Europe, *Proceedings of AAAR 1991*, 7-11 October 1991, Travers City, Michigan, USA.

Covert, D. S., and Heintzenberg, J. (1993). Size Distributions and Chemical-Properties of Aerosol at Ny Alesund, Svalbard, *Atmos. Environ.*, 27:2989-2997.

Crahan, K. K., Hegg, D., Covert, D. S., and Jonsson, H. (2004). An Exploration of Aqueous Oxalic Acid Production in the Coastal Marine Atmosphere, *Atmos. Environ.*, 38:3757-3764.

Cruz, C. N., and Pandis, S. N. (2000). Deliquescence and hygroscopic growth of mixed inorganic-organic atmospheric aerosol, *Environ. Sci. Technol.*, 34:4313-4319.

Dougle, P. G., Veefkind, J. P., and ten Brink, H. M. (1998). Crystallisation of Mixtures of Ammonium Nitrate, Ammonium Sulphate and Soot, *J. Aerosol Sci.*, 29:375-386.

Ferron, G. A., Karg, E., Busch, B., and Heyder, J. (2005). Ambient Particles at an Urban, Semi-Urban and Rural Site in Central Europe: Hygroscopic Properties, *Atmos. Environ.*, 39:343-352.

Fisseha, R., Dommen, J., Gaeggeler, K., Weingartner, E., Samburova, V., Kalberer, M., and Baltensperger, U. (2006). Online Gas and Aerosol Measurement of Water Soluble Carboxylic Acids in Zurich, *J. Geophys. Res.*, 111(D12316), doi:10.1029/2005JD006782.

Flagan, R. C. (1999). On Differential Mobility Analyzer Resolution, *Aerosol Sci. Tech.*, 30:556-570.

Gasparini, R., Li, R. J., Collins, D. R., Ferrare, R. A., and Brackett, V. G. (2006). Application of Aerosol Hygroscopicity Measured at the Atmospheric Radiation Measurement Program's Southern Great Plains Site to Examine Composition and Evolution, *J. Geophys. Res.*, 111(D5), doi:10.1029/2004JD005448.

Gysel, M., Weingartner, E., and Baltensperger, U. (2002): Hygroscopicity of Aerosol Particles at Low Temperatures. 2. Theoretical and Experimental Hygroscopic Properties of Laboratory Generated Aerosols, *Environ. Sci. Technol.*, 36:63-68.

Gysel, M., Weingartner, E., Nyeki, S., Paulsen, D., Baltensperger, U., Galambos, I., and Kiss, G. (2004). Hygroscopic Properties of Water-Soluble Matter and Humic-like Organics in Atmospheric Fine Aerosol, *Atmos. Chem. Phys.*, 4:35-50.

Hameri, K., Laaksonen, A., Vakeva, M., and Suni, T. (2001). Hygroscopic Growth of Ultrafine Sodium Chloride Particles, *J. Geophys. Res.*, 106(D18):20749-20757.

Hameri, K., Vakeva, M., Hansson, H. C., and Laaksonen, A. (2000). Hygroscopic Growth of Ultrafine Ammonium Sulphate Aerosol Measured Using an Ultrafine Tandem Differential Mobility Analyzer, *J. Geophys. Res.*, 105(D17):22231-22242.

- Hand, J. L., Ames, R. B., Kreidenweis, S. M., Day, D. E., and Malm, W. C. (2000). Estimates of Particle Hygroscopicity During the Southeastern Aerosol and Visibility Study, *J. Air Waste Manage.*, 50:677-685.
- Hand, J. L., and Kreidenweis, S. M. (2002). A New Method for Retrieving Particle Refractive Index and Effective Density from Aerosol Size Distribution Data, *Aerosol Sci. Tech.*, 36:1012-1026.
- Hansson, H. C., Rood, M. J., Koloutsou-Vakakis, S., Hameri, K., Orsini, D., and Wiedensohler, A. (1998). NaCl aerosol particle hygroscopicity dependence on mixing with organic compounds, *J. Atmos. Chem.*, 31:321-346.
- Hegg, D. A., Covert, D. S., Crahan, K. K., Jonsson, H., and Liu, Y. (2006). Measurements of Aerosol Size-Resolved Hygroscopicity at Sub and Supermicron Sizes, *Geophys. Res. Lett.*, 33, doi:10.1029/2006GL026747.
- Hegg, D. A., Covert, D. S., Jonsson, H., and Covert, P. A. (2007). An Instrument for Measuring Size-Resolved Aerosol Hygroscopicity at Both Sub- and Super-Micron Sizes, *Aerosol Sci. Tech.*, 41:873-883.
- Hering, S. V., and McMurry, P. H. (1991). Optical Counter Response to Monodisperse Atmospheric Aerosols, *Atmos. Environ.*, 25:463-468.
- Hinds, W. C. (1999). *Aerosol Technology: Properties, Behavior, and Measurement of Airborne Particles, Second Edition*, John Wiley & Sons, New York.
- Huang, X. F., Hu, M., He, L. Y., and Tang, X. Y. (2005). Chemical Characterization of Water-Soluble Organic Acids in PM<sub>2.5</sub> in Beijing, China, *Atmos. Environ.*, 39:2819-2827.
- Huang, X. F., Yu, J. Z., He, L. Y., and Yuan, Z. B. (2006). Water-Soluble Organic Carbon and Oxalate in Aerosols at a Coastal Urban Site in China: Size Distribution Characteristics, Sources, and Formation Mechanisms, *J. Geophys. Res.*, 111, D22212, doi:10.1029/2006JD007408.
- Kawamura, K., and Ikushima, K. (1993). Seasonal-Changes in the Distribution of Dicarboxylic-Acids in the Urban Atmosphere, *Environ. Sci. Technol.*, 27:2227-2235.
- Kawamura, K., and Sakaguchi, F. (1999). Molecular Distributions of Water Soluble Dicarboxylic Acids in Marine Aerosols Over the Pacific Ocean Including Tropics, *J. Geophys. Res.*, 104(D3):3501-3509.
- Kerminen, V. M., Ojanen, C., Pakkanen, T., Hillamo, R., Aurela, M., and Merilainen, J. (2000). Low-Molecular-Weight Dicarboxylic Acids in an Urban and Rural Atmosphere, *J. Aerosol Sci.*, 31:349-362.

- Khwaja, H. A. (1995). Atmospheric Concentrations of Carboxylic-Acids and Related-Compounds at a Semiurban Site, *Atmos. Environ.*, 29:127-139.
- Kim, J., Yoon, S. C., Jefferson, A., and Kim, S. W. (2006). Aerosol Hygroscopic Properties During Asian Dust, Pollution, and Biomass Burning Episodes at Gosan, Korea in April 2001, *Atmos. Environ.*, 40:1550-1560.
- Knutson, E. O., and Whitby, K. T. (1975). Aerosol Classification by Electric Mobility: Apparatus, Theory, and Applications, *J. Aerosol Sci.*, 6:443-451.
- Kotchenruther, R. A., and Hobbs, P. V. (1998). Humidification Factors of Aerosols from Biomass Burning in Brazil, *J. Geophys. Res.*, 103(D24):32081-32089.
- Kreisberg, N. M., Stolzenburg, M. R., Hering, S. V., Dick, W. D., and McMurry, P. H. (2001). A New Method for Measuring the Dependence of Particle Size Distributions on Relative Humidity, with Application to the Southeastern Aerosol and Visibility Study, *J. Geophys. Res.*, 106(D14):14935-14949.
- Li, Z. D., Williams, A. L., and Rood, M. J. (1998). Influence of Soluble Surfactant Properties on the Activation of Aerosol Particles Containing Inorganic Solute, *J. Atmos. Sci.*, 55:1859-1866.
- Lide, D. R. (2005). *CRC Handbook of Chemistry and Physics*, 86<sup>th</sup> Edition, CRC Press, Florida.
- Lightstone, J. M., Onasch, T. B., Imre, D., and Oatis, S. (2000). Deliquescence, Efflorescence, and Water Activity in Ammonium Nitrate and Mixed Ammonium Nitrate/Succinic Acid Microparticles, *J. Phys. Chem. A.*, 104:9337-9346.
- Liu, B. Y. H., and Lee, K. W. (1975). Aerosol Generator of High Stability, *Am. Ind. Hyg. Assoc. J.*, 36:861-865.
- Liu, B. Y. H., Pui, D. Y. H., Whitby, K. T., Kittelson, D. B., Kousaka, Y., and McKenzie, R. L. (1978). Aerosol Mobility Chromatograph - New Detector for Sulfuric-Acid Aerosols, *Atmos. Environ.*, 12:99-104.
- Magi, B. I., and Hobbs, P. V. (2003). Effects of Humidity on Aerosols in Southern Africa During the Biomass Burning Season, *J. Geophys. Res.*, 108(D13), doi:10.1029/2002JD002144.
- Malm, W. C., Day, D. E., Kreidenweis, S. M., Collett, J. L., Carrico, C., McMeeking, G., and Lee, T. (2005). Hygroscopic Properties of an Organic-Laden Aerosol, *Atmos. Environ.*, 39:4969-4982.

Massling, A., Wiedensohler, A., Busch, B., Neususs, C., Quinn, P., Bates, T., and Covert, D. (2003). Hygroscopic Properties of Different Aerosol Types Over the Atlantic and Indian Oceans, *Atmos. Chem. Phys.*, 3:1377-1397.

Massling, A., Leinert, S., Wiedensohler, A., and Covert, D. (2007). Hygroscopic Growth of Sub-Micrometer and One-Micrometer Aerosol Particles Measured During ACE-Asia, *Atmos. Chem. Phys.*, 7:3249-3259.

McMurry, P. H., and Stolzenburg, M. R. (1989). On the Sensitivity of Particle-Size to Relative-Humidity for Los-Angeles Aerosols, *Atmos. Environ.*, 23:497-507.

Peng, C., Chan, M. N., and Chan, C. K. (2001). The Hygroscopic Properties of Dicarboxylic and Multifunctional Acids: Measurements and UNIFAC Predictions, *Environ. Sci. Technol.*, 35:4495-4501.

Peng, C. G., and Chan, C. K. (2001). The Water Cycles of Water-Soluble Organic Salts of Atmospheric Importance, *Atmos. Environ.*, 35:1183-1192.

Pilinis, C., Seinfeld, J. H., and Grosjean, D. (1989). Water-Content of Atmospheric Aerosols, *Atmos. Environ.*, 23:1601-1606.

Poore, M. W. (2000). Oxalic Acid in PM<sub>2.5</sub> Particulate Matter in California, *J. Air Waste Manage.*, 50:1874-1875.

Prenni, A. J., DeMott, P. J., Kreidenweis, S. M., Sherman, D. E., Russell, L. M., and Ming, Y. (2001). The Effects of Low Molecular Weight Dicarboxylic Acids on Cloud Formation, *J. Phys. Chem. A.*, 105:11240-11248.

Prenni, A. J., De Mott, P. J., and Kreidenweis, S. M. (2003). Water Uptake of Internally Mixed Particles Containing Ammonium Sulfate and Dicarboxylic Acids, *Atmos. Environ.*, 37:4243-4251.

Rader, D. J., and McMurry, P. H. (1986). Application of the Tandem Differential Mobility Analyzer to Studies of Droplet Growth or Evaporation, *J. Aerosol Sci.*, 17:771-787.

Rood, M. J., Larson, T. V., Covert, D. S., and Ahlquist, N. C. (1985). Measurement of Laboratory and Ambient Aerosols with Temperature and Humidity Controlled Nephelometry, *Atmos. Environ.*, 19:1181-1190.

Saxena, P., Hildemann, L. M., McMurry, P. H., and Seinfeld, J. H. (1995). Organics Alter Hygroscopic Behavior of Atmospheric Particles, *J. Geophys. Res.*, 100(D9):18755-18770.

- Saxena, P., and Hildemann, L. M. (1996). Water-Soluble Organics in Atmospheric Particles: A Critical Review of the Literature and Application of Thermodynamics to Identify Candidate Compounds, *J. Atmos. Chem.*, 24:57-109.
- Saxena, P., and Hildemann, L. M. (1997). Water Absorption by Organics: Survey of Laboratory Evidence and Evaluation of UNIFAC for Estimating Water Activity, *Environ. Sci. Technol.*, 31:3318-3324.
- Seinfeld, J. H., and Pandis, S. N. (2006). *Atmospheric Chemistry and Physics, Second Edition*, Wiley-Interscience, New York.
- Sekigawa, K. (1983). Estimation of the Volume Fraction of Water-Soluble Material in Sub-Micron Aerosols in the Atmosphere, *J. Meteorol. Soc. Jpn.*, 61:359-367.
- Sheridan, P. J., Jefferson, A., and Ogren, J. A. (2002). Spatial Variability of Submicrometer Aerosol Radiative Properties Over the Indian Ocean During INDOEX, *J. Geophys. Res.*, 107(D19), doi:10.1029/2000JD000166.
- Snider, J. R., and Petters, M. D. (2007). Optical Particle Counter Measurement of Marine Aerosol Hygroscopic Growth, *Atmos. Chem. Phys. Disc.*, 7:12381-12415.
- Sorooshian, A., Varutbangkul, V., Brechtel, F. J., Ervens, B., Feingold, G., Bahreini, R., Murphy, S. M., Holloway, J. S., Atlas, E. L., Buzorius, G., Jonsson, H., Flagan, R. C., and Seinfeld, J. H. (2006a). Oxalic Acid in Clear and Cloudy Atmospheres: Analysis of Data from International Consortium for Atmospheric Research on Transport and Transformation 2004, *J. Geophys. Res.*, 111, D23S45, doi:10.1029/2005JD006880.
- Sorooshian, A., Brechtel, F. J., Ma, Y. L., Weber, R. J., Corless, A., Flagan, R. C., and Seinfeld, J. H. (2006b). Modeling and Characterization of a Particle-into-Liquid Sampler (PILS), *Aerosol Sci. Tech.*, 40:396-409.
- Sorooshian, A., Ng, N. L., Chan, A. W. H., Feingold, G., Flagan, R. C., and Seinfeld, J. H. (2007a). Particulate Organic Acids and Overall Water-Soluble Aerosol Composition Measurements from the 2006 Gulf of Mexico Atmospheric Composition and Climate Study (GoMACCS), *J. Geophys. Res.*, 112, D13201, doi:10.1029/2007JD008537.
- Sorooshian, A., Lu, M. -L., Brechtel, F. J., Jonsson, H., Feingold, G., Flagan, R. C., and Seinfeld, J. H. (2007b). On the Source of Organic Acid Aerosol Layers Above Clouds, *Environ. Sci. Technol.* 41:4647-4654.
- Stolzenburg, M., Kreisberg, N., and Hering, S. (1998). Atmospheric Size Distributions Measured by Differential Mobility Optical Particle Size Spectrometry, *Aerosol Sci. Tech.*, 29:402-418.



Svenningsson, I. B., Hansson, H. C., Wiedensohler, A., Ogren, J. A., Noone, K. J., and Hallberg, A. (1992). Hygroscopic Growth of Aerosol-Particles in the Po Valley, *Tellus B.*, 44:556-569.

Svenningsson, B., Hansson, H. C., Wiedensohler, A., Noone, K., Ogren, J., Hallberg, A., and Colville, R. (1994). Hygroscopic Growth of Aerosol-Particles and its Influence on Nucleation Scavenging In-Cloud - Experimental Results from Kleiner-Feldberg, *J. Atmos. Chem.*, 19:129-152.

Svenningsson, B., Hansson, H. C., Martinsson, B., Wiedensohler, A., Swietlicki, E., Cederfelt, S. I., Wendisch, M., Bower, K. N., Choularton, T. W., and Colville, R. N. (1997). Cloud Droplet Nucleation Scavenging in Relation to the Size and Hygroscopic Behaviour of Aerosol Particles, *Atmos. Environ.*, 31:2463-2475.

Swietlicki, E., Zhou, J. C., Berg, O. H., Martinsson, B. G., Frank, G., Cederfelt, S. I., Dusek, U., Berner, A., Birmili, W., Wiedensohler, A., Yuskiewicz, B., and Bower, K. N. (1999). A Closure Study of Sub-Micrometer Aerosol Particle Hygroscopic Behaviour, *Atmos. Res.*, 50:205-240.

Swietlicki, E., Zhou, J. C., Covert, D. S., Hameri, K., Busch, B., Vakeva, M., Dusek, U., Berg, O. H., Wiedensohler, A., Aalto, P., Makela, J., Martinsson, B. G., Papaspiropoulos, G., Menten, B., Frank, G., and Stratmann, F. (2000). Hygroscopic Properties of Aerosol Particles in the Northeastern Atlantic During ACE-2, *Tellus B.*, 52:201-227.

Tang, I. N., and Munkelwitz, H. R. (1993). Composition and Temperature-Dependence of the Deliquescence Properties of Hygroscopic Aerosols, *Atmos. Environ.*, 27:467-473.

Tang, I. N., and Munkelwitz, H. R. (1994a). Water Activities, Densities, and Refractive-Indexes of Aqueous Sulfates and Sodium-Nitrate Droplets of Atmospheric Importance, *J. Geophys. Res.*, 99:18801-18808.

Tang, I. N., and Munkelwitz, H. R. (1994b). Aerosol Phase-Transformation and Growth in the Atmosphere, *J. Appl. Meteorol.*, 33:791-796.

Videen, G., Pellegrino, P., Ngo, D., Videen, J. S., and Pinnick, R. G. (1997). Light-Scattering Intensity Fluctuations in Microdroplets Containing Inclusions, *Appl. Optics.*, 36:6115-6118.

Wang, J., Flagan, R. C., and J. H. Seinfeld (2003). A Differential Mobility Analyzer (DMA) System for Submicron Aerosol Measurements at Ambient Relative Humidity, *Aerosol Sci. Tech.*, 37:46-52.

Weast, R. C. (1987). *CRC Handbook of Chemistry and Physics*, 68<sup>th</sup> Edition, CRC Press, Florida.

Wise, M. E., Surratt, J. D., Curtis, D. B., Shilling, J. E., and Tolbert, M. A. (2003). Hygroscopic Growth of Ammonium Sulfate/Dicarboxylic Acids, *J. Geophys. Res.*, 108(D20), doi:10/1029/2003JD003775.

Yao, X. H., Fang, M., Chan, C. K., Ho, K. F., and Lee, S. C. (2004). Characterization of Dicarboxylic Acids in PM<sub>2.5</sub> in Hong Kong, *Atmos. Environ.*, 38:963-970.

Yu, J. Z., Huang, S. F., Xu, J. H., and Hu, M. (2005). When Aerosol Sulfate Goes Up, so does Oxalate: Implication for the Formation Mechanisms of Oxalate, *Environ. Sci. Technol.*, 39:128-133.

Zhang, X. Q., McMurry, P. H., Hering, S. V., and Casuccio, G. S. (1993). Mixing Characteristics and Water-Content of Submicron Aerosols Measured in Los-Angeles and at the Grand-Canyon, *Atmos. Environ.*, 27:1593-1607.

Table 3.1. Aerosol Hygroscopicity Measurement Techniques

Measurement Category	Measurement Description	Notes	Studies
Single particle levitation to directly measure mass change in response to humidity variation	Electrodynamic balance	Suitable only for laboratory studies; can study full RH hysteresis behavior	Cohen et al. 1987a, 1987b; Tang and Munkelwitz 1993, 1994a, 1994b; Peng et al. 2001; Peng and Chan 2001
Variation in aerosol light scattering coefficient with changing RH	Humidity-controlled nephelometry: either one or multiple RH-conditioned nephelometers, each typically operated at 3 wavelengths	Growth factor is estimated by the ratio of the humidification factor at a dry RH and an elevated RH	Rood et al. 1985; Carrico et al. 1998, 2000; Kotchenruther and Hobbs 1998; Sheridan et al. 2002; Magi and Hobbs 2003; Malm et al. 2005; Kim et al. 2006
Parallel unit operations to estimate growth factor of total aerosol from size distribution shifts	Comparison of size distributions from two aircraft wing probes: Passive cavity aerosol spectrometer probe (PCASP; dry RH) and forward scattering spectrometer probe (FSSP or F300; ambient RH)	Cannot compare aerosol at one particular size and is limited by the RH at ambient conditions	Kotchenruther and Hobbs 1998; Snider and Petters 2007
	Aerosol hydration spectrometer: Two OPCs in parallel at different RHs (48 - 53% and 88 - 92%)	Cannot compare aerosol at one particular size; typically requires 20 min for each sample (maximum = 40 min) (Hegg et al. 2006)	Hegg et al. 2006, 2007
	Dual Automated Classified Aerosol Detector: Two DMAs in parallel at different RHs	Cannot compare aerosol at one particular size	Wang et al. 2003
Unit operations in series to measure growth factor of size-classified aerosol from size distribution shifts	Humidified tandem DMA (HTDMA): Two DMAs in series with a humidification step in between	Usually restricted to sizes less than ~ 500 nm; limited by one RH at one time; time resolution can be as low as 15 min (Busch et al. 2002)	Sekigawa 1983; McMurry and Stolzenberg 1989; Covert et al. 1991; Zhang et al. 1993; Berg et al. 1998; Covert and Heintzenberg 1993; Swietlicki et al. 1999, 2000; Svenningsson et al. 1992, 1994, 1997; Cocker et al. 2001; Baltensperger et al. 2002; Busch et al. 2002; Massling et al. 2003; Gysel et al. 2004; Ferron et al. 2005; Carrico et al. 2005; Gasparini et al. 2006; Aklilu et al. 2006; Massling et al. 2007
	Relative humidity-moderated differential mobility optical particle size spectrometer (RH-DMOPSS): high flow DMA followed by an OPC and CPC operating in parallel. DMA and OPC are operated at different RHs; dry aerosol is used to calibrate the OPC continuously during operation	Can study only one wet RH at a time; measures shrinkage upon drying rather than growth upon humidification; initial humid diameters can be as large as 1.1 $\mu\text{m}$ ; time resolution is better than that of the HTDMA	Kreisberg et al. 2001
	Hygroscopic-differential mobility analyzer-aerodynamic particle sizer (H-DMA-APS): DMA followed by a dry APS and a separate RH-conditioned APS	Can study only one wet RH at a time	Massling et al. 2007
	Differential aerosol sizing and hygroscopicity spectrometer probe (DASH-SP): DMA followed by a parallel system of one WCPC and four OPCs, each of which has an upstream RH-conditioning module	Can study multiple RHs simultaneously; DMA upper size limit near 1 $\mu\text{m}$ ; OPCs detect particles in excess of 1 $\mu\text{m}$ ; time resolution as short as a few seconds	This study

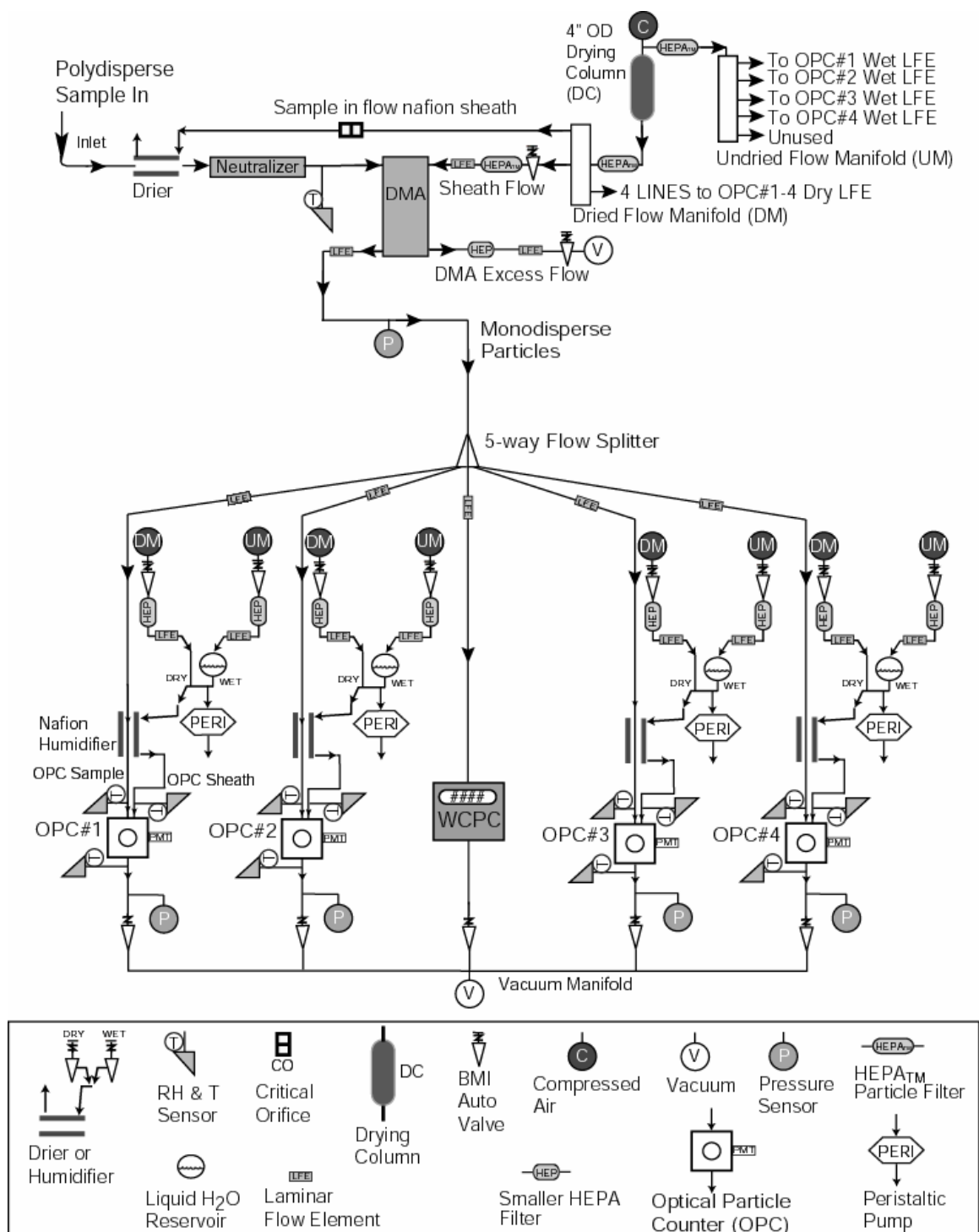


Figure 3.1. Schematic of DASH-SP.

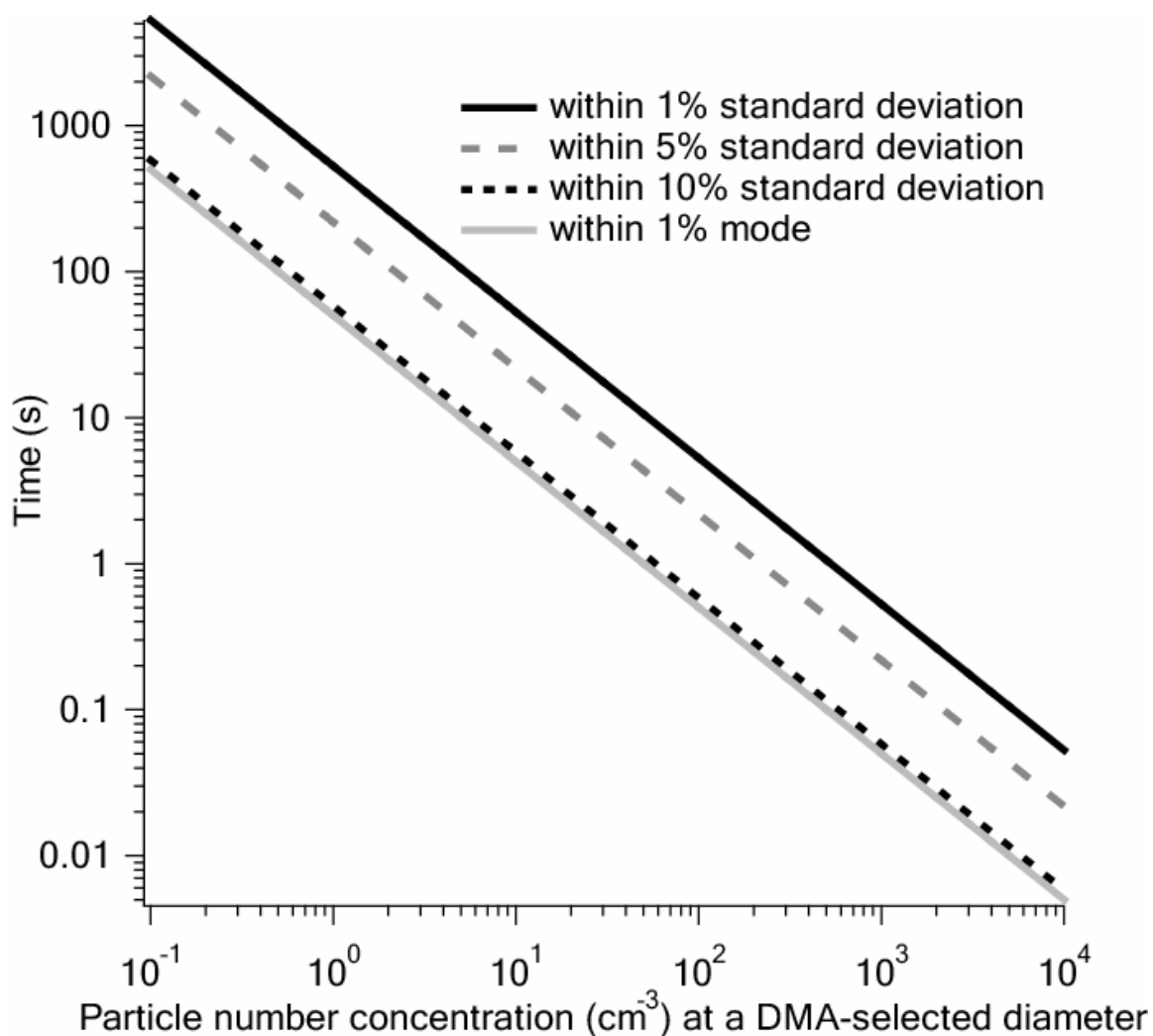


Figure 3.2. Time required as a function of particle number concentration to obtain sufficient pulses for the modal pulse height to be within 1% of the mode that would be obtained when counting at least 10,000 particles at constant particle composition. Also shown is the time needed for the standard deviation to be within 1%, 5%, and 10% of the standard deviation that would be obtained when counting at least 10,000 particles at constant particle composition.

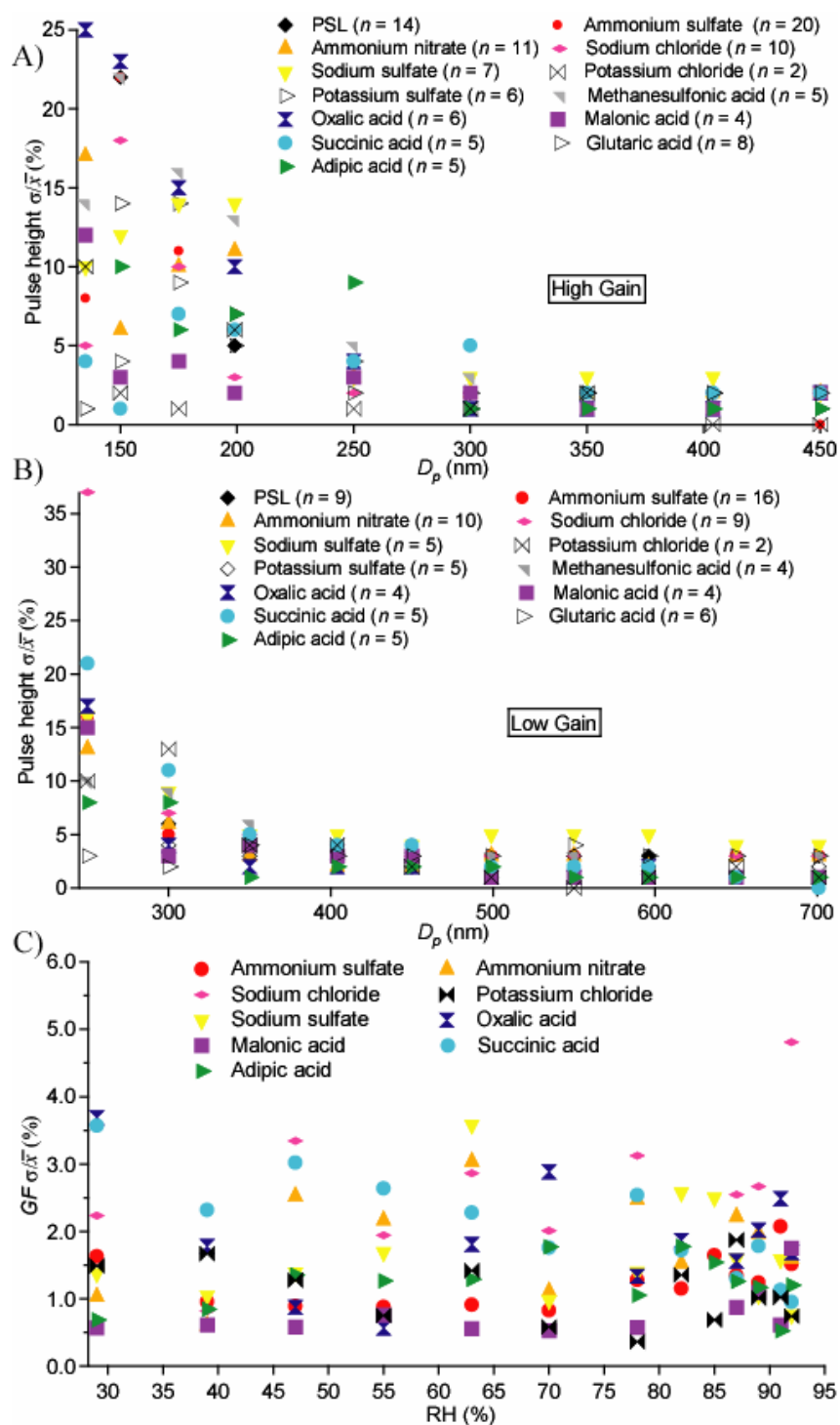


Figure 3.3. Stability statistics for different species and sizes over a time span of four months. Panel A corresponds to the high-gain OPC setting, and Panel B represents the low-gain setting for dry tests. Panel C represents stability statistics for growth factor during wet studies using the high-gain OPC configuration ( $n > 20$  for each salt in the bottom panel).

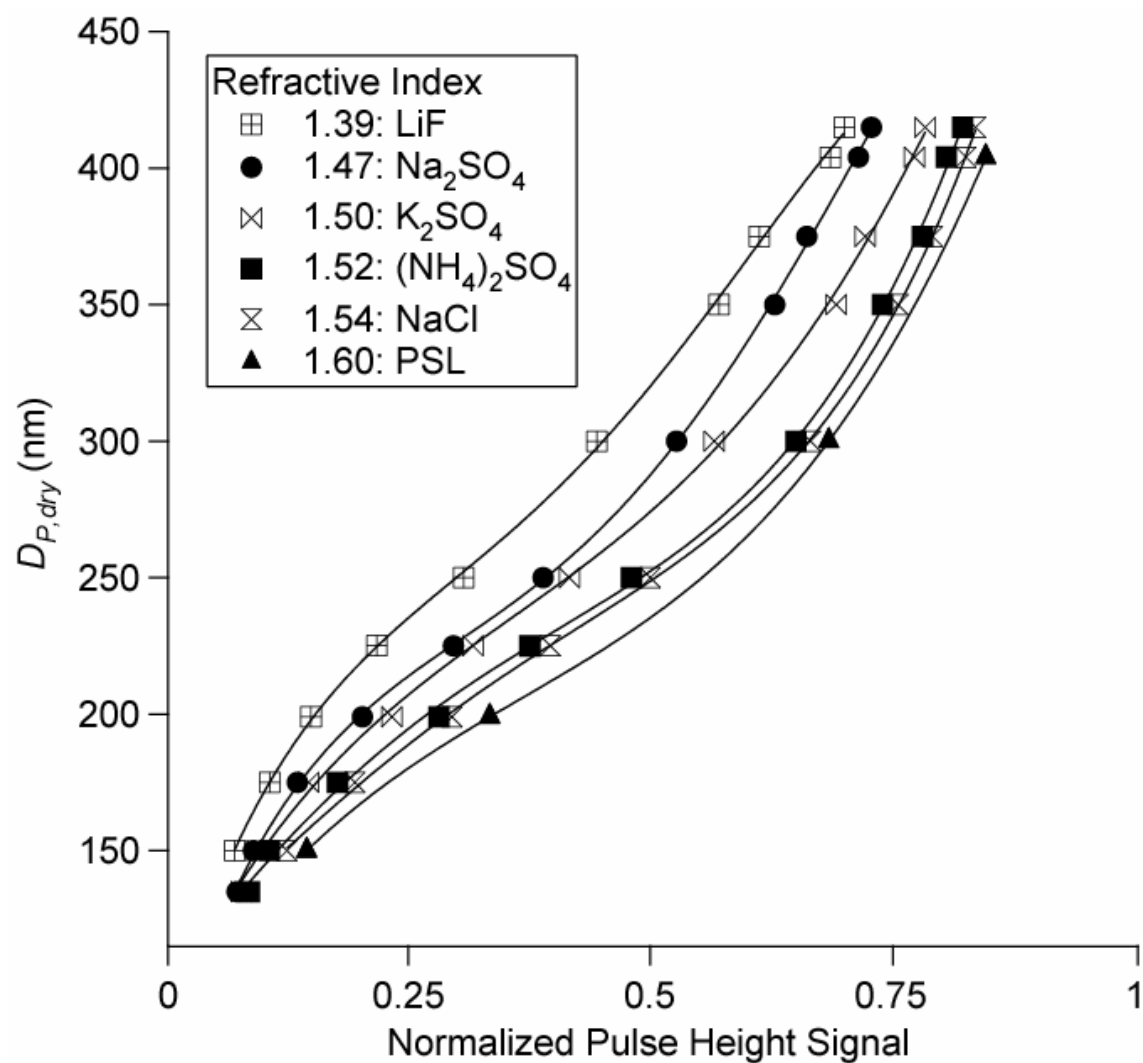


Figure 3.4. OPC response as a function of dry particle size for salts of different refractive index. These results are from one OPC for a single set of calibrations performed for each salt. All OPCs show the same general behavior.

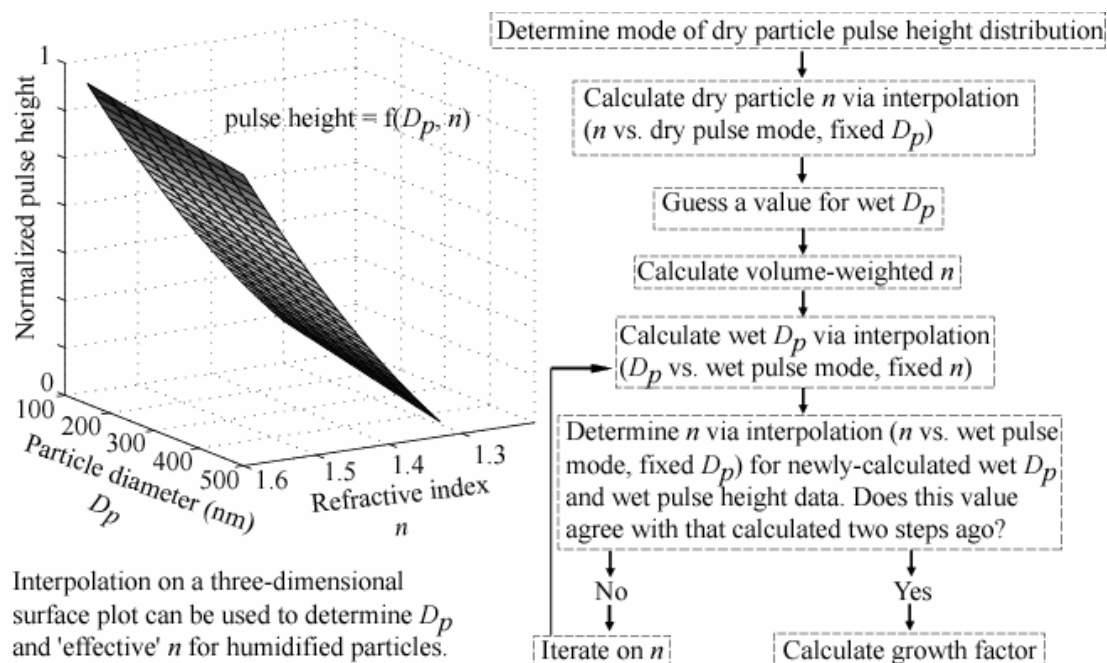


Figure 3.5. Data processing procedure from DASH-SP raw pulse height data to growth factors ( $GF$ s) for both laboratory-generated aerosol, for which the composition and refractive index ( $n$ ) of the dry particles are known, and for ambient aerosol, where the composition and refractive index of the dry particles are unknown. The dry pulse height distribution mode is first used to determine the dry particle refractive index, which is used to calculate a volume-weighted wet particle refractive index, taking into account the volume fractions of water and the particle. Iterations are subsequently carried out on the three-dimensional surface shown to converge on a wet particle refractive index. The  $D_p$  corresponding to the latter value of refractive index and the wet pulse height distribution mode is subsequently used to calculate growth factor.



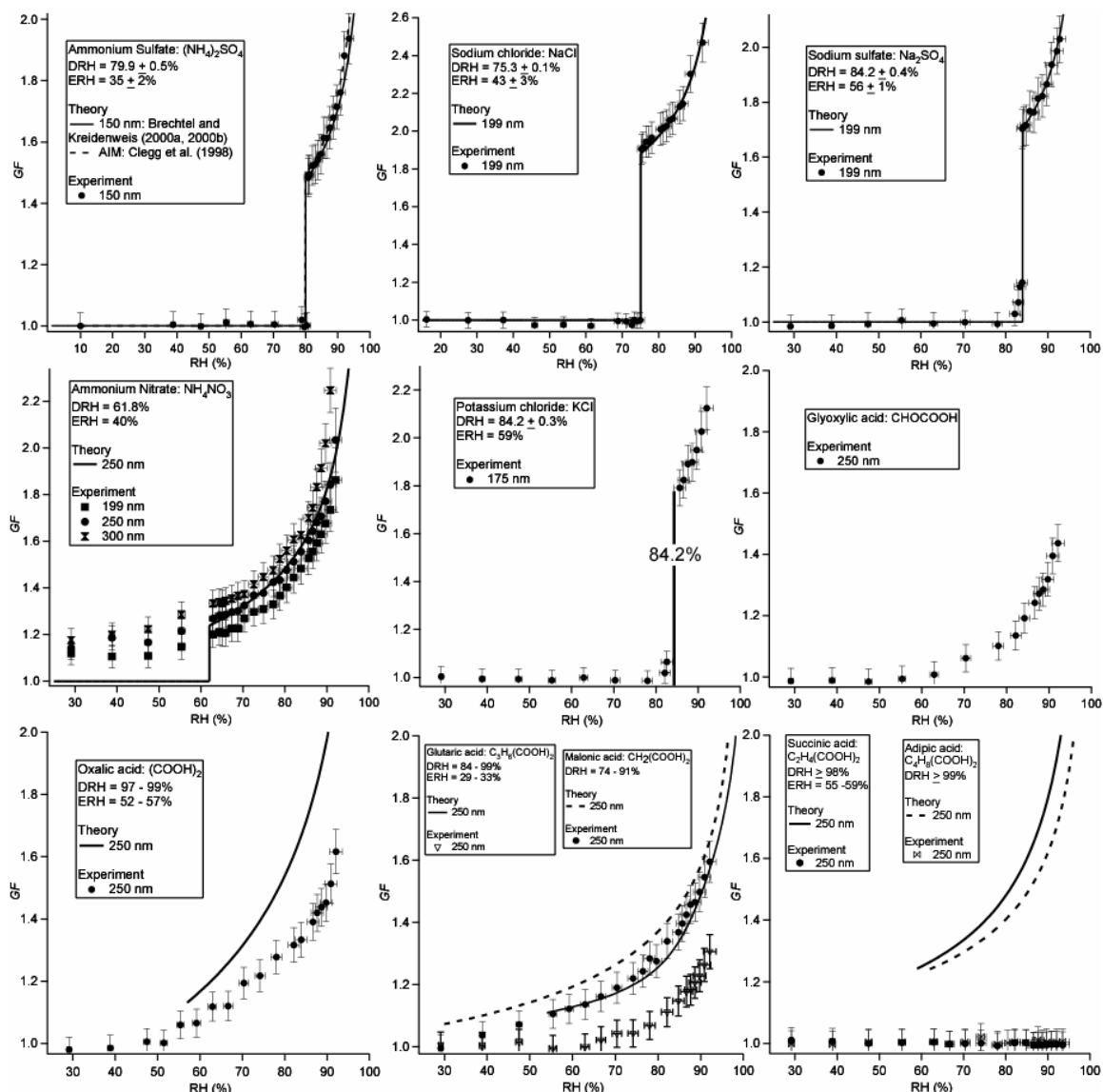


Figure 3.6. Experimentally determined growth factor curves for inorganic and organic acid species. Predictions from the Brechtel and Kreidenweis (2000a, 2000b) model are shown for all salts except for glyoxylic acid and potassium chloride, while predictions from the Clegg et al. (1998) model are also shown for ammonium sulfate. It should be noted that these two models differ in that the Brechtel and Kreidenweis (2000a, 2000b) model includes the Kelvin term to account for droplet curvature. Sampled particles within the size range of the DASH-SP are sufficiently large so that the Kelvin effect correction is relatively small. The error bars reflect uncertainties associated with the RH and sizing (DMA and OPC) measurements. The reported deliquescence RH (DRH) and efflorescence RH (ERH) values are from the following references: Saxena and Hildemann (1997) and Peng et al. (2001) for organic acids, and Seinfeld and Pandis (2006) for the inorganic species.

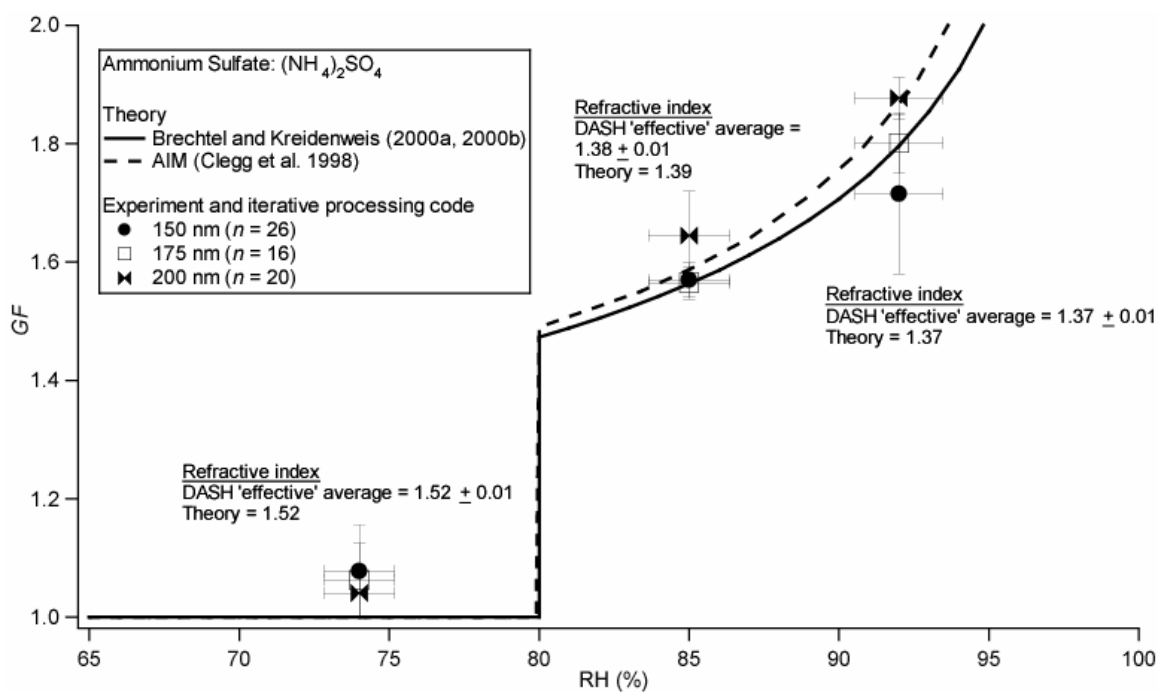


Figure 3.7. Comparison between two thermodynamic models and DASH-SP data for ammonium sulfate particles. The reported DASH-SP results were calculated by using iterative procedure in Figure 3.5 to process the OPC pulse height data. The RH error bars reflect uncertainties in the RH measurement, while the *GF* error bars reflect the precision of the measurement after several repetitive trials.

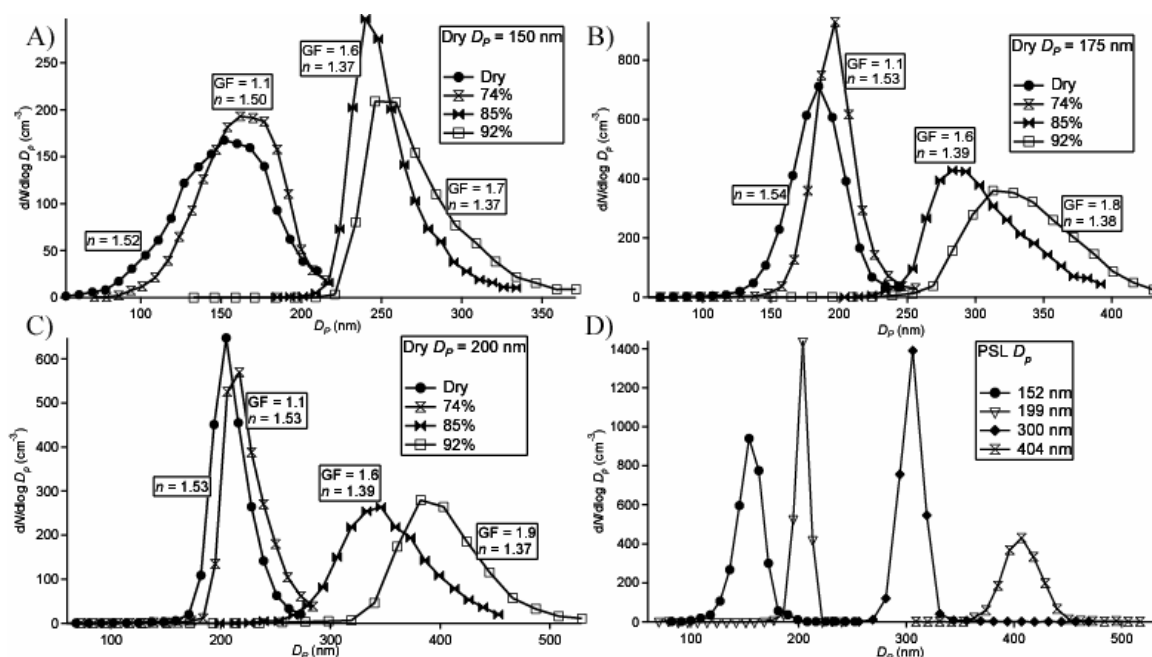


Figure 3.8. Size distributions from wet ammonium sulfate and dry PSL aerosol laboratory tests. Panels A, B, and C correspond to ammonium sulfate tests in which DMA-selected dry particle sizes of 150, 175, and 200 nm, respectively, were exposed to RHs of < 8% (dry), 74%, 85%, and 92%. Each curve is labeled with its calculated growth factor and “effective” refractive index ( $n$ ), as calculated from the iterative data processing procedure in Figure 3.5. Panel D corresponds to dry PSL size distributions to show that for spherical particles the distributions are narrower than those for salts that may not be perfectly spherical. The size distributions tend to be broader near the minimum and maximum size detection limits of the OPCs.

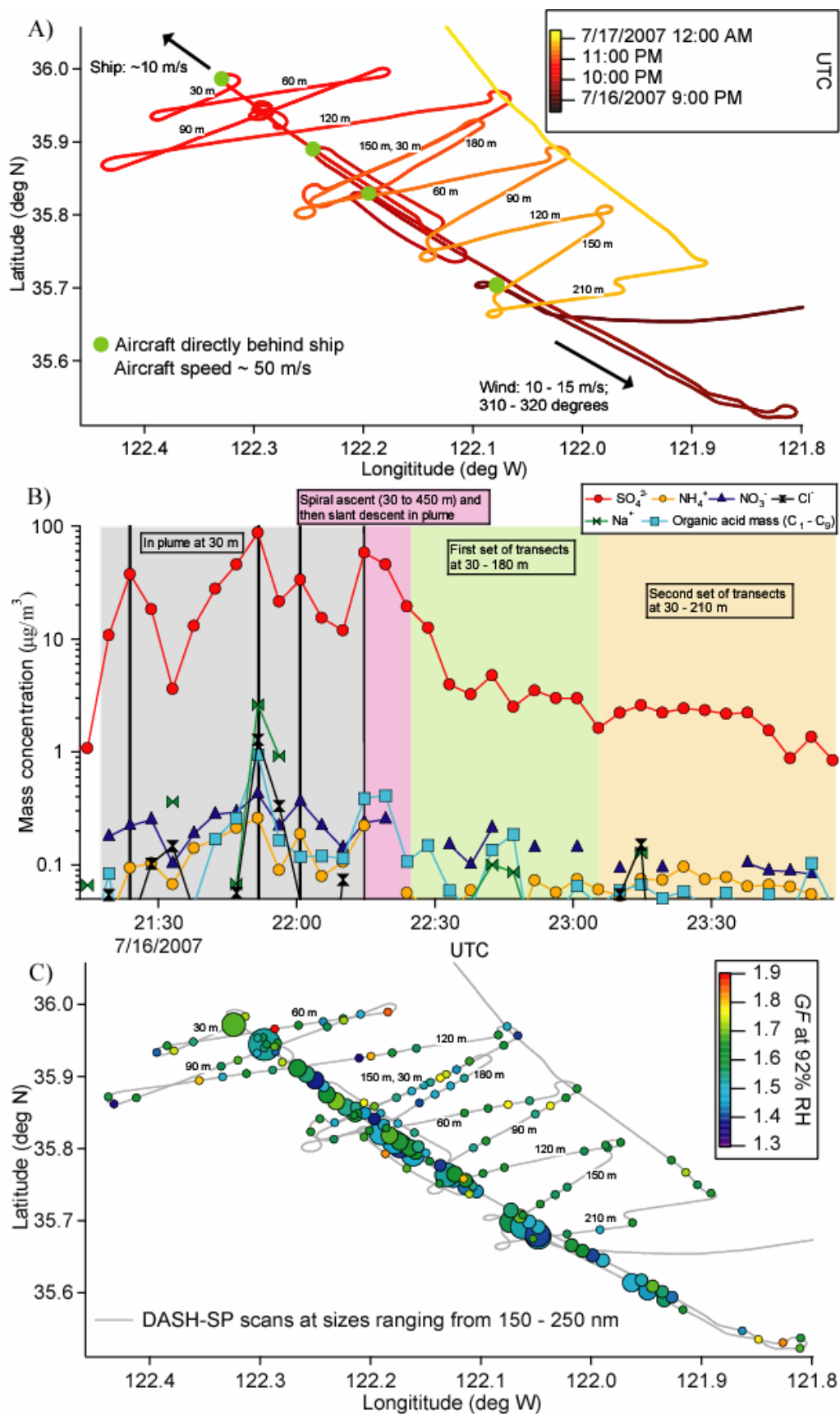


Figure 3.9. Panel A) Flight tracks during a MASE II flight (July 16, 2007) during which the Twin Otter aircraft sampled emissions from a large cargo ship off the central coast of California. The duration of the ship exhaust plume measurements was approximately 2.5 h. The plane flew at an altitude of 30 m in the ship's plume, before performing multiple cross-wind transects of the plume at the labeled altitudes. Panel B) Water-soluble species concentrations as measured by a PILS onboard the Twin Otter. The four, black vertical lines indicate when the aircraft was immediately behind the ship. Panel C) Growth factors at an RH of 92%. Marker sizes are proportional to the submicrometer particle number concentration (range =  $50 - 365,000 \text{ cm}^{-3}$ ), as determined by a DMA.

## **Chapter 4**

# **Oxalic Acid in Clear and Cloudy Atmospheres: Analysis of Data from International Consortium for Atmospheric Research on Transport and Transformation 2004\***

---

\*This chapter is reproduced by permission from “Oxalic Acid in Clear and Cloudy Atmospheres: Analysis of Data from International Consortium for Atmospheric Research on Transport and Transformation 2004” by A. Sorooshian, V. Varutbangkul, F. J. Brechtel, B. Ervens, G. Feingold, R. Bahreini, S. M. Murphy, J. S. Holloway, E. L. Atlas, G. Buzorius, H. Jonsson, R. C. Flagan, and J. H. Seinfeld, *J. Geophys. Res.*, *111*, D23S45, doi:10.1029/2005JD006880, 2006. Copyright 2006. American Geophysical Union.

## 4.1 Abstract

Oxalic acid is often the leading contributor to the total dicarboxylic acid mass in ambient organic aerosol particles. During the 2004 International Consortium for Atmospheric Research on Transport and Transformation (ICARTT) field campaign, nine inorganic ions (including  $\text{SO}_4^{2-}$ ) and five organic acid ions (including oxalate) were measured onboard the Center for Interdisciplinary Remotely-Piloted Aircraft Studies (CIRPAS) Twin Otter research aircraft by a particle-into-liquid sampler (PILS) during flights over Ohio and surrounding areas. Five local atmospheric conditions were studied: (1) cloud-free air, (2) power plant plume in cloud-free air with precipitation from scattered clouds overhead, (3) power plant plume in cloud-free air, (4) power plant plume in cloud, and (5) clouds uninfluenced by local pollution sources. The aircraft sampled from two inlets: a counterflow virtual impactor (CVI) to isolate droplet residuals in clouds and a second inlet for sampling total aerosol. A strong correlation was observed between oxalate and  $\text{SO}_4^{2-}$  when sampling through both inlets in clouds. Predictions from a chemical cloud parcel model considering the aqueous-phase production of dicarboxylic acids and  $\text{SO}_4^{2-}$  show good agreement for the relative magnitude of  $\text{SO}_4^{2-}$  and oxalate growth for two scenarios: power plant plume in clouds and clouds uninfluenced by local pollution sources. The relative contributions of the two aqueous-phase routes responsible for oxalic acid formation were examined; the oxidation of glyoxylic acid was predicted to dominate over the decay of longer-chain dicarboxylic acids. Clear evidence is presented for aqueous-phase oxalic acid production as the primary mechanism for oxalic acid formation in ambient aerosols.

## 4.2. Introduction

Dicarboxylic acids are ubiquitous in atmospheric aerosols (Norton et al., 1983; Kawamura and Kaplan, 1987; Kawamura and Ikushima, 1993; Khwaja et al., 1995; Kawamura et al., 1995, 1996, 2003, 2005; Liu et al., 1996; Kawamura and Sakaguchi, 1999; Limbeck and Puxbaum, 1999; Kerminen et al., 2000; Poore, 2000; Puxbaum et al., 2000; Pakkanen et al., 2001; Rohrl and Lammel, 2001; Yao et al., 2002a, 2004; Salam et al., 2003a, 2003b; Crahan et al., 2004; Shantz et al., 2004; Yu et al., 2005) and cloud droplets (Weathers et al., 1988; Limbeck and Puxbaum, 2000; Hegg et al., 2002; Loflund et al., 2002; Crahan et al., 2004); however, the physical and chemical routes by which these compounds form and are sequestered in particulate matter are not fully understood. The presence of dicarboxylic acids in pure and mixed aerosols may affect both deliquescence relative humidity and hygroscopic behavior (Cruz and Pandis, 1998; Brooks et al., 2002; Kumar et al., 2003); the radiative impact of particles containing dicarboxylic acids depends on their effectiveness in absorbing water as a function of relative humidity.

Oxalic acid,  $(\text{COOH})_2$ , a by-product of fossil fuel combustion, biomass burning, and biogenic activity, has been shown in many studies to be the most abundant dicarboxylic acid in tropospheric aerosols (Kawamura and Kaplan, 1987; Kawamura and Ikushima, 1993; Kawamura et al., 1995, 1996, 2003, 2005; Liu et al., 1996; Kawamura and Sakaguchi, 1999; Kerminen et al., 2000; Poore, 2000; Loflund et al., 2002; Yao et al., 2002a, 2004; Salam et al., 2003a, 2003b; Crahan et al., 2004; Yu et al., 2005). Studies have suggested, however, that primary sources of particulate oxalic acid cannot



account for ambient levels that have been measured globally (Poore, 2000; Warneck, 2003; Yao et al., 2004; Yu et al., 2005).

Oxalate, the anion of oxalic acid, is typically detected by analytical techniques such as ion chromatography (IC). In some observations, oxalate-containing particles show two distinct accumulation modes at  $0.2 \pm 0.1 \mu\text{m}$  and  $0.7 \pm 0.2 \mu\text{m}$ , with the larger mode being associated with  $\text{SO}_4^{2-}$  (Kerminen et al., 1999, 2000; Kalberer et al., 2000; Yao et al., 2002b, 2003; Crahan et al., 2004). Suggested oxalate formation mechanisms in the fine particulate mode include in-cloud processing, oxidation of gaseous species followed by condensation, and aerosol surface reactions (Kawamura and Ikushima, 1993; Faust, 1994; Chebbi and Carlier, 1996; Blando and Turpin, 2000; Yao et al., 2002b, 2003; Mochida et al., 2003; Turekian et al., 2003). Crahan et al. (2004) measured in a coastal marine environment the air-equivalent concentrations of  $\text{SO}_4^{2-}$  and oxalate in cloudwater as approximately two and three times greater, respectively, than concentrations measured below cloud. They also detected glyoxylic acid, an intermediate in aqueous-phase oxalate production (Leitner and Dore, 1997), in cloudwater samples. Based on data from the literature and results from their own study, Yu et al. (2005) argue that a dominant in-cloud pathway can explain the close correlation between  $\text{SO}_4^{2-}$  and oxalate.

During the 2004 International Consortium for Atmospheric Research on Transport and Transformation (ICARTT) study, measurements made by surface, airborne, and satellite platforms focused on examining the nature of air masses in the northeastern United States, the western Atlantic Ocean, and the Maritime Provinces of Canada. In August 2004, the Center for Interdisciplinary Remotely-Piloted Aircraft

Studies (CIRPAS) Twin Otter (TO), based at Hopkins International Airport in Cleveland, Ohio, participated in the ICARTT field campaign. The focus of the CIRPAS participation was to study aerosol and cloud condensation nuclei (CCN) physics and chemistry.

The goal of the present work is to elucidate oxalic acid formation in the atmosphere. We analyze airborne measurements of  $\text{SO}_4^{2-}$  and oxalate in different conditions in the atmosphere around Ohio during ICARTT. The majority of the oxalate measurements were made while sampling either droplet residuals (the particle remaining after a cloud droplet has evaporated) or the total aerosol in clouds (the sum of interstitial aerosol and droplet residuals). We investigate the correlation between  $\text{SO}_4^{2-}$  and oxalate, and the role of other organic acids in aqueous-phase production of oxalate. The relative contributions of different aqueous-phase reactions are examined, as well as the magnitude of  $\text{SO}_4^{2-}$  and oxalate mass production rates in cloud-processed air. Finally, we assess the extent to which these rates agree with those predicted by a cloud parcel model containing a state-of-the-art mechanism for aqueous-phase production of  $\text{SO}_4^{2-}$  and oxalate.

#### **4.3. Twin Otter (TO) Research Aircraft**

Table 4.1 summarizes the instruments that were operated on the TO. Chemical composition data analyzed here were obtained by a particle-into-liquid sampler (PILS), which will be described below. A quadrupole Aerodyne Aerosol Mass Spectrometer (AMS) (Jayne et al., 2000) provided chemical composition data for non-refractory aerosol species. Aerosol size distribution data (10 - 800 nm diameter) were obtained by a Caltech dual differential mobility analyzer (DMA) system (Wang et al., 2003), also

called the Dual Automated Classified Aerosol Detector (DACAD). An external Passive Cavity Aerosol Spectrometer Probe (PCASP, PMS, modified by DMT Inc.) and an external Forward Scattering Spectrometer Probe (FSSP, PMS, modified by DMT Inc.) provided cloud and aerosol size distributions for the following particle diameter ranges, respectively: 0.1 to 2.0  $\mu\text{m}$  and 2.0 to 40.0  $\mu\text{m}$ .

The main inlet was the primary inlet supplying sample flow to all instruments anytime the TO was outside of clouds and sometimes when it was inside clouds. The main inlet of the TO uses two diffusers to decelerate air by a factor of ten before it is sent to the sampling instruments. Hegg et al. (2005) characterized the behavior of the TO inlet; they report that the transmission efficiency of the inlet under standard flight conditions for particle diameters less than 3.5  $\mu\text{m}$  is near unity, decreasing for larger particles until 5.5  $\mu\text{m}$  and above, where the transmission efficiency remains slightly in excess of 60%. This transmission efficiency persists for particle diameters up to 9  $\mu\text{m}$ , the upper limit of the characterization tests. When used in clouds, the main inlet sampled the total aerosol, which included interstitial aerosol and residual particles from evaporated cloud droplets. Evidence that droplet residuals were being sampled through the main inlet during ICARTT included the detection of aqueous-phase precursors to oxalic acid.

A counterflow virtual impactor (CVI) inlet was employed only in clouds. The CVI selectively samples cloud droplets larger than a cut-off diameter of 10 ( $\pm 20\%$ )  $\mu\text{m}$  by isolating them from the interstitial aerosol, by means of inertial impaction. During the time the CVI was used, sample flow was diluted and divided for supply only to the PILS, AMS, a particle soot absorption photometer (PSAP, Radiance Research Inc.), and a

condensation particle counter (TSI CPC 3010), during which time, all other instruments still sampled air entering through the main inlet. The instruments behind the CVI sampled residual particles from evaporated cloud droplets. PILS concentrations reported during CVI sampling should be considered as the lower limit to their true value due to uncertainties in the CVI transmission efficiency.

#### **4.4. PILS-IC Measurements**

The PILS-IC is a quantitative technique for measuring water-soluble ions, including inorganic and organic acid ions in aerosol particles. The PILS developed and used in this study (Brechtel Manufacturing Inc., [www.brechtel.com](http://www.brechtel.com)) is based on the prototype design (Weber et al., 2001) with key modifications, including integration of a liquid sample fraction collector and real-time control of the steam injection tip temperature (Sorooshian et al., 2006). Ambient air is sampled through a 1 - micrometer cut-size impactor and a set of three denuders (URG and Sunset Laboratories) to remove inorganic and organic gases that may bias aerosol measurements. The two annular glass denuders (URG-2000-30x242-3CSS) used for removal of inorganic gases are coated with solutions of either 2% sodium carbonate or 2% phosphoric acid (for removal of acidic and basic gases, respectively) in a solution of 100 mL of Milli Q water, 80 mL of methanol, and 2 g of glycerol. The third denuder (Sunset Laboratory Inc.), composed of 15 thin carbon filter paper sheets (3.15 cm x 20.32 cm x 0.04 cm thick) with 0.2 cm gaps between them, removes organic gases. Sample air mixes with steam in a condensation chamber where rapid adiabatic mixing produces a high water supersaturation. Droplets grow sufficiently large to be collected by inertial impaction before being delivered to

vials held on a rotating carousel. The contents of the vials are subsequently analyzed off-line using a dual IC system (ICS-2000 with 25  $\mu\text{L}$  sample loop, Dionex Inc.) for simultaneous anion and cation analysis. A fraction of each liquid sample was frozen for future re-analysis with a longer IC program capable of better detection of organic acid ions.

Nine inorganic ions ( $\text{Na}^+$ ,  $\text{NH}_4^+$ ,  $\text{K}^+$ ,  $\text{Mg}^{2+}$ ,  $\text{Ca}^{2+}$ ,  $\text{Cl}^-$ ,  $\text{NO}_2^-$ ,  $\text{NO}_3^-$ , and  $\text{SO}_4^{2-}$ ) and five organic acid ions (oxalate, malonate, glutarate, pyruvate, and glyoxylate) were measured during the field campaign. The limit of detection (LOD) for each ion was determined by running the lowest concentration standard detectable by the IC and using the average concentration plus three times the standard deviation ( $n = 50$ ) to calculate the air-equivalent concentration of each ion. The LODs for the ions measured using the PILS-IC technique for this study are all below  $0.1 \mu\text{g}/\text{m}^3$ , with the organic anions and  $\text{SO}_4^{2-}$  exhibiting LOD's below  $0.03 \mu\text{g}/\text{m}^3$ .

Measurements presented for glyoxylate, pyruvate, and glutarate are derived from re-analyzing the stored liquid volumes (they were frozen for 13 months). It should be noted that all vials were spiked with 5  $\mu\text{L}$  of dichloromethane prior to storage to prevent biological processing. The mass concentrations of  $\text{SO}_4^{2-}$ ,  $\text{NH}_4^+$ , and oxalate from the original and re-analyzed vials were compared for Flight 5 on 9 August 2004 to determine the magnitude of variability between the two batches (Table 4.2). The concentrations measured in the original vials for the three ions exceeded the re-analyzed concentrations by factors between 1.54 and 1.83, indicating that there was degradation of ion levels during storage; potential explanations for degradation include the freezing and thawing process, the interaction of the sample with the vial surface, and the effect of

dichloromethane. The reported concentrations of glyoxylate, pyruvate, and glutarate should be viewed as a lower limit, assuming that their degradation rates were similar to those measured for  $\text{SO}_4^{2-}$ ,  $\text{NH}_4^+$ , and oxalate.

## **4.5. Field Measurements**

### **4.5.1. Field Data Summary**

The TO flight tracks for all twelve flights between 1 and 21 August 2004 are shown in Figure 4.1. Several flights focused on areas downwind of the Monroe Power Plant (Monroe County, Michigan) and the Conesville Power Plant (Coshocton County, Ohio), both of which are coal-burning plants. The following types of atmospheric conditions were encountered over the entire 12-flight mission: (1) cloud-free air, (2) power plant plume in cloud-free air with precipitation from scattered clouds overhead, (3) power plant plume in cloud-free air, (4) power plant plume in cloud, and (5) clouds uninfluenced by local pollution sources. Figure 4.2 illustrates the sampling strategy used by the TO during flights when atmospheric condition types 2 and 4 were encountered; the TO flew a number of horizontal transect legs perpendicular to the studied plume. Figure 4.2b represents the case of type 3 as well, but in the absence of precipitation. Data grouped in the two cloud cases were identified by elevated relative humidities ( $\text{RH} > 100\%$ ) and high liquid water content ( $\text{LWC} > 0.1 \text{ g/m}^3$ ). Plumes were identified by a dramatic increase in aerosol number concentration. It should be noted that the clouds uninfluenced by local pollution sources may have still been influenced by long-range transport of urban pollution.

Characteristics of the clouds observed during Flights 5 and 12 (9 and 21 August 2004, respectively), which are flights that will be examined in detail subsequently, are

representative of the clouds encountered over the entire mission. The clouds were typically cumulus, which broadly encompasses stratocumulus, fair-weather cumulus, and cumulus congestus clouds, with thicknesses between 500 to 700 m. Cloud bases stayed on the order of 1500 m, and as the day proceeded, the tops grew from around 2000 m to between 2300 and 2700 m. Typical LWC vertical profiles indicate that there were slightly variable cloud base altitudes, and some entrainment drying. The LWC in clouds typically ranged from 0.1 to 1.0 g/m<sup>3</sup>. The lower troposphere in the sampling region was marked by turbulence and convective instability. Soundings obtained on the ascents out of Cleveland show ambient and dew point temperatures tracing nearly straight lines to cloud base altitudes, reflecting instability and vigorous mixing. On average, vertical velocities near the cloud bases tended to be 1 m/s, increasing to 2 m/s during passes at higher levels in cloud.

Figure 4.3 displays the vertical distribution of specific ions and the total mass measured through both inlets for the entire 12-flight mission. The mass concentrations of oxalate and SO<sub>4</sub><sup>2-</sup> were evenly scattered at all altitudes up to about 2250 m, where they start to decrease, indicating the beginning of the free troposphere. Oxalate constituted up to 6.3% of the total water-soluble ionic mass as measured by the PILS. Table 4.3 shows the variation of the molar ratio of oxalate relative to three of the major inorganic ions for each atmospheric condition encountered and each inlet used. Overall, oxalate exhibits the strongest correlation with SO<sub>4</sub><sup>2-</sup>, followed by NH<sub>4</sub><sup>+</sup> and then NO<sub>3</sub><sup>-</sup>. Ammonium is correlated with SO<sub>4</sub><sup>2-</sup>, since acidic sulfate-containing particles absorb ammonia. Oxalate and NO<sub>3</sub><sup>-</sup> show a poor correlation, suggesting that these ions arise from different processes.

The strongest correlations between  $\text{SO}_4^{2-}$  and oxalate were seen for the power plant plume in cloud category when droplet residual particles ( $R^2 = 0.97$ ,  $n = 11$ ) and the total aerosol ( $R^2 = 0.77$ ,  $n = 44$ ) were being individually sampled through the CVI and the main inlet, respectively. The next strongest correlation ( $R^2 = 0.75$ ,  $n = 54$ ) was observed when the total aerosol was measured in clouds uninfluenced by local pollution sources. During ICARTT, the highest single oxalate measurement ( $0.94 \mu\text{g}/\text{m}^3$ ) occurred in a droplet residual sample from a power plant plume in cloud. Aerosol samples in that category represented the largest average oxalate ( $0.28 \mu\text{g}/\text{m}^3$ ) and  $\text{SO}_4^{2-}$  ( $6.51 \mu\text{g}/\text{m}^3$ ) loadings. Flight 5, the flight with the majority of the data points representing power plant plume in cloud, will be addressed in the next section.

The lowest  $\text{SO}_4^{2-}$  and oxalate loadings occurred in cloud-free air (Figure 4.4); these samples showed no correlation between  $\text{SO}_4^{2-}$  and oxalate. Oxalate exceeded detection limits in only 24 out of 196 samples collected in cloud-free air. For total aerosol samples collected in power plant plume in cloud-free air, a moderate correlation between  $\text{SO}_4^{2-}$  and oxalate ( $R^2 = 0.56$ ,  $n = 18$ ) was observed only for the precipitation case, where oxalate levels exceeded  $0.1 \mu\text{g}/\text{m}^3$ . In the absence of precipitation, the correlation was much lower ( $R^2 = 0.21$ ,  $n = 10$ ) and oxalate levels were less than  $0.1 \mu\text{g}/\text{m}^3$ . All samples representing power plant plume in cloud-free air with precipitation from scattered clouds overhead are from Flight 4 on 8 August 2004, where oxalate constituted up to 5.1% of the water-soluble ionic mass, which corresponded to the vial with the maximum oxalate loading ( $0.33 \mu\text{g}/\text{m}^3$ ). Table 4.3 shows that oxalate was measured in the greatest amount relative to  $\text{SO}_4^{2-}$  during this flight compared to all total aerosol samples from other atmospheric condition categories; however, no key aqueous-



phase intermediates in oxalic acid formation were detected. Therefore, we cannot preclude sources of oxalic acid other than cloud processing, such as gas-phase oxidation of parent organic species followed by condensation.

As noted in the Introduction, previous studies have ruled out primary sources as the main formation mechanism for oxalic acid based on spatial and temporal characteristics (Poore, 2000; Yao et al., 2004; Yu et al., 2005). If primary sources were responsible for observed oxalate levels, then comparable levels should have been measured in all of the aforementioned atmospheric conditions encountered. That the oxalate-to-sulfate molar ratios in the two cloud categories (power plant plume in cloud and clouds uninfluenced by local pollution sources) show consistency and that the oxalate mass concentrations in cloud-free air were significantly lower is consistent with the hypothesis of an in-cloud production pathway for oxalate. Although  $\text{SO}_4^{2-}$  and oxalate are not directly linked chemically, the correlation between their levels is a result of the fact that both formation mechanisms require the aqueous medium. While information regarding the size distribution of oxalate and  $\text{SO}_4^{2-}$  is not available from the PILS measurements, past studies have noted similar size distributions of these two species, suggesting a common source (Yao et al., 2003; Crahan et al., 2004). Further evidence for aqueous oxalate production is provided by the detection of aqueous intermediates in oxalate formation, including glyoxylate, which was measured in 6 CVI samples (clouds uninfluenced by local pollution sources) and 13 total aerosol samples (9 in clouds uninfluenced by local pollution sources and 4 in clouds influenced by power plant plumes).

#### 4.5.2. Case Study: Power Plant Plume in Cloud (Flight 5 on 9 August 2004)

On 9 August 2004 (1709–2216 UT), the TO sampled the Conesville Power Plant plume in cloud (Figure 4.5a). Located south of Cleveland, this plant emits  $\text{SO}_2$  and  $\text{NO}_x$  at rates of  $1.31 \times 10^8$  kg/yr and  $2.16 \times 10^7$  kg/yr, respectively, and VOCs at  $1.21 \times 10^5$  kg/yr (<http://www.emissionsonline.org/nei99v3/plant/pl44374x.htm>, 1999). The plume was transported northeast ( $\sim 230^\circ$ ) at wind speeds between 6 and 12 m/s. Figure 4.5b shows the TO altitude, LWC, and aerosol number concentration. The TO flew a stair-step pattern between altitudes of 1500 and 2200 m downwind of the plant between 1815 and 2140 UT. LWC measurements reached values as high as  $0.94 \text{ g/m}^3$ .

Typical FSSP cloud droplet size distributions showed a number concentration mode ranging from 7.7 to 9.0  $\mu\text{m}$  with a geometric standard deviation ranging between 1.2 and 1.5. All instruments were sampling the total aerosol through the main inlet, which when used in cloud, as noted earlier, contained a mixture of interstitial aerosol, particles that contain significant amounts of water but are not activated (usually  $< 2 \mu\text{m}$ ), and droplet residuals. The DACAD measured a consistent bimodal size distribution with increasing distance downwind of the power plant in cloud, with a smaller mode that grew from 25 to 42 nm (Figure 4.6). The aerosol number concentration outside of cloud and close to the power plant was dominated by particles with  $D_p < 40 \text{ nm}$ . A cloud-processing mode in the range between 100 and 200 nm was measured throughout the flight. The hygroscopic growth factor for the larger mode ranged between 1.16 and 1.20 at the relative humidities shown in Figure 4.6. The growth factors are low relative to that for pure ammonium sulfate particles (1.17 compared to 1.44 for pure ammonium sulfate

at 77% RH), suggesting that the sampled aerosol was composed of less hygroscopic components.

Figure 4.5c shows a time series of  $\text{SO}_4^{2-}$ , various organic ions, and the volume concentration, from the DACAD, of the total aerosol sampled ( $D_p < 1 \mu\text{m}$ ). There is significant growth in  $\text{SO}_4^{2-}$ , oxalate, and the aerosol volume concentration in the plume proceeding downwind of the power plant. The aerosol volume concentration and the  $\text{SO}_4^{2-}$  loadings are correlated and close in magnitude, suggesting that most of the volume growth was a result of the conversion of  $\text{SO}_2$  to  $\text{SO}_4^{2-}$ . The ammonium-to-sulfate molar ratio was between 1.1 and 1.6 for most of the flight downwind of the plant, indicating that there was insufficient ammonia to neutralize the relatively high level of sulfuric acid. This high level of acidity can also explain why virtually no  $\text{NO}_3^-$  was detected ( $< 0.3 \mu\text{g}/\text{m}^3$ ). The aerosol volume concentration reached a maximum close to 40 km downwind of the plant (2043 UT), the point at which the highest  $\text{SO}_4^{2-}$  and oxalate loadings occurred ( $18.90$  and  $0.61 \mu\text{g}/\text{m}^3$ , respectively). Oxalate grew with increasing distance from the plant as well, representing between 0.5 and 3.1% of the total water-soluble mass for the majority of the flight and 2.6% in the vial with its maximum mass. Out-of-plume, oxalate concentrations dropped below  $0.1 \mu\text{g}/\text{m}^3$ , and  $\text{SO}_4^{2-}$  dropped to between 1 and  $5 \mu\text{g}/\text{m}^3$ .

Aqueous-phase precursors to oxalate were only identified in cloud, offering support to the hypothesis of an aqueous formation pathway. Glyoxylate, the anion of glyoxylic acid, was measured in two successive vials, at a level on the order of  $0.06 \mu\text{g}/\text{m}^3$ , while oxalate was measured as  $0.26 \mu\text{g}/\text{m}^3$  and  $0.39 \mu\text{g}/\text{m}^3$  in these two vials. Two other vials contained  $0.03 \mu\text{g}/\text{m}^3$  glyoxylate, while oxalate was at  $0.19 \mu\text{g}/\text{m}^3$  and

0.36  $\mu\text{g}/\text{m}^3$ . Pyruvate, the anion of pyruvic acid, which is thought to be a precursor of glyoxylic acid (Lim et al., 2005), was measured at a level between 0.09 and 0.10  $\mu\text{g}/\text{m}^3$ . Glutarate, the anion of the glutaric acid ( $\text{C}_5$  dicarboxylic acid), reached a maximum level of 0.24  $\mu\text{g}/\text{m}^3$ . One vial contained 0.05  $\mu\text{g}/\text{m}^3$  of malonate, the anion of malonic acid ( $\text{C}_3$  dicarboxylic acid). Longer-chain dicarboxylic acids such as glutaric acid are oxidized in the aqueous phase leading to smaller dicarboxylic acids, ultimately reaching oxalic acid (Kawamura and Sakaguchi, 1999). The aforementioned data alone do not reveal the relative contribution from the decay of longer-chain acids such as glutarate and the oxidation of glyoxylate to the production of oxalate mass; this will be explored subsequently.

Since the concentrations of  $\text{SO}_4^{2-}$  and oxalate are correlated and they are both typically found in the same mode in the submicrometer aerosol size range, it is hypothesized that oxalate is formed in the aqueous phase, for which the presence of key aqueous intermediates to oxalic acid provides evidence. The mass concentrations of  $\text{SO}_4^{2-}$  and oxalate were higher in the Flight 5 total aerosol samples as compared to the total aerosol and droplet residual measurements in clouds uninfluenced by local pollution sources from other flights. This is hypothesized to be a result of longer cloud processing times for sampled particles during Flight 5 since the clouds were more abundant and closely packed. Also, some of the highest LWC values from the entire mission were observed, leading to increased partitioning of gases (specifically  $\text{SO}_2$ , organic precursors to oxalic acid, and oxidants) into the droplets, yielding higher mass production rates of  $\text{SO}_4^{2-}$  and oxalate. The highly turbulent nature of the lower atmosphere on 9 August 2004 may have also promoted the re-activation of evaporated droplets, via cycling in- and

out-of-cloud, to produce increasing amounts of  $\text{SO}_4^{2-}$  and oxalate. We note that although the  $\text{SO}_2$  concentrations were measured to be higher in plume compared to non-plume conditions, the concentrations of volatile organic carbon (VOC) species were essentially similar, which highlights the importance of non-VOC factors in oxalic acid production.

## **4.6. Cloud Parcel Model**

### **4.6.1. Description and Modifications**

The overall goal of this study is to understand the mechanism of occurrence of oxalic acid in atmospheric aerosols. The hypothesis is that aqueous-phase chemistry provides the dominant route for oxalic acid formation. To evaluate the extent to which the data support this hypothesis, we compare ambient oxalate measurements to predictions of a state-of-the-art microphysical/chemical cloud parcel model (Ervens et al., 2004) that simulates the activation of a population of aerosol particles. The model also simulates cloud cycles that are intended to represent the trajectory of a typical air parcel in a cloudy atmosphere, including gas and aqueous-phase chemical reactions. Four gas-phase VOC precursors of dicarboxylic acids are included; toluene and ethene represent anthropogenic emissions, isoprene represents biogenic emissions, and cyclohexene serves as a model compound for symmetrical alkenes similar to monoterpenes emitted by biogenic sources. The oxidation products of these species in the gas phase (glyoxal, glyoxylic acid, glycolic acid, hydroxyacetaldehyde, methylglyoxal, pyruvic acid, acetic acid, adipic acid, and glutaric acid) can transfer to the aqueous phase. Key multiphase organic reactions leading to the formation and depletion of oxalic acid are shown in Figure 4.7, whereas  $\text{SO}_4^{2-}$  production in the model is simply governed by  $\text{SO}_2$  oxidation

with  $\text{H}_2\text{O}_2$  and  $\text{O}_3$  (Seinfeld and Pandis, 1998). The model does not consider the volatilization of particulate dicarboxylic acids as their vapor pressures are sufficiently low ( $< 10^{-5}$  mm Hg) (Saxena and Hildemann, 1996; Tong et al., 2004).

Oxalic acid has two sources and one sink in the aqueous phase; it is consumed by OH oxidation to yield  $\text{CO}_2$ , and it is formed by OH oxidation of longer-chain dicarboxylic acids and glyoxylic acid (including its anion, glyoxylate). The formation route arising from the decay of longer dicarboxylic acids begins with adipic acid, which is formed primarily by the aqueous uptake of gas-phase products from cyclohexene oxidation by ozone and OH. Glutaric acid is formed by the aqueous oxidation of adipic acid and by the aqueous uptake of gas-phase products from the ozonolysis of cyclohexene. A series of oxidation steps leads, in order, from glutaric acid to succinic, malonic, and oxalic acids. The second formation route considers the oxidation of glyoxylic acid, which is formed by the OH oxidation of glyoxal, glycolate, methylglyoxal, and acetic acid. These intermediates are formed in the mechanisms associated with toluene, isoprene, and ethene. Lim et al. (2005) have proposed that methylglyoxal yields low volatility organic acids through oxidation to glyoxylic acid, via intermediate steps involving pyruvic and acetic acids, and finally to oxalic acid. The Ervens et al. (2004) aqueous-phase mechanism for isoprene oxidation has been modified to account for these reactions (Figure 4.7).

The model was applied to match the conditions encountered in the ICARTT flights. To estimate the soluble aerosol fraction (by mass), the total PILS water-soluble mass (inorganic and organic acid species) was divided by the sum of the PILS inorganic water-soluble mass and the organic mass measured by the AMS. The AMS organic

measurement includes both water-soluble and non-water soluble species. The model was also modified to incorporate measured ambient particle size distributions.

Since measurements were carried out in plumes, it is necessary to account for plume dispersion. Using measurements and estimates for various properties in the background air (including concentrations of SO<sub>2</sub>, H<sub>2</sub>O<sub>2</sub>, O<sub>3</sub>, gas-phase organic precursors, and the mixing ratio of water), the following parameterized factor, which will be called the entrainment rate, is applied to simultaneously simulate open system conditions and plume dilution,

$$\frac{\partial \phi_c}{\partial t} = -\frac{\eta}{b}(\phi_c - \phi_e)$$

where  $\phi_c$  and  $\phi_e$  are the values of a property in the moving parcels and in the entrained air, respectively. As will be discussed later, a constant measured value representative of background air in the ambient Ohio atmosphere was used for properties represented by  $\phi_e$ , while  $\phi_c$  was initialized with measured values at the source of the ambient process being simulated (one simulation to be addressed in a later section begins near a power plant stack) and subsequently calculated after each time step by the model. The equation above is analogous to the plume entrainment rate presented by Squires and Turner (1962), where a value of  $\eta = 0.2$  is based on their laboratory experiments. The parameter  $b$  is defined as the characteristic length scale for the entrainment process at time  $t$ , and taken here as 500 m, the typical depth of the clouds sampled. It is emphasized that the entrainment rate represents a simplified ad hoc factor.

The model simulates one - hour cloud cycles that are intended to represent the trajectory of a typical air parcel in a cloudy atmosphere. Twelve cloud cycles, limited by the prescribed trajectory used, are simulated for each experiment. One cloud cycle

begins with a parcel of air ascending from near the ground up through the mixed layer until activation in cloud. The parcel continues to rise and then descends through the cloud back to the mixed layer. During each cycle, a parcel is in-cloud for approximately 800 s; the same trajectory is then repeated with the number concentration remaining the same, but with particle sizes altered due to mass addition after each cycle. The LWC time evolution in the prescribed thermodynamic trajectory represents mixing and drying by entrained air, based on the host model from which it is derived. A rough estimate of the in-cloud residence time can be estimated by calculating the volume fraction of the boundary layer (BL) occupied by cloud (Feingold et al., 1998); typical volume fractions observed were between 20 and 25% suggesting that the hourly cloud contact time was between 720 and 900 s for a well-mixed BL, a range that is consistent with the cloud contact time of 800 s assumed in the cloud cycles. Photolysis rates are calculated for 40°N on June 21 at a height of 1 km for 12 hours starting at 6 am. The photolysis rates are time dependent and uninfluenced by the presence of clouds. Gas uptake and chemical aqueous-phase processes during each cycle occur only if the LWC exceeds 1 mg/kg and for each particle size bin if the sum of the ammonium and sulfate concentrations does not exceed 1 M. The model neglects aqueous-phase chemical processes when the ionic strength exceeds 1 M. This assumption is the result of a lack of data for the estimation of rate coefficients and because the solubility of organic gases typically decreases with increasing ionic strength. The model also does not consider aerosol loss by wet and dry deposition. Predictions for  $\text{SO}_4^{2-}$  and oxalate levels are presented here at the end of each cloud cycle. The comparison between field data and predictions should be viewed as semi-quantitative; for instance, the actual trajectories of air parcels are not known. Our



goal is to determine the extent to which the levels of  $\text{SO}_4^{2-}$  and oxalate measured are generally consistent with those predicted by a model that is based on cloud processing and aqueous-phase chemistry.

#### 4.6.2. Sensitivity Analysis

Prior to actually simulating the field data, we explore the sensitivity of the model to key parameters and initial conditions related to the initial particle population and the ambient atmosphere which include meteorological conditions and concentrations of gaseous species. Ervens et al. (2004) simulated generic “clean continental” and “polluted” cases, in which for a closed system (without entrainment of background air)  $\text{SO}_4^{2-}$  reached its ultimate level by the end of the third cloud cycle. With continuous replenishment of  $\text{SO}_2$ , on the other hand,  $\text{SO}_4^{2-}$  is predicted to form continuously. Oxidation of all organic species in the aqueous phase yields  $\text{HO}_2$  which replenishes the  $\text{H}_2\text{O}_2$  supply, also promoting  $\text{SO}_4^{2-}$  production. Sulfate production is controlled mainly by the initial concentrations of  $\text{SO}_2$  and  $\text{H}_2\text{O}_2$ ; a set of simulations show that the percentage change in  $\text{SO}_4^{2-}$  mass depends almost linearly on the percentage change in the initial  $\text{SO}_2$  concentration, while an increase in  $\text{H}_2\text{O}_2$  yields a less than proportional increase in  $\text{SO}_4^{2-}$ . The initial value of  $\text{SO}_4^{2-}$  is governed by the size distribution and soluble fraction of the initial particle population, where the initial soluble portion is assumed to be pure ammonium sulfate.

Ervens et al. (2004) showed that approximately eight cloud cycles are required for aqueous-phase organic oxidation to be completed in “clean continental” and “polluted” cases (since organics are involved in more oxidation steps than  $\text{SO}_4^{2-}$ ). As

with sulfur, with continued replenishment of organic precursor gases, organics continue reacting in the aqueous phase. Oxalic acid production does not exhibit the same degree of sensitivity to its precursor concentrations as does  $\text{SO}_4^{2-}$  to  $\text{SO}_2$ . In some cases, even less oxalic acid was produced when its gaseous precursor concentrations were increased. One explanation is that oxalic acid does not form in direct proportion to its parent precursor VOC (toluene, ethene, isoprene, cyclohexene) levels because of subsequent steps required in its formation and competing reactions that deplete OH, the primary oxidant in the aqueous-phase organic reactions. Examples of such competing reactions include the OH oxidation of hydrogen peroxide, formic acid, formate, and hydrated formaldehyde. In addition, several volatile organic species, including HCHO and  $\text{CO}_2$ , are produced as side-products in the aqueous-phase mechanism and do not contribute to oxalic acid production.

The base value of 500 m used for  $b$  in the entrainment rate was doubled and halved to explore the sensitivity of the production rates of  $\text{SO}_4^{2-}$  and oxalic acid to this parameterized factor. For these sensitivity tests, the concentrations of gas-phase species in the moving parcels ( $\phi_c$ ) and in the entrained air ( $\phi_e$ ) were identical and equal to the initial conditions for the case of clouds uninfluenced by local pollution sources in Table 4.4. As will be discussed later, these conditions are taken from field measurements made at 1000 m in the ambient Ohio atmosphere. With higher entrainment rates, the simulated particles are more effectively replenished with oxidants,  $\text{SO}_2$ , and organic precursors. Sulfate steadily changed to reach a final mass 28.3% greater and 27.2% lower when the entrainment rate was doubled and halved, respectively. Doubling and halving the base entrainment rate yielded 11% more and 3% less oxalic acid, respectively, at the end of

the simulation. Although less oxalic acid was formed in the case with the lowest replenishment rate of oxidants and precursors, oxalic acid was produced more efficiently relative to the total organic mass compared to simulations with higher entrainment rates; the oxalic acid predicted contribution to the total organic aerosol mass in the case with the lowest entrainment rate exceeded that of the other two cases by a minimum of 40% after the second cloud cycle. Concentrations of the first-generation aqueous-phase organic products, like adipic acid, showed the most proportional response to changes in the entrainment rate (they grew with increasing entrainment rate) followed by products in subsequent generations. Thus, the nonlinear response of oxalic acid to the entrainment rate compared to  $\text{SO}_4^{2-}$  can be explained by the multiple steps required in oxalic acid formation and the complex feedbacks of reaction chains in the chemical mechanism, specifically with the oxidant cycles (including  $\text{HO}_x$ ,  $\text{NO}_x$ ,  $\text{O}_3$ , and  $\text{H}_2\text{O}_2$ ). Also, the production of oxalic acid from glyoxylic acid oxidation is less efficient as the pH decreases, with the lowest pH values predicted in the simulation with the highest entrainment rate, because the rate constant of the oxidation of glyoxylic acid is an order of magnitude lower than that of its anion, glyoxylate.

The results of these sensitivity tests emphasize the critical nature of allowing for an open system with entrainment as opposed to a closed system when simulating the production rates of  $\text{SO}_4^{2-}$  and oxalic acid. Sulfate was shown to be the most sensitive to its precursor concentrations ( $\text{SO}_2$ ). Although the total organic aerosol mass and  $\text{SO}_4^{2-}$  are comparably sensitive to their precursor concentrations, oxalic acid is not. This is because the total organic mass is dominated by first-generation products in the aqueous phase, mainly adipic acid. Several oxidation steps are required to form oxalic acid, which

allows for the depletion of OH, the primary oxidant for organic compounds, and the production of volatile organic side-products that do not contribute to the production of oxalic acid.

#### **4.7. Comparison of Model Predictions to Field Measurements**

Measured ambient conditions from two specific flights (Table 4.4) are used here to initialize individual simulations to represent the two types of clouds that were studied; Flights 5 (9 August 2004) and 12 (21 August 2004) represent power plant plume in cloud and clouds uninfluenced by local pollution sources, respectively. The representative measurements from Flight 5 were made directly downwind of the Conesville Power Plant outside of cloud in its plume at 1000 m, whereas the Flight 12 measurements were made at the same altitude at a location in the Ohio atmosphere unaffected by local pollution sources. Gas-phase measurements were not carried out on the TO; estimates of the gaseous precursor concentrations were obtained from the WP-3D and Convair, operated by the National Oceanic and Atmospheric Administration (NOAA) and the Meteorological Service of Canada (MSC), respectively, which flew in the same areas as the TO, but at different times. In both simulations, concentrations of gas-phase species in the entrained air were set equal to those in the case of clouds uninfluenced by local pollution sources (Table 4.4), which represent background air conditions. Two key differences in the plume case are the higher SO<sub>2</sub> and aerosol number concentrations. Although the ethene and toluene levels are each below 0.15 ppb for both cases, they are nearly twice as large in the plume case suggesting that anthropogenic emissions were stronger directly downwind of the Conesville plant compared to a nearby location in the

Ohio atmosphere unaffected by local pollution sources. The soluble fraction of the initial particle population in the plume case is calculated to be 0.45 as opposed to 0.60 for clouds uninfluenced by local pollution sources. These two values agree with an alternate calculation of the soluble fraction by dividing the total PILS water-soluble mass by the DACAD-derived mass concentration assuming a total aerosol density of  $1.3 \text{ g/cm}^3$  in both cases. Measurements show that the sampled particles from the plume flight were composed of less hygroscopic components; the accumulation mode (100 to 200 nm) growth factors for the representative measurements during Flight 5 and 12 were 1.15 (77% RH) and 1.20 (75% RH), respectively. For the aerosol microphysics, it is assumed that the soluble fraction is entirely ammonium sulfate. The measured contribution of ammonium and sulfate to the total water-soluble mass measured by the PILS was on the order of 90% for the representative data for both flights; thus, the predicted  $\text{SO}_4^{2-}$  concentrations are adjusted, accounting for the 10% deficit in the initial water-soluble ammonium sulfate mass.

#### **4.7.1. Case Study: Power Plant Plume in Cloud**

Figure 4.8 shows predictions for the growth rate of  $\text{SO}_4^{2-}$  and various organic ions in the particle phase immediately downwind of the Conesville Power Plant. Sulfate is predicted to continuously increase, reaching a total submicrometer mass of  $31.4 \text{ } \mu\text{g/m}^3$ , with its sharpest increase predicted during cloud cycles 4 and 5. The predicted total organic mass, which grows to  $0.82 \text{ } \mu\text{g/m}^3$  by the end of the simulation, is dominated by oxalic and adipic acids (the model treats the oxidation of cyclohexene as a one-step process leading immediately to adipic acid). Ervens et al. (2004) state that the

cyclohexene mechanism provides an upper estimate for its contribution to the predicted dicarboxylic acid mass due to the simplified (one-step) chemistry in the model. The background concentration of cyclohexene is assumed to be 0.01 ppb, which was chosen to stay consistent with previous measurements showing that its emission rate is an order of magnitude less than that of toluene (Grosjean and Fung, 1984). Even though the background concentration of cyclohexene, which was not measured by the WP-3D or Convaire, in the atmosphere above Ohio may have been lower since adipate was not measured by the PILS, cyclohexene can be considered to serve as a surrogate compound for all symmetrical alkenes similar to monoterpenes.

Adipic and glutaric acids are oxidized, forming the shorter-chain acids starting with succinic acid, which then fuels malonic acid production. Succinic and malonic acids are each predicted to remain below  $0.01 \mu\text{g}/\text{m}^3$  and 0.3% of the total organic mass throughout the simulation. The oxidation of malonic acid leads to oxalic acid, which is predicted to grow to levels comparable to those of adipic acid ( $0.27 \mu\text{g}/\text{m}^3$  and  $0.24 \mu\text{g}/\text{m}^3$ , respectively) after three cloud cycles, since it is also produced by glyoxylic acid oxidation. Oxalic acid reaches a peak mass of  $0.38 \mu\text{g}/\text{m}^3$  after the sixth cloud cycle before steadily decreasing to  $0.17 \mu\text{g}/\text{m}^3$  by the end of the simulation. It grows the most during the third and fourth cloud cycles, which correspond to the two cycles with the highest average droplet pH values (2.61 and 2.46, respectively) and when glyoxylic acid and its precursors reached their highest concentrations (droplet pH values from the simulations will be displayed subsequently).

Figure 4.9 compares predictions to field measurements from Flight 5, where first-order plume age is based on the distance away from the power plant and the wind speed.

Selected measurements from the field data were taken to represent different distances downwind of the Conesville Power Plant where transects were made. The field measurements for  $\text{SO}_4^{2-}$  show continuous growth until the last transect, where plume dilution may have dominated. The initial  $\text{SO}_4^{2-}$  mass predicted prior to the first cloud cycle (cloud cycle 0 in Figure 4.9) is highly dependent on the assumed particle size distribution and soluble fraction of the particles used to initialize the simulation. Using the measured values for these two parameters, the initial  $\text{SO}_4^{2-}$  predicted ( $7.37 \mu\text{g}/\text{m}^3$ ) is already more than  $2 \mu\text{g}/\text{m}^3$  greater than that measured in the first transect downwind of the Conesville Power Plant ( $5.00 \mu\text{g}/\text{m}^3$  at a plume age of 0.6 hours). The model predicted that  $3.46 \mu\text{g}/\text{m}^3$  of  $\text{SO}_4^{2-}$  grew after the first cloud cycle, while the most growth occurs in the fourth and fifth cloud cycles ( $4.83 \mu\text{g}/\text{m}^3$  and  $5.42 \mu\text{g}/\text{m}^3$ , respectively). Sulfate grows between  $0.5$  and  $2 \mu\text{g}/\text{m}^3$  in each of the other cloud cycles. It is hypothesized that  $\text{SO}_4^{2-}$  increased the most during cloud cycles 4 and 5 because the average cloud cycle droplet pH value experienced its largest decline in the simulation from 2.61 in the third cycle to 1.95 in the fifth cycle, which enhanced  $\text{SO}_4^{2-}$  production.

Oxalic acid first increases and eventually decreases slightly with downwind distance in both the field data and the predictions. The decrease in oxalic acid is predicted to be due to its oxidation in the particle phase to  $\text{CO}_2$ . The predicted oxalate-to-sulfate molar ratio agrees with the field data points (between 0.01 and 0.05) from the third cloud cycle until the end of the eighth cloud cycle.

As mentioned earlier, it is difficult to compare plume age, as measured by the aircraft, to a specific cloud cycle, as represented by the model. A tracer species such as  $\text{SO}_2$  can give an indication of the comparison of field data at different transects to

predictions from specific cloud cycles. The NOAA WP-3D made measurements of  $\text{SO}_2$  on 6 August 2004 in the Conesville plume at distances corresponding to plume ages of 1.1 hours (51 ppb) and 1.8 hours (36 ppb), which occur during the second cloud cycle. Figure 4.9 shows how the predicted  $\text{SO}_2$  concentration changes at one-half the base entrainment rate. At this lower rate, the second measured point for  $\text{SO}_2$  is predicted to occur during the third cloud cycle. The oxalate measurement between plume ages of 1.1 and 1.8 hours ( $0.45 \mu\text{g}/\text{m}^3$ ) substantially exceeds predictions between the first and second cloud cycles ( $9 \times 10^{-5} - 0.01 \mu\text{g}/\text{m}^3$ ); it does, however, agree within an order of a magnitude with the predictions starting from the third cloud cycle until the last cycle, ranging between  $0.17$  and  $0.38 \mu\text{g}/\text{m}^3$ . The ambient  $\text{SO}_4^{2-}$  measurement ( $12.8 \mu\text{g}/\text{m}^3$ ) lies between the values predicted between the second and third cloud cycles ( $12.68 - 14.55 \mu\text{g}/\text{m}^3$ ). Thus, measurements and predictions for the relative levels of  $\text{SO}_4^{2-}$  and oxalate agree to within one cloud cycle when considering the same amount of  $\text{SO}_2$  measured and predicted.

The measured glyoxylate concentrations during Flight 5 ranged between  $0.03$  and  $0.06 \mu\text{g}/\text{m}^3$  (Figure 4.5c), which exceed the predicted values by an order of magnitude. The model predicted up to  $0.08 \mu\text{g}/\text{m}^3$  of pyruvic acid, which is close to that observed Flight 5 ( $0.09 - 0.10 \mu\text{g}/\text{m}^3$ ). Glutaric acid, measured at levels between  $0.02$  and  $0.24 \mu\text{g}/\text{m}^3$  during Flight 5, is predicted to reach a peak of  $0.03 \mu\text{g}/\text{m}^3$  after the second cloud cycle. Malonic acid ( $0.05 \mu\text{g}/\text{m}^3$ ) was measured as an order of magnitude larger than predictions, which were stable after the fourth cloud cycle at  $0.001 \mu\text{g}/\text{m}^3$ . In summary, measured and predicted mass concentrations of organic acids other than oxalic acid in the



particle phase show general agreement, providing support for the aqueous-phase chemical mechanism used to predict oxalic acid formation.

#### **4.7.2. Case Study: Clouds Uninfluenced by Local Pollution Sources**

Figure 4.10 shows predictions from a simulation initialized with conditions representative of the absence of local pollution sources, including power plant plumes. Sulfate is predicted to grow almost linearly with each successive cloud cycle from 1.4 to 12.5  $\mu\text{g}/\text{m}^3$ . The total organic mass, which is predicted to grow to 3.06  $\mu\text{g}/\text{m}^3$  at the end of the simulation, once again has its largest dicarboxylic acid mass contributions from oxalic and adipic acids. Oxalic acid is predicted to achieve its peak concentration after the fourth cloud cycle (0.61  $\mu\text{g}/\text{m}^3$ ), which corresponds to the cycle with the highest average droplet pH value (3.28), before steadily decreasing to 0.35  $\mu\text{g}/\text{m}^3$  at the end of the simulation. Glyoxylic acid is predicted to increase in concentration with each successive cloud cycle, in contrast to its behavior in the power plant plume in cloud case. Glyoxylic acid is also predicted to attain higher concentrations in this case as compared to the previous case study (0.2  $\mu\text{g}/\text{m}^3$  versus 0.002  $\mu\text{g}/\text{m}^3$ ). The concentrations of the precursors to glyoxylic acid (including acetic, pyruvic, and glycolic acids) are also predicted to be greater in this case, suggesting that the mechanisms associated with toluene, ethene, and isoprene (only these three parent organic species produce glyoxylic acid) are more efficient at producing oxalic acid. The pathway associated with cyclohexene, which consists of the decay of dicarboxylic acids (from  $\text{C}_6$  to  $\text{C}_2$ ) by OH oxidation and does not involve any other aqueous-phase intermediate species, is more

efficient in the previous case at producing oxalic acid since a greater amount of the C<sub>3</sub>-C<sub>6</sub> acids were produced.

That more oxalic acid is predicted to form in this case as compared to that of the power plant plume in cloud case is a result of the predicted relative effectiveness of glyoxylic acid oxidation vs. the decay of longer-chain dicarboxylic acids. The production of glyoxylic acid was less efficient in the previous simulation due partly to the lower soluble fraction of the initial particle population (0.45 versus 0.60 for plume and non-plume cases, respectively). The partitioning of gas-phase species into droplets was reduced in the plume simulation since the LWC was lower. Also, the effective Henry's Law coefficients are a function of pH; the more acidic particles in the plume simulation (total simulation pH average of 1.88 versus 2.46 for plume and non-plume cases, respectively) resulted in a reduction of the droplets' uptake efficiency for some aqueous-phase precursors to oxalic acid, including acetic and pyruvic acids. As stated before, although sulfate production is enhanced at lower pH, the production of oxalic acid from glyoxylic acid is slower at lower pH because the rate constant of the oxidation of glyoxylic acid is an order of magnitude lower than that of its anion, glyoxylate.

#### **4.7.3. Comparison of Predictions From Both Cases to all In-Cloud Field Measurements**

Figure 4.11 compares all of the measured oxalate and SO<sub>4</sub><sup>2-</sup> data from total aerosol and droplet residual samples to the predictions of the two previous case studies. Predictions of the relative growth of SO<sub>4</sub><sup>2-</sup> vs. oxalate from the first three cloud cycles, corresponding to up to 40 minutes of cloud contact time, agree most closely with ambient

measurements for clouds uninfluenced by local pollution sources. The high droplet pH values during the fourth and fifth cloud cycles yielded greater predicted oxalate growth relative to  $\text{SO}_4^{2-}$  compared to observations; however, the relative amounts of the two species are again predicted to come close to agreement with observations after the fifth cycle. Predictions during the third and fourth cloud cycles (between 40 and 55 minutes of cloud contact time) agree with the power plant plume in cloud measurements. Cumulatively, for both cloud types studied, the relative loadings of  $\text{SO}_4^{2-}$  and oxalate predicted during the third cloud cycle agree the best with observations, suggesting that the average air parcel experienced nearly 40 minutes of cloud contact time. In addition, the ranges of  $\text{SO}_4^{2-}$  and oxalate measured agree with those predicted for both cloud types, with the exception of the large amount of  $\text{SO}_4^{2-}$  predicted after the fourth cloud cycle for the case of power plant plume in cloud.

As noted earlier, the measured amounts of oxalate relative to  $\text{SO}_4^{2-}$  downwind of the Conesville plant exceeded those predicted, indicating that the model overestimated  $\text{SO}_4^{2-}$  production relative to oxalate in the case of power plant plume in cloud. If the aerosol number concentration or the soluble fraction used to initialize the particle population in the power plant plume in cloud simulation were slightly lower, the  $\text{SO}_4^{2-}$  levels would be reduced to a greater extent compared to oxalate, yielding better agreement between measurements and predictions. Even though these two values were derived from measurements, any error in the determination of these initial values could have led to inaccurate predicted  $\text{SO}_4^{2-}$  levels. Also, the overestimate in  $\text{SO}_4^{2-}$  may be due to the actual plume dilution in Flight 5 being higher than assumed. Excess  $\text{SO}_4^{2-}$  and oxalate predicted in the latter cloud cycles for clouds uninfluenced by local pollution

sources may have resulted from a replenishment rate of oxidants, organic precursors, and  $\text{SO}_2$  that is too high. However, the latter cloud cycles that predicted excessive  $\text{SO}_4^{2-}$  and oxalate in both simulations may also represent particles that were processed longer compared to the sampled particles.

The model predicts a range of particulate oxalic acid levels that are consistent with measurements of both total aerosol and droplet residuals in clouds. The predicted growth of oxalate relative to  $\text{SO}_4^{2-}$  is most consistent with measurements assuming that the sampled particles experienced an average of 40 minutes of cloud contact time. However, if the sampled particles had been processed longer, the predicted replenishment of gaseous species in the entrained air may have been too high, leading to an overestimate in the latter cloud cycles for  $\text{SO}_4^{2-}$  (both simulations) and oxalate (only in the case of clouds uninfluenced by local pollution sources). Also, uncertainties in the characteristics of the initial particle population may have led to inaccurate predicted  $\text{SO}_4^{2-}$  growth relative to oxalate.

#### **4.7.4. Contribution of Different Aqueous-Phase Pathways to Production of Oxalic Acid**

Comparison of observations and predictions can help address the relative importance of different aqueous-phase oxalic acid formation pathways. Three simulations were performed, using the conditions from the case of clouds uninfluenced by local pollution sources in Table 4.4 (the initial concentration of cyclohexene was set to 0.05 ppb instead of 0.01 ppb to compare the predicted oxalic acid growth to the simulation presented in Section 6.2), to analyze the effect of the two pathways, decay of

larger dicarboxylic acids vs. oxidation of glyoxylic acid. In the first case, only cyclohexene was considered as an organic precursor; in this case, oxalic acid is produced only from the decay of longer-chain dicarboxylic acids. The second case considered toluene, isoprene, and ethene as organic precursors in the absence of cyclohexene; this case assesses oxalic acid formation solely from the oxidation of glyoxylic acid. The third simulation, which is that presented for the case of clouds uninfluenced by local pollution sources, included all four of the organic precursors.

Figure 4.12 shows the evolution of oxalic acid in all three simulations. The cyclohexene-only simulation predicts a peak in oxalic acid concentration after the sixth cloud cycle of  $0.0008 \mu\text{g}/\text{m}^3$ . The simulation with the other three organic precursors predicts a maximum of oxalic acid after the fourth cloud cycle of  $0.64 \mu\text{g}/\text{m}^3$ . The simulation with all four organic precursors leads to an oxalic acid peak after the fifth cloud cycle of  $0.57 \mu\text{g}/\text{m}^3$ . These results show clearly that the oxidation of glyoxylic acid dominates the aqueous-phase production of oxalic acid. The predicted levels of malonic, succinic, glutaric, and adipic acids from the cumulative case and that considering only cyclohexene are nearly identical, but the difference in predicted oxalic acid levels is significant. The oxalic acid levels predicted in the case considering all the organic precursors nearly matches that in the absence of cyclohexene, demonstrating the dependence of oxalic acid formation on the oxidation of glyoxylic acid. The key difference after increasing the initial cyclohexene concentration from 0.01 to 0.05 ppb was a near five-fold increase in the production of glutaric and adipic acids. As explained above, these two species do not contribute significantly to oxalic acid production making little difference in the oxalic acid concentrations during the simulation.

#### 4.8. Conclusions

Airborne measurements made during ICARTT 2004 in the vicinity of Ohio provide clear evidence for aqueous-phase production of oxalic acid. In addition, a correlation between measured oxalate and  $\text{SO}_4^{2-}$  is indicative of common aqueous-phase processing, as these two species are not directly linked in their production chemistry. The highest mass loadings for oxalate were measured for total aerosol and droplet residual samples in clouds influenced by power plant plumes. Virtually no oxalate was measured in cloud-free air aerosols; however, values slightly higher than detection limits were observed for aerosol samples in a power plant plume in cloud-free air. The strongest correlation between  $\text{SO}_4^{2-}$  and oxalate ( $R^2 = 0.80$ ,  $n = 40$ ) is seen in Flight 5 (9 August 2004) where the aircraft was sampling the total aerosol downwind of a coal-fired power plant in the presence of clouds. Both masses evolved chemically in clouds while being transported away from the power plant. Oxalate reached some of its highest levels on this particular flight presumably due to the elevated LWC in the clouds and abundance of clouds in a stratified deck allowing for additional cloud processing time.

A chemical cloud parcel model, initialized with measured aerosol size distributions, gas-phase concentrations, and meteorological conditions, predicted the same relative magnitudes of oxalic acid and  $\text{SO}_4^{2-}$  production as those measured in the field. Agreement between measurements and predictions for the growth of glyoxylate, malonate, pyruvate, and glutarate lends further support to the aqueous-phase mechanism. The production of oxalic acid is less sensitive to the initial concentration of its gas-phase precursors as compared to production of  $\text{SO}_4^{2-}$ ; this may be a result of the complex multi-

step nature of oxalic acid production, which leads to the production of volatile side-product species and the depletion of its main aqueous-phase oxidant, OH, by competing reactions. Oxalic acid production is shown to be enhanced with increasing amounts of both LWC and pH in droplets. Based on a state-of-the-art aqueous-phase chemical mechanism, the oxidation of glyoxylic acid dominates over that of longer-chain dicarboxylic acids in the production of oxalic acid.

#### 4.9. Acknowledgments

This work was supported by the National Science Foundation grant ATM-0340832. Graham Feingold and Barbara Ervens were supported by NOAA's Climate Goal. Elliot L. Atlas acknowledges support from the NOAA Office of Global Programs and NOAA Health of the Atmosphere Program. We thank Kurt Anlauf, Art Tham, and Maurice Watt of the Meteorological Service of Canada for providing hydrogen peroxide measurements. Appreciation is extended to William C. Conant for helpful discussions.

#### 4.10. References

- Blando, J. D., and B. J. Turpin (2000), Secondary organic aerosol formation in cloud and fog droplets: a literature evaluation of plausibility, *Atmos. Environ.*, 34, 1623-1632.
- Brooks, S. D., M.E. Wise, M. Cushing, and M.A. Tolbert (2002), Deliquescence behavior of organic/ammonium sulfate aerosol, *Geophys. Res. Lett.*, 29(10), 1917, doi:10.1029/2002GL014733.
- Chebbi, A., and P. Carlier (1996), Carboxylic acids in the troposphere, occurrence, sources, and sinks: A review, *Atmos. Environ.*, 30, 4233-4249.
- Crahan, K. K., D. Hegg, D. S. Covert, and H. Jonsson (2004), An exploration of aqueous oxalic acid production in the coastal marine atmosphere, *Atmos. Environ.*, 38, 3757-3764.

- Cruz, C. N., and S. N. Pandis (1998), The effect of organic coatings on the cloud condensation nuclei activation of inorganic atmospheric aerosol, *J. Geophys. Res.*, 103(D11): 13111-13123.
- Ervens, B., G. Feingold, G. J. Frost, and S. M. Kreidenweis (2004), A modeling study of aqueous production of dicarboxylic acids: 1. Chemical pathways and speciated organic mass production, *J. Geophys. Res.*, 109, D15205, doi:10.1029/2003JD004387.
- Faust, B. C. (1994), Photochemistry of clouds, fogs, and aerosols, *Environ. Sci. Technol.*, 28, A217-A222.
- Feingold, G., S. M. Kreidenweis, and Y. Zhang (1998), Stratocumulus processing of gases and cloud condensation nuclei: 1. Trajectory ensemble model, *J. Geophys. Res.*, 103(D16), 19,527– 19,542.
- Grosjean, D. and K. Fung (1984), Hydrocarbons and carbonyls in Los-Angeles air, *J. Air Pollut. Control Assoc.*, 34, 537-543.
- Hegg, D. A., S. Gao, and H. Jonsson (2002), Measurements of selected dicarboxylic acids in marine cloud water, *Atmos. Res.*, 62, 1-10.
- Hegg, D. A., D. S. Covert, P. A. Covert, and H. Jonsson (2005), Determination of the efficiency of an aircraft aerosol inlet. *Aerosol Sci. Tech.*, 39, 966-971.
- Jayne, J. T., D. C. Leard, X. F. Zhang, P. Davidovits, K. A. Smith, C. E. Kolb, and D. R. Worsnop (2000), Development of an aerosol mass spectrometer for size and composition analysis of submicron particles, *Aerosol Sci. Tech.*, 33, 49-70.
- Kalberer, M., J. Yu, D. R. Cocker, R. C. Flagan, and J. H. Seinfeld (2000), Aerosol formation in the cyclohexene-ozone system, *Environ. Sci. Technol.*, 34, 4894-4901.
- Kawamura, K., and I. R. Kaplan (1987), Motor exhaust emissions as a primary source for dicarboxylic-acids in Los-Angeles ambient air, *Environ. Sci. Technol.*, 21, 105-110.
- Kawamura, K., and K. Ikushima (1993), Seasonal-changes in the distribution of dicarboxylic-acids in the urban atmosphere, *Environ. Sci. Technol.*, 27, 2227-2235.
- Kawamura, K., H. Kasukabe, O. Yasui, and L. A. Barrie (1995), Production of dicarboxylic-acids in the Arctic atmosphere at polar sunrise, *Geophys. Res. Lett.*, 22, 1253-1256.
- Kawamura, K., R. Sempéré, Y. Imai, Y. Fujii, and M. Hayashi (1996), Water soluble dicarboxylic acids and related compounds in Antarctic aerosols, *J. Geophys. Res.*, 101(D13), 18721-18728.



Kawamura, K., and F. Sakaguchi (1999), Molecular distributions of water soluble dicarboxylic acids in marine aerosols over the Pacific Ocean including tropics, *J. Geophys. Res.*, 104(D3), 3501-3509.

Kawamura, K., N. Umemoto, M. Mochida, T. Bertram, S. Howell, and B. J. Huebert (2003), Water-soluble dicarboxylic acids in the tropospheric aerosols collected over east Asia and western North Pacific by ACE-Asia C-130 aircraft, *J. Geophys. Res.*, 108(D23), 8639, doi:10.1029/2002JD003256.

Kawamura, K., Y. Imai, and L. A. Barrie (2005), Photochemical production and loss of organic acids in high Arctic aerosols during long-range transport and polar sunrise ozone depletion events, *Atmos. Environ.*, 39, 599-614.

Kerminen, V. M., K. Teinila, R. Hillamo, and T. Makela (1999), Size-segregated chemistry of particulate dicarboxylic acids in the Arctic atmosphere, *Atmos. Environ.*, 33, 2089-2100.

Kerminen, V. M., C. Ojanen, T. Pakkanen, R. Hillamo, M. Aurela, and J. Merilainen (2000), Low-molecular-weight dicarboxylic acids in an urban and rural atmosphere, *J. Aerosol Sci.*, 31, 349-362.

Khwaja, H. A., S. Brudnoy, and L. Husain (1995), Chemical characterization of 3 summer cloud episodes at Whiteface Mountain, *Chemosphere*, 31, 3357-3381.

Kumar, P. P., K. Broekhuizen, and J. P. D. Abbatt (2003), Organic acids as cloud condensation nuclei: Laboratory studies of highly soluble and insoluble species, *Atmos. Chem. Phys.*, 3, 509-520.

Leitner, N. K. V., and M. Dore (1997), Mechanism of the reaction between hydroxyl radicals and glycolic, glyoxylic, acetic and oxalic acids in aqueous solution: Consequence on hydrogen peroxide consumption in the  $\text{H}_2\text{O}_2/\text{UV}$  and  $\text{O}_3/\text{H}_2\text{O}_2$  systems, *Water Res.*, 31, 1383-1397.

Lim, H. J., A. G. Carlton, and B. J. Turpin (2005), Isoprene forms secondary organic aerosol through cloud processing: Model simulations, *Environ. Sci. Technol.*, 39, 4441-4446.

Limbeck, A., and H. Puxbaum (1999), Organic acids in continental background aerosols, *Atmos. Environ.*, 33, 1847-1852.

Limbeck, A., and H. Puxbaum (2000), Dependence of in-cloud scavenging of polar organic aerosol compounds on the water solubility, *J. Geophys. Res.*, 105(D15): 19857-19867.

Liu, P. S. K., W. R. Leaitch, C. M. Banic, S. M. Li, D. Ngo, and J. W. Megaw (1996), Aerosol observations at Chebogue Point during the 1993 North Atlantic Regional

Experiment: Relationships among cloud condensation nuclei, size distribution, and chemistry, *J. Geophys. Res.*, 101(D22), 28971-28990.

Loflund, M., A. A. Kasper-Giebl, B. Schuster, H. Giebl, R. Hitzenberger, and H. Puxbaum (2002), Formic, acetic, oxalic, malonic and succinic acid concentrations and their contribution to organic carbon in cloud water, *Atmos. Environ.*, 36, 1553-1558.

Mochida, M., N. N. Umemoto, K. Kawamura, and M. Uematsu (2003), Bimodal size distribution of C<sub>2</sub>-C<sub>4</sub> dicarboxylic acids in the marine aerosols, *Geophys. Res. Lett.*, 30(13), 1672, doi:10.1029/2003GL017451.

Norton, R. B., J. M. Roberts, and B. J. Huebert (1983), Tropospheric oxalate, *Geophys. Res. Lett.*, 10(7), 517-520.

Pakkanen, T. A., K. Loukkola, C. H. Korhonen, M. Aurela, T. Makela, R. E. Hillamo, P. Aarnio, T. Koskentalo, A. Kousa, and W. Maenhaut (2001), Sources and chemical composition of atmospheric fine and coarse particles in the Helsinki area, *Atmos. Environ.*, 35, 5381-5391.

Poore, M. W. (2000), Oxalic acid in PM<sub>2.5</sub> particulate matter in California, *J. Air Waste Manage.*, 50, 1874-1875.

Puxbaum, H., J. Rendl, R. Allabashi, L. Otter, and M.C. Scholes (2000), Mass balance of the atmospheric aerosol in a South African subtropical savanna (Nylsvley, May 1997), *J. Geophys. Res.*, 105(D16): 20697-20706.

Rohrl, A., and G. Lammel (2001), Low molecular weight dicarboxylic acids and glyoxylic acid: Seasonal and air mass characteristics, *Environ. Sci. Technol.*, 35, 95-101.

Salam, A., H. Bauer, K. Kassin, S. M. Ullah, and H. Puxbaum (2003a), Aerosol chemical characteristics of a mega-city in Southeast Asia (Dhaka-Bangladesh), *Atmos. Environ.*, 37, 2517-2528.

Salam, A., H. Bauer, K. Kassin, S. M. Ullah, and H. Puxbaum (2003b), Aerosol chemical characteristics of an island site in the Bay of Bengal (Bhola-Bangladesh), *J. Environ. Monitor.*, 5, 483-490.

Saxena, P., and L. M. Hildemann (1996), Water-soluble organics in atmospheric particles: A critical review of the literature and application of thermodynamics to identify candidate compounds, *J. Atmos. Chem.*, 24, 57-109.

Seinfeld, J. H., and S. N. Pandis (1998), *Atmospheric Chemistry and Physics*, Wiley-Interscience, New York.

Shantz, N. C., Y. A. Aklilu, N. Ivanis, W. R. Leaitch, P. C. Brickell, J. R. Brook, Y. Cheng, D. Halpin, S. M. Li, Y. A. Tham, D. Toom-Saunty, A. J. Prenni, and L. Graham

(2004), Chemical and physical observations of particulate matter at Golden Ears Provincial Park from anthropogenic and biogenic sources, *Atmos. Environ.*, 38, 5849-5860.

Sorooshian, A., Brechtel, F. J., Ma, Y., Weber, R. J., Corless, A., Flagan, R. C., Seinfeld, J. H. (2006), Modeling and characterization of a particle-into-liquid sampler (PILS), *Aerosol Sci. Tech.*, 40, 396-409.

Squires, P., and J. S. Turner (1962), An entraining jet model for cumulo-nimbus updraughts, *Tellus*, 14, 422-434.

Tong, C. H., M. Blanco, W. A. Goddard III, and J. H. Seinfeld (2004), Thermodynamic properties of multifunctional oxygenates in atmospheric aerosols from quantum mechanics and molecular dynamics: Dicarboxylic acids, *Environ. Sci. Technol.*, 38, 3941-3949.

Turekian, V. C., S. A. Macko, and W. C. Keene (2003), Concentrations, isotopic compositions, and sources of size-resolved, particulate organic carbon and oxalate in near-surface marine air at Bermuda during spring, *J. Geophys. Res.*, 108(D5), 4157, doi:10.1029/2002JD002053.

Wang, J., R. C. Flagan, and J. H. Seinfeld (2003), A differential mobility analyzer (DMA) system for submicron aerosol measurements at ambient relative humidity, *Aerosol Sci. Tech.*, 37, 46-52.

Warneck, P. (2003), In-cloud chemistry opens pathway to the formation of oxalic acid in the marine atmosphere, *Atmos. Environ.*, 37, 2423-2427.

Weathers, K. C., G. E. Likens, F. H. Bormann, S. H. Bicknell, B. T. Bormann, B. C. Daube, J. S. Eaton, J. N. Galloway, W. C. Keene, K. D. Kimball, W. H. McDowell, T. G. Siccama, D. Smiley, and R. A. Tarrant (1988), Cloudwater chemistry from 10 sites in North-America, *Environ. Sci. Technol.*, 22, 1018-1026.

Weber, R. J., D. Orsini, Y. Daun, Y. N. Lee, P. J. Klotz, and F. J. Brechtel (2001), A particle-into-liquid collector for rapid measurement of aerosol bulk chemical composition, *Aerosol Sci. Tech.*, 35, 718-727.

Yao, X. H., C. K. Chan, M. Fang, S. Cadle, T. Chan, P. Mulawa, K. B. He, and B. M. Ye (2002a), The water-soluble ionic composition of PM<sub>2.5</sub> in Shanghai and Beijing, China, *Atmos. Environ.*, 36, 4223-4234.

Yao, X. H., M. Fang, and C. K. Chan (2002b), Size distributions and formation of dicarboxylic acids in atmospheric particles, *Atmos. Environ.*, 36, 2099-2107.

Yao, X. H., A. P. S. Lau, M. Fang, C. K. Chan, and M. Hu (2003), Size distributions and formation of ionic species in atmospheric particulate pollutants in Beijing, China: 2-dicarboxylic acids, *Atmos. Environ.*, 37, 3001-3007.

Yao, X. H., M. Fang, C. K. Chan, K. F. Ho, and S. C. Lee (2004), Characterization of dicarboxylic acids in PM<sub>2.5</sub> in Hong Kong, *Atmos. Environ.*, 38, 963-970.

Yu, J. Z., S. F. Huang, J. H. Xu, and M. Hu (2005), When aerosol sulfate goes up, so does oxalate: Implication for the formation mechanisms of oxalate, *Environ. Sci. Technol.*, 39, 128-133.

Table 4.1. Twin Otter Payload Description

Instrument	Data
Condensation particle counter (CPC) <sup>a</sup>	Aerosol number concentration
Cloud condensation nucleus counter (CCN)	Cloud condensation nucleus number concentration at 3 supersaturations
Counterflow virtual impactor (CVI)	Virtual impactor for isolating cloud droplets
Dual automated classified aerosol detector (DACAD)	Submicrometer aerosol size distribution (10-800 nm) at low and high RH
Aerosol spectrometer probe (PCASP), aerodynamic particle sizer (APS), forward scattering spectrometer probe (FSSP), cloud and aerosol particle spectrometer (CAPS)	Aerosol/cloud droplet size distribution (120 nm-1.6 mm)
Aerodyne aerosol mass spectrometer (AMS) <sup>a</sup>	Non-refractory aerosol chemistry
Particle-into-liquid sampler (PILS) <sup>a</sup>	Submicrometer aerosol chemistry (IC: inorganic and some organic acid ions)
Filters	Bulk aerosol chemistry (FTIR: functional group analysis)
PSAP <sup>a</sup> , photoacoustic, SP2	Soot absorption (multi-wavelength/incandescence)
Miscellaneous navigational and meteorology probes	Navigational data, temperature, dew point, RH, pressure, liquid water content, wind direction/speed, updraft velocity, etc.

<sup>a</sup>These are the only instruments that sampled air coming through the CVI inlet.

Table 4.2. Comparison of PILS Original (Old) and Re-Analyzed (New) Vials from Flight 5 on 9 August 2004

	$\text{SO}_4^{2-} (n = 42)$	$\text{NH}_4^+ (n = 38)$	Oxalate ( $n = 34$ )
	Slope ( $R^2$ )	Slope ( $R^2$ )	Slope ( $R^2$ )
[Old]/[New]	1.66 (0.84)	1.54 (0.50)	1.83 (0.50)

Table 4.3. Molar Ratio of Oxalate Relative to Sulfate, Nitrate, and Ammonium<sup>a</sup>

Atmospheric condition type	Inlet (# vials with oxalate above detection limits/total # vials)	SO <sub>4</sub> <sup>2-</sup>	NO <sub>3</sub> <sup>-</sup>	NH <sub>4</sub> <sup>+</sup>
		Slope (R <sup>2</sup> )	Slope (R <sup>2</sup> )	Slope (R <sup>2</sup> )
Clouds uninfluenced by local pollution sources	CVI (34/131)	0.014 (0.37)	0.010 (0.15)	0.006 (0.24)
	Main (54/92)	0.024 (0.75)	-0.007 (0.01)	0.015 (0.59)
	Cumulative (88/223)	0.023 (0.71)	0.000 (0.00)	0.013 (0.55)
Power plant plume in cloud	CVI (11/32)	0.083 (0.97)	-0.009 (0.00)	0.073 (0.45)
	Main (44/79)	0.028 (0.77)	-0.110 (0.03)	0.026 (0.81)
	Cumulative (55/111)	0.028 (0.82)	-0.031 (0.04)	0.026 (0.84)
Cloud-free air	Main (24/196)	0.000 (0.00)	0.010 (0.08)	0.002 (0.17)
Power plant plume in cloud-free air	Main (10/24)	0.015 (0.21)	0.011 (0.10)	0.011 (0.28)
Power plant plume in cloud-free air with precipitation from scattered clouds overhead	Main (18/21)	0.051 (0.56)	0.031 (0.09)	0.024 (0.52)

<sup>a</sup>CVI samples correspond to cloud droplet residual particles; Main inlet samples correspond to total aerosol, which includes a mixture of interstitial aerosol and droplet residuals in clouds.

Table 4.4. Initial Conditions for Two Simulations<sup>a</sup>

	Power plant plume in cloud	Clouds uninfluenced by local pollution sources
	ppb unless otherwise stated	
SO <sub>2</sub>	69.5	0.5
O <sub>3</sub>	40.0	40.0
H <sub>2</sub> O <sub>2</sub>	1.0	1.0
NH <sub>3</sub>	0.25	0.25
HNO <sub>3</sub>	2.0	2.0
CO <sub>2</sub>	360 ppm	360 ppm
N <sub>2</sub> O <sub>5</sub>	0.02	0.02
HCHO	1.5	1.5
CH <sub>2</sub> OHCHO	1.0	1.0
(CHO) <sub>2</sub>	1.0	1
CH <sub>3</sub> C(O)CHO	1.0	1.0
HCOOH	0.5	0.5
CH <sub>3</sub> COOH	1.0	1.0
CH <sub>3</sub> CHO	1.0	1.0
CH <sub>3</sub> C(O)CH <sub>3</sub>	1.0	1.0
C <sub>6</sub> H <sub>5</sub> CH <sub>3</sub> (toluene)	0.11	0.06
C <sub>2</sub> H <sub>4</sub> (ethene)	0.13	0.05
C <sub>6</sub> H <sub>10</sub> (cyclohexene)	0.01	0.01
C <sub>5</sub> H <sub>8</sub> (isoprene)	0.04	0.04
NO	3.27	0.07
NO <sub>2</sub>	9.42	0.50
CO	118.0	114.1
CH <sub>4</sub>	1842.0	1825.0
Initial D <sub>p</sub> (nm)	N, cm <sup>-3</sup> (Sum = 4890 cm <sup>-3</sup> )	N, cm <sup>-3</sup> (Sum = 1755 cm <sup>-3</sup> )
828.2	20	0
574.4	2.34	0.435
340.6	88	9.8
212.8	471	52.3
140.1	711	146.6
113.6	502	90.7
97.2	549	129.6
51.9	1219	486
36.0	343	351
17.3	767	489
9.7	238	0.426
Soluble fraction by mass (%)	45	60
T (C)	15	
P (bar)	900	
Alt (m)	1000	
RH (%)	70	

<sup>a</sup>Conditions for clouds uninfluenced by local pollution sources are also those representing the background air in the entrainment rate for both simulations.



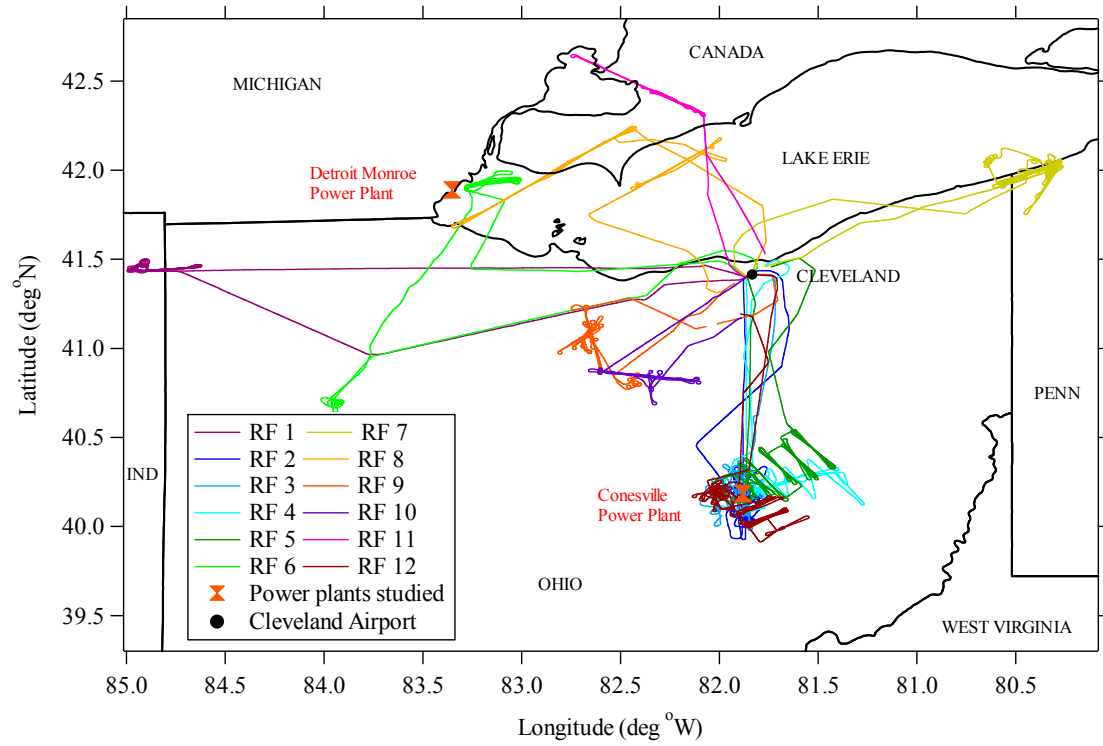


Figure 4.1. Twin Otter flight tracks during the ICARTT field study. RF refers to Research Flight.

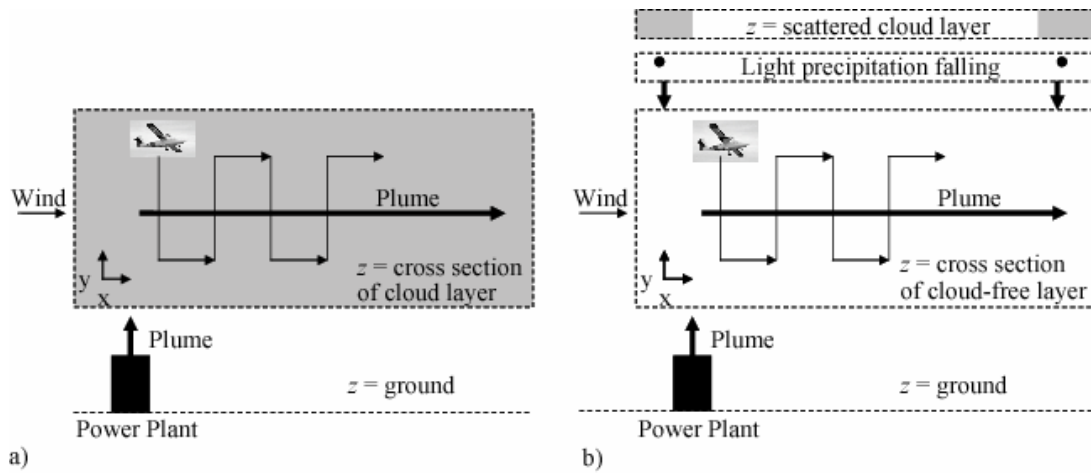


Figure 4.2. Simplified illustration of how the Twin Otter flew when it encountered two specific atmospheric conditions: (a) Power plant plume in cloud; (b) Power plant plume in cloud-free air with precipitation from scattered clouds overhead.

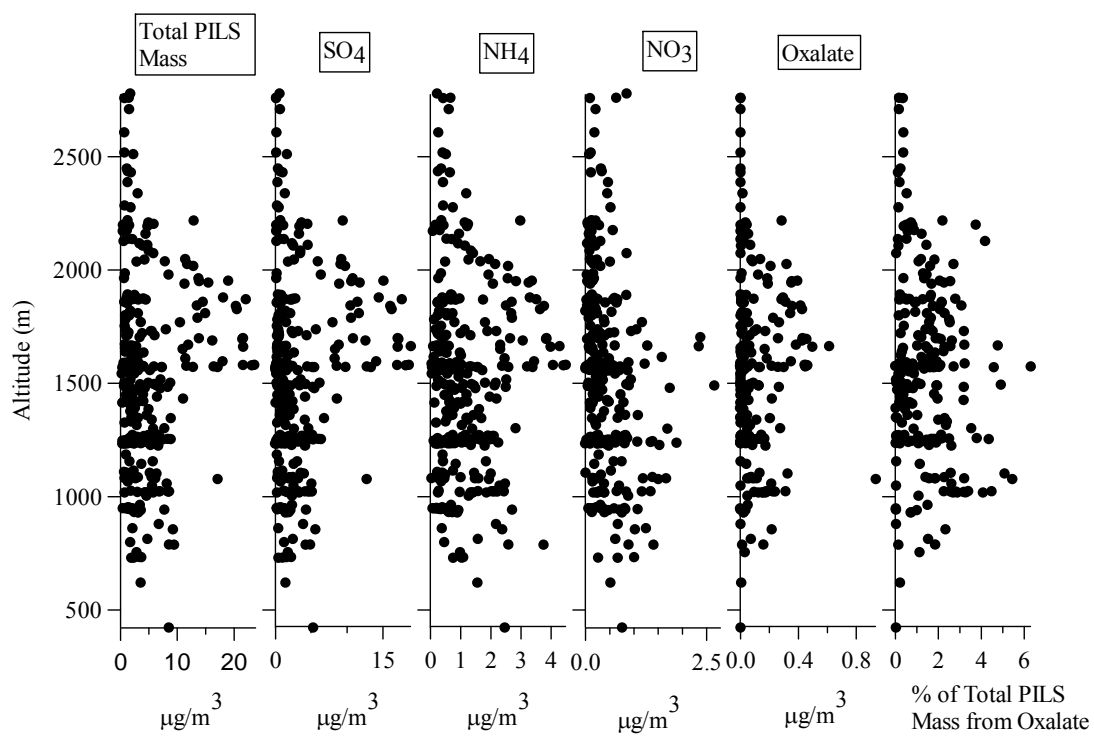


Figure 4.3. Vertical distribution of ions measured by the PILS during ICARTT.

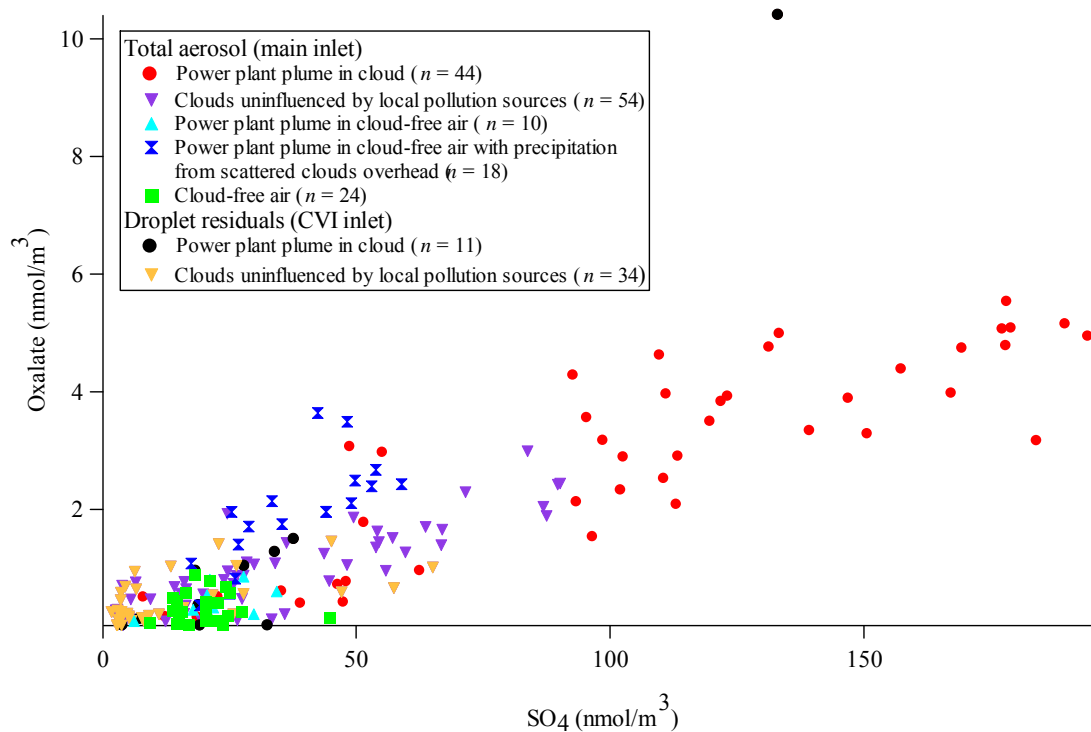


Figure 4.4. Oxalate and  $\text{SO}_4^{2-}$  molar concentrations for each atmospheric condition encountered. The total aerosol samples collected in cloud consist of a mixture of interstitial aerosol and droplet residuals.

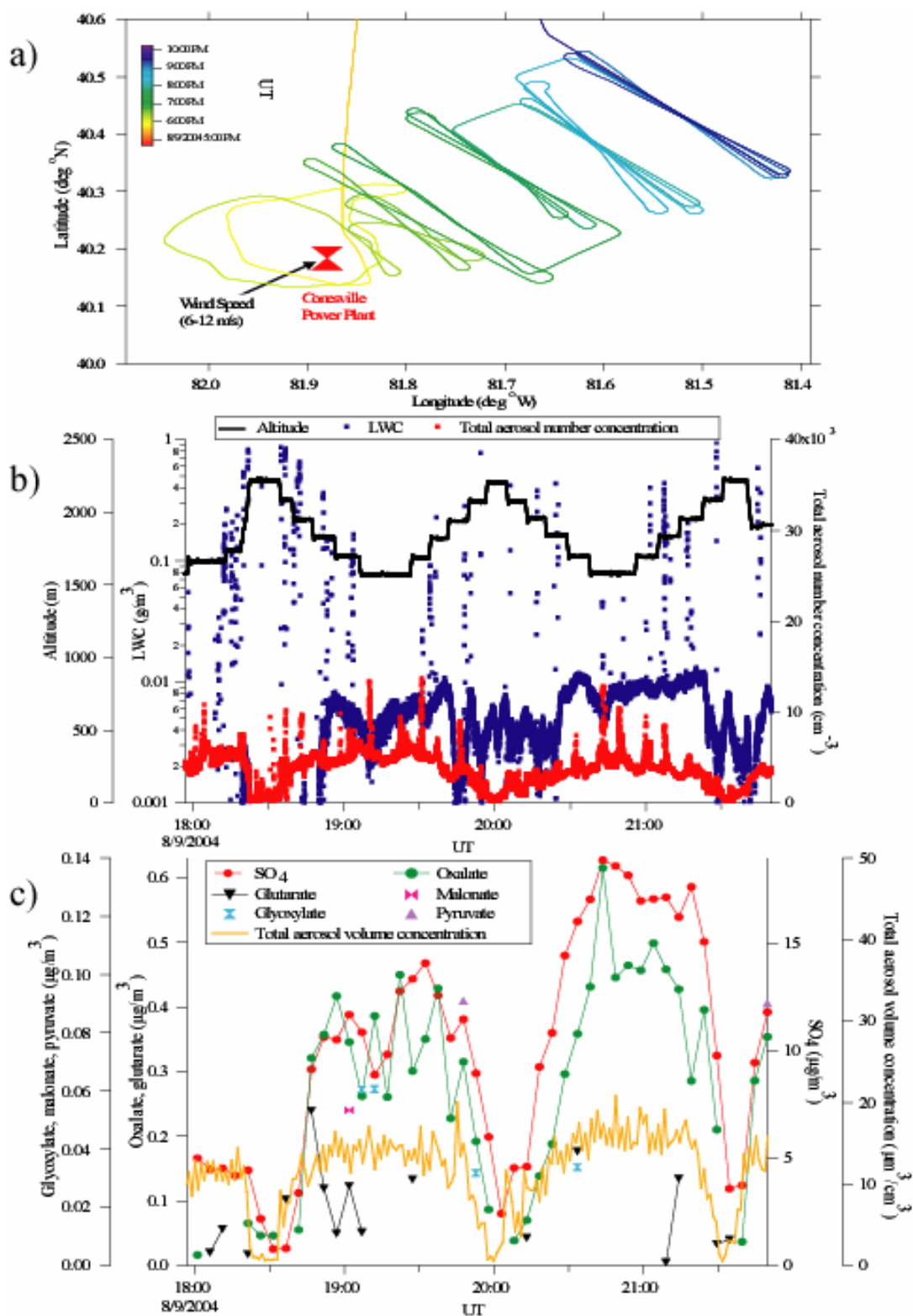


Figure 4.5. Flight 5 (9 August 2004): (a) Flight tracks; (b) Time series of altitude, LWC, and aerosol number concentration; (c) Time series of  $\text{SO}_4^{2-}$ , organic ions, and the aerosol volume concentration.

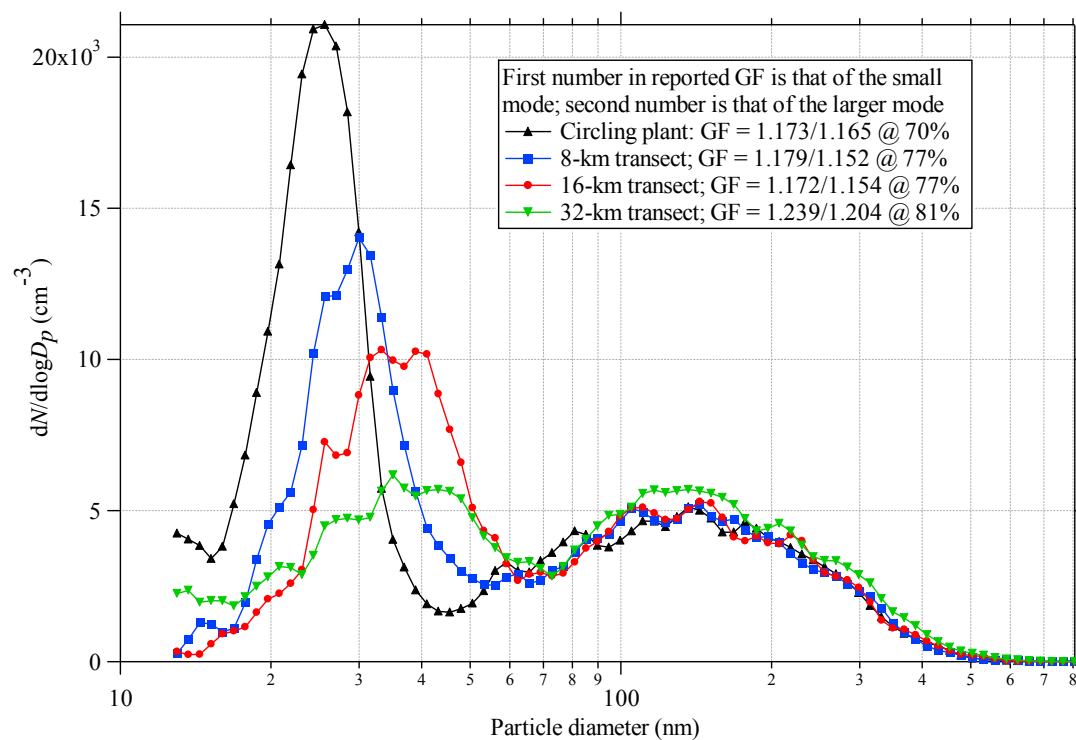


Figure 4.6. Evolution of the DACAD aerosol size distribution (dry: < 20%) for Flight 5 on 9 August 2004. GF refers to the aerosol growth factor at the RH value given.

Figure 4.7. Multiphase organic chemistry (shadowed area: aqueous phase). References: Ervens et al. (2004) and Lim et al. (2005).

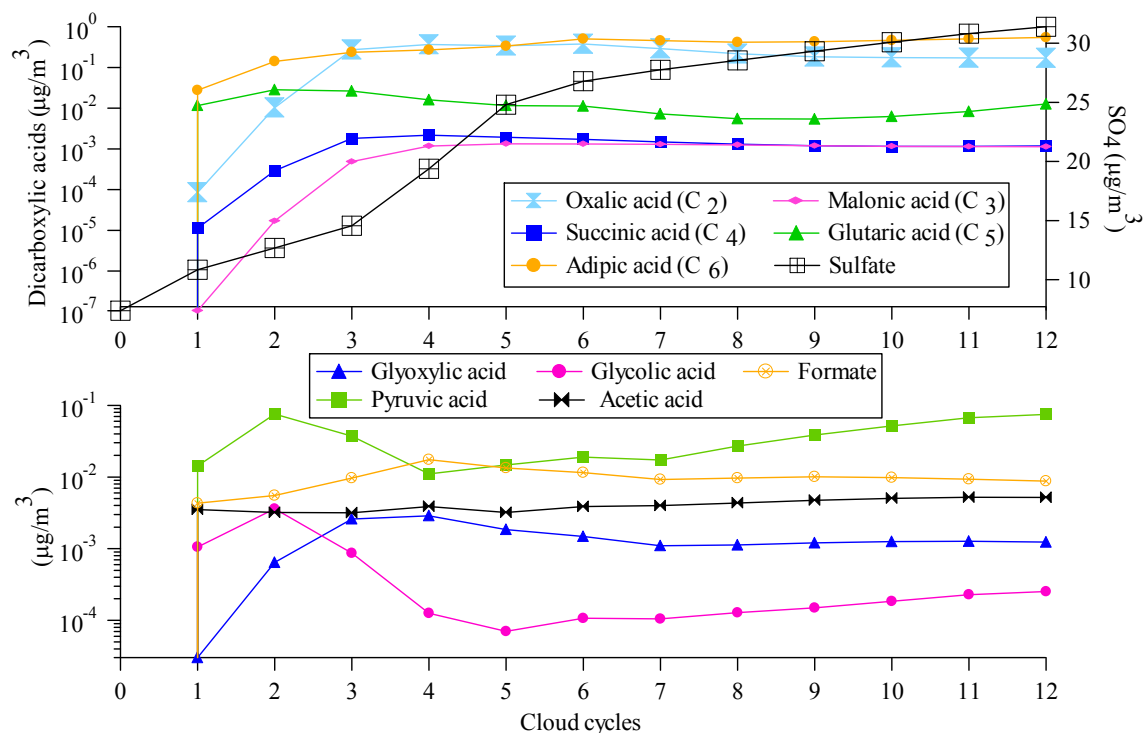


Figure 4.8. Model predictions for the power plant plume in cloud case (simulation of Flight 5 on 9 August 2004).



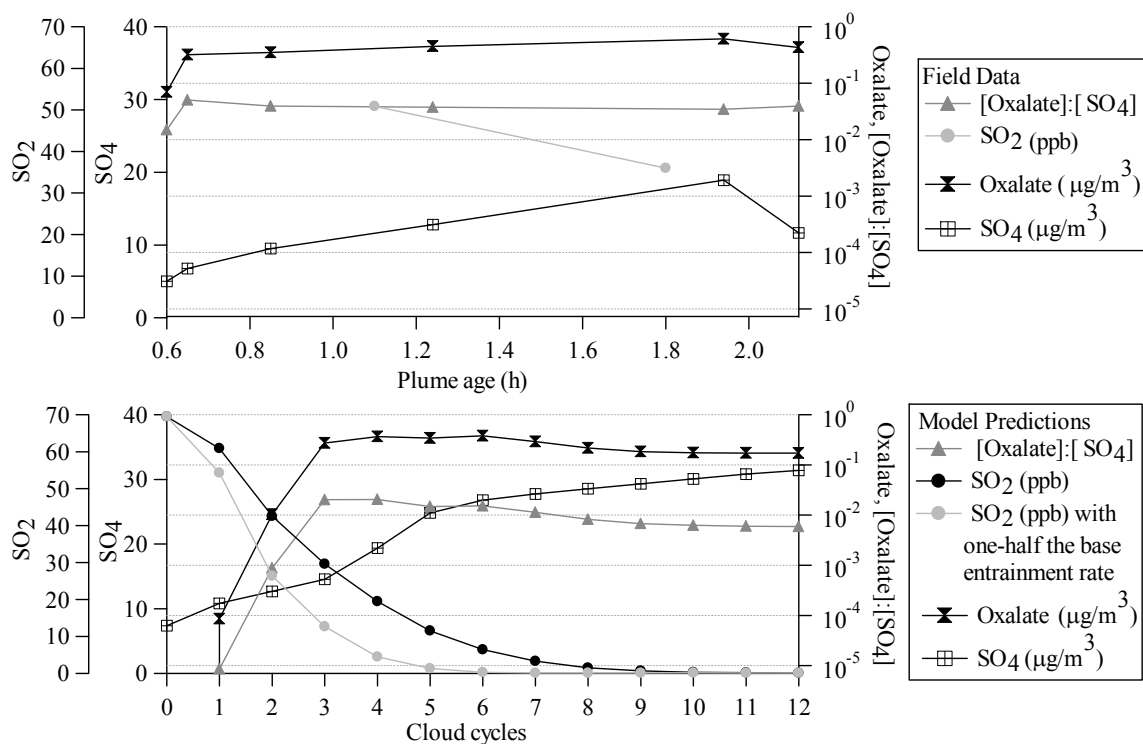


Figure 4.9. Comparison of Flight 5 (9 August 2004) field data and model predictions for  $\text{SO}_4^{2-}$  and oxalate growth.

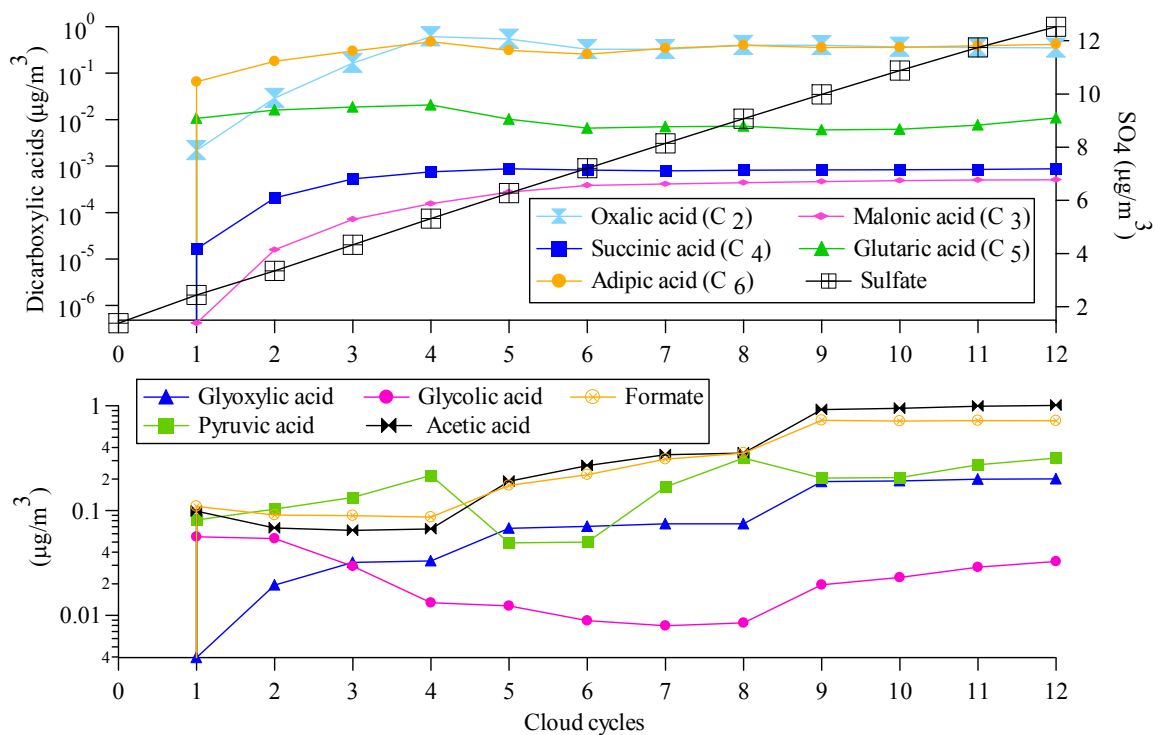


Figure 4.10. Model predictions for the case of clouds uninfluenced by local pollution sources.

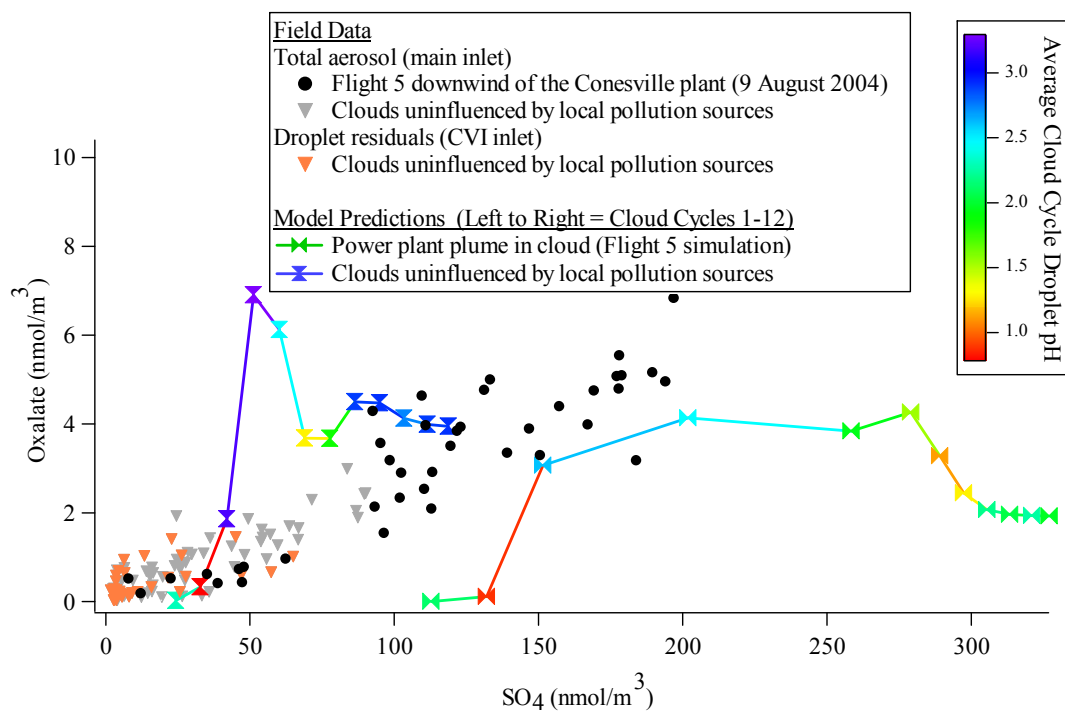


Figure 4.11. Comparison of oxalate and  $\text{SO}_4^{2-}$  molar concentrations between model predictions and field data for clouds with and without power plant plume influence. The model prediction points are color coded to represent the average droplet pH during each cloud cycle.

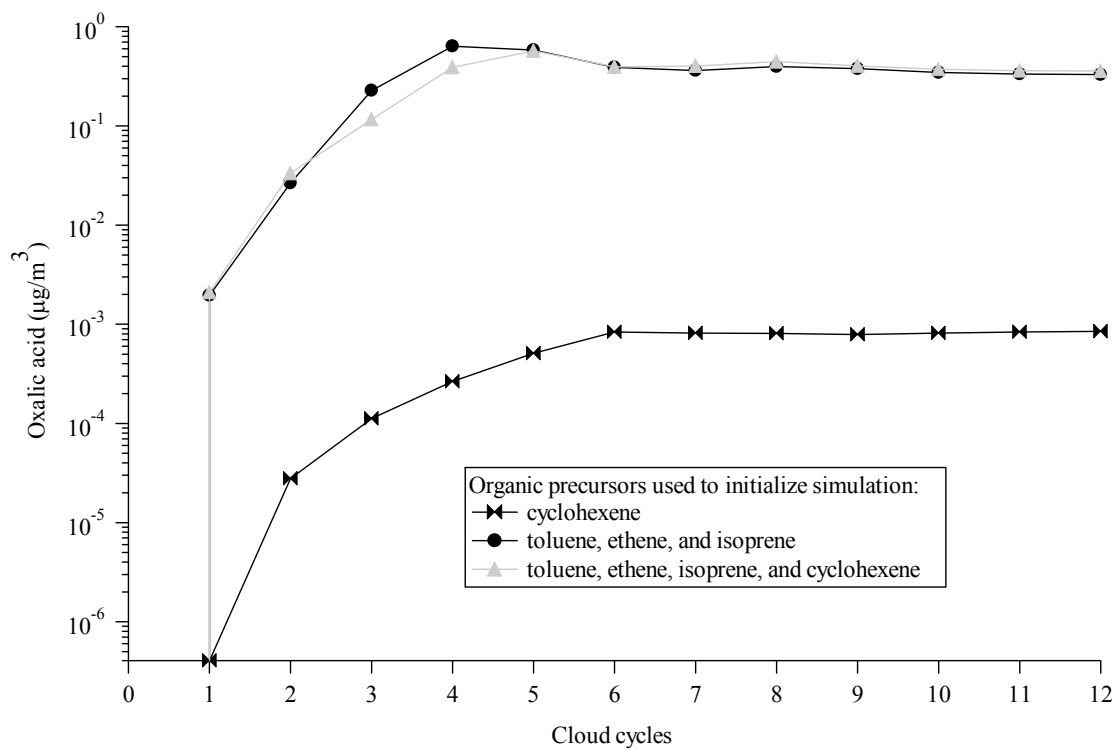


Figure 4.12. Contribution of different aqueous-phase pathways to production of oxalic acid.

## **Chapter 5**

# **On the Source of Organic Acid Aerosol Layers Above Clouds\***

---

\*This chapter is reproduced by permission from “On the Source of Organic Acid Aerosol Layers Above Clouds” by A. Sorooshian, M. –L. Lu, F. J. Brechtel, H. Jonsson, G. Feingold, R. C. Flagan, and J. H. Seinfeld, *Environ. Sci. Technol.*, 41(13), 4647-4654, 2007. Copyright 2007. American Chemical Society.

## 5.1 Abstract

During the July 2005 Marine Stratus/Stratocumulus Experiment (MASE) and the August-September 2006 Gulf of Mexico Atmospheric Composition and Climate Study (GoMACCS), the Center for Interdisciplinary Remotely-Piloted Aircraft Studies (CIRPAS) Twin Otter probed aerosols and cumulus clouds in the eastern Pacific Ocean off the coast of northern California and in southeastern Texas, respectively. An on-board particle-into-liquid sampler (PILS) quantified inorganic and organic acid species with  $\leq 5$ -min time resolution. Ubiquitous organic aerosol layers above cloud with enhanced organic acid levels were observed in both locations. The data suggest that aqueous-phase reactions to produce organic acids, mainly oxalic acid, followed by droplet evaporation is a source of elevated organic acid aerosol levels above cloud. Oxalic acid is observed to be produced more efficiently relative to sulfate as the cloud liquid water content increases, corresponding to larger and less acidic droplets. As derived from large eddy simulations of stratocumulus under the conditions of MASE, both Lagrangian trajectory analysis and diurnal cloudtop evolution provide evidence that a significant fraction of the aerosol mass concentration above cloud can be accounted for by evaporated droplet residual particles. Methanesulfonate data suggest that entrainment of free tropospheric aerosol can also be a source of organic acids above boundary layer clouds.

## 5.2 Introduction

Organic carbon (OC) is a major component of atmospheric particulate matter (*1-7*). Organic acids constitute a significant fraction of particulate organic carbon (*1, 8-11*). Dicarboxylic acids, the most abundant of which in the troposphere is oxalic acid

[(COOH)<sub>2</sub>], contributed as much as 50% to particulate organic aerosol mass in at least one study in central Japan (8). Primary emissions from fossil fuel combustion, biomass burning, and biogenic activity are sources of particulate oxalic acid (12-14); photooxidation of volatile organic compounds (VOCs), particularly aromatic hydrocarbons, followed by condensation onto preexisting aerosols is also a source (15, 16). Blando and Turpin (17) suggested that organic acids are likely particle-phase compounds formed by cloud and fog processing. Oxalic acid, which has also been shown to be formed by aqueous-phase chemistry in cloud droplets, remains in the aerosol phase after subsequent droplet evaporation (18-28). In the aqueous phase, oxalic acid is formed by oxidation of either glyoxylic acid or by the oxidative decay of malonic acid, which, in turn, is formed by the oxidation of higher-order dicarboxylic acids (18-19, 21-28). Sorooshian et al. (21) showed that the glyoxylic acid oxidation pathway is significantly more efficient at producing oxalic acid, as compared to malonic acid oxidation. Aqueous-phase intermediates to glyoxylic acid include glyoxal, methylglyoxal, glycolic acid, pyruvic acid, and acetic acid (18, 19, 21-28).

In July 2005, the Center for Interdisciplinary Remotely-Piloted Aircraft Studies (CIRPAS) Twin Otter (TO), based at Marina, CA, participated in the Marine Stratus/Stratocumulus Experiment (MASE), focused on probing aerosols and stratocumulus clouds over the eastern Pacific Ocean off the coast of northern California (29; <http://www.cirpas.org>). During August - September 2006, the CIRPAS TO also participated in the Gulf of Mexico Atmospheric Composition and Climate Study (25; GoMACCS; <http://esrl.noaa.gov/csd/2006/>), in which 22 flights were devoted largely to probing aerosol-cloud relationships over the Gulf of Mexico and the inland Houston area.

In both MASE and GoMACCS, a ubiquitous layer of organic aerosol was found above cloud. These observations in the MASE experiment have been noted by Alexander et al. (30). At present, there is uncertainty as to what mechanism(s) can explain these observations. It should be noted that Heald et al. (31, 32) also observed a layer of enhanced organic aerosol levels, but in the free troposphere (FT), and argued that likely explanations include the formation of secondary organic aerosol (SOA) following the venting of insoluble VOCs to the FT, and also cloud processing.

The goal of the present work is to evaluate, on the basis of the two field datasets, evidence and possible mechanisms for the existence of pervasive organic aerosol layers above clouds. We focus especially on organic acid levels in this work; particulate concentrations of organic acids and sulfate, and their ratios to each other, are compared above the boundary layer (BL) and below, inside, and above BL cumulus clouds. Results from large eddy simulations (LES) are used to provide support for a source of organic acid aerosols above cloud as residual particles from evaporated droplets.

### **5.3 Aircraft Measurements**

The instrument payload on the TO aircraft is described elsewhere (29 <http://www.cirpas.org>). In both field experiments, two different inlets were employed for sampling clear air and clouds. A counterflow virtual impactor (CVI) inlet was used in cloud to isolate particles resulting from evaporation of cloud droplets (so-called residual particles). The transmission efficiency of the total aerosol inlet under standard flight conditions for particle diameters less than 3.5  $\mu\text{m}$  is near unity (33). Submicrometer aerosol chemical composition measurements were carried out by a particle-into-liquid



sampler (PILS, Brechtel Manufacturing Inc.) (34). In the PILS, submicrometer-sized ambient particles are grown into droplets sufficiently large to be collected by inertial impaction, allowing subsequent chemical analysis by ion chromatography (IC, Dionex). A series of three denuders immediately downstream of the PILS inlet removes inorganic and organic gases that may bias aerosol measurements. Samples are deposited in vials held on a rotating carousel, where each vial contains material representing a period of time between 3.5 and 5 min of flight. IC analysis quantified the ambient air concentrations of water-soluble ions, including inorganic and organic acid ions.

The PILS-IC instrument uncertainty is calculated to be  $\pm 7\%$  and the detection limit (calculated as the average concentration plus three standard deviations of the smallest detectable peak for each ion in the IC baseline noise and then converted to air-equivalent units) is  $< 0.04 \mu\text{g}/\text{m}^3$  for the inorganic ions ( $\text{NH}_4^+$ ,  $\text{SO}_4^{2-}$ , and  $\text{NO}_3^-$ ) and  $< 0.01 \mu\text{g}/\text{m}^3$  for the organic acid ions (dicarboxylic acids  $\text{C}_2$  -  $\text{C}_9$ , acetate, formate, pyruvate, glyoxylate, maleate, malate, methacrylate, benzoate, and methanesulfonate) pertinent to this study. Methanesulfonate ( $\text{MSA}^-$ ) was detected during MASE and GoMACCS, but was only quantified for GoMACCS flights because of uncertainties in its measurement during MASE; therefore, only the presence of  $\text{MSA}^-$  in MASE samples is reported, not its concentration. Oxalate is the only organic acid ion for which quantitative data are shown from MASE, as it was the only organic acid observed above detection limits.

The aircraft flight strategy consisted of probing either cloud fields (MASE and GoMACCS) or a single growing cumulus cloud (GoMACCS). The flight path generally comprised multiple level legs below cloud, at different altitudes in cloud, and above

cloud. The cloud field legs were usually sufficiently long for at least two PILS samples to be collected, while individual samples collected during shorter single cloud profiling legs combined residual particles from up to three different altitude transects. Relative ratios of species in individual droplet residual particle samples are reported in this study, as opposed to absolute concentrations, to account for the variable amount of time the aircraft spent in cloud when collecting a particular sample.

During MASE, stratocumulus cloud bases typically ranged between 100 and 400 m, with tops between 350 and 700 m. Cumulus cloud bases during GoMACCS ranged between 500 and 800 m, with tops between 800 and 3000 m. Typical stratocumulus liquid water content (LWC) values ranged between 0.1 and 0.5 g/m<sup>3</sup>, with a maximum of 0.7 g/m<sup>3</sup>, during MASE; cumulus LWC values between 0.1 and 1 g/m<sup>3</sup> were typically observed during GoMACCS, with a maximum of 2.1 g/m<sup>3</sup>. Sounding profiles up to cloud bases indicate that the BL tended to be well-mixed during both field campaigns. An estimate of the in-cloud residence time of an air parcel in a well-mixed BL can be obtained from the cloud volume fraction of the BL (35), values of which for both field studies were usually between 20 - 50%. The volume fraction was calculated by dividing the average cloud depth observed during cloud field legs by the BL height; uncertainties in this calculation include the assumption that there was a continuous cloud deck of the same depth everywhere in the BL and that there was no deviation in cloud thickness. For GoMACCS, this likely represents an upper bound since cloud fractions were on the order of 10%. Organic acids constituted a significant portion of the above-cloud aerosol mass during both campaigns; on average, organic acid mass above cloud during MASE and

GoMACCS was  $0.07 \pm 0.04 \text{ } \mu\text{g}/\text{m}^3$  ( $4.9 \pm 3.6\%$  of PILS mass) and  $0.14 \pm 0.14 \text{ } \mu\text{g}/\text{m}^3$  ( $6.5 \pm 5.1\%$  of PILS mass), respectively.

#### 5.4 Sources of Oxalate above Cloud

Figure 5.1 is a schematic of processes that can lead to enhanced organic acid levels above cloud. Gases such as  $\text{SO}_2$  and VOCs ascend into cloud and partition into droplets before participating in aqueous-phase chemistry to form  $\text{SO}_4^{2-}$  and organic species (such as oxalic acid), respectively (18-28). At the same time, ambient particles already containing  $\text{SO}_4^{2-}$  and organic acids are lofted into cloud. Above cloudtop, droplets evaporate leaving residual particles, which contain newly-formed species such as sulfate and oxalic acid. Also, aerosol containing organic acids can be entrained into the BL from the FT. Although not discussed here, new particle formation can also occur above cloud (36).

Oxalate was consistently the dominant organic acid species measured in both field experiments; during GoMACCS, for example, the largest contributor to above-cloud organic acids was oxalate, on average  $87 \pm 17\%$  by mass (Figure 5.1). Less abundant species included acetate ( $7 \pm 13\%$ ), formate ( $2 \pm 8\%$ ), malonate ( $1 \pm 6\%$ ), glutarate ( $1 \pm 7\%$ ),  $\text{MSA}^-$  ( $1 \pm 5\%$ ), succinate ( $0.5 \pm 3\%$ ), and glyoxylate ( $0.5 \pm 2\%$ ). During both MASE and GoMACCS, the oxalate concentration, on average, increased from below to above cloud by between 25 - 30%, then decreased above the BL to its lowest values in the FT (Figure 5.1).

Of 14 cloud field profiling events during MASE, oxalate concentration was higher above cloud as compared to below in 12 events (Figure 5.2). Sulfate was greater above

cloud as compared to below in three of these 14 events (7/16a, 7/13b, 7/17), two of which were influenced by ship emissions; there was usually slightly less sulfate above cloud as compared to below. Situations in which the increase in  $\text{NH}_4^+:\text{SO}_4^{2-}$  from below to above cloud was largest tended to exhibit the greatest amount of oxalate growth as well (7/16a-c). The greatest increase in both oxalate concentration and the relative amount of oxalate to sulfate from below to above cloud was usually associated with higher in-cloud LWC values and larger BL cloud volume fractions. Four out of nine cloud events, in which at least four droplet residual samples were collected, exhibited a strong correlation between sulfate and oxalate ( $R^2 > 0.5$ ); this is consistent with in-cloud production of oxalic acid (19, 21, 25, 26).

During GoMACCS, higher organic acid and oxalate mass concentrations were observed above cloud as compared to below in 13 and 16 out of 22 cloud profiling events, respectively (Figure 5.3). Only one event (8/23b), which was directly influenced by the plume from the W.A. Parish Power Plant, exhibited a higher sulfate concentration above cloud; sulfate was usually more abundant below cloud due to the high background levels at lower altitudes from local  $\text{SO}_2$  sources. When BL cloud volume fractions exceeded 55% in GoMACCS, the contribution of oxalate to organic acid mass in aerosol below and above cloud always exceeded 85% and 90%, respectively; these values were lower when the BL cloud volume fraction was smaller, presumably because the cloud droplet medium in which organic acids are converted to oxalic acid was less abundant. Similar to MASE, oxalate was well-correlated with sulfate in cloud ( $R^2 > 0.5$  in 14 out of the 22 events). It should be noted that in cloud events from both field campaigns where

oxalate increased from below to above cloud, the increases were significant beyond the PILS-IC measurement uncertainty.

During strong GoMACCS pollution events ( $> 8000$  particles/cm<sup>3</sup> below cloud) the contribution of oxalate to the total organic acid mass increased from below to above cloud even though the total organic acid mass itself decreased (8/23b, 9/2b). Under more polluted conditions, photooxidation of primary VOCs may have led to lower volatility organic acids that could have partitioned into below-cloud aerosols. It is hypothesized that subsequent cloud processing increased the oxalate mass above these polluted clouds, with simultaneous depletion of the other organic acids by deposition, reaction to form volatile organic side-products, or further oxidation to produce oxalic acid.

### **5.5 Physical Processes at the Cloudtop Interface (Large Eddy Simulations)**

In order to assess the likelihood of there being evaporated droplet residual particles above cloud, we report on LES results for the stratocumulus cloud observed July 5, 2005, which was influenced by ship emissions. For vertical resolution, we use  $\Delta z = 5$  m near the cloudtop interface ( $z = 630\text{--}730$  m); outside that range, a resolution of 15 m is employed, giving a total of 94 vertical grid cells. The horizontal resolution is 55 m with 60 grid cells in each horizontal direction. Periodic boundary conditions are specified (37). The sea surface temperature is taken to be 287 K. The large scale divergence estimated from the National Centers for Environmental Prediction (NCEP) reanalysis is set at  $10^{-5}$ /s. The initial wind field is assumed to be constant with  $u = 5.75$  m/s and  $v = -9.96$  m/s, as derived from the aircraft measurements. The initial sounding profiles are based on the smoothed vertical profiles of potential temperature and total liquid water mixing ratio

sampled by the aircraft. The model is spun up at 4 AM local time with random noise on temperature over the initially assumed well-mixed sounding profile. The model used is the LES version of RAMS coupled with bin microphysics, a detailed description of which is given by Lu and Seinfeld (37).

The dry aerosol size distribution obtained by the differential mobility analyzer in the sub-cloud region ( $\sim 227$  m) is fitted with a trimodal log-normal distribution:  $r_g$  [nm] = (56, 65, 175),  $\sigma_g$  = (1.24, 2.43, 1.31), and  $N$  [cm<sup>-3</sup>] = (140, 513, 81). Based on aircraft measurements, the simulated CCN is largely ammonium bisulfate with dry density of 1.79 g/cm<sup>3</sup> and soluble fraction of 1. Organic carbon is not considered as an aerosol component in the LES simulations.

Lagrangian air parcel trajectories from the LES simulations are derived following the methodology of Stevens et al. (38). The parcels are released at 10 AM local time and tracked for three hours; 3600 parcels are released at each altitude. The integration time interval for parcel trajectories is 10 s. Parcels initialized just below cloudtop have the highest probability of ascending above cloud (Figure 5.4A-C); at least 10% of cloud parcels that originate within the 10 m-layer below cloudtop can ascend above cloud (Table 5.1). These above-cloud parcels can be recycled back into cloud or remain above cloud. Cloudtop residence times of simulated trajectories in nonprecipitating stratocumulus have been shown to be on the order of 10 min or longer (38); a significant portion of droplets near cloudtop, as represented by trajectories in the present simulations, are likely to undergo evaporation once they are out of cloud.

Stratocumulus clouds typically exhibit a clear diurnal evolution in cloud top and base (37, 39), and the cloud layer is thinner during daytime as compared to nighttime.

LES results in Figure 5.4D show that the simulated cloudtop drops by about 15 m from 8 to 10 AM. Extrapolating these results to the actual measurements suggests that the thin layer above cloud sampled by the aircraft possibly contained droplet residual particles from evaporated cloudtops during the day. Moreover, modeling studies of marine stratocumulus clouds have shown that cloudtops are not the limit of mixing of BL air and that turbulence and mixing tend to exist up to tens of meters above cloud (40, 41). Hegg et al. (42) reported measurements directly above stratocumulus off the coast of California, as in the present experiment; their measurements also indicate that cloud-processed aerosol detraining from the marine cloud layer were being sampled. In summary, both Lagrangian trajectory analysis and diurnal cloudtop evolution provide evidence that a significant fraction of aerosol particles above cloud are likely residual particles from evaporated cloud droplets. Both mechanisms work concomitantly and continuously during the day, as the resultant residual particle layer thickens. This conceptual model provides support for physical mechanisms leading to a residual organic acid aerosol layer above clouds.

We utilize the results from the trajectory analysis to assess the amount of organic acid mass measured above cloud. Using results from Table 5.1, specifically that 56% of 159 droplets/cm<sup>3</sup> ascend above cloudtop, and assuming that residual particles from these evaporated droplets have diameters of 150 nm, the density of ammonium bisulfate (1.79 g/cm<sup>3</sup>), and an organic acid mass fraction of 5% (based on measurements), the particulate organic acid concentration calculated ( $\sim 0.01 \mu\text{g}/\text{m}^3$ ) is less than those measured. An increase in any of the input variables will increase this value, and this calculation still does not account for the thickening of the residual particle layer during the day.

Assuming that all the aerosol above cloud consisted of evaporated droplets at 1000 particles/cm<sup>3</sup>, 0.16 µg/m<sup>3</sup> of organic acids is predicted to be present, which approaches the highest measurement made above cloud during MASE (Figure 5.2: 7/16c = 0.14 µg/m<sup>3</sup>). The more convective clouds encountered during GoMACCS, as compared to the stratocumulus clouds in MASE, would have been more effective at pumping cloud-processed aerosol above their tops. Vigorous mixing and transient cloud evolution (clouds grow and dissipate rapidly during the day) during GoMACCS likely contributed to the observed organic acid aerosol layer above cloud; during above-cloud legs, the aircraft was frequently sampling in areas that were recently occupied by the top portions of a cloud that evaporated.

## 5.6 Oxalic Acid Chemistry

Detection of aqueous-phase intermediates to oxalic acid in several cloud events provides evidence for a cloud processing mechanism. Glyoxylate was detected in droplet residual particles in six GoMACCS cloud events. Typically, the glyoxylate concentration in total aerosol samples was an order of magnitude lower than that of oxalate, with glyoxylate peaking at 0.03 µg/m<sup>3</sup>. Acetic acid, an aqueous precursor to glyoxylic acid, was measured during the same six events as well. The six cloud events were marked by higher LWC values as compared to others, which may explain why aqueous oxalic acid precursors reached measurable concentrations. Higher LWC values increase partitioning of gases (including organic precursors to oxalic acid) into droplets, which promotes enhanced production of oxalic acid from oxidation of intermediates such as glyoxylic and acetic acids.



It has been shown that glyoxylic acid produces oxalic acid more efficiently at higher droplet pH values, because the rate constant of the oxidation of glyoxylic acid is an order of magnitude lower than that of its anion, glyoxylate (43). Also, effective Henry's Law coefficients are a function of pH; higher acidity reduces droplet uptake efficiency for aqueous-phase precursors to oxalic acid. Similarly, the solubility of sulfate precursors and the aqueous oxidation of these precursors both have pH dependence. However, the production rate of oxalic acid is greater than that of sulfate at pH levels expected in cloud droplets; the Henry's Law coefficients for oxalic acid VOC precursors (for example, glyoxal =  $3 \times 10^5$  M/atm; acetic acid = 5500 M/atm, pyruvic acid =  $3.11 \times 10^5$  M/atm; glycolic and glyoxylic acids = 9000 M/atm) exceed that of SO<sub>2</sub> (1.24 M/atm) (1, 44). In addition, at higher droplet pH conditions, the reaction rate constant for oxalic acid production from OH oxidation of glyoxylate,  $2.9 \times 10^9 \text{ M}^{-1} \text{ s}^{-1}$  (OH oxidation of glyoxylic acid =  $3.6 \times 10^8 \text{ M}^{-1} \text{ s}^{-1}$ ), exceeds that of sulfate-producing reactions (SO<sub>2</sub> + O<sub>3</sub> =  $2.4 \times 10^4 \text{ M}^{-1} \text{ s}^{-1}$ ; HSO<sub>3</sub><sup>-</sup> + O<sub>3</sub> =  $3.7 \times 10^5 \text{ M}^{-1} \text{ s}^{-1}$ ; SO<sub>3</sub><sup>2-</sup> + O<sub>3</sub> =  $1.5 \times 10^9 \text{ M}^{-1} \text{ s}^{-1}$ ; H<sub>2</sub>O<sub>2</sub> + HSO<sub>3</sub><sup>-</sup> + H<sup>+</sup> =  $7.2 \times 10^7 \text{ M}^{-2} \text{ s}^{-1}$ ) (43, 44).

GoMACCS cloud data are consistent with a role of acidity in in-cloud processes. The oxalate:SO<sub>4</sub><sup>2-</sup> ratio increased when ascending from below to above cloud in all MASE and GoMACCS cloud events, before decreasing above the BL. The below- to above-cloud ratio of oxalate to sulfate exhibited the largest increase when BL cloud volume fractions exceeded 55%; these cases also included cloud fields with some of the highest LWC values. During a single cloud profiling event (Figure 5.5: bottom), seven residual particle samples were collected with ascending altitude in a growing cumulus cloud, and the oxalate:SO<sub>4</sub><sup>2-</sup> ratio increased in strong correlation with the maximum LWC

amount. The greatest increases in the oxalate:SO<sub>4</sub><sup>2-</sup> ratio occurred in the fourth and sixth sample when the greatest increases in the maximum LWC occurred. Cloud LWC increased with altitude, but decreased near cloudtop due to entrainment drying. In another cloud profiling event where two adjacent growing cumulus clouds were probed (Figure 5.5: top), the same trends were observed for six residual particle samples collected. The oxalate:SO<sub>4</sub><sup>2-</sup> ratio grew with altitude as the maximum LWC increased, with the sharpest increases occurring with the maximum LWC increase. The cumuli in the two events were almost the same depth and exhibited similar oxalate:SO<sub>4</sub><sup>2-</sup> mass ratios with altitude (0.10-0.40); the highest ratios were observed in the top half of the clouds. Observations from these cloud profiling events show that higher altitudes in cloud have increased LWC (with the exception of near the top due to entrainment drying) and as a result, higher droplet pH; the rate of oxalic acid production is enhanced relative to sulfate with increasing LWC in cloud. Also, higher oxalic acid concentrations relative to sulfate in the upper levels of clouds are a consequence of multi-step aqueous-phase oxalic acid production (several subsequent oxidation steps are necessary before oxalic acid is formed from VOC precursors, whereas fewer steps are required for sulfate production; 18-28), which is facilitated by more time in cloud. The oxalate:SO<sub>4</sub><sup>2-</sup> ratio showed no increasing trend with altitude on clear days; most of the higher clear air ratios were observed during flights when the plane was performing a spiral ascent or descent in an area near clouds. These results offer an explanation of high ratios of oxalate to sulfate above cloud.

Of 22 flights during GoMACCS, only two showed consistent particulate nitrate levels above 0.5 µg/m<sup>3</sup> in the BL. In these, the sampled particles exhibited NH<sub>4</sub><sup>+</sup>:SO<sub>4</sub><sup>2-</sup>

molar ratios above two, indicating that there was sufficient  $\text{NH}_3$  to neutralize  $\text{SO}_4^{2-}$ , thereby allowing  $\text{HNO}_3$  to partition into the particle phase, forming  $\text{NO}_3^-$ . Four total cloud profiling events were carried out during these two flights (Figure 5.3: 8/29a-c, 8/31) in the high-nitrate area. Three of these events exhibited lower particulate oxalate and organic acid concentrations above cloud as compared to below. The oxalate: $\text{SO}_4^{2-}$  ratio showed either no change or only a small increase from below to above cloud. In the presence of high  $\text{HNO}_3$  levels and relatively lower LWC values, the droplets are more acidic, presumably suppressing organic acid formation. That the in-cloud production rate of oxalate seemed to be reduced during these cloud events suggests again that FT entrainment is not the dominant source of above-cloud oxalate levels.

## 5.7 Methanesulfonate

Methanesulfonate data from both campaigns show that the aerosol both above the BL and below clouds can be a source for this species above clouds. Methanesulfonic acid is formed by dimethylsulfide (DMS) oxidation by free radicals such as OH, where DMS is excreted by phytoplankton in sea water (45). Data from MASE and GoMACCS show that, on average, oxalate increased in concentration with altitude from below to above cloud;  $\text{MSA}^-$  exhibited the opposite behavior (Figure 5.1).  $\text{MSA}^-$  was most frequently detected below cloud; its frequency of detection decreased with altitude until eventually increasing above cloud. Since the occurrence of  $\text{MSA}^-$  was not observed to be enhanced in cloud, its source above cloud is more likely to be from above the BL. Most of the GoMACCS  $\text{MSA}^-$  measurements occurred over the Gulf of Mexico; although not reflected in the average concentrations in Figure 5.1, comparable levels of  $\text{MSA}^-$  were

measured above cloud and in the FT over the Gulf ( $0.02 - 0.05 \mu\text{g}/\text{m}^3$ ), with a decrease observed in cloud.

Five-day back-trajectories computed from the NOAA HYSPLIT model (46) for MASE indicate that the air tended to originate from areas over the Pacific Ocean farther north up the coast of the US and from farther west over the ocean. Five-day back-trajectories indicate that air parcels in the GoMACCS flights with  $\text{MSA}^-$  detected originated farther southeast over the Gulf of Mexico. Vertical transport from the marine BL injects  $\text{MSA}^-$  or its precursors, such as DMS, into the lower FT. It is hypothesized that the MASE marine BL, which exhibited continuous decks of stratocumulus clouds, was more effective at entraining  $\text{MSA}^-$ -enriched aerosol above clouds. The data indicate that the FT is a source of above-cloud  $\text{MSA}^-$  in both regions studied, and organic acids other than  $\text{MSA}^-$  may also be contained within these entraining aerosol particles.

## 5.8 Acknowledgements

This work was supported by NOAA grant NA06OAR4310082 and Office of Naval Research grant N00014-04-1-0118. The authors gratefully acknowledge the NOAA Air Resources Laboratory (ARL) for the provision of the HYSPLIT transport and dispersion model.

## 5.9 References

(1) Saxena, P.; Hildemann, L. M. Water-soluble organics in atmospheric particles: A critical review of the literature and application of thermodynamics to identify candidate compounds. *J. Atmos. Chem.* 1996, 24, 57–109.

- (2) Kanakidou, M.; Seinfeld, J. H.; Pandis, S. N.; Barnes, I.; Dentener, F. J.; Facchini, M. C.; Van Dingenen, R.; Ervens, B.; Nenes, A.; Nielsen, C. J.; Swietlicki, E.; Putaud, J. P.; Balkanski, Y.; Fuzzi, S.; Horth, J.; Moortgat, G. K.; Winterhalter, R.; Myhre, C. E. L.; Tsigaridis, K.; Vignati, E.; Stephanou, E. G.; Wilson, J. Organic aerosol and global climate modelling: a review. *Atmos. Chem. Phys.* 2005, 5, 1053-1123.
- (3) Lim, H. J.; Turpin, B. J. Origins of primary and secondary organic aerosol in Atlanta: Results of time-resolved measurements during the Atlanta supersite experiment. *Environ. Sci. Technol.* 2002, 36, 4489-4496.
- (4) Balasubramanian, R.; Qian, W. B.; Decesari, S.; Facchini, M. C.; Fuzzi, S. Comprehensive characterization of PM<sub>2.5</sub> aerosols in Singapore. *J. Geophys. Res.* 2003, 108, D16, 4523, doi:10.1029/2002JD002517.
- (5) Putaud, J. P.; Raes, F.; Van Dingenen, R.; Brüggemann, E.; Facchini, M. C.; Decesari, S.; Fuzzi, S.; Gehrig, R.; Hüglin, C.; Laj, P.; Lorbeer, G.; Maenhaut, W.; Mihalopoulos, N.; Müller, K.; Querol, X.; Rodriguez, S.; Schneider, J.; Spindler, G.; ten Brink, H.; Tørseth, K.; Wiedensohler, A. European aerosol phenomenology-2: chemical characteristics of particulate matter at kerbside, urban, rural and background sites in Europe. *Atmos. Environ.* 2004, 38, 2579-2595.
- (6) Russell, M.; Allen, D. T.; Collins, D. R.; Fraser, M. P. Daily, seasonal, and spatial trends in PM<sub>2.5</sub> mass and composition in Southeast Texas. *Aerosol Sci. Tech.* 2004, 38, 14-26.
- (7) Murphy, D. M.; Cziczo, D. J.; Froyd, K. D.; Hudson, P. K.; Matthew, B. M.; Middlebrook, A. M.; Peltier, R. E.; Sullivan, A.; Thomson, D. S.; Weber, R. J. Single-

particle mass spectrometry of tropospheric aerosol particles. *J. Geophys. Res.* 2006, *111*, D23S32, doi:10.1029/2006JD007340.

(8) Satsumabayashi, H.; Kurita, H.; Yokouchi, Y.; Ueda, H. Photochemical formation of particulate dicarboxylic-acids under long-range transport in central Japan. *Atmos. Environ.* 1990, *24*, 1443-1450.

(9) Kavouras, I. G.; Mihalopoulos, N.; Stephanou, E. G. Formation of atmospheric particles from organic acids produced by forests. *Nature*, 1998, *395*, 683-686.

(10) Kawamura, K.; Sakaguchi, F. Molecular distributions of water soluble dicarboxylic acids in marine aerosols over the Pacific Ocean including tropics. *J. Geophys. Res.* 1999, *104*, D3, 3501-3509.

(11) Raman, R. S.; Hopke, P. K. An ion chromatographic analysis of water-soluble, short-chain organic acids in ambient particulate matter. *Int. J. Environ. An. Ch.* 2006, *86*, 767-777.

(12) Kawamura, K.; Kaplan, I. R. Motor exhaust emissions as a primary source for dicarboxylic-acids in Los-Angeles ambient air. *Environ. Sci. Technol.* 1987, *21*, 105-110.

(13) Narukawa, M.; Kawamura, K.; Takeuchi, N.; Nakajima, T. Distribution of dicarboxylic acids and carbon isotopic compositions in aerosols from 1997 Indonesian forest fires. *Geophys. Res. Lett.* 1999, *26*, 3101-3104.

(14) Yamasoe, M. A.; Artaxo, P.; Miguel, A. H.; Allen, A. G. Chemical composition of aerosol particles from direct emissions of vegetation fires in the Amazon Basin: water-soluble species and trace elements. *Atmos. Environ.* 2000, *34*, 1641-1653.

(15) Kleindienst, T. E.; Smith, D. F.; Li, W.; Edney, E. O.; Driscoll, D. J.; Speer, R. E.; Weathers, W. S. Secondary organic aerosol formation from the oxidation of aromatic

hydrocarbons in the presence of dry submicron ammonium sulfate aerosol. *Atmos. Environ.* 1999, *33*, 3669-3681.

(16) Kalberer, M.; Yu, J.; Cocker, D. R.; Flagan, R. C.; Seinfeld, J. H. Aerosol formation in the cyclohexene-ozone system. *Environ. Sci. Technol.* 2000, *34*, 4894-4901.

(17) Blando, J. D.; Turpin, B. J. Secondary organic aerosol formation in cloud and fog droplets: a literature evaluation of plausibility. *Atmos. Environ.* 2000, *34*, 1623-1632.

(18) Warneck, P. In-cloud chemistry opens pathway to the formation of oxalic acid in the marine atmosphere. *Atmos. Environ.* 2003, *37*, 2423-2427.

(19) Crahan, K. K.; Hegg, D.; Covert, D. S.; Jonsson, H. An exploration of aqueous oxalic acid production in the coastal marine atmosphere. *Atmos. Environ.* 2004, *38*, 3757-3764.

(20) Gelencser, A.; Varga, Z. Evaluation of the atmospheric significance of multiphase reactions in atmospheric secondary organic aerosol formation. *Atmos. Chem. Phys.* 2005, *5*, 2823-2831.

(21) Sorooshian, A.; Varutbangkul, V.; Brechtel, F. J.; Ervens, B.; Feingold, G.; Bahreini, R.; Murphy, S. M.; Holloway, J. S.; Atlas, E. L.; Buzorius, G.; Jonsson, H.; Flagan, R. C.; Seinfeld, J. H. Oxalic acid in clear and cloudy atmospheres: Analysis of data from International Consortium for Atmospheric Research on Transport and Transformation 2004. *J. Geophys. Res.* 2006, *111*, D23S45, doi:10.1029/2005JD006880.

(22) Ervens, B.; Feingold, G.; Frost, G. J.; Kreidenweis, S. M. A modeling study of aqueous production of dicarboxylic acids: 1. Chemical pathways and speciated organic mass production. *J. Geophys. Res.* 2004, *109*, D15205, doi:10.1029/2003JD004387.

- (23) Lim, H. J.; Carlton, A. G.; Turpin, B. J. Isoprene forms secondary organic aerosol through cloud processing: Model simulations. *Environ. Sci. Technol.* 2005, 39, 4441-4446.
- (24) Carlton, A. G.; Turpin, B. J.; Lim, H. J.; Altieri, K. E.; Seitzinger, S. Link between isoprene and secondary organic aerosol (SOA): Pyruvic acid oxidation yields low volatility organic acids in clouds. *Geophys. Res. Lett.* 2006, 33, L06822, doi:10.1029/2005GL025374.
- (25) Sorooshian, A.; Ng, N. L.; Chan, A. W. H.; Feingold, G.; Flagan, R. C.; Seinfeld, J. H. Particulate organic acids and overall water-soluble aerosol composition measurements from the 2006 Gulf of Mexico Atmospheric Composition and Climate Study (GoMACCS). *J. Geophys. Res.*, 2007, 112, D13201, doi:10.1029/2007JD008537.
- (26) Yu, J. Z.; Huang, S. F.; Xu, J. H.; Hu, M. When aerosol sulfate goes up, so does oxalate: Implication for the formation mechanisms of oxalate. *Environ. Sci. Technol.* 2005, 39, 128-133.
- (27) Altieri, K. E.; Carlton, A. G.; Lim, H. J.; Turpin, B. J.; Seitzinger, S. P. Evidence for oligomer formation in clouds: Reactions of isoprene oxidation products. *Environ. Sci. Technol.* 2006, 40, 4956-4960.
- (28) Carlton, A. G.; Turpin, B. J.; Altieri, K. E.; Seitzinger, S.; Reff, A.; Lim, H. J.; Ervens, B. Atmospheric oxalic acid and SOA production from glyoxal: results of aqueous photooxidation experiments. *Atmos. Environ.* 2007, 41:7588-7602.
- (29) Lu, M.-L.; Conant, W. C.; Jonsson, H.; Varutbangkul, V.; Flagan, R. C.; Seinfeld, J. H. The Marine Stratus/Stratocumulus Experiment (MASE): Aerosol-cloud relationships



in marine stratocumulus. *J. Geophys. Res.* 2007, 112, D10209, doi:10.1029/2006JD007985.

(30) Alexander, M.; Hubbe, J.; Lee, Y.; Daum, P.; Senum, G.; Wang, J.; Flagan, R. C.; Varutbangkul, V.; Murphy, S. M.; Rissman, T. A.; Sorooshian, A.; Seinfeld, J. H.; Hudson, J.; Jayne, J. Observation of persistent layer of enhanced organic aerosol concentrations above cloudtops off the Northern California Coast. 2006, Seventh International Aerosol Conference, American Association for Aerosol Research, St. Paul, Minnesota, USA, September 10-15.

(31) Heald, C. L.; Jacob, D. J.; Park, R. J.; Russell, L. M.; Huebert, B. J.; Seinfeld, J. H.; Liao, H.; Weber, R. J. A large organic aerosol source in the free troposphere missing from current models. *Geophys. Res. Lett.* 2005, 32, L18809, doi:10.1029/2005GL023831.

(32) Heald, C. L.; Jacob, D. J.; Turquety, S.; Hudman, R. C.; Weber, R. J.; Sullivan, A. P.; Peltier, R. E.; Atlas, E. L.; de Gouw, J. A.; Warneke, C.; Holloway, J. S.; Neuman, J. A.; Flocke, F. M.; Seinfeld, J. H. Concentrations and sources of organic carbon aerosols in the free troposphere over North America. *J. Geophys. Res.* 2006, 111, D23S47, doi:10.1029/2006JD007705.

(33) Hegg, D. A.; Covert, D. S.; Covert, P. A.; Jonsson, H. Determination of the efficiency of an aircraft aerosol inlet. *Aerosol Sci. Tech.* 2005, 39, 966–971.

(34) Sorooshian, A.; Brechtel, F. J.; Ma, Y. L.; Weber, R. J.; Corless, A.; Flagan, R. C.; Seinfeld, J. H. Modeling and characterization of a particle-into-liquid sampler (PILS). *Aerosol Sci. Tech.* 2006, 40, 396-409.

- (35) Feingold, G.; Kreidenweis, S. M.; Zhang, Y. Stratocumulus processing of gases and cloud condensation nuclei: 1. Trajectory ensemble model. *J. Geophys. Res.* 1998, *103*, D16, 19527–19542.
- (36) Hegg, D. A.; Radke, L. F.; Hobbs, P. V. Particle-production associated with marine clouds. *J. Geophys. Res.* 1990, *95*, D9, 13917-13926.
- (37) Lu, M. -L.; Seinfeld, J. H. Study of the aerosol indirect effect by large-eddy simulation of marine stratocumulus. *J. Atmos. Sci.* 2005, *62*, 3909-3932.
- (38) Stevens, B.; Feingold, G.; Cotton, W. R.; Walko, R. L. Elements of the microphysical structure of numerically simulated nonprecipitating stratocumulus. *J. Atmos. Sci.* 1996, *53*, 980-1006.
- (39) Duynkerke, P. G.; de Roode, S. R.; van Zanten, M. C.; Calvo, J.; Cuxart, J.; Cheinet, S.; Chlond, A.; Grenier, H.; Jonker, P. J.; Kohler, M.; Lenderink, G.; Lewellen, D.; Lappen, C. L.; Lock, A. P.; Moeng, C. H.; Muller, F.; Olmeda, D.; Piriou, J. M.; Sanchez, E.; Sednev, I. Observations and numerical simulations of the diurnal cycle of the EUROCS stratocumulus case. *Q. J. Roy. Meteor. Soc.* 2004, *130*, 3269-3296.
- (40) Moeng, C. H.; Stevens, B.; Sullivan, P. P. Where is the interface of the stratocumulus-topped PBL?. *J. Atmos. Sci.* 2005, *62*, 2626-2631.
- (41) Lenschow, D. H.; Zhou, M. Y.; Zeng, X. B.; Chen, L. S.; Xu, X. D. Measurements of fine-scale structure at the top of Marine Stratocumulus. *Bound-Lay. Meteorol.* 2000, *97*, 331-357.
- (42) Hegg, D. A.; Covert, D. S.; Jonsson, H.; Khelif, D.; Friehe, C. A. Observations of the impact of cloud processing on aerosol light-scattering efficiency. *Tellus B.* 2004, *56*, 285-293.

- (43) Ervens, B.; Gligorovski, S.; Herrmann, H. Temperature-dependent rate constants for hydroxyl radical reactions with organic compounds in aqueous solutions. *Phys. Chem. Chem. Phys.* 2003, 5, 1811-1824.
- (44) Ervens, B.; George, C.; Williams, J. E.; Buxton, G. V.; Salmon, G. A.; Bydder, M.; Wilkinson, F.; Dentener, F.; Mirabel, P.; Wolke, R.; Herrmann, H. CAPRAM 2.4 (MODAC mechanism): An extended and condensed tropospheric aqueous phase mechanism and its application. *J. Geophys. Res.* 2003, 108, D14, 4426, doi:10.1029/2002JD002202.
- (45) Charlson, R. J.; Lovelock, J. E.; Andreae, M. O.; Warren, S. G. Oceanic phytoplankton, atmospheric sulphur, cloud albedo and climate. *Nature*. 1987, 326, 655–661.
- (46) Draxler, R. R.; Rolph, G. D. *HYSPLIT (HYbrid Single-Particle Lagrangian Integrated Trajectory) Model access via NOAA ARL READY Website* (<http://www.arl.noaa.gov/ready/hysplit4.html>). 2003, NOAA Air Resources Laboratory, Silver Spring, MD.

Table 5.1. Summary of Lagrangian Trajectory Results

<b>Initial trajectory altitude (m) (Cloudtop = 675 m)</b>	<b>Fraction of trajectories penetrating above cloudtop at least once (%)</b>	<b>Mean cloud droplet number concentration (#/cm<sup>3</sup>)</b>
672.5	56	159 $\pm$ 67
667.5	13	303 $\pm$ 112
662.5	4	284 $\pm$ 185






Data Row 1: Oxalate ( $\mu\text{g}/\text{m}^3$ );[100*oxalate/organic acid mass]			
Data Row 2: Oxalate: $\text{SO}_4^{2-}$ by mass			
Data Row 3: % samples with MSA detected;[MSA ( $\text{ng}/\text{m}^3$ )]			
		MASE	GoMACCS
→ Long-range transport ←		FT averages	
Top of BL	 FT aerosol containing sulfate and organic acids	0.03±0.03	0.03±0.05[54±39]
		0.06±0.06	0.05±0.07
		28	13[3.0±7.4]
		Above-cloud averages	
	 Above-cloud aerosol with sulfate and organic acids	0.07±0.04	0.11±0.11[87±17]
		0.09±0.07	0.12±0.12
		24	2[1.5±11.1]
		In-cloud averages	
Cloud	 Droplets producing oxalic acid and sulfate  Interstitial aerosol	NA	NA[81±24]
		0.08±0.06	0.08±0.08
		12	3
		Below-cloud averages	
SO <sub>2</sub> , VOCs Surface	 Below cloud aerosol containing sulfate and organic acids	0.05±0.03	0.08±0.10[69±30]
		0.05±0.05	0.02±0.03
		36	13[5.3±18.5]

Figure 5.1. Schematic of physical processes leading to an organic acid aerosol layer above clouds. Average oxalate, sulfate, and methanesulfonate data are shown next to the respective region of the atmosphere where they were measured (below cloud, in cloud, above cloud, and the FT) for MASE and GoMACCS. During MASE, oxalate represented the entire organic acid mass (mass fraction is not shown) and absolute concentrations of  $\text{MSA}^-$  were not measured. In addition, only species ratios are reported for the in-cloud category since absolute concentrations were not measured (NA).

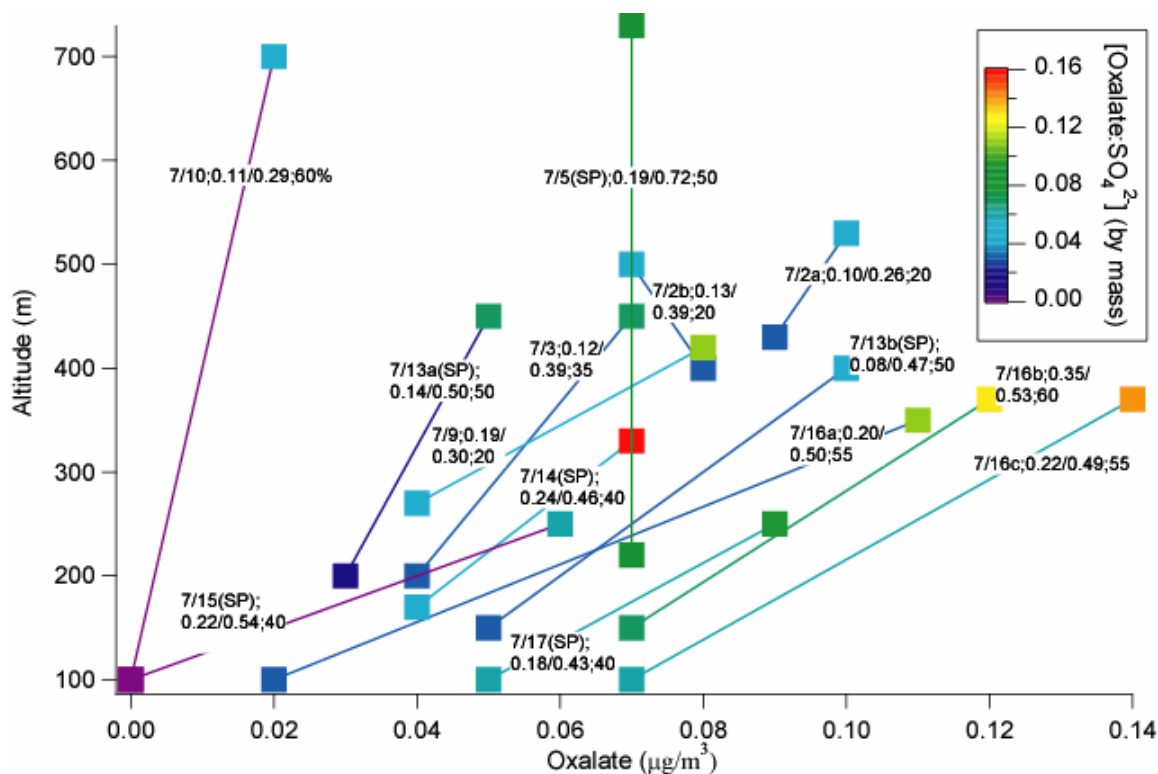


Figure 5.2. Particulate oxalate concentrations below and above 14 different cloud fields probed during MASE (lines connect below- and above-cloud measurements for individual cloud profiling events). The points are color coded with their respective oxalate: $\text{SO}_4^{2-}$  mass ratios, which typically increased above cloud. The information in each text box corresponds to the following in order: date of flight; LWC average/maximum ( $\text{g}/\text{m}^3$ ); BL cloud volume fraction (%). Letters after the date signify multiple cloud fields studied during the same flight. "SP" corresponds to clouds influenced by ship plumes.

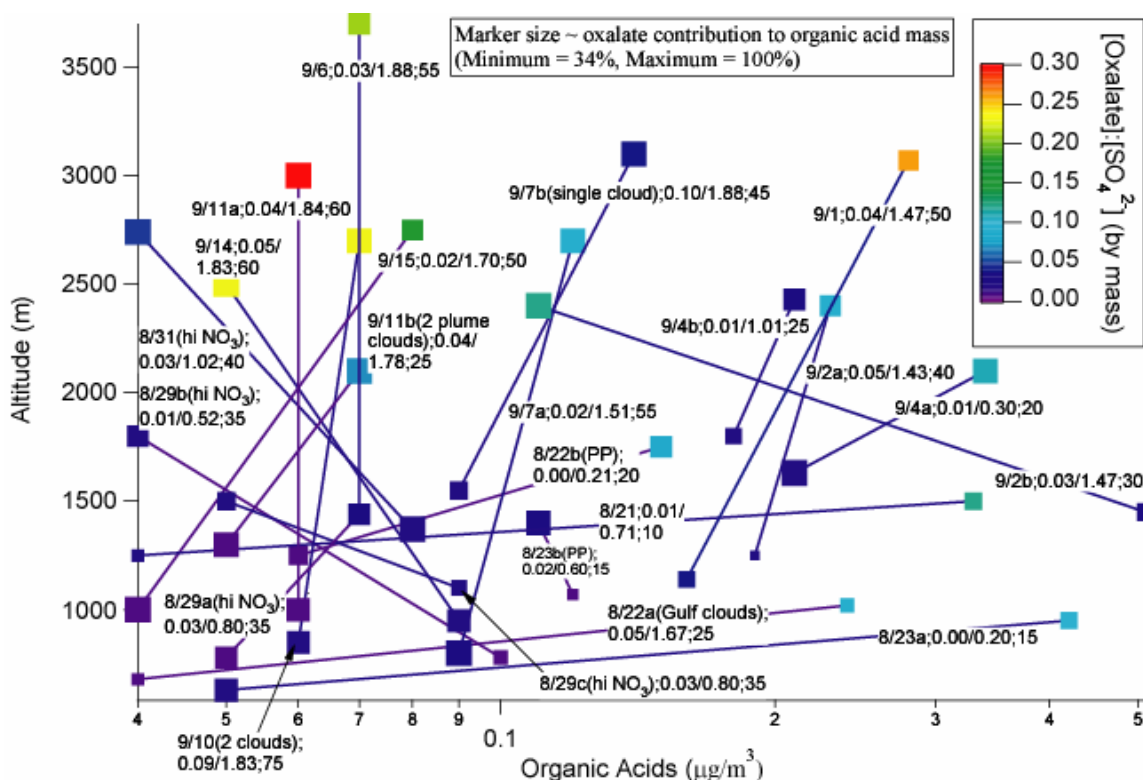


Figure 5.3. Particulate organic acid concentrations below and above 22 different cloud systems probed during GoMACCS (lines connect below- and above-cloud measurements for individual cloud profiling events). The points are color coded with their respective oxalate: $\text{SO}_4^{2-}$  mass ratios, which typically increased above cloud. Larger marker sizes, usually above cloud, also denote that oxalate contributed relatively more to the total organic acid mass. The information in each text box corresponds to the following in order: date of flight; LWC average/maximum ( $\text{g}/\text{m}^3$ ); BL cloud volume fraction (%). Letters after the date signify multiple cloud fields studied during the same flight. "PP" corresponds to clouds influenced by the Parish Plant plume.

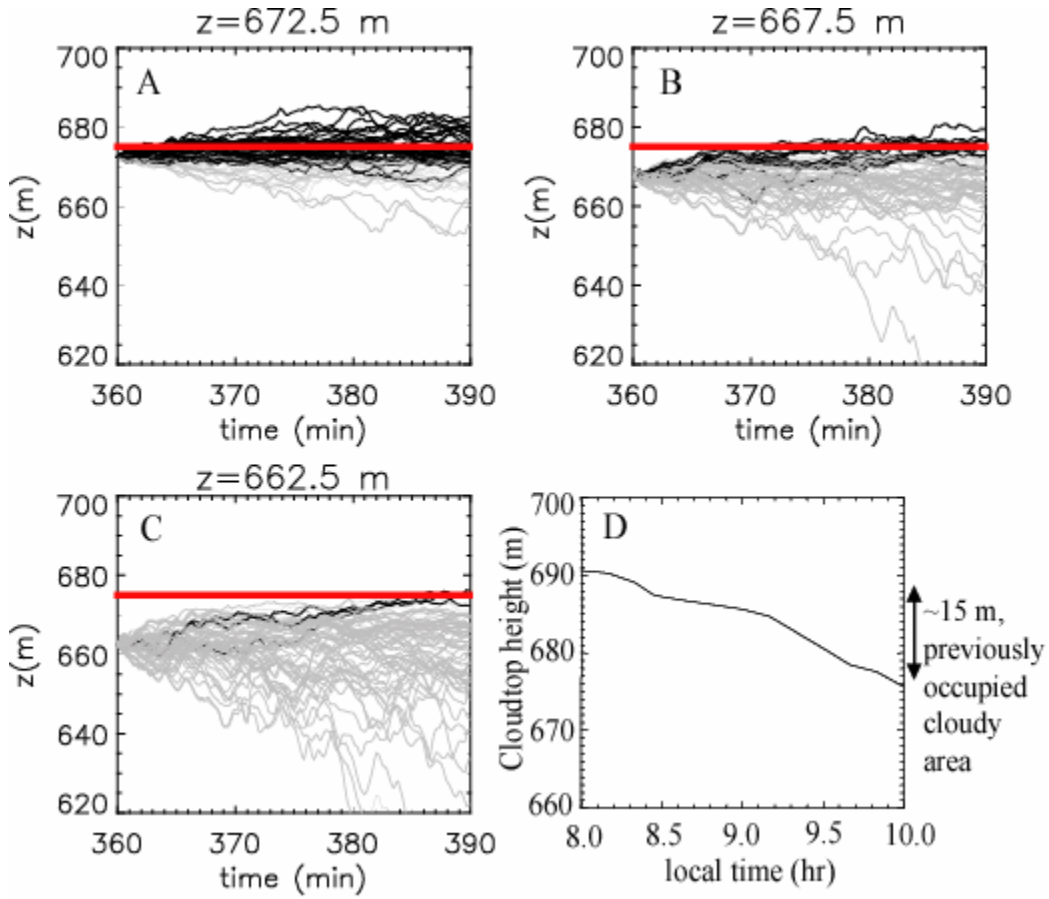


Figure 5.4. A-C: Example of the temporal evolution of trajectories from a 2D slice of the 3D LES simulation. Trajectories are initialized at various altitudes ( $z$ ) near cloudtop. Trajectories that always stay inside cloud are shown as gray lines; those that penetrate above cloud at least once are represented by black lines. The thick red horizontal line marks the cloudtop (675 m). D: Temporal evolution of cloudtop from the LES simulation of the stratocumulus cloud observed July 5, 2005, which was influenced by ship emissions (corresponds to 7/5 in Figure 5.2). Detailed discussion of this cloud can be found in Lu et al. (29).



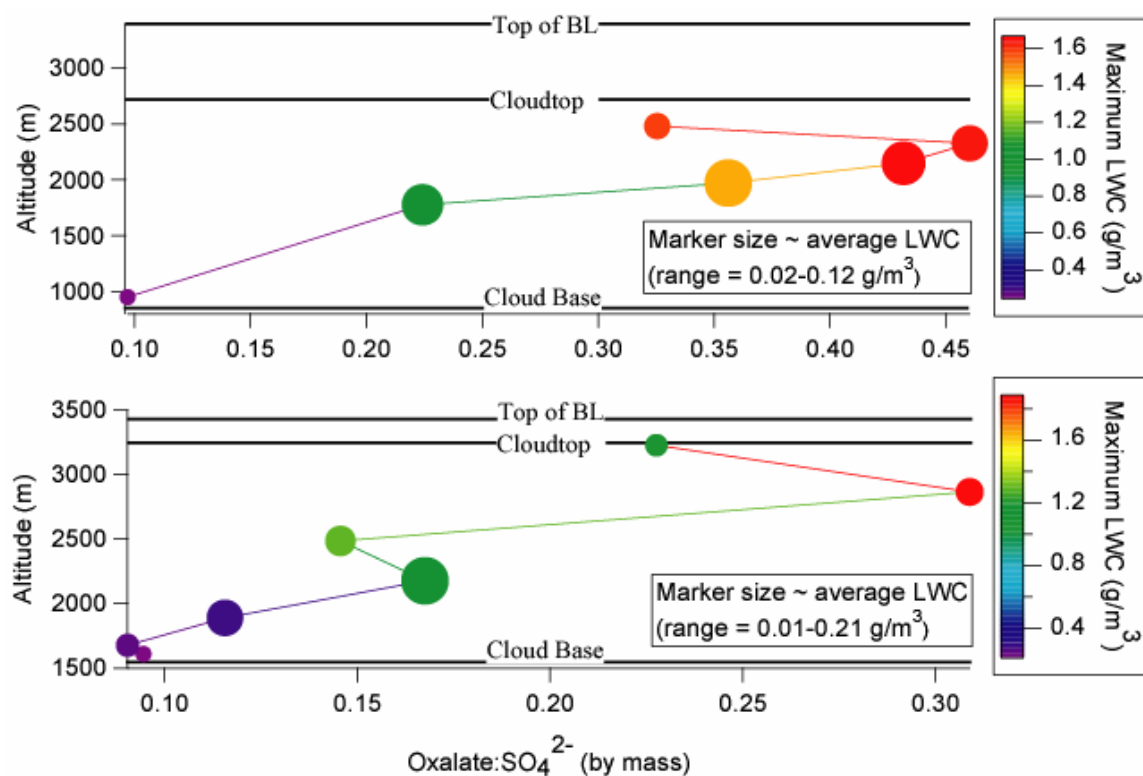


Figure 5.5. Droplet residual particle data from two different GoMACCS cloud profiling events. (Top) The TO probed two adjacent cumuli (corresponds to 9/10 in Figure 5.3); (Bottom) the TO probed one cumulus cloud (corresponds to 9/7b in Figure 5.3). The mass ratio of oxalate to sulfate usually increased with increasing LWC.

## **Chapter 6**

# **Particulate Organic Acids and Overall Water-Soluble Aerosol Composition Measurements from the 2006 Gulf of Mexico Atmospheric Composition and Climate Study (GoMACCS)\***

---

\*This chapter is reproduced by permission from “Particulate Organic Acids and Overall Water-Soluble Aerosol Composition Measurements from the 2006 Gulf of Mexico Atmospheric Composition and Climate Study (GoMACCS)” by A. Sorooshian, N. L. Ng, A. W. H. Chan, G. Feingold, R. C. Flagan, and J. H. Seinfeld, *J. Geophys. Res.*, 112, D13201, doi:10.1029/2007JD008537, 2007. Copyright 2007. American Geophysical Union.

## 6.1 Abstract

The Center for Interdisciplinary Remotely-Piloted Aircraft Studies (CIRPAS) Twin Otter participated in the Gulf of Mexico Atmospheric Composition and Climate Study (GoMACCS) mission during August - September 2006. A particle-into-liquid sampler (PILS) coupled to ion chromatography was used to characterize the water-soluble ion composition of aerosol and cloud droplet residual particles (976 5-min PM<sub>1.0</sub> samples in total). Sulfate and ammonium dominated the water-soluble mass ( $\text{NH}_4^+ + \text{SO}_4^{2-} = 84 \pm 14\%$ ), while organic acids contributed  $3.4 \pm 3.7\%$ . The average  $\text{NH}_4^+ : \text{SO}_4^{2-}$  molar ratio was  $1.77 \pm 0.85$ . Particulate concentrations of organic acids increased with decreasing carbon number from C<sub>9</sub> to C<sub>2</sub>. Organic acids were most abundant above cloud, presumably as a result of aqueous-phase chemistry in cloud droplets, followed by subsequent droplet evaporation above cloudtops; the main product of this chemistry was oxalic acid. The evolution of organic acids with increasing altitude in cloud provides evidence for the multi-step nature of oxalic acid production; predictions from a cloud parcel model are consistent with the observed oxalate:glyoxylate ratio as a function of altitude in GoMACCS cumuli. Suppressed organic acid formation was observed in clouds with relatively acidic droplets, as determined by high particulate nitrate concentrations (presumably high HNO<sub>3</sub> levels too) and lower liquid water content, as compared to other cloud fields probed. In the Houston Ship Channel region, an area with significant volatile organic compound emissions, oxalate, acetate, formate, benzoate, and pyruvate, in decreasing order, were the most abundant organic acids. Photooxidation of *m*-xylene in laboratory chamber experiments leads to a particulate organic acid product distribution consistent with the Ship Channel area observations.

## 6.2 Introduction

Organic acids are ubiquitous in atmospheric aerosols (Kawamura and Ikushima, 1993; Stephanou and Stratigakis, 1993; Khwaja, 1995; Chebbi and Carlier, 1996; Kerminen et al., 2000; Yao et al., 2004); however, their formation mechanisms are not entirely understood. Dicarboxylic acids have much lower vapor pressures (factor of 2 to 4) compared to monocarboxylic acids, which allows them to partition more easily into the aerosol phase (Ludwig and Klemm, 1988; Chebbi and Carlier, 1996). Studies have shown that the particulate mass concentration of dicarboxylic acids tends to increase with decreasing carbon number (Kawamura and Ikushima, 1993; Sempere and Kawamura, 1994; Kawamura et al., 1995; Kawamura and Sakaguchi, 1999; Limbeck and Puxbaum, 1999; Kerminen et al., 2000; Neususs et al., 2000); consequently, oxalic acid  $[(\text{COOH})_2]$  is the dominant particulate dicarboxylic acid. Oxalic acid occurs both in primary emissions from fossil fuel combustion, biomass burning, and biogenic activity, as well as from photooxidation of volatile organic compounds (VOCs) and aqueous-phase chemistry in cloud droplets (Norton et al., 1983; Kawamura and Kaplan, 1987; Kawamura and Ikushima, 1993; Faust, 1994; Chebbi and Carlier, 1996; Kerminen et al., 1999; Narukawa et al., 1999; Blando and Turpin, 2000; Yamasoe et al., 2000; Yao et al., 2002, 2003; Mochida et al., 2003; Turekian et al., 2003; Crahan et al., 2004; Yu et al., 2005; Sorooshian et al., 2006a). (Huang and Yu (2007) recently showed that vehicle exhaust is not a significant primary source for oxalate.) Sources of longer chain dicarboxylic acids ( $\text{C}_9$  is the longest acid detected in the present study) include pyrolysis of vegetative material, vehicular emissions, photooxidation of aromatic hydrocarbons, and the oxidative decay of higher carbon number organic acids (Pereira et al., 1982;

Rogge et al., 1991; Kawamura and Sakaguchi, 1999). A major source of  $\geq C_9$  organic acids includes the oxidation of unsaturated *n*-fatty acids, which are emitted from microbial sources and the processing of plant and animal constituents (Rogge et al., 1993; Kawamura et al., 2005); meat cooking is an especially significant source of fatty acid emissions (Rogge et al., 1991). Lower carbon number dicarboxylic acids have been more frequently detected and at higher concentrations. The decrease in concentration of dicarboxylic acids with increasing carbon number, especially at higher altitudes, is suggestive of an oxidative decay mechanism; it is not certain, however, whether the lower carbon number acids are more abundant at lower altitudes simply as a result of larger primary emission rates.

The monocarboxylic acids, of which formic and acetic acids are the most dominant in the gas phase, usually exhibit concentrations one to two orders of magnitude lower in the aerosol phase as compared to the gas phase (Chebbi and Carlier, 1996). Formation mechanisms for these and other monocarboxylic acids include reactions of precursors in gas, aqueous, and particulate phases, and primary biogenic and anthropogenic emissions (Simoneit and Mazurek, 1982; Simoneit, 1986; Talbot et al., 1988; Rogge et al., 1991; Khwaja, 1995; Chebbi and Carlier, 1996; Souza et al., 1999; Kanakidou et al., 2005). Although exceptions such as formic acid exist, monocarboxylic acids are generally thought to be oxidized to form dicarboxylic acids via intermediates such as hydroxyacids and ketocarboxylic acids (Kawamura and Ikushima, 1993).

During August - September 2006, the Center for Interdisciplinary Remotely-Piloted Aircraft Studies (CIRPAS) Twin Otter (TO), based at Houston, Texas, participated in the Gulf of Mexico Atmospheric Composition and Climate Study

(GoMACCS; <http://www.esrl.noaa.gov/csd/2006/>); 22 flights were devoted largely to probing aerosol-cloud relationships over the Gulf of Mexico and the inland Houston area. Previous field campaigns in southeastern Texas have addressed chemical characterization of aerosol in the Houston area (2000 Texas Air Quality Study (TexAQS; [www.utexas.edu/research/ceer/texaqs](http://www.utexas.edu/research/ceer/texaqs)); 2000 - 2001 Gulf Coast Aerosol Research and Characterization Study (GC-ARCH; Russell and Allen, 2004)); absent in those studies were rapid ( $< 5$  min) airborne measurements of speciated organic acids, in addition to inorganic species, in aerosol and cloud droplet residual particles. Table 6.1 provides a summary of reported urban organic aerosol measurements, with an emphasis on organic acids. These past measurements provide a body of urban data to which data from the Houston area during GoMACCS can be compared.

The goal of the present work is twofold: (1) to provide a chemical characterization of inorganic and organic acid ions in southeastern Texas aerosol, including cloud droplet residual particles; and (2) to gain insight into formation mechanisms for organic acids and their role in cloud droplet chemistry. Measurements of inorganic and organic acid species are first presented to gain insight into the spatial distribution of their mass concentrations, ionic charge balance closure, mass and volume concentration ratios in different air categories, and cross-correlations between the different species. An in-depth analysis of each organic acid follows. The evolution of organic acids with increasing altitude in cloud is examined, and cloud parcel model predictions are compared to measurements to explain trends in the oxalate:glyoxylate ratio observed. Unique findings from cloud field measurements in high-nitrate areas are reported. Special attention is given to evidence of secondary organic aerosol (SOA)

formed from aromatic VOCs, in which airborne data in the Houston Ship Channel area are compared to those from laboratory chamber photooxidation of *m*-xylene.

### 6.3 Twin Otter (TO) Research Aircraft

The instrument payload on the TO aircraft is described elsewhere (<http://www.cirpas.org>). Two different inlets were employed for sampling clear air and clouds. A counterflow virtual impactor (CVI) inlet was used in cloud to isolate particles resulting from evaporation of cloud droplets (so-called residual particles). The main aircraft inlet sampled total aerosol outside of clouds and occasionally inside clouds, where the total aerosol consisted of interstitial aerosol and some evaporated droplet residual particles. Submicrometer aerosol chemical composition was measured by a particle-into-liquid sampler (PILS, Brechtel Manufacturing Inc.) (Sorooshian et al., 2006b). In the PILS, submicrometer-sized ambient particles are grown into droplets sufficiently large to be collected by inertial impaction, allowing subsequent chemical analysis by ion chromatography (IC, Dionex). Samples are deposited in vials held on a rotating carousel, with each vial containing material representing a period of 5 min of flight, or alternatively, 62.5 L of sampled air (PILS sample flow rate = 12.5 L/min). IC analysis quantified the ambient air concentrations of water-soluble ions, including inorganic and organic acid ions.

The detection limit (calculated as the average concentration plus three standard deviations of the smallest detectable peak for each ion in the IC baseline noise, converted to air-equivalent units) is  $< 0.1 \mu\text{g}/\text{m}^3$  for the inorganic ions ( $\text{Na}^+$ ,  $\text{NH}_4^+$ ,  $\text{K}^+$ ,  $\text{Mg}^{2+}$ ,  $\text{Ca}^{2+}$ ,  $\text{Cl}^-$ ,  $\text{NO}_2^-$ ,  $\text{NO}_3^-$ , and  $\text{SO}_4^{2-}$ ),  $< 0.01 \mu\text{g}/\text{m}^3$  for the organic acid ions (saturated

dicarboxylic acids C<sub>2</sub>-C<sub>9</sub>, acetic, formic, pyruvic, glyoxylic, maleic, malic, methacrylic, benzoic, and methanesulfonic acids), and 0.06 µg/m<sup>3</sup> for the one amine measured, diethylamine. Since acetate, lactate, and glycolate co-elute, these three are reported as a collective mass using the calibration equation of acetate; therefore, the contribution of acetate reported is likely an overestimate. Compared to acetate, using the calibration equation of glycolate would yield values lower by < 10%, with increasing peak area allowing for better agreement between the two calibration equations. A list of all organic acids studied with their respective structures and chemical formulas is given in Table 6.2.

#### 6.4 Water-soluble Chemical Characterization of Southeastern Texas Aerosol

The PILS collected 976 samples up to an altitude of 5 km over 22 flights during GoMACCS. Data were collected in the following regions of the atmosphere: free troposphere (called “FT”; determined by meteorological sounding profiles), above cloud, inside cloud, below cloud, and in clear air in the boundary layer (BL) away from the vicinity of clouds (called “clear air”).

Figure 6.1 displays the spatial distribution of total water-soluble mass concentrations; the highest water-soluble mass concentrations (reported here with respective mass fraction of sulfate) in the BL occurred downwind of the W.A. Parish Power Plant (8.9±3.7 µg/m<sup>3</sup>; SO<sub>4</sub><sup>2-</sup> = 76±6%), followed by the urban core of Houston (7.7±3.4 µg/m<sup>3</sup>; SO<sub>4</sub><sup>2-</sup> = 69±10%), the Beaumont-Port Arthur area (7.1±4.5 µg/m<sup>3</sup>; SO<sub>4</sub><sup>2-</sup> = 66±12%), the Houston Ship Channel (6.3±3.9 µg/m<sup>3</sup>; SO<sub>4</sub><sup>2-</sup> = 69±8%), and over the Gulf of Mexico (2.9±1.4 µg/m<sup>3</sup>; SO<sub>4</sub><sup>2-</sup> = 56±10%). The maximum mass concentration



during the entire study ( $25.74 \mu\text{g}/\text{m}^3$ ;  $\text{SO}_4^{2-} = 79\%$ ) was observed downwind of the Parish Plant.

The overall water-soluble aerosol charge balance, as shown in Figure 6.2, has a slope of 0.80, indicating that there were unmeasured cations. The zero y-intercept indicates the absence of high background levels of anions and cations. Since sulfate and ammonium were the dominant species in aerosol sampled, the  $\text{NH}_4^+:\text{SO}_4^{2-}$  molar ratio is a reliable indicator of the overall aerosol acidity in the region; Figure 6.2 shows that ratios  $< 2$  usually are associated with a negative charge balance. On average, the  $\text{NH}_4^+:\text{SO}_4^{2-}$  molar ratio was  $1.77 \pm 0.85$  during GoMACCS, indicating that ammonia ( $\text{NH}_3$ ) was generally prevalent in the region. The vertical distribution of the charge balance shows that the most acidic aerosol occurred in clear air and at low altitudes close to  $\text{SO}_2$  sources; the  $\text{NH}_4^+:\text{SO}_4^{2-}$  molar ratio was close to unity downwind of the Parish Plant.

The PILS mass concentrations were reasonably correlated with DMA volume concentrations for aerosol in different vertical layers of the troposphere ( $R^2 > 0.5$ ) with the exception of the FT ( $R^2 = 0.19$ ) (Figure 6.3). The highest correlation ( $R^2 = 0.64$ ) was observed above cloud where the slope (aerosol density) was  $1.46 \text{ g}/\text{cm}^3$  (density of pure ammonium sulfate =  $1.769 \text{ g}/\text{cm}^3$ ). The slopes for other regions of the atmosphere in Figure 6.3 are less than unity. Many of the points exhibiting a higher volume concentration as compared to mass concentration (indicative of an aerosol density  $< 1 \text{ g}/\text{cm}^3$ ), especially in clear air, are downwind of major VOC sources. These samples may have contained organic species not detectable by the PILS-IC technique owing to insufficient water solubility and polarity. The FT data exhibited the lowest slope, suggesting that much of the mass was organic aerosol not quantifiable by the PILS-IC

technique. The greatest mass fraction of organic acids occurred in above-cloud aerosol particles, as this layer has been shown to be enriched in water-soluble organic acids (Sorooshian et al., submitted). A significant fraction of the organic acids above cloud may have been produced by in-cloud oxidation of less-polar below-cloud species not able to be detected by the PILS-IC technique.

The vertical mass distribution of the major inorganic species and total organic acids is shown in Figure 6.4. The total mass concentration usually peaked near 1 km, and was lowest ( $< 5 \mu\text{g}/\text{m}^3$ ) above 3 km, an approximate altitude indicating the division between the BL and the FT. For all of the five air categories shown in Figure 6.4, the total mass was dominated by sulfate (55 - 68%), followed by ammonium (16 - 22%), and then nitrate (5 - 12%). The mass fraction of organic acids increased with altitude from below cloud (2%) to above cloud (7%), while an intermediate mass fraction was observed in cloud droplet residual particles (6%). The total organic acid mass did not decrease above cloud. Sulfate was highly correlated with ammonium ( $R^2 = 0.84$ ), followed by oxalate ( $R^2 = 0.33$ ), which dominated the total organic acid mass. Cloud chemistry is likely the explanation for the observed correlation between sulfate and oxalic acid (Sorooshian et al., 2006a; Sorooshian et al., submitted). Although sulfate and oxalic acid are known to be produced by in-cloud oxidation of their gaseous precursors, sulfate typically decreased from below to above cloud while the sum of all organic acids, which was dominated by oxalic acid, exhibited the opposite behavior. This can be explained by the high background levels of sulfate at lower altitudes from local  $\text{SO}_2$  sources. Although there were local VOC sources as well, more lengthy chemistry, and consequently more

time, is required to form oxalic acid from its parent gas-phase precursors as compared to sulfate production from  $\text{SO}_2$ .

The mass fractions of the other inorganic species measured ( $\text{Na}^+$ ,  $\text{K}^+$ ,  $\text{Ca}^{2+}$ ,  $\text{Mg}^{2+}$ ,  $\text{Cl}^-$ ,  $\text{NO}_2^-$ ,  $\text{NO}_3^-$ ) were highest in the FT (cumulative = 13%), presumably from long-range transport, and then above cloud (cumulative = 3%). Sodium and chloride are best correlated with each other ( $R^2 = 0.45$ ), likely owing to sea salt from the Gulf of Mexico. Nitrate shows poor correlation ( $R^2 < 0.1$ ) with all other species except diethylamine ( $R^2 = 0.53$ ), suggesting the presence of diethylamine nitrate in the atmosphere. Previous studies provide experimental and theoretical evidence for diethylamine nitrate being present in atmospheric aerosol (Angelino et al., 2001; Murphy et al., 2007). Diethylamine reached levels as high as  $0.08 \mu\text{g}/\text{m}^3$  ( $n = 4$ ; Figure 6.5). When nitrite was measured ( $n = 4$ ), it was best-correlated with calcium ( $R^2 = 0.85$ ); this suggests that nitrite was formed heterogeneously on the surface of calcium-containing particles in these samples. The heterogeneous uptake and reactions of nitrogen oxides on the surface of calcium-containing particles have been well-characterized (Grassian, 2001).

Two flights over the Gulf of Mexico addressed cloud-processed and clear air aerosol. When comparing measurements at the same altitude range below 1100 m on these two days, the clear day was characterized by an average concentration of  $0.05 \mu\text{g}/\text{m}^3$  and  $0.02 \mu\text{g}/\text{m}^3$  for organic acids and oxalate, respectively, while the cloudy day yielded respective averages of  $0.11 \mu\text{g}/\text{m}^3$  and  $0.09 \mu\text{g}/\text{m}^3$ . Cloud processing is hypothesized to have led to higher organic acid levels, especially oxalic acid, on the cloudy day. It is uncertain though the extent to which other conditions differed between the two days, such as VOC and oxidant levels. Methanesulfonate (MSA) was measured

during these two Gulf flights, exhibiting its highest organic acid mass fractions below cloud (5%) and in the FT (11%), as compared to other data categories in Figure 6.6.

## 6.5 Sources and Character of Organic Acids

As an average over 22 flights, the total concentration of the nine dicarboxylic acids measured ( $C_2 - C_9$ ; includes saturated and unsaturated acids) was larger than those of seven monocarboxylic acids ( $C_1 - C_7$ ; includes saturated and unsaturated acids) ( $0.09 \pm 0.10 \mu\text{g}/\text{m}^3$  vs.  $0.03 \pm 0.05 \mu\text{g}/\text{m}^3$ ). Secondary organic carbon (SOC) measurements (difference between total OC and primary OC, averaged over two years) at urban sites in southeastern Texas during the 2000 - 2001 GC-ARCH study ranged from  $0.65 \pm 1.11$  to  $1.15 \pm 1.52 \mu\text{g C}/\text{m}^3$  (Table 6.1) (Russell and Allen, 2004); the total organic acids measured in GoMACCS account for an estimated 5 - 10% of the SOC reported in this prior study.

### 6.5.1 Saturated Dicarboxylic Acids

Oxalate was the most abundant organic acid anion measured in GoMACCS. It exhibited higher organic acid mass fractions below ( $0.08 \pm 0.10 \mu\text{g}/\text{m}^3$ ; 68%), inside ( $0.09 \pm 0.07 \mu\text{g}/\text{m}^3$ ; 80%), and above clouds ( $0.11 \pm 0.11 \mu\text{g}/\text{m}^3$ ; 85%), as compared to in clear air ( $0.09 \pm 0.09 \mu\text{g}/\text{m}^3$ ; 64%) and the FT ( $0.03 \pm 0.05 \mu\text{g}/\text{m}^3$ ; 52%) (Figures 6.5, 6.6). These values tend to be less than those measured in other polluted urban atmospheres (as shown in Table 6.1, the measurements, the majority of which are from ground sites, are reported for different particle size ranges); oxalic acid exhibited a mean concentration of  $1.14 \mu\text{g}/\text{m}^3$  in Sao Paulo, Brazil (Souza et al., 1999),  $0.27 \mu\text{g}/\text{m}^3$  (Kawamura and

Ikushima, 1993) and  $1.35 \mu\text{g}/\text{m}^3$  (Sempere and Kawamura, 1994) in Tokyo,  $0.22 \mu\text{g}/\text{m}^3$  in Beijing (Huang et al., 2005),  $0.21 \mu\text{g}/\text{m}^3$  (Grosjean, 1988) and  $0.06 - 0.36 \mu\text{g}/\text{m}^3$  (semiurban site; Khwaja, 1995) in New York,  $0.49 \mu\text{g}/\text{m}^3$  in Los Angeles (Kawamura et al., 1985),  $0.35 - 0.37 \mu\text{g}/\text{m}^3$  in Hong Kong during the winter ( $0.09 - 0.17 \mu\text{g}/\text{m}^3$  during summer) (Yao et al., 2004),  $0.23 \mu\text{g}/\text{m}^3$  in Leipzig, Germany (Rohrl and Lammel, 2001), and  $0.34 \mu\text{g}/\text{m}^3$  in Vienna, Austria (Limbeck and Puxbaum, 1999).

In cloud droplets, oxalic acid is formed by oxidation of glyoxylic acid, the precursors of which include glyoxal, methylglyoxal, glycolic acid, pyruvic acid, and acetic acid (Warneck, 2003; Ervens et al., 2004; Lim et al., 2005; Carlton et al., 2006). Elevated organic acid layers above clouds, dominated by oxalic acid, can be explained, in part, by two likely mechanisms: evaporation of droplets near cloudtops, leaving residual particles that have newly formed oxalic acid, and entrainment from the FT above BL clouds (Sorooshian et al., submitted). Oxalate is the most abundant organic acid in the FT, as it is a product of the oxidation of higher carbon number organic acids. For example, malonic acid is oxidized to form oxalic acid via intermediates such as hydroxymalonic acid or ketomalonic acid (Kawamura and Ikushima, 1993; Kawamura et al., 1996a; Kawamura and Sakaguchi, 1999). Mainly because of the double bond, unsaturated dicarboxylic acids are oxidized to produce oxalic acid (Kawamura and Ikushima, 1993).

The organic acid mass fractions of malonate ( $\text{C}_3$ ), succinate ( $\text{C}_4$ ), glutarate ( $\text{C}_5$ ), and adipate ( $\text{C}_6$ ) were greater in the FT (3.4%, 2.2%, 2.7%, and 1.6%, respectively), as compared to below in the BL (Figure 6.6). Malonic acid is thought to be formed by oxidative decay of larger acids like succinic acid (Kawamura and Ikushima, 1993;

Kawamura and Sakaguchi, 1999). (Measurements, however, made in the Helsinki metropolitan area are not consistent with major malonic acid production from succinic acid (Kerminen et al., 2000).) A source of  $C_4$ - $C_6$  dicarboxylic acids is the ozonolysis of cyclic alkenes, such as cyclohexene, which are emitted by vehicles and have been reported to be present in urban atmospheres (Grosjean et al., 1978; Grosjean and Fung, 1984; Hatakeyama et al., 1985, 1987).

Kawamura and Ikushima (1993) suggested that the  $C_3$ : $C_4$  ratio can be used as an indicator of enhanced photochemical production of dicarboxylic acids; they showed that malonate is less abundant than succinate in automobile exhaust, yet more abundant in Tokyo aerosol, presumably owing to secondary atmospheric production. In the present study, the  $C_3$ : $C_4$  ratio increased with increasing altitude up to 4 km (average  $C_3$ : $C_4$  up to 500 m = 0.05;  $C_3$ : $C_4$  > 1 from 500 - 4000 m), above which no malonate was detected. At a ground sampling site in Los Angeles in 1984, an average  $C_3$ : $C_4$  ratio of 0.35 was reported for direct primary emissions from vehicular exhaust (Kawamura and Kaplan, 1987), while ratios > 1 were reported for atmospheric aerosol in other studies (Kawamura and Ikushima, 1993; Kawamura et al., 1996b; Kawamura and Sakaguchi, 1999; Yao et al., 2002; Huang et al., 2005); these values are consistent with the measurements in the present study. Because of oxidative decay, the  $C_n$  and  $C_{n+1}$  dicarboxylic acid pairs were usually well-correlated [oxalate:malonate ( $R^2 = 0.72$ ); succinate:glutarate ( $R^2 = 0.47$ ); glutarate:adipate ( $R^2 = 0.67$ )].

The fraction of organic acid mass contributed by suberate peaked below cloud (1.3%), with a clear air value of 0.7%. Azelate was detected only in one clear air sample at ~ 600 m (~ 0.01  $\mu\text{g}/\text{m}^3$ ). Azelaic acid is known to be an oxidation product from

biogenic unsaturated fatty acids, mainly those containing a double bond at the C-9 position (Yokouchi and Ambe; 1986; Kawamura and Gagosian, 1987; Kawamura and Kaplan, 1987; Narukawa et al., 1999). C<sub>8</sub> and C<sub>9</sub> dicarboxylic acids decreased in concentration rapidly with increasing altitude, presumably because the aged aerosol has undergone oxidative decay of these and other longer-chain acids.

### 6.5.2 Unsaturated and Hydroxylated Dicarboxylic Acids

Photooxidation of aromatic hydrocarbons is known to lead to ring-cleavage reactions and produce C<sub>2</sub> - C<sub>5</sub> dicarbonyls that are subsequently oxidized to form dicarboxylic acids (Kawamura and Ikushima, 1993; Calvert et al., 2002). Maleic acid, an unsaturated dicarboxylic acid, is produced by photooxidation of benzene (Kawamura and Ikushima, 1993; Kawamura et al., 1996a) and is emitted from diesel and gasoline engines (Rogge et al., 1993). The organic acid mass fraction of maleate was highest in the FT (3.2%) (Figure 6.6). It was correlated most closely with benzoate ( $R^2 = 1$ ,  $n = 3$ ), followed by glutarate ( $R^2 = 0.52$ ), formate ( $R^2 = 0.39$ ), succinate ( $R^2 = 0.16$ ), and acetate ( $R^2 = 0.15$ ). Maleic and succinic acids exhibit similar vertical distributions; the most direct link between these two species is formation of succinic acid by hydrogenation of maleic acid, although there is no clear evidence from the present data to support this mechanism. Benzoic acid, like maleic acid, is also produced by the oxidation of aromatic hydrocarbons, specifically toluene (Forstner et al., 1997; Jang and Kamens, 2001). Maleic acid is expected to be further oxidized to produce malonic and oxalic acids, or transformed to fumaric acid, an isomer of maleic acid (Kawamura et al., 2005).

Kawamura and Ikushima (1993) reported that the cis-configuration (maleic acid) is generally more abundant than the trans-configuration (fumaric acid).

Malic acid, whose anion (malate) was detected in only four samples, is a hydroxylated dicarboxylic acid that can be formed by hydration of maleic acid and hydroxylation of succinic acid (Kawamura and Ikushima, 1993; Kawamura and Sakaguchi, 1999; Kawamura et al., 2005). Evidence for the hydroxylation reaction is based on detection of C<sub>5</sub> and C<sub>6</sub> hydroxyacids (Appel et al., 1979). It has been proposed that the oxidation of succinic acid can form malonic acid with malic acid acting as an intermediate (Kawamura and Ikushima, 1993). Succinate was not measured in the same samples as malic acid, but it was twice measured in samples collected immediately after a sample containing malate. Malate and maleate were measured together in one sample. Malate was best-correlated with acetate ( $R^2 = 0.89$ ) and oxalate ( $R^2 = 0.77$ ); oxalic and malonic acids are known oxidation products of malic acid (Kawamura and Ikushima, 1993), but it is uncertain as to whether acetic acid is also an oxidative product. Malate exhibited low concentrations (maximum of 0.02  $\mu\text{g}/\text{m}^3$ ) and was detected only below 2 km.

### 6.5.3 Saturated Monocarboxylic Acids

After oxalate, the next most abundant particulate organic acid measured in GoMACCS was acetate, with formate and several other acids with similar concentrations following. Acetate was measured more frequently than formate; acetic acid has a higher Henry's Law coefficient and a lower vapor pressure as compared to formic acid, which allows it to partition more easily into the aerosol phase (Saxena and Hildemann, 1996).



The organic acid mass fraction of acetate peaked in the FT ( $20 \pm 28\%$ ) (Figure 6.6). Acetate and formate were the most abundant organic acids in droplet residual particles after oxalate, contributing 13% and 3% to the total organic acid mass, respectively. This suggests that acetate and formate are active components in droplet chemistry; acetic acid is further oxidized in the aqueous phase to yield oxalic (with glyoxylic acid as an intermediate) and formic acids (Lim et al., 2005; Carlton et al., 2006). Some of the highest acetate concentrations (maximum of  $0.6 \mu\text{g}/\text{m}^3$ ) occurred in the Houston Ship Channel area. As will be discussed later, the oxidation of aromatic VOCs leads preferentially to acetate and formate, as compared to other organic acids studied.

Pyruvic acid, the main oxidation product of methylglyoxal, has been shown to originate from biogenic sources such as isoprene (Talbot et al. 1995); it is also a precursor to oxalic acid in the aqueous phase (Lim et al., 2005; Carlton et al., 2006). Pyruvate was detected only in clear air and below cloud, suggesting that it is rapidly oxidized in the condensed phase to form products of higher polarity such as acetic and oxalic acids (Lim et al., 2005; Carlton et al., 2006). Pyruvate has been reported in other urban areas (Table 6.1); pyruvic acid concentrations ranged between  $0.06 - 1.15 \mu\text{g}/\text{m}^3$  in Sao Paulo (Souza et al., 1999), between  $0.04 - 0.10 \mu\text{g}/\text{m}^3$  in Schenectady, New York (Khwaja, 1995), and exhibited an average of  $0.03 \mu\text{g}/\text{m}^3$  in Beijing (Huang et al., 2005) and  $0.06 \mu\text{g}/\text{m}^3$  in Vienna (Limbeck and Puxbaum, 1999). In the present study, pyruvate is most closely correlated with benzoate ( $R^2 = 0.42$ ) and methacrylate ( $R^2 = 0.26$ ). Souza et al. (1999) showed that oxalic and pyruvic acids were well-correlated ( $R^2 = 0.67$ ) in Sao Paulo. As will be discussed, pyruvate is a product in the photooxidation of aromatic VOCs, similar to benzoate, acetate, and oxalate.

The fraction of organic acid mass contributed by glyoxylate was a maximum in droplet residual samples (1.1%), because it is likely an immediate precursor to oxalic acid in the aqueous phase (Sorooshian et al., 2006a). As evidenced by its vertical distribution, glyoxylate was usually detected at altitudes corresponding to those where clouds were present. Glyoxylic acid is produced by the oxidation of glyoxal and glycolic acid (Kawamura et al., 1996a; Ervens et al., 2004). Glyoxylate exhibited its strongest correlation with formate ( $R^2 = 0.91$ ), followed by benzoate ( $R^2 = 0.58$ ). As will be discussed, glyoxylate is an oxidative product, similar to formic and benzoic acids, from the photooxidation of aromatic VOCs.

#### 6.5.4 Unsaturated Monocarboxylic Acids

Methacrylic acid is a second-generation gas-phase oxidation product of isoprene, formed from methacrolein ( $C_4H_6O$ ) oxidation (Claeys et al., 2004). The methacrolein Henry's Law constant, 6.5 M/atm, is too low for it to participate directly in SOA formation (Iraci et al., 1999; Gelencser and Varga, 2005). Methacrylic acid has a Henry's Law constant of  $2 \times 10^3$  M/atm; this value is such that it is a possible precursor for other organic acids in the aqueous phase (Meylan and Howard, 1991; Gelencser and Varga, 2005). (Assuming a pH range of 2–5 for cloud droplets, the effective Henry's Law constant,  $K_{H,eff} = K_H \cdot (1 + K_a/[H^+])$ , is calculated to be between  $2 \times 10^3$  M/atm and  $6.4 \times 10^3$  M/atm.) An IC peak corresponding to that at which methacrylate normally elutes was detected in both clear air and cloud droplet residual samples. Tests were done to see if another anion, 2-methylglycerate, elutes at the same time as methacrylate; methacrylic acid is thought to form 2-methylglyceric acid ( $C_3H_7O_2COOH$ ; also called

2,3-dihydroxy-2-methylpropanoic acid) via oxidation (Claeys et al., 2004). After synthesizing standards for 2-methylglyceric acid and analyzing them by IC, no conclusive evidence was found that 2-methylglycerate co-elutes with methacrylate. In addition, field samples were too dilute to give any signal by LC/ESI-MS (liquid chromatography/electrospray ionization-mass spectrometry) in the negative ion mode for methacrylic and 2-methylglyceric acids. It is also unclear as to whether methacrylic acid was formed in the droplet growth chamber of the PILS as a decomposition product of larger species such as polymers. This species, measured to be  $< 0.04 \mu\text{g}/\text{m}^3$ , will be termed methacrylate henceforth; it was best-correlated with pyruvate ( $R^2 = 0.26$ ) and glyoxylate ( $R^2 = 0.15$ ), two other species active in the aqueous-phase chemistry of isoprene oxidation products (Lim et al., 2005; Carlton et al., 2006). Methacrylate will be discussed in more detail subsequently.

Benzoate was measured most frequently in clear air and in the vicinity of the Houston Ship Channel and urban core area. Benzoate was detected only below 1 km, suggesting that it is likely oxidized rapidly. Aromatic hydrocarbons are emitted by numerous point sources in the Houston area, with a high density of sources in the Ship Channel area (<http://www.esrl.noaa.gov/csd/2006/fieldops/emission.html>). Toluene constitutes one of these species emitted, and its gas-phase oxidation leads to benzoic acid as a product (Forstner et al., 1997; Jang and Kamens, 2001; Hamilton et al., 2005). Jang and Kamens (2001) showed that in the presence of  $\text{NO}_x$  and 1-propene, 7-12% of the toluene-OH radical reaction yields benzaldehyde after H-abstraction from the methyl group. Based on data from five different studies, Calvert et al. [2002] suggested an average yield of  $6 \pm 1\%$  for the same reaction pathway. After subsequent oxidation of

benzaldehyde, benzoic acid is produced from the benzoylperoxy radical - HO<sub>2</sub> reaction. It should be noted, however, that Kleindienst et al. (2004) did not detect particulate benzoic acid in toluene photooxidations and attributed its detection in the previous studies of Forstner et al. (1997) and Jang and Kamens (2001) to be a result of high initial concentrations of aromatic and NO<sub>x</sub> gases, which lead to significant levels of ring-retaining products. When detected during GoMACCS, benzoate was well-correlated with glutarate and succinate ( $R^2 = 0.98$  and  $0.63$ , respectively), which represent ring-opening products from the oxidation of C<sub>5</sub>-C<sub>7</sub> cycloalkenes (Hatakeyama et al., 1985; Kalberer et al., 2000). Benzoate was highly correlated with maleate ( $R^2 = 1$ ,  $n = 3$ ), glyoxylate ( $R^2 = 0.58$ ), and pyruvate ( $R^2 = 0.42$ ), all of which will be shown later to be products from the photooxidation of aromatic VOCs.

## **6.6 Role of Organic Acids in Cloud Droplet Chemistry**

### **6.6.1 Oxalic Acid as a Reaction Product in Clouds**

The below-cloud organic acid product distribution was dominated by oxalate (69%), followed by acetate (10%), formate (9%), and MSA (6%) (Figure 6.6). In cloud droplet residual particles, the distribution of organic acids changed as a result of cloud-phase reactions forming oxalic acid through its main intermediate, glyoxylic acid (Sorooshian et al., 2006a; Sorooshian et al., submitted). Glyoxylate, which contributed an average of 0.2% to the organic acid mass below cloud, accounted for 1.1% in droplet residual particles. Oxalic acid can also be produced by malonic acid oxidation (Ervens et al., 2004; Sorooshian et al., 2006a), and malonate contributed 1.7% to the organic acid mass in droplet residual particles, as compared to a 0.3% contribution to below-cloud

aerosol. The source of malonic acid was most likely the decarboxylation of larger dicarboxylic acids such as succinic acid (Ervens et al., 2004). Acetic acid is an aqueous-phase precursor to glyoxylic acid (Lim et al., 2005; Carlton et al., 2006), and it contributed 12.6% to the organic acid mass in droplet residual particles as opposed to 9.9% in below-cloud aerosol. The oxalate contribution to the organic acid mass increased to 77% in cloud droplet residual particles as a result of aqueous-phase reactions (Ervens et al., 2004; Sorooshian et al., 2006a). As the droplets above cloud evaporated, the organic acid product distribution was shifted even more towards oxalic acid, as it contributed 87% to the organic acid mass, while acetate, glyoxylate, and malonate decreased to 7%, 1%, and 0.7%, respectively.

Droplet residual particle composition was studied as a function of altitude in cloud. With increasing altitude in cloud, the cumulative average of the oxalate:glyoxylate ratio in all clouds studied decreased and then increased (just above base = 78; mid-level = 19; just below top = 232); this behavior suggests that glyoxylic acid is produced most rapidly in the bottom half of clouds, while oxalic acid is produced most efficiently in the top half of the clouds by glyoxylic acid oxidation. An average is reported here since glyoxylate did not achieve sufficiently high concentrations at multiple heights in more than a couple individual cloud fields. In-cloud data from all samples containing both oxalate and glyoxylate from different flights are shown together in Figure 6.7 as a function of normalized height in cloud (height above cloud base/cloud thickness). The oxalate:glyoxylate ratio decreases from the lower portions of clouds to the mid-point, at which point the ratio increases with increasing altitude.

Ambient measurements of the oxalate:glyoxylate ratio are compared to predictions of a state-of-the-art microphysical/chemical cloud parcel model [Ervens et al., 2004] that simulates the activation of a population of aerosol particles. The model simulates cloud cycles that are intended to represent the trajectory of a typical air parcel in a cloudy atmosphere, including gas and aqueous-phase chemical reactions. The parcel follows a prescribed trajectory that encounters a cloud for a fixed period of time ( $\sim 850$  s each cycle). During a cloud cycle, a parcel ascends from the base of a cloud to its top and then descends back down. Four gas-phase VOC precursors of dicarboxylic acids are included in the model chemistry; toluene and ethene represent anthropogenic emissions, isoprene represents biogenic emissions, and cyclohexene serves as a model compound for symmetrical alkenes similar to monoterpenes emitted by biogenic sources. Oxidation products of these species in the gas phase (glyoxal, glyoxylic acid, glycolic acid, hydroxyacetaldehyde, methylglyoxal, pyruvic acid, acetic acid, adipic acid, and glutaric acid) can transfer to the aqueous phase to undergo reactions to form lower-volatility products. The same initial conditions used by Sorooshian et al. (2006a) are used to simulate two conditions: clouds uninfluenced by local pollution sources (“clean” initial concentrations:  $1755 \text{ particles/cm}^3$ ,  $0.5 \text{ ppb SO}_2$ ,  $40 \text{ ppb O}_3$ ,  $1 \text{ ppb H}_2\text{O}_2$ ,  $0.04 - 0.06 \text{ ppb}$  each for isoprene, toluene, cyclohexene, ethene) and clouds immediately impacted by pollution sources (“polluted” initial concentrations:  $4890 \text{ particles/cm}^3$ ,  $69.5 \text{ ppb SO}_2$ ,  $40 \text{ ppb O}_3$ ,  $1 \text{ ppb H}_2\text{O}_2$ ,  $0.04 - 0.11 \text{ ppb}$  each for isoprene, toluene, cyclohexene, ethene).

In order to evaluate the comparison between the predicted and observed oxalate:glyoxylate ratio, it is necessary to compare cloud-contact times in the model and in the Houston cumulus clouds studied. Ervens et al. (2004) used trajectories derived

from modeling of stratocumulus clouds and showed mean contact times with cloud on the order of  $\sim 850$  s (14 min). For the current study we use model trajectories for shallow cumulus clouds based on model simulations of GoMACCS cases as well as simple calculations based on updraft velocities and cloud depth. The stratocumulus clouds in the previous work were shallower ( $< 200$  m) as compared to GoMACCS clouds (average depth  $\sim 1100$  m), but the more convective clouds in GoMACCS exhibited higher updraft velocities ( $1.2 \pm 1.3$  m/s). Using the average GoMACCS cloud depth and updraft velocity measured, an estimate of the cloud-contact time for one cloud cycle is  $\sim 900$  s (15 min). There are obvious uncertainties in this estimate such as the assumption of no variability in cloud depth or updraft velocity during the time the aircraft was probing a single cloud field. Model simulations of air parcel trajectories in cumulus clouds in the Houston area show that among 500 parcels initialized in the BL, approximately 30% spent more than 6 min in cloud, and some parcels spent up to 21 min in cloud. Since the oxalate:glyoxylate data are reported from some of the largest clouds studied, it is likely that many of the parcels were in contact with these large clouds for times in the order of 10 - 20 min. Therefore, the predicted trend of the ratio of oxalate:glyoxylate as a function of in-cloud time should provide a meaningful comparison to GoMACCS measurements.

The general trend predicted for a typical cloud cycle is that the ratio of oxalate:glyoxylate decreases and then increases with increasing cloud-contact time (Figure 6.7). The trend and absolute values of the oxalate:glyoxylate ratio predicted were similar for the “clean” and “polluted” simulations. The range of values predicted agree with ambient GoMACCS measurements; thus, the residence times of parcels in GoMACCS clouds are consistent with that needed for the observed chemical changes in

the oxalate:glyoxylate ratio in cloud. The multi-step nature of oxalic acid production leads to more efficient production in the upper portions of clouds; in addition, the upper portions of clouds usually exhibit higher liquid water content (LWC) values, which increases droplet pH, a condition favorable for oxalic acid production from glyoxylate oxidation (Sorooshian et al., submitted).

It should also be noted that some of the highest oxalate levels were observed during spirals performed in clear air with clouds nearby. For instance, after profiling a single growing cumulus cloud, the aircraft performed a spiral descent from 3400 m to 700 m between the profiled cloud and other deep cumuli. Three total PILS samples were collected, where each sample represents aerosol over a third of the height range during the descent; the oxalate concentration increased with increasing altitude (0.23, 0.34, 0.41  $\mu\text{g}/\text{m}^3$ ). This suggests that significant amounts of cloud-processed aerosol containing organic acids might exist outside the edges of these deep cumuli. Sources of cloud-processed aerosol around the edges of cumulus clouds include detrainment out of the sides of clouds and transport from the cloudtop region by downdrafts.

#### **6.6.2 High Nitrate Episodes: Methacrylic Acid in Cloud Droplets and Suppressed Organic Acid Formation**

During two flights, the TO probed cloud fields above agricultural areas west of Houston where elevated levels of particulate nitrate ( $> 0.6 \mu\text{g}/\text{m}^3$ ; up to 40% of total PILS mass) were observed. The TO also probed cloud fields within this same vicinity during three other flights when there were lower nitrate levels. During the five flights, the TO flew within the same altitude range (1000 - 3000 m). The below-cloud aerosol



during high-nitrate flights exhibited higher  $\text{NH}_4^+:\text{SO}_4^{2-}$  molar ratios (usually  $> 2$ ) as opposed to low-nitrate flights, indicating that there was enough  $\text{NH}_3$  to neutralize the  $\text{SO}_4^{2-}$ , thereby allowing  $\text{NO}_3^-$  to form in the particle phase from gaseous nitric acid ( $\text{HNO}_3$ ) condensation with available  $\text{NH}_3$ .

During the flight with the largest average nitrate levels, the frequency of detection of methacrylate was relatively high compared to other flights, and was the only flight in which methacrylate was detected in droplet residual particle samples. Glyoxylic acid was also measured in the droplet residual samples. These data are consistent with the multiphase mechanism proposed by Claeys et al. (2004); they observed that the ambient concentrations of 2-methyltetrols and 2-3 dihydroxymethacrylic acid, the latter of which is proposed to have methacrylic acid as an intermediate, were enhanced under high- $\text{NO}_x$  conditions and that they could be formed by acid-catalyzed oxidation with hydrogen peroxide. Owing to the high particulate nitrate levels, both in and out of cloud, it is thought that high- $\text{NO}_x$  conditions existed and that the droplets were relatively acidic since the cloud LWC values were lower this flight compared to other flights. Methacrolein could have produced methacrylate in these acidic droplets, which could have been further oxidized to form 2-methylglyceric acid.

Unlike the majority of the other cloud fields sampled during GoMACCS, the cloud fields experienced during the high-nitrate flights exhibited lower organic acid levels above cloud as compared to below (Sorooshian et al., submitted). In the presence of high  $\text{HNO}_3$  levels and relatively lower LWC values, the droplets are more acidic (larger droplets would be more dilute), presumably suppressing organic acid formation. For example, the net production rate of oxalic acid in acidic droplets is suppressed

because the rate constant of glyoxylic acid oxidation is an order of magnitude lower than that of glyoxylate (Ervens et al., 2003; Sorooshian et al., 2006a).

### 6.7 Organic Acids Downwind of the Houston Ship Channel

One flight (Flight 7; 28 August 2006) was devoted to studying the evolution of three different plumes from sources on the Houston Ship Channel (Figure 6.8), an area emitting a significant amount of VOCs, including aromatic hydrocarbons (<http://www.esrl.noaa.gov/csd/2006/fieldops/emission.html>). Several crosswind transects were made to identify the largest plumes and then the plane flew 10 - 15 min legs at ~ 500 m going downwind inside three separate plumes. The fine particle number concentration was strongest at the source of plume B ( $37,000 \text{ cm}^{-3}$ ), followed by plume A ( $14,000 \text{ cm}^{-3}$ ), and then plume C ( $8000 \text{ cm}^{-3}$ ). At a plume age of 1.5 h (plume ages calculated with distance from source and wind speed), plumes A and B were diluted to approximately  $8000 \text{ cm}^{-3}$ , while plume C decreased to  $1000 \text{ cm}^{-3}$ . On the other hand, the PCASP ( $0.1 - 2.5 \text{ }\mu\text{m}$ ) number concentrations grew with plume age in plumes A, B, and C, reaching more than  $20,000 \text{ cm}^{-3}$  at plume ages of 1.5 h; the majority of the particles in these plumes exceeded  $1 \text{ }\mu\text{m}$  in diameter.

The mass fractions of sulfate and ammonium together exceeded 80% in all three plumes from the source to a corresponding plume age of 1.5 h. On average, the mass fraction of organic acids was greatest in plume A (2.7%), followed by plumes B (1%) and C (0.5%). Plume C exhibited the lowest volume ( $2 - 2.5 \text{ }\mu\text{m}^3/\text{cm}^3$ ) and PILS mass ( $2.5 - 3.5 \text{ }\mu\text{g}/\text{m}^3$ ) concentrations both at the source and downwind up to 40 km, with little variation in the aerosol composition. Plumes A and B showed an increase in aerosol

volume ( $\sim 3$  to  $4 \mu\text{m}^3/\text{cm}^3$ ) and mass concentration ( $\sim 4$  to  $6 \mu\text{g}/\text{m}^3$ ) from the source to a plume age of 1.5 h. Sulfate continuously increased with downwind distance in both plume A and B. Between a plume age of 0.5 to 1.5 h, the total organic acid concentration in plume A was stable at approximately  $0.09 \mu\text{g}/\text{m}^3$ , unlike plume B, where it grew from 0.03 to  $0.12 \mu\text{g}/\text{m}^3$ . Of the total organic acid mass, acetate and formate collectively accounted for  $\sim 5\%$  and oxalate contributed  $\sim 55\%$  upwind of the three plumes, while downwind, acetate and formate accounted for 29 - 77% and oxalate contributed 6 - 56%. During the early stages of the plumes ( $< 0.5$  h), the organic acid mass fraction of benzoate reached up to 9% and 25% in plumes A and B, respectively. It is likely that the SOA formed by gas-to-particle conversion from aromatic emissions initially contained species such as benzoic acid, that were subsequently oxidized to form lower molecular weight organic acids (that were less volatile and more polar), dominated by acetic and formic acids and followed by oxalic acid. Plume C was composed entirely of acetate among all of the organic acids. An average of all clear air Ship Channel samples during the campaign show that the most abundant organic acids in decreasing order of their organic acid mass fractions are as follows: oxalate (37%), acetate (36%), formate (9%), benzoate (9%), and pyruvate (4%); these results differ from other areas sampled because benzoate was actually detected, and oxalate contributed the least to the organic acid mass in this area, while acetate, formate, and pyruvate contributed relatively more.

## 6.8 Evaluation of Ambient Data Relative to Laboratory Chamber Experiments of *m*-xylene Photooxidation

The GoMACCS observations prompt the question of the extent to which particulate products measured in the Houston atmosphere match those of aromatic oxidation in a laboratory chamber. Laboratory tests in the dual 28 m<sup>3</sup> Teflon chambers at Caltech were performed to study the organic acid product distribution from the photooxidation of a model aromatic hydrocarbon, *m*-xylene. A detailed description of these experiments and SOA yield are addressed elsewhere (Ng et al., 2007), but selected results are briefly discussed here in relation to the field measurements. The chambers are surrounded by banks of black lights that are turned on after the injection of seed aerosol and gas-phase reactants to initiate photooxidation. Seed aerosol, produced by atomizing a solution of ammonium sulfate, was first introduced into the chambers in these experiments. Sulfuric acid was added to the atomizing solution when studying the effects of acidic seed aerosol. For nucleation experiments, no seed was added. Nitrous acid (HONO) was introduced as a source of OH and NO<sub>x</sub> for a series of high-NO<sub>x</sub> tests; extra NO was added to ensure a NO<sub>x</sub> level near ~ 1 ppm. For the low-NO<sub>x</sub> experiments, H<sub>2</sub>O<sub>2</sub> served as the OH source. The range of initial VOC:NO<sub>x</sub> ratios during the experiments, 0.3 – 2500 (Table 6.3), encompasses values expected in the Houston atmosphere.

For the experiments conducted with *m*-xylene and the different NO<sub>x</sub> and seed conditions, the SOA mass fraction of organic acids was between 17% and 41% (Table 6.3); SOA mass was determined by multiplying the DMA volume concentration by a calculated SOA density (as determined by comparing DMA size distribution to the AMS size distribution; error =  $\pm 0.10$  g/cm<sup>3</sup>). Higher organic acid mass fractions were

exhibited during the low-NO<sub>x</sub> experiments (35 - 41%), as compared to high-NO<sub>x</sub> conditions (17 - 26%); however, the high-NO<sub>x</sub> organic acid mass fractions are likely an underestimate due to observed nitrate contamination in the laboratory chambers (5 - 10 µg/m<sup>3</sup>), which increased the volume concentration. The organic acid product distribution was similar for all the experiments; acetate (22 - 45%) and formate (28 - 37%) were the dominant products, followed by pyruvate (15 - 28%), oxalate (5 - 8%), and a set of other acids (malonate, succinate, glutarate, glyoxylate, and maleate were each ≤ 4%). As stated earlier, acetate, lactate, and glycolate co-elute, so it is likely that the contribution of acetate reported is an overestimate, while glycolate and lactate could have been products.

Figure 6.9 shows the time evolution of all organic acids during one photooxidation experiment (75 ppb *m*-xylene/low NO<sub>x</sub>/non-acidic ammonium sulfate seed aerosol). The first organic acid products formed are acetate/glycolate/lactate, formate, pyruvate, and oxalate, in decreasing level of concentration. Less abundant products included malonate, succinate, glutarate, maleate, and glyoxylate. All species stabilize in concentration within approximately four hours with the exception of oxalate, malonate, succinate, and glutarate, which continue to grow until the end of the experiment. For the first two hours of irradiation, the oxalate:malonate mass ratio increases from 2 to 4, and then decreases steadily to 1.7 by the end of the experiment (9 h of irradiation). The malonate:succinate and succinate:glutarate ratios do not show such a trend over the duration of the experiment. One possibility is that in the first two hours, malonic acid was more efficiently being photooxidized to form oxalic acid, and then in the final hours, malonate was being formed more efficiently. It has been suggested that some of the dicarboxylic acids from the photooxidation of aromatic VOCs

could be dimers of monocarboxylic acids (Fisseha et al., 2004), which is consistent with the first step of polymerization as reported by Kalberer et al. (2004). This could explain why oxalate, malonate, succinate, and glutarate were still increasing in concentration until the end of the experiment. Pyruvic acid, which exhibited most of its growth in the first two hours after lights were turned on, may be a compound involved in polymerization processes (Kalberer et al., 2004).

Fisseha et al. (2004) also reported higher particulate concentrations of monocarboxylic acids as compared to dicarboxylic acids in their study of the photooxidation of 1,3,5 trimethylbenzene in the presence of 300 ppb propene and 300 ppb NO<sub>x</sub>; they reported that organic acids accounted for 20 - 45% of the aerosol mass formed, similar to results in this study. However, it should be noted that the aerosol sampling techniques used both in this study and that of Fisseha et al. (2004) rely on steam condensation, which may break down polymers to their monomers resulting in higher concentrations of organic acids such as acetic, formic, and pyruvic acids.

These laboratory chamber results are consistent with acetate, formate, and pyruvate contributing more to the organic acid mass in the Ship Channel area compared to all other locations during GoMACCS. The higher contribution of oxalate in the Ship Channel area as compared to the laboratory chamber may be a result of a higher background level of oxalate in the area.

## **6.9 Conclusions**

Ambient measurements of water-soluble aerosol species were made on board the CIRPAS Twin Otter during the 2006 GoMACCS field campaign in southeastern Texas.

Sulfate and ammonium dominated the water-soluble mass ( $\text{NH}_4^+ + \text{SO}_4^{2-} = 84 \pm 14\%$ ). The average  $\text{NH}_4^+:\text{SO}_4^{2-}$  molar ratio was  $1.77 \pm 0.85$ . The most acidic samples and highest sulfate loadings occurred downwind of the W. A. Parish Power Plant. The mass fraction of nitrate was usually less than 10%, but elevated levels were observed west of Houston during two particular flights ( $> 0.6 \mu\text{g}/\text{m}^3$ ; up to 40% of total PILS mass). The cloud fields in these areas were unique in that the droplet residual particles contained methacrylate, which is known to be formed under high- $\text{NO}_x$  conditions by the acid-catalyzed reaction of isoprene with hydrogen peroxide. Suppressed organic acid formation was also observed in the high nitrate-containing clouds since they were suspected of containing relatively acidic droplets.

The average particulate water-soluble mass fraction of organic acids measured was  $3.4 \pm 3.7\%$ ; concentrations of organic acids increased with decreasing carbon number from  $\text{C}_9$  to  $\text{C}_2$ . The organic acid mass fraction of oxalate, the most abundant organic acid measured, was greatest above cloud as a result of aqueous-phase chemistry in cloud droplets followed by subsequent droplet evaporation above cloudtops. The observed distribution of organic acids as a function of altitude in cloud is consistent with the multi-step nature of liquid-phase oxalic acid production; predictions from a cloud parcel model agree with measurements that show that the oxalate:glyoxylate ratio decreases and then increases as a function of altitude in GoMACCS cumuli. Glyoxylate is likely formed rapidly with increasing altitude in the lower portion of clouds, which then allows it to efficiently produce oxalic acid in the upper portion.

Oxalate, acetate, formate, benzoate, and pyruvate, in decreasing order, contributed the most to the organic acid mass in the Houston Ship Channel region, an area with

significant VOC emissions. The chemical composition of the aerosol in this region was different from that in other areas around Houston in that benzoate was detected, oxalate contributed the least to the organic acid mass, while acetate, formate, and pyruvate contributed relatively more. In laboratory chamber experiments, the photooxidation of *m*-xylene, a model aromatic VOC, leads to a particulate organic acid product distribution consistent with Ship Channel observations. The chamber SOA mass fraction accounted for by organic acids ranged from 17-41%, with higher values observed under low-NO<sub>x</sub> conditions, as compared to high-NO<sub>x</sub> conditions. Acetate/glycolate/lactate, formate, and pyruvate were the dominant products, accounting for 22-45%, 28-37%, and 15-28% of the total organic acid mass, respectively.

Atmospheric measurements of water-soluble aerosol species, especially organic acids, provide valuable data to constrain gas- and particle/droplet-phase chemistry. Organic acids identified in the Houston atmosphere give important clues as to the sources of the atmospheric organic aerosol in that region and in urban atmospheres in general.

## 6.10 Acknowledgements

This work was supported by National Oceanic and Atmospheric Administration grant NA06OAR4310082.

## 6.11 References

Angelino, S., D. T. Suess, and K. A. Prather (2001), Formation of aerosol particles from reactions of secondary and tertiary alkylamines: Characterization by aerosol time-of-flight mass spectrometry, *Environ. Sci. Technol.*, 35, 3130-3138.



Appel, B. R., E. M. Hoffer, E. L. Kothny, S. M. Wall, M. Haik, and R. L. Knights (1979), Analysis of carbonaceous material in Southern-California atmospheric aerosols. 2., *Environ. Sci. Technol.*, *13*, 98-104.

Blando, J. D., and B. J. Turpin (2000), Secondary organic aerosol formation in cloud and fog droplets: a literature evaluation of plausibility, *Atmos. Environ.*, *34*, 1623-1632.

Calvert, J. G., R. Atkinson, K. H. Becker, R. M. Kamens, J. H. Seinfeld, T. J. Wallington, and G. Yarwood (2002), *The Mechanisms of Atmospheric Oxidation of Aromatic Hydrocarbons*, Oxford University Press, New York, N. Y.

Carlton, A. G., B. J. Turpin, H. J. Lim, K. E. Altieri, and S. Seitzinger (2006), Link between isoprene and secondary organic aerosol (SOA): Pyruvic acid oxidation yields low volatility organic acids in clouds, *Geophys. Res. Lett.*, *33*, L06822, doi:10.1029/2005GL025374.

Chebbi, A., and P. Carlier (1996), Carboxylic acids in the troposphere, occurrence, sources, and sinks: A review, *Atmos. Environ.*, *30*, 4233-4249.

Claeys, M., W. Wang, A. C. Ion, I. Kourchev, A. Gelencser, and W. Maenhaut (2004), Formation of secondary organic aerosols from isoprene and its gas-phase oxidation products through reaction with hydrogen peroxide, *Atmos. Environ.*, *38*, 4093-4098.

Crahan, K. K., D. Hegg, D. S. Covert, and H. Jonsson (2004), An exploration of aqueous oxalic acid production in the coastal marine atmosphere, *Atmos. Environ.*, *38*, 3757-3764.

Ervens, B., S. Gligorovski, and H. Herrmann (2003), Temperature-dependent rate constants for hydroxyl radical reactions with organic compounds in aqueous solutions, *Phys. Chem. Chem. Phys.*, *5*, 1811-1824.

Ervens, B., G. Feingold, G. J. Frost, and S. M. Kreidenweis (2004), A modeling study of aqueous production of dicarboxylic acids: 1. Chemical pathways and speciated organic mass production, *J. Geophys. Res.*, *109*, D15205, doi:10.1029/2003JD004387.

Faust, B. C. (1994), Photochemistry of clouds, fogs, and aerosols, *Environ. Sci. Technol.*, *28*, A217-A222.

Fisseha, R., J. Dommen, M. Sax, D. Paulsen, M. Kalberer, R. Maurer, F. Hofler, E. Weingartner, and U. Baltensperger (2004), Identification of organic aerosol and the acids in secondary corresponding gas phase from chamber experiments, *Anal. Chem.*, *76*, 6535-6540.

Forstner, H. J. L., R. C. Flagan, and J. H. Seinfeld (1997), Secondary organic aerosol from the photooxidation of aromatic hydrocarbons: Molecular composition, *Environ. Sci. Technol.*, *31*, 1345-1358.

Gelencser, A., and Z. Varga (2005), Evaluation of the atmospheric significance of multiphase reactions in atmospheric secondary organic aerosol formation, *Atmos. Chem. Phys.*, **5**, 2823-2831.

Grassian, V. H. (2001), Heterogeneous uptake and reaction of nitrogen oxides and volatile organic compounds on the surface of atmospheric particles including oxides, carbonates, soot and mineral dust: implications for the chemical balance of the troposphere, *Int. Rev. Phys. Chem.*, **20**, 467-548.

Grosjean, D., K. Vancauwenberghe, J. P. Schmid, P. E. Kelley, and J. N. Pitts (1978), Identification of C3-C10 aliphatic dicarboxylic-acids in airborne particulate matter, *Environ. Sci. Technol.*, **12**, 313-317.

Grosjean, D., and K. Fung (1984), Hydrocarbons and carbonyls in Los-Angeles air, *Japca. J. Air Waste Ma.*, **34**, 537-543.

Grosjean, D. (1988), Aldehydes, carboxylic-acids and inorganic nitrate during NSMCS, *Atmos. Environ.*, **22**, 1637-1648.

Hamilton, J. F., P. J. Webb, A. C. Lewis, and M. M. Reviejo (2005), Quantifying small molecules in secondary organic aerosol formed during the photo-oxidation of toluene with hydroxyl radicals, *Atmos. Environ.*, **39**, 7263-7275.

Hatakeyama, S., T. Tanonaka, J. H. Weng, H. Bandow, H. Takagi, and H. Akimoto (1985), Ozone cyclohexene reaction in air - quantitative-analysis of particulate products and the reaction-mechanism, *Environ. Sci. Technol.*, **19**, 935-942.

Hatakeyama, S., M. Ohno, J. H. Weng, H. Takagi, and H. Akimoto (1987), Mechanism for the formation of gaseous and particulate products from ozone-cycloalkene reactions in air, *Environ. Sci. Technol.*, **21**, 52-57.

Huang, X. F., M. Hu, L. Y. He, and X. Y. Tang (2005), Chemical characterization of water-soluble organic acids in PM<sub>2.5</sub> in Beijing, China, *Atmos. Environ.*, **39**, 2819-2827.

Huang, X. F., J. Z. Yu, L. Y. He, and Z. B. Yuan (2006), Water-soluble organic carbon and oxalate in aerosols at a coastal urban site in China: Size distribution characteristics, sources, and formation mechanisms, *J. Geophys. Res.*, **111**, D22212, doi:10.1029/2006JD007408.

Huang, X. F., and J. Z. Yu (2007), Is vehicle exhaust a significant primary source of oxalic acid in ambient aerosols?, *Geophys. Res. Lett.*, **34**, L02808, doi:10.1029/2006GLO28457.

Iraci, L. T., B. M. Baker, G. S. Tyndall, and J. J. Orlando (1999), Measurements of the Henry's law coefficients of 2-methyl-3-buten-2-ol, methacrolein, and methylvinyl ketone, *J. Atmos. Chem.*, **33**, 321-330.

Jang, M. S., and R. M. Kamens (2001), Characterization of secondary aerosol from the photooxidation of toluene in the presence of NO<sub>x</sub> and 1-propene, *Environ. Sci. Technol.*, **35**, 3626-3639.

Kalberer, M., J. Yu, D. R. Cocker, R. C. Flagan, and J. H. Seinfeld (2000), Aerosol formation in the cyclohexene-ozone system, *Environ. Sci. Technol.*, **34**, 4894-4901.

Kalberer, M., D. Paulsen, M. Sax, M. Steinbacher, J. Dommen, A. S. H. Prevot, R. Fisseha, E. Weingartner, V. Frankevich, R. Zenobi, and U. Baltensperger (2004), Identification of polymers as major components of atmospheric organic aerosols, *Science*, **303**, 1659-1662.

Kanakidou, M., J. H. Seinfeld, S. N. Pandis, I. Barnes, F. J. Dentener, M. C. Facchini, R. Van Dingenen, B. Ervens, A. Nenes, C. J. Nielsen, E. Swietlicki, J. P. Putaud, Y. Balkanski, S. Fuzzi, J. Horth, G. K. Moortgat, R. Winterhalter, C. E. L. Myhre, K. Tsigaridis, E. Vignati, E. G. Stephanou, and J. Wilson (2005), Organic aerosol and global climate modelling: a review, *Atmos. Chem. Phys.*, **5**, 1053-1123.

Kawamura, K., L. L. Ng, and I. R. Kaplan (1985), Determination of organic-acids (C<sub>1</sub>-C<sub>10</sub>) in the atmosphere, motor exhausts, and engine oils, *Environ. Sci. Technol.*, **19**, 1082-1086.

Kawamura, K., and R. B. Gagosian (1987), Implications of omega-oxocarboxylic acids in the remote marine atmosphere for photooxidation of unsaturated fatty-acids, *Nature*, **325**, 330-332.

Kawamura, K., and I. R. Kaplan (1987), Motor exhaust emissions as a primary source for dicarboxylic-acids in Los-Angeles ambient air, *Environ. Sci. Technol.*, **21**, 105-110.

Kawamura, K., and K. Ikushima (1993), Seasonal-changes in the distribution of dicarboxylic-acids in the urban atmosphere, *Environ. Sci. Technol.*, **27**, 2227-2235.

Kawamura, K., H. Kasukabe, O. Yasui, and L. A. Barrie (1995), Production of dicarboxylic-acids in the Arctic atmosphere at polar sunrise, *Geophys. Res. Lett.*, **22**, 1253-1256.

Kawamura, K., H. Kasukabe, and L. A. Barrie (1996a), Source and reaction pathways of dicarboxylic acids, ketoacids and dicarbonyls in Arctic aerosols: one year of observations, *Atmos. Environ.*, **30**, 1709-1722.

Kawamura, K., R. Semere, Y. Imai, Y. Fujii, and M. Hayashi (1996b), Water soluble dicarboxylic acids and related compounds in Antarctic aerosols, *J. Geophys. Res.*, **101**(D13), 18721-18728.

Kawamura, K., and F. Sakaguchi (1999), Molecular distributions of water soluble dicarboxylic acids in marine aerosols over the Pacific Ocean including tropics, *J. Geophys. Res.*, *104*(D3), 3501-3509.

Kawamura, K., Y. Imai, and L. A. Barrie (2005), Photochemical production and loss of organic acids in high Arctic aerosols during long-range transport and polar sunrise ozone depletion events, *Atmos. Environ.*, *39*, 599-614.

Kerminen, V. M., K. Teinila, R. Hillamo, and T. Makela (1999), Size-segregated chemistry of particulate dicarboxylic acids in the Arctic atmosphere, *Atmos. Environ.*, *33*, 2089-2100.

Kerminen, V. M., C. Ojanen, T. Pakkanen, R. Hillamo, M. Aurela, and J. Merilainen (2000), Low-molecular-weight dicarboxylic acids in an urban and rural atmosphere, *J. Aerosol Sci.*, *31*, 349-362.

Khwaja, H. A. (1995), Atmospheric concentrations of carboxylic-acids and related-compounds at a semiurban site, *Atmos. Environ.*, *29*, 127-139.

Kleindienst, T. E., T. S. Conver, C. D. McIver, and E. O. Edney (2004), Determination of secondary organic aerosol products from the photooxidation of toluene and their implications in ambient PM<sub>2.5</sub>, *J. Atmos. Chem.*, *47*, 79-100.

Kondo, Y., Y. Miyazaki, N. Takegawa, T. Miyakawa, R. J. Weber, J. L. Jimenez, Q. Zhang, and D. R. Worsnop (2007), Oxygenated and water-soluble organic aerosols in Tokyo, *J. Geophys. Res.*, *112*, D01203, doi:10.1029/2006JD007056.

Lim, H. J., A. G. Carlton, and B. J. Turpin (2005), Isoprene forms secondary organic aerosol through cloud processing: Model simulations, *Environ. Sci. Technol.*, *39*, 4441-4446.

Limbeck, A., and H. Puxbaum (1999), Organic acids in continental background aerosols, *Atmos. Environ.*, *33*, 1847-1852.

Ludwig J., and O. Klemm (1988), Organic acids in different classes of atmospheric particulate material, *Tellus*, *40*13, 340-347.

Meylan, W. M., and P. H. Howard (1991), Bond contribution method for estimating Henry's law constants, *Environ. Toxicol. Chem.*, *10*, 1283-1293.

Mochida, M., N. N. Umemoto, K. Kawamura, and M. Uematsu (2003), Bimodal size distribution of C-2-C-4 dicarboxylic acids in the marine aerosols, *Geophys. Res. Lett.*, *30*(13), 1672, doi:10.1029/2003GL017451.

Murphy, S. M., A. Sorooshian, J. H. Kroll, N. L. Ng, P. Chhabra, C. Tong, J. D. Surratt, E. Knipping, R. C. Flagan, and J. H. Seinfeld (2007), Secondary aerosol formation from atmospheric reactions of aliphatic amines, *Atmos. Chem. Phys. Disc.*, 7, 289–349.

Narukawa, M., K. Kawamura, N. Takeuchi, and T. Nakajima (1999), Distribution of dicarboxylic acids and carbon isotopic compositions in aerosols from 1997 Indonesian forest fires, *Geophys. Res. Lett.*, 26, 3101-3104.

Neususs, C., M. Pelzing, A. Plewka, and H. Herrmann (2000), A new analytical approach for size-resolved speciation of organic compounds in atmospheric aerosol particles: Methods and first results, *J. Geophys. Res.*, 105(D4), 4513-4527.

Ng, N. L., J. H. Kroll, A. W. H. Chan, P. S. Chhabra, R. C. Flagan, and J. H. Seinfeld (2007), Secondary organic aerosol formation from m-xylene, toluene, and benzene, *Atmos. Chem. Phys. Disc.*, 7, 4085–4126.

Norton, R. B., J. M. Roberts, and B. J. Huebert (1983), Tropospheric oxalate, *Geophys. Res. Lett.*, 10(7), 517-520.

Peltier, R. E., A. P. Sullivan, R. J. Weber, A. G. Wollny, J. S. Holloway, C. A. Brock, J. A. de Gouw, and E. L. Atlas (2007), No evidence for acid-catalyzed secondary organic aerosol formation in power plant plumes over metropolitan Atlanta, Georgia, *Geophys. Res. Lett.*, 34(6), L06801, doi:10.1029/2006GL028780.

Pereira, W. E., C. E. Rostad, H. E. Taylor, and J. M. Klein (1982), Characterization of Organic Contaminants in Environmental-Samples Associated with Mount St-Helens 1980 Volcanic-Eruption, *Environ. Sci. Technol.*, 16, 387-396.

Rogge, W. F., L. M. Hildemann, M. A. Mazurek, G. R. Cass, and B. R. T. Simoneit (1991), Sources of fine organic aerosol .1. Charbroilers and meat cooking operations, *Environ. Sci. Technol.*, 25, 1112-1125.

Rogge, W. F., M. A. Mazurek, L. M. Hildemann, G. R. Cass, and B. R. T. Simoneit (1993), Quantification of urban organic aerosols at a molecular-level - identification, abundance and seasonal-variation, *Atmos. Environ.*, 27, 1309-1330.

Rohrl, A., and G. Lammel (2001). Low molecular weight dicarboxylic acids and glyoxylic acid: Seasonal and air mass characteristics. *Environ. Sci. Technol.*, 35, 95-101.

Russell, M., and D. T. Allen (2004), Seasonal and spatial trends in primary and secondary organic carbon concentrations in southeast Texas, *Atmos. Environ.*, 38, 3225-3239.

Salam, A., H. Bauer, K. Kassin, S. M. Ullah, and H. Puxbaum (2003), Aerosol chemical characteristics of a mega-city in Southeast Asia (Dhaka-Bangladesh), *Atmos. Environ.*, 37, 2517-2528.

Satsumabayashi, H., H. Kurita, Y. Yokouchi, and H. Ueda (1989), Mono- and dicarboxylic acids under long-range transport of air pollution in central Japan, *Tellus*, *41B*, 219-229.

Saxena, P., and L. M. Hildemann (1996), Water-soluble organics in atmospheric particles: A critical review of the literature and application of thermodynamics to identify candidate compounds, *J. Atmos. Chem.*, *24*, 57-109.

Sempere, R., and K. Kawamura (1994), Comparative distributions of dicarboxylic-acids and related polar compounds in snow rain and aerosols from urban atmosphere. *Atmos. Environ.*, *28*, 449-459.

Simoneit, B. R. T., and M. A. Mazurek (1982), Organic-matter of the troposphere .2. Natural background of biogenic lipid matter in aerosols over the rural Western United-States, *Atmos. Environ.*, *16*, 2139-2159.

Simoneit, B. R. T. (1986), Characterization of organic-constituents in aerosols in relation to their origin and transport - a review, *Int. J. Environ. An. Ch.*, *23*, 207-237.

Sorooshian, A., V. Varutbangkul, F. J. Brechtel, B. Ervens, G. Feingold, R. Bahreini, S. M. Murphy, J. S. Holloway, E. L. Atlas, G. Buzorius, H. Jonsson, R. C. Flagan, and J. H. Seinfeld (2006a), Oxalic acid in clear and cloudy atmospheres: Analysis of data from International Consortium for Atmospheric Research on Transport and Transformation 2004, *J. Geophys. Res.* *111*, D23S45, doi:10.1029/2005JD006880.

Sorooshian, A., F. J. Brechtel, Y. L. Ma, R. J. Weber, A. Corless, R. C. Flagan, and J. H. Seinfeld (2006b), Modeling and characterization of a particle-into-liquid sampler (PILS), *Aerosol Sci. Tech.*, *40*, 396-409.

Sorooshian, A., M. -L. Lu, F. J. Brechtel, H. Jonsson, G. Feingold, R. C. Flagan, and J. H. Seinfeld (2007), On the source of organic acid aerosol layers above clouds, *Environ. Sci. Technol.*, *41*, 4647-4654.

Souza, S. R., P. C. Vasconcellos, and L. R. F. Carvalho (1999), Low molecular weight carboxylic acids in an urban atmosphere: Winter measurements in Sao Paulo City, Brazil, *Atmos. Environ.*, *33*, 2563-2574.

Stephanou, E. G., and N. Stratigakis (1993), Oxocarboxylic and alpha,omega-dicarboxylic acids - photooxidation products of biogenic unsaturated fatty-acids present in urban aerosols, *Environ. Sci. Technol.*, *27*, 1403-1407.

Sullivan, A. P., R. E. Peltier, C. A. Brock, J. A. de Gouw, J. S. Holloway, C. Warneke, A. G. Wollny, and R. J. Weber (2006), Airborne measurements of carbonaceous aerosol soluble in water over northeastern United States: Method development and an investigation into water-soluble organic carbon sources, *J. Geophys. Res.*, *111*, D23S46, doi:10.1029/2006JD007072.

Talbot, R. W., K. M. Beecher, R. C. Harriss, and W. R. Cofer (1988), Atmospheric geochemistry of formic and acetic-acids at a mid-latitude temperate site, *J. Geophys. Res.*, *93*(D2), 1638-1652.

Talbot, R. W., B. W. Mosher, B. G. Heikes, D. J. Jacob, J. W. Munger, B. C. Daube, W. C. Keene, J. R. Maben, and R. S. Artz (1995), Carboxylic-acids in the rural continental atmosphere over the Eastern United-States during the Shenandoah Cloud and Photochemistry Experiment, *J. Geophys. Res.*, *100*(D5), 9335-9343.

Turekian, V. C., S. A. Macko, and W. C. Keene (2003), Concentrations, isotopic compositions, and sources of size-resolved, particulate organic carbon and oxalate in near-surface marine air at Bermuda during spring, *J. Geophys. Res.*, *108*(D5), 4157, doi:10.1029/2002JD002053.

Warneck, P. (2003), In-cloud chemistry opens pathway to the formation of oxalic acid in the marine atmosphere, *Atmos. Environ.*, *37*, 2423-2427.

Yamasoe, M. A., P. Artaxo, A. H. Miguel, and A. G. Allen (2000), Chemical composition of aerosol particles from direct emissions of vegetation fires in the Amazon Basin: water-soluble species and trace elements, *Atmos. Environ.*, *34*, 1641-1653.

Yao, X. H., M. Fang, and C. K. Chan (2002), Size distributions and formation of dicarboxylic acids in atmospheric particles, *Atmos. Environ.*, *36*, 2099-2107.

Yao, X. H., A. P. S. Lau, M. Fang, C. K. Chan, and M. Hu (2003), Size distributions and formation of ionic species in atmospheric particulate pollutants in Beijing, China: 2-dicarboxylic acids, *Atmos. Environ.*, *37*, 3001-3007.

Yao, X. H., M. Fang, C. K. Chan, K. F. Ho, and S. C. Lee (2004), Characterization of dicarboxylic acids in PM<sub>2.5</sub> in Hong Kong, *Atmos. Environ.*, *38*, 963-970.

Yokouchi, Y., and Y. Ambe (1986), Characterization of polar organics in airborne particulate matter, *Atmos. Environ.*, *20*, 1727-1734.

Yu, J. Z., S. F. Huang, J. H. Xu, and M. Hu (2005), When aerosol sulfate goes up, so does oxalate: Implication for the formation mechanisms of oxalate, *Environ. Sci. Technol.*, *39*, 128-133.

Table 6.1. Selected Organic Acid Measurements in Urban Atmospheres

Study	Location	Measurements	Amount ( $\mu\text{g}/\text{m}^3$ )
Grosjean et al., 1978	Los Angeles, USA	Dicarboxylic acids ( $\text{C}_4\text{-C}_6$ )	$\text{C}_4\text{-C}_6$ range = 0.2-0.5
Appel et al., 1979	Southern California, USA	Dicarboxylic acids ( $\text{C}_5\text{-C}_6$ )	$\text{C}_5\text{-C}_6$ range = 0.84-1.80
Satsumabayashi et al., 1989	Takasaki; suburban area near Tokyo, Japan	Dicarboxylic acids ( $\text{C}_2\text{-C}_8$ )	$\text{C}_2\text{-C}_8$ ave = 0.17; May have been serious underestimation of oxalic and malonic acids [Kawamura and Ikushima, 1993]
Kawamura and Ikushima, 1993	Tokyo, Japan	Dicarboxylic acids ( $\text{C}_2\text{-C}_{10}$ ) (total suspended particulate matter; TSP)	$\text{C}_2\text{-C}_{10}$ ave = $0.48 \pm 0.33$ (range = 0.09-1.37); ave oxalate = 0.27 (range = 0.04-0.73); $\text{C}_2\text{-C}_4$ dicarboxylic acids ~ 80% of total dicarboxylic acid mass
Sempere and Kawamura, 1994	Tokyo, Japan	Dicarboxylic acids ( $\text{C}_2\text{-C}_5$ )	$\text{C}_2\text{-C}_5$ ave = 2.25
Kawamura and Kaplan, 1987	Los Angeles, USA	Dicarboxylic acids ( $\text{C}_2\text{-C}_{10}$ ) (TSP)	$\text{C}_2\text{-C}_{10}$ ave = 1.41 (range = 0.59-2.50); ave oxalate = 0.46 (range = 0.19-0.78)
Souza et al., 1999	Sao Paulo, Brazil	Carboxylic acids ( $\text{C}_1\text{-C}_4$ )	$\text{C}_1\text{-C}_4$ ave = $2.75 \pm 2.28$ (range = 0.24-7.42)
Limbeck and Puxbaum, 1999	Vienna, Austria	Oxalate, malonate, succinate, glutarate, adipate, glyoxylate, pyruvate (TSP)	0.34, 0.24, 0.12, 0.03, 0.12, 0.02, 0.06, respectively
Rohrl and Lammel, 2001	Eichstadt and Leipzig, Germany	Dicarboxylic acids ( $\text{C}_2\text{-C}_5$ ) and glyoxylate (TSP)	$\text{C}_2\text{-C}_5$ ave = 0.34-0.35; Leipzig: oxalate = 0.23 (range = 0.06-0.50), glyoxylate = 0.008
Salam et al., 2003	Dhaka, Bangladesh	Oxalate, malonate, succinate, malate, formate, acetate (TSP)	0.71, 0.07, 0.04, 0.05, 0.10, 0.13, respectively; organic acids ~ 0.72% of OC mass; ave OC = $45.7 \mu\text{g}/\text{m}^3$
Yao et al., 2004	Hong Kong	Winter: oxalate, malonate, succinate ( $\text{PM}_{2.5}$ ) Summer: oxalate, malonate, succinate ( $\text{PM}_{2.5}$ )	0.35-0.37, 0.02-0.03, 0.05-0.07, respectively 0.09-0.17, 0.01, 0.01, respectively
<sup>a</sup> Russell and Allen, 2004	Southeast Texas, USA	Total secondary organic carbon (SOC; $\text{PM}_{2.5}$ ) Mean fraction of SOC ( $\text{PM}_{2.5}$ )	SOC range = $(0.65 \pm 1.11) - (1.15 \pm 1.52)$ Range = $(0.05 \pm 0.06) - (0.10 \pm 0.33)$
Sullivan et al., 2006	Northeastern USA	Water-soluble organic carbon (WSOC; $\text{PM}_{1.0}$ ) (airborne measurements below 1 km)	WSOC range = $2\text{-}6 \mu\text{g C}/\text{m}^3$
Huang et al., 2005	Beijing, China	Dicarboxylic acids ( $\text{C}_2\text{-C}_5$ ) and malate, glyoxylate, pyruvate ( $\text{PM}_{2.5}$ )	$\text{C}_2\text{-C}_5$ range = 0.17-0.53, ave oxalate = 0.22 (range = 0.1-0.4), malate = 0.03, glyoxylate = 0.02, pyruvate = 0.03
Huang et al., 2006/2007	Shenzhen, China	Winter: Oxalate ( $\text{PM}_{3.2}$ ), WSOC ( $\text{PM}_{1.8}$ ), OC/EC (organic/elemental carbon) Summer: Oxalate ( $\text{PM}_{3.2}$ ), WSOC ( $\text{PM}_{1.8}$ ), OC/EC	Ave oxalate = 0.32; ave WSOC = $4.5 \mu\text{g C}/\text{m}^3$ ; WSOC/TC = 0.34 Ave oxalate = 0.29; ave WSOC = $2.2 \mu\text{g C}/\text{m}^3$ ; WSOC/TC = 0.30
Kondo et al., 2007	Tokyo, Japan	Winter: WSOC, OC/EC, AMS oxygenated organic aerosol (OOA) and hydrocarbon-like organic aerosol (HOA) ( $\text{PM}_{1.0}$ ) Summer: WSOC, OC/EC, AMS OOA and HOA ( $\text{PM}_{1.0}$ )	WSOC < $6 \mu\text{g C}/\text{m}^3$ ; 39% (total mass base) and 23% (carbon mass base) of organic aerosols were oxygenated; 88 $\pm$ 29% of OOA was water-soluble WSOC < $8 \mu\text{g C}/\text{m}^3$ ; 80% (total mass base) and 42-65% (carbon mass base) of organic aerosols were oxygenated; 88 $\pm$ 29% of OOA was water-soluble
Peltier et al., 2007	Atlanta, USA	WSOC (airborne measurements at ~ 1 km)	Median concentrations ( $\mu\text{g C}/\text{m}^3$ ): in plume = $2.5 \pm 0.2$ ; out of plume = $2.4 \pm 0.2$

<sup>a</sup>Ground site measurements made by Russell and Allen (2004) were in the same area as the GoMACCS measurements.



Table 6.2. Chemical Formulas and Structures for the Organic Acids Studied

Organic acid	Chemical Formula	Structure
Oxalic	$(\text{COOH})_2$	
Malonic	$\text{CH}_2(\text{COOH})_2$	
Succinic	$\text{C}_2\text{H}_4(\text{COOH})_2$	
Glutaric	$\text{C}_3\text{H}_6(\text{COOH})_2$	
Adipic	$\text{C}_4\text{H}_8(\text{COOH})_2$	
Suberic	$\text{C}_6\text{H}_{12}(\text{COOH})_2$	
Azelaic	$\text{C}_7\text{H}_{14}(\text{COOH})_2$	
Maleic	$\text{C}_2\text{H}_2(\text{COOH})_2$	
Malic	$\text{C}_2\text{H}_4\text{O}(\text{COOH})_2$	
Formic	$\text{HCOOH}$	
Acetic	$\text{CH}_3\text{COOH}$	
Glyoxylic	$\text{CHOCOOH}$	
Pyruvic	$\text{C}_2\text{H}_3\text{OCOOH}$	
Methacrylic	$\text{C}_3\text{H}_5\text{COOH}$	
Benzoic	$\text{C}_6\text{H}_5\text{COOH}$	
Methanesulfonic	$\text{CH}_3\text{SO}_2\text{OH}$	

Table 6.3. Organic Acid Product Distribution for a Series of *m*-xylene Laboratory Chamber Photooxidation Experiments. (C<sub>2</sub>-C<sub>5</sub> = dicarboxylic acids; For=formate; Ace=acetate; Pyr=pyruvate; Gly=glyoxylate; Mle=maleate; Glyc=glycolate; Lac=lactate). Those labels with “Det” indicate that glyoxylate exceeded detection limits during the experiment, but not in the sample representing the maximum organic acid mass observed.

	% contribution to total organic acid mass in the PILS sample representing maximum total organic acid mass											
	Initial VOC: NO <sub>x</sub> ratio	DMA-derived SOA mass (µg/m <sup>3</sup> )	Organic acid mass fraction of SOA	Ace/ Glyc /Lac	For	Pyr	C <sub>2</sub>	C <sub>3</sub>	C <sub>4</sub>	C <sub>5</sub>	Gly	Mle
75 ppb <i>m</i> -xylene/low NO <sub>x</sub> /non-acid seed	17.1	90	0.41	41	29	20	5	2	2	1	Det	0.6
75 ppb <i>m</i> -xylene/low NO <sub>x</sub> /non-acid seed	8.5	81	0.38	45	28	17	5	2	2	1	0.2	0.9
75 ppb <i>m</i> -xylene/low NO <sub>x</sub> /acid seed	2500.0	93	0.35	42	33	15	6	1	1	1	Det	0.0
75 ppb <i>m</i> -xylene/low NO <sub>x</sub> /nucleation	29.2	97	0.36	37	37	16	5	1	1	2	Det	1.0
300 ppb <i>m</i> -xylene/high NO <sub>x</sub> /non-acid seed	0.3	65	0.18	30	31	21	8	4	4	2	0.1	0.0
300 ppb <i>m</i> -xylene/high NO <sub>x</sub> /acid seed	0.3	81	0.26	22	33	28	8	3	3	1	0.2	1.0
300 ppb <i>m</i> -xylene/high NO <sub>x</sub> /nucleation	0.3	75	0.17	30	34	21	7	2	3	1	0.2	2.0

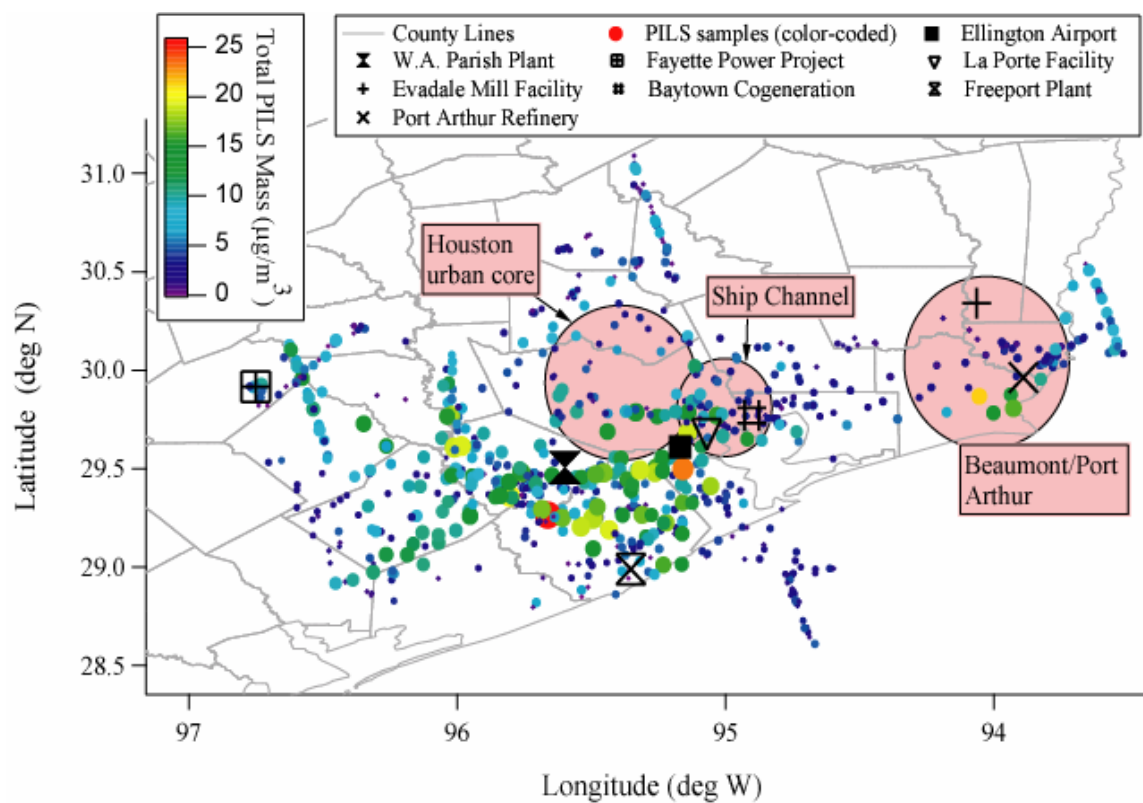


Figure 6.1. Spatial distribution of the PILS water-soluble mass concentration during GoMACCS. Marker sizes are proportional to sulfate concentration, where larger markers represent higher concentrations (range = 0.2–23.3  $\mu\text{g}/\text{m}^3$ ).

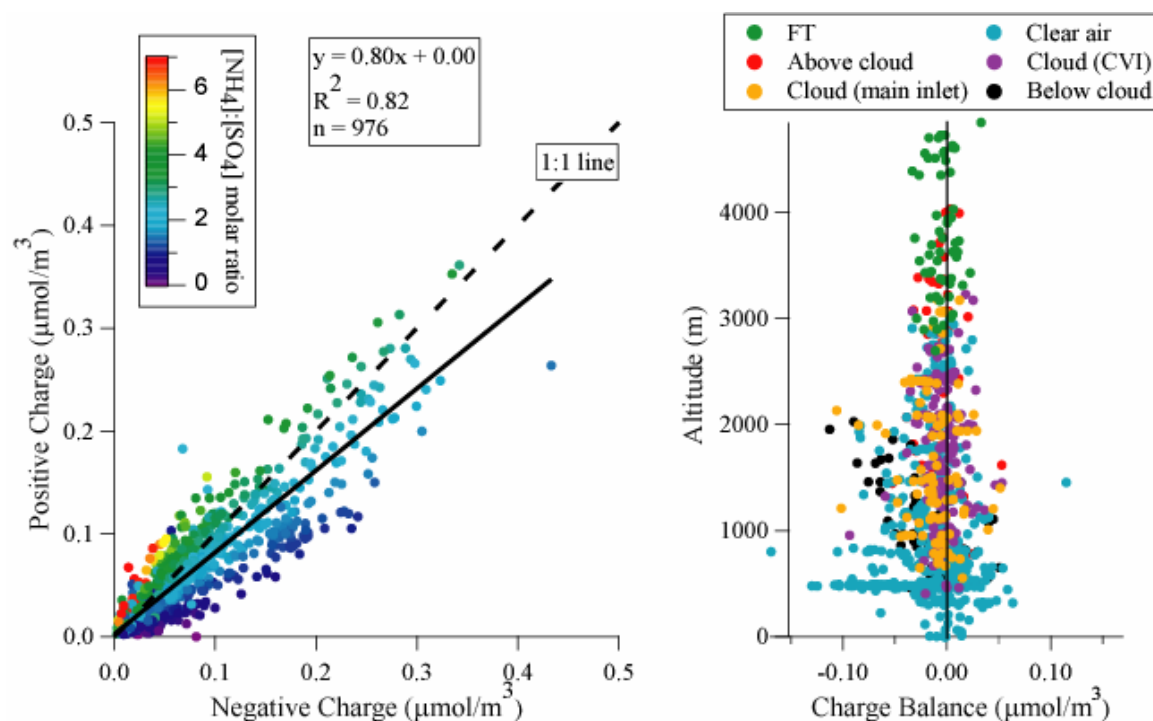


Figure 6.2. (Left) Total water-soluble charge balance for all samples collected during GoMACCS. Markers are color coded with their respective  $\text{NH}_4^+:\text{SO}_4^{2-}$  molar ratios. (Right) Vertical distribution of the charge balance for samples categorized by the region of the lower troposphere they were collected in. Main inlet data in cloud refer to total aerosol samples, which contain interstitial aerosol and evaporated droplet residual particles. CVI data represent only evaporated droplet residual particles in cloud.

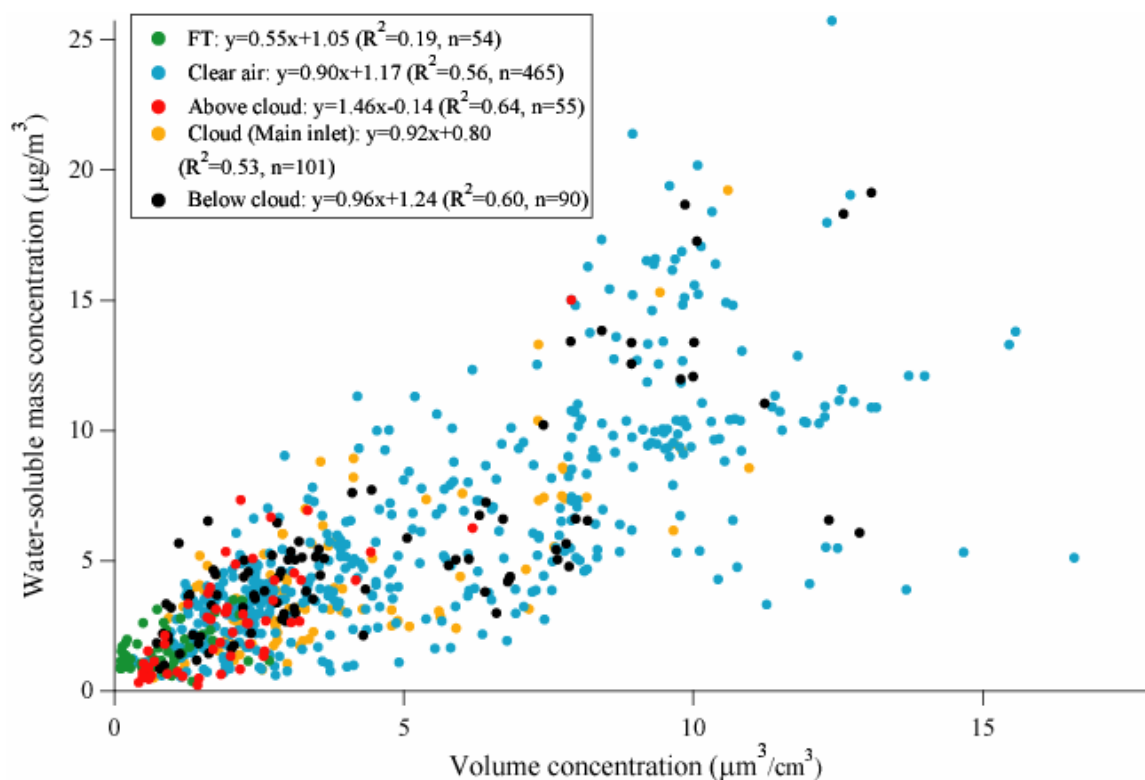


Figure 6.3. Comparison between the water-soluble mass concentration and DMA volume concentration in different regions of the lower troposphere. It should be noted that the size cut-off of the DMA was slightly less than the PILS ( $0.8\ \mu\text{m}$  versus  $1\ \mu\text{m}$ ), which may have led to an overestimate of the aerosol density, as represented by the slopes. The positive y-intercepts suggest that there may have been a systematic increase in the mass concentration as compared to what would be expected and this could also be due to the difference in the instrument size cut-off points. Forcing the intercepts of the regression lines to zero would compromise the relative nature of the individual data points. (The slopes in the case of a y-intercept of zero are as follows: FT = 1.34, clear air = 1.06, above cloud = 1.41, in cloud (total aerosol inlet) = 1.07, below cloud = 1.13.)

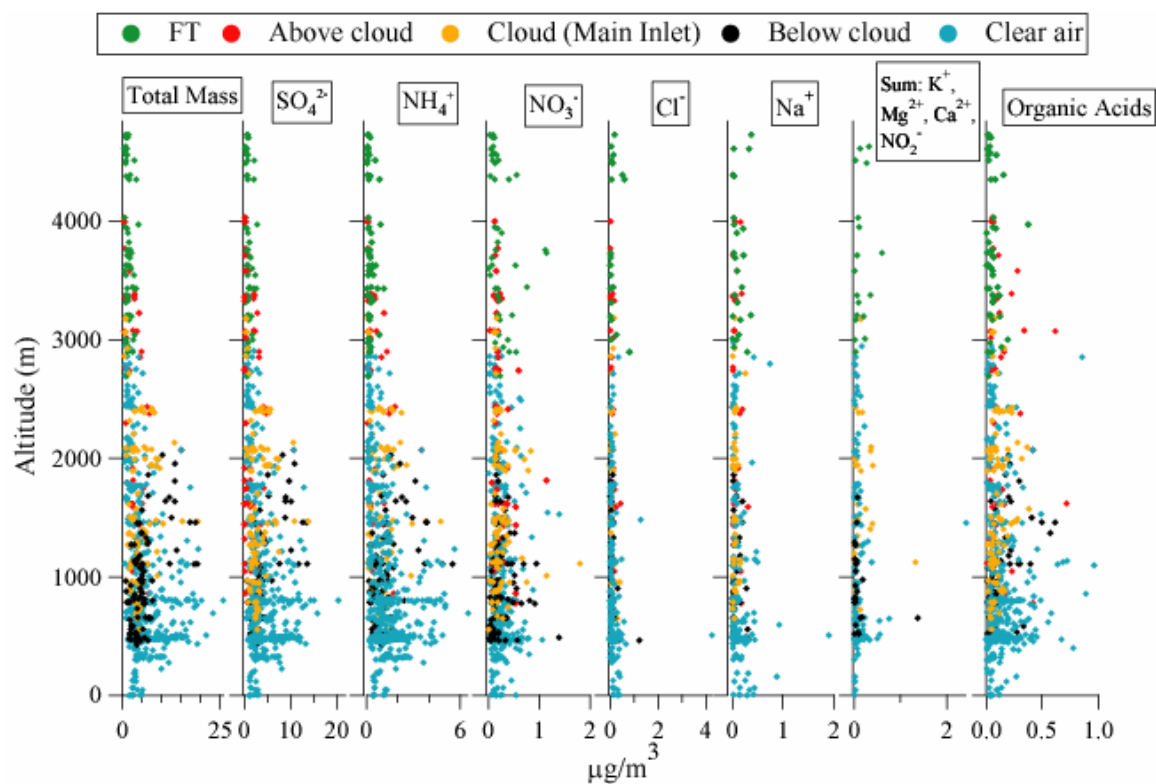


Figure 6.4. Vertical distribution of the total water-soluble mass and different ionic components. The data are categorized by what region of the lower troposphere the samples were collected in. Main inlet data in cloud refer to total aerosol samples, which contain interstitial aerosol and evaporated droplet residual particles.

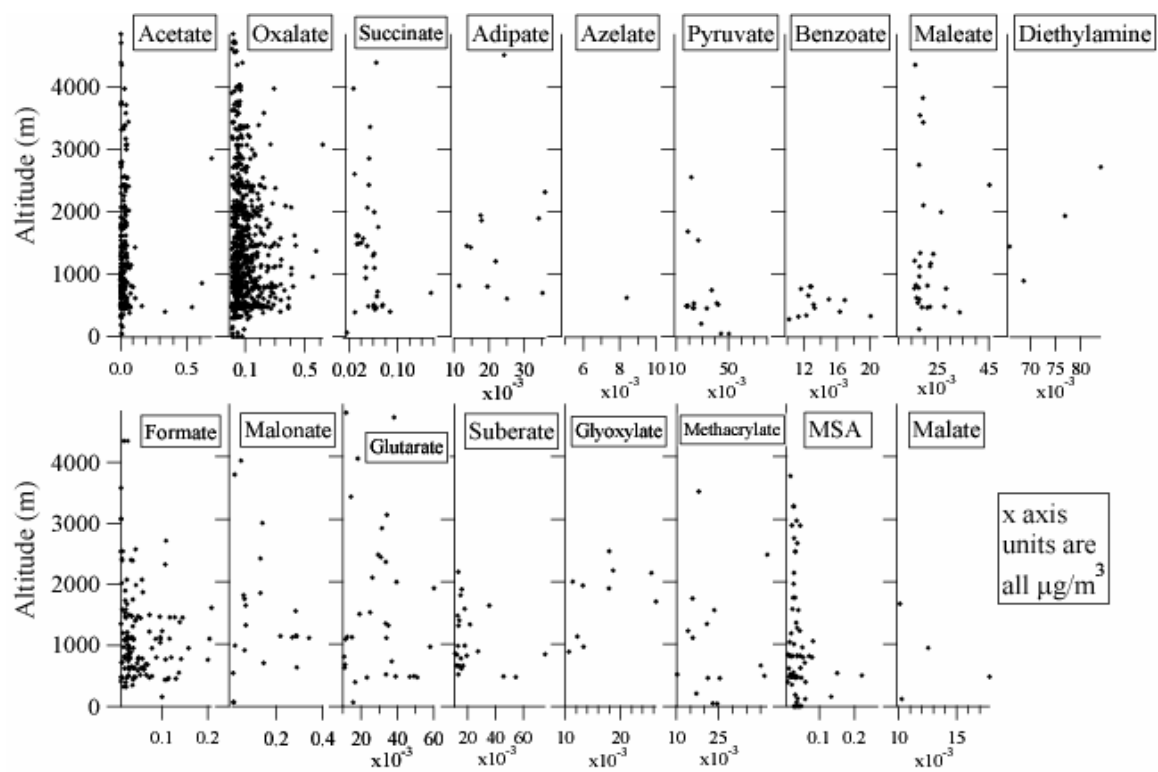


Figure 6.5. Vertical distribution of the different organic acids and diethylamine.

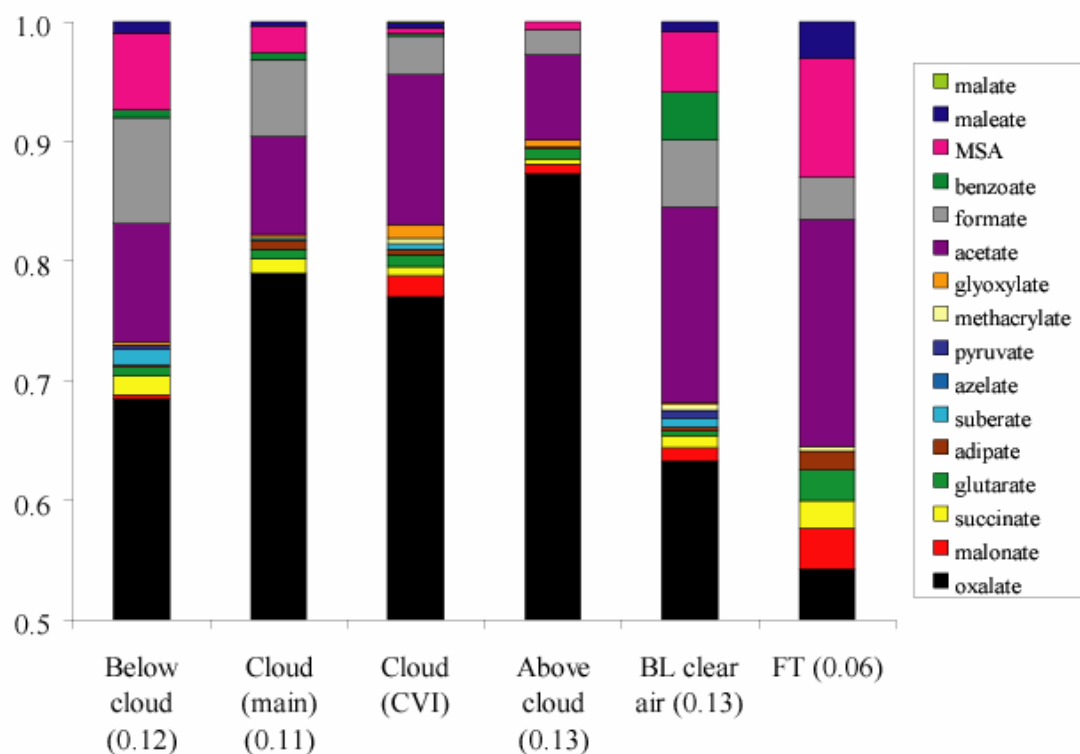


Figure 6.6. Contribution of individual organic acids to the total organic acid mass in different regions of the lower troposphere. To highlight less abundant organic acids, the y axis begins at 50% as oxalate contributes > 50% in each category. Average organic acid mass concentrations ( $\mu\text{g}/\text{m}^3$ ) for each category are shown in parentheses by each label on the x axis. Main inlet data in cloud refer to total aerosol samples, which contain interstitial aerosol and evaporated droplet residual particles. CVI data represent only evaporated droplet residual particles in cloud.



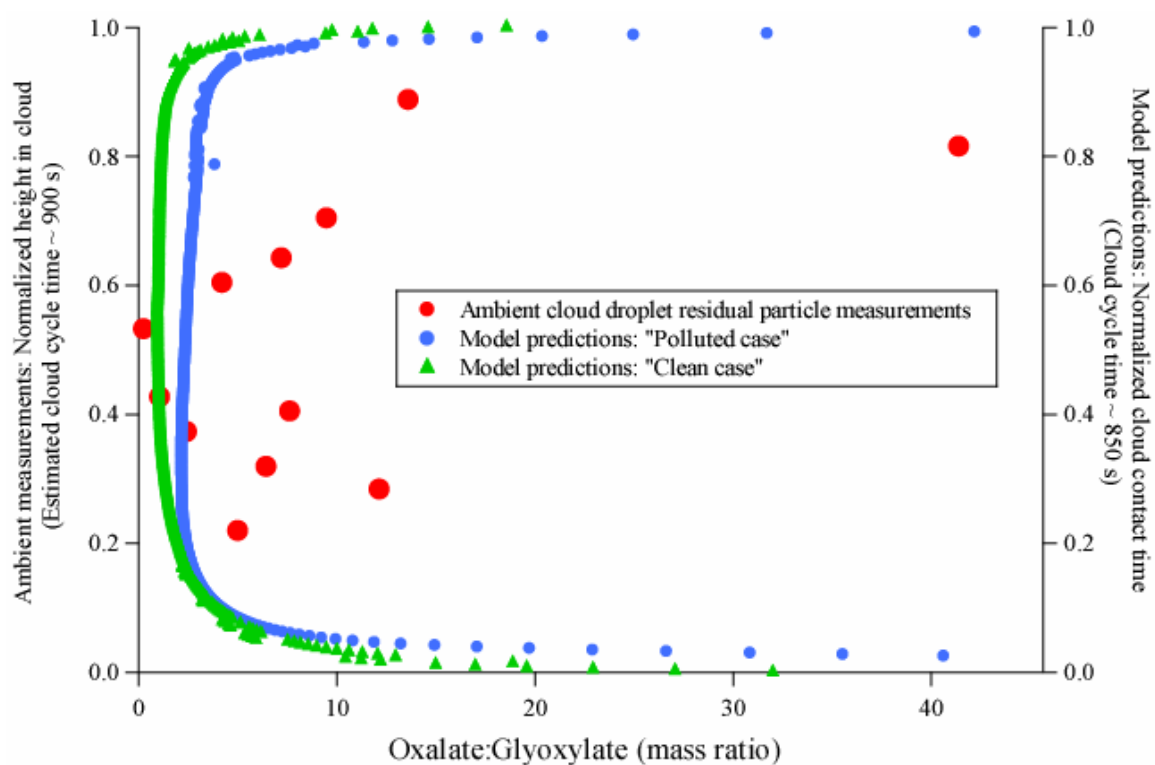


Figure 6.7. Comparison of the oxalate:glyoxylate mass ratio between ambient measurements of cloud droplet residual particles and model predictions for clouds influenced by pollution sources ("polluted") and those that are not ("clean"). The chemical cloud parcel model considers mean cloud-contact times on the order of  $\sim 850$  s, while the estimated value for the ambient case, using average cloud depth and updraft velocity, is  $\sim 900$  s.

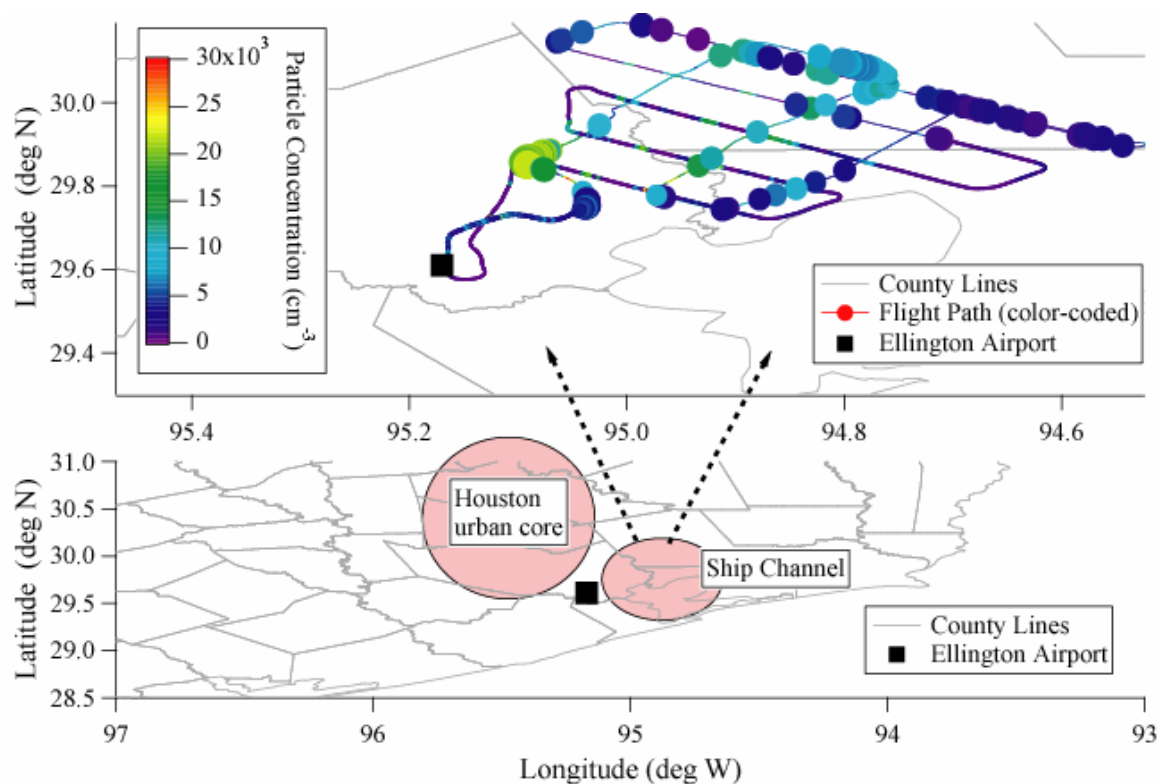


Figure 6.8. Flight tracks during a study aimed at analyzing the evolution of aerosol properties in three major plumes originating in the Houston Ship Channel. Markers are color-coded to represent fine particle (< 1 μm) number concentration, while marker sizes are proportional to PCASP (0.1 - 2.5 μm) number concentration (range = 0 – 29,000 cm<sup>-3</sup>). There were southwesterly winds (205 - 230°; 5 - 10 m/s).

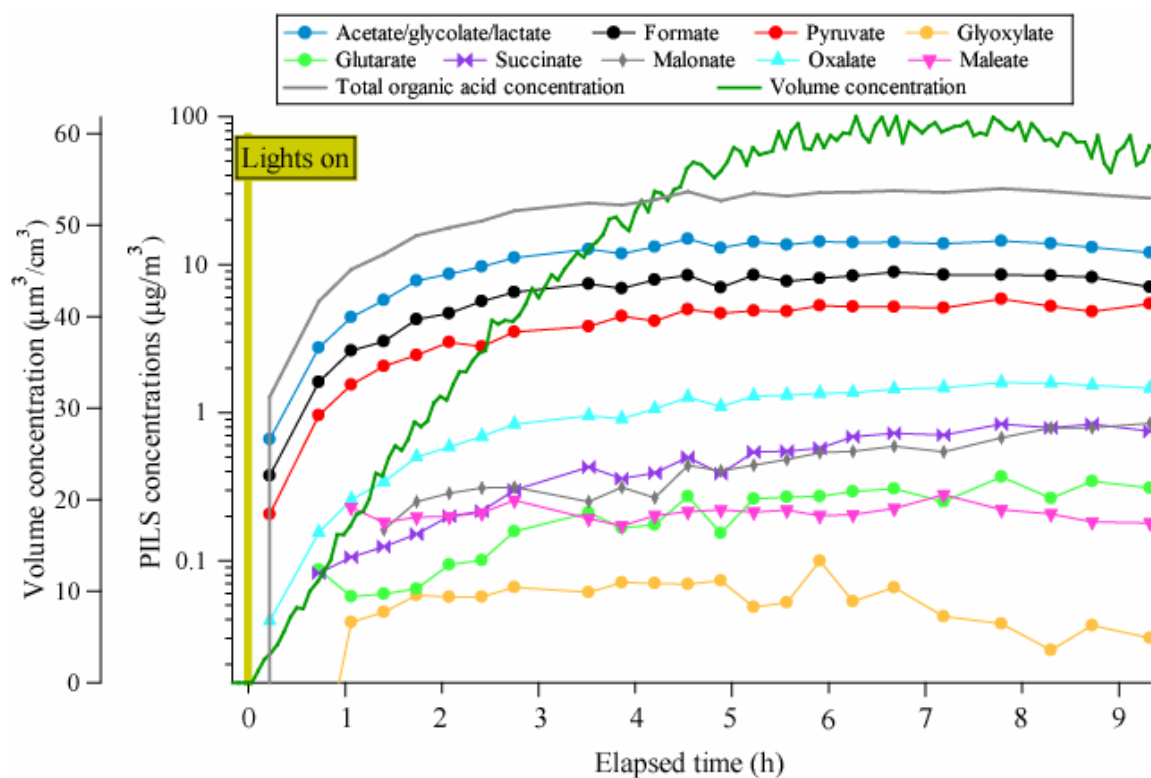


Figure 6.9. Organic acid product evolution from a photooxidation experiment with the following conditions: 75 ppb *m*-xylene/low NO<sub>x</sub>/non-acid ammonium sulfate seed aerosol. The organic acid mass fraction of the DMA-derived SOA mass was estimated to be approximately 39% at the time the sample with the maximum mass concentration was collected.

## **Chapter 7**

# **Comprehensive Airborne Characterization of Aerosol From a Major Bovine Source\***

---

\*This chapter is prepared for journal submission as “Comprehensive Airborne Characterization of Aerosol From a Major Bovine Source” by A. Sorooshian, S. Hersey, S. M. Murphy, H. Gates, L. Padro, A. Nenes, F. J. Brechtel, H. Jonsson, R. C. Flagan, and J. H. Seinfeld.

## 7.1 Abstract

We report an extensive airborne characterization of aerosol downwind of a massive bovine source in the San Joaquin Valley (California) on two flights during July 2007. The Center for Interdisciplinary Remotely-Piloted Aircraft Studies (CIRPAS) Twin Otter probed chemical composition, particle size distribution, mixing state, sub- and supersaturated water uptake behavior, light scattering properties, and the interrelationship between these parameters and meteorology. Total  $PM_{1.0}$  levels and concentrations of organics, nitrate, and ammonium were enhanced in the plume from the source as compared to the background aerosol. Organics dominated the plume aerosol mass ( $\sim 56 - 64\%$ ), followed either by sulfate or nitrate, and then ammonium. Particulate amines were detected in the plume aerosol by a particle-into-liquid sampler (PILS) and via mass spectral markers in the Aerodyne cToF-AMS. Amines were found to be a significant atmospheric base even in the presence of ammonia; particulate amine concentrations are estimated as at least 14 – 23% of that of ammonium in the plume. Enhanced sub- and supersaturated water uptake and reduced refractive indices were coincident with lower organic mass fractions, higher nitrate mass fractions, and the detection of amines. Kinetic limitations due to hydrophobic organic material are shown to have likely suppressed droplet growth. After removing effects associated with size distribution and mixing state, the normalized activated fraction of cloud condensation nuclei (CCN) increased as a function of the subsaturated hygroscopic growth factor, with the highest activated fractions being consistent with relatively lower organic mass fractions and higher nitrate mass fractions. Subsaturated hygroscopic growth factors for the organic fraction of the aerosol are estimated based on employing the Zdanovskii-Stokes Robinson (ZSR) mixing

rule. Representative values for a parameterization treating particle water uptake in both the sub- and supersaturated regimes are reported for incorporation into atmospheric models.

## 7.2 Introduction

Bovine emissions are major sources of methane ( $\text{CH}_4$ ), nitrous oxide ( $\text{N}_2\text{O}$ ), and ammonia ( $\text{NH}_3$ ); they are also the dominant anthropogenic source for amines (Schade and Crutzen, 1995). Ammonia is the dominant base in the atmosphere, efficiently neutralizing acidic substances. The main global sources of ammonia are from livestock waste, fertilizer applications, biomass burning, motor vehicle emissions, and coal combustion (Apsimon et al., 1987; Asman and Janssen, 1987; Kleeman et al., 1999; Anderson et al., 2003; Battye et al., 2003). Typical ammonia mixing ratios over continents range between 0.1 and 10 ppb (Edgerton et al., 2007, and references therein), while levels as high as a few ppm have been reported near areas of extensive livestock operations (Rumburg et al., 2006).

The principal inorganic aerosol components involving ammonia are ammonium nitrate and ammonium sulfate. The formation of these inorganic salts depends on temperature, relative humidity (RH), and concentrations of  $\text{NH}_3$ , nitric acid ( $\text{HNO}_3$ ) and sulfur dioxide ( $\text{SO}_2$ ). Ammonium nitrate tends to form after sulfuric acid is completely neutralized. Atmospheric ammonium nitrate generally obeys thermodynamic equilibrium with gaseous nitric acid and ammonia (Stelson et al., 1979; Doyle et al., 1979; Stelson and Seinfeld, 1982a, 1982b; Russell et al., 1983; Hildemann et al., 1984; Zhang et al., 2002; Takahama et al., 2004; Yu et al., 2005), although some studies have pointed out that factors such as mass transport limitations can, at times, result in departures from

equilibrium (Wexler and Seinfeld, 1992; Meng and Seinfeld, 1996; Fridlind and Jacobson, 2000; Fridlind et al., 2000). The equilibrium between particulate ammonium nitrate and gaseous nitric acid and ammonia shifts to the gas phase as ambient temperature increases, and RH decreases. Similar to ammonia, amines undergo neutralization reactions with nitric and sulfuric acids to form amine salts (Mozurkewich, 1993; Stelson and Seinfeld, 1982a; Angelino et al., 2001; Murphy et al., 2007). The photooxidation of gas-phase amines has been shown to form aerosol based on recent laboratory experiments (Angelino et al., 2001; Murphy et al., 2007).

Gaseous amines, including methylamine, dimethylamine, trimethylamine, ethylamine, diethylamine, triethylamine, ethanoloamine, *n*-butylamine, amylamine, 1,4-butanediamine, isobutylamine, and isopropylamine, have been identified in emissions from bovine sources (Mosier et al., 1973; Hutchinson et al., 1982; Schade and Crutzen, 1995; Rabaud et al., 2003; Ngwabie et al., 2005). Amine emission rates from animal husbandry sources are typically two to three orders of magnitude lower than those of ammonia (Schade and Crutzen, 1995; Ngwabie et al., 2005). Gaseous amines are also present in vehicular exhaust (Cadle and Mulawa, 1980; Westerholm et al., 1993), the marine atmosphere (Vanneste et al., 1987), biomass burning plumes (Lobert et al., 1991), as well as emissions from decaying organic matter, waste incineration, and sewage treatment plants (Manahan, 2005). Amine salts have sufficiently low vapor pressures to partition to the aerosol phase; moreover, they exhibit greater water-solubility as compared to other particulate organic nitrogen species (Milne and Zika, 1993; Gorzelska et al., 1994; Murphy and Thomson, 1997; Glagolenko and Phares, 1994; Abalos et al., 1999; Angelino et al., 2001; Makela et al., 2001; Tan et al., 2002; Zhang et al., 2002;

Zhang and Anastasio, 2003; Maria et al., 2003; Beddows et al., 2004; Denkenberger et al., 2007; Murphy et al., 2007; Sorooshian et al., 2007a).

The availability of a massive, concentrated source of ammonia and amines offers a unique opportunity to probe the response of the resulting aerosol. During July 2007, the Center for Interdisciplinary Remotely Piloted Aircraft Studies (CIRPAS) Twin Otter probed the aerosol downwind of a major cattle feedlot in the San Joaquin Valley in California. The San Joaquin Valley, the major geographical feature in central California, is bordered on its west and east sides by mountain ranges and is characterized by relatively stagnant air circulation (Figure 7.1A). Consequently, this region is one of the largest nonattainment areas for ozone and particulate matter in the United States (Chow et al., 2006). The San Joaquin Valley contains numerous animal husbandry operations, the largest of which is the focus of this study. This feedlot operation covers several hundred acres and contains up to 100,000 head of cattle at any one time. Although gas-phase measurements were not carried out, the presence of ammonia and amines is inferred from established emissions inventories from animal husbandry sources and from measurements of the ammonium and amine content of the aerosol downwind of the plume source.

The goal of the present study is to provide a comprehensive airborne characterization of the aerosol downwind of a major bovine source. First, the aircraft instrument payload and flight path strategy are presented. Detailed measurements were obtained for: meteorology, aerosol size distributions and number concentrations, aerosol composition, mixing state, refractive index, hygroscopic growth factors at three different relative humidities, and cloud condensation nucleus (CCN) behavior. Special attention is



given to the sub- and supersaturated water uptake properties of the aerosol, and how these relate to chemical composition. Subsaturated hygroscopic growth factors for the organic fraction of the aerosol are reported based on a closure analysis employing the Zdanovskii-Stokes Robinson mixing rule. Subsaturated hygroscopic growth data are then compared to measured supersaturated CCN activity to evaluate the level of consistency between observed water uptake in the two regimes.

### **7.3 Experimental Methods**

The data on which the present study is based were acquired during two clear air flights in the San Joaquin Valley on 12 July 2007 and 30 July 2007. Henceforth, these two flights will be termed flight A (12 July 2007) and flight B (30 July 2007). The aircraft total aerosol inlet, characterized by Hegg et al. (2005), provided sample air to instruments on the aircraft. The instrument payload on the Twin Otter aircraft is described elsewhere (<http://www.cirpas.org>), however, attention is given below to those instruments the data from which will be discussed in detail.

#### **7.3.1. Aerosol Chemical Composition (PILS)**

Water-soluble aerosol chemical composition was measured by a particle-into-liquid sampler (PILS, Brechtel Mfg Inc.; Sorooshian et al., 2006a). In the PILS, submicrometer ambient particles are grown into droplets sufficiently large to be collected by inertial impaction for subsequent chemical analysis. At the entrance to the instrument a series of three denuders (URG and Sunset Laboratories) remove inorganic (basic and acidic) and organic gases that would otherwise bias aerosol measurements. The denuders

have been shown to successfully remove gaseous amine species (Murphy et al., 2007). The impacted droplets are delivered to a rotating carousel containing 72 vials, with each vial containing material representing a period of  $\sim 5$  min of flight, or alternatively, a distance of 15 km in flight (aircraft speed  $\sim 50$  m/s). The contents of the vials are subsequently analyzed off-line using a dual ion chromatography (IC) system (ICS-2000, Dionex Inc.) for simultaneous anion and cation analysis.

The PILS-IC instrument uncertainty has been established as  $\pm 7\%$ , and the detection limit (calculated as air-equivalent concentration of the lowest concentration standard that is distinct from baseline noise in the IC plus three times the standard deviation of this measurement) is  $< 0.1 \mu\text{g}/\text{m}^3$  for the inorganic ions ( $\text{Na}^+$ ,  $\text{NH}_4^+$ ,  $\text{K}^+$ ,  $\text{Mg}^{2+}$ ,  $\text{Ca}^{2+}$ ,  $\text{Cl}^-$ ,  $\text{NO}_2^-$ ,  $\text{NO}_3^-$ , and  $\text{SO}_4^{2-}$ ) and  $< 0.01 \mu\text{g}/\text{m}^3$  for the organic acid ions (carboxylic acids with one to nine carbon atoms) (Sorooshian et al., 2007b). The PILS-IC technique has been demonstrated to speciate amines, including ethylamine, diethylamine, triethylamine, methylamine, dimethylamine, and trimethylamine (Sorooshian et al., 2007a); however, only ethylamine and diethylamine were measured above detection limits ( $0.01 \mu\text{g}/\text{m}^3$ ) in the present study. It should be noted that ammonium and ethylamine co-elute in the IC cation column; however, ethylamine was detected at sufficiently high concentrations for its peak to be distinguishable from that of ammonium. The reported concentrations of ethylamine represent a lower limit due to this co-elution effect. Since acetate, lactate, and glycolate also co-elute, these three species are reported as a collective mass using the calibration equation of acetate; therefore, the contribution of acetate reported is likely an overestimate. As compared to acetate, using the calibration equation of glycolate would reduce the estimates by  $< 10\%$ .

### 7.3.2. Aerosol Chemical Composition (Aerodyne cToF-AMS)

Chemical composition measurements for non-refractory aerosol species (sulfate, nitrate, ammonium, and organics) were performed using an Aerodyne compact Time of Flight Aerosol Mass Spectrometer (cToF-AMS; Drewnick et al., 2004a, 2004b). At the entrance to the instrument, an aerodynamic lens focuses particles with vacuum aerodynamic diameters between approximately 50 nm and 800 nm through a 3.5% chopper and onto a tungsten vaporizer ( $\sim 550^{\circ}\text{C}$ ) (Murphy et al., 2007). The chopper can be operated in three modes to gather either background mass spectra, ensemble average mass spectra over all particle sizes, or size-resolved mass spectra. Once vaporized, molecules undergo electron impact ionization and travel through a time of flight mass analyzer. The cToF-AMS detects the presence of amines in the form of characteristic amine peaks at  $m/z$  30, 56, 58, 73, and 86 (McClafferty and Turecek, 1993; Angelino et al., 2001; Murphy et al., 2007). The detection limit, calculated as three times the standard deviation of the noise for filtered air, is  $< 0.05\ \mu\text{g}/\text{m}^3$  for all species measured.

The cToF-AMS can be used to calculate a quantity that will be referred to subsequently as *excess nitrate*. *Excess nitrate* is defined as the nitrate mass, derived from cToF-AMS spectra, remaining after both sulfate and nitrate have been fully neutralized by ammonium. A zero or slightly negative value indicates that sufficient ammonia exists to neutralize both sulfate and nitrate, while a positive value indicates that some nitrate is associated with other cations besides ammonium. cToF-AMS calibrations allow an assessment of the error associated with the *excess nitrate* calculation; introducing pure ammonium nitrate into the instrument should result in an *excess nitrate* value of zero. After flight A, calibrations were conducted with monodisperse ammonium nitrate

particles ranging from 50 nm to 400 nm and mass concentrations ranging from  $1.5 \mu\text{g}/\text{m}^3$  to  $7.0 \mu\text{g}/\text{m}^3$ , similar to concentrations in flight. Thirty-three calibration points were collected that exhibited an average *excess nitrate* of  $0.08 \pm 0.31 \mu\text{g}/\text{m}^3$ . Similarly during a calibration on the day of flight B, 350 and 400 nm ammonium nitrate particles were introduced into the instrument at levels near  $\sim 3 \mu\text{g}/\text{m}^3$ , which exceeds the peak nitrate concentration observed during the flight. The average *excess nitrate* was  $-0.014 \pm 0.095 \mu\text{g}/\text{m}^3$  ( $n = 17$ ). As will be shown, ambient *excess nitrate* concentrations in the plume aerosol significantly exceeded the background values for pure ammonium nitrate.

Nitrate species can be detected by peaks at  $m/z$  30 and 46. A problem innate to cToF-AMS unit mass-resolution spectra is differentiating between  $\text{NO}^+$ ,  $\text{CH}_2\text{O}^+$ , and  $\text{C}_2\text{H}_6^+$ , all of which give peaks at  $m/z$  30. If the contribution of organic fragments to the signal at  $m/z$  30 is not correctly accounted for, the mass of nitrate, as inferred from  $\text{NO}^+$ , can be overestimated. A relatively conservative approach is to calculate nitrate mass using the peak intensity at  $m/z$  46 ( $\text{NO}_2^+$ ), which rarely corresponds to an organic fragment (McClafferty and Turecek, 1993). Calibration of the instrument with pure ammonium nitrate allows observation of the ratio of the peak intensities at  $m/z$  30 and 46 when  $\text{NO}^+$  and  $\text{NO}_2^+$  are present without organic interference. During such a calibration conducted after flight A, the peak at  $m/z$  30 was observed to be 2.2 times that at  $m/z$  46. Thus, for this flight, nitrate mass at  $m/z$  30 was calculated to be 2.2 times the mass at  $m/z$  46. Based on calibrations on the day of flight B, the peak at  $m/z$  30 was observed to be 2.8 times that at  $m/z$  46. The two calibrations were seventeen days apart, and instrumental drift is responsible for the difference in the  $m/z$  30:46 ratio between the two days; typical values observed with this instrument range between two and three. The mass remaining at

$m/z$  30 after the nitrate contribution is subtracted is assumed to be organic, including amine species, which often exhibit a major peak here.

### 7.3.3. Aerosol Hygroscopicity and Refractive Index (DASH-SP)

A differential aerosol sizing and hygroscopicity spectrometer probe (DASH-SP; Brechtel Mfg Inc.; Sorooshian et al., 2008) was included in the instrument payload on the aircraft. The DASH-SP consists of a single classification differential mobility analyzer (DMA) followed by a set of parallel hygroscopic growth chambers operated at different relative humidities. A  $\sim 0.5$  LPM aerosol sample flow passes first through a Nafion drier, and then through a  $^{210}\text{Po}$  neutralizer that brings the dried particles to a stable, steady-state charge distribution. A cylindrical DMA selects particles in a narrow interval of mobility-equivalent diameters in the 0.1 to 1.0  $\mu\text{m}$  range. The classified aerosol leaving the DMA is split into five separate flows. In one of the five streams, the total concentration of classified particles is determined using an integral TSI Model 3831 water-based condensation particle counter (CPC). The remaining four classified aerosol flows pass through a Nafion humidifier (Perma Pure, LLP, Model MD-070-24FS-4) to achieve thermodynamic equilibrium with water vapor at a constant, predetermined RH. The four conditioned aerosol flows pass directly to dedicated, custom-built OPCs ( $\lambda = 532$  nm, World Star Technologies, Model TECGL-30) designed to size particles in the 100 nm to 3  $\mu\text{m}$  diameter size range. An iterative data processing algorithm quantifies an “effective” aerosol refractive index that is used to calculate hygroscopic growth factors ( $GF = D_{p,wet}/D_{p,dry}$ ) corrected for the refractive-index dependence of the OPC response (Sorooshian et al., 2008). During this study, the DASH-SP provided simultaneous

measurements of  $GF$ s at different RHs for dry DMA-selected particle diameters between  $D_p = 150 - 200$  nm. One humidifier was operated dry ( $RH < 8\%$ ), and the other three were at RHs of 74%, 85%, and 92%. (No data from the  $RH = 85\%$  channel were available during flight A.) The uncertainty associated with growth factor measurements is  $\sim \pm 4.5\%$ , and the uncertainty in the RH is  $\pm 1.5\%$ .

#### **7.3.4. Cloud Condensation Nuclei Counter (CCNc)**

A continuous flow thermal gradient cloud condensation nuclei counter (CCNc, Droplet Measurement Technologies Inc.; Roberts and Nenes, 2005; Lance et al., 2006) was used to quantify the number of particles that activate at supersaturations ranging from 0.1% to 0.6%. In the instrument a supersaturation is generated in an axisymmetric flow by applying a constant streamwise temperature gradient, using three sets of thermal electric coolers across a wetted column. At the exit of the CCNc column, those particles that activate and grow sufficiently large ( $D_p > 0.75$   $\mu\text{m}$ ) for detection by an OPC were quantified. The activated fraction is determined as the ratio of the CCN number concentration to the total particle (CN) number concentration.

#### **7.3.5. Size Distributions and Particle Number Concentration**

Aerosol size distribution data were obtained by a DMA ( $D_p = 10 - 800$  nm) and an external passive cavity aerosol spectrometer probe (0.1 – 3  $\mu\text{m}$ ) (PCASP, PMS Inc., modified by DMT Inc.). Particle number concentrations were quantified with two condensation particle counters (CPC Model 3010, TSI Inc.,  $D_p > 10$  nm; UFCPC Model 3025, TSI Inc.,  $D_p > 3$  nm). When the two CPCs experienced electrical saturation,

particle number concentrations from the DMA are reported. The DMA time resolution is 74 s as opposed to 1 s for the CPCs.

### **7.3.6. Flight Strategy**

Complete flight tracks from flights A and B are shown in Figure 7.1A. Both flights were intended to resemble each other in the time of the day and flight path. Starting from the Marina, CA airport, the aircraft transited east before descending to 50 m above the surface of the San Joaquin Valley. Then the aircraft flew southeast directly towards the feedlot, approaching to within one kilometer of the feedlot. A close-up of the flight tracks near the plume source with step-by-step details of the flight strategy is shown in Fig. 7.1B/C. In each flight, the Twin Otter circled above the perimeter of the source several times, performed a spiral ascent to characterize the meteorological profile, performed several downwind transects of the plume at various altitudes below the boundary layer top, flew directly in the plume for several legs (only flight B), and transited northwest back up the valley. Sampling lasted for more than three hours starting just before noon during both flights. The feedlot operation is slightly larger than 3 km<sup>2</sup> in area (~ 800 acres). The feedlot is bordered on the west side by the Interstate 5 roadway, which is a major transportation route and source of vehicular emissions, connecting northern and southern California.

## 7.4 Results

### 7.4.1 Meteorology

Figures 7.2 (flight A) and 7.3 (flight B) display the time evolution of meteorological and particle number concentration data, while Figure 7.4 presents vertical profiles. During flight B, ambient temperatures ( $27.5 \pm 2.4^{\circ}\text{C}$ ) were higher and RHs ( $25.8 \pm 5.9\%$ ) were lower than observed in flight A ( $21.8 \pm 2.3^{\circ}\text{C}$ ;  $49.0 \pm 7.8\%$ ). During both flights, the aircraft performed three vertical profiles of the boundary layer. The temperature inversions were weak ( $< 1^{\circ}\text{C}$ ), so decreases in RH and particle number concentrations, as quantified by the DMA and PCASP, are used as indicators for inversion layers. The boundary layer exhibited multiple inversions, the highest of which was observed at the end of the flights ( $\sim 3\text{ PM}$  local time) at  $\sim 630\text{ m}$ . The depth of the inversion layers increased with time as the surface warmed. The vertical temperature and RH profiles, and the relatively uniform particle concentrations with altitude (Fig. 7.4) provide evidence for a vigorously-mixed boundary layer, as was previously observed by Neuman et al. (2003) in the San Joaquin Valley in May 2002.

Five-day back-trajectories, computed using the NOAA HYSPLIT model (Draxler and Rolph, 2003), show that the background air during flight A originated over the Pacific Ocean, whereas the background air during flight B was transported over land from the north (Fig. 7.5). This suggests that the background aerosol in flight A may have carried the signature of cleaner marine air, while that measured during flight B was more exposed to urban and agricultural emissions.



## 7.4.2 Particle Number Concentrations and Size Distributions

Average submicrometer particle number concentrations in the plume were  $30,528 \pm 8,987 \text{ cm}^{-3}$  (flight A) and  $16,606 \pm 4,286 \text{ cm}^{-3}$  (flight B) (Table 7.1). Particle number concentrations in and out of the plume were similar, indicating the absence of significant emissions of particles from the source. (As noted in Section 7.4.3, nitrate enhancement is used to identify the location of the plume.) During the downwind plume transects, number concentrations decreased slightly with increasing altitude until a sharp decrease near the top of the boundary layer to below  $300 \text{ cm}^{-3}$  (flight A) and  $800 \text{ cm}^{-3}$  (flight B) at altitudes of 550 m and 400 m, respectively. The ratio of the number concentration of particles with  $D_p > 3 \text{ nm}$  to the number concentration of particles with  $D_p > 10 \text{ nm}$  was  $1.1 \pm 0.1$  and  $1.2 \pm 0.1$  for flights A and B, respectively. This ratio showed no difference in and out of the plume and decreased with altitude.

The vertical structure of the PCASP ( $D_p = 0.1 - 3 \text{ }\mu\text{m}$ ) and CPC number concentrations were similar. Average PCASP concentrations in the plume for flights A and B were  $1,065 \pm 330$  and  $675 \pm 220 \text{ cm}^{-3}$ , respectively, indicating that most of the particles were smaller than 100 nm in diameter. The number of 0.1 to 3  $\mu\text{m}$  diameter particles in the plume was enhanced by a factor of 2.5 - 3 times as much over that in the background aerosol. This is especially evident by the increase in number concentration ( $D_p > 100 \text{ nm}$ ) observed when passing through the beginning of the plume over the perimeter of the source (upper panels of Figure 7.2/7.3; see the flight segments labeled “2” when the aircraft was circling the perimeter of the plume source); this likely is a result of smaller particles growing into this size range. However, the increase in number concentration for particles with  $D_p = 0.1 - 3 \text{ }\mu\text{m}$  was not sufficiently large to result in a

significant difference in the submicrometer number concentration ( $D_p = 0.01 - 1 \mu\text{m}$ ) in and out of the plume.

Aerosol number and volume distributions were similar both between the two flights, and in and out of the plume. Multiple modes normally existed in the number and volume distributions. A number concentration mode was generally present between  $D_p = 20 - 60 \text{ nm}$ , with a weaker mode between  $D_p = 60 - 100 \text{ nm}$  (lower panels of Fig. 7.2/7.3). There was also a dominant number concentration mode, which will be referred to as the nucleation mode, at sizes smaller than the detection limit of the DMA ( $10 \text{ nm}$ ); this mode is evident from the difference in number concentration measured by the DMA and the UFCPC 3025. Volume concentration modes existed at  $D_p = 30 - 60 \text{ nm}$ ,  $D_p \sim 100 \text{ nm}$ , and frequently at  $D_p > 100 \text{ nm}$ . The number and volume distributions in the plume shifted slightly to larger sizes with downwind distance from the plume source.

### 7.4.3 Submicrometer Aerosol Chemical Composition

Figures 7.6 (time series), 7.7/7.8 (spatial distribution), and 7.9 (vertical distribution) summarize the submicrometer aerosol composition data, in addition to Table 7.1, which reports the background and in-plume composition for both flights. The reported total organic mass is non-refractory organic mass that was measured by the cToF-AMS. The total aerosol mass is determined as the sum of inorganic mass, as determined by the PILS and cToF-AMS, and non-refractory organic mass from the cToF-AMS. Nitrate enhancement is used to define the location of the plume. Then, knowing where the plume is, local enhancements in other species concentrations and aerosol properties can be determined. Plume ages are noted on the spatial plots in Fig. 7.1B/C

and were calculated using downwind distance and average wind speed in the vicinity of the source. The highest plume age encountered in flights A and B was 0.9 h and 1.2 h, respectively.

#### 7.4.3.1 Total Aerosol Mass and Major Components

The average total aerosol mass in the boundary layer was  $8.85 \pm 1.79 \mu\text{g}/\text{m}^3$  and  $3.40 \pm 0.98 \mu\text{g}/\text{m}^3$  during flights A and B, respectively, with significant enhancements in the plume (Table 7.1). The highest concentrations,  $17.07 \mu\text{g}/\text{m}^3$  (flight A) and  $6.27 \mu\text{g}/\text{m}^3$  (flight B), occurred in the plume while the lowest concentrations were observed at the highest altitudes when the aircraft performed spiral ascents (flight A =  $1.40 \mu\text{g}/\text{m}^3$ ; flight B =  $0.24 \mu\text{g}/\text{m}^3$ ).

Overall, organic species dominated the total mass. Organics accounted for  $61.9\% \pm 2.6\%$  (flight A) and  $55.5\% \pm 6.4\%$  (flight B) of the plume aerosol mass, and  $63.5\% \pm 3.3\%$  (flight A) and  $63.1\% \pm 11.9\%$  (flight B) of the background aerosol mass. The organic mass concentration in the plume was  $6.48 \pm 0.98 \mu\text{g}/\text{m}^3$  (flight A) and  $2.46 \pm 0.29 \mu\text{g}/\text{m}^3$  (flight B), and in the background aerosol was  $5.10 \pm 1.07 \mu\text{g}/\text{m}^3$  (flight A) and  $1.73 \pm 0.70 \mu\text{g}/\text{m}^3$  (flight B). The next largest contributor to the particulate mass was either sulfate or nitrate, depending on the day and aerosol type, followed by either ammonium or nitrate (see Table 7.1). The ratio of organic mass to inorganic mass in the plume was  $1.64 \pm 0.19$  (flight A) and  $1.30 \pm 0.39$  (flight B), while the ratio in the background aerosol was  $1.77 \pm 0.29$  (flight A) and  $1.92 \pm 0.68$  (flight B). Previous measurements in the San Joaquin Valley have also shown that organic aerosol contributes significantly to the fine particle mass (Chow et al., 1996; Neuman et al., 2003).

### 7.4.3.2 Inorganic Aerosol

Within the source plume, the levels of nitrate and ammonium increased significantly above their respective values in the background valley aerosol (Fig. 7.6 – 7.8). The ammonium-to-sulfate molar ratio is an important indicator of the level of partitioning of ammonium nitrate between the gas and aerosol phases. Since this ratio usually exceeded two, ammonia was available to foster partitioning of nitrate to the aerosol phase in the plume. The vertical distribution of nitrate and ammonium exhibited similar trends in each flight, unlike sulfate, which did not increase in concentration at plume altitudes ( $\sim 100 - 300$  m) (Fig. 7.9).

Generally, other inorganic species, including chloride, sodium, potassium, calcium, magnesium, and nitrite, did not contribute significantly ( $> 0.1 \mu\text{g}/\text{m}^3$ ) to the aerosol mass. Many of these species are expected to be found primarily in the coarse particle fraction ( $D_p > 1 \mu\text{m}$ ), owing to their origins in sea salt ( $\text{Na}^+$ ,  $\text{Cl}^-$ ) and dust and soil ( $\text{Ca}^{2+}$ ,  $\text{Mg}^{2+}$ ,  $\text{Na}^+$ ,  $\text{K}^+$ ). Magnesium, calcium, and potassium concentrations were all below detection limits ( $< 0.05 \mu\text{g}/\text{m}^3$ ). Sodium and chloride were sparsely detected in both flights, usually in the background aerosol during the transits, with concentrations near  $\sim 0.1 \mu\text{g}/\text{m}^3$ . Nitrite above detection limits was found in only one PILS sample ( $0.10 \mu\text{g}/\text{m}^3$ ) during flight A while circling the feedlot near the beginning of the flight (UT  $\sim 19:00$ ).

### 7.4.3.3 Organic Aerosol

The concentration of total organics, as determined by the cToF-AMS, in the plume aerosol significantly exceeded those in the background valley aerosol (Figure 7.6 –

7.8). The vertical distribution of total organic concentrations was somewhat similar to those of nitrate and ammonium, with the exception that there was not as sharp an enhancement in concentration at plume altitudes, as was especially evident in flight B (Fig. 7.9).

Figure 7.10 shows the representative mass spectra of the organic fragments detected by the cToF-AMS in the background valley aerosol, the plume aerosol close to the source, and farther downwind. All non-organic contributions to the mass spectra have been removed using the methodology described in Allan et al. (2004); fragmentation at  $m/z$  30 was further modified as described in Section 7.3.2. Figure 7.11 indicates that the signal at  $m/z$  30 represents a large fragment for organics, including amines. The chemical signatures of the organic aerosol in the three categories appear to be quite similar. One difference, which is highlighted also in Figure 7.11, is that the  $m/z$  30 (common amine marker) peak intensity is enhanced by  $\sim 150\%$  at the closest point to the plume source as compared to background aerosol, and decreases by  $\sim 25\%$  at the farthest downwind distance. Figure 7.11 shows comparisons of the plume aerosol organic mass spectra to the background spectra for both flights. The overall organic aerosol appears to be similar in and out of the plume; however, peak intensities at  $m/z$  30, 56, 74, and 86 are enhanced in plume. These are all peaks in the electron impact mass spectrum of amines, including diethylamine and triethylamine (McClafferty and Turecek, 1993; Angelino et al., 2001; Murphy et al., 2007). A similar analysis for plume organics close to the feedlot and farther downwind reveals no significant difference in most peaks, although the intensity of the  $m/z$  30 peak decreases with increasing plume age; as will be discussed subsequently, this is likely attributed to increased partitioning of particulate

amines to the gas phase to maintain thermodynamic equilibrium as the plume dilutes with background air. An analysis of the background valley aerosol spectra during the transit portions of the flights indicates that the organic aerosol composition was similar throughout the valley.

Two amines were detected by the PILS, diethylamine and ethylamine; these were found only in the plume (Fig. 7.6 – 7.8). Diethylamine reached higher concentrations (up to  $0.18 \mu\text{g}/\text{m}^3$  and 6.0% of the organic mass) and was more abundant farther downwind of the feedlot as compared to ethylamine; diethylamine was observed at plume ages up to 0.9 h (flight A) and 0.7 h (flight B). Ethylamine was detected by the PILS only in three samples collected during the two flights. It was found immediately downwind of the feedlot up to plume ages of 0.7 h (flight A) and 0.3 h (flight B) at concentrations near  $0.02 \mu\text{g}/\text{m}^3$ , which corresponds to 0.8% of the total organic mass, as inferred from the cToF-AMS data.

The collective organic acid concentration, as determined by the PILS, reached levels of up to  $0.23 \mu\text{g}/\text{m}^3$  (flight A) and  $0.41 \mu\text{g}/\text{m}^3$  (flight B), accounting for 0.4% ( $\pm$  0.8%) and 0.4% ( $\pm$  0.6%) of the cToF-AMS total organic mass during flights A and B, respectively. Oxalate was the most abundant organic acid, followed by succinate, formate, and acetate. The concentration of the organic acids ( $\text{C}_1 - \text{C}_9$ ) were not found to be correlated with those of total organics, amines, or any inorganic species.

#### 7.4.4 Aerosol Mixing State

Figure 7.12 shows speciated size distributions for the background and in-plume aerosol at various downwind distances for both flights. Organics, nitrate, and sulfate all

appear to be externally mixed to some extent. This is especially clear when examining the plume aerosol at various downwind distances in flight B; the distribution of nitrate aerosol grows in diameter, while the organic distribution shows relatively less growth and the sulfate distribution does not exhibit any corresponding shift in size. Speciated size distributions for the valley aerosol during transit are similar to the background aerosol in the vicinity of the feedlot, indicating chemically similar particles.

#### **7.4.5 Refractive Index**

The background aerosol exhibited a consistent average dry-particle refractive index of  $1.54 \pm 0.07$  and  $1.54 \pm 0.04$  for flights A and B, respectively (Table 7.2). Since these values are close to those of ammonium nitrate (1.55) and ammonium sulfate (1.52 – 1.53) (Weast, 1987; Tang, 1996), which are the dominant inorganic components of the aerosol, assuming a volume-weighted overall refractive index, the organic component refractive index is calculated also to be 1.54. Notably, Zhang et al. (1994) reported a similar refractive index of 1.55 for particulate organic compounds in Grand Canyon aerosol. The overall aerosol refractive indices were slightly lower in the plume, with the lowest values observed closest to the feedlot during the aircraft circling maneuvers ( $1.48 \pm 0.09$  and  $1.51 \pm 0.01$  for flights A and B, respectively). Organic species, such as amines, may be responsible for this decrease as the organic mass fraction dominated the total mass; ethylamine and diethylamine have refractive indices of 1.37 and 1.39, respectively (Dean, 1999). Although only two particulate amines were speciated at low concentrations (< 4% of total mass), other amine compounds may well have existed in the total organic mass with comparable refractive indices.

## 7.4.6 Hygroscopic Properties of the Aerosol

### 7.4.6.1 Subsaturated Water Uptake

Figures 7.13 and 7.14 present the spatial distribution of hygroscopic growth factors at the RHs studied for flights A and B, respectively. Aerosol growth factors ranged from 1.00 to 1.27 at 74% RH, 1.21 to 1.62 at 85% RH, and 1.30 to 2.04 at 92% RH (Table 7.2), depending on location, altitude, and proximity to the plume source. For reference, growth factors for pure ammonium nitrate ( $D_{p,dry} = 150$  nm) at RHs of 74%, 85%, and 92% are 1.37, 1.60, and 1.94, respectively (deliquescence RH = 61.8%; Brechtel and Kreidenweis, 2000). Growth factors for pure ammonium sulfate ( $D_{p,dry} = 150$  nm) at RHs of 85% and 92% are 1.56 and 1.80, respectively (deliquescence RH = 79.9%; Brechtel and Kreidenweis, 2000). Overall, the plume aerosol exhibited higher hygroscopic growth factors as compared to the background aerosol. Hygroscopic growth factors in the immediate vicinity of the source were usually between 1.75 – 1.90 at RH = 92%.

Hygroscopic growth factors are now related to the mass fractions of the aerosol components. Figure 7.15 shows the dependence of growth factors at an RH of 92% on mass fractions of nitrate and organics measured for flight B. (Similar effects occur at the other RHs.) Increasing growth factors coincide with higher nitrate mass fractions. This effect is most evident during flight B, in terms of slope (0.31) and correlation ( $R^2 = 0.43$ ), partly because of the larger range of nitrate mass fractions observed. In addition, growth factors exhibited a negative correlation ( $R^2 = 0.46$ , slope = -0.28) with organic mass fractions. Less correlation exists between observed growth factors and mass fractions of ammonium and sulfate ( $R^2 < 0.21$ ). The data show that subsaturated hygroscopicity



increases as a function of increasing fraction of ammonium nitrate, a highly hygroscopic salt, and decreasing fraction of organics, the growth factor of which will be explored subsequently.

#### **7.4.6.2 CCN**

The CCN data acquired are summarized in Table 7.3 and Figure 7.16. Owing to the large number of particles with diameters below about 60 nm, in the background atmosphere as well as in the plume, the activated fractions were quite small. An enhancement in activated fraction was observed in the plume, which is consistent with the observed behavior of subsaturated hygroscopic growth factors.

An important issue is the extent to which aerosol composition influences CCN behavior. This can be manifested in two ways: (1) by affecting the critical supersaturation of the particles; and (2) by influencing the growth rate once the particle activates. Figure 7.17 shows the normalized activation fraction as a function of hygroscopic growth factor for flight B. The normalization is done by computing the activation fraction assuming the CCN are composed of pure ammonium sulfate. The normalization removes any variations due to shifts in the shape of the size distribution. It is noted that, in general, higher supersaturations are required to activate particles composed of less hygroscopic material.

Regarding the effect of particle composition on growth rate, consider two particles each having the same critical supersaturation. If the ambient supersaturation exceeds the critical supersaturation, then each particle will activate. The subsequent rate of growth by water condensation depends on the uptake of water molecules. If the two

particles have different composition, then the uptake coefficients for water vapor can be different; the particle with the smaller water uptake coefficient will exhibit a slower rate of growth after activation. In a CCN instrument, like the CCNc employed here, the more slowly growing particle may not reach its ultimate size before it exits the growth chamber of the instrument and is detected by the OPC. The growth rate of pure ammonium sulfate particles of the same critical supersaturation as that of the particle in question can be taken as the standard against which particle growth rates can be compared. Since an entire distribution of particles enter the CCNc, with different critical supersaturations (as a result of size and composition), the standard used is ammonium sulfate with a critical supersaturation equal to the supersaturation of the instrument. Based on this standard, if all particles grow as quickly as those composed entirely of ammonium sulfate, all particles will have droplet sizes equal to or larger than the standard. Hence, at a given supersaturation, the presence of droplets with a size less than that of the standard indicates retarded growth. We express this effect in terms of the fraction of droplets less than the standard at the supersaturation of the instrument.

Figure 7.18 shows the cToF-AMS – derived ratio of  $m/z$  57:44 as a function of organic mass fraction. (A larger  $m/z$  57:44 ratio is correlated with the organic material being less oxidized, and hence more hydrophobic.) The color coding of the data points corresponds to the fraction of droplets that have a size ( $D_i$ ) less than the ammonium sulfate standard ( $D_{AS}$ ), as described above. The size of the symbols reflects the hygroscopic growth factor at 92% RH. The data indicate that at high organic mass fractions when the particles are composed of less oxidized material, there is a tendency,

although weak, towards retardation of growth. The growth factor exhibits a clear anti-correlation with organic mass fraction.

## **7.5 Discussion**

In this section we explore key findings in this study. The observations reveal significant differences in aerosol properties in and out of the plume, and as a function of plume age. Significant enhancements in nitrate, ammonium, and organic levels in the plume were observed; this coincided with an increased potential for water uptake in both the sub- and supersaturated regimes. While trends in the data from the two flights were similar, particle number and mass concentrations were larger in flight A. Explanations for this discrepancy will be pursued.

Owing to the range of organic fractions observed, the present study provides an opportunity to evaluate the sensitivity of mixed inorganic/organic particle hygroscopicity to the organic fraction. Subsaturated hygroscopic growth factors are calculated for the organic fraction based on a closure analysis using the Zdanovskii-Stokes Robinson (ZSR) mixing rule. Measurement of CCN activity in this study also presents an opportunity to assess the consistency of observed supersaturated water uptake with the subsaturated water uptake measurements.

### **7.5.1 Enhancements in Mass Production and Water Uptake in the Plume Aerosol**

Significant production of ammonium nitrate and organic mass in the plume occurred during both flights. Ammonium nitrate production is expected due to the high ammonia levels and the presumed abundance of nitric acid from the daytime

photochemistry. Organic aerosol mass production results from both condensation of semi-volatile organic species and acid – base chemistry of amines, followed by condensation of low-volatility products onto pre-existing aerosols.

Enhanced sub- and supersaturated water uptake coincides with greater fractions of ammonium, nitrate, and amines. Dinar et al. (2008) have shown, for example, that the reactive uptake of ammonia by aerosols containing slightly soluble organics leads to substantial increases in hygroscopic growth and CCN activity. This observation appears to be consistent with the present measurements. Speciated size distributions show that the aerosol is, in part, externally mixed, with different species growing independently during plume aging (Fig. 7.12). The high organic fractions, particularly during flight A, may have masked the expected and significant growth exhibited by pure ammonium nitrate and ammonium sulfate salts; however, amines, which represent one class of organic species in the plume, are thought to be highly hygroscopic. Aklilu et al. (2006) also suggested that the organic fraction of the aerosol can suppress the growth normally associated with nitrate based on ambient measurements at two rural, urban-influenced sites.

## **7.5.2 Amines as an Atmospheric Base**

### **7.5.2.1 Is Nitric Acid or Ammonia the Limiting Reactant?**

Previous studies of particulate ammonium nitrate formation in the San Joaquin Valley suggest that the limiting reactant is nitric acid because of abundant ammonia emissions (Blanchard et al., 2000; Pun and Seigneur, 1999). During an aircraft study in the San Joaquin Valley in May 2002, Neuman et al. (2003) reported simultaneous nitric

acid depletion and aerosol mass enhancements when the aircraft either encountered large ammonia sources or reached lower temperatures at higher altitudes in the boundary layer. Ammonia is emitted from the ground, whereas nitric acid is efficiently produced photochemically throughout the entire boundary layer, especially during the summer in the daytime San Joaquin Valley atmosphere.

Since gas-phase ammonia and nitric acid were not measured in the present study, observed particulate levels of ammonium, nitrate, sulfate, and amines can help determine the limiting reactant in chemical processing inside the plume. *Excess nitrate* is most abundant within the plume, reaching levels as high as  $1.72 \mu\text{g}/\text{m}^3$  (flight A) and  $0.89 \mu\text{g}/\text{m}^3$  (flight B). (As defined in Section 7.3.2, *excess nitrate* is the amount of nitrate remaining after both sulfate and nitrate have been fully neutralized by ammonium.) The greatest *excess nitrate* values coincide with relatively lower ambient temperatures, higher altitudes, the presence of diethylamine and ethylamine, and are correlated with amine markers in the cToF-AMS spectra ( $m/z$  58, 73, 86) (Figure 7.7B/7.8B/7.9). The background aerosol tends to exhibit *excess nitrate* values close to zero, indicating that just enough ammonia was present, on average, to neutralize both sulfate and nitrate. The data suggest either of two conclusions: (1) insufficient ammonia was present to neutralize both sulfate and nitrate within the plume, thereby distinguishing ammonia as the limiting reactant; or (2) sufficient ammonia was present, but a significant amount of nitric acid formed salts preferentially with amines rather than ammonia. The detection of amines by the PILS and the large amount of organic mass, with representative amine markers detected by the cToF-AMS, suggests that the second explanation may be more plausible. This is a significant finding in the atmosphere that is consistent with laboratory

observations made in photooxidation experiments of aliphatic amines (Angelino et al., 2001; Murphy et al., 2007). The affinity of inorganic acids for amines in the presence of ammonia has even greater implications during the winter and at night, when lower temperatures and higher RHs enable increasing partitioning of both ammonium nitrate and amine salts into the aerosol phase.

#### **7.5.2.2 Sources and Character of Amines**

The formation of particulate amine salts depends on temperature, the identity and concentrations of the amine and acidic species present, and the concentration of ammonia that competes with amines for the acidic species. Once the particulate amine salts are formed, they may revolatilize, undergo subsequent particle-phase reactions including oxidation, or serve as a site for the condensation of other organic compounds. Chamber experiments performed by Murphy et al. (2007) showed that the dominant formation mechanism for amines is that of acid-base reactions (amine + nitric acid) rather than from photooxidation to form non-salt condensable organics. These experiments showed that nitric acid preferentially reacts with amines, depending on the species, rather than ammonia. It is expected that particulate amines should be prevalent close to the source of amine emissions where gaseous amine concentrations are highest. If the temperature dependence of amine salt equilibria resembles that of ammonium nitrate, then amines should partition more favorably to the aerosol phase at lower temperature (higher altitudes) within the plume. Of the six amines studied by Murphy et al. (2007), diethylamine was shown to have the most favorable equilibrium constant for salt formation in the presence of ammonia, an observation that is consistent with the present

field measurements since diethylamine was the most abundant amine detected in the aerosol. The amine salts produced in the laboratory chamber experiments eventually repartitioned back to the gas phase. In the present study, amine concentrations decreased as a function of plume age, as evident in the ethylamine and diethylamine data and the  $m/z$  30 peak intensity data from the cToF-AMS. The decreasing amine levels in the aerosol phase presumably occur because of two reasons: (1) amine concentrations, like those of ammonium and nitrate, decrease due to dilution as a function of plume age; and (2) amines partition back to the gas phase to maintain thermodynamic equilibrium due to the decreasing gas-phase concentrations owing to dilution.

Diethylamine, measured exclusively in the plume, exhibited a strong and positive correlation with nitrate, ammonium, sulfate, and total organics during flight A ( $n = 8$ ,  $R^2$ : nitrate = 0.65, ammonium = 0.73, sulfate = 0.72, organics = 0.68), but showed a weaker correlation with the same species during flight B ( $n = 7$ ,  $R^2$ : nitrate = 0.35, ammonium = 0.04, sulfate = 0.13, total organics = 0.40). The positive correlation between diethylamine and nitrate suggests that nitric acid exhibits an affinity for amines as an atmospheric base, even in the presence of ammonia. Diethylamine concentrations correlated more weakly with sulfate than to nitrate during flight B, possibly because nitric acid levels were higher than those of sulfuric acid causing the formation of particulate amines to proceed only through the amine +  $\text{HNO}_3$  acid - base reaction. When diethylamine was detected, its average mass ratio relative to nitrate was 0.31 (flight A) and 0.36 (flight B); relative to sulfate it was 0.16 (flight A) and 0.36 (flight B), and relative to ammonium it was 0.31 (flight A) and 0.17 (flight B).

### 7.5.2.3 Total Amine Mass Calculations

One can estimate the total mass of amines present in the plume. This calculation assumes that *excess nitrate* is in a 1:1 molar ratio with amines. Amine mass is then determined by assuming a representative molecular weight for the amine population. We choose to use methylamine and triethylamine as lower and upper limits, respectively, since these species represent the smallest and largest amines that can be speciated using the PILS-IC technique (Murphy et al., 2007); the molecular weight of the two amines detected in this study, ethylamine and diethylamine, fall within the range of those of methylamine and triethylamine.

On the basis of the molecular weight of methylamine (31.1 g/mol), average amine concentrations in the plume are calculated to have been  $0.23 \pm 0.13 \mu\text{g}/\text{m}^3$  (4% of total organic mass) (flight A) and  $0.06 \pm 0.10 \mu\text{g}/\text{m}^3$  (2% of total organic mass) (flight B), while maximum plume concentrations were  $0.86 \mu\text{g}/\text{m}^3$  (13% of total organic mass) (flight A) and  $0.44 \mu\text{g}/\text{m}^3$  (19% of total organic mass) (flight B). On the basis of the molecular weight of triethylamine (101.1 g/mol), average amine concentrations are calculated to have been  $0.76 \pm 0.43 \mu\text{g}/\text{m}^3$  (12% of total organic mass) (flight A) and  $0.20 \pm 0.32 \mu\text{g}/\text{m}^3$  (8% of total organic mass) (flight B), while maximum levels were  $2.81 \mu\text{g}/\text{m}^3$  (43% of total organic mass) (flight A) and  $1.45 \mu\text{g}/\text{m}^3$  (63% of total organic mass) (flight B). Using the conservative molecular weight of methylamine, amine mass was at least 23% (flight A) and 14% (flight B) of ammonium mass in this plume. In addition, speciated amines (ethylamine and diethylamine via the PILS) accounted for at least 25% (flight A) and 45% (flight B) of the estimated total amine mass (via the *excess nitrate* calculation from the cToF-AMS).



### 7.5.3 Degree of Oxidation and Volatility in the Aerosol

In the absence of strong signals in the data representing primary particulate emission sources, the submicrometer aerosol in the sampling region is presumed to originate mainly from secondary production. No obvious signs of primary aerosol vehicular emissions existed based on organic markers in the cToF-AMS spectra. The ratio of  $m/z$  57:44 peak intensities from the cToF-AMS can provide some insight into the relative ratio of hydrocarbon-like (HOA) and oxygenated organic (OOA) aerosols (Zhang et al., 2005). This ratio was  $\sim 0.07 \pm 0.01$  during both flights, with no major changes during the flights, nor between plume and background aerosol (Table 7.1). Based on this ratio, it appears that the aerosol was highly oxygenated with relatively little hydrocarbon-like organic aerosol (HOA). The ratio of the peak intensity between  $m/z$  44 and total organics was, on average,  $0.10 \pm 0.01$  in the plume aerosol and  $0.11 \pm 0.02$  in the background aerosol (Table 7.1). Peak intensities at  $m/z$  44 (and 29 for flight A) are slightly greater in the background aerosol relative to plume aerosol, indicating a greater degree of oxidation out of the plume than within it (Fig. 7.11). This is presumably because the background aerosol had aged longer than the fresh emissions in the plume.

Organic acids represent a pool of organic species that are water-soluble and highly oxidized. In previous aircraft measurements, organic acids ( $C_1 - C_9$ ) contributed  $3.4 \pm 3.7\%$  to the total PILS mass in an urban atmosphere (Houston, Texas; Sorooshian et al., 2007a) and  $3.5 \pm 3.1\%$  in a marine atmosphere (Eastern Pacific Ocean; Sorooshian et al., 2007b). In the present study, organic acids contributed  $2.4 \pm 5.5\%$  to the total PILS mass, indicating greater variability and a lower average mass fraction of organic acids than seen in the other field data. Since the lower organic acid contributions are likely not

a result of less photochemical processing, gas-particle partitioning of these water-soluble organic species may have been affected by the high ambient temperatures in the present flights. In addition, the relatively low humidities and lack of clouds prevented organic acid production via aqueous-phase processing during the measurement period (Sorooshian et al., 2006b). Organic acid concentrations were not correlated with ammonium or nitrate, which represent semi-volatile species, during the present flights. The ammonium nitrate levels varied significantly in the plume, but concentrations of the organic acids were relatively stable. Thus, the data do not allow one to conclude whether volatility or RH was the dominant factor controlling organic acid levels.

#### **7.5.4 Factors Influencing Aerosol Number/Mass Concentrations**

Particle number and mass concentrations were significantly higher during flight A than in flight B. The presence of nucleation cannot explain this discrepancy, especially in terms of mass concentration (Table 7.1). The background aerosol concentration in the valley was also higher during flight A than in flight B. Since there are no significant sources of SO<sub>2</sub> in the sampling region, sulfate can be employed as a tracer for accumulated aerosol originating from long-range transport. It should be noted that comparable levels of vehicular emissions could be expected both days as both flights occurred on weekdays. Sulfate concentrations were significantly higher during flight A. The lower temperatures and higher RH during flight A favored partitioning of semi-volatile species, such as ammonium nitrate and organics, to the aerosol phase. The back-trajectory analysis indicates that the sampled air mass during flight A originated three days previously over the Pacific Ocean, while the air sampled in flight B originated in a

more polluted inland area. We conclude that ventilation of the valley during flight B was more effective than in flight A, reducing aerosol number and mass concentrations.

Over the flight durations, aerosol concentrations were influenced by competition between a growing boundary layer, decreasing RH, and increasing temperatures. Although the aerosol was well-mixed locally in the valley, the timescale for equilibration between the gas and particle phases is shorter than the boundary layer mixing time (Neuman et al., 2003); this may explain fluctuations in the concentrations of aerosol species at various altitudes and distances downwind of the plume source. The topography of the sampling region downwind of the source and general buoyancy in the boundary layer facilitated vertical transport of emissions to lower temperature regions, reducing the dissociation constant of ammonium nitrate aerosol and, presumably, semi-volatile organics. This might explain why the concentrations of organics (diethylamine in particular), nitrate, and ammonium peaked at the highest altitude and farthest downwind distance from the plume source in flight A.

#### **7.5.5 Estimated Subsaturated Hygroscopic Growth Factors for the Organic Fraction**

Calculations were carried out to determine the effective growth factor for the organic fraction needed to achieve composition – hygroscopicity closure. Due to its simplicity and frequent application (Cruz and Pandis, 2000; Dick et al., 2000; Choi and Chan, 2002a, 2002b; Prenni et al., 2003; Wise et al., 2003; Clegg et al., 2003; Clegg and Seinfeld, 2004, 2006a, 2006b; Khlystov et al., 2005; Rissler et al., 2005; Aklilu et al., 2006; Svenningsson et al., 2006; Varutbangkul et al., 2006; Gysel et al., 2007; Sjogren et al., 2007; Dinar et al., 2008), the Zdanovskii-Stokes Robinson (ZSR) (Zdanovskii, 1948;

Stokes and Robinson, 1966) mixing rule is employed to predict hygroscopic growth factors. This procedure of estimating hygroscopic growth based on specified composition is based on the assumption that water uptake by each individual component of a particle is independent and additive. We use the following form of the ZSR mixing rule (Aklilu et al., 2006; Gysel et al., 2007):

$$GF_{mixed}(a_w) \approx \left( \sum_i \varepsilon_i GF_i(a_w)^3 \right)^{\frac{1}{3}} \quad (1)$$

where  $GF_{mixed}$  is the hygroscopic growth factor of the mixed particle,  $GF_i$  is the hygroscopic growth factor of pure compound  $i$ ,  $a_w$  is the activity coefficient of water, and  $\varepsilon_i$  is the volume fraction of pure compound  $i$  in the dry particle.  $a_w = RH$  in equation (1) (Seinfeld and Pandis, 2006). Growth factors for the pure inorganic components were obtained from the Aerosol Inorganics Model (AIM; <http://mae.ucdavis.edu/~sclegg/aim.html>; Clegg et al., 1998). At an RH of 74%, a growth factor of unity is employed for ammonium sulfate rather than the predicted value of 1.40 on its metastable branch of the hygroscopic hysteresis. It is reasonable to assume that the sampled aerosol did not have sufficient time to be processed in the atmosphere at high RHs. A growth factor of unity is also assumed for EC, as suggested by Aklilu et al. (2006).

Calculating the individual volume fractions requires an estimate of the organic density. If it is assumed that the aerosol is composed of ammonium sulfate (AS), ammonium nitrate (AN), organic carbon (OC), and elemental carbon (EC), then total aerosol density can be expressed as:

$$\rho = x_{OC} m_{OC} \rho_{OC} + x_{AS} m_{AS} \rho_{AS} + x_{AN} m_{AN} \rho_{AN} + x_{EC} m_{EC} \rho_{EC} \quad (2)$$

where  $x_i$  are mass fractions,  $m_i$  are mass concentrations, and  $\rho$  is density of the multicomponent particle, as determined by the ratio of aerosol volume (via the DMA) to the aerosol mass (via the PILS and cToF-AMS); in equation (2),  $\rho_{OC}$  is the unknown quantity that we desire to determine. Elemental carbon was not quantified in the present study; however, based on extensive chemical characterization of San Joaquin Valley  $PM_{2.5}$  by Chow et al. (2006), the mass fraction of EC tends to be  $\sim 5 - 10\%$  near the present sampling site. In the absence of a quantitative measure of EC, it is assumed that 5% of the total submicrometer mass is composed of EC. It is assumed for the purpose of this calculation that all of the sulfate is neutralized by ammonium, and the remaining ammonium occurs as ammonium nitrate. Densities of 1.725, 1.769, and 1.9  $g/cm^3$  are used for AN, AS, and EC respectively. A wide range of densities are reported for EC (0.625 – 2.25  $g/cm^3$ ) (Fuller et al., 1999); here we assume a value of 1.9  $g/cm^3$ , similar to that employed by Dillner et al. (2001). From the mass concentrations and respective densities of AN, AS, OC, and OC, the volume fraction of each component can be calculated.

On average, the in-plume organic growth factors needed to match the data (flight A/B) are 1.07/1.02 (74% RH), NA/1.28 (85% RH), and 1.49/1.53 (92% RH) (Figure 7.19). The background aerosol organic growth factors (flight A/B) are 1.08/1.03 (74% RH), NA/1.21 (85% RH), and 1.29/1.24 (92% RH). Flight B is characterized by a wider range in the mass fractions of organics, thus this flight presents a better indication of trends in organic growth factor with changing mass fractions. During this flight, inferred organic growth factors increase in the plume as a function of decreasing organic fraction. The lowest organic fractions in flight B coincide with the detection of amines, which

likely enhance the hygroscopicity of the organic fraction. There is a significant amount of variation in predicted growth factors at constant organic mass fractions and the absolute values of some of the predicted organic growth factors ( $< 1$  and  $> 2$ ) are unrealistic. Possible explanations for the unrealistic organic hygroscopic growth factors include: (1) complex particle morphology; (2) complex interactions between the components in the particles leading to non-additive water uptake among the individual components; and (3) errors associated with the calculation of the volume fractions and uncertainties in the measurements.

#### **7.5.6 Relationship Between Sub- and Supersaturated Water Uptake**

One anticipates a direct correspondence between subsaturated hygroscopic behavior and supersaturated CCN activity. For example, Mochida et al. (2006) explored the relationship between hygroscopicity and CCN activity for urban aerosols using a hygroscopic tandem DMA (HTDMA) coupled in series to a CCNc; enhanced CCN activity coincided with higher subsaturated growth factors. A similar analysis for the present data (Figure 7.17) shows that the normalized CCN activation ratio is generally consistent with water uptake in the subsaturated regime. Also, higher activated fractions are consistent with smaller markers, which represent lower organic mass fractions and higher nitrate mass fractions. Enhancements in water uptake for aerosols with lower organic content are likely due to increasing dissolution of water-soluble species, including ammonium nitrate and amine salts, and the possible reduction in surface tension by surface-active species. Organics have previously been shown to influence

CCN activity by adding solute and suppressing surface tension (Shulman et al., 1996; Facchini et al., 1999; Feingold and Chuang, 2002; Nenes et al., 2002).

Recent work has shown that kinetic limitations, including surface films and slow dissolution of particulate substances, can suppress droplet growth (Asa-Awuku and Nenes, 2007; Ruehl et al., 2008). With few exceptions including solute being physically “trapped” within some type of waxy material, dissolution kinetics is governed by diffusion of solute from the solid “core” at the center of a droplet to the growing droplet. It has been argued that the latter process is slow enough for compounds with high molecular weights to influence droplet growth kinetics and the Köhler curve (Asa-Awuku and Nenes, 2007; Taraniuk et al., 2007; Moore et al., 2008). According to Figure 7.18, droplet growth was at times less than that expected for pure ammonium sulfate. In addition, it is shown to some extent that the droplet growth was suppressed for CCN with relatively greater amounts of hydrophobic organic material. This suggests kinetic limitations may have played a role in suppressing water uptake. This issue will be revisited in subsequent work that will address size-resolved CCN data from this experiment.

#### **7.5.7 Parameterization for Sub- and Supersaturated Water Uptake**

To effectively represent the process of water uptake by multicomponent particles in atmospheric models, parameterizations are used. A number of investigators have attempted to introduce parameters to describe water uptake in both the sub- and supersaturated regimes. Expanding upon the earlier work of Fitzgerald et al. (1982), Svenningsson et al. (1992) used a parameter termed  $\varepsilon$  to link subsaturated water uptake to

cloud and fog activation. Subsequent work introduced closely related parameters for sub- and supersaturated regimes (Kreidenweis et al., 2005; Rissler et al., 2006; Petters and Kreidenweis, 2007). A recently introduced parameter,  $\kappa$  (Petters and Kreidenweis, 2007), can be calculated without knowledge of the particle properties such as density, molecular weight, and surface tension.

Kappa can be determined from either CCN activity data or subsaturated hygroscopic growth data. Since the subsaturated DASH-SP growth factors are measured for size-resolved particles, we use the subsaturated hygroscopicity data to predict the value of  $\kappa$  with the following equation (Petters and Kreidenweis, 2007):

$$\frac{RH}{\exp\left(\frac{A}{D_d GF}\right)} = \frac{GF^3 - 1}{GF^3 - (1 - \kappa)} \quad (3)$$

where  $A = \frac{4\sigma_{s/a}M_w}{RT\rho_w}$ ,  $D_d$  is the dry particle diameter,  $GF$  is the growth factor at the corresponding RH,  $M_w$  is the molecular weight of water,  $\rho_w$  is the density of water,  $R$  is the universal gas constant,  $T$  is temperature, and  $\sigma_{s/a}$  is the surface tension at the air/water interface. The water surface tension of  $0.072 \text{ J/m}^2$  is assumed, as in the analysis of Petters and Kreidenweis (2007). Briefly,  $\kappa$  values of 0.5 to 1.4 represent highly hygroscopic salts such as sodium chloride, values of 0.01 to 0.5 represent slightly to very hygroscopic organics, and a value of 0 represents a non-hygroscopic component (Petters and Kreidenweis, 2007; see Table 7.1).  $\kappa$  values representative of urban, maritime, continental, and remote areas, as derived by Petters and Kreidenweis (2007) using data



from previous ambient studies (Fitzgerald and Hoppel, 1982; Hudson and Da, 1996; Dusek et al., 2006), have been reported to range from 0.1 to 0.94.

Table 7.4 summarizes the values of  $\kappa$  derived in the present study. A noticeable enhancement in  $\kappa$  occurs within the plume as compared to the background aerosol, which is consistent with the enhancement in subsaturated growth factors.  $\kappa$  is enhanced by between 21% and 67% in the plume, with typical values being between 0.36 – 0.44. The range of  $\kappa$  values, based on DASH-SP data at RHs of 85% and 92%, is 0.11 – 0.87. The correlation between  $\kappa$  values and the mass fraction of organics is more pronounced for flight B;  $\kappa$  increases as the mass fraction of organics decreases and that of nitrate increases. Representative  $\kappa$  values are assigned to two categories: aerosol from the strong bovine source ( $\kappa=0.40$ ) and aerosol in an agricultural area ( $\kappa=0.30$ ). Values of  $\kappa$  determined here fall within the range of those derived from previous ambient studies.

## 7.6 Conclusions

An extensive set of airborne aerosol and meteorological measurements were performed downwind of a massive bovine source in the San Joaquin Valley of California during two flights in July 2007; these include meteorology, particle size distributions, aerosol composition and mixing state, sub- and supersaturated water uptake behavior, aerosol refractive index, and interrelationships between these properties.

Concentrations of total mass, organics, nitrate, and ammonium were elevated within the plume as compared to the background aerosol during both flights. Evidence exists of some degree of external mixing of particles in the plume. Organics constituted the dominant fraction of the total mass in the plume and background aerosol (~ 56 –

64%), followed either by sulfate or nitrate, and then ammonium. Particulate amines were detected in the plume and are shown to be a significant atmospheric base even in the presence of ammonia; the total amine concentration accounted for at least 23% (flight A) and 14% (flight B) of that of ammonium.

The refractive index of the background aerosol in the valley was on average 1.54, but reductions were observed in the plume, especially in the immediate vicinity of the plume source (flight A  $\sim$  1.48; flight B  $\sim$  1.51). Measurements indicate that increasing uptake of ammonia by aerosols, in the form of ammonium nitrate and ammonium sulfate, relative to the organic fraction, results in an enhancement in particle water uptake and a reduction in refractive index. Amine salts are also hypothesized to have contributed to significant hygroscopic growth in the plume. Hygroscopic growth factors in the immediate vicinity of the source were generally between 1.75 – 1.90 at RH = 92%. Estimated hygroscopic growth factors (RH = 92%) for the organic fraction on average were 1.49 – 1.53 in the plume and 1.24 – 1.29 in the background aerosol. It is shown that kinetic limitations associated with hydrophobic organic species likely suppressed droplet growth. After removing effects associated with size distribution and mixing state, enhanced CCN activated fractions were generally observed as a function of increasing subsaturated growth factors, with the highest activated fractions being consistent with the lowest organic mass fractions. Representative  $\kappa$  values (Petters and Kreidenweis, 2007) are assigned to two categories: aerosol from the bovine source ( $\kappa$  = 0.40) and aerosol in an agricultural area ( $\kappa$  = 0.30). Since organics dominated the particle mass, these values of  $\kappa$  are indicative of fairly hygroscopic organics.

## 7.7 Acknowledgements

This work was supported, in part, by NOAA grant NA06OAR4310082. A. N. acknowledges support from an NSF CAREER award, NOAA, and NASA. L. T. P. acknowledges support from a NASA Earth System Science Fellowship. The authors gratefully acknowledge the NOAA Air Resources Laboratory (ARL) for provision of the HYSPLIT transport and dispersion model.

## 7.8 References

- Abalos, M., Bayona, J. M., and Ventura, F.: Development of a solid-phase microextraction GC-NPD procedure for the determination of free volatile amines in wastewater and sewage-polluted waters, *Anal. Chem.*, 71, 3531-3537, 1999.
- Aklilu, Y., Mozurkewich, M., Prenni, A. J., Kreidenweis, S. M., Alfarra, M. R., Allan, J. D., Anlauf, K., Brook, J., Leaitch, W. R., Sharma, S., Boudries, H., and Worsnop, D. R.: Hygroscopicity of particles at two rural, urban influenced sites during Pacific 2001: Comparison with estimates of water uptake from particle composition, *Atmos. Environ.*, 40, 2650-2661, 2006.
- Allan, J. D., Delia, A. E., Coe, H., Bower, K. N., Alfarra, M. R., Jimenez, J. L., Middlebrook, A. M., Drewnick, F., Onasch, T. B., Canagaratna, M. R., Jayne, J. T., and Worsnop, D. R.: A generalised method for the extraction of chemically resolved mass spectra from aerodyne aerosol mass spectrometer data, *J. Aerosol Sci.*, 35, 909-922, 2004.
- Anderson, N., Strader, R., and Davidson, C.: Airborne reduced nitrogen: ammonia emissions from agriculture and other sources, *Environ. Int.*, 29, 277-286, 2003.
- Angelino, S., Suess, D. T., and Prather, K. A.: Formation of aerosol particles from reactions of secondary and tertiary alkylamines: Characterization by aerosol time-of-flight mass spectrometry, *Environ. Sci. Technol.*, 35, 3130-3138, 2001.
- Apsimon, H. M., Kruse, M., and Bell, J. N. B.: Ammonia emissions and their role in acid deposition, *Atmos. Environ.*, 21, 1939-1946, 1987.
- Asa-Awuku, A. and Nenes, A.: Effect of solute dissolution kinetics on cloud droplet formation: Extended Kohler theory, *J. Geophys. Res.*, 112, D22201, doi:10.1029/2005JD006934, 2007.

Asman, W. A. H. and Janssen, A. J.: A long-range transport model for ammonia and ammonium for Europe, *Atmos. Environ.*, 21, 2099-2119, 1987.

Battye, W., Aneja, V. P., and Roelle, P. A.: Evaluation and improvement of ammonia emissions inventories, *Atmos. Environ.*, 37, 3873-3883, 2003.

Beddows, D. C. S., Donovan, R. J., Harrison, R. M., Heal, M. R., Kinnersley, R. P., King, M. D., Nicholson, D. H., and Thompson, K. C.: Correlations in the chemical composition of rural background atmospheric aerosol in the UK determined in real time using time-of-flight mass spectrometry, *J. Environ. Monitor.*, 6, 124-133, 2004.

Blanchard, C. L., Roth, P. M., Tanenbaum, S. J., Ziman, S. D., and Seinfeld, J. H.: The use of ambient measurements to identify which precursor species limit aerosol nitrate formation, *J. Air Waste Manage.*, 50, 2073-2084, 2000.

Brechtel, F. J. and Kreidenweis, S. M.: Predicting particle critical supersaturation from hygroscopic growth measurements in the humidified TDMA. part I: Theory and sensitivity studies, *J. Atmos. Sci.*, 57, 1854-1871, 2000.

Cadle, S. H. and Mulawa, P. A.: Low-molecular weight aliphatic-amines in exhaust from catalyst-equipped cars, *Environ. Sci. Technol.*, 14, 718-723, 1980.

Choi, M. Y. and Chan, C. K.: The effects of organic species on the hygroscopic behaviors of inorganic aerosols, *Environ. Sci. Technol.*, 36, 2422-2428, 2002a.

Choi, M. Y. and Chan, C. K.: Continuous measurements of the water activities of aqueous droplets of water-soluble organic compounds, *J. Phys. Chem. A*, 106, 4566-4572, 2002b.

Chow, J. C., Watson, J. G., Lu, Z. Q., Lowenthal, D. H., Frazier, C. A., Solomon, P. A., Thuillier, R. H., and K. Magliano (1996), Descriptive analysis of PM(2.5) and PM(10) at regionally representative locations during SJVAQS/AUSPEX, *Atmos. Environ.*, 30, 2079-2112.

Chow, J. C., Chen, L. W. A., Watson, J. G., Lowenthal, D. H., Magliano, K. A., Turkiewicz, K., and Lehrman, D. E.: PM<sub>2.5</sub> chemical composition and spatiotemporal variability during the California Regional PM<sub>10</sub>/PM<sub>2.5</sub> Air Quality Study (CRPAQS), *J. Geophys. Res.*, 111, D10S04, doi:10.1029/2005JD006457, 2006.

Chuang, P. Y.: Measurement of the timescale of hygroscopic growth for atmospheric aerosols, *J. Geophys. Res.*, 108, 4282, doi:10.1029/2002JD002757, 2003.

Clegg, S. L., Brimblecombe, P., and Wexler, A. S.: Thermodynamic model of the system  $\text{H}^+ - \text{NH}_4^+ - \text{Na}^+ - \text{SO}_4^{2-} - \text{NO}_3^- - \text{Cl}^- - \text{H}_2\text{O}$  at 298.15 K, *J. Phys. Chem. A*, 102, 2155-2171, 1998.

Clegg, S. L., Seinfeld, J. H., and Edney, E. O.: Thermodynamic modelling of aqueous aerosols containing electrolytes and dissolved organic compounds. II. An extended Zdanovskii-Stokes-Robinson approach, *J. Aerosol Sci.*, 34, 667-690, 2003.

Clegg, S. L. and Seinfeld, J. H.: Improvement of the Zdanovskii-Stokes-Robinson model for mixtures containing solutes of different charge types, *J. Phys. Chem. A*, 108, 1008-1017, 2004.

Clegg, S. L. and Seinfeld, J. H.: Thermodynamic models of aqueous solutions containing inorganic electrolytes and dicarboxylic acids at 298.15 K. 1. The acids as nondissociating components, *J. Phys. Chem. A*, 110, 5692-5717, 2006a.

Clegg, S. L. and Seinfeld, J. H.: Thermodynamic models of aqueous solutions containing inorganic electrolytes and dicarboxylic acids at 298.15 K. 2. Systems including dissociation equilibria, *J. Phys. Chem. A*, 110, 5718-5734, 2006b.

Cruz, C. N. and Pandis, S. N.: Deliquescence and hygroscopic growth of mixed inorganic-organic atmospheric aerosol, *Environ. Sci. Technol.*, 34, 4313-4319, 2000.

Dean, J. A.: *Lange's Handbook of Chemistry, Fifteenth Edition*, McGraw-Hill, 1999.

Denkenberger, K. A., Moffet, R. C., Holecek, J. C., Rebotier, T. P., and Prather, K. A.: Real-time, single-particle measurements of oligomers in aged ambient aerosol particles, *Environ. Sci. Technol.*, 41, 5439-5446, 2007.

Dick, W. D., Saxena, P., and McMurry, P. H.: Estimation of water uptake by organic compounds in submicron aerosols measured during the Southeastern Aerosol and Visibility Study, *J. Geophys. Res.*, 105, 1471-1479, 2000.

Dillner, A. M., Stein, C., Larson, S. M., and Hitztenberger, R.: Measuring the mass extinction efficiency of elemental carbon in rural aerosol, *Aerosol Sci. Tech.*, 35, 1009-1021, 2001.

Dinar, E., Anttila, T., and Rudich, Y.: CCN activity and hygroscopic growth of organic aerosols following reactive uptake of ammonia, *Environ. Sci. Technol.*, 42, 793-799, 2008.

Doyle, G. J., Tuazon, E. C., Graham, R. A., Mischke, T. M., Winer, A. M., and Pitts, J. N.: Simultaneous concentrations of ammonia and nitric-acid in a polluted atmosphere and their equilibrium relationship to particulate ammonium-nitrate, *Environ. Sci. Technol.*, 13, 1416-1419, 1979.

Draxler, R. R. and Rolph, G. D.: *HYSPLIT (HYbrid Single-Particle Lagrangian Integrated Trajectory) Model access via NOAA ARL READY Website* (<http://www.arl.noaa.gov/ready/hysplit4.html>), NOAA Air Resources Laboratory, Silver Spring, MD, 2003.

Drewnick, F., Schwab, J. J., Jayne, J. T., Canagaratna, M., Worsnop, D. R., and Demerjian, K. L.: Measurement of ambient aerosol composition during the PMTACS-NY 2001 using an aerosol mass spectrometer. Part I: Mass concentrations, *Aerosol Sci. Tech.*, 38, 92-103, 2004a.

Drewnick, F., Jayne, J. T., Canagaratna, M., Worsnop, D. R., and Demerjian, K. L.: Measurement of ambient aerosol composition during the PMTACS-NY 2001 using an aerosol mass spectrometer. Part II: Chemically speciated mass distributions, *Aerosol Sci. Tech.*, 38, 104-117, 2004b.

Dusek, U., Frank, G. P., Hildebrandt, L., Curtius, J., Schneider, J., Walter, S., Chand, D., Drewnick, F., Hings, S., Jung, D., Borrmann, S., and Andreae, M. O.: Size matters more than chemistry for cloud-nucleating ability of aerosol particles, *Science*, 312, 1375-1378, 2006.

Edgerton, E. S., Saylor, R. D., Hartsell, B. E., Jansen, J. J., and Hansen, D. A.: Ammonia and ammonium measurements from the southeastern United States, *Atmos. Environ.*, 41, 3339-3351, 2007.

Facchini, M. C., Mircea, M., Fuzzi, S., and Charlson, R. J.: Cloud albedo enhancement by surface-active organic solutes in growing droplets, *Nature*, 401, 257-259, 1999.

Feingold, G. and Chuang, P. Y.: Analysis of the influence of film-forming compounds on droplet growth: Implications for cloud microphysical processes and climate, *J. Atmos. Sci.*, 59, 2006-2018, 2002.

Fitzgerald, J. W., Hoppel, W. A., and Vietti, M. A.: The size and scattering coefficient of urban aerosol-particles at Washington, DC as a function of relative-humidity, *J. Atmos. Sci.*, 39, 1838-1852, 1982.

Fitzgerald, J. W. and Hoppel, W. A.: Measurement of the relationship between the dry size and critical supersaturation of natural aerosol particles, *J. Hung. Meteorol. Serv.*, 86, 242-248, 1982.

Fridlind, A. M. and Jacobson, M. Z.: A study of gas-aerosol equilibrium and aerosol pH in the remote marine boundary layer during the First Aerosol Characterization Experiment (ACE 1), *J. Geophys. Res.*, 105, 17325-17340, 2000.

Fridlind, A. M., Jacobson, M. Z., Kerminen, V. M., Hillamo, R. E., Ricard, V., and Jaffrezo, J. L.: Analysis of gas-aerosol partitioning in the Arctic: Comparison of size-resolved equilibrium model results with field data, *J. Geophys. Res.*, 105, 19891-19903, 2000.

Fuller, K. A., Malm, W. C., and Kreidenweis, S. M.: Effects of mixing on extinction by carbonaceous particles, *J. Geophys. Res.*, 104, 15941-15954, 1999.

Glagolenko, S. and Phares, D. J.: Single-particle analysis of ultrafine aerosol in College Station, Texas. *J. Geophys. Res.*, 109, D18205, doi:10.1029/2004JD004621, 2004.

Gorzelska, K., Talbot, R. W., Klemm, K., Lefer, B., Klemm, O., Gregory, G. L., Anderson, B., and Barrie, L. A.: Chemical-composition of the atmospheric aerosol in the troposphere over the Hudson-Bay Lowlands and Quebec-Labrador Regions of Canada. *J. Geophys. Res.*, 99, 1763-1779, 1994.

Gysel, M., Crosier, J., Topping, D. O., Whitehead, J. D., Bower, K. N., Cubison, M. J., Williams, P. I., Flynn, M. J., McFiggans, G. B., and Coe, H.: Closure study between chemical composition and hygroscopic growth of aerosol particles during TORCH2, *Atmos. Chem. Phys.*, 7, 6131-6144, 2007.

Hegg, D. A., Covert, D. S., Jonsson, H., and Covert, P. A.: Determination of the transmission efficiency of an aircraft aerosol inlet, *Aerosol Sci. Tech.*, 39, 966-971, 2005.

Hildemann, L. M., Russell, A. G., and Cass, G. R.: Ammonia and nitric-acid concentrations in equilibrium with atmospheric aerosols - experiment vs theory, *Atmos. Environ.*, 18, 1737-1750, 1984.

Hudson, J. G. and Da, X. Y.: Volatility and size of cloud condensation nuclei, *J. Geophys. Res.*, 101, 4435-4442, 1996.

Hutchinson, G. L., Mosier, A. R., and Andre, C. E.: Ammonia and amine emissions from a large cattle feedlot, *J. Environ. Qual.*, 11, 288-293, 1982.

Khlystov, A., Stanier, C. O., Takahama, S., and Pandis, S. N.: Water content of ambient aerosol during the Pittsburgh air quality study, *J. Geophys. Res.*, 110, D07S10, doi:10.1029/2004JD004651, 2005.

Kleeman, M. J., Hughes, L. S., Allen, J. O., and Cass, G. R.: Source contributions to the size and composition distribution of atmospheric particles: Southern California in September 1996, *Environ. Sci. Technol.*, 33, 4331-4341, 1999.

Kreidenweis, S. M., Koehler, K., DeMott, P. J., Prenni, A. J., Carrico, C., and Ervens, B.: Water activity and activation diameters from hygroscopicity data - Part I: Theory and application to inorganic salts, *Atmos. Chem. Phys.*, 5, 1357-1370, 2005.

Lance, S., Medina, J., Smith, J. N., and Nenes, A.: Mapping the operation of the DMT Continuous Flow CCN counter, *Aerosol Sci. Tech.*, 40, 242-254, 2006.

Lobert, J. M., Scharffe, D. H., Hao, W. M., Kuhlbusch, T. A., Warneck, P., and Crutzen, P. J.: Experimental evaluation of biomass burning emissions: Nitrogen and carbon containing compounds, in J. S. Levine (ed.), *Global Biomass Burning: Atmospheric, Climate and Biospheric Implications*, MIT Press, Cambridge, MA, 1991.

Makela, J. M., Yli-Koivisto, S., Hiltunen, V., Seidl, W., Swietlicki, E., Teinila, K., Sillanpaa, M., Koponen, I. K., Paatero, J., Rosman, K., and Hameri, K.: Chemical composition of aerosol during particle formation events in boreal forest, *Tellus B*, 53, 380-393, 2001.

Manahan, S. E.: *Environmental Chemistry, Eighth Edition*, CRC Press, Boca Raton, Florida, 2005.

Maria, S. F., Russell, L. M., Turpin, B. J., Porcja, R. J., Campos, T. L., Weber, R. J., and Huebert, B. J.: Source signatures of carbon monoxide and organic functional groups in Asian Pacific Regional Aerosol Characterization Experiment (ACE-Asia) submicron aerosol types, *J. Geophys. Res.*, 108, 8637, doi:10.1029/2003JD003703, 2003.

McLafferty, F. W. and Turecek, F.: *Interpretation of Mass Spectra, Fourth Edition*, University Science Books, Mill Valley, California, 1993.

Meng, Z. Y. and Seinfeld, J. H.: Time scales to achieve atmospheric gas-aerosol equilibrium for volatile species, *Atmos Environ.*, 30, 2889-2900, 1996.

Milne, P. J. and Zika, R. G.: Amino-acid nitrogen in atmospheric aerosols - occurrence, sources and photochemical modification, *J. Atmos. Chem.*, 16, 361-398, 1993.

Mochida, M., Kuwata, M., Miyakawa, T., Takegawa, N., Kawamura, K., and Kondo, Y.: Relationship between hygroscopicity and cloud condensation nuclei activity for urban aerosols in Tokyo, *J. Geophys. Res.*, 111, D23204, doi:10.1029/2005JD006980, 2006.

Moore, R. H., Ingall, E. D., Sorooshian, A., and Nenes, A.: Molar mass, surface tension, and droplet growth kinetics of marine organics from measurements of CCN activity, *Geophys. Res. Lett.*, 35, L07801, doi:10.1029/2008GL033350, 2008.

Mosier, A. R., Andre, C. E., and Viets, F. G.: Identification of Aliphatic-Amines Volatilized from Cattle Feedyard, *Environ. Sci. Technol.*, 7, 642-644, 1973.

Mozurkewich, M.: The dissociation-constant of ammonium-nitrate and Its dependence on temperature, relative-humidity and particle-size, *Atmos Environ.*, 27, 261-270, 1993.

Murphy, D. M. and Thomson, D. S.: Chemical composition of single aerosol particles at Idaho Hill: Positive ion measurements, *J. Geophys. Res.*, 102, 6341-6352, 1997.

Murphy, S. M., Sorooshian, A., Kroll, J. H., Ng, N. L., Chhabra, P., Tong, C., Surratt, J. D., Knipping, E., Flagan, R. C., and J. H. Seinfeld (2007), Secondary aerosol formation from atmospheric reactions of aliphatic amines, *Atmos. Chem. Phys.*, 7, 2313-2337.



Nenes, A., Charlson, R. J., Facchini, M. C., Kulmala, M., Laaksonen, A., and Seinfeld, J. H.: Can chemical effects on cloud droplet number rival the first indirect effect?, *Geophys. Res. Lett.*, 29, 1848, doi:10.1029/2002GL015295, 2002.

Neuman, J. A., Nowak, J. B., Brock, C. A., Trainer, M., Fehsenfeld, F. C., Holloway, J. S., Hubler, G., Hudson, P. K., Murphy, D. M., Nicks, D. K., Orsini, D., Parrish, D. D., Ryerson, T. B., Sueper, D. T., Sullivan, A., and Weber, R.: Variability in ammonium nitrate formation and nitric acid depletion with altitude and location over California, *J. Geophys. Res.*, 108, 4557, doi:10.1029/2003JD003616, 2003.

Ngwabie, N. M., Custer, T. G., Schade, G. W., Linke, S., and Hinz, T.: Mixing ratio measurements and flux estimates of volatile organic compounds (VOC) from a cowshed with conventional manure treatment indicate significant emissions to the atmosphere, *Geophys. Res. Abstr.*, 7(01175), 2005.

Petters, M. D. and Kreidenweis, S. M.: A single parameter representation of hygroscopic growth and cloud condensation nucleus activity. *Atmos. Chem. Phys.*, 7, 1961-1971, 2007.

Prenni, A. J., De Mott, P. J., and Kreidenweis, S. M.: Water uptake of internally mixed particles containing ammonium sulfate and dicarboxylic acids, *Atmos Environ.*, 37, 4243-4251, 2003.

Pun, B. K. and Seigneur, C.: Understanding particulate matter formation in the California San Joaquin Valley: conceptual model and data needs, *Atmos. Environ.*, 33, 4865-4875, 1999.

Rabaud, N. E., Ebeler, S. E., Ashbaugh, L. L., and Flocchini, R. G.: Characterization and quantification of odorous and non-odorous volatile organic compounds near a commercial dairy in California, *Atmos. Environ.*, 37, 933-940, 2003.

Rissler, J., Pagels, J., Swietlicki, E., Wierzbicka, A., Strand, M., Lillieblad, L., Sanati, M., and Bohgard, M.: Hygroscopic behavior of aerosol particles emitted from biomass fired grate boilers, *Aerosol Sci. Tech.*, 39, 919-930, 2005.

Rissler, J., Vestin, A., Swietlicki, E., Fisch, G., Zhou, J., Artaxo, P., and Andreae, M. O.: Size distribution and hygroscopic properties of aerosol particles from dry-season biomass burning in Amazonia, *Atmos. Chem. Phys.*, 6, 471-491, 2006.

Roberts, G. C. and Nenes, A.: A continuous-flow streamwise thermal-gradient CCN chamber for atmospheric measurements, *Aerosol Sci. Tech.*, 39, 206-221, 2005.

Ruehl, C. R., Chuang, P. Y., and Nenes, A.: How quickly do cloud droplets form on atmospheric particles?, *Atmos. Chem. Phys.*, 8, 1043-1055, 2008.

Rumburg, B., Mount, G. H., Yonge, D., Lamb, B., Westberg, H., Filipy, J., Bays, J., Kincaid, R., and Johnson, K.: Atmospheric flux of ammonia from sprinkler application of dairy waste, *Atmos Environ.*, 40, 7246-7258, 2006.

Russell, A. G., Mcrae, G. J., and Cass, G. R.: Mathematical-modeling of the formation and transport of ammonium-nitrate aerosol, *Atmos. Environ.*, 17, 949-964, 1983.

Schade, G. W. and Crutzen, P. J.: Emission of aliphatic-amines from animal husbandry and their reactions - potential source of N<sub>2</sub>O and HCN, *J. Atmos. Chem.*, 22, 319-346, 1995.

Seinfeld, J. H. and Pandis, S. N.: *Atmospheric Chemistry and Physics, Second Edition*, Wiley-Interscience, New York, 2006.

Shulman, M. L., Jacobson, M. C., Carlson, R. J., Synovec, R. E., and Young, T. E.: Dissolution behavior and surface tension effects of organic compounds in nucleating cloud droplets, *Geophys. Res. Lett.*, 23, 277-280, 1996.

Sjogren, S., Gysel, M., Weingartner, E., Baltensperger, U., Cubison, M. J., Coe, H., Zardini, A. A., Marcolli, C., Krieger, U. K., and Peter, T.: Hygroscopic growth and water uptake kinetics of two-phase aerosol particles consisting of ammonium sulfate, adipic and humic acid mixtures, *J. Aerosol Sci.*, 38, 157-171, 2007.

Sorooshian, A., Brechtel, F. J., Ma, Y. L., Weber, R. J., Corless, A., Flagan, R. C., and Seinfeld, J. H.: Modeling and characterization of a particle-into-liquid sampler (PILS), *Aerosol Sci. Tech.*, 40, 396-409, 2006a.

Sorooshian, A., Varutbangkul, V., Brechtel, F. J., Ervens, B., Feingold, G., Bahreini, R., Murphy, S. M., Holloway, J. S., Atlas, E. L., Buzorius, G., Jonsson, H., Flagan, R. C., and Seinfeld, J. H.: Oxalic acid in clear and cloudy atmospheres: Analysis of data from International Consortium for Atmospheric Research on Transport and Transformation 2004, *J. Geophys. Res.*, 111, D23S45, doi:10.1029/2005JD006880, 2006b.

Sorooshian, A., Ng, N. L., Chan, A. W. H., Feingold, G., Flagan, R. C., and Seinfeld, J. H.: Particulate organic acids and overall water-soluble aerosol composition measurements from the 2006 Gulf of Mexico Atmospheric Composition and Climate Study (GoMACCS), *J. Geophys. Res.*, 112, D13201, doi:10.1029/2007JD008537, 2007a.

Sorooshian, A., Lu, M. L., Brechtel, F. J., Jonsson, H., Feingold, G., Flagan, R. C., and Seinfeld, J. H.: On the source of organic acid aerosol layers above clouds, *Environ. Sci. Technol.*, 41, 4647-4654, 2007b.

Sorooshian, A., S. Hersey, F. J. Brechtel, A. Corless, R. C. Flagan, and Seinfeld, J. H.: Rapid, size-resolved aerosol hygroscopic growth measurements: differential aerosol sizing and hygroscopicity spectrometer probe (DASH-SP), *Aerosol Sci. Tech.*, (in press), 2008.

Stelson, A. W., Friedlander, S. K., and Seinfeld, J. H.: Note on the equilibrium relationship between ammonia and nitric-acid and particulate ammonium-nitrate, *Atmos. Environ.*, 13, 369-371, 1979.

Stelson, A. W. and Seinfeld, J. H.: Relative-humidity and temperature-dependence of the ammonium-nitrate dissociation-constant, *Atmos. Environ.*, 16, 983-992, 1982a.

Stelson, A. W. and Seinfeld, J. H.: Relative-humidity and Ph-dependence of the vapor-pressure of ammonium-nitrate nitric acid-solutions at 25 degrees C, *Atmos. Environ.*, 16, 993-1000, 1982b.

Stokes, R. H. and Robinson, R. A.: Interactions in aqueous nonelectrolyte solutions .I. Solute-solvent equilibria, *J. Phys. Chem.*, 70, 2126-2130, 1966.

Svenningsson, I. B., Hansson, H. C., Wiedensohler, A., Ogren, J. A., Noone, K. J., and Hallberg, A.: Hygroscopic growth of aerosol-particles in the Po Valley, *Tellus B*, 44, 556-569, 1992.

Svenningsson, B., Rissler, J., Swietlicki, E., Mircea, M., Bilde, M., Facchini, M. C., Decesari, S., Fuzzi, S., Zhou, J., Monster, J., and Rosenorn, T.: Hygroscopic growth and critical supersaturations for mixed aerosol particles of inorganic and organic compounds of atmospheric relevance, *Atmos. Chem. Phys.*, 6, 1937-1952, 2006.

Takahama, S., Wittig, A. E., Vayenas, D. V., Davidson, C. I., and Pandis, S. N.: Modeling the diurnal variation of nitrate during the Pittsburgh Air Quality Study, *J. Geophys. Res.*, 109, D16S06, doi:10.1029/2003JD004149, 2004.

Tan, P. V., Evans, G. J., Tsai, J., Owega, S., Fila, M. S., and Malpica, O.: On-line analysis of urban particulate matter focusing on elevated wintertime aerosol concentrations, *Environ. Sci. Technol.*, 36, 3512-3518, 2002.

Tang, I. N.: Chemical and size effects of hygroscopic aerosols on light scattering coefficients, *J. Geophys. Res.*, 101, 19245-19250, 1996.

Taraniuk, I., Graber, E. R., Kostinski, A., and Rudich, Y.: Surfactant properties of atmospheric and model humic-like substances (HULIS), *Geophys. Res. Lett.*, 34, L16807, doi:10.1029/2007GL029576, 2007.

Vanneste, A., Duce, R. A., and Lee, C.: Methylamines in the marine atmosphere, *Geophys. Res. Lett.*, 14, 711-714, 1987.

Varutbangkul, V., Brechtel, F. J., Bahreini, R., Ng, N. L., Keywood, M. D., Kroll, J. H., Flagan, R. C., Seinfeld, J. H., Lee, A., and Goldstein, A. H.: Hygroscopicity of secondary organic aerosols formed by oxidation of cycloalkenes, monoterpenes, sesquiterpenes, and related compounds, *Atmos. Chem. Phys.*, 6, 2367-2388, 2006.

Weast, R. C.: *CRC Handbook of Chemistry and Physics, Sixty Eighth Edition*, CRC Press, Florida, 1987.

Westerholm, R., Li, H., and Almen, J.: Estimation of aliphatic amine emissions in automobile exhausts, *Chemosphere*, 27, 1381-1384, 1993.

Wexler, A. S. and Seinfeld, J. H.: Analysis of aerosol ammonium-nitrate - departures from equilibrium during Scaqs, *Atmos. Environ.*, 26, 579-591, 1992.

Wise, M. E., Surratt, J. D., Curtis, D. B., Shilling, J. E., and Tolbert, M. A.: Hygroscopic growth of ammonium sulfate/dicarboxylic acids, *J. Geophys. Res.*, 108, 4638, doi:10.1029/2003JD003775, 2003.

Xiong, J. Q., Zhong, M. H., Fang, C. P., Chen, L. C., and Lippmann, M.: Influence of organic films on the hygroscopicity of ultrafine sulfuric acid aerosol, *Environ. Sci. Technol.*, 32, 3536-3541, 1998.

Yu, S. C., Dennis, R., Roselle, S., Nenes, A., Walker, J., Eder, B., Schere, K., Swall, J., and Robarge, W.: An assessment of the ability of three-dimensional air quality models with current thermodynamic equilibrium models to predict aerosol  $\text{NO}_3^-$ , *J. Geophys. Res.*, 110, D07S13, doi:10.1029/2004JD004718, 2005.

Zdanovskii, A.: New methods for calculating solubilities of electrolytes in multicomponent systems, *Zhur. Fiz. Khim.*, 22, 1475-1485, 1948.

Zhang, J., Chameides, W. L., Weber, R., Cass, G., Orsini, D., Edgerton, E., Jongejan, P., and Slanina, J.: An evaluation of the thermodynamic equilibrium assumption for fine particulate composition: Nitrate and ammonium during the 1999 Atlanta Supersite Experiment, *J. Geophys. Res.*, 108, 8414, doi:10.1029/2001JD001592, 2002.

Zhang, X. Q., Turpin, B. J., McMurry, P. H., Hering, S. V., and Stolzenburg, M. R.: Mie theory evaluation of species contributions to 1990 wintertime visibility reduction in the Grand-Canyon, *J. Air Waste Manage.*, 44, 153-162, 1994.

Zhang, Q., Anastasio, C., and Jimenez-Cruz, M.: Water-soluble organic nitrogen in atmospheric fine particles ( $\text{PM}_{2.5}$ ) from northern California, *J. Geophys. Res.*, 107, 4112, doi:10.1029/2001JD000870, 2002.

Zhang, Q. and Anastasio, C.: Free and combined amino compounds in atmospheric fine particles ( $\text{PM}_{2.5}$ ) and fog waters from Northern California, *Atmos. Environ.*, 37, 2247-2258, 2003.

Zhang, Q., Alfarra, M. R., Worsnop, D. R., Allan, J. D., Coe, H., Canagaratna, M. R., and Jimenez, J. L.: Deconvolution and quantification of hydrocarbon-like and oxygenated

organic aerosols based on aerosol mass spectrometry, *Environ. Sci. Technol.*, 39, 4938-4952, 2005.

**Table 7.1.** Summary of In-plume and Out-of-plume Measurements of Composition and Particle Number and Mass Concentration.

			Total Mass	Organic	NO <sub>3</sub> <sup>-</sup>	SO <sub>4</sub> <sup>2-</sup>	NH <sub>4</sub> <sup>+</sup>	Excess NO <sub>3</sub> <sup>-</sup>	[NH <sub>4</sub> <sup>+</sup> :SO <sub>4</sub> <sup>2-</sup>	%	%	%	%	DMA particle concentration	(UFCPC 3025:CPC 3010) <sup>a</sup>	cToF- AMS: <i>m/z</i> 57:44	cToF-AMS: <i>m/z</i> 44/Total Organic
			(μg/m <sup>3</sup> )	(μg/m <sup>3</sup> )	(μg/m <sup>3</sup> )	(μg/m <sup>3</sup> )	(μg/m <sup>3</sup> )	(μg/m <sup>3</sup> )	molar ratio	Organic	NO <sub>3</sub> <sup>-</sup>	SO <sub>4</sub> <sup>2-</sup>	NH <sub>4</sub> <sup>+</sup>	(#/cm <sup>3</sup> )			
Flight A	In plume	AVE	10.48	6.48	0.93	2.06	1.02	0.04	2.64	61.9	8.6	19.8	9.7	30528	1.1	0.07	0.10
		ST DEV	1.64	0.98	0.40	0.24	0.23	0.50	0.51	2.6	2.4	1.7	1.7	8987	0.0	0.01	0.01
	Out of plume	AVE	8.01	5.10	0.30	1.81	0.80	-0.16	2.38	63.5	3.7	22.8	10.1	30778	1.1	0.07	0.10
		ST DEV	1.48	1.07	0.11	0.31	0.17	0.41	0.47	3.3	1.1	2.6	1.8	11026	0.0	0.02	0.01
Flight B	In plume	AVE	4.53	2.46	1.08	0.54	0.44	0.02	4.61	55.5	22.7	12.3	9.6	16606	1.2	0.07	0.11
		ST DEV	0.87	0.29	0.50	0.10	0.14	0.34	2.25	6.4	7.3	3.0	2.1	4286	0.1	0.02	0.01
	Out of plume	AVE	2.65	1.73	0.19	0.56	0.19	0.00	1.94	63.1	7.2	23.1	7.0	18139	1.2	0.09	0.12
		ST DEV	0.95	0.70	0.12	0.26	0.10	0.21	1.42	11.9	2.4	11.0	3.8	8910	0.1	0.08	0.02

<sup>a</sup>The ratio of the particle number concentration for  $D_p > 3$  nm (UFCPC 3025) to that for  $D_p > 10$  nm (CPC 3010).

**Table 7.2.** DASH-SP Hygroscopicity and Dry Particle Refractive Index Data Categorized by the Time of Flight as Shown in Figure 7.1. Data at RH = 85% are not available for flight A.

		<i>GF</i> (74%)	<i>GF</i> (85%)	<i>GF</i> (92%)	Dry Refractive Index
Flight A	Valley transit	1.10 ± 0.05		1.64 ± 0.17	1.52 ± 0.08
	Circle above plume source	1.16 ± 0.12		1.79 ± 0.22	1.48 ± 0.08
	First set of transects (1 - 4)	1.07 ± 0.03		1.55 ± 0.19	1.52 ± 0.06
	Transect 1 (plume age = 0.3 h)	1.04 ± 0.03		1.59 ± 0.17	1.54 ± 0.04
	Transect 2 (plume age = 0.5 h)	1.05 ± 0.03		1.51 ± 0.22	1.56 ± 0.05
	Transect 3 (plume age = 1.1 h)	1.08 ± 0.03		1.70 ± 0.18	1.48 ± 0.05
	Transect 4 (plume age = 1.5 h)	1.06 ± 0.01		1.74 ± 0.08	1.51 ± 0.01
	Spiral up to 600 m	1.07 ± 0.05		1.47 ± 0.15	1.53 ± 0.10
	Second set of transects (5 - 7)	1.09 ± 0.04		1.61 ± 0.13	1.54 ± 0.05
	Transect 5 (plume age = 1.2 h)	1.06 ± 0.01		1.68 ± 0.06	1.54 ± 0.05
	Transect 6 (plume age = 1.3 h)	1.12 ± 0.05		1.60 ± 0.08	1.54 ± 0.05
	Transect 7 (plume age = 0.8 h)	1.12 ± 0.01		1.69 ± 0.16	1.54 ± 0.09
	Spiral down above plume source	1.33 ± 0.30		1.80 ± 0.19	1.40 ± 0.10
	Valley transit	1.06 ± 0.02		1.53 ± 0.15	1.56 ± 0.05
Flight B	Valley transit	1.03 ± 0.04	1.35 ± 0.06	1.49 ± 0.07	1.55 ± 0.04
	Circle above plume source	1.10 ± 0.07	1.50 ± 0.10	1.88 ± 0.22	1.51 ± 0.01
	First set of transects (plume age < 0.9 h)	1.12 ± 0.05	1.39 ± 0.08	1.65 ± 0.20	1.52 ± 0.01
	Directly in plume (plume age < 0.9 h)	1.15 ± 0.06	1.44 ± 0.06	1.86 ± 0.14	1.52 ± 0.01
	Spiral up to 400 m	1.07 ± 0.04	1.37 ± 0.06	1.57 ± 0.07	1.52 ± 0.01
	Second set of transects (plume age < 0.9 h)	1.08 ± 0.04	1.39 ± 0.06	1.65 ± 0.17	1.53 ± 0.03
	Directly in plume (plume age < 0.9 h)	1.09 ± 0.05	1.40 ± 0.09	1.65 ± 0.16	1.51 ± 0.02
	Valley transit	1.11 ± 0.04	1.39 ± 0.08	1.55 ± 0.11	1.53 ± 0.05

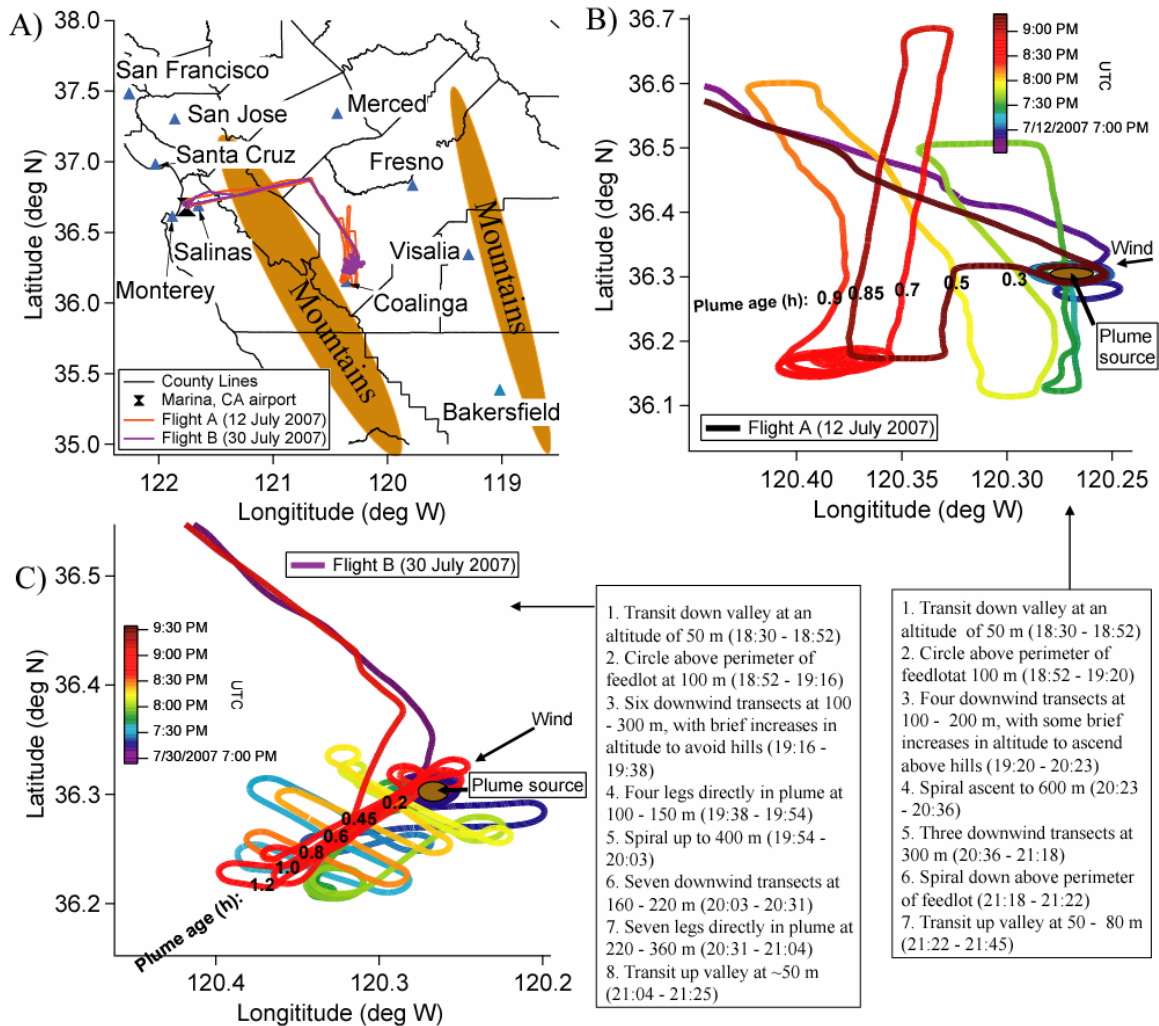
**Table 7.3.** Summary of CCN Data for Flights A and B.

			CCN (#/cm <sup>3</sup> )	Activated fraction	CCN (#/cm <sup>3</sup> )	Activated fraction	CCN (#/cm <sup>3</sup> )	Activated fraction	CCN (#/cm <sup>3</sup> )	Activated fraction		
			SS ~ 0.1%		SS ~ 0.2%		SS ~ 0.3%		SS ~ 0.4 - 0.45%		SS ~ 0.5%	
Flight A	In plume	AVE	92	0.01	329	0.02	1114	0.06	1882	0.08	2265	0.08
		ST DEV	123	0.01	354	0.02	628	0.05	526	0.04	478	0.02
	Out of plume	AVE	141	0.01	252	0.01	1124	0.05	1641	0.06	1966	0.08
		ST DEV	218	0.01	295	0.01	561	0.03	484	0.02	478	0.02
			SS ~ 0.2%		SS ~ 0.25 - 0.35%		SS ~ 0.4 - 0.45%		SS ~ 0.6%			
Flight B	In plume	AVE	855	0.05	1246	0.07	2027	0.11	2436	0.15		
		ST DEV	584	0.03	713	0.04	523	0.03	834	0.05		
	Out of plume	AVE	707	0.04	1073	0.06	1796	0.08	4168	0.14		
		ST DEV	596	0.03	770	0.05	768	0.03	2052	0.04		

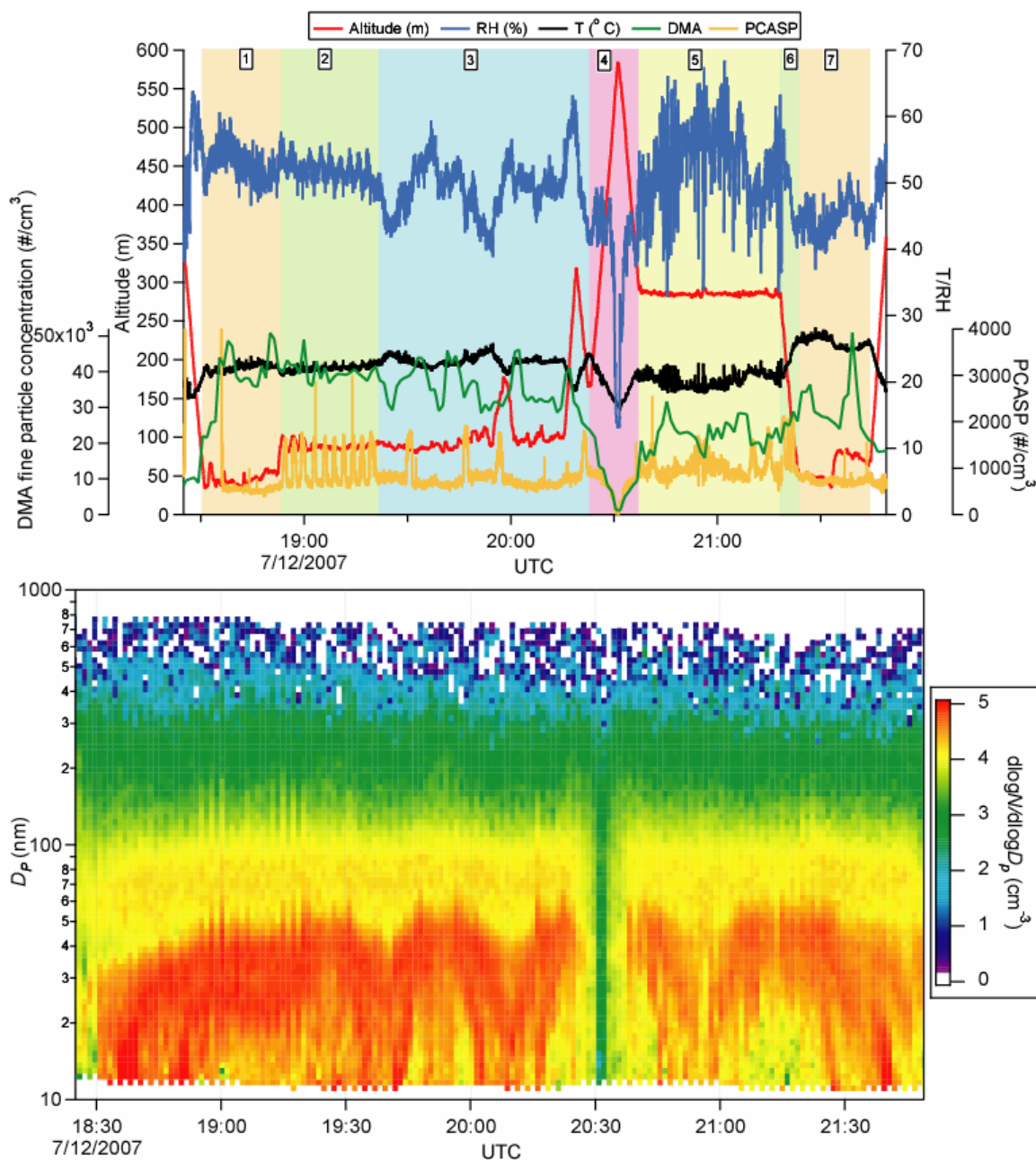


**Table 7.4.** Summary of  $\kappa$  Values (Petters and Kreidenweis, 2007) Derived From Subsaturated Hygroscopic Growth Factor Data at RHs of 85%, and 92%. Data at RH = 85% are not available for flight A.

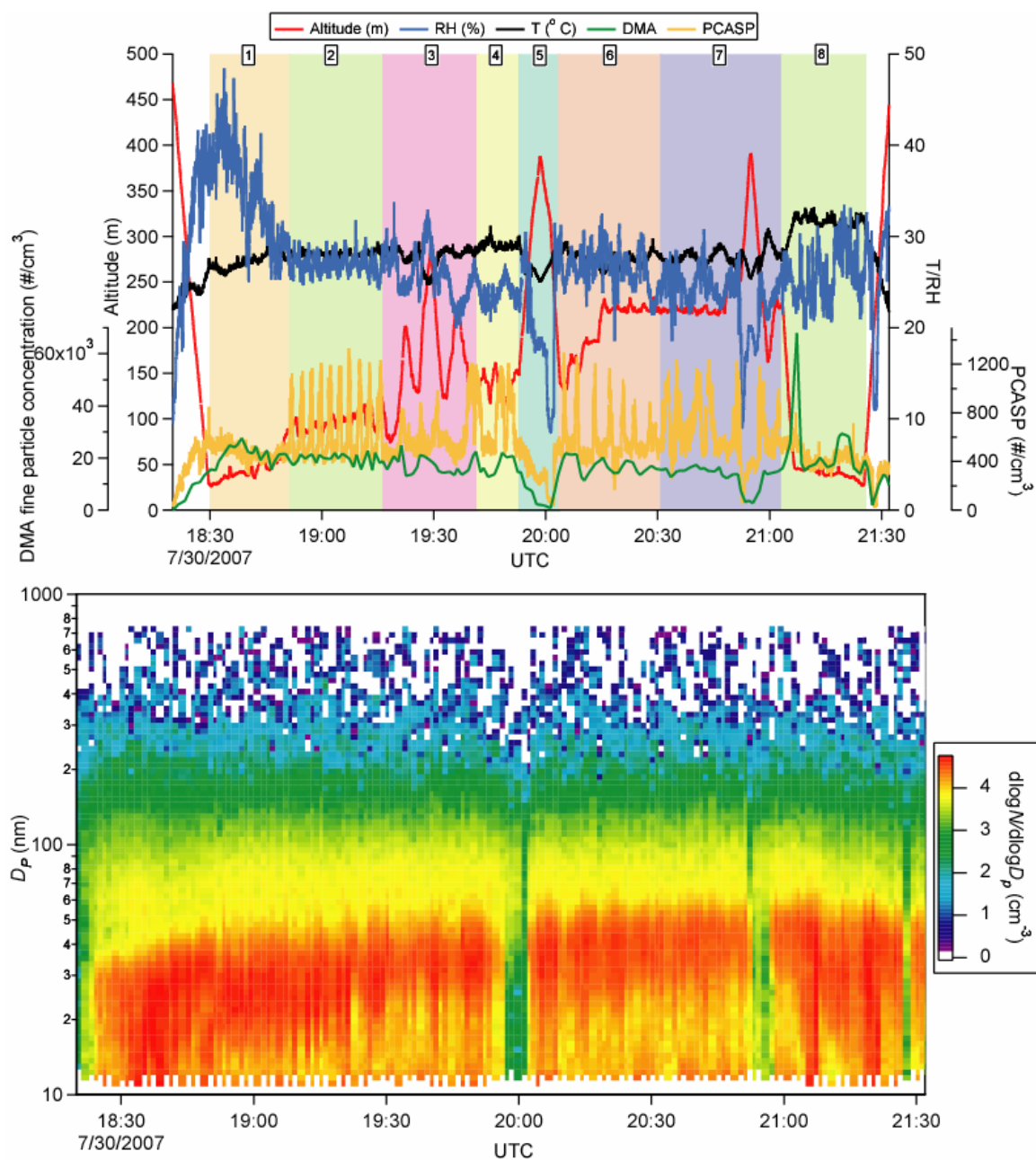
	In plume		Out of plume	
	Flight A	Flight B	Flight A	Flight B
$\kappa$ (85%)	NA	$0.40 \pm 0.12$	NA	$0.33 \pm 0.09$
$\kappa$ (92%)	$0.36 \pm 0.12$	$0.44 \pm 0.19$	$0.29 \pm 0.12$	$0.28 \pm 0.10$



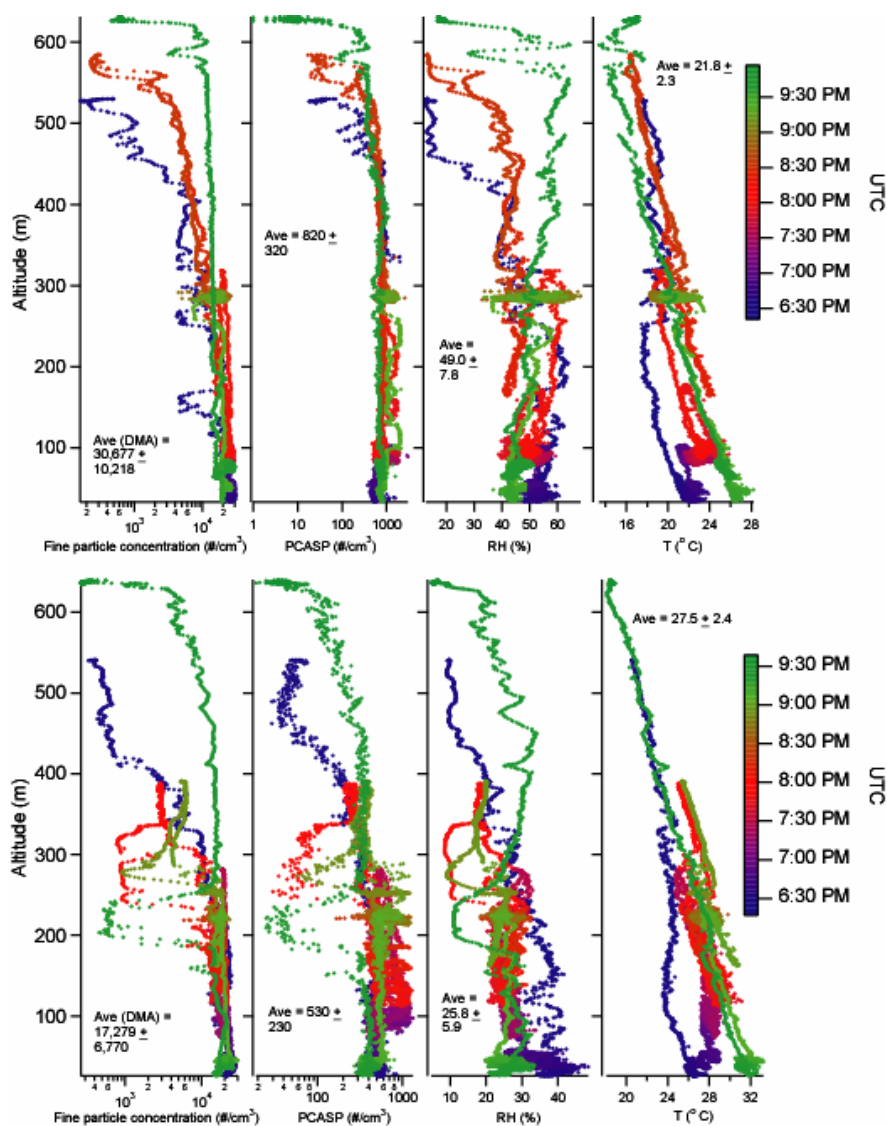
**Figure 7.1.** A) Complete flight tracks for the two flights in the San Joaquin Valley of California. The shaded mountain areas are meant to provide a relative view of how the San Joaquin Valley is bordered by major topographical features. B/C) Detailed tracks for flights A (12 July 2007) and B (30 July 2007) with a step-by-step description of the aircraft maneuvers. Plume ages were calculated using downwind distance and average wind speed in the vicinity of the feedlot.



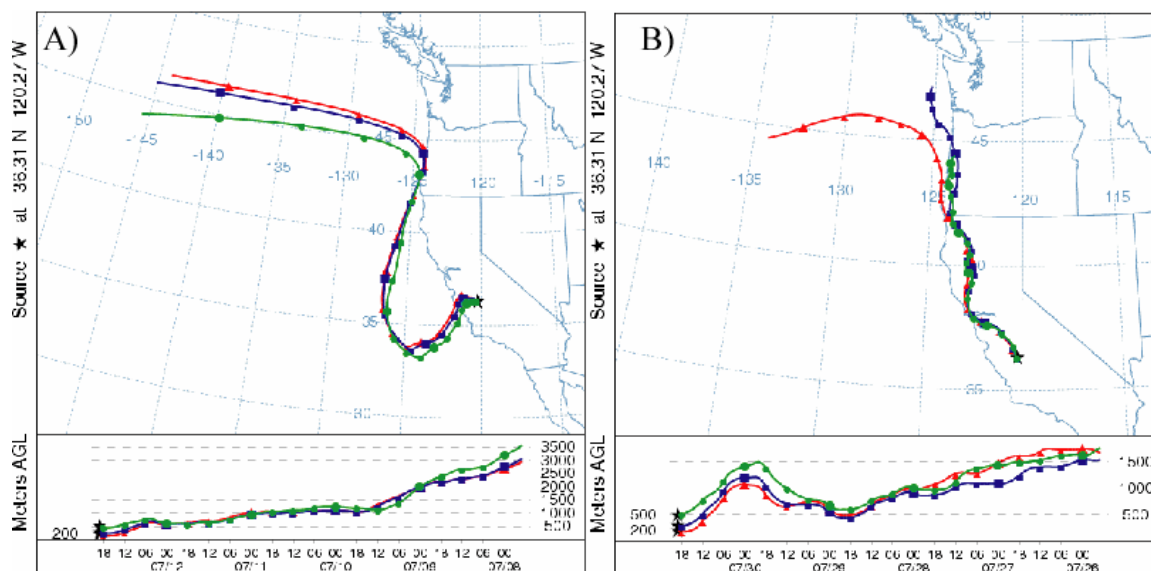
**Figure 7.2.** Upper panel) Time series of particle number concentration and meteorological data for flight A. Lower panel) Time series of aerosol size distribution. The number labels at the top of each shaded block correspond to the respective flight segment listed in Figure 7.1.



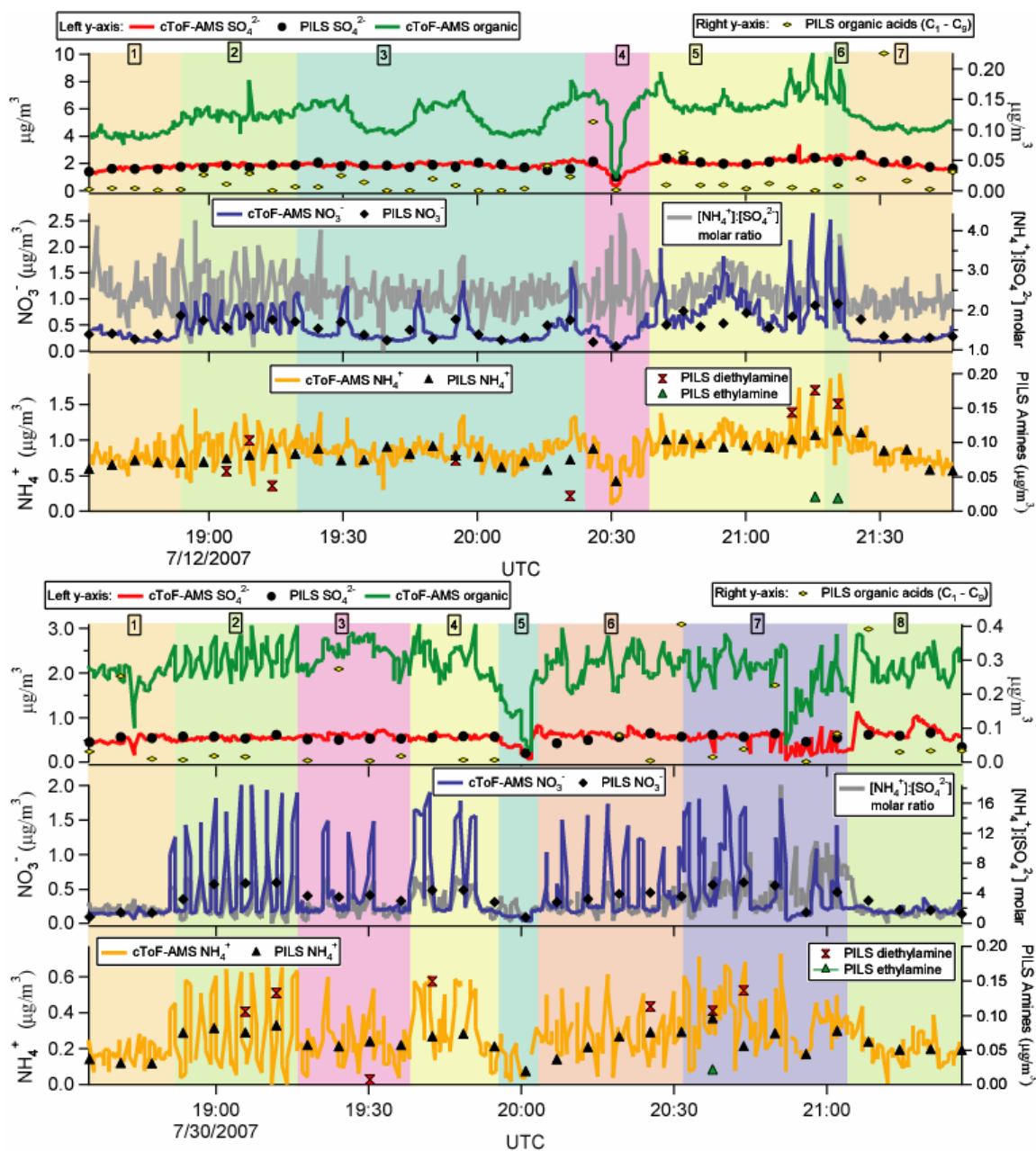
**Figure 7.3.** Upper panel) Time series of particle number concentration and meteorological data for flight B. Lower panel) Time series of aerosol size distribution. The number labels at the top of each shaded block correspond to the respective flight segment listed in Figure 7.1.



**Figure 7.4.** Vertical profiles of particle number concentration and meteorological data for flights A (upper panel) and B (lower panel). For the submicrometer particle concentration data (CPC 3010), it should be noted that the absolute concentrations are not accurate due to electrical saturation of the instrument; these data are plotted because of the 1 s time resolution of the data. The DMA and CPC 3010 number concentrations were proportional throughout both flights, therefore, the CPC 3010 values are useful for qualitative purposes to identify the mixing layer height. DMA number concentrations indicated are accurate.

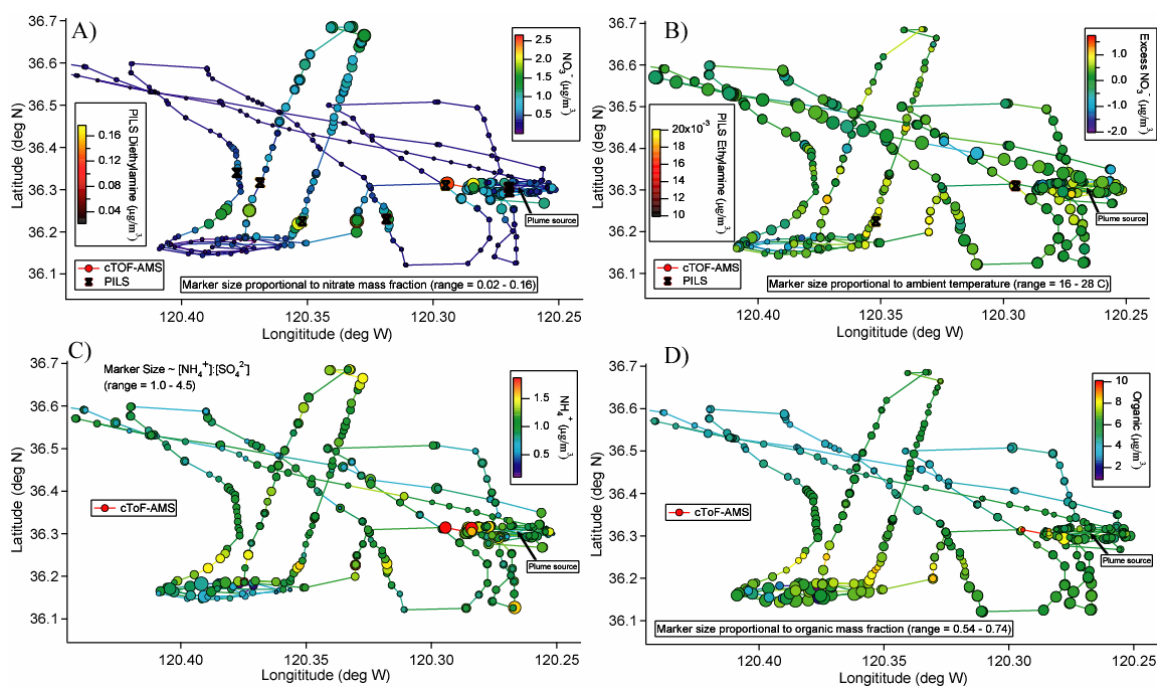


**Figure 7.5.** HYSPLIT five-day backward trajectory analysis for flights A (panel A) and B (panel B). Six hours of time separate each marker on the trajectories.



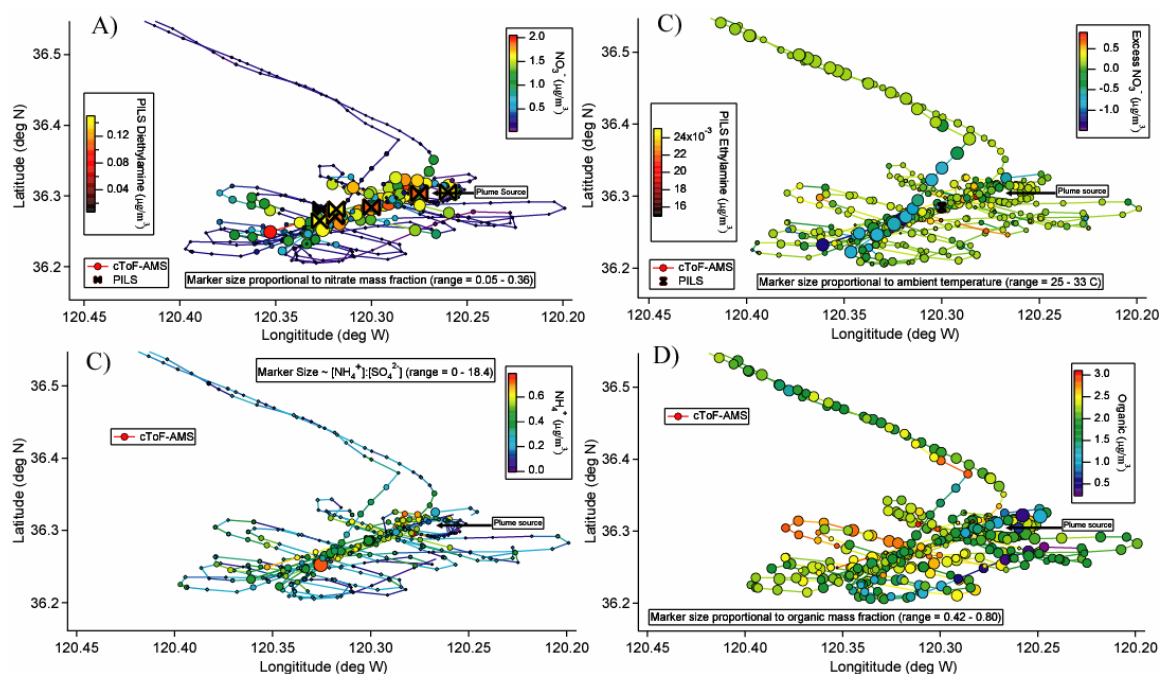
**Figure 7.6.** Time series of PILS water-soluble aerosol composition and cToF-AMS composition for flights A (upper panel) and B (lower panel). The number labels for each shaded box correspond to the portion of each flight represented in Figure 7.1. The shaded areas representing the plume are characterized by significant increases in organics, ammonium, nitrate, and amines. The ammonium-to-sulfate molar ratio exceeds 2.0 in the plume, allowing nitrate to partition into the aerosol phase. The multiple cToF-AMS spikes in the species concentrations cannot be resolved by the PILS since the 5 - min time intervals for sample collection average out the quick plume passes with the longer legs outside of the plume. Agreement between the PILS and cToF-AMS is most evident for sulfate, since this species was relatively level in concentration during the flights.



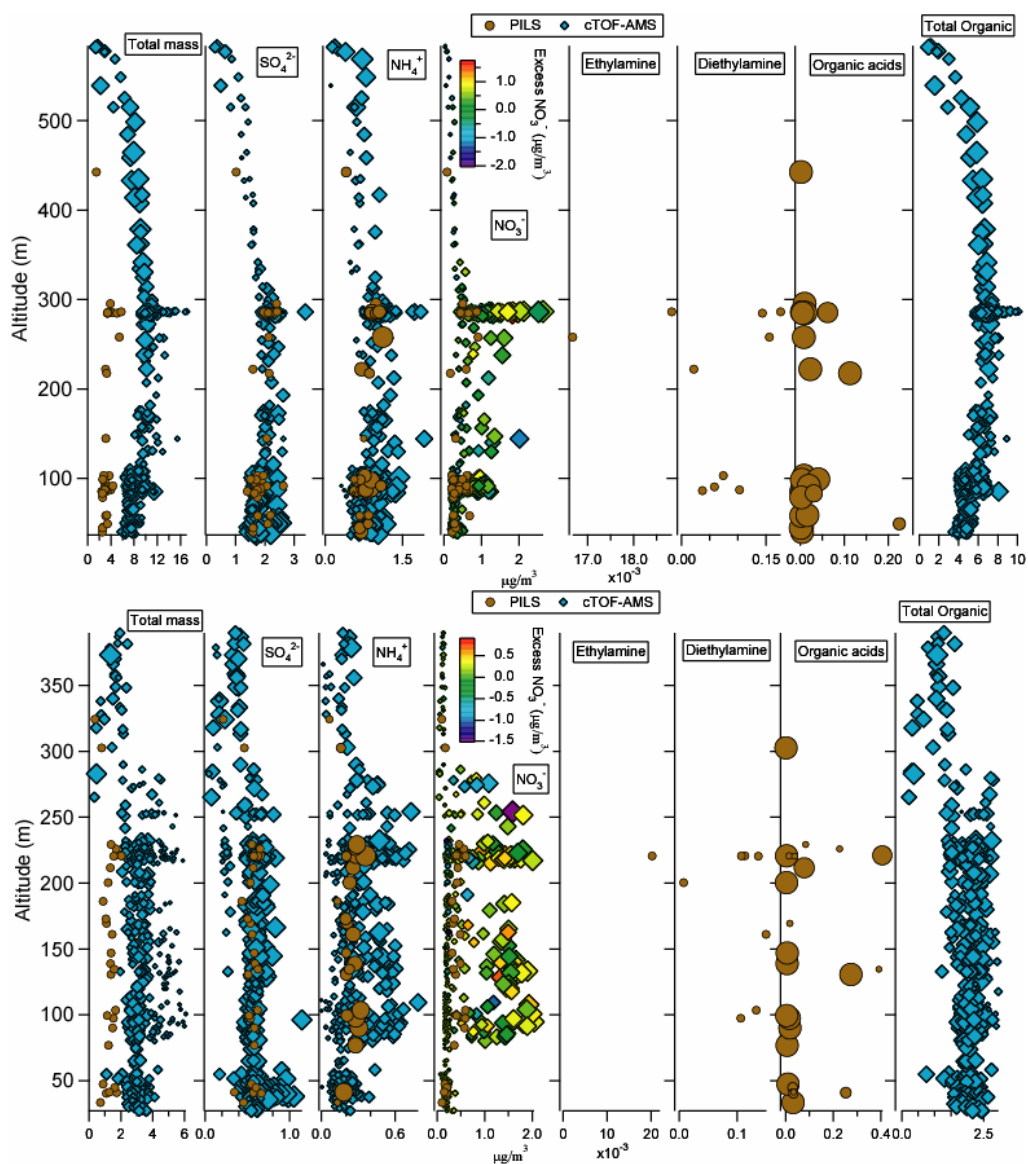


**Figure 7.7.** Spatial distribution of various aerosol species during flight A. A) Nitrate and diethylamine; B) *Excess nitrate* remaining after both sulfate and nitrate have been neutralized by ammonium (see Section 7.3.2 for further explanation); C) ammonium; D) organics. The PILS markers are spatially placed wherever the aircraft was at the midpoint of the time when a particular sample was collected (after being corrected for liquid residence time in the instrument); therefore the amine markers are spatially distinct from the core of the plume (especially the two markers representing the highest plume ages).

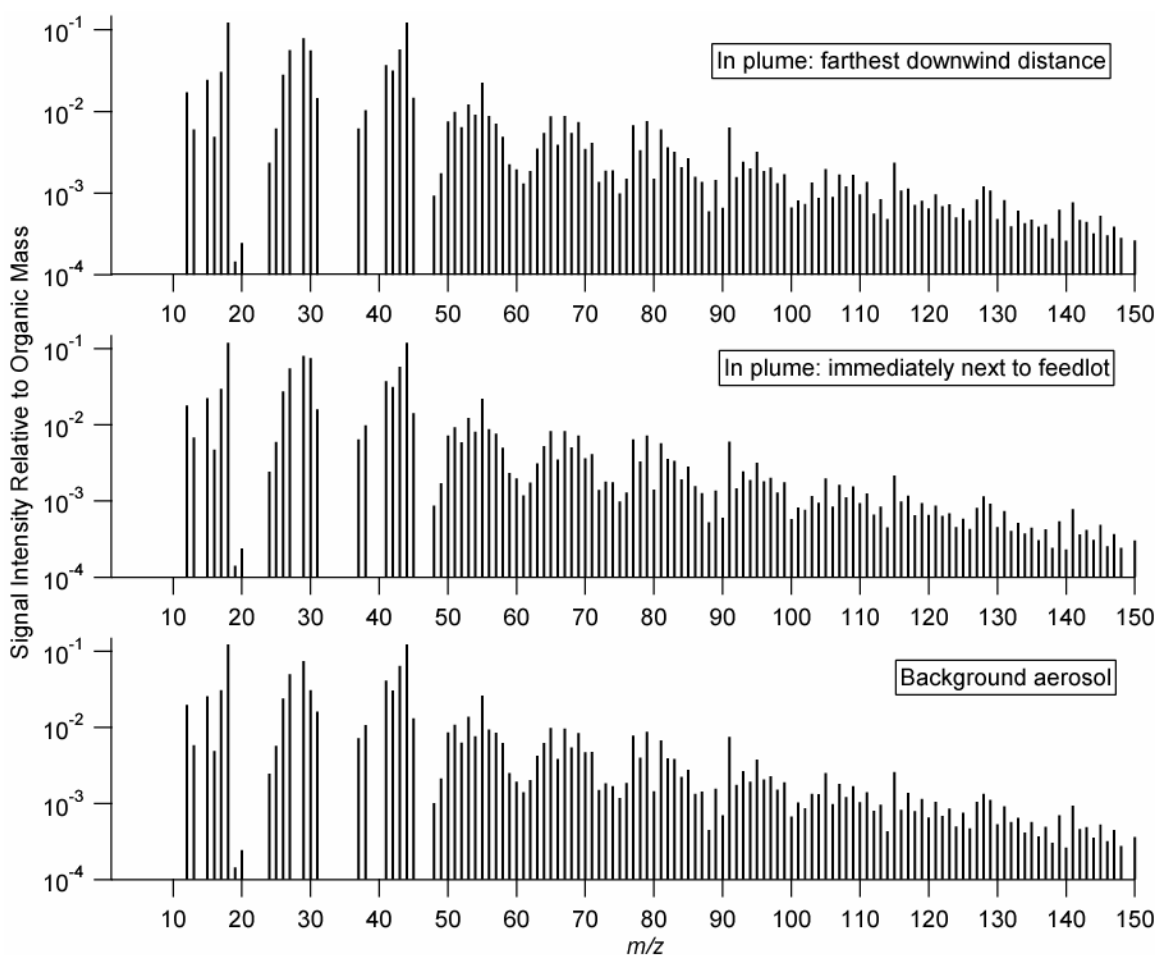




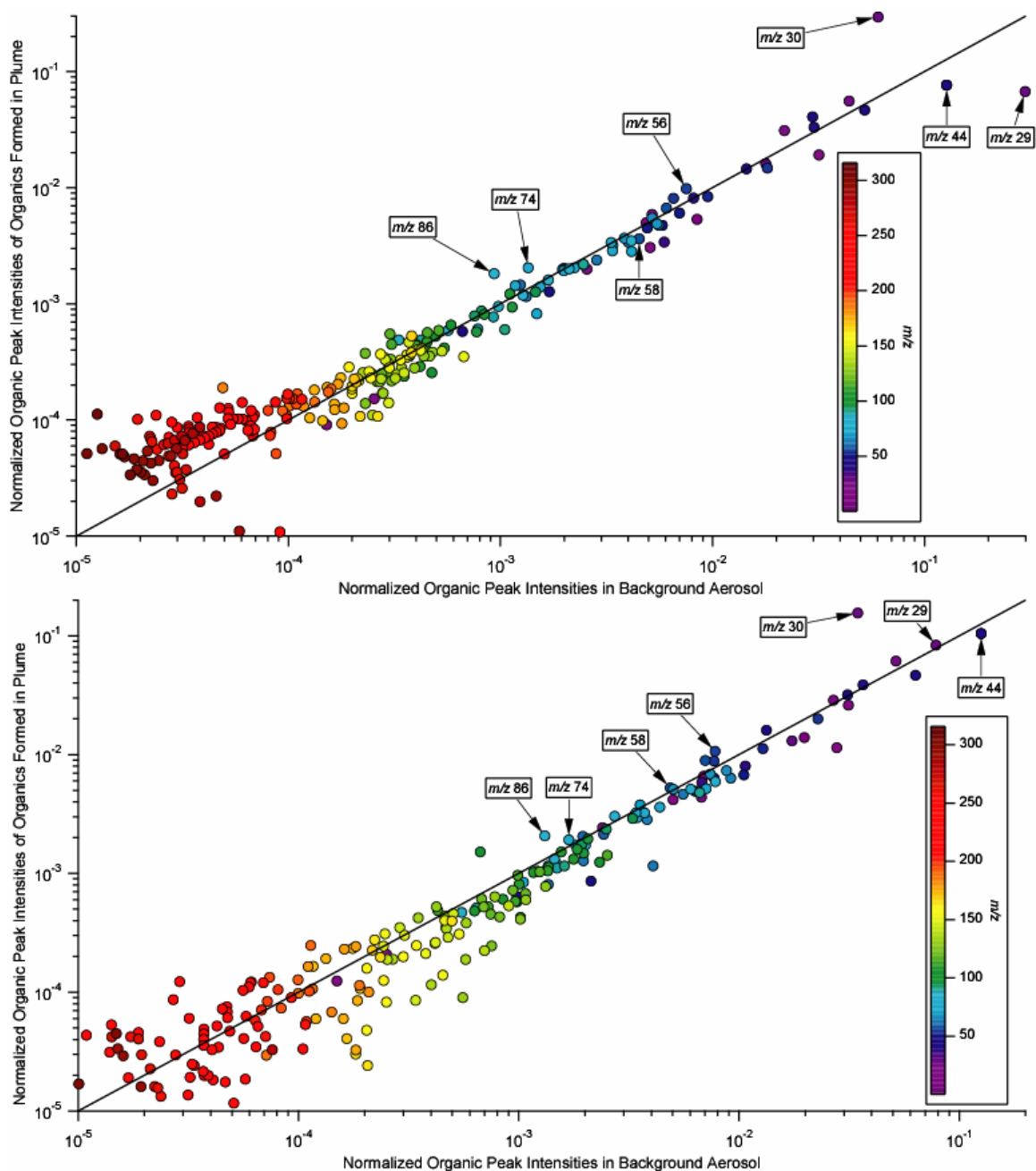
**Figure 7.8.** Spatial distribution of various aerosol species during flight B. A) Nitrate and diethylamine; B) *Excess nitrate* remaining after both sulfate and nitrate have been neutralized by ammonium (see Section 7.3.2 for further explanation); C) ammonium; D) organics. The PILS markers are spatially placed wherever the aircraft was at the midpoint of the time when a particular sample was collected (after being corrected for liquid residence time in the instrument).



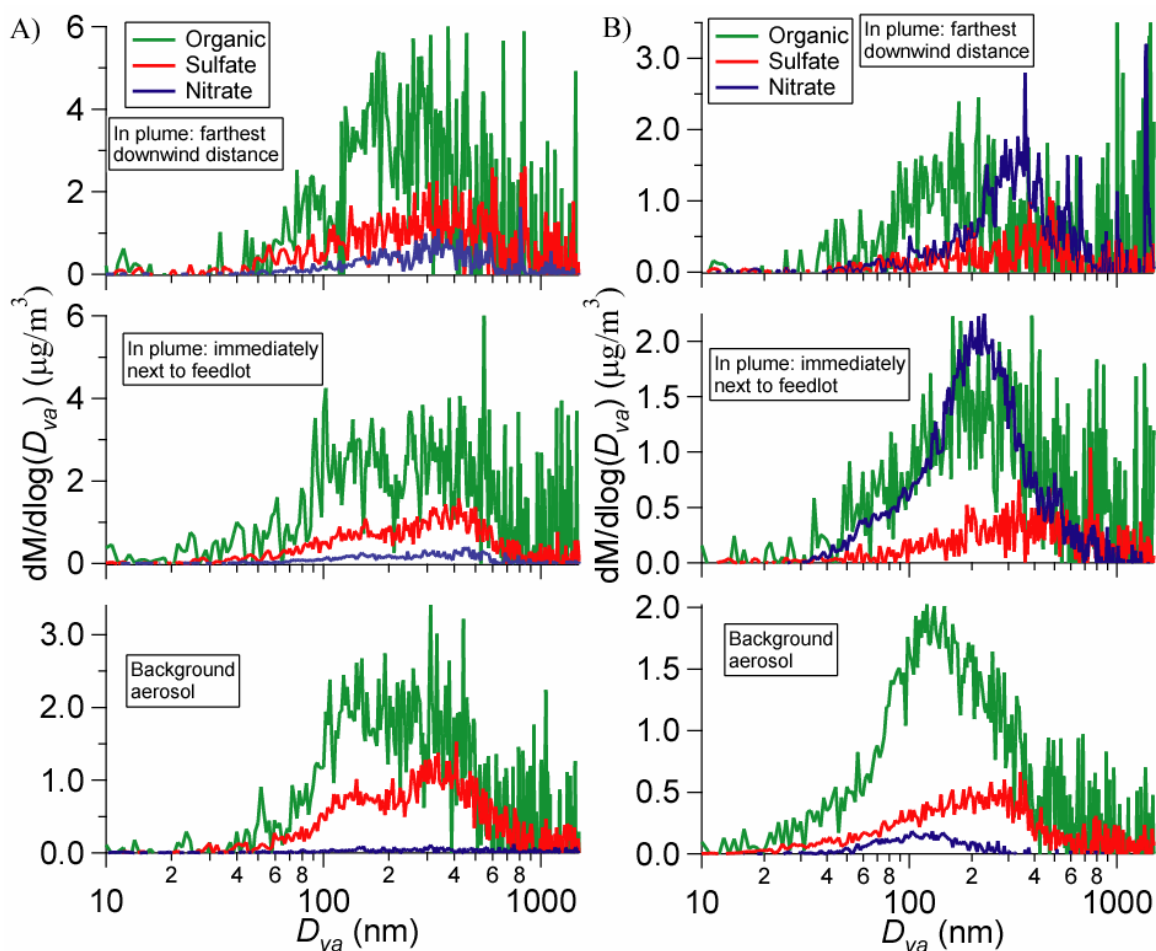
**Figure 7.9.** Vertical distribution of total submicrometer particulate mass and species concentrations from both the PILS and cToF-AMS, for flights A (upper panel) and B (lower panel). The cToF-AMS marker sizes for “Total mass” are proportional to the organic:inorganic ratio. Marker sizes for the individual cToF-AMS species are proportional to the respective mass fraction of that species. Marker sizes for PILS “Organic acids” are proportional to the relative contribution by oxalate. Marker sizes for PILS ammonium are proportional to the ammonium-to-sulfate molar ratio. Total mass, nitrate, ammonium, and organics increase in concentration with increasing altitude up to  $\sim 250 - 300$  m, before decreasing in both flights. cToF-AMS concentrations exceed those of the PILS for commonly detected species in the plume, especially nitrate and ammonium, since the PILS averages 5 - min worth of aerosol composition whereas the cToF-AMS has a time resolution of  $\sim 20 - 30$  s. Total PILS mass includes inorganics and organic acids, whereas total cToF-AMS mass includes inorganics and nonrefractory organic mass.



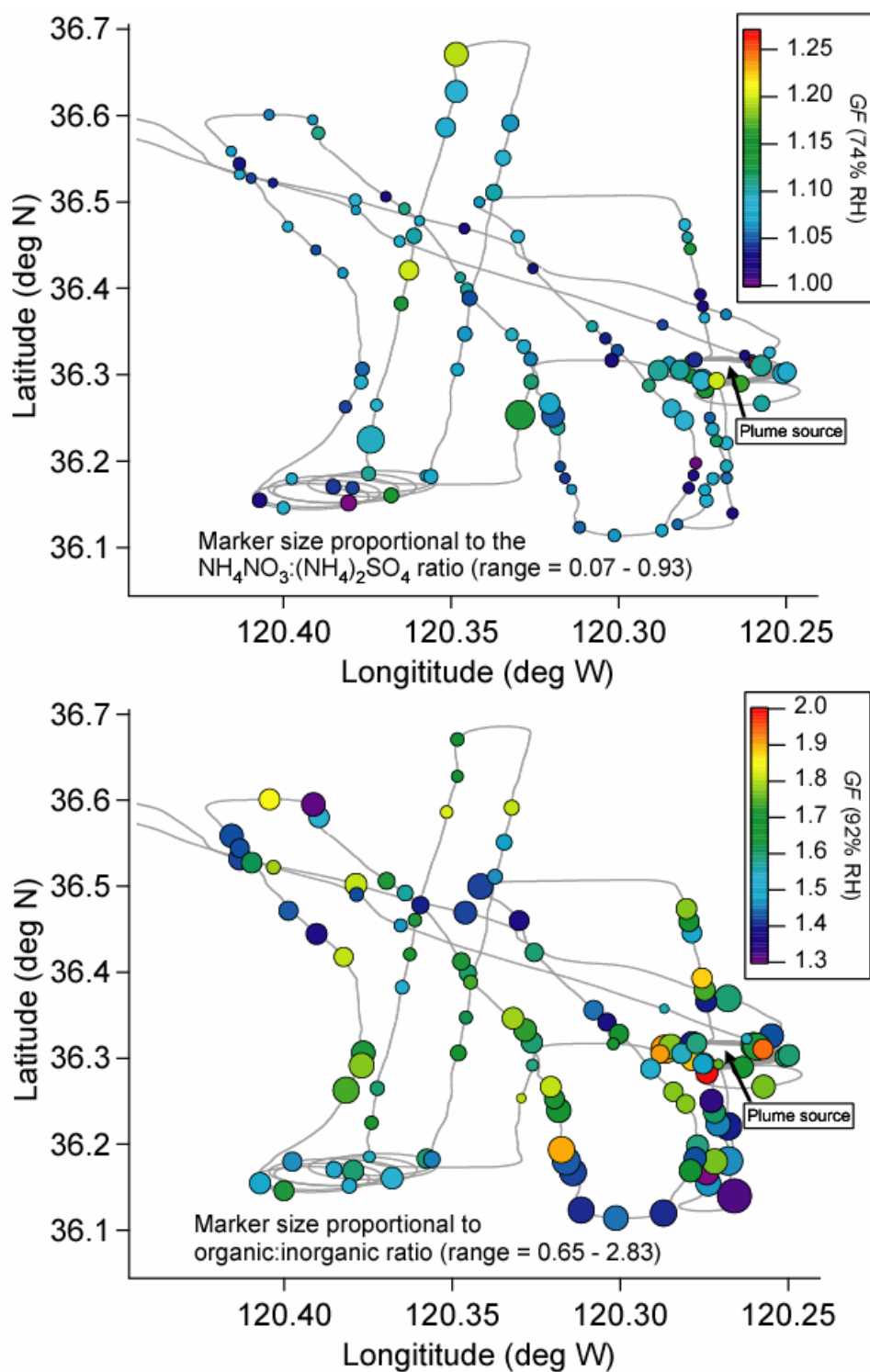
**Figure 7.10.** Aerosol mass spectra from the cToF-AMS in the background aerosol and in the plume at various downwind distances from the feedlot for flight B. There is no significant difference in the chemical signature of the aerosol in the three categories shown, with the notable exception of an enhancement in the  $m/z$  30 peak, a common amine marker, at the closest point to the source. The flight A spectra are similar to those presented here.



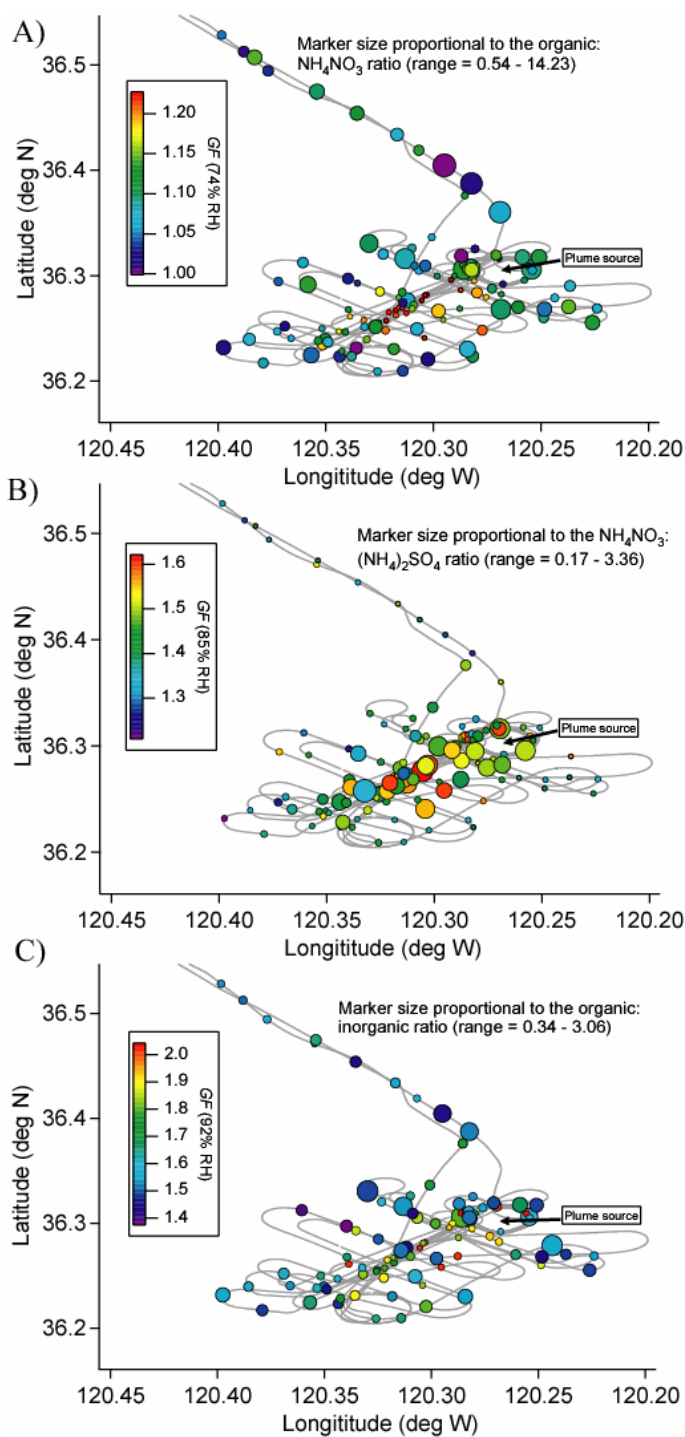
**Figure 7.11.** A comparison of the plume organic mass spectra versus the background aerosol organic mass spectra for flights A (upper panel) and B (lower panel). All non-organic contributions to the mass spectra have been removed by fragmentation calculations described in Section 7.4.3.3. This means that the signal at  $m/z$  30 represents a fragment of organics, including amines. The data on the y-axis were generated by taking the difference in the organic spectra in the plume and out of the plume. The organic aerosol appears to be very similar except this plot shows that there is an increase in peak intensities at  $m/z$  30, 56, 74, and 86, common amine peaks, in the plume. The peak intensity at  $m/z$  44 (and 29 in flight A) are greater in the background aerosol spectra indicating increased oxidation out of the plume as compared to inside the plume.



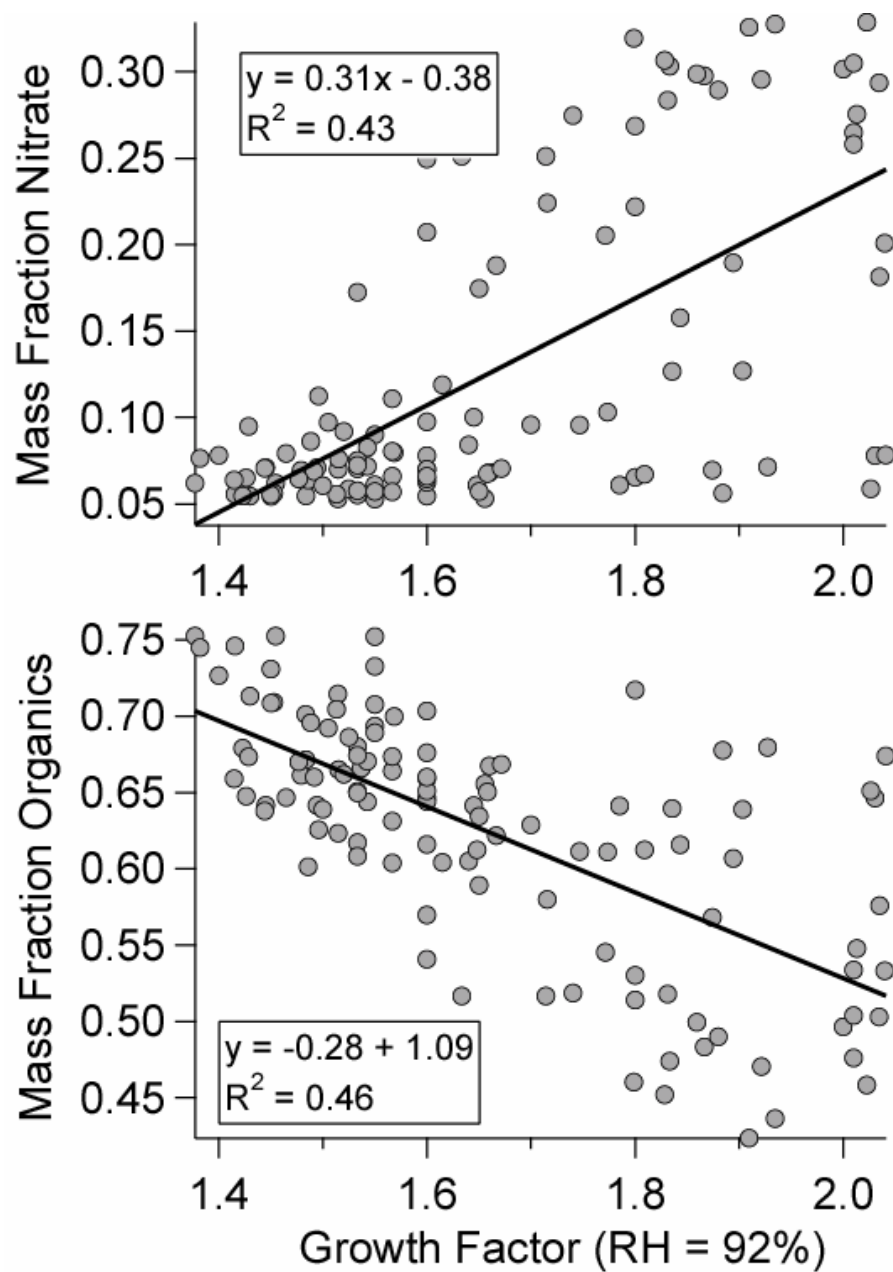
**Figure 7.12.** Speciated size distributions as determined by the cToF-AMS for flights A (panel A) and B (panel B). The x-axis is the vacuum aerodynamic diameter. There is evidence of externally mixed aerosols, evident by the independent shifts of various species as a function of increasing plume age. This is clearest in flight B where nitrate is shown to grow in size with plume age with less growth for organics and no growth for sulfate.



**Figure 7.13.** Growth factor data from flight A at RHs of 74% (upper panel) and 92% (lower panel). The markers represent individual DASH-SP scans at dry diameters between 150 and 200 nm. Marker sizes in upper panel are proportional to the ammonium nitrate:ammonium sulfate ratio, while marker sizes in the lower panel are proportional to the organic:inorganic ratio (inorganic = ammonium sulfate + ammonium nitrate).

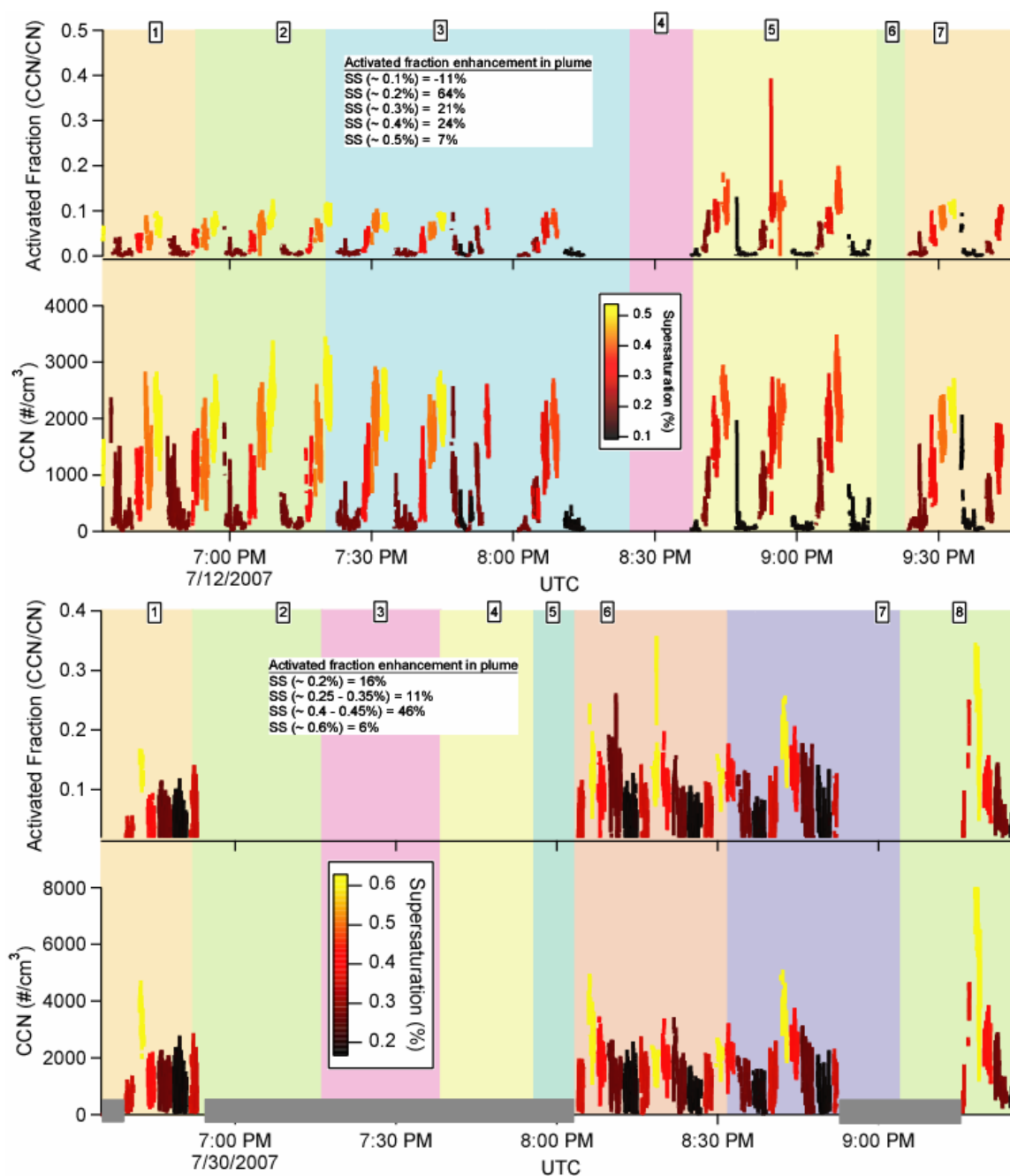


**Figure 7.14.** Growth factor data from flight B at RHs of 74% (A), 85% (B), and 92% (C). The markers represent individual DASH-SP scans at dry diameters between 150 and 200 nm. A) Marker sizes are proportional to the organic:ammonium nitrate ratio; B) marker sizes are proportional to the ammonium nitrate:ammonium sulfate ratio; C) marker sizes are proportional to the organic:inorganic ratio (inorganic = ammonium sulfate + ammonium nitrate).

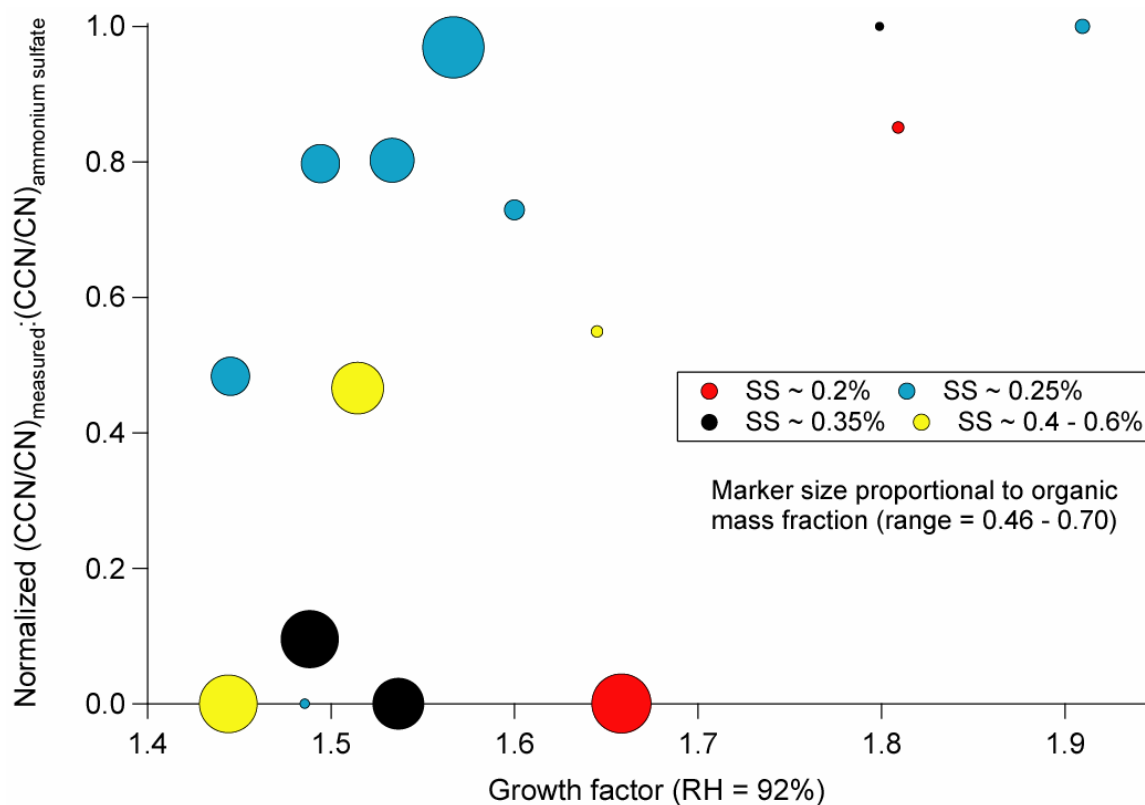


**Figure 7.15.** Relationship between the hygroscopic growth factor at 92% RH and mass fractions of nitrate and organics during flight B. Less correlation exists between the subsaturated hygroscopic growth factors and the mass fractions of ammonium ( $R^2 = 0.19$ , slope = 0.07) and sulfate ( $R^2 = 0.21$ , slope = -0.10).

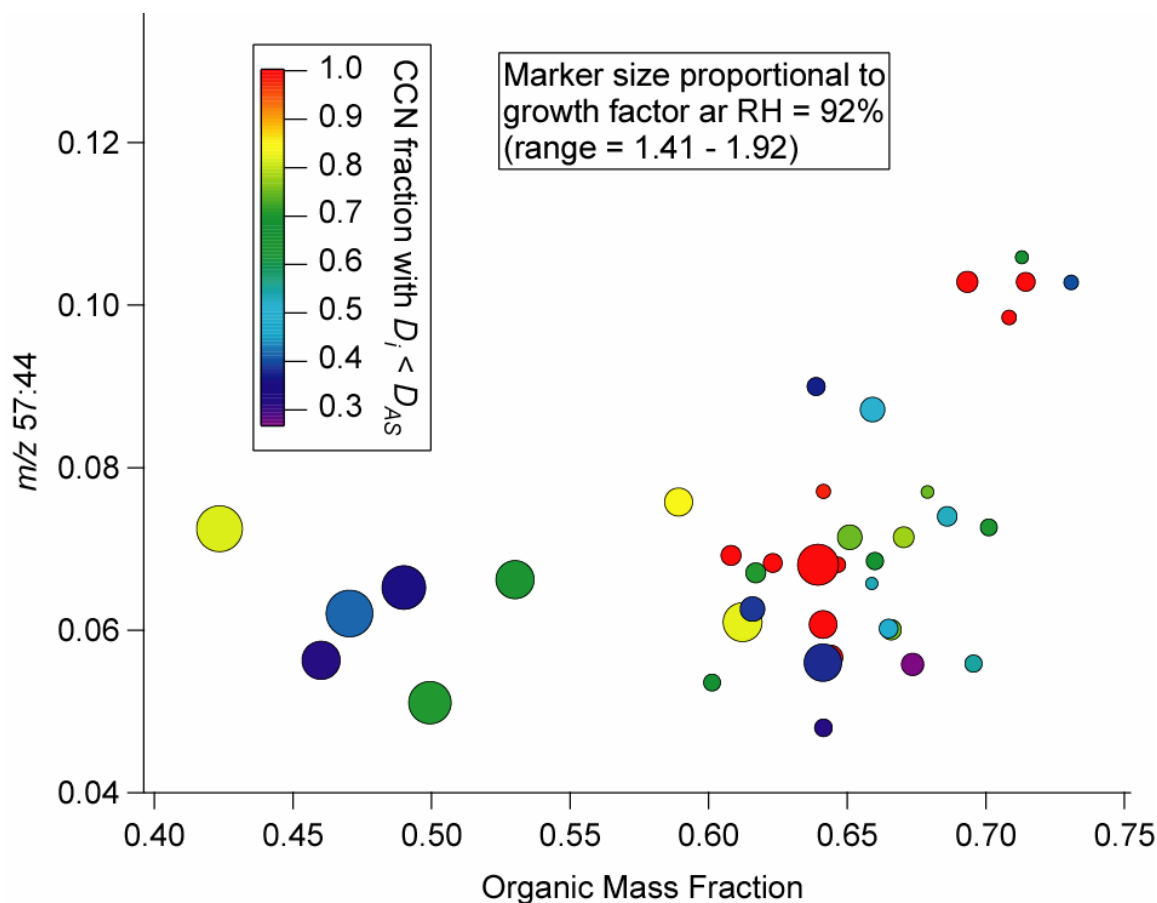




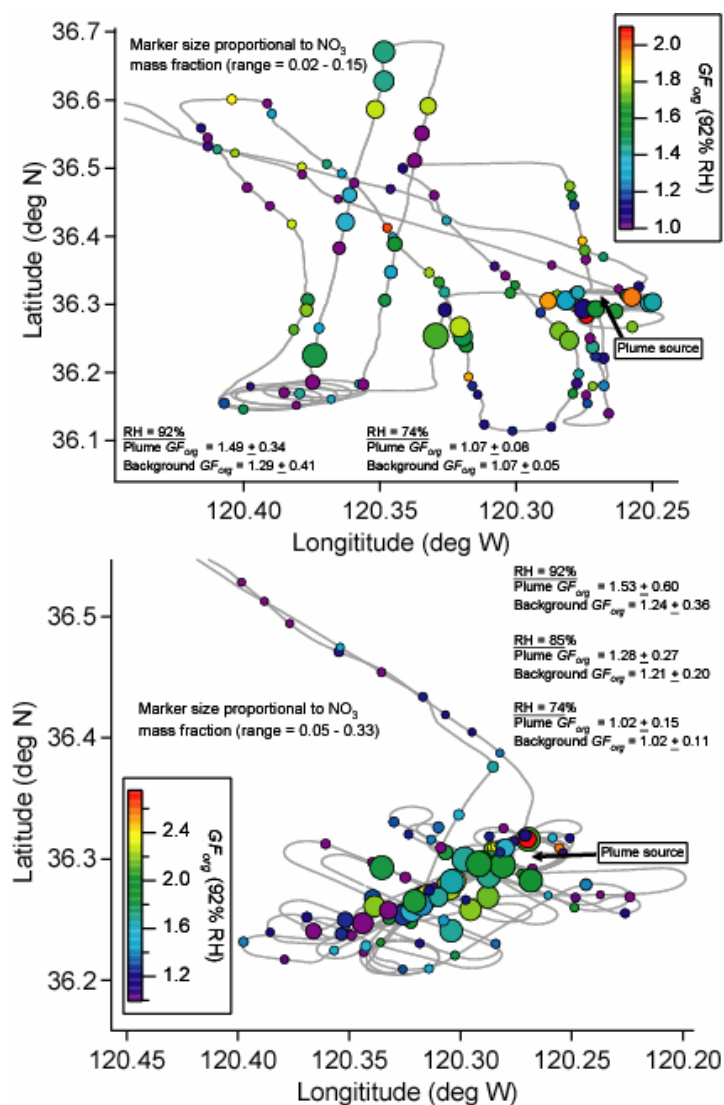
**Figure 7.16.** Time series of activated fraction of aerosol (CCN/CN), and total CCN concentration during flights A (upper panel) and B (lower panel). Data points are color-coded with instrument supersaturation. The shaded gray boxes in the lower panel indicate portions of flight B when the CCNc was operating in an alternative mode and those data are not presented here.



**Figure 7.17.** Normalized CCN activation ratio,  $(\text{CCN}/\text{CN})_{\text{measured}} : (\text{CCN}/\text{CN})_{\text{ammonium sulfate}}$ , as a function of hygroscopic growth factors for flight B. The effects of size distribution and mixing state have been removed from the data and the calculated activation ratio to isolate the impact of composition on the relationship between water uptake in the sub- and supersaturated regimes (see Section 7.4.6.2).



**Figure 7.18.** The relationship between the  $m/z$  57:44 ratio, the organic mass fraction, the CCN fraction with less droplet growth than ammonium sulfate ( $D_i < D_{AS}$ ), and the hygroscopic growth factor at RH = 92%. The CCN fraction with  $D_i < D_{AS}$  is a qualitative measure of kinetic limitations to droplet growth. The majority of the markers representing the lowest values of  $D_i < D_{AS}$  occur at  $m/z$  57:44 < 0.07, while most of the higher values of  $D_i < D_{AS}$  coincide with the highest organic mass fractions (> 0.6). The highest growth factors at RH = 92% occur at the lowest organic mass fractions and  $m/z$  57/44 ratios.



**Figure 7.19.** Spatial distribution of the calculated organic growth factors, using the ZSR mixing rule, for flights A (upper panel) and B (lower panel). Marker sizes are proportional to the mass fraction of nitrate.

## **Chapter 8**

## **Conclusions**

This thesis has focused on the development and characterization of aerosol instrumentation, the application of these instruments in field and laboratory studies, and the evaluation models and parameterizations with measurements. In order to reduce uncertainties associated with aerosol radiative forcing, rapid measurements of key aerosol properties, including composition and hygroscopicity, are needed. Two novel aerosol instruments have been designed specifically for aircraft operation.

Chapter 2 introduces the particle-into-liquid sampler (PILS), which grows particles into droplets sufficiently large to be collected by inertial impaction. The collected liquid sample can be analyzed using a variety of analytical techniques, including ion chromatography to quantify water-soluble aerosol composition. Forward and backward instruments models, which consider plumbing transmission efficiencies, droplet growth, mixing effects, and volatilization losses, were developed to predict mass concentrations that are consistent with laboratory tests for step changes in concentration. Results from characterization experiments summarize the overall performance of the instrument, including uncertainties, volatilization effects, and time resolution. Sample data from the 2004 International Consortium for Atmospheric Research on Transport and Transformation (ICARTT) field campaign show that this instrument is suitable for aircraft deployment and can quantify ambient mass concentrations of both inorganic and organic acid ions with 5 - min time resolution.

Chapter 3 reports on a new instrument developed to perform rapid, size-resolved aerosol hygroscopicity measurements. The differential aerosol sizing and hygroscopicity spectrometer probe (DASH-SP) employs differential mobility analysis in-concert with multiple humidification and optical sizing steps to determine dry optical size and

hygroscopic growth factors for size-selected aerosols simultaneously at three elevated RHs. Results from an extensive set of characterization tests summarize the time and size resolution, accuracy, precision, stability, and uncertainties associated with the instrument. An iterative data processing algorithm is introduced that quantifies growth factors and “effective” refractive indices for humidified particles using an empirically-derived three-dimensional surface (OPC pulse height - refractive index – particle size), based on a calculated value of the “effective” dry particle refractive index. Growth factor data are presented for several inorganic and organic acid salts and compared to thermodynamic predictions. Oxalic, malonic, glutaric, and glyoxylic acids grow gradually with increasing relative humidity up to 94%, while succinic and adipic acids show no growth. Airborne measurements of hygroscopic growth factors of ship exhaust aerosol during the 2007 Marine Stratus/Stratocumulus Experiment (MASE II) field campaign off the central coast of California are presented as the first report of the aircraft integration of the DASH-SP.

In-cloud production of secondary organic aerosol is discussed in Chapters 4 - 6. Airborne PILS measurements carried out on the CIRPAS Twin Otter from three field campaigns (ICARTT, MASE I, GoMACCS) are presented and show that sulfate and oxalate are strongly correlated in ambient aerosols, including evaporated cloud droplet residual particles. Since their chemical formation mechanisms are not directly linked, this correlation can be explained by a common medium necessary for production: droplets. Enhanced organic acid aerosol layers have been observed directly above cloudtops in both marine and urban atmospheres; as derived from large eddy simulations of stratocumulus under the conditions of MASE I, both Lagrangian trajectory analysis

and diurnal cloudtop evolution provide evidence that a significant fraction of the aerosol mass concentration above cloud can be accounted for by evaporated droplet residual particles. Predictions from a chemical cloud parcel model considering the aqueous-phase production of organic acids and sulfate show good agreement with ambient data for the relative magnitude of sulfate and organic acid growth in clouds and also the evolution of oxalic acid and its aqueous-phase precursors with increasing altitude in cloud. Aircraft measurements show that cloud processing is a significant source for organic acids, especially oxalic acid, in the ambient aerosols.

Chapter 6 additionally discusses the sources and character of water-soluble aerosol species, including both inorganic and organic acid species, during the 2006 GoMACCS campaign. Sulfate and ammonium dominated the water-soluble mass, with the most acidic samples and highest sulfate loadings observed downwind of the W. A. Parish Power Plant. The average particulate water-soluble mass fraction of organic acids measured was  $3.4 \pm 3.7\%$ ; concentrations of organic acids increased with decreasing carbon number from  $C_9$  to  $C_2$ . Specific attention was given to the sources and character of various organic acids in both clear and cloudy conditions; organic acids identified in the Houston atmosphere give important clues as to the sources of the atmospheric organic aerosol in that region and in urban atmospheres in general.

Chapter 7 reports an extensive airborne characterization of aerosol downwind of a massive bovine source in the San Joaquin Valley (California) on two flights during July 2007. Total submicrometer aerosol levels and concentrations of organics, nitrate, and ammonium were enhanced in the plume from the source as compared to the background aerosol. Amines were found to be a significant atmospheric base even in the presence of



ammonia; particulate amine concentrations are estimated as at least 14 – 23% of that of ammonium in the plume. Enhanced sub- and supersaturated water uptake and reduced refractive indices were coincident with lower organic volume fractions, higher ammonium nitrate volume fractions, and the detection of amines. Kinetic limitations due to hydrophobic organic material are shown to have likely suppressed droplet growth. After removing effects associated with size distribution and mixing state, the normalized activated fraction of CCN increased as a function of the subsaturated hygroscopic growth factor, with the highest activated fractions being consistent with relatively lower organic mass fractions and higher nitrate mass fractions.

Looking ahead to the future, it is necessary to continue to make ambient aerosol measurements in order to advance knowledge of the climatic and environmental effects associated with aerosols, and to assess the level of accuracy of atmospheric models. Since discrepancies invariably exist, models need to be improved in order to increase the accuracy of future climate change predictions. To increase understanding and predictive capabilities of global climate change, it is also imperative to monitor and analyze changes in properties that alter the radiative budget, such as trace gases, aerosols, and cloud cover, with large-scale systematic measurements. Remote sensing of aerosols and other components of the atmosphere, such as water vapor, are needed to understand the relationship between aerosols, clouds, and the hydrological cycle. The synergism of remote sensing data analysis, in-situ observations, and modeling provides a solid framework to study causal relationships between aerosols, clouds, and precipitation, and their resulting climatic implications.

## **Appendices**

## Appendix A

# Chemical Composition of Secondary Organic Aerosol Formed from the Photooxidation of Isoprene\*

---

\*This chapter is reproduced by permission from “Chemical Composition of Secondary Organic Aerosol Formed from the Photooxidation of Isoprene” by J. D. Surratt, S. M. Murphy, J. H. Kroll, N. L. Ng, L. Hildebrandt, A. Sorooshian, R. Szmigielski, R. Vermeylen, W. Maenhaut, M. Claeys, R. C. Flagan, and J. H. Seinfeld, *J. Phys. Chem. A*, 110, 9665-9690, 2006. Copyright 2006. American Chemical Society.

# Chemical Composition of Secondary Organic Aerosol Formed from the Photooxidation of Isoprene

Jason D. Surratt,<sup>†</sup> Shane M. Murphy,<sup>‡</sup> Jesse H. Kroll,<sup>§</sup> Nga L. Ng,<sup>‡</sup> Lea Hildebrandt,<sup>‡</sup> Armin Sorooshian,<sup>‡</sup> Rafal Szmigielski,<sup>||</sup> Reinhilde Vermeylen,<sup>||</sup> Willy Maenhaut,<sup>⊥</sup> Magda Claeys,<sup>||</sup> Richard C. Flagan,<sup>§</sup> and John H. Seinfeld<sup>\*,§</sup>

Department of Chemistry, California Institute of Technology, Pasadena, California 91125, Department of Chemical Engineering, California Institute of Technology, Pasadena, California 91125, Departments of Environmental Science and Engineering and Chemical Engineering, California Institute of Technology, Pasadena, California 91125, Department of Pharmaceutical Sciences, University of Antwerp (Campus Drie Eiken), Universiteitsplein 1, BE-2610 Antwerp, Belgium, and Department of Analytical Chemistry, Institute for Nuclear Sciences, Ghent University, Proefuinststraat 86, BE-9000 Gent, Belgium

Received: March 20, 2006; In Final Form: June 15, 2006

Recent work in our laboratory has shown that the photooxidation of isoprene (2-methyl-1,3-butadiene, C<sub>5</sub>H<sub>8</sub>) leads to the formation of secondary organic aerosol (SOA). In the current study, the chemical composition of SOA from the photooxidation of isoprene over the full range of NO<sub>x</sub> conditions is investigated through a series of controlled laboratory chamber experiments. SOA composition is studied using a wide range of experimental techniques: electrospray ionization–mass spectrometry, matrix-assisted laser desorption ionization–mass spectrometry, high-resolution mass spectrometry, online aerosol mass spectrometry, gas chromatography/mass spectrometry, and an iodometric-spectroscopic method. Oligomerization was observed to be an important SOA formation pathway in all cases; however, the nature of the oligomers depends strongly on the NO<sub>x</sub> level, with acidic products formed under high-NO<sub>x</sub> conditions only. We present, to our knowledge, the first evidence of particle-phase esterification reactions in SOA, where the further oxidation of the isoprene oxidation product methacrolein under high-NO<sub>x</sub> conditions produces polyesters involving 2-methylglyceric acid as a key monomeric unit. These oligomers comprise ~22–34% of the high-NO<sub>x</sub> SOA mass. Under low-NO<sub>x</sub> conditions, organic peroxides contribute significantly to the low-NO<sub>x</sub> SOA mass (~61% when SOA forms by nucleation and ~25–30% in the presence of seed particles). The contribution of organic peroxides in the SOA decreases with time, indicating photochemical aging. Hemiacetal dimers are found to form from C<sub>5</sub> alkene triols and 2-methyltetrols under low-NO<sub>x</sub> conditions; these compounds are also found in aerosol collected from the Amazonian rainforest, demonstrating the atmospheric relevance of these low-NO<sub>x</sub> chamber experiments.

## 1. Introduction

Secondary organic aerosol (SOA) is formed in the troposphere from the oxidation of volatile organic compounds (VOCs), where the resultant low-vapor-pressure oxidation products partition between the gas and aerosol phases. Recent laboratory experiments have established that SOA formation can also result from the heterogeneous reactions between particle-associated substances and relatively volatile species resulting in the formation of high-molecular-weight (MW) products via oligomerization (polymerization).<sup>1–5</sup> Until recently, the formation of SOA from the photooxidation of isoprene, the atmosphere's most abundant nonmethane hydrocarbon, was considered insignificant.<sup>6,7</sup> This was largely due to the known volatility of first-generation gas-phase oxidation products, such as meth-

acrolein (MACR), methyl vinyl ketone (MVK), and formaldehyde, from isoprene oxidation in the presence of NO<sub>x</sub>, and a previous chamber study that concluded that isoprene oxidation does not lead to SOA formation.<sup>8</sup> Recent field observations of certain organic aerosol compounds, diastereoisomeric 2-methyltetrols (2-methylerythritol and 2-methylthreitol), and 2-methylglyceric acid, attributable to isoprene oxidation, and the experimental observation that isoprene under highly acidic conditions can lead to the formation of polymeric, humic-like substances through heterogeneous reactions, re-opened the issue of SOA formation from isoprene.<sup>7,9–13</sup> After their ambient identification, Edney et al.<sup>14</sup> and Böge et al.<sup>15</sup> detected 2-methyltetrols in SOA formed from laboratory chamber studies of isoprene.

Recent work in our laboratory has shown that SOA formation from isoprene oxidation can be significant.<sup>16,17</sup> Extensive experiments were carried out under both low- and high-NO<sub>x</sub> conditions using either nitrous acid (HONO) or hydrogen peroxide (H<sub>2</sub>O<sub>2</sub>) as the OH radical source. Photooxidation experiments were also conducted using isoprene first-generation gas-phase oxidation products as the VOC precursor. Although no aerosol growth was observed from MVK oxidation, SOA

\* To whom correspondence should be addressed. Phone: (626) 395-4635. Fax: (626) 796-2591. E-mail seinfeld@caltech.edu.

<sup>†</sup> Department of Chemistry, California Institute of Technology.

<sup>‡</sup> Department of Chemical Engineering, California Institute of Technology.

<sup>§</sup> Departments of Environmental Science and Engineering and Chemical Engineering, California Institute of Technology.

<sup>||</sup> University of Antwerp.

<sup>⊥</sup> Ghent University.

formation was observed from MACR at high- $\text{NO}_x$  conditions. High-molecular-weight (MW) species were observed to form from isoprene oxidation under both low- and high- $\text{NO}_x$  conditions.<sup>17</sup> Moreover, SOA yields were observed to exhibit a dependence on the  $\text{NO}_x$  level. This dependence appears to be attributed to differences in organic peroxy radical ( $\text{RO}_2$ ) chemistry. At high  $[\text{NO}]$  (i.e., high- $\text{NO}_x$  conditions),  $\text{RO}_2$  radicals react mainly with NO to produce small alkoxy radicals (RO) that likely fragment into smaller organics, which are expected to be too volatile to partition appreciably to the aerosol phase, or form organic nitrate species ( $\text{RONO}_2$ ). In the absence of  $\text{NO}_x$  (i.e., low- $\text{NO}_x$  conditions),  $\text{RO}_2$  radicals instead react with  $\text{HO}_2$  radicals (present in the chamber experiments in large quantities from the  $\text{OH} + \text{H}_2\text{O}_2$  reaction) to form organic hydroperoxides, which have been experimentally shown to be important SOA components from other VOC precursors.<sup>18,19</sup> Hydroperoxides have been suggested to be involved in polymerization in the aerosol phase via reactions with aldehydes to form peroxyhemiacetals.<sup>18,19</sup>

Although it is now established that OH-initiated oxidation of isoprene leads to SOA, a detailed understanding of the chemical reaction pathways leading to the production of isoprene SOA is lacking. Results from chamber studies have elucidated the importance of the further oxidation of MACR as a primary route for SOA formation from isoprene under high- $\text{NO}_x$  conditions. Known  $\text{RO}_2$  chemistry at low- $\text{NO}_x$  conditions leads to the initial gas-phase oxidation products, likely hydroxyhydroperoxides, of isoprene, which upon further oxidation leads to SOA production. Nonetheless, detailed evaluation of the mechanism of SOA formation from the oxidation of isoprene has not yet been carried out.

In the present work, a suite of offline analytical techniques is used in conjunction with online aerosol mass spectrometry to investigate the detailed chemical composition of SOA from isoprene oxidation. SOA is produced from the photooxidation of isoprene under varying  $\text{NO}_x$  conditions and is collected onto filters for offline chemical analyses. Offline mass spectrometry (MS) techniques are used to detect organic species from aerosol filter samples, including oligomeric components of isoprene SOA (as detected in prior studies only by online time-of-flight aerosol mass spectrometry (TOF-AMS) measurements). Tandem MS and gas chromatography (GC)/MS derivatization techniques are employed to structurally elucidate oligomeric components. Organic peroxides are detected and quantified from low- $\text{NO}_x$  isoprene SOA using a conventional iodometric-spectroscopic method. Tracer compounds for isoprene oxidation in the ambient atmosphere, as found in the Amazonian rainforest, are detected here for the first time in the low- $\text{NO}_x$  chamber experiments. The low- $\text{NO}_x$  conditions are most relevant to understanding SOA formation in highly vegetated, remote regions.<sup>7</sup> In some cases, such as the southeastern U.S., where atmospheric transport of pollutants from urban areas can influence SOA formation,<sup>20</sup> conditions closer to those of the high- $\text{NO}_x$  experiments may be applicable.

## 2. Experimental Section

**2.1. Chamber Experiments.** Experiments were carried out in Caltech's dual indoor 28  $\text{m}^3$  Teflon smog chambers.<sup>21,22</sup> Experimental protocols are similar to those described previously,<sup>16,17</sup> so they will be described only briefly here. Most experiments were carried out with hydrogen peroxide ( $\text{H}_2\text{O}_2$ ) as the hydroxyl radical (OH) precursor; in some cases, HONO was used instead to demonstrate that the particular OH source has no effect on the outcome of the experiments. For some

experiments, ammonium sulfate seed particles were introduced into the chamber (at volume concentrations of 20–30  $\mu\text{m}^3/\text{cm}^3$ ) by atomization of a 0.015 M ammonium sulfate solution. A known concentration of isoprene (or any other precursor, such as MACR) was then introduced by sending air over a measured volume of the pure compound (Aldrich, 99.8%) into the chamber. For  $\text{H}_2\text{O}_2$ /high- $\text{NO}_x$  experiments, NO was also introduced into the chamber from a gas mixture (500 ppm gas cylinder in  $\text{N}_2$ , Scott Specialty Gases). In low- $\text{NO}_x$  experiments, NO was not added and  $\text{NO}_x$  concentrations were  $<1$  ppb. When the isoprene (monitored by gas chromatography–flame ionization detection (GC-FID)),  $\text{NO}_x$ , and seed concentrations became constant inside the chamber, irradiation by UV lights (centered at 354 nm) was started, initiating the reaction.

SOA volume growth ( $\mu\text{m}^3/\text{cm}^3$ ) was monitored with a differential mobility analyzer (DMA). For quantification of SOA products collected on filter samples, the DMA volumes were used for each experiment to determine the total SOA mass collected. Filter sampling commenced when the particle growth had terminated, that is, when the aerosol volume had reached its maximum value. Depending on the total volume concentration of aerosol in the chamber, the filter sampling time was 2–4 h, which typically resulted in 3–7  $\text{m}^3$  of total chamber air sampled.

**2.2. Filter Extractions.** Collected Teflon filters (PALL Life Sciences, 47-mm diameter, 1.0- $\mu\text{m}$  pore size, teflo membrane) were extracted in 5 mL of HPLC-grade methanol by 40 min of sonication. The filters were then removed from the methanol sample extracts and archived at  $-20^\circ\text{C}$ . Each extract was blown dry under a gentle  $\text{N}_2$  stream (without added heat) and then reconstituted with 1 mL of a 50:50 (v/v) solvent mixture of HPLC-grade methanol and 0.1% aqueous acetic acid solution. The reconstituted extracts were then stored at  $-20^\circ\text{C}$  until analysis was performed. In most cases, filter extracts were chemically analyzed within 1–2 days after filter extraction. Lab control filters were extracted and treated in the same manner as the samples. Aliquots of each of these filter extracts were analyzed by the four mass spectrometry techniques to follow.

To ensure that  $\text{H}_2\text{O}_2$  was not condensing onto filter media and introducing artifacts in the chemical analyses, we collected several blank filters under dark conditions from the chamber containing typical experimental well-mixed concentrations of isoprene, NO, and ammonium sulfate seed aerosol, sampled for the same duration ( $\sim 2$ –4 h) as a sample filter. No significant chemical artifacts or contaminants were observed in the analytical techniques from these blank filters, consistent with the lack of observed aerosol growth under dark conditions.

**2.3. Liquid Chromatography/Electrospray Ionization–Mass Spectrometry (LC/ESI-MS).** A Hewlett-Packard 1100 Series HPLC instrument, coupled with a single quadrupole mass analyzer and equipped with an electrospray ionization (ESI) source, was used to identify and quantify relatively polar, acidic SOA components. Data were collected in both positive (+) and negative (–) ionization modes; the quantitative analysis presented here is limited to the negative ionization mode. An Agilent Eclipse  $\text{C}_{18}$  column (3.0  $\times$  250 mm) was used to separate the organic species before detection. The eluents used were 0.1% aqueous acetic acid (A) and methanol (B). In the 40-min gradient elution program used, the concentration of eluent B increased from 5% to 90% in 35 min, and then decreased to 5% in 5 min. The total flow rate of the eluent used in the LC/MS analysis was 0.8  $\text{mL min}^{-1}$ . Optimum electrospray conditions were found using a 60 psig nebulizing pressure, 3.5 kV capillary voltage, 13  $\text{L min}^{-1}$  drying gas

flowrate, and a 330 °C drying gas temperature. During the full scan mode of analysis, the cone voltage was set at 60 V, avoiding fragmentation of most species and allowing their detection as deprotonated molecules ( $[M - H]^-$ ). During the upfront collision-induced dissociation (CID) mode of analysis, the cone voltage was set to 110 V, resulting in partial fragmentation of the  $[M - H]^-$  ions. By comparing these two sets of MS data (upfront CID mode to the full scan mode of analysis) and by examining the fragmentation patterns of the species, some structural information on the analyzed species was obtained. This was particularly useful in confirming results from other MS/MS techniques used and for the identification of oligomeric components.

Using a set of six acidic species (*meso*-erythritol, citramalic acid, 2-hydroxy-3-methylbutyric acid, pimelic acid, pinic acid, and suberic acid monomethyl ester) as surrogate standards, this method was also used to quantify the amount of polar acidic species. Filter extraction efficiency was established by standard additions of these surrogate standards to blank filters. On average, the extraction efficiency for each standard was ~60% with an estimated error bar of ca.  $\pm 15\%$  over the concentration range used to generate the LC/MS calibration curves. This average extraction efficiency was included in the calculations to quantify identified isoprene SOA products.

As we will note shortly, to investigate the probable importance of a  $C_4$  hydroxy dialdehyde species formed under high- $NO_x$  conditions, we derivatized selected sample extracts using Girard Reagent P (1-(carboxymethyl)pyridinium chloride hydrazide, MW = 187) to increase sensitivity for aldehydic species in the (+)LC/MS mode. Girard Reagent P (GirP) reacts with aldehydes and ketones to form water-soluble hydrazones with a permanently charged pyridine moiety, and water is eliminated in this reaction.<sup>23</sup> The organic unit that adds to aldehydes and ketones has a mass of 152 Da. A series of aldehyde standards, glyoxal (MW = 58), succinic semialdehyde (MW = 102), and glutaraldehyde (MW = 100), were derivatized using the GirP and analyzed with (+)LC/MS. These small polar aldehyde standards typically go undetected using (+)ESI techniques such as in LC/MS; however, upon derivatization they were detected as the singly charged  $[M - H_2O + 152(\text{GirP})]^+$  ions (glyoxal was also detected as doubly charged  $[M - 2H_2O + 152(\text{GirP})]^{2+}$  ion), where M is the MW of the aldehyde species. These compounds eluted between 1 and 2 min from the LC column, including a derivatized compound corresponding to the proposed  $C_4$  hydroxy dialdehyde species (MW = 102 and  $[M - H_2O + 152(\text{GirP})]^+ = 236$ ).

**2.4. ESI-Ion Trap Mass Spectrometry (ESI-ITMS).** Aliquots of the filter extracts were also analyzed by a ThermoElectron LCQ ion trap mass spectrometer equipped with an ESI source, via direct infusion. This instrument does not provide chromatographic separation, precluding quantification. Instead, the instrument was used for the qualitative detection of product species. In addition, specific ions of interest were isolated from the rest of the sample ion matrix and further fragmented to produce product ion mass spectra, aiding in structural elucidation.

Data were collected in both positive and negative ionization modes. Because the same species were detected in both modes ( $[M - H]^-$  and  $[M + Na]^+$  ions), we only present here the data collected under negative ionization; the data collected under positive ionization serve as confirmation of the negative ionization data.

**2.5. Matrix-Assisted Laser Desorption Ionization–Time-of-Flight Mass Spectrometer (MALDI-TOFMS).** Another

aliquot of the filter extract was analyzed on an Applied Biosystems Voyager-DE Pro MALDI-TOFMS instrument. After 6  $\mu\text{L}$  of each extract had been dried on the steel target plate, the plate was gently brushed with graphite particles, which served as the matrix. The samples were analyzed in the linear mode, in both positive and negative ionization modes. 400–500 laser shots were summed to obtain a representative mass spectrum of each sample. This method was mainly used to assess the molecular weight (MW) range of the aerosol, to detect oligomeric signatures, and to confirm the MWs of species identified by the ESI techniques.

**2.6. High-Resolution ESI-MS.** Extracts were also analyzed by a Waters LCT Premier Electrospray time-of-flight mass spectrometer with W geometry in the Department of Chemistry at the University of California, Irvine, operated in the negative ionization mode. Samples were analyzed by flow injection. The calibration was carried out using sodium formate clusters with co-injection of fmoc-amino acids of appropriate mass spiked into the analytical sample for lock-mass corrections to obtain accurate mass for the oligomeric ions with  $m/z$  266, 323, 365, 368, 467, and 470. These ions were only detected in the high- $NO_x$  experiments, and elemental compositions were determined with reasonable accuracy (within  $\pm 5$  ppm) and were consistent with other analytical observations (such as ESI-MS/MS and GC/MS derivatization data).

**2.7. Aerodyne Time-of-Flight Aerosol Mass Spectrometer (TOF-AMS).** During most chamber experiments, real-time particle mass spectra were collected continuously by an Aerodyne Time-of-Flight Aerosol Mass Spectrometer (TOF-AMS), and averaged spectra were saved every 5 min. The design and capabilities of the TOF-AMS instrument are described in detail elsewhere.<sup>24</sup> Briefly, chamber air enters the instrument through a 100- $\mu\text{m}$  critical orifice at a flowrate of 1.4  $\text{cm}^3/\text{s}$ . Particles with vacuum aerodynamic diameters between 50 and 800 nm are efficiently focused by an aerodynamic lens, passed through a chopper, and then impacted onto a tungsten vaporizer. The chopper can be operated in three modes: (1) completely blocking the beam to gather background mass spectra; (2) out of the beam's path to collect ensemble average mass spectra over all particles sizes; and (3) chopping the beam to create size-resolved mass spectra. The vaporizer is typically run at  $\sim 550$  °C to ensure complete volatilization of the SOA and the inorganic seed; during several runs the vaporizer temperature was lowered to  $\sim 160$  °C to reduce thermally induced fragmentation of oligomers. Once vaporized, molecules undergo electron ionization at 70 eV and are orthogonally pulsed every 19  $\mu\text{s}$  into the time-of-flight mass analyzer.

**2.8. Gas Chromatography/Mass Spectrometry (GC/MS).** Extracts of selected filters were analyzed for polar organic compounds by GC/MS using a method that was adapted from that reported by Pashynska et al.<sup>25</sup> The sample workup consisted of extraction of all or half of the filter with methanol under ultrasonic agitation and derivatization of carboxyl and hydroxyl functions into trimethylsilyl (TMS) derivatives. The extract was divided into two parts; one part was trimethylsilylated while the other part was stored in a refrigerator at 4 °C for eventual further analysis. GC/MS analyses were performed with a system comprising a TRACE GC2000 gas chromatograph, which was coupled to a Polaris Q ion trap mass spectrometer equipped with an external ionization source (ThermoElectron, San Jose, CA). A Heliflex AT-5MS fused-silica capillary column (5% phenyl, 95% methylpolysiloxane, 0.25  $\mu\text{m}$  film thickness, 30 m  $\times$  0.25 mm i.d.) preceded by a deactivated fused-silica precolumn (2 m  $\times$  0.25 mm i.d.) (Alltech, Deerfield, IL) was



used to separate the derivatized extracts. Helium was used as carrier gas at a flow rate of 1.2 mL min<sup>-1</sup>. The temperature program was as follows: isothermal hold at 50 °C for 5 min, temperature ramp of 3 °C min<sup>-1</sup> up to 200 °C, isothermal hold at 200 °C for 2 min, temperature ramp of 30 °C min<sup>-1</sup> up to 310 °C; and isothermal hold at 310 °C for 2 min. The analyses were performed in the full scan mode (mass range: *m/z* 50–800), and were first carried out in the electron ionization (EI) mode and subsequently in the chemical ionization (CI) mode. The ion source was operated at an electron energy of 70 eV and temperatures of 200 °C and 140 °C in the EI and CI modes, respectively. The temperatures of the GC injector and the GC/MS transfer line were 250 °C and 280 °C, respectively. For chemical ionization, methane was introduced as reagent gas at a flow rate of 1.8 mL min<sup>-1</sup>. We present here mainly the data collected in the EI mode; the data collected in the CI mode are used if insufficient MW information is obtained in the EI mode.

Selected extracts were also subjected to a hydrolysis/ethylation and/or a methoximation procedure prior to trimethylsilylation. The purpose of the hydrolysis/ethylation procedure was to confirm the presence of ester linkages, while that of the methoximation procedure was to evaluate the presence of aldehyde/keto groups, in oligomeric SOA. The hydrolysis/ethylation procedure involved reaction of the extract residues with 40  $\mu$ L of analytical-grade ethanol and 8  $\mu$ L of trimethylchlorosilane (Supelco, Bellefonte, PA) for 1 h at 60 °C. Details about the methoximation procedure can be found in Wang et al.<sup>12</sup>

**2.9. Gas Chromatography–Flame Ionization Detection (GC-FID).** Quantitative determination of the 2-methyltetrols (i.e., 2-methylthreitol and 2-methylerythritol), the C<sub>5</sub> alkene triols [i.e., 2-methyl-1,3,4-trihydroxy-1-butene (cis and trans) and 3-methyl-2,3,4-trihydroxy-1-butene], and 2-methylglyceric acid, in selected filters, was performed by GC-FID with a GC 8000 Top instrument (Carlo Erba, Milan, Italy). The sample workup was the same as that for GC/MS analysis except that filter parts were spiked with a known amount of erythritol (Sigma, St. Louis, MO) as an internal recovery standard; it was assumed that the GC-FID responses of the trimethylsilyl derivatives of the analytes and the internal recovery standard were similar. The GC column and conditions were comparable with those used for GC/MS; the column was a CP-Sil 8 CB capillary column (5% diphenyl, 95% methylpolysiloxane, 0.25  $\mu$ m film thickness, 30 m  $\times$  0.25 mm i.d.) (Chrompack, Middelburg, The Netherlands) and the temperature program was as follows: isothermal hold at 45 °C for 3 min, temperature ramp of 20 °C min<sup>-1</sup> up to 100 °C, isothermal hold at 100 °C for 10 min, temperature ramp of 5 °C min<sup>-1</sup> up to 315 °C, and isothermal hold at 315 °C for 20 min. Measurement of the 2-methyltetrols in the low-NO<sub>x</sub> SOA samples was performed after the unstable products tentatively characterized as 2-methyltetrol performate derivatives had decayed to 2-methyltetrols, that is, after leaving the reaction mixture for 2 days at room temperature.

**2.10. Total Aerosol Peroxide Analysis.** The total amount of peroxides in the low-NO<sub>x</sub> isoprene SOA was quantified using an iodometric-spectrophotometric method adapted from that used by Docherty et al.<sup>18</sup> to analyze peroxides formed by  $\alpha$ -pinene-ozonolysis. The method employed here differed only in the choice of extraction solvent: we used a 50:50 (v/v) mixture of methanol and ethyl acetate, rather than pure ethyl acetate. Calibration and measurements were performed at 470 nm on a Hewlett-Packard 8452A diode array spectrophotometer. A standard calibration curve was obtained from a series of

benzoyl peroxide solutions. Benzoyl peroxide was the standard used for quantification of organic peroxides formed from low-NO<sub>x</sub> experiments, because its MW is close to the average MW determined from the mass spectrometry techniques, in particular the MALDI-TOFMS measurements. The molar absorptivity determined from the standard curve was  $\sim$ 852, in excellent agreement with that determined by Docherty et al. and with the value of 845 determined with the original method development paper.<sup>18,26</sup> As a confirmation that the technique was reproducible, we extracted and analyzed in the same fashion, three  $\alpha$ -pinene-ozonolysis filters collected from our laboratory chambers. We measured  $\sim$ 49% of the SOA mass, produced from  $\alpha$ -pinene ozonolysis, to be organic peroxides, in excellent agreement to that of Docherty et al.'s measurement of  $\sim$ 47% for the same system. A few high-NO<sub>x</sub> isoprene filter samples were also analyzed by this method, but resulted in the detection of no organic peroxides (below detection limits of this technique).

**2.11. Particle-Into-Liquid Sampler Coupled to Ion Chromatography (PILS/IC).** The PILS/IC (particle-into-liquid sampler coupled to ion chromatography) is a quantitative technique for measuring water-soluble ions in aerosol particles. The PILS developed and used in this study<sup>27</sup> is based on the prototype design<sup>28</sup> with key modifications, including integration of a liquid sample fraction collector and real-time control of the steam injection tip temperature. Chamber air is sampled through a 1- $\mu$ m cut-size impactor and a set of three denuders (URG and Sunset Laboratories) to remove inorganic and organic gases that may bias aerosol measurements. Sample air mixes with steam in a condensation chamber where rapid adiabatic mixing produces a high water supersaturation. Droplets grow sufficiently large to be collected by inertial impaction before being delivered to vials held on a rotating carousel. The contents of the vials are subsequently analyzed off-line using a dual IC system (ICS-2000 with 25  $\mu$ L sample loop, Dionex Inc.) for simultaneous anion and cation analysis. The background levels of individual species (Na<sup>+</sup>, NH<sub>4</sub><sup>+</sup>, K<sup>+</sup>, Mg<sup>2+</sup>, Ca<sup>2+</sup>, SO<sub>4</sub><sup>2-</sup>, Cl<sup>-</sup>, NO<sub>2</sub><sup>-</sup>, NO<sub>3</sub><sup>-</sup>, oxalate, acetate, formate, methacrylate, pyruvate) concentrations for analyzed filter samples, presented as the average concentration plus three times the standard deviation ( $\sigma$ ), are less than 0.28  $\mu$ g m<sup>-3</sup>.

### 3. Results

As noted, experiments were conducted at high- and low-NO<sub>x</sub> conditions. High-NO<sub>x</sub> conditions were achieved through the addition of substantial NO<sub>x</sub> ( $\sim$ 800 to 900 ppb NO<sub>x</sub>) to the reaction chamber, leading to isoprene/NO<sub>x</sub> molar ratios of  $\sim$ 0.56 to 0.63. Under low-NO<sub>x</sub> conditions no NO<sub>x</sub> is added to the chamber, where NO<sub>x</sub> mixing ratios of  $<1$  ppb (small amounts of NO<sub>x</sub> likely desorb from chamber walls) were observed. The low-NO<sub>x</sub> condition simulates a remote (NO<sub>x</sub>-free) atmosphere; for example, at typical isoprene and NO<sub>x</sub> mixing ratios observed in the Amazonian rainforest ( $\sim$ 4 to 10 ppb and 0.02 to 0.08 ppb, respectively),<sup>7,29</sup> the isoprene/NO<sub>x</sub> ratios that result are  $\sim$ 50 to 500, comparable to the isoprene/NO<sub>x</sub> ratio of the present experiments ( $\sim$ 500).

**3.1. High-NO<sub>x</sub> Condition.** Table 1 lists nine high-NO<sub>x</sub> chamber experiments that were conducted to generate SOA for aerosol filter sampling. All experiments were conducted with 500 ppb of isoprene or MACR in order to produce sufficient aerosol mass for all offline analytical measurements. In most of the experiments conducted, H<sub>2</sub>O<sub>2</sub> served as the OH radical precursor; in this manner, initial oxidation of isoprene is dominated by OH. It is estimated that  $\sim$ 3–5 ppm of H<sub>2</sub>O<sub>2</sub> was

TABLE 1: High-NO<sub>x</sub> Chamber Experiments Conducted

expt no.	VOC <sup>a</sup>	OH precursor <sup>b</sup>	seeded/ <sup>c</sup> nucleation	initial [NO] ppb	initial [NO <sub>2</sub> ] ppb	initial [NO <sub>x</sub> ] ppb	[O <sub>3</sub> ] <sup>d</sup> ppb	T, °C <sup>d</sup>	total SOA mass concentration <sup>d,e,f</sup> μg/m <sup>3</sup>
1	isoprene	H <sub>2</sub> O <sub>2</sub>	nucleation	827	34	860	498	28.5	74
2	isoprene	H <sub>2</sub> O <sub>2</sub>	dry AS	759	112	869	525	28.3	73
3	MACR	H <sub>2</sub> O <sub>2</sub>	dry AS	791	60	850	540	25.2	181
4	MACR	H <sub>2</sub> O <sub>2</sub>	nucleation	898	30	926	519	25.0	197
5	isoprene	H <sub>2</sub> O <sub>2</sub>	nucleation	805	87	891	294	24.3	104
6	isoprene	H <sub>2</sub> O <sub>2</sub>	AAS	825	80	904	450	24.6	111
7 <sup>g</sup>	isoprene	HONO	dry AS	50	333	382	132	20.1	68
8 <sup>g</sup>	isoprene	HONO	nucleation	89	279	366	134	21.4	73
9	isoprene	H <sub>2</sub> O <sub>2</sub>	dry AS	891	74	963	325	24.9	95

<sup>a</sup> All VOC gas phase mixing ratios were 500 ppb. MACR = methacrolein. <sup>b</sup> H<sub>2</sub>O<sub>2</sub> and HONO are not measured directly, but from isoprene decay during irradiation we estimate ~3 ppm of H<sub>2</sub>O<sub>2</sub>, and [HONO] is unlikely greater than measured [NO<sub>2</sub>]. <sup>c</sup> AS = ammonium sulfate seed, AAS = acidic ammonium sulfate seed. <sup>d</sup> Averaged over the course of the filter sampling. <sup>e</sup> Subtraction of seed aerosol taken into account when necessary. SOA volume derived from DMA wall loss uncorrected measurements for use in mass closure from filter sample analyses. <sup>f</sup> Assuming a SOA density of 1.35 g/cm<sup>3</sup>. This value is derived from comparison of DMA aerosol mass measurements. <sup>g</sup> 10% of light bank used and hence lower temperature observed. Also lower amounts of initial NO due to HONO as precursor.

used in each of these experiments based upon isoprene decay during irradiation.<sup>17</sup> All of these experiments were conducted at low relative humidity ( $RH < 5\%$ ) in order to limit the uptake of H<sub>2</sub>O<sub>2</sub> into the particle phase. In the high-NO<sub>x</sub> experiments using H<sub>2</sub>O<sub>2</sub> as an OH source, ~800 to 900 ppb of NO was injected into the chamber. With the HONO source, lower initial NO concentrations were achieved, because the source of NO was HONO photolysis and a NO<sub>x</sub> side-product from the HONO synthesis. Nucleation (seed-free) and ammonium sulfate seeded experiments were also conducted to examine if the presence of seed aerosol has an effect on the chemistry observed. In Experiment 6, acidified ammonium sulfate seed (0.015 M (NH<sub>4</sub>)<sub>2</sub>SO<sub>4</sub> + 0.015 M H<sub>2</sub>SO<sub>4</sub>) was used to investigate the possible effect of acid catalysis on oligomerization reactions, which has previously been observed to occur for other VOC precursors, such as  $\alpha$ -pinene and 1,3,5-trimethylbenzene.<sup>1,3–5,30</sup> No discernible increase in SOA mass is observed for this acid-seeded experiment (Experiment 6) when comparing to its corresponding dry-seeded and nucleation (seed-free) experiments (Experiments 5 and 9).

To illustrate the overall chemical composition typically observed under high-NO<sub>x</sub> conditions, shown in Figure 1a is a first-order (–)ESI-IT mass spectrum obtained via direct infusion analysis of an isoprene SOA sample collected from Experiment 1. Prior work in our laboratory has shown that most organics detected in the negative ion mode occur as the deprotonated molecules ( $[M - H]^-$  ions),<sup>2,3,20</sup> making (–)ESI sensitive for the detection of polar acidic species. As can be seen in Figure 1a, many such species are detected. Observable 102 Da differences between many of the  $[M - H]^-$  ions and the detection of high-MW species (up to MW ~470) indicate the presence of oligomeric species with more than the five carbons of the parent isoprene. Organic nitrate species are detected in this spectrum as even-mass  $[M - H]^-$  ions ( $m/z$  266, 368, and 470).

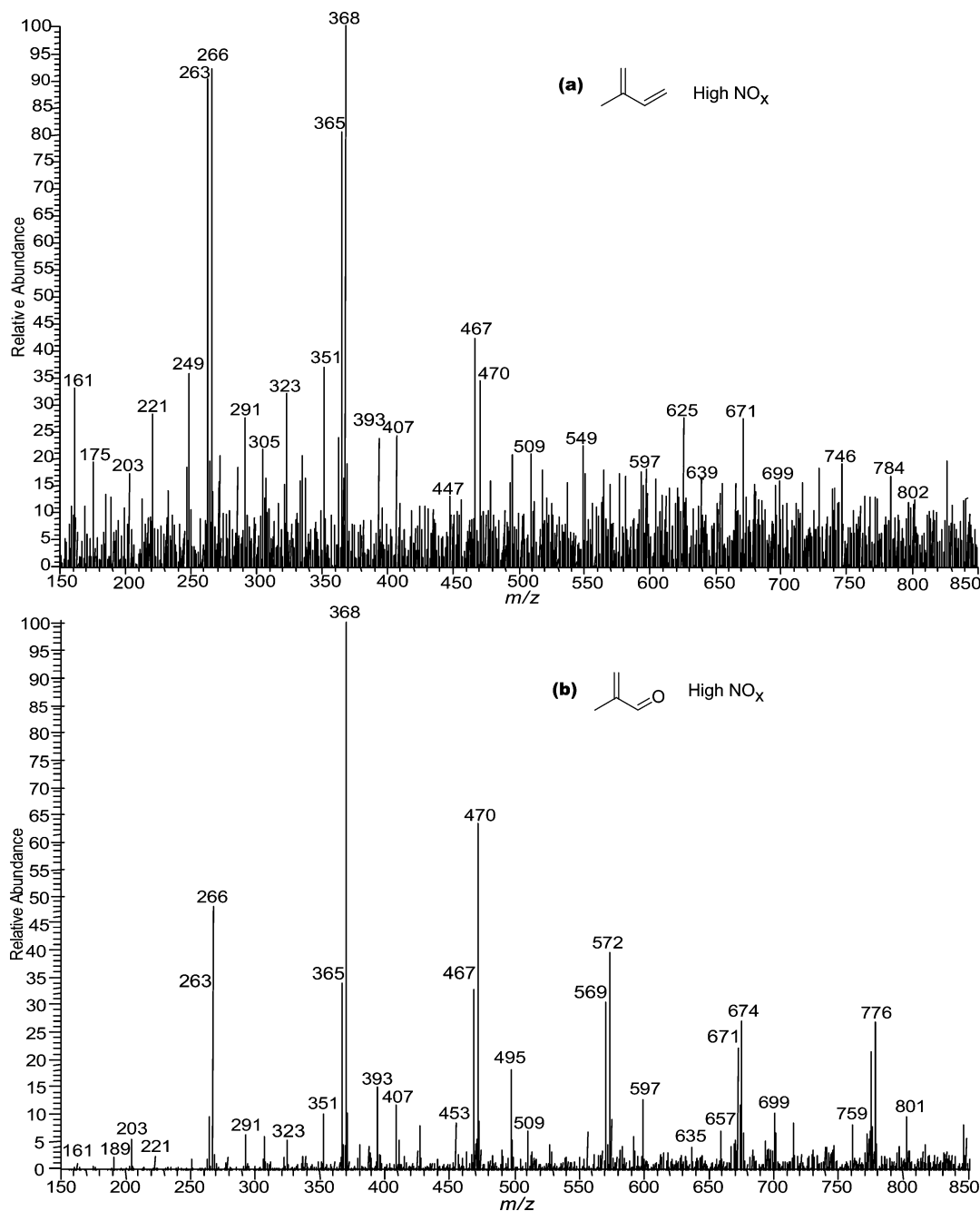
Figure 1b shows, by comparison, a first-order (–)ESI-IT spectrum, also obtained via direct infusion analysis, for a MACR high-NO<sub>x</sub> sample (Experiment 3). Many of the ions detected correspond exactly to those observed from isoprene oxidation (Figure 1a). It should be noted that when the MACR, H<sub>2</sub>O<sub>2</sub>, and dry ammonium sulfate seed aerosol are well-mixed in the chamber under dark conditions, no aerosol growth is observed, confirming that photooxidation is required to produce SOA. The SOA components formed in this MACR experiment (as shown in Figure 1b) extend out to higher MWs than those of isoprene, which is likely a result of the amount of MACR precursor

available in this experiment and also owing to the removal of one oxidation step (the oxidation of isoprene).

The SOA products detected in Figure 1a and b are confirmed by additional mass spectrometry techniques. Figure 2 shows a mass spectrum collected using the MALDI-TOFMS instrument in the positive ion mode for a high-NO<sub>x</sub>, seeded isoprene photooxidation experiment (Experiment 9). SOA components observed here are detected mainly as the sodiated molecules ( $[M + Na]^+$  ions), which is consistent with our experiences in analyzing polymeric standards, such as aqueous glyoxal, with a graphite matrix. In Figure 2, only species that correspond to ions detected in the (–)ESI-IT spectra are highlighted. For example, for the  $[M - H]^-$  ion series detected in (–)ESI-IT spectra at  $m/z$  161, 263, 365, and 467, a corresponding  $[M + Na]^+$  ion series is detected at  $m/z$  185, 287, 389, and 491, respectively, using MALDI-TOFMS. It should be noted that the (+)-ESI-IT spectra also detected the same ions ( $[M + Na]^+$ ) as those of the MALDI technique, confirming that the species observed in Figures 1 and 2 are not a result of ionization artifacts specific to individual techniques.

The LC/MS results obtained in the negative ionization mode are used to quantify the SOA components common to all high-NO<sub>x</sub> isoprene SOA (as detected in Figures 1 and 2). Figure 3a and b show total ion chromatograms (TICs) for an isoprene photooxidation experiment (Experiment 1) and a MACR photooxidation experiment (Experiment 4), respectively, both carried out at high NO<sub>x</sub> in the absence of seed aerosol. These TICs show that many of the SOA products formed in each system are the same because the retention times ( $RT$ s) are comparable and the  $m/z$  values of the molecular ion species ( $[M - H]^-$ ) associated with each chromatographic peak are the same. Shown in Figure 3c–e are extracted ion chromatograms (EICs) for three organic nitrate species ( $[M - H]^-$  at  $m/z$  266, 368, and 470) common to both isoprene and MACR high-NO<sub>x</sub> photooxidation experiments. For each chamber experiment, EICs were used instead of TICs for the quantification of each  $[M - H]^-$  ion detected in order to deconvolute any coeluting species. Figure 4a shows a mass spectrum recorded for the largest chromatographic peak ( $RT = 15.7$  min) from the EIC of  $m/z$  368 (Figure 3d). The  $m/z$  759 ion that is also detected in this mass spectrum is a cluster ion corresponding to  $[2M + Na - 2H]^-$ ; such cluster ions are commonly observed in (–)LC/ESI-MS conditions. In Figure 4b is a resultant upfront CID mass spectrum taken for this same chromatographic peak, showing many product ions from the dissociation of  $m/z$  368. The product ion  $m/z$  305 corresponds to a neutral loss of 63 Da, which is



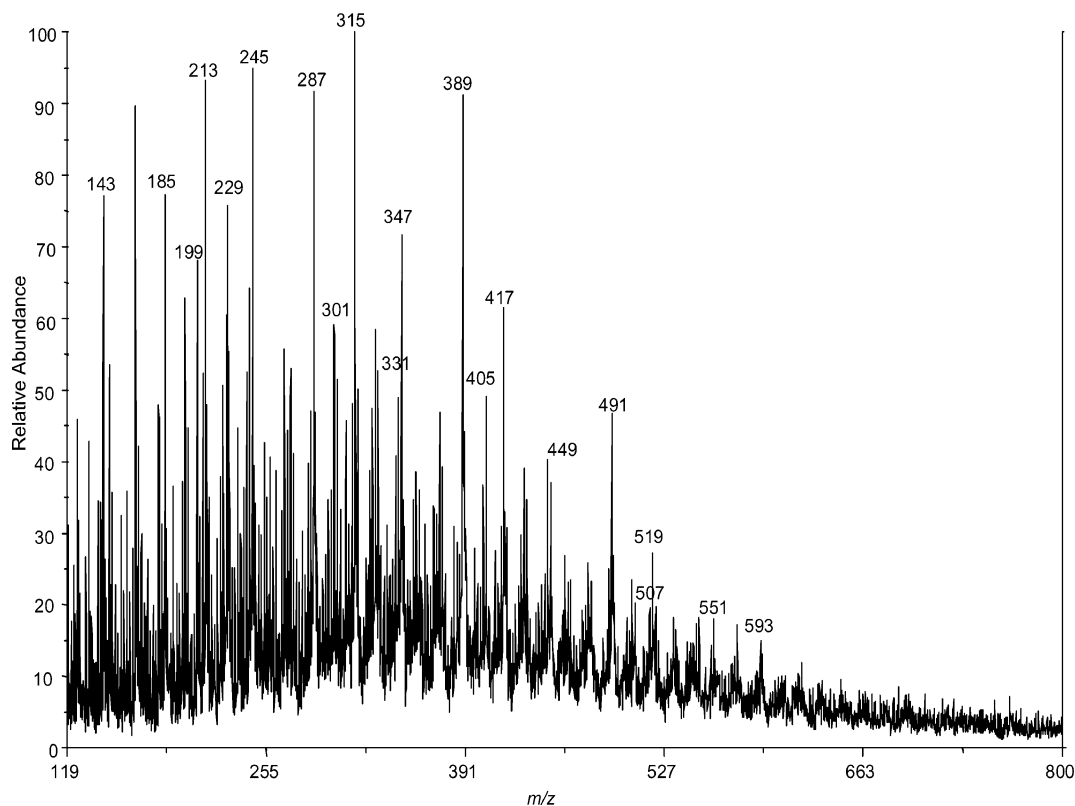


**Figure 1.** ESI-ITMS negative mode spectra collected via direct infusion analyses. (a) MS scan of a filter extract obtained from a 500 ppb isoprene, high- $\text{NO}_x$ , seeded experiment. (b) MS scan of a filter extract obtained from a 500 ppb MACR, high- $\text{NO}_x$ , seeded experiment. These mass spectra show that MACR oxidation produces many of the same SOA products as that of isoprene oxidation under high- $\text{NO}_x$  conditions. Common 102 Da differences between ions in both spectra are observed indicating the presence of oligomers.

likely nitric acid ( $\text{HNO}_3$ ). Another product ion  $m/z$  291 corresponds to neutral loss of 77 Da, likely from the combined losses of a methyl ( $\text{CH}_3$ ) radical and a nitrate ( $\text{NO}_3$ ) radical (or  $\text{CH}_3\text{ONO}_2$ ). The neutral loss of 102 Da results in the product ion  $m/z$  266; these types of product ions are used to aid in the structural elucidation of SOA components and will be discussed subsequently. Owing to the lack of available authentic oligomeric standards, quantification was carried out by using a series of calibration curves generated from surrogate standards (listed in the Experimental Section) covering the wide range of  $R_T$ s for all detected species. Each surrogate standard contained a carboxylic acid group, the likely site of ionization for detected SOA components, except for the *meso*-erythritol standard. Because of the initial high percentage of aqueous buffer present in the LC/MS gradient, we were able to detect small polar

organics, such as 2-methylglyceric acid. To quantify this compound, the polyol *meso*-erythritol, detected as the  $[M - \text{H} + \text{acetic acid}]^-$  ion, was used. Unlike *meso*-erythritol, 2-methyltetrols (and other polyols) were not detected using the  $(-)$ -LC/MS technique. All surrogate standards were within ca.  $\pm 1.5$  min of the  $R_T$ s of the detected SOA components. Table 2 shows the LC/MS quantification results for high- $\text{NO}_x$  SOA. Four types of oligomers are quantified here. For ease of comparison, experiments corresponding to the same VOC and OH precursor type are grouped together under the same column heading.

SOA components observed thus far are not artifacts formed on filters and are observed over varying isoprene concentrations, as confirmed by online particle mass spectrometry. Figure 5 shows mass spectra collected from three high- $\text{NO}_x$  chamber experiments using the Aerodyne TOF-AMS instrument. In these



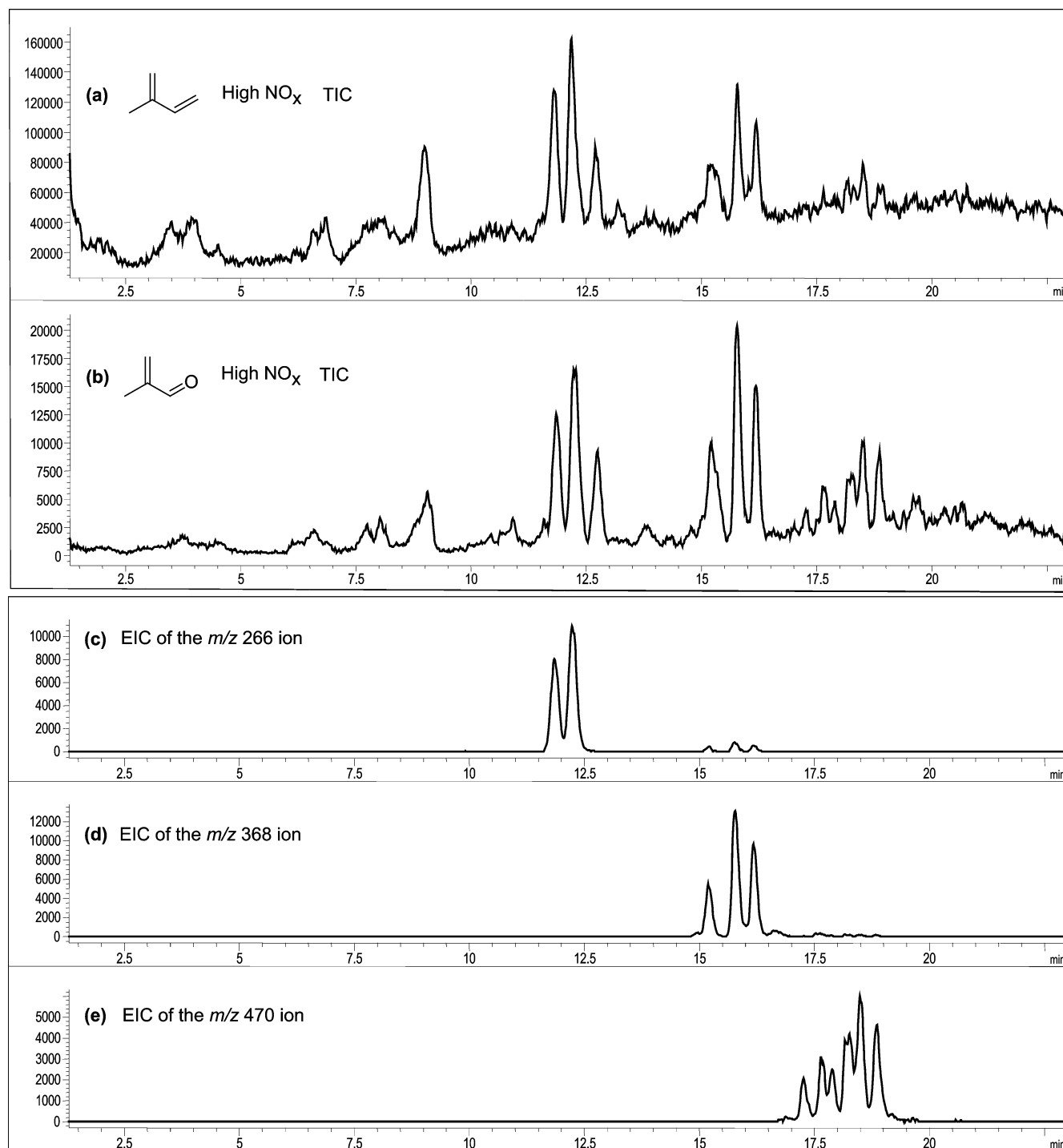
**Figure 2.** MALDI positive mode spectrum obtained with a graphite matrix for a 500 ppb isoprene, high- $\text{NO}_x$ , dry seeded experiment (Experiment 9). Highlighted  $\text{Na}^+$  adduct ions confirm the existence of the species detected by ESI.

experiments, the TOF-AMS instrument was operated at  $\sim 160^\circ\text{C}$  to lessen the degree of thermal fragmentation of the high-MW SOA components. Figure 5a shows a TOF-AMS spectrum collected for a 50 ppb isoprene, high- $\text{NO}_x$  nucleation experiment (not included in Table 1 because of insufficient aerosol mass for offline chemical analysis techniques). Even at these isoprene concentrations, high-MW species are detected in the SOA produced. Differences of 102 Da are noted in this spectrum, again indicating the presence of oligomers. The oligomers present here confirm the species detected by the  $(-)$ ESI and  $(+)$ MALDI techniques (Figures 1 and 2, respectively), where the observed TOF-AMS ions result from a loss of a hydroxyl (OH) radical from the molecular ion (i.e.,  $\alpha$ -cleavage of a hydroxyl radical from a carboxylic acid group). ESI detects these oligomers as the  $[M - \text{H}]^-$  ion and MALDI as the  $[M + \text{Na}]^+$  ion, so ions measured in the TOF-AMS instrument are lower by 16 and 40 units, respectively. For example, ions of  $m/z$  145, 187, 247, and 289 measured by the TOF-AMS instrument (Figure 5), correspond to  $m/z$  161, 203, 263, and 305, respectively, using  $(-)$ ESI (Figure 1). Four different series of oligomers are highlighted in this spectrum, where ions of the same oligomeric series are indicated in a common color. Figure 5b corresponds to a MACR high- $\text{NO}_x$ , dry seeded experiment, in which a filter sample was collected (Experiment 3), showing the same oligomeric signature to that of the low concentration (50 ppb) isoprene experiment. Figure 5c corresponds to an isoprene high- $\text{NO}_x$ , HONO experiment (Experiment 8). Again, many ions at the same  $m/z$  values are detected, as those of Figures 5a and 5b, suggesting the chemical components of the SOA are the same in these samples. Though probably present, oligomeric compounds formed under conditions similar to those of Figure 5c were not detected in the original study of SOA formation from this laboratory<sup>16</sup> because a less-sensitive quadrupole AMS was used; such high-MW species were reported

in a subsequent study using the TOF-AMS.<sup>17</sup> These online chemical results confirm that the 102 Da differences observed in the offline analytical techniques (ESI and MALDI) are not a result of sample workup or ionization artifacts. Also, these online chemical results suggest that seeded versus nucleation experiments do not lead to significant differences in the chemistry observed, in agreement with the ESI analyses. The OH precursor ( $\text{HONO}$  or  $\text{H}_2\text{O}_2$ ) also does not have a substantial effect on the chemistry observed (i.e., similar products formed, however, abundances may vary), an observation that is also consistent with the offline mass spectrometry analyses.

PILS/IC measurements were carried out for Experiments 1 (nucleation) and 2 (dry seeded). In both experiments, the acetate anion was the most abundant organic anion detected ( $14.72\ \mu\text{g}/\text{m}^3$  in Experiment 1 and  $23.47\ \mu\text{g}/\text{m}^3$  in Experiment 2) followed by the formate anion ( $1.18\ \mu\text{g}/\text{m}^3$  in Experiment 1 and  $2.90\ \mu\text{g}/\text{m}^3$  in Experiment 2). It should be noted that these two ions elute off the IC column immediately after sample injection, and there is a possibility that other early-eluting monocarboxylic acid species coeluted with these two species leading to an overestimate of their mass. In addition, the extent to which the acetate and formate levels quantified here represent decay products from oligomers detected in the particle phase is uncertain. It is likely that a significant fraction of this mass results from the decomposition of oligomers at the sample collection conditions (high water concentrations and temperatures) in the PILS instrument and possibly by the use of potassium hydroxide (KOH) as the eluent for anion analyses in the IC instrument.

GC/MS with TMS derivatization (restricted to carboxyl and hydroxyl groups) was employed to determine the functional groups present within SOA components formed under high- $\text{NO}_x$  conditions. Figure 6a shows a GC/MS TIC of a high- $\text{NO}_x$  isoprene nucleation experiment (Experiment 5). 2-methylglyceric

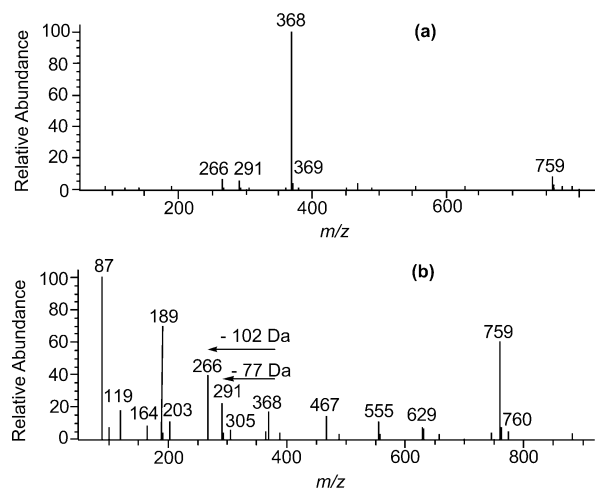


**Figure 3.** (a) LC/MS TIC of a filter extract from a 500 ppb isoprene, high-NO<sub>x</sub>, nucleation experiment. (b) LC/MS TIC of a filter extract from a 500 ppb MACR, high-NO<sub>x</sub>, nucleation experiment. The similar retention times and mass spectra associated with each chromatographic peak in these two TICs indicate that MACR is an important SOA precursor from isoprene oxidation under high-NO<sub>x</sub> conditions. c–e are LC/MS EICs of organic nitrate species common to both MACR and isoprene high-NO<sub>x</sub> samples. These organic nitrate ions are a part of the same oligomeric series confirmed by MS/MS analyses.

acid (2-MG), detected previously in ambient and laboratory filter samples,<sup>10,11,13,14</sup> was found to elute from the GC column at 29.08 min. The corresponding EI mass spectrum for this peak is shown in Figure 6b. The chemical structure of trimethylsilylated 2-MG, along with its respective MS fragmentation, is also shown in this mass spectrum. Using GC-FID to quantify the amount of 2-MG present in this same sample, it was found that 3.8  $\mu\text{g}/\text{m}^3$  was formed, which accounted for  $\sim 3.7\%$  of the SOA mass. This was consistent with LC/MS measurements of 2-MG from other high-NO<sub>x</sub> isoprene nucleation experiments

(such as 2.7% of the SOA mass for Experiment 1). A *di*-ester peak was observed to elute from the GC column at 51.59 min. The corresponding EI mass spectrum for this chromatographic peak is shown in Figure 6c along with its proposed chemical structure and MS fragmentation pattern.

**3.2. Low-NO<sub>x</sub> Condition.** Table 3 lists nine low-NO<sub>x</sub> chamber experiments. All experiments were conducted with H<sub>2</sub>O<sub>2</sub> as the OH radical precursor with no added NO<sub>x</sub>. Ozone formation is attributed mainly to residual NO<sub>x</sub> emitted by the chamber walls; these O<sub>3</sub> concentrations observed likely have a



**Figure 4.** (a) Mass spectrum for the largest chromatographic peak ( $RT = 15.7$  min) from Figure 3d (EIC of  $m/z$  368 ion). (b) Upfront CID mass spectrum for the same chromatographic peak in Figure 3d (EIC of  $m/z$  368 ion). The neutral losses observed in the upfront CID mass spectrum are associated with a trimeric organic nitrate species. This fragmentation pattern of  $m/z$  368 is consistent with ion trap MS/MS results. The product ion  $m/z$  266 corresponds to a neutral loss of 102 Da (common to all MS techniques), the product ion  $m/z$  291 corresponds to a neutral loss of 77 Da (likely  $\text{CH}_3$  radical and  $\text{NO}_3$  radical,  $\text{CH}_3\text{-NO}_3$ ), the product ion  $m/z$  305 corresponds to a neutral loss of 63 Da (likely  $\text{HNO}_3$ ), the product ion  $m/z$  203 corresponds to a neutral loss of 165 Da, and the product ion  $m/z$  164 corresponds to a neutral loss of 204 Da (two losses of common monomer).

negligible effect on the gas-phase chemistry because of the slow reactivity of  $\text{O}_3$  toward isoprene. Experiments were conducted with 50% of the light banks in the chamber except for Experiments 10 and 11, in which 100% of the light banks were used and resulted in the higher temperatures observed. All experiments were conducted with 500 ppb of isoprene except for Experiment 17, in which 100 ppb of isoprene was used. As in the high- $\text{NO}_x$  experiments, these experiments were conducted at low relative humidity ( $RH < 9\%$ ) in order to limit the uptake of  $\text{H}_2\text{O}_2$  into the particle phase. Nucleation (seed-free) and seeded (ammonium sulfate and acidified ammonium sulfate) experiments were conducted in order to examine if the presence of seed aerosol has an effect on the chemistry observed. Assuming a density of  $\sim 1.25 \text{ g/cm}^3$  (derived from the comparison of DMA aerosol volume and TOF-AMS aerosol mass measurements), acid seeded ( $0.015 \text{ M } (\text{NH}_4)_2\text{SO}_4 + 0.015 \text{ M } \text{H}_2\text{SO}_4$ ) experiments formed the largest amounts of SOA mass ( $\sim 259 \mu\text{g/m}^3$  for Experiment 14) compared to the corresponding nucleation ( $\sim 72.5 \mu\text{g/m}^3$  for Experiment 12) and ammonium sulfate seeded experiments ( $\sim 72.8 \mu\text{g/m}^3$  for Experiment 15). Lower mixing ratios of isoprene (Experiment 17) in the presence of acid seed also resulted in larger amounts of SOA when compared to the nucleation and ammonium sulfate seeded experiments.

No particle-phase organics were detected using (–) and (+)-ESI techniques. Analysis of filter sample extracts using these techniques were nearly identical to the blank and control filters. This shows that SOA components at low- $\text{NO}_x$  conditions are not acidic in nature like those of the high- $\text{NO}_x$  SOA. Because of the expected presence of hydroperoxides and polyols, other analytical techniques, such as the iodometric-spectrophotometric method and GC/MS with TMS derivatization, were employed to understand the chemical nature of low- $\text{NO}_x$  SOA. The peroxide aerosol mass concentration was measured for all experiments except for Experiments 12, 13, and 16. The

iodometric-spectrophotometric method measures the total peroxide content (sum of  $\text{ROOH}$ ,  $\text{ROOR}$ , and  $\text{H}_2\text{O}_2$ ) of the aerosol, but because no peroxides were measured from filters collected from air mixtures containing isoprene,  $\text{H}_2\text{O}_2$ , and seed aerosol, it is assumed that the peroxides measured are organic peroxides. The nucleation experiments (Experiments 10 and 18a) had the highest contribution of peroxides ( $\sim 61\%$  on average) to the SOA mass observed. Dry ammonium sulfate (Experiments 11 and 15) and acidified ammonium sulfate seeded experiments (Experiments 14 and 17) led to comparable contributions of organic peroxides to the overall SOA mass ( $\sim 25$  and  $30\%$ , respectively). Quality control tests were conducted by the addition of ammonium sulfate to standard solutions of benzoyl peroxide to test if the seed had an effect on the UV–vis measurement of total peroxides. The amount of ammonium sulfate added to the benzoyl peroxide standards was determined by the ratio of SOA volume growth to the typical ammonium sulfate seed volume employed ( $\sim 3:1$ ) as determined from the DMA. Little difference was observed ( $\sim 0.6\%$ ), showing that ammonium sulfate seed has a negligible effect on the measurement of peroxide content from seeded experiments. As observed previously,<sup>17</sup> the SOA mass was found to decrease rapidly in nucleation experiments after reaching peak growth, and as a result, the peroxide content of the SOA was measured at different times in Experiment 18. The iodometric-spectrophotometric measurement made at the peak growth in the aerosol volume, as determined from the DMA, for Experiment 18, showed that the peroxides accounted for  $\sim 59\%$  of the total SOA mass. Twelve hours later, once the aerosol volume decay reached its constant value, the peroxide contribution to the SOA mass was found to have dropped to  $26\%$ .

Figure 7 shows a (+)MALDI mass spectrum for a low- $\text{NO}_x$  acid-seed experiment (Experiment 14). The  $m/z$  range (49–620) of ion species observed was not significantly different from (+)-MALDI results obtained for nonacid-seeded experiments. The abundances of these ions were higher for the acid experiments, but quantification of these species is not possible because of uncertainties in the ionization efficiencies. In the absence of seed MALDI signal was low or nonexistent, likely due to very low ionization efficiencies in the absence of a sulfate matrix. Quantification is also difficult with MALDI because of inconsistencies and inhomogeneities of sample preparation and lack of understanding of sample matrix effects.<sup>31</sup> It is clear, however, that oligomerization occurs in low- $\text{NO}_x$  SOA. Common 14, 16, and 18 Da differences are observed between many peaks throughout this spectrum. Structural elucidation of these peaks in Figure 7 was not possible using the (+)MALDI technique owing to the inability of performing MS/MS experiments on selected ions from the sample matrix.

Figure 8 shows two TOF-AMS mass spectra for a 500 ppb, low- $\text{NO}_x$  nucleation experiment (Experiment 12) in the  $m/z$  range of 200–450. These mass spectra also indicate the existence of oligomeric components for low- $\text{NO}_x$  SOA. The mass spectrum in Figure 8a was collected at a low vaporizer temperature ( $\sim 150^\circ\text{C}$ ) while that in Figure 8b was collected at a higher temperature ( $\sim 600^\circ\text{C}$ ). The presence of more higher-mass peaks at high vaporizer temperatures (Figure 8b) may indicate that the low- $\text{NO}_x$  oligomers are heterogeneous, with some series of oligomers being easily volatilized below  $200^\circ\text{C}$  while others are not volatile at these temperatures.

The chemical composition of the SOA formed under low- $\text{NO}_x$  conditions was found to change over the course of the experiment. The evolution of selected ions and of the total organic mass measured by the TOF-AMS instrument is shown

**TABLE 2: Quantified SOA Products (in ng/m<sup>3</sup>) from High-NO<sub>x</sub> Chamber Experiments**

			isoprene/high NO <sub>x</sub> /H <sub>2</sub> O <sub>2</sub>				MACR/high NO <sub>x</sub> /H <sub>2</sub> O <sub>2</sub>		isoprene/HONO	
	[M - H] <sup>-</sup> ion	surrogate standard used for quantification <sup>a</sup>	expt 1	expt 2	expt 6	expt 9	expt 3	expt 4	expt 7	expt 8
mono-nitrate oligomers	266	pimelic acid	1970	4170	3890	3910	9360	3860	1470	830
	368	pinic acid	1350	2450	3700	4440	20600	10100	830	750
	470	pinic acid	2330	2930	2300	2640	28900	16700		210
	572	pinic acid	<sup>b</sup>				2960	6810		
	674	suberic acid monomethyl ester					670	710		
	776	suberic acid monomethyl ester					220	450		
	878	suberic acid monomethyl ester						210		
total mass from mono-nitrate oligomers (μg/m <sup>3</sup> )			5.65	9.55	9.89	11.0	62.7	38.8	2.30	1.79
% contribution to the total SOA mass			8	13	9	12	35	20	3	2
2-MG <sup>c</sup> oligomers	119	meso-erythritol	2050	3170	9680	4500	1240	460	4170	11600
	221	citramalic acid	1170	2590	2330	2110	3840	1720	550	1000
	323	2-hydroxy-3-methylbutyric acid	630	970	430	470	2740	1320	70	160
	425	pimelic acid		280	290	260	1650	680		130
	527	pimelic acid					720	480		
total mass from 2-MG oligomers (μg/m <sup>3</sup> )			3.85	7.01	12.7	7.34	10.2	4.66	4.79	12.9
% contribution to the total SOA mass			5	10	11	8	6	2	7	18
mono-acetate oligomers	161	citramalic acid		40	100		90		110	70
	263	2-hydroxy-3-methylbutyric acid	680	1720	600	670	4070	1300	360	160
	365	pimelic acid	770	1890	820	1240	4830	1760	250	290
	467	pinic acid	340	450	180	420	3750	1310		130
	569	pinic acid		790			8600	2960		
	671	suberic acid monomethyl ester					450	360		
total mass from mono-acetate oligomers (μg/m <sup>3</sup> )			1.79	4.89	1.70	2.33	21.8	7.69	0.72	0.65
% contribution to the total SOA mass			2	7	2	2	12	4	1	1
mono-formate oligomers	147	meso-erythritol	200	380	11300		200			1370
	249	2-hydroxy-3-methylbutyric acid	460	1340		40	1970	810	60	
	351	2-hydroxy-3-methylbutyric acid	370	1000		60	2880	1390	30	
	453	pimelic acid	290	380			1800	710		
total mass from mono-formate oligomers (μg/m <sup>3</sup> )			1.32	3.10	11.3	0.10	6.85	2.91	0.09	1.37
% contribution to the total SOA mass			2	4	10	0.1	4	1	0.1	2
total mass identified (g/m <sup>3</sup> )			12.6	24.6	35.6	20.8	102	54.1	7.90	16.7
% of SOA identified			17	34	32	22	56	27	12	23

<sup>a</sup> Surrogate standards used covered the range of retention times for detected [M-H]<sup>-</sup> ions. All standards used were within ± 1.5 minutes of retention times for sample [M-H]<sup>-</sup> ions. <sup>b</sup> A blank cell indicates that the corresponding species was below the detection limit. <sup>c</sup> 2-MG = 2-methylglyceric acid.

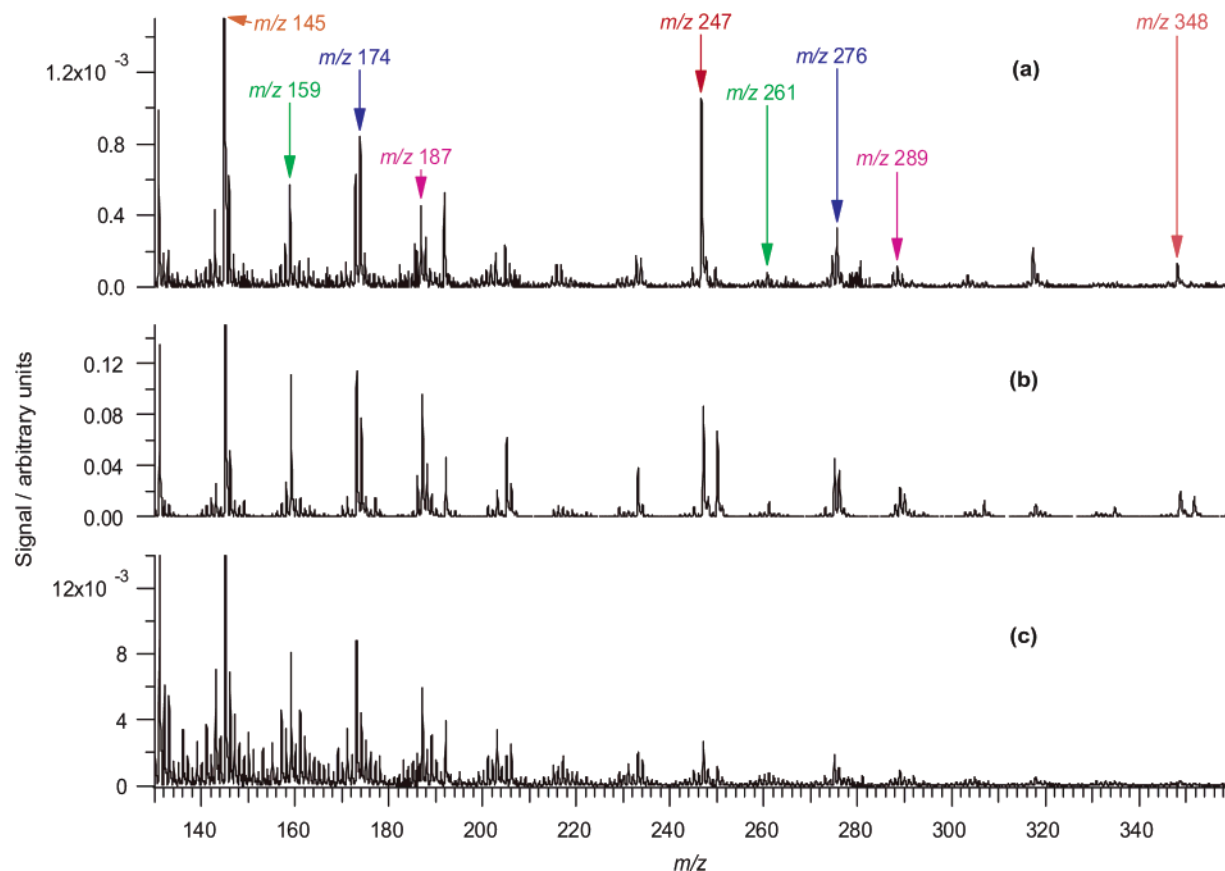
in Figure 9. All ion signal intensities shown here are divided by the signal intensity of sulfate to correct for loss of particle mass to the chamber walls. Figure 9a shows the evolution of two prominent high-mass fragment ions *m/z* 247 and 327. These high-mass fragment ions increase in abundance with time, with the increase in *m/z* 327 being more significant. This increase is observed for all high-mass (*m/z* > 200) fragment ions. Figure 9b shows the change in the intensity of the fragment ion *m/z* 91, which is proposed to serve as a tracer ion for peroxides formed under low-NO<sub>x</sub> conditions, where the proposed formula for this fragment ion is C<sub>3</sub>H<sub>7</sub>O<sub>3</sub>, and the structure for one of its isomers is shown in Figure 9b. This peroxide tracer ion reaches its maximum signal after 7 h have elapsed in the experiment. Over the next 6 h, this ion decreases to a lower constant value; such a loss cannot be attributed to wall loss processes because the *m/z* 91 signal has already been normalized to the sulfate signal. Figure 9c shows the time evolution of the organic mass from Experiment 13. The organic mass also decreases slightly after reaching its peak value; however, the decrease observed for the organic mass is much lower than that of the peroxide tracer ion (*m/z* 91).

PILS/IC data were collected for some low-NO<sub>x</sub> experiments. Aerosol mass concentrations of acetate were much lower than those in the high-NO<sub>x</sub> case. For example, for Experiment 12, the acetate anion accounted for only 1.67 μg/m<sup>3</sup>, ~14–22 times lower than that of high-NO<sub>x</sub> levels. Formate anion was detected

at comparable mass concentrations to that of the high-NO<sub>x</sub> experiments (~1.51 μg/m<sup>3</sup>). Again, it should be noted that these two ions elute off the IC column immediately after sample injection and there is a possibility that other early-eluting monocarboxylic acid species coeluted with these two species, leading to an overestimate of their mass. No other organic anions were detected at significant levels from these low-NO<sub>x</sub> experiments.

Figure 10a shows a GC/MS TIC of a low-NO<sub>x</sub>, dry ammonium sulfate seeded experiment (Experiment 13). The chromatographic peaks at *RT* = 31.21, 32.25, and 32.61 min correspond to isomeric C<sub>5</sub> alkene triol species (*cis*-2-methyl-1,3,4-trihydroxy-1-butene, 3-methyl-2,3,4-trihydroxy-1-butene, *trans*-2-methyl-1,3,4-trihydroxy-1-butene, respectively), which have been measured previously in ambient aerosol from the Amazonian rainforest and Finnish boreal forests.<sup>11,12</sup> This is the first detection of these species in a controlled laboratory chamber experiment. The chromatographic peaks at *RT*s 38.22 and 38.97 min correspond to the 2-methyltetrols (2-methylthreitol and 2-methylerythritol, respectively), which also have been detected in ambient aerosol studies,<sup>7,10,11,13</sup> as well as in one previous photooxidation chamber study.<sup>14</sup> The C<sub>5</sub> alkene triols and 2-methyltetrols have received much attention in prior studies; the corresponding mass spectra for their respective chromatographic peaks can be found in Figure 1S (Supporting Information). GC-FID measurements were made to quantify the





**Figure 5.** TOF-AMS spectra collected at low vaporizer temperatures for the following high- $\text{NO}_x$  chamber experiments: (a) 50 ppb isoprene, 250 ppb  $\text{NO}_x$ ,  $\text{H}_2\text{O}_2$  as the OH precursor, no seed; (b) 500 ppb MACR, 800 ppb  $\text{NO}_x$ ,  $\text{H}_2\text{O}_2$  as the OH precursor, with seed; and (c) 500 ppb isoprene, HONO as the OH precursor, no seed. These spectra indicate that the OH precursor does not have a substantial effect on the chemistry observed, that MACR is an important SOA precursor from isoprene oxidation, and that the 102 Da differences observed in the offline mass spectrometry data are not a result of sample workup or ionization artifacts.

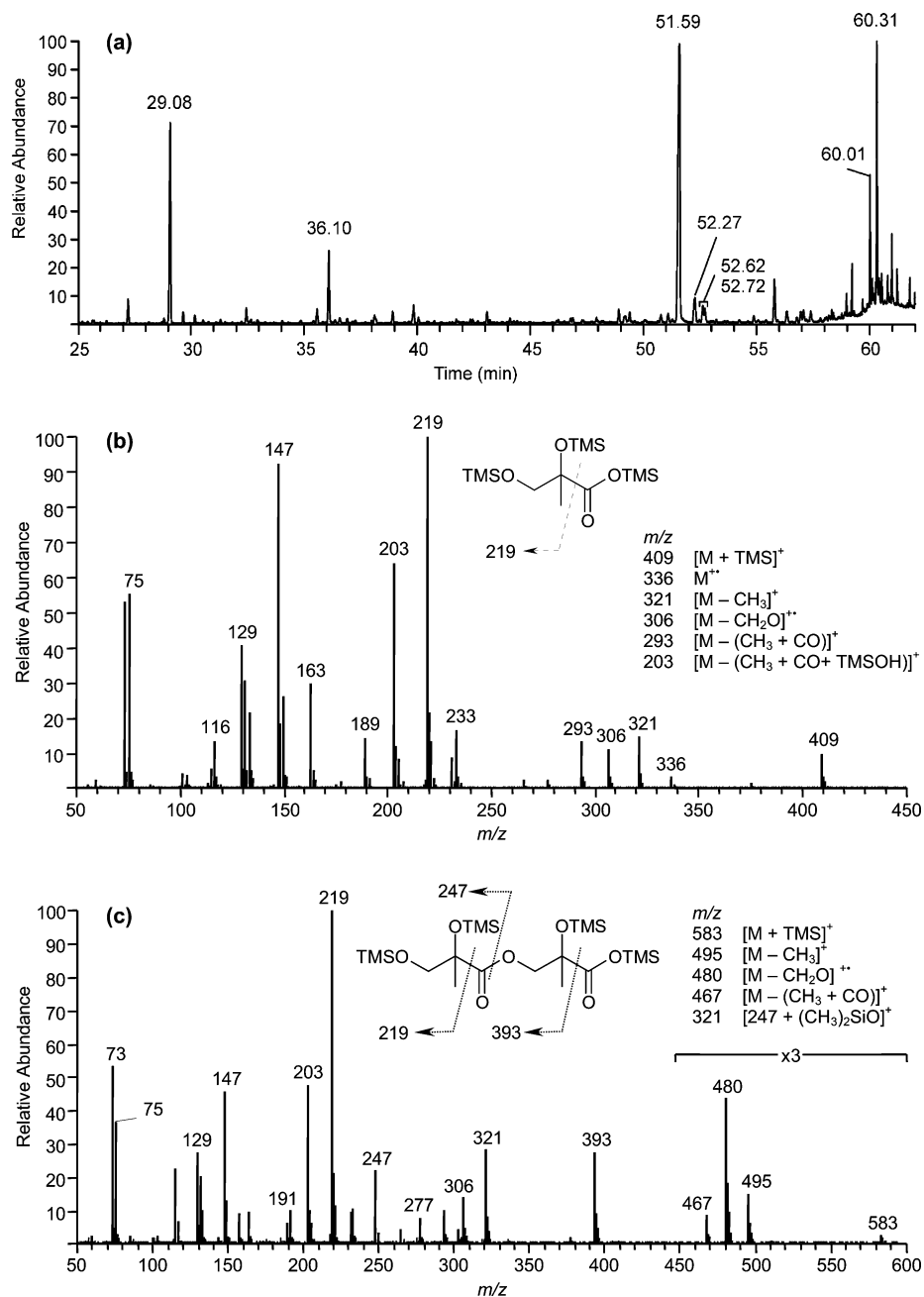
2-methyltetrols and  $\text{C}_5$  alkene triols for a low- $\text{NO}_x$  dry seeded experiment (Experiment 13—peaks in Figure 10a) and a low- $\text{NO}_x$  acid seeded experiment (Experiment 14). It was found that the 2-methyltetrols and  $\text{C}_5$  alkene triols accounted for 3.91% and 0.60% of the SOA mass, respectively, for the dry seeded experiment (Experiment 13), and decreased to 0.46% and 0.06% of the SOA mass, respectively, for the acid seeded experiment (Experiment 14). The inset shown in Figure 10a is the  $m/z$  219 EIC for six isomeric dimers ( $\text{MW} = 254$ ) eluting between 58.8 and 59.2 min. The corresponding averaged EI mass spectrum for these chromatographic peaks is shown in Figure 10b. The general chemical structure of the trimethylsilylated dimer, along with its respective MS fragmentation, is also shown in this mass spectrum. The fragmentation pattern shown here indicates that the dimer forms by the reaction of a  $\text{C}_5$  alkene triol (indicated by the  $m/z$  335 fragment ion) with a 2-methyltetrol (indicated by the  $m/z$  219 fragment ion) to form the hemiacetal dimer shown. To confirm the MW of the isomeric hemiacetal dimers eluting between 58.8 and 59.2 min, an averaged CI( $\text{CH}_4$ ) mass spectrum was also collected and is shown in Figure 10c. The MW of the trimethylsilylated dimer (derivatized MW = 686) is confirmed by the  $[M + \text{H} - \text{CH}_4]^+$  ion at  $m/z$  671. The SOA products that elute at 34.91 and 35.47 min were tentatively characterized as diastereoisomeric 2-methyltetrol performate derivatives, which are unstable and upon reaction in the trimethylsilylation reagent mixture are converted into 2-methyltetrols. Their corresponding EI mass spectra can also be found in Figure 1S (Supporting Information). It should be noted that the peaks labeled \*1, \*2, and \*3 in the GC/MS TIC (Figure

10a) were also present in the laboratory controls and were identified as palmitic acid, stearic acid, and palmitoyl monoglyceride, respectively. Table 4 summarizes all low- $\text{NO}_x$  SOA components elucidated by GC/MS.

#### 4. Discussion

**4.1. Gas-Phase Chemistry.** Gas-phase oxidation of isoprene is dominated by the reaction with OH.<sup>16,17</sup> Under high- $\text{NO}_x$  conditions,  $\text{O}_3$  and  $\text{NO}_3$  radicals play only a minor role in the initial oxidation of isoprene because they form only once  $[\text{NO}]$  approaches zero, by which time most of the isoprene is consumed. Under low- $\text{NO}_x$  conditions,  $\text{O}_3$  and  $\text{NO}_3$  radicals also contribute negligibly to isoprene oxidation. Figure 11 shows the initial gas-phase reactions that occur under both low- and high- $\text{NO}_x$  conditions. In both cases, the initial oxidation of isoprene occurs by reaction with OH, followed by the immediate addition of  $\text{O}_2$  to form eight possible isomeric isoprene hydroperoxy ( $\text{RO}_2$ ) radicals (for simplicity, only three are shown).

Under high- $\text{NO}_x$  conditions, the isoprene hydroperoxy radicals react predominantly with NO; however, they may also react with  $\text{NO}_2$  to form peroxy nitrates ( $\text{ROONO}_2$ , not shown in Figure 11), but these are likely unimportant to the formation of isoprene SOA because of their thermal instability.  $\text{RO}_2 + \text{NO}$  reactions result in the formation of either hydroxynitrates or hydroxyalkoxy ( $\text{RO}$ ) radicals. Our observations of organic nitrates in high- $\text{NO}_x$  SOA as observed in Figure 1 ( $[M - \text{H}]^-$  ions with even  $m/z$  values) indicate that these hydroxynitrates



**Figure 6.** (a) TIC of a high- $\text{NO}_x$  isoprene nucleation experiment (Experiment 5) collected using GC/MS in the EI mode. (b) EI mass spectrum for the 2-MG residue ( $RT = 29.08$  min). (c) EI mass spectrum for a linear dimer made up of two 2-MG residues ( $RT = 51.59$  min). These two mass spectra confirm that 2-MG is present in high- $\text{NO}_x$  SOA and that it is involved in particle-phase esterification reactions resulting in polyesters (as shown by the dimer structure above).

are likely SOA precursors. Two of the hydroxyalkoxy radicals decompose into MVK and MACR, where their yields are 32–44% and 22–28%, respectively.<sup>32–35</sup> The remaining hydroxyalkoxy radical forms a 1,4-hydroxycarbonyl, which may isomerize and dehydrate to form 3-methylfuran.<sup>36</sup> SOA formation has been observed from the photooxidation of MACR and 3-methylfuran, indicating that these are SOA precursors (indicated by black boxes in Figure 11).<sup>17</sup> However, 3-methylfuran is not expected to contribute greatly to the SOA formed by isoprene oxidation because of its low gas-phase product yield (<2–5%).<sup>33–35</sup> The higher gas-phase product yields observed for MACR suggest that it is the most important SOA precursor from isoprene oxidation under high- $\text{NO}_x$  conditions; this is consistent with the similarities of the chemical products observed in isoprene and MACR SOA (Figure 1 and Table 2). Even though

MVK typically has the highest gas-phase product yield observed, it is not a contributor to SOA formation under high- $\text{NO}_x$  conditions because negligible amounts of aerosol were produced from the high- $\text{NO}_x$  photooxidation of 500 ppb MVK. Other products of isoprene oxidation under high- $\text{NO}_x$  conditions (not shown in Figure 11) include  $\text{C}_5$  hydroxycarbonyls,  $\text{C}_4$  hydroxycarbonyls, and  $\text{C}_5$  carbonyls; these may contribute to SOA formation, but experimental evidence is currently lacking.

Under low- $\text{NO}_x$  conditions, the isoprene hydroxyperoxy radicals react predominantly with  $\text{HO}_2$ . These reactions result in the formation of hydroxy hydroperoxides, which are highlighted in dotted boxes to indicate that these species are possible SOA precursors. Under similar reaction conditions, Miyoshi et al.<sup>32</sup> observed by IR spectroscopy that hydroperoxides are major gas-phase products from isoprene oxidation under  $\text{NO}_x$ -

TABLE 3: Low-NO<sub>x</sub> Chamber Experiments Conducted

expt no. <sup>a,b</sup>	seeded <sup>c</sup> / nucleation	[O <sub>3</sub> ] <sup>d</sup> ppb	T, °C <sup>d</sup>	total SOA mass concentration <sup>d,e,f</sup> μg/m <sup>3</sup>	peroxide aerosol mass concentration μg/m <sup>3</sup>	% contribution of peroxides to the SOA mass concentration observed
10 <sup>g</sup>	nucleation	32	29.1	186	116	62
11 <sup>g</sup>	dry AS	36	28.7	282	97	34
12	nucleation	b.d.l.	23.7	73	<sup>h</sup>	<sup>h</sup>
13	dry AS	12	24.1	69	<sup>h</sup>	<sup>h</sup>
14	AAS	b.d.l.	23.8	259	67	26
15	dry AS	11	23.9	73	19	25
16 <sup>i</sup>	dry AS	2	25.6	24	<sup>h</sup>	<sup>h</sup>
17	AAS	b.d.l.	23.6	93	23	24
18a	nucleation	7	26.2	55	32	59
18b <sup>j</sup>	nucleation	37	27.0	22	6	26

<sup>a</sup> All VOC gas-phase mixing ratios were 500 ppb, except for Experiment 17 (100 ppb). <sup>b</sup> H<sub>2</sub>O<sub>2</sub> was the OH precursor used for each low NO<sub>x</sub> isoprene experiment. H<sub>2</sub>O<sub>2</sub> is not measured directly, but from isoprene decay during irradiation we estimate ~3 ppm of H<sub>2</sub>O<sub>2</sub>. <sup>c</sup> AS = ammonium sulfate seed, AAS = acidic ammonium sulfate seed. <sup>d</sup> Averaged over the course of filter sampling. <sup>e</sup> Subtraction of seed aerosol taken into account when necessary. SOA volume derived from DMA wall loss uncorrected measurements for use in mass closure from filter sample analyses. <sup>f</sup> Assuming a SOA density of 1.25 g/cm<sup>3</sup>. This value is derived from comparison of DMA aerosol volume and AMS aerosol mass measurements. <sup>g</sup> 100% of light bank used and hence higher temperatures in chamber observed during sampling. <sup>h</sup> No peroxide measurement made for this sample. <sup>i</sup> Half of the typical [H<sub>2</sub>O<sub>2</sub>] used ~1.5 ppm. <sup>j</sup> Late sampling, after peak growth, during the rapid decay of the aerosol mass/volume typical of low NO<sub>x</sub> experiments.

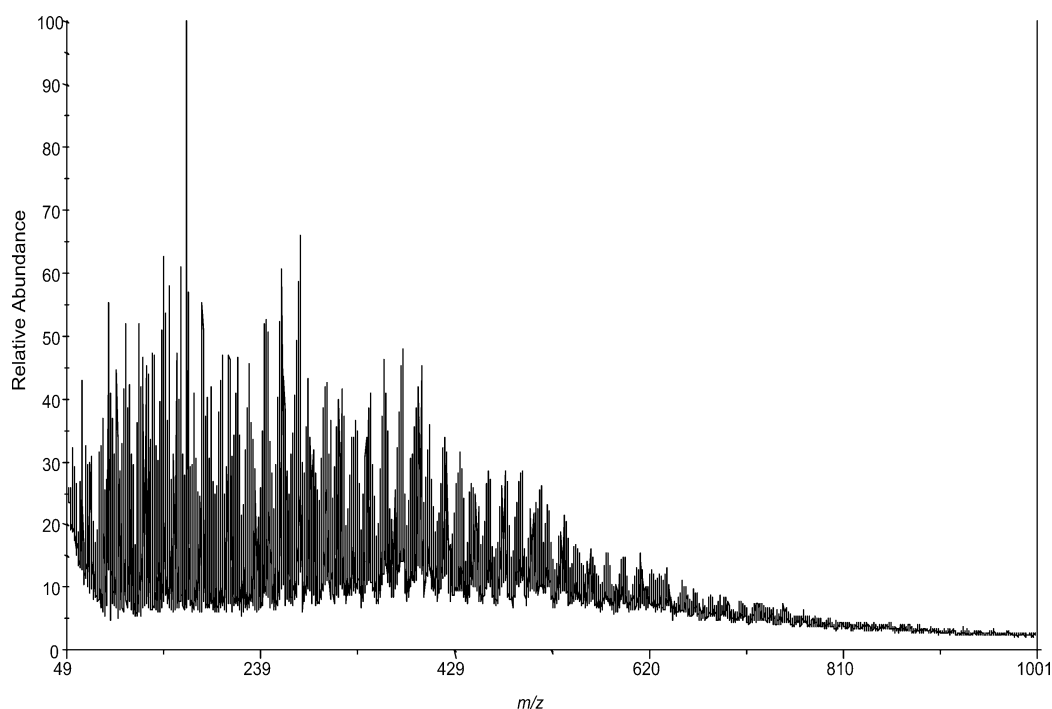


Figure 7. MALDI positive mode spectrum obtained with a graphite matrix for a 500 ppb isoprene, low-NO<sub>x</sub>, acid seeded experiment (Experiment 14). High-molecular mass species formed up to ~620 Da.

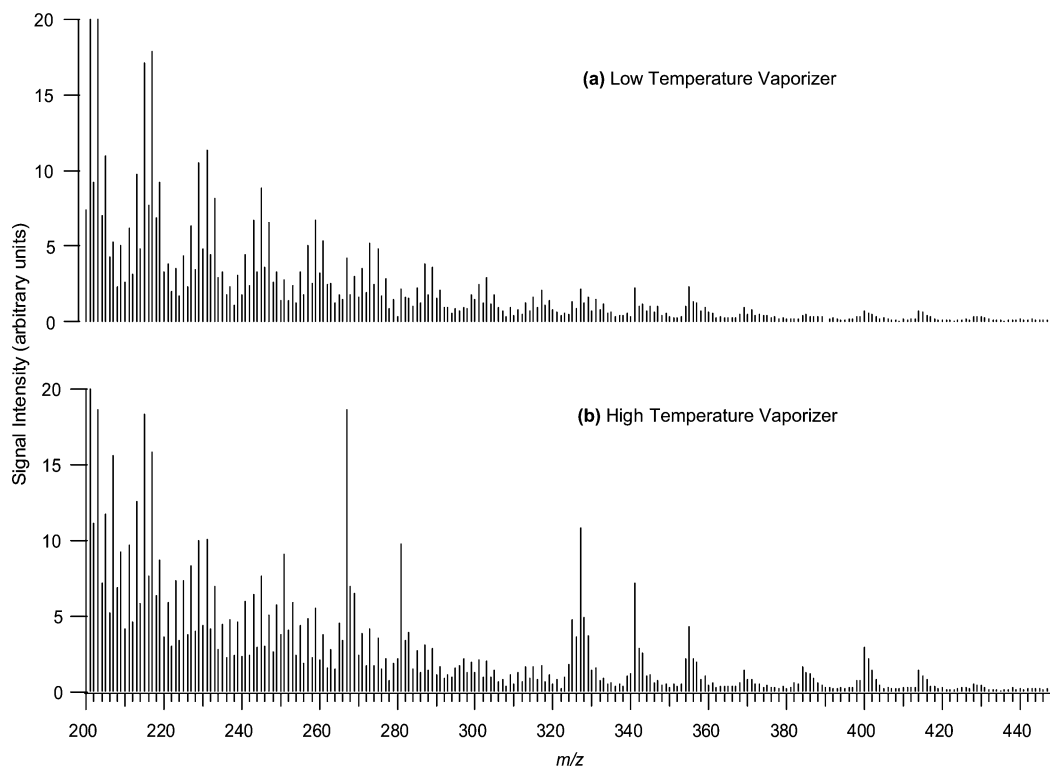
free conditions. Aerosol formation was also observed; however, the composition of the resultant aerosol was not investigated.

In contrast to Kroll et al.,<sup>16</sup> under the present conditions there may be some contribution (~10–30%) of RO<sub>2</sub> + RO<sub>2</sub> reactions under low-NO<sub>x</sub> conditions owing to the higher [isoprene]/[H<sub>2</sub>O<sub>2</sub>] ratios used in the current study.<sup>32</sup> For simplicity, only the RO<sub>2</sub> + RO<sub>2</sub> reactions that lead to hydroxyalkoxy radicals are shown in Figure 11. As in the high-NO<sub>x</sub> case, these hydroxyalkoxy radicals will likely form MVK, MACR, and hydroxycarbonyls. The RO<sub>2</sub> + RO<sub>2</sub> reactions not shown can lead to the formation of diols and other isomeric hydroxycarbonyls. As will be discussed subsequently, the diols that result from RO<sub>2</sub> + RO<sub>2</sub> reactions (not shown) may form SOA as well.<sup>15</sup>

#### 4.2. High-NO<sub>x</sub> SOA. 4.2.1. Importance of MACR Oxidation.

MACR oxidation under high-NO<sub>x</sub> conditions produces significant amounts of SOA (Experiments 3 and 4). When comparing the SOA products from isoprene and MACR oxidation at high-NO<sub>x</sub> conditions, many of the same products are observed (Figure 1). Tandem MS data obtained for selected ions common to both isoprene and MACR samples, like the *m/z* 368 ion shown in Figure 4, produced similar product ion spectra, further indicating that these species are indeed the same. This observation is consistent with our previous proton-transfer reaction-mass spectrometry (PTR-MS) studies of isoprene oxidation, which demonstrate a strong correlation between the amount of SOA formed and the MACR reacted in the gas phase.<sup>37,38</sup> In these studies, aerosol growth continued well after isoprene was fully consumed, indicating the likely importance of second- (or later-)





**Figure 8.** TOF-AMS spectra for a 500 ppb isoprene low- $\text{NO}_x$  experiment (Experiment 12). (a) Mass spectrum obtained with a low temperature vaporizer ( $\sim 150^\circ\text{C}$ ). (b) Mass spectrum obtained with a high temperature vaporizer ( $\sim 600^\circ\text{C}$ ). The spectrum is richer at higher  $m/z$ , indicating that the high- MW oligomers that are not easily volatilized at  $<200^\circ\text{C}$ .

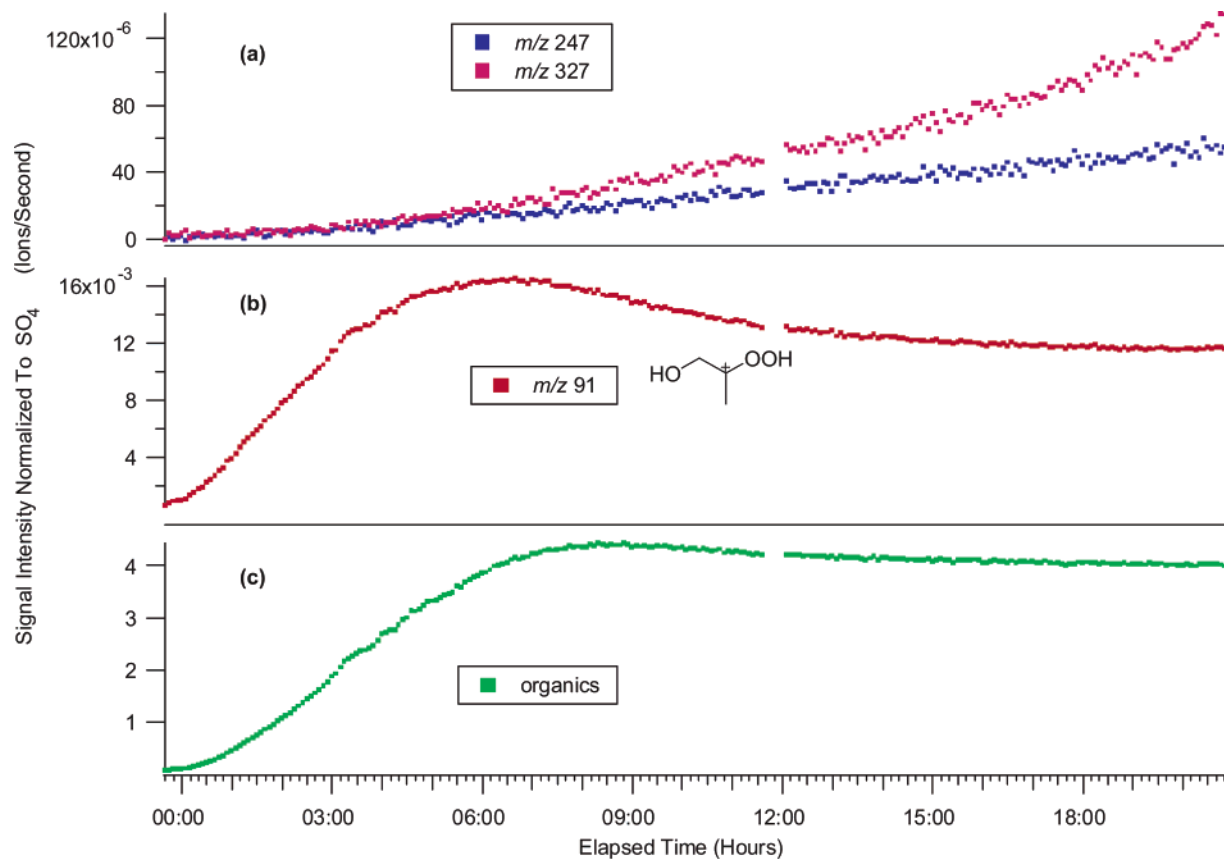
generation gas-phase products and/or heterogeneous (particle-phase) reactions. It should be noted that when the MACR,  $\text{H}_2\text{O}_2$ , and dry ammonium sulfate seed aerosol are well mixed in the chamber before irradiation begins, no aerosol growth is observed. This rules out the possibility of reactive uptake of MACR into the particle phase; instead the oxidation of MACR is a necessary step in SOA formation from the photooxidation of isoprene.

**4.2.2. Oligomers.** Oligomerization occurs in SOA formed under high- $\text{NO}_x$  conditions, where both offline and online mass spectrometry techniques (Figures 1, 2, and 5) measure species with much higher MWs than those of the parent isoprene, with characteristic 102 Da differences. Tandem MS techniques, such as upfront CID on the LC/MS instrument, confirm that oligomers are indeed formed from a common 102 Da monomeric unit. For example, when isolating the  $m/z$  368 ion from the rest of the sample matrix and further fragmenting it to generate a product ion spectrum, two successive neutral losses of 102 Da were observed at  $m/z$  266 and 164 (Figure 4b). Two isomeric compounds with  $m/z$  266 in Figure 3c were found to elute off the LC column at  $\sim 2.5$ – $3$  min earlier than the compound with  $m/z$  368 studied here. The fact that the compounds with  $m/z$  266 ions elute off the LC column at earlier  $RT$ s, and that  $m/z$  266 is a product ion of  $m/z$  368, strongly suggests that these two ions are characteristic of the same oligomeric series. The compounds characterized by  $m/z$  368 and 266 are likely a trimer and dimer, respectively. The other series of oligomers quantified in Table 2 also had 102 Da differences observed and similar LC/MS behaviors, with ions with lower mass eluting from the LC column at earlier  $RT$ s.

**4.2.3. Organic Nitrates.** Organic nitrates, detected as even-mass  $[M - \text{H}]^-$  ions in  $(-)\text{ESI}$  spectra, were measured in all high- $\text{NO}_x$  experiments. All organic nitrates detected in high- $\text{NO}_x$  SOA samples had similar product ion spectra as  $m/z$  368

(Figure 4b), with neutral losses of 63 ( $\text{HNO}_3$ ), 77 ( $\text{CH}_3$  radical +  $\text{NO}_3$  radical, possibly  $\text{CH}_3\text{NO}_3$ ), and 102 Da, suggesting that all even-mass  $[M - \text{H}]^-$  ions are oligomeric organic nitrate species. Unlike the  $(-)\text{ESI}$  techniques (Figures 1 and 3), the GC/MS technique did not allow for the detection of organic nitrate species, likely a result of their instability at the high temperature of the GC injector and/or derivatization techniques used during sample workup. Organic nitrates were also not clearly detected in the MALDI-TOFMS (Figure 2) and TOF-AMS (Figure 5) instruments. This is likely a result of the harsh ionization techniques employed by these instruments. Even with  $(-)\text{ESI}$ , these organic nitrates were not completely stable, as shown in Figure 4a for the  $m/z$  368 ion. Organic nitrates found in the high- $\text{NO}_x$  SOA likely form from the further oxidation of the hydroxynitrate species found in the gas phase from  $\text{RO}_2 + \text{NO}$  reactions.

**4.2.4. 2-MG as Monomeric Units.** As shown in Table 2, other varieties of oligomers were observed as well. From further use of tandem MS techniques, it was found that one of these series of oligomers likely involved 2-MG (2-methylglyceric acid), a recently discovered SOA tracer compound for isoprene oxidation in the ambient atmosphere,<sup>10,13,14</sup> as an important monomer. Confirmation of the 2-MG monomer in high- $\text{NO}_x$  SOA was provided by GC/MS with TMS derivatization (Figure 6a and b). Because monomeric 2-MG is small and polar, it was not retained effectively by the LC reverse phase column ( $RT \approx 1.3$  min) and was detected in its deprotonated form at  $m/z$  119. Figure 12 shows product ion spectra obtained with  $(-)\text{ESI}$ -ITMS for Experiment 9. In Figure 12a, the  $m/z$  323 ion is isolated in the ion trap from the rest of the ion matrix and is collisionally activated to produce the  $\text{MS}^2$  spectrum shown here. The  $m/z$  221 ion is the base peak in this spectrum, and the  $m/z$  119 ion also detected as the result of further fragmentation of the  $m/z$  221 product ion. The fact that the  $m/z$  119 ion was



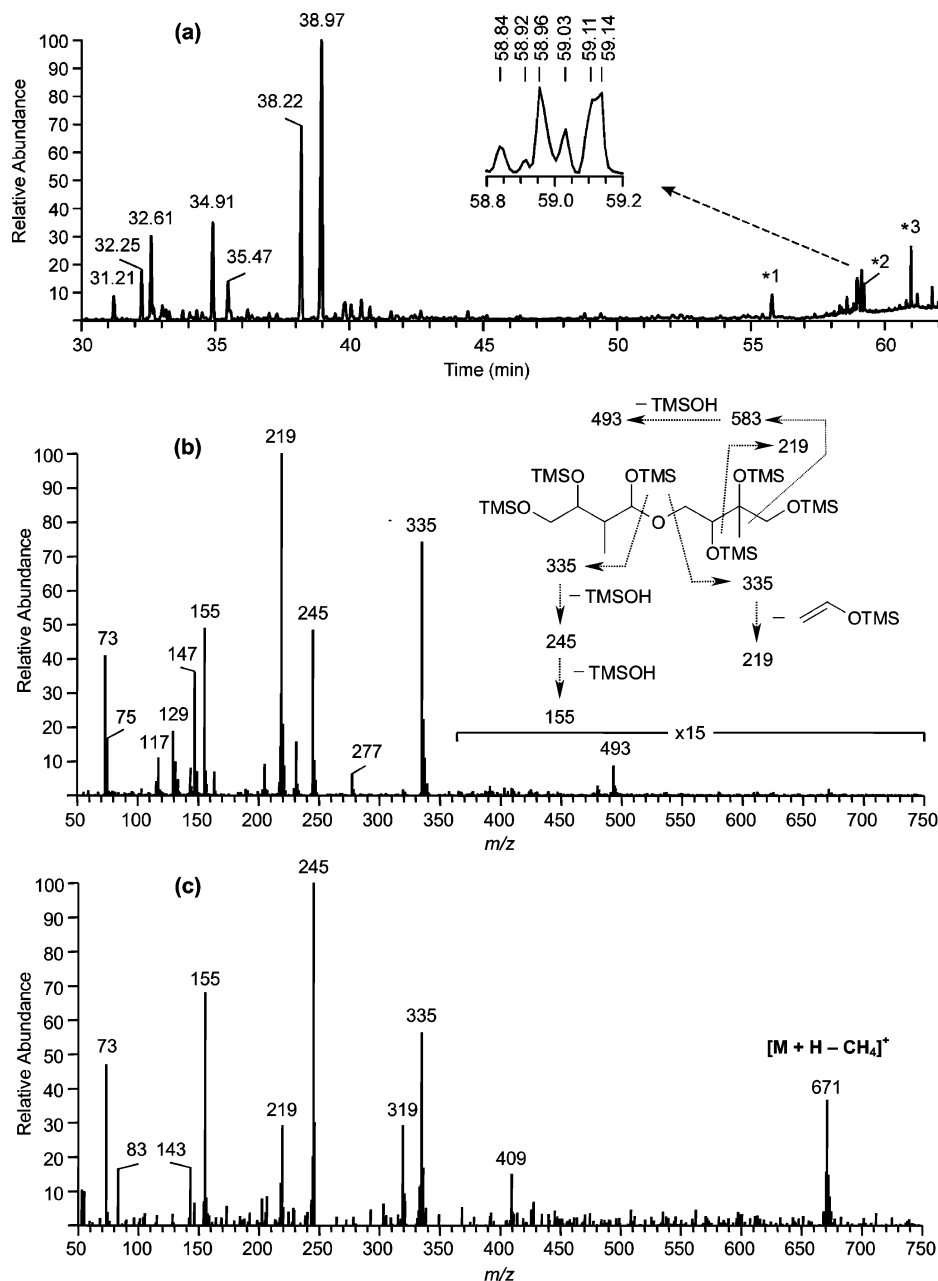
**Figure 9.** Time evolution plots produced from the TOF-AMS instrument for selected fragment ions and the total organic mass observed from a typical low- $\text{NO}_x$  experiment (Experiment 13). All ion signal intensities are divided by the signal intensity of sulfate. Because sulfate concentration is a tracer for wall loss (neither created nor removed during the run), the ratio of ion signal to sulfate signal should give an indication of the behavior without wall loss. (a) Time evolution plot for high-mass fragment ions  $m/z$  247 and 327. (b) Time evolution plot for the proposed peroxide fragment ion  $m/z$  91 ( $\text{C}_3\text{H}_7\text{O}_3$ ), where the structure of one isomer is shown. (c) Time evolution plot for the total organic mass. These plots indicate that the chemical composition changes with experimental time, where the decomposition of organic peroxides correlates to oligomerization within low- $\text{NO}_x$  SOA. The missing data points (11:30 to 12:00 hours) in these plots are due to the vaporizer in the TOF-AMS instrument being turned off.

detected as a product ion in the  $\text{MS}^2$  and  $\text{MS}^3$  spectra shown in Figure 12 strongly suggests that 2-MG is a monomer in this oligomeric series. It is important to note that  $m/z$  119 was also a fragment ion produced in the upfront CID spectrum for the  $m/z$  368 ion in Figure 4b. It was found that  $m/z$  119 was a common product ion to each oligomeric series, suggesting the importance of 2-MG in oligomerization reactions.

**4.2.5. Mono-Acetate and Mono-Formate Oligomers.** The PILS/IC measurements of high levels of particulate acetate and formate anions in both the seeded (Experiment 1) and nucleation (Experiment 2) experiments, coupled with the high volatilities of their acid forms produced in the gas phase from the oxidation of isoprene, suggests that these compounds resulted from the decomposition of oligomeric SOA. The formation of *mono*-acetate and *mono*-formate oligomers was observed by tandem (–)ESI-MS measurements. Figure 13 shows two product ion spectra for a *mono*-acetate dimer ( $[M - \text{H}]^-$  at  $m/z$  161) and *mono*-formate trimer ( $[M - \text{H}]^-$  at  $m/z$  249), respectively. The observation of a neutral loss of 42 Da (ketene,  $\text{H}_2\text{C}=\text{C}=\text{O}$ ) and a dominant product ion  $m/z$  59 (acetate anion) in the  $\text{MS}^2$  spectrum of the  $m/z$  161 ion (Figure 13a), provides strong evidence for acetylation. In the  $\text{MS}^2$  spectrum of the  $m/z$  249 ion (Figure 13b), the major product ion  $m/z$  147 results from the common neutral loss of 102 Da. The product ion  $m/z$  221 results from a neutral loss of 28 Da (CO), a rearrangement reaction that is characteristic of formates. The product ion  $m/z$  119 (deprotonated 2-MG) resulting from the combined neutral losses of 102 and 28 Da is also observed. *Mono*-acetate

oligomers were also detected by the GC/MS TMS derivatization method; the details of these findings will be discussed in a forthcoming GC/MS complementary paper.

**4.2.6. Heterogeneous Esterification Reactions.** Oligomer species containing the  $m/z$  119, 221, and 323 ions as detected by the (–)ESI techniques were also observed by GC/MS as their respective TMS derivatives as shown Figure 6a. As in previous measurements of 2-MG,<sup>14</sup> the EI mass spectrum shown in Figure 6b confirms the formation of monomeric 2-MG in high- $\text{NO}_x$  isoprene SOA. The dimer detected at  $m/z$  221 by (–)ESI techniques (as shown in Figure 12b) involving 2-MG as an important monomer, is detected at 51.59 min in Figure 6a. The chemical structure of this species likely contains one carboxyl and three hydroxyl groups, as shown in Figure 6c. The formation of an ester linkage is also denoted in this structure, which is the expected site of oligomerization. The ions  $m/z$  583 ( $[M + \text{TMS}]^+$ ) and  $m/z$  495 ( $[M - \text{CH}_3]^+$ ) confirm that the MW of this dimer species is 222 (which is also in agreement with the ESI results). The ion  $m/z$  467 ( $[M - (\text{CH}_3 + \text{CO})]^+$ ) is consistent with a terminal trimethylsilylated carboxylic group, while the ion  $m/z$  480 ( $[M - \text{CH}_2\text{O}]^+$ ) is explained by a rearrangement of a trimethylsilyl group and points to a terminal trimethylsilylated hydroxymethyl group. The elemental composition ( $\text{C}_8\text{H}_{14}\text{O}_7$ ) of the structure shown in Figure 6c was also confirmed by high-resolution ESI-TOFMS measurements. These results strongly suggest that particle-phase esterification reactions occurred between 2-MG molecules, where a hydroxyl group of one 2-MG molecule reacted with a



**Figure 10.** (a) GC/MS TIC of isoprene low- $\text{NO}_x$  SOA. The inset shows the  $m/z$  219 EIC for the dimeric products eluting between 58.8 and 59.2 min. Peak identifications:  $R_t$ s 31.21, 32.25, and 32.61 min:  $\text{C}_5$  alkene triols;  $R_t$ s 34.91 and 35.47 min: unstable products tentatively characterized as 2-methyltetrol performatate derivatives;  $R_t$ s 38.22 and 38.97 min: 2-methylthreitol and 2-methylerythritol, respectively). The EI spectra for the latter seven compounds are provided in Figure 1S (Supporting Information). The peaks labeled \*1, \*2, and \*3 were also present in the laboratory controls and were identified as palmitic acid, stearic acid, and palmitoyl monoglyceride, respectively. (b) Averaged EI spectrum for the dimeric products eluting between 58.8 and 59.2 min and fragmentation scheme; and (c) averaged  $\text{CI}(\text{CH}_4)$  spectrum for the latter products.

carboxylic acid group of another one. The products that result from this reaction would be the ester compound shown in Figure 6c and a water molecule. The neutral loss of 102 Da, likely corresponding to dehydrated 2-MG or a 2-MG residue in the form of a lactone (i.e., 2-hydroxy-2-methylpropiolactone), observed from the ESI-MS/MS techniques can be explained by the charge-directed nucleophilic reaction shown in Figure 14. To our knowledge, this is the first evidence of particle-phase esterification reactions in SOA. It should be noted that the mass spectra, not shown here, for the chromatographic peaks in Figure 6a at 60.01 and 60.31 min, correspond to branched and linear 2-MG acid trimers (corresponding to MW = 324), respectively. A detailed discussion of the EI mass spectral behavior of the TMS derivatives of 2-MG and 2-MG dimer and trimers will be presented in a complimentary GC/MS study.

Figure 15a and b compares the GC/MS EICs, using the  $m/z$  219 ion as the base peak, for a filter sample from Experiment 5 treated with trimethylsilylation only to that of a filter sample (also from Experiment 5) treated by hydrolysis/ethylation + trimethylsilylation, respectively, to show further confirmation of polyesters formed via esterification reactions between 2-MG molecules. When treating SOA from the same chamber experiment with the hydrolysis/ethylation procedure, a noticeable decrease in 2-MG and 2-MG oligomers is observed. For example, the peaks at 29.08, 51.59, and 60.31 min (Figure 15a) observed after trimethylsilylation appear as smaller peaks upon the hydrolysis/ethylation experiment, as shown in the second chromatogram (Figure 15b). This decrease is a result of the formation of ethyl esters of 2-MG and of linear dimer ( $R_t$ s = 27.42 and 50.48 min, respectively). The mass spectra confirming

TABLE 4: Low-NO<sub>x</sub> Isoprene SOA Products Elucidated by GC/MS

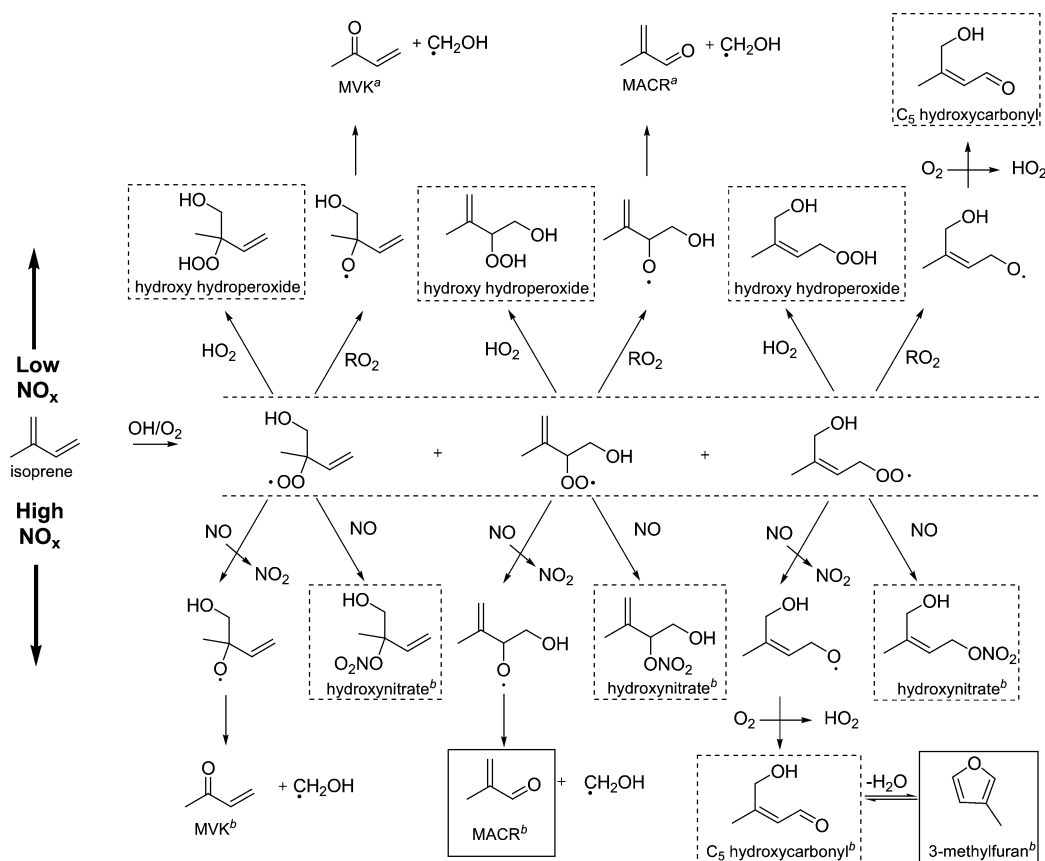
Compound / Structure	MW (MW TMS- derivative)	Elemental composition	Detection in Ambient Atmospheres
<b>C<sub>5</sub> alkene triols / ald form</b> 	118 (334)	C <sub>5</sub> H <sub>10</sub> O <sub>3</sub>	[Wang et al., 2005] <sup>12</sup> [Kourtchev et al., 2005] <sup>11</sup>
<b>C<sub>5</sub> alkene triols / keto form</b> 	118 (334)	C <sub>5</sub> H <sub>10</sub> O <sub>3</sub>	[Wang et al., 2005] <sup>12</sup> [Kourtchev et al., 2005] <sup>11</sup>
<b>2-methyltetrols</b>  <i>threo</i> + <i>erythro</i>	136 (424)	C <sub>5</sub> H <sub>12</sub> O <sub>4</sub>	[Claeys et al., 2004] <sup>7</sup> [Edney et al., 2005] <sup>14</sup> [Böge et al., 2006] <sup>15</sup> [Ion et al., 2005] <sup>10</sup> [Kourtchev et al., 2005] <sup>11</sup>
<b>C<sub>5</sub> trihydroxy monocarboxylic acid</b>  <i>threo</i> + <i>erythro</i> (minor compounds)	150 (438)	C <sub>5</sub> H <sub>10</sub> O <sub>5</sub>	Not yet detected in ambient aerosol
<b>C<sub>5</sub> trihydroxy monocarboxylic acid</b>  <i>threo</i> + <i>erythro</i> (minor compounds)	150 (438)	C <sub>5</sub> H <sub>10</sub> O <sub>5</sub>	Not yet detected in ambient aerosol
<b>2-methyltetrol performate derivatives</b>  (unstable products)	180 (396)	C <sub>6</sub> H <sub>12</sub> O <sub>6</sub>	Not yet detected in ambient aerosol
<b>Dimers (6 isomers)</b>  (minor compounds)	254 (686)	C <sub>10</sub> H <sub>22</sub> O <sub>7</sub>	Detected in ambient aerosol for the first time in this study

the formation of these ethyl ester species are shown in Figure 15c and d, respectively. The  $m/z$  365 and 277 ions in Figure 15c confirm the MW of the ethyl ester of 2-MG to be 148, where its formation is the result of polyesters decomposing into this derivatized monomer. The detection of  $m/z$  539 and 451 in Figure 15d confirm the MW of the ethyl ester of the linear 2-MG dimer, likely a result of the incomplete decomposition of larger polyesters (i.e., trimers, tetramers, pentamers, etc.) in high-NO<sub>x</sub> SOA.

Figure 16 shows the overall proposed reaction mechanism for SOA formation from the photooxidation of isoprene under high-NO<sub>x</sub> conditions. This figure denotes important initial gas-phase and particle-phase reactions that lead to the observed SOA products. As was discussed earlier, further gas-phase oxidation of MACR is required in order to form SOA from isoprene under high-NO<sub>x</sub> conditions. Oligomeric organic nitrates, such as the  $m/z$  368 ion, are comprised of an organic nitrate monomer, which is detected as the deprotonated  $m/z$  164 product ion (Figure 4b); therefore, it is possible that one gas-phase product of MACR oxidation is its hydroxynitrate form, as shown in Figure 16. Through further oxidation of the aldehyde group in this hydroxynitrate species, it is expected that the acid form of

this species results in the particle phase, thus being available for esterification reactions with 2-MG (Reaction 2 in Figure 16). To our knowledge, no organic nitrates have been measured in the gas phase from MACR oxidation (though nitrate formation has been inferred from OH-methacrolein reaction kinetics<sup>39</sup>); however, the detection of organic nitrates in the particle phase suggests that this is possibly a minor channel for SOA formation. However, the formation of 2-MG from the oxidation of MACR is still uncertain because of the unknown intermediates leading to its formation. Recently, it was proposed that 2-MG forms from the reaction of methacrylic acid or MACR with H<sub>2</sub>O<sub>2</sub> in the liquid aerosol phase under acidic conditions.<sup>13</sup> No aerosol growth was observed for MACR, H<sub>2</sub>O<sub>2</sub>, and dry ammonium sulfate seed aerosol under dark conditions; however, it is possible that other products such as formic and acetic acid, as well as oxidants formed during isoprene photooxidation, may promote the reactive uptake of MACR into the aerosol phase. Further measurements of MACR oxidation products are needed in order to better understand the formation of 2-MG, which might occur in either the particle or gas phase.

From our detailed analytical measurements discussed above, the importance of 2-MG to particle-phase reactions in high-



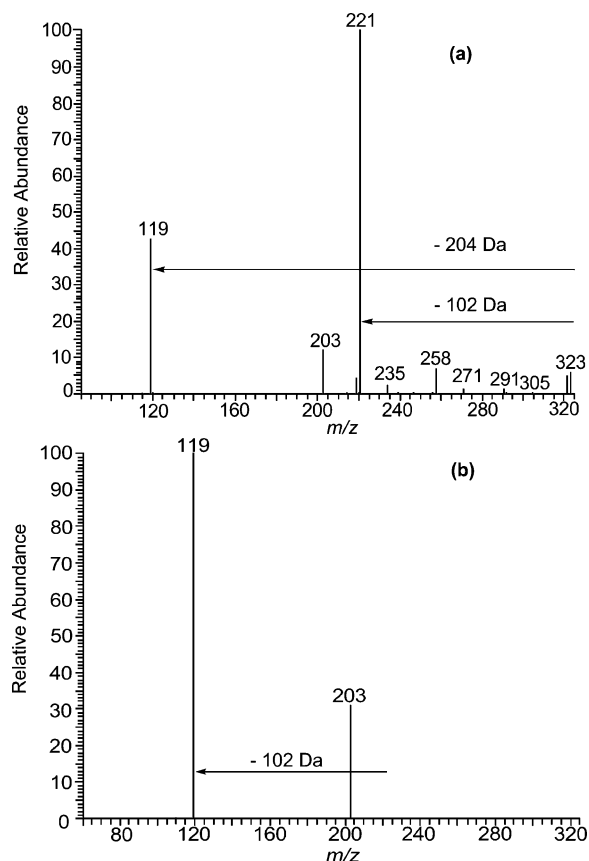
**Figure 11.** Reaction mechanism of isoprene oxidation under low- and high- $\text{NO}_x$  conditions. Dotted boxes indicate possible SOA precursors, whereas black boxes indicate known SOA precursors. For simplicity, only three of the eight initial isoprene hydroxyperoxy ( $\text{RO}_2$ ) radicals are shown.  $\text{RO}_2 + \text{RO}_2$  reactions leading to diols and other hydroxycarbonyls have been omitted for simplicity. <sup>a</sup>Miyoshi et al.<sup>31</sup> showed that  $[\text{isoprene}]/[\text{H}_2\text{O}_2]$  determines molar yields of MVK, MACR, and formaldehyde under low- $\text{NO}_x$  conditions. <sup>b</sup>Kroll et al.<sup>16</sup> summarized molar yields of gas-phase products from isoprene oxidation under high- $\text{NO}_x$  conditions reported in the literature.

$\text{NO}_x$  SOA is now well established. 2-MG monomers can react intermolecularly via esterification to produce 2-MG oligomers (Reaction 1), or react with *mono*-nitrate monomers to produce *mono*-nitrate oligomers (Reaction 2), or react with acetic or formic acid to produce *mono*-acetate and *mono*-formate oligomers, respectively (Reactions 3 and 4). These proposed esterification reactions are equilibrium reactions, and as a result, the addition of an acid or removal of water could promote the formation of these esters. As stated earlier, the high- $\text{NO}_x$  experiments were conducted at very low relative humidities ( $RH < 5\%$ ); therefore, this condition could allow for the ester formation we observe. We also observe high concentrations of organic acids (2-methylglyceric, acetic, and formic acid) at high- $\text{NO}_x$  conditions, which could provide the acidity needed to drive these reactions. It has been shown<sup>40</sup> that heterogeneous esterification of polyols by vapor-phase treatment with acetic acid and trifluoroacetic anhydride (used as an alternative to the sulfuric acid catalyst) will occur at room temperature without the use of liquids. Thus, it is reasonable to infer that esterification reactions may occur under the dry, room-temperature conditions of our chamber experiments. It should be noted that there is also evidence from the TOF-AMS that supports this reaction mechanism. The ratio of the TOF-AMS ion signals associated with the 2-MG dimer ( $m/z$  205) to that of the 2-MG monomer ( $m/z$  103) increases during the course of the high- $\text{NO}_x$  experiments, therefore providing additional confirmation of our proposed reaction mechanism in Figure 16. These results from the TOF-AMS, however, are not quantitative because of the majority of these molecules being fragmented (thermally or by the electron impact ionization) to smaller ions.

In comparison to MACR oxidation, the further oxidation of MVK likely does not produce SOA under high- $\text{NO}_x$  conditions because of its ketone moiety. The lack of an aldehydic hydrogen precludes the formation of acidic products (like that of 2-MG from MACR oxidation), which are necessary components needed for the particle-phase esterification reactions (Figure 16). One of the most abundant gas-phase products produced from MVK oxidation under high- $\text{NO}_x$  conditions is methylglyoxal. It was shown in a prior chamber study by Kroll et al.<sup>41</sup> that methylglyoxal does not reactively uptake onto inorganic seed aerosol; therefore, this could explain the lack of SOA growth from the further oxidation of MVK.

For the isoprene/ $\text{H}_2\text{O}_2$  experiments, except for Experiment 6, the most abundant oligomer series was the *mono*-nitrate oligomers (Table 2). The *mono*-nitrate oligomers accounted for  $\sim 8$ – $13\%$  of the SOA mass formed in these experiments. As for the isoprene/ $\text{H}_2\text{O}_2$  experiments, the *mono*-nitrate oligomers were the most abundant oligomers for the MACR/ $\text{H}_2\text{O}_2$  experiments ( $\sim 35\%$  of SOA mass for the seeded experiment versus  $\sim 20\%$  for the nucleation experiment). Even though most of the chemical products are the same in the  $\text{H}_2\text{O}_2$  and HONO experiments, the abundances of these products are different. In contrast to the  $\text{H}_2\text{O}_2$  experiments, the 2-MG oligomers are the most abundant oligomers for the HONO experiments. These differences could be due to different  $\text{NO}_x$  levels. SOA mass closure was observed to be the highest for the MACR/ $\text{H}_2\text{O}_2$ /seeded experiment ( $\sim 57\%$  of SOA identified) and the isoprene/ $\text{H}_2\text{O}_2$ /seeded experiments (22–34% identified). It is important to stress that the organic aerosol mass loadings formed in these isoprene high- $\text{NO}_x$  chamber experiments ( $\sim 50$ – $200 \mu\text{g m}^{-3}$ )

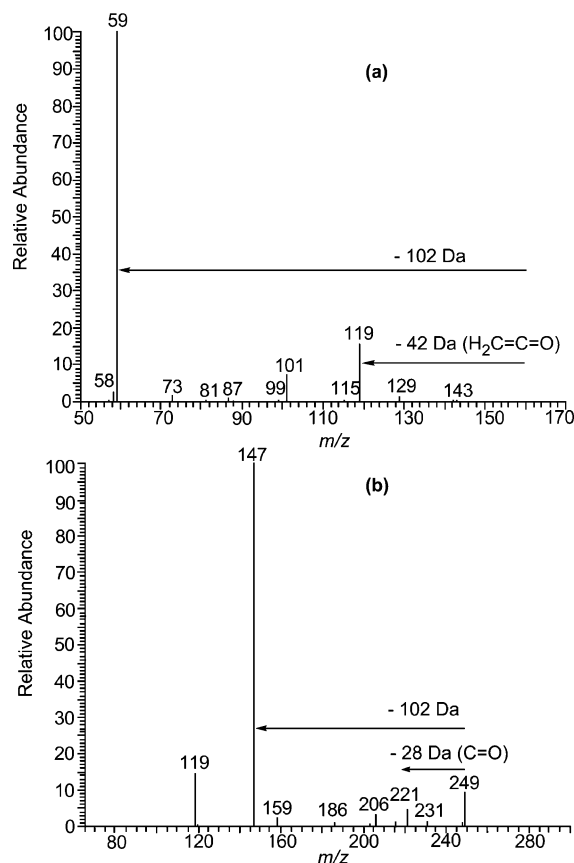




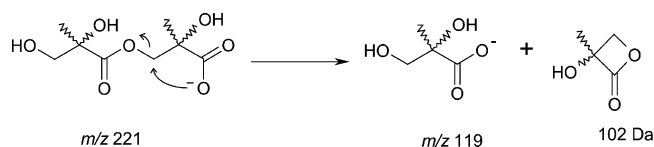
**Figure 12.** ESI-ITMS negative mode product ion spectra from a high- $\text{NO}_x$  isoprene SOA sample (Experiment 9). (a)  $\text{MS}^2$  spectrum for an isolated  $m/z$  323 ion. Two neutral losses of 102 Da are observed as shown by the product ions  $m/z$  221 and 119. (b)  $\text{MS}^3$  spectrum for an isolated  $m/z$  323 ion generated from the further fragmentation of the dominant daughter ion ( $= m/z$  221) in the  $\text{MS}^2$  spectrum. These spectra indicate that 2-MG ( $[M - \text{H}]^-$  ion  $= m/z$  119) is a monomer for the oligomeric  $m/z$  323 ion.

are much higher than those found in ambient aerosol where isoprene emissions are the highest ( $\sim 5 \mu\text{g m}^{-3}$ ). The amount of organic aerosol mass controls the gas-particle partitioning of semi-volatile species produced from the oxidation of hydrocarbons because more organic aerosol mass allows for more uptake of these species; therefore, the mass closure results presented apply only to the aerosol mass loadings produced in this current study and are not absolute for the isoprene system. The key insight from our analysis is the detection of these various oligomeric products formed from particle-phase esterification reactions.

**4.2.7. Additional Routes for SOA Formation.** As shown in Table 2, the polyester products from oligomerization of 2-MG and related components account only for a portion (22–34%) of the SOA formed from isoprene oxidation under high- $\text{NO}_x$  conditions. This lack of mass closure could result from the LC/MS technique underestimating the amount of polyesters, possibly related to the use of a  $\text{C}_{18}$  reverse phase column and the unavailability of authentic standards. The  $\text{C}_{18}$  reverse phase column could have degraded the oligomers into smaller units as they pass through the column, or very large oligomers could have permanently been retained onto the reverse phase material, and hence were not detected. Negative bias associated with filter sampling, such as evaporative losses during sampling or storage, could also be a source of incomplete mass closure. The presence of acetic acid in eluent mixture used for the LC/MS runs could also have caused an underestimation of the oligomers formed



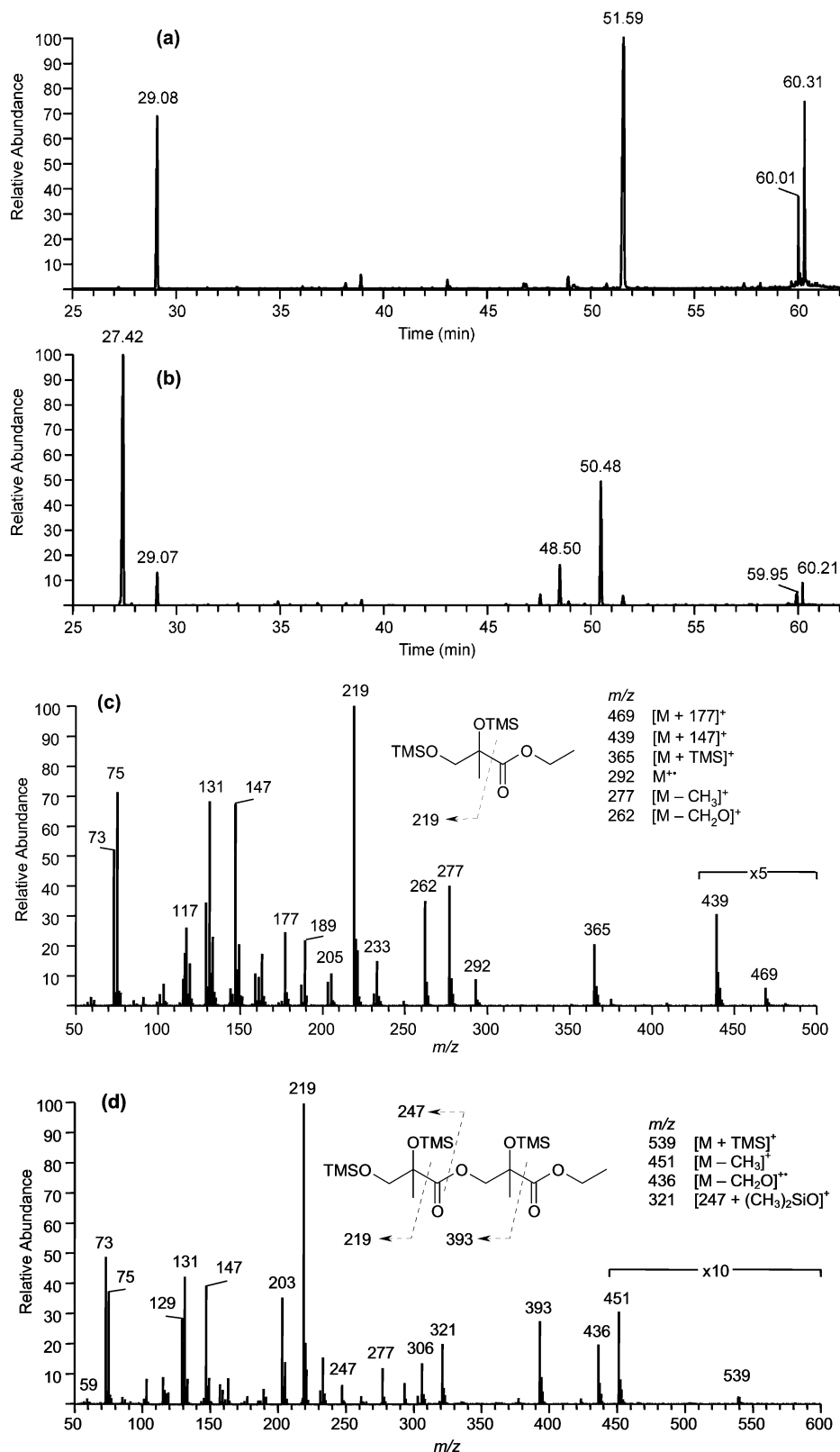
**Figure 13.** ESI-ITMS negative mode product ion mass spectra providing evidence for *mono*-acetate and *mono*-formate oligomers in high- $\text{NO}_x$  SOA. (a) Product ion mass spectrum for a *mono*-acetate dimer ( $m/z$  161). (b) Product ion mass spectrum for a *mono*-formate trimer ( $m/z$  249).



**Figure 14.** Proposed charge-directed nucleophilic reaction occurring during collisional activation in (–)ESI-ITMS, explaining the observation of 102 Da (2-hydroxy-2-methylpropiolactone) losses from oligomeric high- $\text{NO}_x$  SOA.

due to the possibility of acid-catalyzed hydrolysis during ESI, a process that would lead to a decrease in the detection of oligomeric compounds. Besides possible errors associated with quantifying esterification products identified by the LC/MS technique, the possibility still exists that other unidentified second- (or later-) generation gas- or particle-phase products from isoprene oxidation contribute to SOA formation, and as a result, would increase the mass closure significantly.

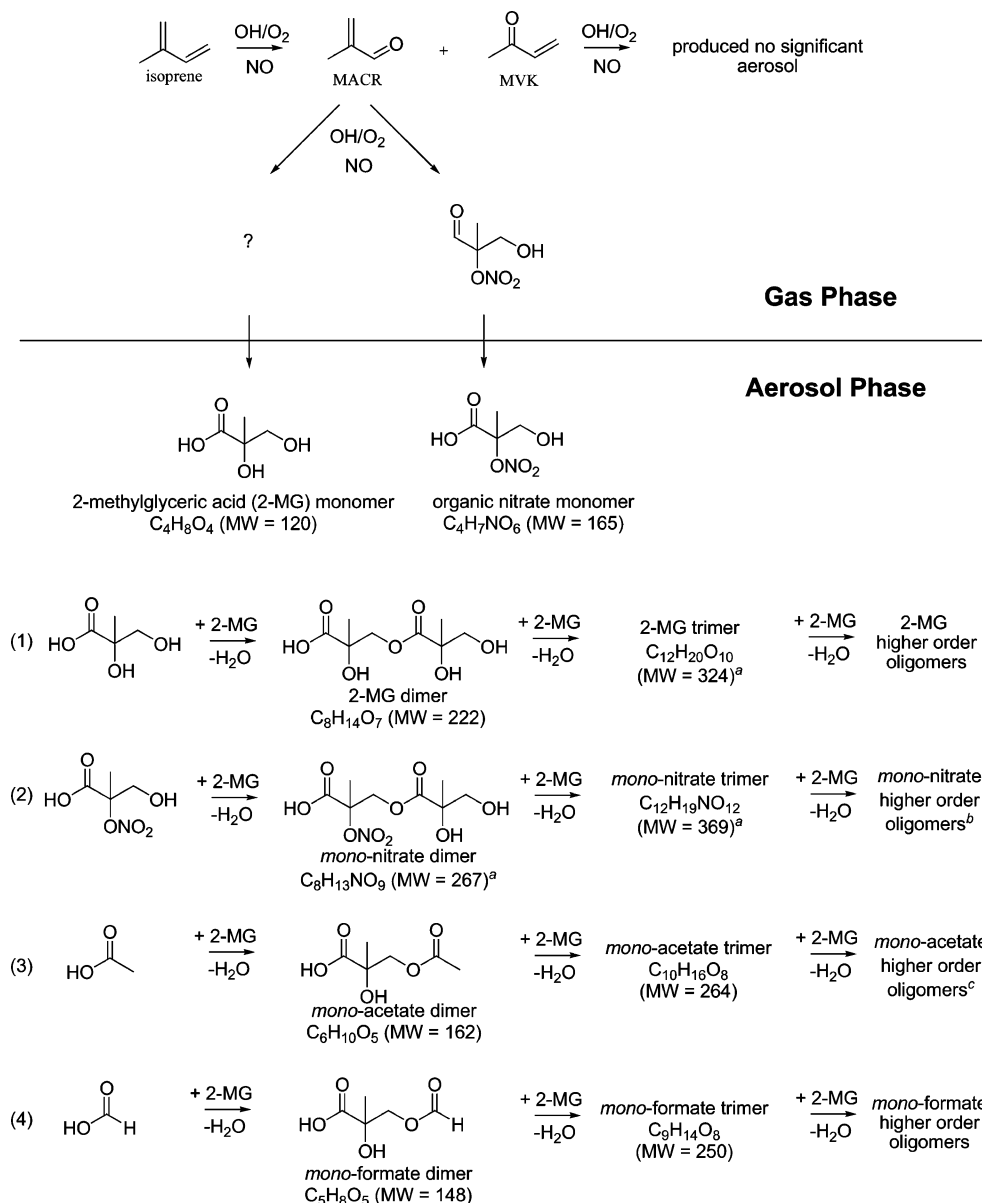
Glyoxal, a  $\text{C}_2$  dialdehyde, has been recently shown to be reactively taken up into particulate matter,<sup>41,42</sup> however, not at the low  $RH$ s employed in this study ( $RH < 5\%$ ). Theoretically, it has been shown that this reactive uptake of glyoxal results from thermodynamically favorable hydration and oligomerization.<sup>43,44</sup> When first interpreting the MS data from the ESI and MALDI techniques, it was considered that a dialdehyde species possibly corresponded to the 102 Da neutral losses observed from the oligomeric components. Figure 17 shows a proposed gas-phase reaction scheme for the formation of a  $\text{C}_4$  hydroxy dialdehyde species ( $\text{MW} = 102$ ) from the further oxidation of MACR. In contrast to glyoxal, dissolution may not be required



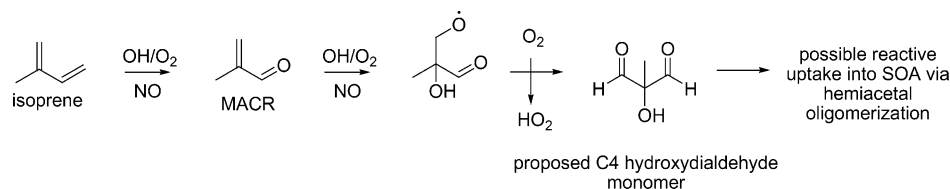
**Figure 15.** (a) GC/MS EIC ( $= m/z$  219) for high- $\text{NO}_x$  isoprene nucleation sample (Experiment 5) treated only with TMS derivatization. (b) GC/MS EIC ( $= m/z$  219) for a duplicate sample of the same experiment (Experiment 5) in part a, but treated this time by hydrolysis/ethylation followed by TMS derivatization. (c) EI mass spectrum for ethyl ester of 2-MG acid detected in part b ( $RT = 27.42$  min). (d) EI mass spectrum for ethyl ester of linear 2-MG acid dimer detected in part b ( $RT = 50.48$  min). The hydrolysis/ethylation followed by TMS derivatization results presented here confirm the existence of polyesters in high- $\text{NO}_x$  SOA.

for this proposed dialdehyde species to form SOA; therefore, other heterogeneous processes may occur. The detailed analysis of the GC/MS derivatization and the ESI tandem MS results, however, provides strong chemical evidence for the formation

of polyesters, where the neutral loss of 102 Da is explained by the dehydrated lactone form of 2-MG (Figure 14). In addition, a GC/MS derivatization analysis made for MACR high- $\text{NO}_x$  SOA (Experiment 3) that included a methoximation step prior



**Figure 16.** Proposed mechanism for SOA formation from isoprene photooxidation under high- $\text{NO}_x$  conditions. Symbol used: ?, further study needed in order to understand the formation (in gas/particle phase) of 2-MG. <sup>a</sup>Elemental compositions confirmed by high-resolution ESI-MS. <sup>b</sup>Elemental composition of mono-nitrate tetramer (MW = 471) confirmed by high-resolution ESI-MS. <sup>c</sup>Elemental compositions of mono-acetate tetramer and pentamer (MW = 366 and 468, respectively) confirmed by high-resolution ESI-MS.



**Figure 17.** Proposed gas-phase formation mechanism for a  $\text{C}_4$  hydroxydialdehyde monomer, possibly accounting for a fraction of the unidentified SOA mass in high- $\text{NO}_x$  experiments.

to trimethylsilylation to reveal aldehyde functions in the formed oligomers was negative.

To investigate further the probable importance of a  $\text{C}_4$  hydroxy dialdehyde species and its respective hemiacetal oligomers, selected sample extracts were derivatized using Girard Reagent P to increase sensitivity for aldehydic species in the (+)ESI mode. A high- $\text{NO}_x$  isoprene and a MACR sample were treated with this derivatizing agent, and as a result, the detection of the  $m/z$  236, 206, and 192 ions resulted for both

samples, which likely corresponds to the detection of the proposed  $\text{C}_4$  dialdehyde, glyoxal, and methylglyoxal, respectively. However, the proposed hemiacetal oligomers that would be produced from this  $\text{C}_4$  dialdehyde were not detected, consistent with observations made in the methoximation GC/MS experiment. It is possible that the detection of the proposed  $\text{C}_4$  dialdehyde resulted from the decomposition of oligomers during the derivatization step of the sample workup procedure (which is equivalent for the detection of glyoxal and methylgly-



lyoxal in the particle phase). As a confirmation that the observed ions were derivatized species of the proposed C<sub>4</sub> dialdehyde, glyoxal, and methylglyoxal, upfront CID LC/MS analysis was used to detect common neutral mass losses and fragment ions associated with derivatized aldehydes and ketones. The common neutral losses and fragment ions associated with the GirP derivatization detected were similar to those found by Lai et al.,<sup>23</sup> providing further evidence of the detection of these small aldehyde species in high-NO<sub>x</sub> isoprene and MACR SOA. The detection of these small dicarbonyls provides some evidence that aldehydes may account for a fraction of the unquantified (unidentified) SOA mass (Table 2) produced from isoprene oxidation under high-NO<sub>x</sub> conditions. The mechanism (reactive uptake and/or oligomerization) and the degree in which these aldehydes form SOA, however, remains unclear and bears further study.

**4.3. Low-NO<sub>x</sub> SOA.** **4.3.1. Hydroperoxides: Key Component to SOA Formation.** As discussed previously, in the absence of NO<sub>x</sub>, the RO<sub>2</sub> radical chemistry is dominated by RO<sub>2</sub> + HO<sub>2</sub> reactions, owing to the large amounts of HO<sub>2</sub> formed from the OH + H<sub>2</sub>O<sub>2</sub> reactions.<sup>17</sup> RO<sub>2</sub> + RO<sub>2</sub> reactions are expected to be less substantial (10–30% contribution) because of the high HO<sub>2</sub>/RO<sub>2</sub> ratios in these experiments, and as a result, hydroperoxides are expected to be the dominant gas-phase products. Because of their expected low volatilities, hydroperoxide species can partition to the aerosol phase and likely form high-MW species via peroxyhemiacetal formation with aldehydic species.<sup>18,19</sup> Hydroperoxides resulting from the oxidation of aromatic and biogenic VOCs have been observed and calculated to be important contributors to the overall SOA mass.<sup>18,45,46</sup> Indeed, as shown in Table 3, organic peroxides (i.e., hydroperoxides or ROOR) are also a significant component (~61% of the SOA mass for nucleation experiments and ~25% and 30% of the SOA mass for dry seeded and acid seeded experiments, respectively) of the low-NO<sub>x</sub> isoprene SOA. The large discrepancy in peroxide content observed between nucleation (seed-free) and seeded experiments is currently not understood. As discussed in the results section, there is no evidence of interference from ammonium sulfate on the peroxide content measurement. Owing to the neutral nature of the hydroperoxides (and ROOR) measured by the iodometric-spectrophotometric method, no tandem ESI-MS measurements could be made to structurally elucidate this fraction. Thus, it is difficult to explain the differences in the peroxide content observed between nucleation and seeded experiments. It is possible that in the seeded cases the hydroperoxide species are heterogeneously converted into neutral species other than peroxidic compounds, such as polyols. Further studies should be conducted to investigate the role of inorganic seed on the amount of peroxides formed in the aerosol phase. As noted in the high-NO<sub>x</sub> case, the mass closure results presented here apply only to the aerosol mass loadings produced in this current study and cannot be concluded as absolute for the isoprene system at low-NO<sub>x</sub> conditions.

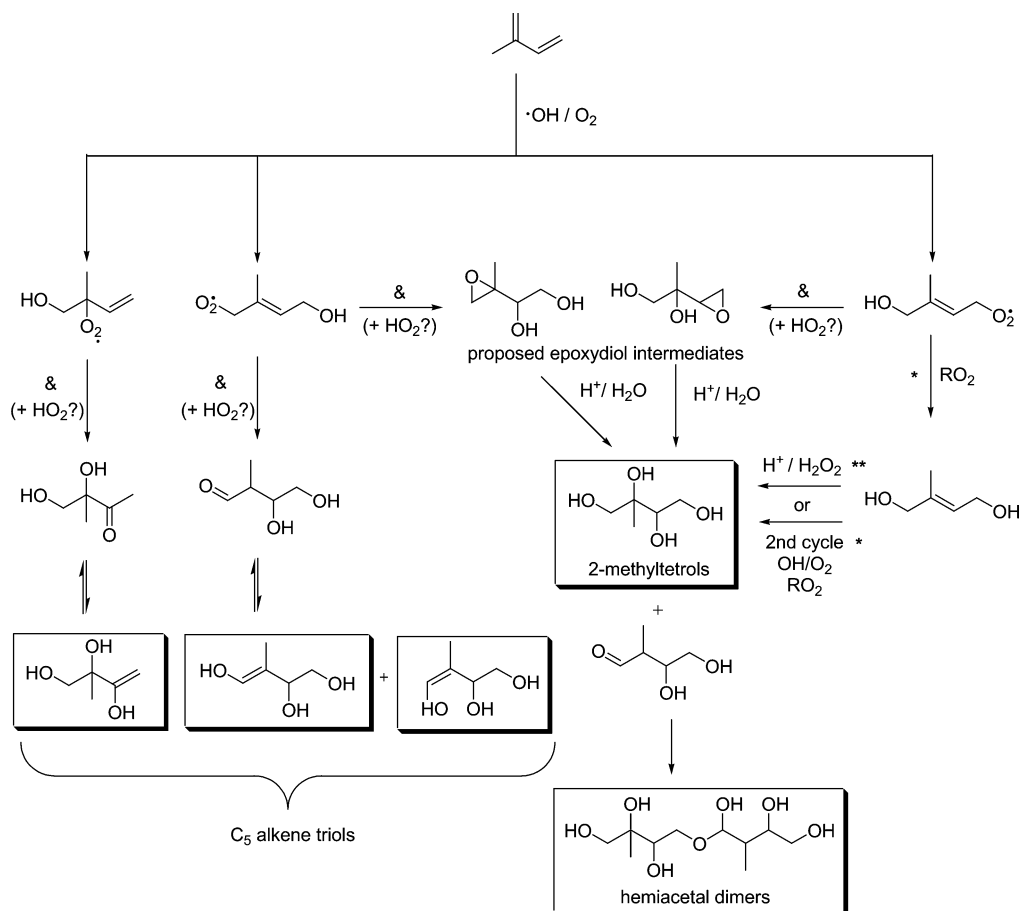
**4.3.2 Oligomerization.** Oligomers were found to form under low-NO<sub>x</sub> conditions, as shown in the (+)MALDI (Figure 7), GC/MS with TMS derivatization (Figure 10), and TOF-AMS (Figures 8 and 9) data. In contrast to high-NO<sub>x</sub> conditions, no distinct pattern or obvious monomeric unit, like the 102 Da differences observed in the high-NO<sub>x</sub> oligomeric SOA (Figures 1, 2, and 5), was observed in the low-NO<sub>x</sub> oligomers. The oligomers formed in the low-NO<sub>x</sub> case are not acidic in nature like those in the high-NO<sub>x</sub> case. Structural elucidation of these oligomers is limited because these neutral products are not

ionizable using ESI-MS. MALDI (Figure 7) was able to provide some indication of the MW ranges of the oligomeric SOA, but structural elucidation was not possible. The large mass contribution of organic peroxides to the low-NO<sub>x</sub> SOA (Table 3) provides some insight into the oligomerization reactions occurring. It is possible that some fraction of the oligomeric SOA is formed by peroxyhemiacetals, which result from heterogeneous reactions of hydroperoxides and aldehydes.

Because of the neutral nature of the oligomeric SOA produced under low-NO<sub>x</sub> conditions, only the GC/MS derivatization technique provides structural elucidation of the oligomers formed owing to the presence of polyols. Hemiacetal formation reactions between C<sub>5</sub> alkene triols (Table 4) and 2-methyltetrols (Table 4) were found to occur using this technique (Figure 10b). The reaction involves a terminal hydroxyl group of a 2-methyltetrol, which serves as a nucleophile, reacting with the tautomeric keto form of one C<sub>5</sub> alkene triol (Table 4) to form the hemiacetal dimer shown in Figure 10b. As was observed by the GC/MS *m/z* 219 EIC, six isomeric forms of this hemiacetal dimer could be partially resolved. However, further elucidation of higher-order hemiacetal (acetal) oligomers could not be conducted owing to their likely thermal decomposition in the GC injector of the GC/MS instrument, their high MW preventing their elution from the GC column, and lack of ionization when using ESI-MS techniques. As for the confirmation of peroxyhemiacetal oligomers, analytical techniques need to be developed in order to further elucidate the neutral higher-order hemiacetal (acetal) oligomers likely present in low-NO<sub>x</sub> SOA.

**4.3.3. Acid Catalysis.** The SOA mass for the acid seed experiment (Experiment 14) is significantly larger (~3.6 times) than that of the dry seeded/nucleation experiments (Experiments 15/12), in contrast to high-NO<sub>x</sub> conditions, in which acid seed had no such observable effect. Note that the SOA mass concentration was virtually identical in experiments using dry (nonacid) seed aerosol and in those in the absence of seed aerosol, where particle formation takes place by nucleation (Experiments 12, 13, and 15). GC-FID measurements made for selected low-NO<sub>x</sub> experiments also provide evidence for acid-catalyzed particle-phase reactions. The C<sub>5</sub> alkene triols and 2-methyltetrols decreased in their contributions to the overall SOA mass when acid seed was present. For example, the 2-methyltetrols and C<sub>5</sub> alkene triols contributed ~3.91% and 0.6%, respectively, to the SOA mass for Experiment 13 (nonacid case), whereas in Experiment 14 (acid case), the 2-methyltetrols and C<sub>5</sub> alkene triols were found to decrease to ~0.46% and 0.06%, respectively, of the SOA mass. This result is in contrast to that observed by Edney et al.<sup>14</sup> in which isoprene tracer compounds were observed to increase in concentration, and is possibly due to the differing isoprene/NO<sub>x</sub> ratios employed. In conjunction with the above GC-FID results, the fact that C<sub>5</sub> alkene triols and 2-methyltetrols were found to form hemiacetal dimers (and likely higher order oligomers) suggests that the presence of acidified aerosol catalyzes hemiacetal (and likely acetal) oligomer formation under low-NO<sub>x</sub> conditions. The same may be the case for peroxyhemiacetal formation reactions.

**4.3.4. Formation Mechanism of Low-NO<sub>x</sub> SOA products Observed by GC/MS.** The detection of organic peroxides in the particle phase (Table 3) by the iodometric-spectrophotometric method provides strong evidence that the hydroperoxides that result from the gas-phase RO<sub>2</sub> + HO<sub>2</sub> reactions are sufficiently polar (nonvolatile) to partition to the aerosol phase, thereby elucidating one major reaction pathway leading to SOA formation under low-NO<sub>x</sub> conditions. The detection of 2-methyltetrols,



**Figure 18.** Low- $\text{NO}_x$  SOA formation pathways as elucidated by GC/MS. Boxes indicate products detected in low- $\text{NO}_x$  SOA. Symbols used:  $\&$ , further study needed for the formations of the hypothetical carbonyl diol and epoxydiol intermediates which may result from the rearrangements of  $\text{RO}_2$  radicals and/or hydroperoxides;  $*$ , for details about this pathway leading to 2-methyltetrols and also holding for isomeric products, see reference 7;  $**$ , for details about this alternative pathway, see ref 14. 2-methyltetrol performate derivatives (shown in Table 4) were omitted for simplicity; however, these could serve as precursors for 2-methyltetrols if in the presence of acid and water.

$\text{C}_5$  alkene triols, 2-methyltetrol performate derivatives, and hemiacetal dimers (Table 4) suggests that the  $\text{RO}_2$  radicals that form from the initial oxidation ( $\text{OH}/\text{O}_2$ ) of isoprene follow some other route. The formation of 2-methyltetrols has been explained by self- and cross-reactions of the  $\text{RO}_2$  radicals formed from the initial oxidation ( $\text{OH}/\text{O}_2$ ) of isoprene, leading to intermediate 1,2-diols, which may undergo a second cycle of oxidation ( $\text{OH}/\text{O}_2$ ) reactions followed by self- and cross-reactions of the  $\text{RO}_2$  radicals.<sup>7</sup>

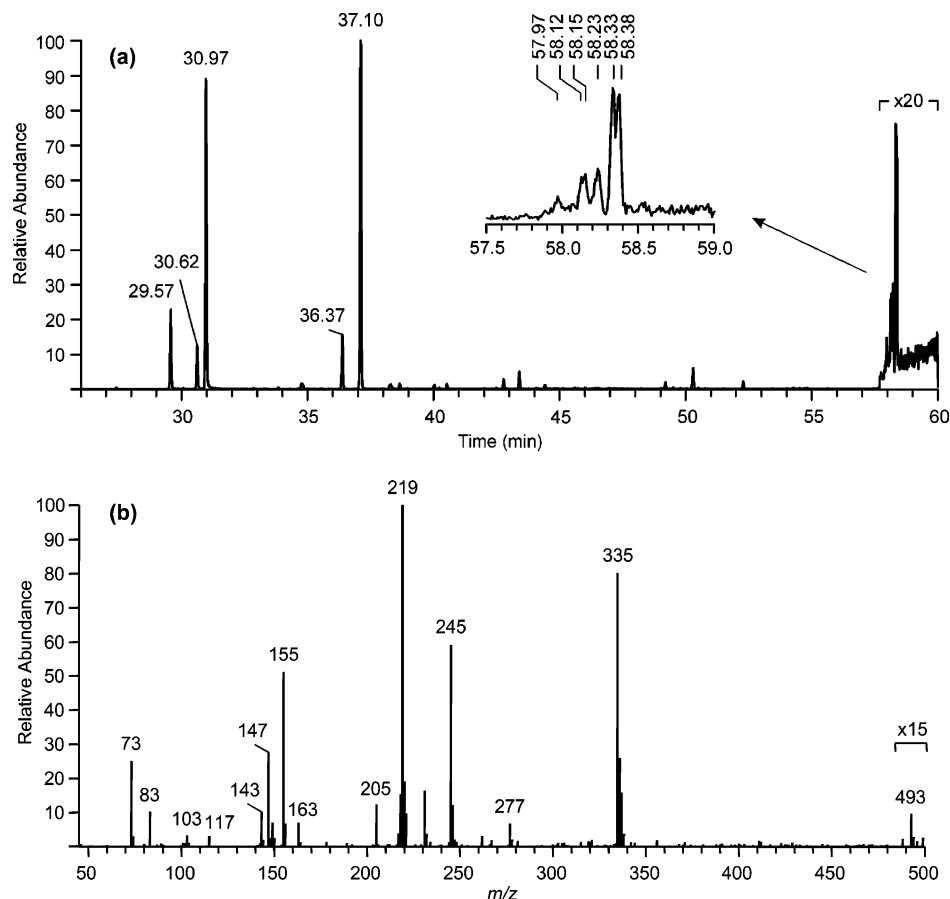
The detection of  $\text{C}_5$  alkene triols in ambient aerosol may indicate the importance of intermediate epoxydiol derivatives of isoprene, which may also be intermediates in the formation of 2-methyltetrols.<sup>11,12</sup> Wang et al.<sup>12</sup> hypothesized from MS evidence that these epoxydiol intermediates could be trapped in the aerosol phase and subsequently converted into  $\text{C}_5$  alkene triols and 2-methyltetrols through acid-catalyzed reactions. Acid-catalyzed reactions of epoxydiols may be a formation pathway for 2-methyltetrols and  $\text{C}_5$  alkene triols, but these monomers may also form from other pathways.

Shown in Figure 18 is a proposed mechanism for the formation of key SOA components from the oxidation of isoprene under low- $\text{NO}_x$  conditions. As suggested by Böge et al.,<sup>15</sup> 2-methyltetrols may form by several possible pathways. The formation of the 2-methyltetrols through two cycles of oxidation ( $\text{OH}/\text{O}_2$ ) reactions followed by self- and cross-reactions of the  $\text{RO}_2$  radicals is only briefly included in this figure. It is possible that epoxydiols may form from rearrangements of hydroxyhydroperoxides or hydroxyperoxy radicals.

Once formed, these epoxydiols could be taken up into the particulate phase, and through hydrolysis form 2-methyltetrols. In addition, an alternative pathway leading to the formation of 2-methyltetrols has been reported in a recent study by Böge et al.<sup>15</sup> That study proposed that intermediates in the formation of 2-methyltetrols (i.e., 2-methyl-3-butene-1,2-diol and 2-methyl-2-vinyloxirane) are converted to 2-methyltetrols through reaction with hydrogen peroxide on acidic particles. The latter pathway is also included in the scheme in Figure 18. Further gas and particle-phase studies are needed in order to fully elucidate the pathways leading to the formation of 2-methyltetrols, the  $\text{C}_5$  alkene triols, and related dimeric products.

**4.3.5. Evolution of SOA Composition.** As in Kroll et al.,<sup>17</sup> a rapid decay of the SOA mass was observed after the initial SOA growth reached its maximum for all low- $\text{NO}_x$  nucleation experiments. This loss is not attributable to wall removal processes because the particles shrink in size rather than reduce in number (as measured by the DMA). The loss of SOA mass was observed to stop immediately after chamber lights were turned off, and resume once the lights were turned back on, indicating a photochemical effect.

Indeed, when comparing the peroxide measurements made at (or around) the initial SOA growth maximum to some later experimental time after SOA mass decay, it was found that the organic peroxide content of the aerosol decreased significantly ( $\sim 59\%$  to  $26\%$  of SOA mass, respectively, for Experiment 18). This observation provides strong evidence that organic peroxides decompose in the particle phase due to photolysis



**Figure 19.** (a) GC/MS EIC using specific ions for the TMS derivatives of 2-methyltetrols ( $m/z$  219),  $C_5$  alkene triols ( $m/z$  231), and hemiacetal dimers ( $m/z$  219 and 335) for a PM<sub>2.5</sub> aerosol sample collected in Rondônia, Brazil, during the onset of the wet season from 10–12 November 2002 (39 h collection time). The inset shows a detail of the isomeric hemiacetal dimers, formed between 2-methyltetrols and  $C_5$  dihydroxycarbonyls, which elute between 57 and 59 min; (b) averaged EI mass spectrum (only limited mass range  $m/z$  50–500 available) for the TMS derivatives of the isomeric hemiacetal dimers.

and/or subsequent particle-phase reactions, or they are driven out of the particle as a result of gas-phase compounds being reacted away, shifting the equilibrium back to the gas phase. TOF-AMS measurements also confirmed that the peroxide content of low- $NO_x$  SOA decreases with time as shown in Figure 9b. This decrease in peroxide content as a function of time also coincided with high-mass fragment ions ( $m/z > 200$ ) increasing in their abundance (in Figure 9a only  $m/z$  247 and 327 are shown), suggesting the possibility that peroxide decomposition causes oligomerization reactions. These oligomerization reactions likely lead to hemiacetals (as elucidated by GC/MS).

**4.3.6. Tracer Compounds for Isoprene Oxidation in the Remote Atmosphere.** The low- $NO_x$  chamber experiments conducted in this study confirm that 2-methyltetrols indeed serve as tracer compounds for isoprene oxidation in the ambient atmosphere, especially in remote regions such as the Amazonian rainforest. The detection of  $C_5$  alkene triols and hemiacetal dimers in the present low- $NO_x$  experiments corresponds well to their observation in ambient aerosol collected from the Amazonian rainforest<sup>12</sup> and Finnish boreal forests (note that hemiacetal dimers in aerosol collected from the Finnish boreal forests is not yet confirmed).<sup>11</sup> From these field studies,  $C_5$  alkene triols were postulated to form by acid-catalyzed ring-opening reactions of epoxydiol derivatives of isoprene in low  $RH$  environments. However, hemiacetal dimers were not recognized in ambient samples; this current study elucidates their formation under low- $NO_x$  conditions. Once it was realized that

hemiacetal dimers form from  $C_5$  alkene triols and 2-methyltetrols, we referred back to data collected from the Amazonian rainforest.<sup>47</sup> When investigating the GC/MS data carefully, it was found that the hemiacetal dimers were indeed detected, suggesting the atmospheric relevance of these low- $NO_x$  chamber experiments. Shown in Figure 19 is a GC/MS EIC of an Amazonian fine aerosol sample (i.e., PM<sub>2.5</sub>; particulate matter with an aerodynamic diameter  $< 2.5 \mu m$ ) collected during the wet season (low- $NO_x$  conditions) using multiple ions, that is,  $m/z$  231 (to show the  $C_5$  alkene triols),  $m/z$  219 (to show 2-methyltetrols as well as the dimers), and  $m/z$  335 (characteristic of the dimers). An averaged EI mass spectrum for the hemiacetal dimers is also included in this Figure to further confirm their presence in ambient aerosol.

## 5. Conclusions

The composition of SOA from the photooxidation of isoprene under both high- and low- $NO_x$  conditions has been thoroughly investigated through a series of controlled laboratory chamber experiments. It is found that the chemical nature of the resultant SOA is significantly different in the two  $NO_x$  regimes. Under high- $NO_x$  conditions, the SOA components are acidic and form upon the further oxidation of MACR. SOA components formed under low- $NO_x$  conditions, by contrast, are not acidic, with primary species identified being polyols and organic peroxides. On the basis of SOA growth, acid-catalysis seems to play a larger role under low- $NO_x$  conditions. Organic peroxides (likely

dominated by hydroperoxides) contribute significantly to the low-NO<sub>x</sub> SOA mass (~61% for nucleation experiments and ~25% and 30% for dry seeded and acid seeded experiments, respectively). However, differences in the organic peroxide contribution and the rate of loss in SOA mass for nucleation (seed-free) and seeded experiments are not well understood and require further investigation. The chemical composition changes with time in the low-NO<sub>x</sub> case, showing evidence of chemical aging.

Oligomerization is an important SOA formation pathway for both low- and high-NO<sub>x</sub> conditions because oligomers were observed in both cases. The nature of the oligomers, however, is distinctly different in each NO<sub>x</sub> regime. Under high-NO<sub>x</sub> conditions, the oligomers have clear monomeric units, with observable 102 Da differences using both online and offline mass spectrometry techniques. Using tandem ESI-MS techniques and GC/MS with trimethylsilylation, it is found that polyesters account for these high-NO<sub>x</sub> oligomers, with 2-MG as the key monomeric unit. These polyesters account only for a fraction (~22–34%) of the SOA mass formed from isoprene oxidation. This lack of mass closure could result from an underestimate of the amount of polyesters formed or additional, unidentified MACR or isoprene oxidation products that contribute to the SOA mass. One key unresolved question is the path by which 2-MG is formed, which at present is not understood. Further gas- and particle-phase studies on isoprene oxidation under high-NO<sub>x</sub> conditions are needed in order to elucidate the 2-MG formation pathway.

Previously detected tracer compounds for isoprene oxidation in the ambient atmosphere were detected in the low-NO<sub>x</sub> experiments. C<sub>5</sub> alkene triols and hemiacetal dimers are reported here for the first time in a controlled laboratory experiment, suggesting that the oxidative conditions used in these experiments are relevant to remote regions. The GC/MS results suggest that hemiacetal dimers formed in these low-NO<sub>x</sub> chamber experiments result from the reactions of 2-methyltetrols and C<sub>5</sub> alkene triols (a reaction that is likely relevant to the real atmosphere). Besides the formation of hemiacetal (acetal) oligomers in low-NO<sub>x</sub> SOA, it is speculated that peroxyhemiacetal oligomers could also form, because of the large amounts of peroxides measured in the particle phase. The formation of low-NO<sub>x</sub> oligomers may correlate to the decomposition of peroxides with experimental time, providing some insight into the mechanism of oligomerization. Additional analytical techniques need to be developed in order to elucidate the neutral/unstable products found in SOA produced from the photooxidation of isoprene.

**Acknowledgment.** Research at Caltech was funded by the U.S. Environmental Protection Agency to Achieve Results (STAR) Program grant no. RD-83107501-0, managed by EPA's Office of Research and Development (ORD), National Center for Environmental Research (NCER), and by the U.S. Department of Energy, Biological, and Environmental Research Program DE-FG02-05ER63983; this work has not been subjected to the EPA's required peer and policy review and therefore does not necessarily reflect the views of the Agency and no official endorsement should be inferred. Jason Surratt was supported in part by the United States Environmental Protection Agency (EPA) under the Science to Achieve Results (STAR) Graduate Fellowship Program. Research at the Universities of Antwerp and Ghent was supported by the Belgian Federal Science Policy Office through the BIOSOL project (contract SD/AT/02A) and a visiting postdoctoral fellowship to Rafal Szmigielski, and by the Research Foundation –

Flanders (FWO). We would like to thank John Greaves at the University of California, Irvine for the accurate mass measurements on the ESI-TOF instrument. We would like to also thank Paul Ziemann at the University of California, Riverside for his useful communications regarding peroxide measurements in SOA.

**Supporting Information Available:** Electron impact (EI) mass spectra for 2-methyltetrols, C<sub>5</sub> alkene triols, and 2-methyltetrol performate derivatives for their respective chromatographic peaks found in Figure 10. This material is available free of charge via the Internet at <http://pubs.acs.org>.

## References and Notes

- (1) Iinuma, Y.; Böge, O.; Gnauk, T.; Herrmann, H. *Atmos. Environ.* **2004**, *38*, 761.
- (2) Gao, S.; Keywood, M.; Ng, N.; Surratt, J. D.; Varutbangkul, V.; Bahreini, R.; Flagan, R. C.; Seinfeld, J. H. *J. Phys. Chem. A* **2004**, *108*, 10147.
- (3) Gao, S.; Ng, N.; Keywood, M.; Varutbangkul, V.; Bahreini, R.; Nenes, A.; He, J.; Yoo, K.; Beauchamp, J.; Hodyss, R.; Flagan, R.; Seinfeld, J. *Environ. Sci. Technol.* **2004**, *38*, 6582.
- (4) Tolocka, M.; Jang, M.; Ginter, J.; Cox, F.; Kamens, R.; Johnston, M. *Environ. Sci. Technol.* **2004**, *38*, 1428.
- (5) Kalberer, M.; Paulsen, D.; Sax, M.; Steinbacher, M.; Dommen, J.; Prevot, A.; Fisseha, R.; Weingartner, E.; Frankevich, V.; Zenobi, R.; Baltensperger, U. *Science* **2004**, *303*, 1659.
- (6) Kanakidou, M.; Seinfeld, J.; Pandis, S.; Barnes, I.; Dentener, F.; Facchini, M.; Van Dingenen, R.; Ervens, B.; Nenes, A.; Nielsen, C.; Swietlicki, E.; Putaud, J.; Balkanski, Y.; Fuzzi, S.; Horth, J.; Moortgat, G.; Winterhalter, R.; Myhre, C.; Tsigaridis, K.; Vignati, E.; Stephanou, E.; Wilson, J. *Atmos. Chem. Phys.* **2005**, *5*, 1053.
- (7) Claeys, M.; Graham, B.; Vas, G.; Wang, W.; Vermeylen, R.; Pashynska, V.; Cafmeyer, J.; Guyon, P.; Andreae, M. O.; Artaxo, P.; Maenhaut, W. *Science* **2004**, *303*, 1173.
- (8) Pandis, S.; Paulson, S.; Seinfeld, J. H.; Flagan, R. C. *Atmos. Environ.* **1991**, *25*, 997.
- (9) Limbeck, A.; Kulmala, M.; Puxbaum, H. *Geophys. Res. Lett.* **2003**, *30*.
- (10) Ion, A. C.; Vermeylen, R.; Kourtchev, I.; Cafmeyer, J.; Chi, X.; Gelencsér, A.; Maenhaut, W.; Claeys, M. *Atmos. Chem. Phys.* **2005**, *5*, 1805.
- (11) Kourtchev, I.; Ruuskanen, T.; Maenhaut, W.; Kulmala, M.; Claeys, M. *Atmos. Chem. Phys.* **2005**, *5*, 2761.
- (12) Wang, W.; Kourtchev, I.; Graham, B.; Cafmeyer, J.; Maenhaut, W.; Claeys, M. *Rapid Commun. Mass Spectrom.* **2005**, *19*, 1343.
- (13) Claeys, M.; Wang, W.; Ion, A.; Kourtchev, I.; Gelencsér, A.; Maenhaut, W. *Atmos. Environ.* **2004**, *38*, 4093.
- (14) Edney, E. O.; Kleindienst, T. E.; Jaoui, M.; Lewandowski, M.; Offenberger, J. H.; Wang, W.; Claeys, M. *Atmos. Environ.* **2005**, *39*, 5281.
- (15) Böge, O.; Miao, Y.; Plewka, A.; Herrmann, H. *Atmos. Environ.* **2006**, *40*, 2501.
- (16) Kroll, J. H.; Ng, N. L.; Murphy, S. M.; Flagan, R. C.; Seinfeld, J. H. *Geophys. Res. Lett.* **2005**, *32*.
- (17) Kroll, J. H.; Ng, N. L.; Murphy, S. M.; Flagan, R. C.; Seinfeld, J. H. *Environ. Sci. Technol.* **2006**, *40*, 1869.
- (18) Docherty, K.; Wu, W.; Lim, Y.; Ziemann, P. *Environ. Sci. Technol.* **2005**, *39*, 4049.
- (19) Johnson, D.; Jenkin, M. E.; Wirtz, K.; Martin-Reviejo, M. *Environ. Chem.* **2004**, *1*, 150.
- (20) Gao, S.; Surratt, J. D.; Knipping, E. M.; Edgerton, E. S.; Shahgholi, M.; Seinfeld, J. H. *J. Geophys. Res.*, in press, 2006.
- (21) Cocker, D.; Flagan, R. C.; Seinfeld, J. H. *Environ. Sci. Technol.* **2001**, *35*, 2594.
- (22) Keywood, M.; Varutbangkul, V.; Bahreini, R.; Flagan, R.; Seinfeld, J. *Environ. Sci. Technol.* **2004**, *38*, 4157.
- (23) Lai, C.; Tsai, C.; Tsai, F.; Lee, C.; Lin, W. *Rapid Commun. Mass Spectrom.* **2001**, *15*, 2145.
- (24) Drewnick, F.; Hings, S.; DeCarlo, P.; Jayne, J.; Gonin, M.; Fuhrer, K.; Weimer, S.; Jimenez, J.; Demerjian, K.; Borrmann, S.; Worsnop, D. *Aerosol Sci. Technol.* **2005**, *39*, 637.
- (25) Pashynska, V.; Vermeylen, R.; Vas, G.; Maenhaut, W.; Claeys, M. *J. Mass Spectrom.* **2002**, *37*, 1249.
- (26) Banerjee, D.; Budke, C. *Anal. Chem.* **1964**, *36*, 792.
- (27) Sorooshian, A.; Brechtel, F. J.; Ma, Y.; Weber, R. J.; Corless, A.; Flagan, R. C.; Seinfeld, J. H. *Aerosol Sci. Technol.* **2006**, *40*, 396.
- (28) Weber, R.; Orsini, D.; Daun, Y.; Lee, Y.; Klotz, P.; Brechtel, F. *Aerosol Sci. Technol.* **2001**, *35*, 718.



- (29) Seinfeld, J. H.; Pandis, S. N. *Atmospheric Chemistry and Physics: From Air Pollution to Climate Change*; Wiley: New York, 1998.
- (30) Iinuma, Y.; Böge, O.; Miao, Y.; Sierau, B.; Gnauk, T.; Herrmann, H. *Faraday Discuss.* **2005**, *130*, 279.
- (31) Knochenmuss, R.; Zenobi, R. *Chem. Rev.* **2003**, *103*, 441.
- (32) Miyoshi, A.; Hatakeyama, S.; Washida, N. *J. Geophys. Res.* **1994**, *99*, 18779.
- (33) Tuazon, E.; Atkinson, R. *Int. J. Chem. Kinet.* **1990**, *22*, 1221.
- (34) Paulson, S.; Flagan, R. C.; Seinfeld, J. H. *Int. J. Chem. Kinet.* **1992**, *24*, 79.
- (35) Sprengnether, M.; Demerjian, K.; Donahue, N.; Anderson, J. *J. Geophys. Res.* **2002**, *107*.
- (36) Baker, J.; Arey, J.; Atkinson, R. *Environ. Sci. Technol.* **2005**, *39*, 4091.
- (37) Ng, N. L.; Kroll, J. H.; Keywood, M. D.; Bahreini, R.; Varutbangkul, V.; Lee, A.; Goldstein, A. H.; Flagan, R. C.; Seinfeld, J. H. *Environ. Sci. Technol.* **2006**, *40*, 2283.
- (38) Lee, A.; Goldstein, A. H.; Ng, N. L.; Kroll, J. H.; Varutbangkul, V.; Flagan, R. C.; Seinfeld, J. H. *J. Geophys. Res.* **2006**, *111*.
- (39) Chuong, B.; Stevens, P. S. *Int. J. Chem. Kinet.* **2004**, *36*, 12.
- (40) Yuan, H.; Nishiyama, Y.; Kuga, S. *Cellulose* **2005**, *12*, 543.
- (41) Kroll, J. H.; Ng, N. L.; Murphy, S. M.; Varutbangkul, V.; Flagan, R. C.; Seinfeld, J. H. *J. Geophys. Res.* **2005**, *110*.
- (42) Liggio, J.; Li, S.; McLaren, R. *Environ. Sci. Technol.* **2005**, *39*, 1532.
- (43) Barsanti, K.; Pankow, J. *Atmos. Environ.* **2005**, *39*, 6597.
- (44) Tong, C.; Blanco, M.; Goddard, W. A., III; Seinfeld, J. H. *Environ. Sci. Technol.* **2006**, *40*, 2333.
- (45) Johnson, D.; Jenkin, M. E.; Wirtz, K.; Martin-Reviejo, M. *Environ. Chem.* **2005**, *2*, 35.
- (46) Bonn, B.; von Kuhlmann, R.; Lawrence, M. *Geophys. Res. Lett.* **2004**, *31*.
- (47) Decesari, S.; Fuzzi, S.; Facchini, M.; Mircea, M.; Emblico, L.; Cavalli, F.; Maenhaut, W.; Chi, X.; Schkolnik, G.; Falkovich, A.; Rudich, Y.; Claeys, M.; Pashynska, V.; Vas, G.; Kourtev, I.; Vermeylen, R.; Hoffer, A.; Andreae, M. O.; Tagliavini, E.; Moretti, F.; Artaxo, P. *Atmos. Chem. Phys.* **2006**, *6*, 375.

## Appendix B

### Evidence for Organosulfates in Secondary Organic Aerosol\*

---

\*This chapter is reproduced by permission from “Evidence for Organosulfates in Secondary Organic Aerosol” by J. D. Surratt, J. H. Kroll, T. E. Kleindienst, E. O. Edney, M. Claeys, A. Sorooshian, N. L. Ng, J. H. Offenberg, M. Lewandowski, M. Jaoui, R. C. Flagan, and J. H. Seinfeld, *Environ. Sci. Technol.*, *41*, 517-527, 2006. Copyright 2006. American Chemical Society.

## Evidence for Organosulfates in Secondary Organic Aerosol

JASON D. SURRATT,<sup>†</sup> JESSE H. KROLL,<sup>‡,\*</sup>  
TADEUSZ E. KLEINDIENST,<sup>§</sup>  
EDWARD O. EDNEY,<sup>§</sup> MAGDA CLAEYS,<sup>⊥</sup>  
ARMIN SOROOSHIAN,<sup>||</sup> NGA L. NG,<sup>||</sup>  
JOHN H. OFFENBERG,<sup>§</sup>  
MICHAEL LEWANDOWSKI,<sup>§</sup>  
MOHAMMED JAOUI,<sup>#</sup>  
RICHARD C. FLAGAN,<sup>‡</sup> AND  
JOHN H. SEINFELD<sup>\*,‡</sup>

Department of Chemistry, California Institute of Technology, Pasadena, California 91125, Departments of Environmental Science and Engineering and Chemical Engineering, California Institute of Technology, Pasadena, California 91125, National Exposure Laboratory, Office of Research and Development, Environmental Protection Agency, Research Triangle Park, North Carolina 27711, Department of Pharmaceutical Sciences, University of Antwerp (Campus Drie Eiken), Universiteitsplein 1, BE-2610 Antwerp, Belgium, Department of Chemical Engineering, California Institute of Technology, Pasadena, California 91125, and Alion Science and Technology, P.O. Box 12313, Research Triangle Park, North Carolina 27709

Recent work has shown that particle-phase reactions contribute to the formation of secondary organic aerosol (SOA), with enhancements of SOA yields in the presence of acidic seed aerosol. In this study, the chemical composition of SOA from the photooxidations of  $\alpha$ -pinene and isoprene, in the presence or absence of sulfate seed aerosol, is investigated through a series of controlled chamber experiments in two separate laboratories. By using electrospray ionization–mass spectrometry, sulfate esters in SOA produced in laboratory photooxidation experiments are identified for the first time. Sulfate esters are found to account for a larger fraction of the SOA mass when the acidity of seed aerosol is increased, a result consistent with aerosol acidity increasing SOA formation. Many of the isoprene and  $\alpha$ -pinene sulfate esters identified in these chamber experiments are also found in ambient aerosol collected at several locations in the southeastern U.S. It is likely that this pathway is important for other biogenic terpenes, and may be important in the formation of humic-like substances (HULIS) in ambient aerosol.

### Introduction

Particle-phase reactions are now understood to play an important role in secondary organic aerosol (SOA) formation

(1). Particle-phase oligomerization leads to the formation of high-molecular-weight (MW) species (2–4); suggested oligomerization reactions include the reactive uptake of volatile aldehydes or ketones via peroxyhemiacetal formation (5, 6), hydration, hemiacetal/acetal formation, and aldol condensation (7, 8). Esterification in isoprene photooxidation (9, 10) has also been reported in SOA formation. The role of these reactions remains in some doubt as some of the proposed reactions (e.g., hemiacetal/acetal formation and aldol condensation) are not thermodynamically favorable at ambient conditions (11, 12).

Laboratory chamber studies have demonstrated that the presence of acidic seed aerosol enhances the SOA yields observed from the oxidation of various volatile organic compounds (VOCs), such as  $\alpha$ -pinene (2, 3, 13, 14), isoprene (8, 14, 15), and several model cycloalkenes (2) over those with a less acidic seed aerosol. Despite recent advances in understanding particle-phase SOA chemistry, the role of particle-phase acidity in enhancing SOA formation remains essentially unexplained. Recent studies have presented mass spectrometric evidence that the reactive uptake of glyoxal and pinonaldehyde (principal gas-phase oxidation products from aromatics and  $\alpha$ -pinene, respectively) on acidic aerosol involves organosulfate formation (sulfate esters or derivatives; for simplicity, we will use hereafter the term sulfate esters to also denote sulfate derivatives; i.e. sulfate derivatives formed from a carbonyl compound) (16–18). In addition, several field studies have reported sulfate ester signatures in aerosol collected on filters using Fourier transform infrared spectroscopy (19, 20) and electrospray ionization (ESI)–mass spectrometry (MS) (21, 22). Nevertheless, the importance of organosulfate formation to SOA remains unclear. Traditional analytical methods, such as gas chromatography/mass spectrometry (GC/MS) with prior derivatization, may not be well suited for identifying organosulfates. It is likely that single derivatization protocols, such as trimethylsilylation, GC injection and column temperatures could cause the degradation or misinterpretation of such species (23). On the other hand, ESI–MS has been shown as an effective method for the detection and quantification of organosulfate species (24, 25).

In the present study ESI–MS is used to detect and structurally elucidate sulfate esters in SOA formed from the photooxidations of isoprene and  $\alpha$ -pinene under differing combinations of  $\text{NO}_x$  levels and seed aerosol acidities. As a result, the formation of sulfate esters may be a major contributor to the observed enhancement in SOA yields in the presence of acidic aerosol.

### Experimental Section

**Isoprene Chamber Experiments.** A summary of experimental conditions for all isoprene photooxidation experiments can be found in Table 1. Isoprene photooxidation experiments were conducted in Caltech's dual indoor 28 m<sup>3</sup> Teflon chambers (26, 27) and in EPA's fixed volume 14.5 m<sup>3</sup> indoor chamber (15). The temperatures, aerosol size distributions, and relative humidities, as well as the  $\text{O}_3$ , nitric oxide ( $\text{NO}$ ),  $\text{NO}_x$  concentrations were continuously measured in both facilities. The isoprene concentrations in both facilities were monitored by GC with flame ionization detection. The Caltech experiments were conducted in the static mode (i.e., batch reactor) whereas the EPA experiments were conducted in the dynamic mode (i.e., continuous stirred tank reactor) with the exception of EPA-326 which was a static mode experiment. Hydroxyl radical ( $\text{OH}$ ) precursors ( $\text{H}_2\text{O}_2$  or  $\text{HONO}$ ) were employed in the Caltech experiments (28, 29). For all Caltech

\* Corresponding author phone: (626) 395-4635; fax: (626) 796-2591; e-mail: seinfeld@caltech.edu.

<sup>†</sup> Department of Chemistry, California Institute of Technology.

<sup>‡</sup> Departments of Environmental Science and Engineering and Chemical Engineering, California Institute of Technology.

<sup>§</sup> Environmental Protection Agency.

<sup>⊥</sup> University of Antwerp.

<sup>||</sup> Department of Chemical Engineering, California Institute of Technology.

<sup>#</sup> Alion Science and Technology.

<sup>\*</sup> Current address: Aerodyne Research, Inc., 45 Manning Road, Billerica, MA 01281.

TABLE 1. Summary of Experimental Conditions and Sulfate Ester Formation from Isoprene Photooxidation

experiment	inorganic seed aerosol <sup>a</sup>	OH precursor	initial isoprene] (ppb)	initial [NO <sub>x</sub> ] (ppb)	average T (°C)	[M-H] <sup>-</sup> detected sulfate ester ions (m/z)
Caltech low-NO <sub>x</sub>	none added	H <sub>2</sub> O <sub>2</sub>	500	none added	23.7	none detected
Caltech low-NO <sub>x</sub>	AS	H <sub>2</sub> O <sub>2</sub>	500	none added	23.9	215, 333
Caltech low-NO <sub>x</sub>	AAS	H <sub>2</sub> O <sub>2</sub>	500	none added	23.8	153, 155, 169, 215, 333, 451
Caltech high-NO <sub>x</sub>	none added	H <sub>2</sub> O <sub>2</sub> /NO	500	891	24.3	none detected
Caltech high-NO <sub>x</sub>	AS	H <sub>2</sub> O <sub>2</sub> /NO	500	963	24.9	199, 215, 244
Caltech high-NO <sub>x</sub>	AAS	H <sub>2</sub> O <sub>2</sub> /NO	500	904	24.6	139, 153, 155, 197, 199, 215, 244, 260, 301, 346
Caltech high-NO <sub>x</sub>	none added	HONO	500	382	20.1	none detected
Caltech high-NO <sub>x</sub>	AS	HONO	500	366	21.4	199, 215, 260, 333
EPA-299 stage 1	AS <sup>b</sup>	<sup>c</sup>	2500	200	29.0	none detected
EPA-299 stage 2	AAS	<sup>c</sup>	2500	200	29.0	153, 155, 167, 169, 181, 197, 199, 215, 244, 260, 333
EPA-299 stage 3	H <sub>2</sub> SO <sub>4</sub> only	<sup>c</sup>	2500	200	29.0	153, 155, 157, 167, 169, 181, 197, 199, 215, 244, 260, 333
EPA-199 stage 1	60 ppb SO <sub>2</sub>	<sup>c</sup>	1598	475	24.6	197, 199, 215, 244, 260, 301, 317, 333
EPA-199 stage 2	200 ppb SO <sub>2</sub>	<sup>c</sup>	1598	475	24.6	155, 169, 197, 199, 215, 244, 260, 301, 317, 333, 346

<sup>a</sup> AS = 15 mM (NH<sub>4</sub>)<sub>2</sub>SO<sub>4</sub>; AAS = 15 mM (NH<sub>4</sub>)<sub>2</sub>SO<sub>4</sub> + 15 mM H<sub>2</sub>SO<sub>4</sub> for Caltech experiments and 0.31 mM (NH<sub>4</sub>)<sub>2</sub>SO<sub>4</sub> + 0.612 mM H<sub>2</sub>SO<sub>4</sub> for EPA-299 experiments; H<sub>2</sub>SO<sub>4</sub> only = 0.92 mM H<sub>2</sub>SO<sub>4</sub>; EPA-199 had no seed nebulized but instead used the photooxidation of SO<sub>2</sub> to generate sulfuric acid aerosol. <sup>b</sup> Due to the low initial inorganic seed aerosol concentration, this condition is more conducive to nucleation. <sup>c</sup> No OH precursor was used.

TABLE 2. Summary of Experimental Conditions and Sulfate Ester Formation from  $\alpha$ -Pinene Photooxidation

experiment	initial [ $\alpha$ -pinene] (ppb)	initial [isoprene] (ppb)	initial [toluene] (ppm)	initial [NO <sub>x</sub> ] (ppb)	SO <sub>2</sub> (ppb)	average T (°C)	[M-H] <sup>-</sup> detected sulfate ester ions (m/z) <sup>a</sup>
EPA-220	220	<sup>b</sup>	<sup>b</sup>	450	<sup>b</sup>	25.5	none detected
EPA-326	186	1108	<sup>b</sup>	248	287	20.5	249, 265, 294, 310, 412, 426
EPA-211 stage 1	105	<sup>b</sup>	<sup>b</sup>	378	<sup>b</sup>	24.3	none detected
EPA-211 stage 2	105	<sup>b</sup>	1.59	378	<sup>b</sup>	24.3	none detected
EPA-211 stage 3	103	820	1.58	378	<sup>b</sup>	24.3	none detected
EPA-211 stage 4	117	854	1.57	378	275	24.3	265, 279, 294, 310, 326, 412, 426
EPA-211 stage 5	115	<sup>b</sup>	1.59	378	275	24.3	249, 265, 279, 294, 310, 326
EPA-211 stage 6	<sup>b</sup>	794	1.56	378	<sup>b</sup>	24.3	none detected
EPA-205	106	592	1.45	599	278	24.0	265, 294, 310, 412, 426

<sup>a</sup> Isoprene sulfate ester products like those in Table 2 were also detected only when SO<sub>2</sub> and isoprene were copresent. No discernible toluene sulfate ester products were detected. <sup>b</sup> This compound was not present during the experiment.

low-NO<sub>x</sub> experiments, only H<sub>2</sub>O<sub>2</sub> was added, resulting in NO<sub>x</sub> concentrations <1 ppb. Caltech high-NO<sub>x</sub> experiments either used H<sub>2</sub>O<sub>2</sub> and an initial amount of NO (~800 ppb), or with HONO and NO<sub>x</sub> as a side product. In the Caltech experiments, three initial inorganic seed aerosol conditions were used: (1) the absence of aerosol where SOA formation was initiated by nucleation; (2) ammonium sulfate (AS) aerosol; and (3) acidified ammonium sulfate (AAS) aerosol. Concentrations of the aqueous solutions that were introduced into the chambers by atomization are shown in Table 1. The initial seed aerosol concentrations that resulted ranged from ~19–24  $\mu\text{g}/\text{m}^3$ . Teflon filters (PALL Life Sciences, 47-mm diameter, 1.0- $\mu\text{m}$  pore size, Teflon filters) were collected for offline chemical analysis from the Caltech experiments at the point at which the aerosol volume reached its maximum value, as determined by the differential mobility analyzer (DMA). All experiments were carried out at relative humidities (RHs) <9%.

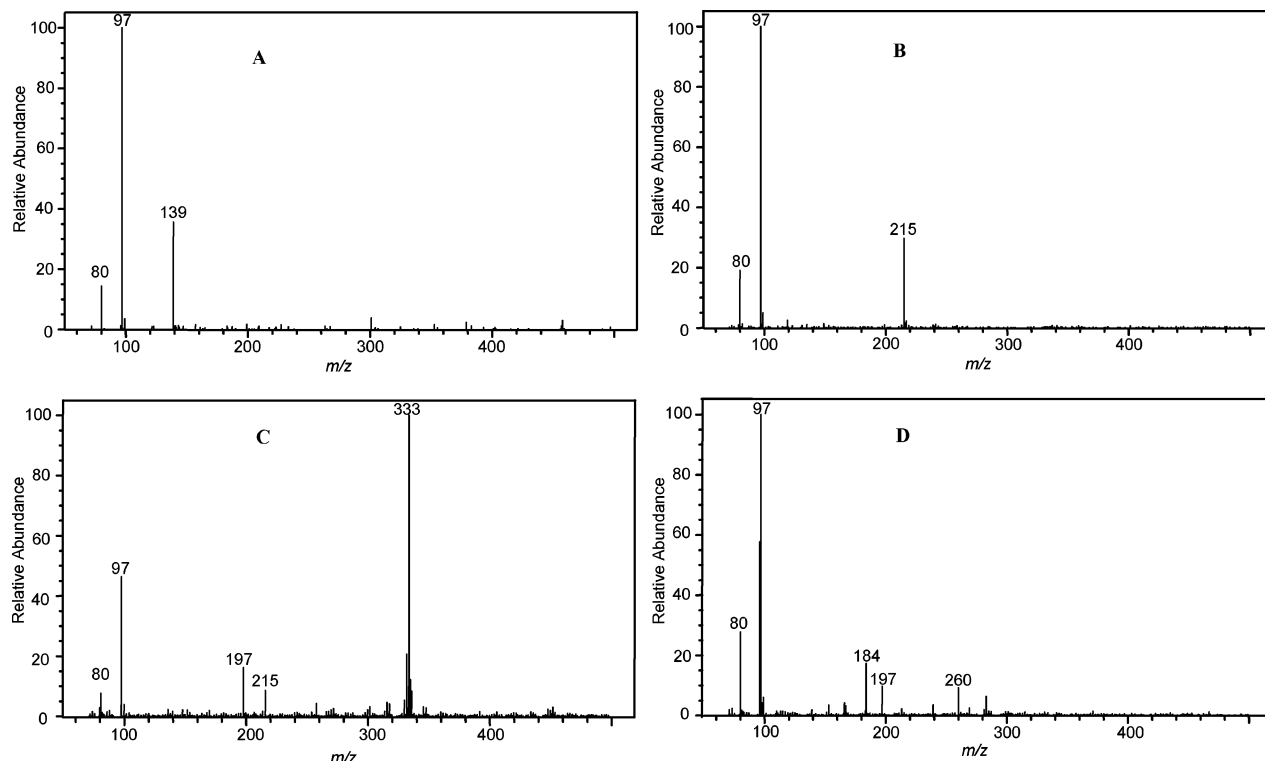
In the dynamic experiments in the EPA chamber, reactants such as NO, SO<sub>2</sub>, and isoprene were continuously added from high-pressure cylinders to the reaction chamber through a mixing manifold. The steady-state nature of chamber operation allows for filter sampling for extended periods for determining the composition of the resultant SOA. Once steady-state conditions were attained (~24 h), samples for determining the composition of the SOA were collected on glass fiber filters preceded by a carbon strip denuder. Two sets of EPA experiments were conducted. In the first set, the

following aerosol conditions were used: AS, AAS, and sulfuric acid, with each of the aqueous solutions atomized into the chamber by atomization. The initial aerosol concentrations were 0.1, 30.0, and 30.0  $\mu\text{g}/\text{m}^3$ , for EPA-299 stage 1, EPA-299 stage 2, and EPA-299 stage 3, respectively. For the second set of EPA experiments, EPA-199 stage 1 and EPA-199 stage 2, acidic aerosol was generated by adding 60 and 200 ppb of SO<sub>2</sub>, respectively to the reactant mixture. All EPA experiments were conducted at a relative humidity of ~30%. Results from both EPA experiments (i.e., SOA yields, gas-phase products, trends, etc.) will be discussed in more detail in forthcoming publications; evidence for organosulfates is the focus here.

**$\alpha$ -Pinene Chamber Experiments.** All  $\alpha$ -pinene experiments were conducted in the EPA dynamic chamber (15). Conditions for each experiment are listed in Table 2. The EPA experiments consisted of one  $\alpha$ -pinene/NO<sub>x</sub> irradiation experiment along with a series of experiments where mixtures of hydrocarbons containing  $\alpha$ -pinene were irradiated in the presence of NO<sub>x</sub>. For some of these experiments, SO<sub>2</sub> was added to the chamber to generate acidity in the aerosol. The same collection protocol was used here as that employed in the EPA isoprene experiments.

**Ambient Aerosol Collection.** Ambient aerosol was collected from the Southeastern Aerosol Research and Characterization Study (SEARCH) network and analyzed for sulfate esters. This network comprises of four urban-rural (or urban-suburban) site pairs at locations across the southeast U.S. and was initiated in mid-1998 to carry out systematic





**FIGURE 1.** (–)LC/ESI–MS upfront CID mass spectra for selected isoprene sulfate ester SOA products shown in Table 2. (A) Product ion mass spectrum for sodium propyl sulfate standard (anionic mass of intact propyl sulfate ester = 139 Da). (B) Product ion mass spectrum for a 2-methyltetrol sulfate ester detected in a Caltech high- $\text{NO}_x$   $\text{H}_2\text{O}_2$  AS seed photooxidation experiment. (C) Product ion mass spectrum for a hemiacetal dimer sulfate ester detected in a Caltech low- $\text{NO}_x$  AAS seed photooxidation experiment. (D) Product ion mass spectrum for a  $\text{C}_5$  trihydroxy nitrate sulfate ester detected in EPA-299 stage 2.

measurements of temporal and spatial variability of PM, in particular  $\text{PM}_{2.5}$ , gases relevant to secondary  $\text{O}_3$  formation, and surface meteorology (22). Twenty-four h composite quartz filters were taken on 4 days at four different sites during June 2004: Birmingham, AL (BHM, urban site), Centerville, AL (CTR, rural site outside of BHM), Jefferson Street (JST, near downtown Atlanta, GA), and Pensacola, FL (PS, marine influenced urban site). Details of these sites (terrain, vegetation, transportation, and industrial sources), sample collection and handling procedures, and specific aerosol and gas-phase measurements obtained are given elsewhere (22, 30).

**Filter Extraction and Chemical Analyses.** Detailed extraction procedures for Teflon and quartz filters are described elsewhere (9, 22). Glass-fiber filters were extracted in the same manner as Teflon filters (9), except resultant extracts were filtered through a PALL Life Sciences Acrodisc CR 25 mm syringe filter (PTFE membrane, 0.2  $\mu\text{m}$  pore size) to remove filter fibers. All sample extracts were analyzed by a Hewlett-Packard 1100 series HPLC instrument, coupled with a quadrupole mass spectrometer, and by direct infusion onto a ThermoElectron LCQ ion trap mass spectrometer (ITMS), both equipped with an ESI source operated in the negative (–) ionization mode. Details of the operating conditions for these instruments are described elsewhere (9). Briefly, all samples were analyzed on the LC/MS instrument in the full scan mode and upfront collision-induced dissociation (CID) mode of analysis. Comparison of the resulting mass spectra produced from these two modes of analyses on the LC/MS instrument allows for some structural information to be obtained on the detected SOA components. Samples were also analyzed on the ThermoElectron LCQ ITMS instrument to confirm these results, and in some cases, provide further structural elucidation. Sulfate standards of sodium propyl sulfate (City Chemical, 98% purity), sodium lauryl sulfate (City Chemical, 98% purity), and 1-butyl-3-methylimidazo-

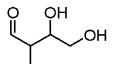
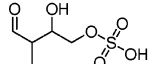
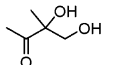
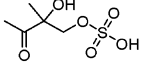
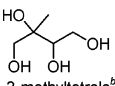
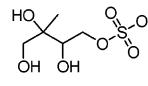
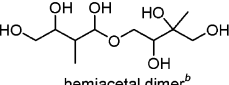
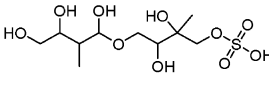
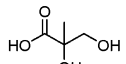
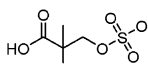
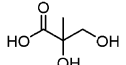
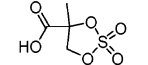
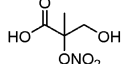
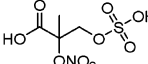
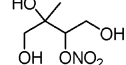
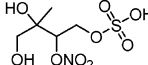
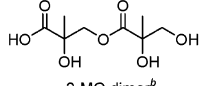
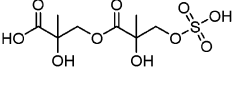
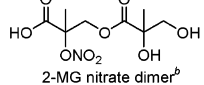
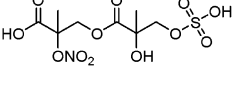

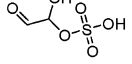

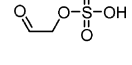
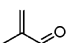
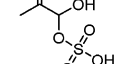
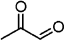
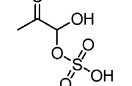
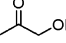
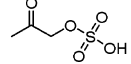
lium 2-(2-methoxyethoxy)ethyl sulfate (Sigma-Aldrich, 95% purity) were analyzed on the LC/MS instrument to determine common product ions associated with sulfate esters. Additional samples were collected with the particle-into-liquid sampler (PILS) with subsequent offline analysis by ion chromatography (IC) (31). The PILS/IC technique allows for the quantitative measurement of water-soluble inorganic ions in aerosol; no IC peaks could be attributed to organosulfates, so for these experiments only inorganic ions are measured.

## Results

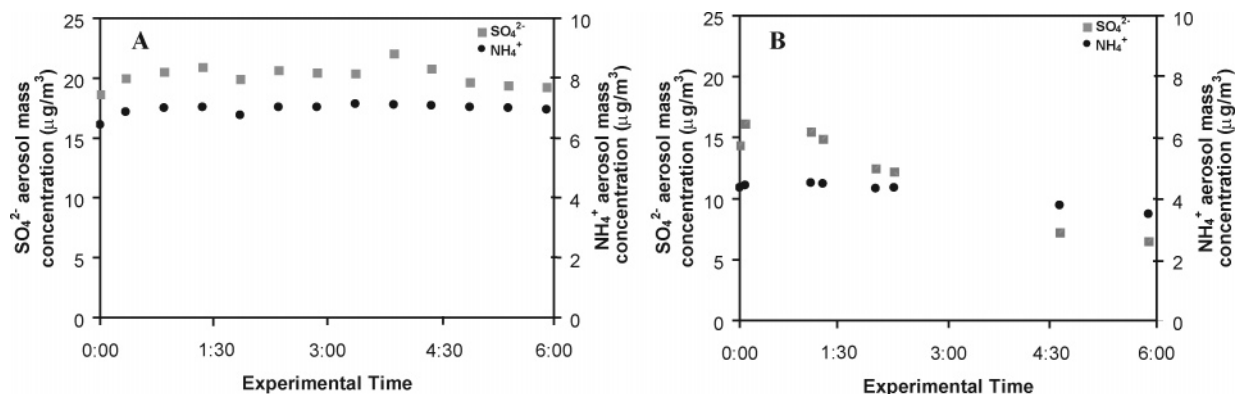
**Sulfate Ester Standards.** (–)ESI–MS studies have shown that sulfate esters produce abundant  $[\text{M}-\text{H}]^-$  ions, and upon collisional activation of these ions, yield  $m/z$  97 ( $\text{HSO}_4^-$ ) and 80 ( $\text{SO}_3^-$ ) product ions (21, 24, 25). In conjunction with the known isotopic distribution of sulfur, which contains  $^{34}\text{S}$  with a natural abundance of 4.2%, these product ions can be used to identify sulfate esters. As confirmation, authentic standards of sodium propyl sulfate (anionic mass = 139 Da), sodium lauryl sulfate (anionic mass = 265 Da), and 1-butyl-3-methylimidazolium 2-(2-methoxyethoxy)ethyl sulfate (anionic mass = 199 Da) were analyzed by the (–)LC/ESI–MS technique in the full scan mode of analysis followed by the upfront CID mode of analysis to generate MS and MS/MS data, respectively. As shown for the sodium propyl sulfate ester standard in Figure 1A, these authentic standards yielded  $m/z$  97 and 80 product ions.

**Sulfate Esters from Isoprene Oxidation.** Previously characterized (9, 10) isoprene SOA products were observed in these experiments and are shown in Table 3; however, the focus here will be on the identification of sulfate esters. Comparison of (–)ESI–MS data collected from experiments employing no sulfate aerosol to those with sulfate aerosol showed that numerous compounds were detected only when sulfate aerosol was present. To understand the nature of

TABLE 3. Proposed Isoprene Sulfate Ester SOA Products

	previously identified isoprene SOA product <sup>a</sup>	MW	proposed sulfate ester structure <sup>a</sup>	observed [M - H] <sup>+</sup> ion (m/z)	major [M - H] <sup>+</sup> product ions (m/z)
Low-NO <sub>x</sub>		118		197	97 80
		118		197	97 80
		136		215 <sup>c,d</sup>	97 80
		254		333 <sup>d</sup>	315 (- H <sub>2</sub> O) <sup>e</sup> 215 (- C <sub>5</sub> alkene triol) 197 (- 2-methyltetrol) 97 80
High-NO <sub>x</sub>		120		199 <sup>c</sup>	119 (- 2-MG) 97 80
		120		181	97 80
		165		244	226 (- H <sub>2</sub> O) 197 (- HONO) 153 (- [CO <sub>2</sub> + HONO]) 97
		181		260 <sup>d</sup>	197 (- HNO <sub>3</sub> ) 183 (- CH <sub>3</sub> NO <sub>3</sub> ) 97 80
		222		301	257 (- CO <sub>2</sub> ) 119 97 80
		267		346	<sup>g</sup>
Highest Acidity Conditions		58		155	<sup>g</sup>
		60		139	<sup>g</sup>
		70		167	<sup>g</sup>
		72		169	<sup>g</sup>
		74		153	<sup>g</sup>

<sup>a</sup> Positional isomers containing nitrate or sulfate groups at other hydroxylated positions are likely. <sup>b</sup> Isoprene SOA products previously identified in prior studies by Surratt et al. (9) and/or Szmigielski et al. (10) and/or Edney et al. (15). <sup>c</sup> Detected in ambient aerosol collected from SEARCH network (summer 2004) for first time. <sup>d</sup> Considered major product due to large MS abundance in chamber studies. <sup>e</sup> Compounds listed in parentheses are neutral losses observed upon (-)ESI-MS/MS. <sup>f</sup> Inferred precursor due to the MS/MS fragmentation of its respective organosulfate product; this parent isoprene product goes undetected by (-)ESI-MS and GC/MS methods. <sup>g</sup> Some evidence for its existence in first-order mass spectra. <sup>h</sup> Detected in ambient aerosol by Matsunaga et al. (32).



**FIGURE 2.** Time evolution of the  $\text{SO}_4^{2-}$  and  $\text{NH}_4^+$  aerosol mass concentrations from the PILS/IC analysis. (A) Caltech high- $\text{NO}_x$   $\text{H}_2\text{O}_2$  isoprene experiment with AS seed aerosol. (B) Caltech low- $\text{NO}_x$  isoprene experiment with AAS seed aerosol. A control experiment was conducted in which seed aerosol is atomized from a solution of 0.015 M AS into the Caltech experimental chamber, and no other reactants such as VOCs or  $\text{NO}_x$  were present. This control experiment produced a similar result to that of Figure 2A (although not evident from the time scale presented,  $\text{SO}_4^{2-}$  and  $\text{NH}_4^+$  decay by  $\sim 20$  and 14%, respectively, over 9 h), indicating that the only loss mechanism for sulfate in this case was wall loss. Of the Caltech isoprene experiments, only the low- $\text{NO}_x$  AAS seed aerosol experiment showed a significant decrease in the  $\text{SO}_4^{2-}$  aerosol mass concentration, indicating that it was likely lost to reaction.

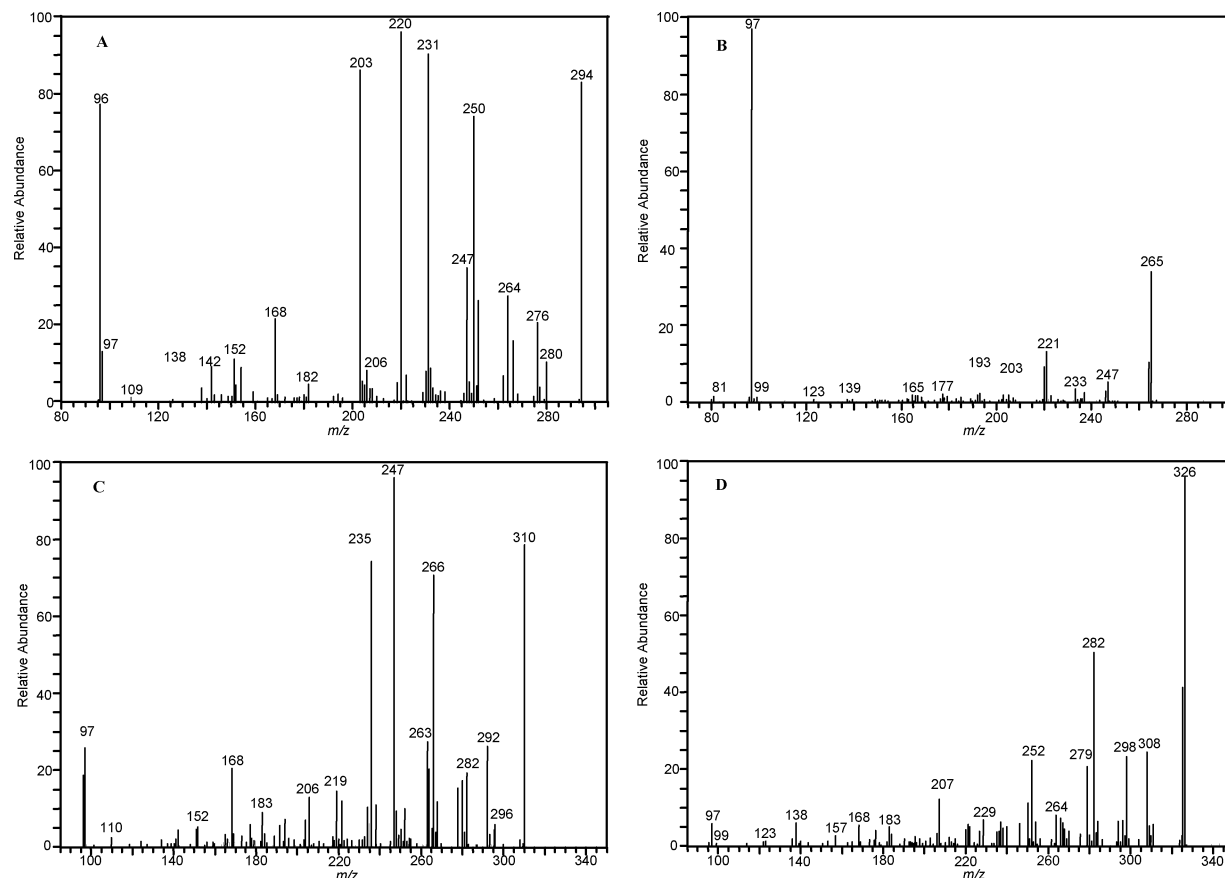
these compounds, tandem MS techniques were employed. Figure 1B–D shows the LC/ESI–MS upfront CID mass spectra collected for large chromatographic peaks common to many of the sulfate aerosol experiments listed in Table 1. The  $[\text{M}-\text{H}]^-$  ions associated with these chromatographic peaks include  $m/z$  215, 333, and 260, respectively. As was the case for the sulfate ester standards, the collisional activation of these  $[\text{M}-\text{H}]^-$  ions yielded  $m/z$  97 and 80 product ions. In addition, these ions also had an isotopic distribution common to sulfur, and as a result, these compounds were identified as sulfate esters. The other product ions, observed in the spectra shown in Figure 1, provided further information on the chemical structures of the identified sulfate esters. Proposed sulfate ester structures for these ions and all other ions listed in Table 1 are given in Table 3. Many of the sulfate esters shown in Table 3 were formed from previously identified isoprene SOA products, including aldehydes, dicarbonyls, hydroxycarbonyls, alcohols, and acids containing an alcohol moiety (9, 10, 32). Sulfate esters formed from small volatile oxidation products, such as glyoxal, hydroxyacetone, and glycolaldehyde, were only detected in experiments involving the highest aerosol acidity. All sulfate esters listed in Table 3 eluted from the reverse-phase LC column within 3 min, indicating their high water solubility. For example, the  $m/z$  215 sulfate ester had a retention time of  $\sim 1.4$  min, close to that of the inorganic sulfate (first peak to elute). On the other hand, the  $m/z$  260 sulfate ester was found to be slightly less polar with isomers eluting at 2.4, 2.7, and 2.9 min. The presence of a nitrate group was confirmed by its even-mass  $[\text{M}-\text{H}]^-$  ion and the observation of a 63 Da ( $\text{HNO}_3$ ) neutral loss shown in Figure 1D. Sulfate ester products given in Table 3 containing nitrate groups were detected only in experiments containing  $\text{NO}_x$ .

In several previous studies, the presence of acidic sulfate aerosol was found to have a pronounced effect on the quantity of SOA formed by the photooxidation of isoprene (9, 14, 15). In the present study, it appears that sulfate ester formation may be similarly enhanced by the introduction of an acidic sulfate aerosol. In the absence of significant levels of inorganic sulfate, no sulfate esters were detected by LC/ESI–MS in any of the isoprene systems considered here. When experiments were carried out in the presence of AS aerosols, a few sulfate esters were detected, including  $[\text{M}-\text{H}]^-$  ions at  $m/z$  199, 215, 244, 260, or 333. Experiments carried out under acidic conditions with AAS aerosol produced a considerably wider array of detectable sulfate ester compounds. In addition, the peak areas of several ions observed in both the AS and AAS experiments were found to be larger in the AAS

experiments. For example, in the low- $\text{NO}_x$  experiments, the LC/MS peak area for the  $m/z$  215 sulfate ester was found to double when AAS aerosol was used rather than nonacidic AS aerosol. Although quantitative data could not be obtained for either the sulfate ester concentrations or the effective acidity of the reaction system, these results suggest that sulfate ester formation is enhanced by the presence of an acidic sulfate aerosol, and that this enhanced sulfate ester formation may be contributing to the increased SOA mass detected previously under acidic conditions. Further work is needed in order to accurately quantify these sulfate esters. It was found that (–)LC/ESI–MS calibration curves generated by surrogate standards lacking sulfate groups (such as *meso*-erythritol) were not suitable for quantifying the identified sulfate esters, resulting from these standards having lower (–)ESI–MS sensitivities. The sulfate ester standards listed in the experimental section were also not suitable for quantification because these compounds had retention times much greater than  $\pm 1$  min of the retention times for the isoprene sulfate esters. Also, these standards lack many structural features common to the identified sulfate esters; therefore, synthesis of more representative standards is needed in order to quantify sulfate esters by (–)LC/ESI–MS.

Sulfate ester aerosol was atomized from a standard solution of sodium propyl sulfate and analyzed directly by the PILS/IC technique; no significant levels of inorganic sulfate were detected, suggesting that organosulfates are thermally stable at the operating conditions of this instrument. In addition, no chromatographic peak in the IC data could be attributed to the sulfate ester standard. These results suggest that the PILS/IC technique will observe decreases in inorganic sulfate if sulfate ester formation occurs.

The time evolution of the  $\text{SO}_4^{2-}$  and  $\text{NH}_4^+$  aerosol mass concentrations obtained using the PILS/IC technique for a Caltech low- $\text{NO}_x$  isoprene AAS seed aerosol experiment is compared to that of a Caltech high- $\text{NO}_x$  AS seed aerosol experiment in Figure 2. As shown in Figure 2A (although not evident from the time scale presented,  $\text{SO}_4^{2-}$  and  $\text{NH}_4^+$  decay by  $\sim 20$  and 14%, respectively, over 9 h), a typical profile for most Caltech isoprene experiments in Table 1, ammonium and sulfate typically decreased slowly with time due to wall-loss processes. However, in the experiment shown in Figure 2B, in which sulfate ester concentrations were exceedingly high, the  $\text{SO}_4^{2-}$  aerosol mass concentration decreased much faster (i.e.,  $\text{SO}_4^{2-}$  decayed by  $\sim 60\%$  over 6 h) than wall loss, suggesting an extra loss process, most likely due to chemical reaction. It should be noted that the initial  $\text{NH}_4^+:\text{SO}_4^{2-}$  molar ratio in Figure 2A was not exactly two due to a known source



**FIGURE 3.** (–)ESI–ITMS product ion mass spectra for sulfate esters of  $\alpha$ -pinene oxidation products. (A) Product ion mass spectrum for  $m/z$  294 detected in EPA-211 stage 5. (B) Product ion mass spectrum for  $m/z$  265 detected in EPA-211 stage 4. (C) Product ion mass spectrum for  $m/z$  310 detected in EPA-211 stage 5. (D) Product ion mass spectrum for  $m/z$  326 detected in EPA-211 stage 5. These sulfate esters were always present when  $\alpha$ -pinene was photooxidized in the presence of  $\text{SO}_2$ .

of ammonium volatilization previously characterized (31). The significant decrease in the  $\text{SO}_4^{2-}$  mass concentration observed for the Caltech low- $\text{NO}_x$  AAS seed aerosol experiment is consistent with previously observed increases in SOA yields (9), strongly suggesting that particle-phase sulfate esterification is at least partly responsible for this “acid-effect.” Filter sampling for most Caltech isoprene experiments began  $\sim 5$ – $7$  h after the experiment was initiated; sulfate esters are formed by this point in the experiments as shown in Figure 2.

**Sulfate Esters from  $\alpha$ -Pinene Oxidation.** As in the isoprene experiments,  $\alpha$ -pinene sulfate esters were found to produce abundant  $[\text{M}-\text{H}]^-$  ions, corresponding  $^{34}\text{S}$  isotopic ions,  $m/z$  97 and 80 product ions, and were not observed in experiments without  $\text{SO}_2$  (Table 2). Isoprene sulfate esters were formed also in experiments involving isoprene and  $\text{SO}_2$  photooxidation; for simplicity, these esters are not listed in Table 2. Shown in Figure 3A–D are the (–)ESI–ITMS product ion spectra for representative  $\alpha$ -pinene sulfate esters; these include esters containing a  $[\text{M}-\text{H}]^-$  ion at  $m/z$  294, 265, 310, and 326, respectively. Analogous to some of the isoprene sulfate esters, the  $m/z$  294, 310, and 326  $\alpha$ -pinene sulfate esters also contain nitrate groups as suggested by their even-mass  $[\text{M}-\text{H}]^-$  ions and observed neutral losses of 63 ( $\text{HNO}_3$ ) and/or 47 Da ( $\text{HONO}$ ). The MS/MS spectra of the  $[\text{M}-\text{H}]^-$  ions for the four  $\alpha$ -pinene sulfate esters yielded  $m/z$  97 product ions. However, the  $m/z$  80 product ion was observed only for the  $m/z$  265 ion due to mass range limits on the mass spectrometer. It should be noted that the MS<sup>3</sup> spectra of high-mass product ions shown in Figure 3 (e.g.,  $m/z$  250 in Figure 1A) did yield the  $m/z$  97 and  $m/z$  80 product ions,

thus supporting that the  $[\text{M}-\text{H}]^-$  ions at  $m/z$  294, 310, and 326 contain a sulfate group. These results were confirmed on the LC/MS instrument operated in the upfront CID mode of analysis.

Sulfate esters from  $\alpha$ -pinene were found to elute from the reverse-phase LC column at much later RTs ( $\sim 10$ – $26$  min) than those formed in isoprene oxidation, indicating differences in water solubility. Identified  $\alpha$ -pinene sulfate esters listed in Table 4 were formed from the reactive uptake of previously identified gas-phase oxidation products (33, 34), consistent with previous work (17, 18). Except for pinonaldehyde, no sulfate esters have been identified to form from previously identified  $\alpha$ -pinene SOA products; however, further investigation is warranted. For quality control purposes, solid-phase extraction (SPE) was used on duplicate filters collected from selected experiments (EPA-211) to remove excess inorganic sulfate; it was found that the  $\alpha$ -pinene sulfate esters were still detected, and in some cases at higher  $[\text{M}-\text{H}]^-$  ion abundances, indicating that these sulfate esters are not a result of inorganic sulfate clusters in the mass spectrometer.

**Sulfate Esters in Ambient Aerosol.** Figures 4A–C compare the LC/MS extracted ion chromatograms (EICs) of  $m/z$  215 obtained from a Caltech low- $\text{NO}_x$  isoprene AAS experiment to that of two SEARCH field samples (JST and BHM, respectively). Both the RTs and mass spectra of the chromatographic peaks shown in the EICs of  $m/z$  215 are the same in all samples, strongly suggesting that this isoprene sulfate ester is present in ambient aerosol. In addition, ambient aerosol recently collected at K-puszt, Hungary indicates that the  $m/z$  199 and 260 isoprene sulfate esters

TABLE 4. Proposed  $\alpha$ -Pinene Sulfate Ester SOA Products

$\alpha$ -pinene oxidation product <sup>a</sup>	MW	proposed sulfate ester structure <sup>a</sup>	observed [M - H] <sup>-</sup> ion (m/z)	major [M - H] <sup>-</sup> product ions (m/z)
	170		249	231 (- H <sub>2</sub> O) <sup>b</sup> 205 97 80
 pinonaldehyde	168 <sup>c</sup>		265 <sup>d,e</sup>	247 (- H <sub>2</sub> O) 221 185 97 (- pinonaldehyde) 80
	200 <sup>c</sup>		279 <sup>e,f</sup>	261 (- H <sub>2</sub> O) 235 199 181 97 80
	200 <sup>c</sup>		279 <sup>e,f</sup>	261 (- H <sub>2</sub> O) 235 199 181 97 80
	215 <sup>c</sup>		294 <sup>g</sup>	247 (- HONO) 231 (- HNO <sub>3</sub> ) 220 96 80
	231 <sup>c</sup>		310 <sup>g,h</sup>	263 (- HONO) 236 247 (- HNO <sub>3</sub> ) 97
	247		326 <sup>e</sup>	308 (- H <sub>2</sub> O) 282 (- CO <sub>2</sub> ) 279 (- HONO) 252 97

<sup>a</sup> Positional isomers containing nitrate or sulfate groups at other hydroxylated positions are possible. <sup>b</sup>Compounds listed in parentheses are neutral losses observed upon ESI-MS/MS. <sup>c</sup>Previously detected  $\alpha$ -pinene oxidation product by Aschmann et al. (33, 34). <sup>d</sup>Proposed by Liggio et al. (17) to form from pinonaldehyde reactive uptake onto acidic seed particles; however, structure was not confirmed. In the current study, we confirm its structure with (-)ESI-MS. <sup>e</sup>Detected in ambient aerosol collected from SEARCH network June 2004 for first time. <sup>f</sup>ESI-MS cannot differentiate between which product is being detected; for completeness both structures are shown here. <sup>g</sup>Observed in an ambient study by Gao et al. (22). <sup>h</sup>No structural information was provided in the previous study by Gao et al. (22).

are present (M. Claeys, unpublished results); however, these compounds are only weakly detected on some days analyzed from the SEARCH network.

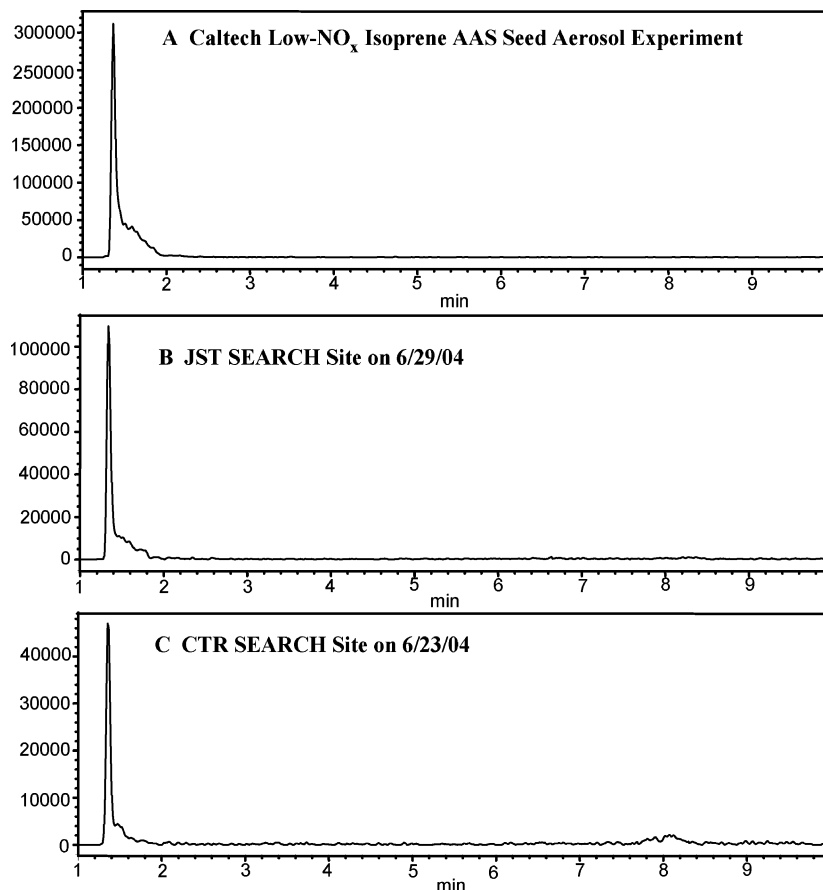
Figure 5A–C compares the LC/MS EICs of  $m/z$  294 obtained from two  $\alpha$ -pinene experiments (EPA-205 and EPA-326, respectively) and with a SEARCH field sample collected at the BHM field site in June 2004. This figure indicates that the  $\alpha$ -pinene  $m/z$  294 sulfate ester is a constituent of ambient aerosol, consistent with previous work (22). Other  $\alpha$ -pinene sulfate esters identified in this study have been observed in ambient aerosol in the southeastern U.S. (22). It is possible that the  $m/z$  294 sulfate ester in the ambient aerosol could also result from the oxidation of other monoterpenes owing

to the lack of detailed connectivity of specific functional groups (e.g., sulfate esters and hydroxyls) provided by ESI-MS/MS methods.

The results above suggest that the chemistry occurring in our laboratory experiments are relevant to the conditions in the southeastern U.S., even though the laboratory aerosol was generated from much higher VOC mixing ratios, lower RHs, and likely higher aerosol acidities observed in the southeastern U.S.

**ESI-MS Quality Control Tests.** To ensure that the sulfate esters elucidated in this study were formed only during SOA formation and not on the filter or during the ESI process, several quality control tests were conducted. First, a filter





**FIGURE 4.** (—)LC/ESI–MS extracted ion chromatograms for  $m/z$  215. The retention times of the  $m/z$  215 EICs are the same as well as the mass spectra associated with each chromatographic peak; therefore, the comparison of these EICs suggests that the photooxidation of isoprene in the presence of acid seed produces these sulfate esters observed in the ambient aerosol. In all chamber experiments involving isoprene in the presence of AS seed aerosol, AAS seed aerosol, or  $\text{SO}_2$ , the  $m/z$  215 ion was detected.

extract from a Caltech low- $\text{NO}_x$  isoprene nucleation (i.e., no inorganic seed aerosol present) experiment was divided into two parts. One part was spiked with a high concentration of  $(\text{NH}_4)_2\text{SO}_4$  and the other part was spiked with pure  $\text{H}_2\text{SO}_4$ . Both of these samples were analyzed by (—)LC/ESI–MS. The sulfate esters listed in Table 1 were not detected in these two test samples, demonstrating that the sulfate esters detected in this study are likely not artifacts formed in the ESI interface. The use of reverse phase chromatography allowed for inorganic sulfate not to be confused with organosulfates, where inorganic sulfate was the very first peak to elute from the column. In the two test samples discussed above, the inorganic sulfate peak was found to have some tailing, which was very similar to the seeded experiments listed in Table 1; however, this tailing seems to have no effect on the formation of sulfate esters.

As a second test, a *meso*-erythritol (a surrogate for the 2-methyltetrols produced from isoprene oxidation) standard was divided into two parts, where one was spiked with  $(\text{NH}_4)_2\text{SO}_4$  and the other with pure  $\text{H}_2\text{SO}_4$ . As for the first quality control test above, these two samples produced no sulfate esters in (—)LC/ESI–MS.

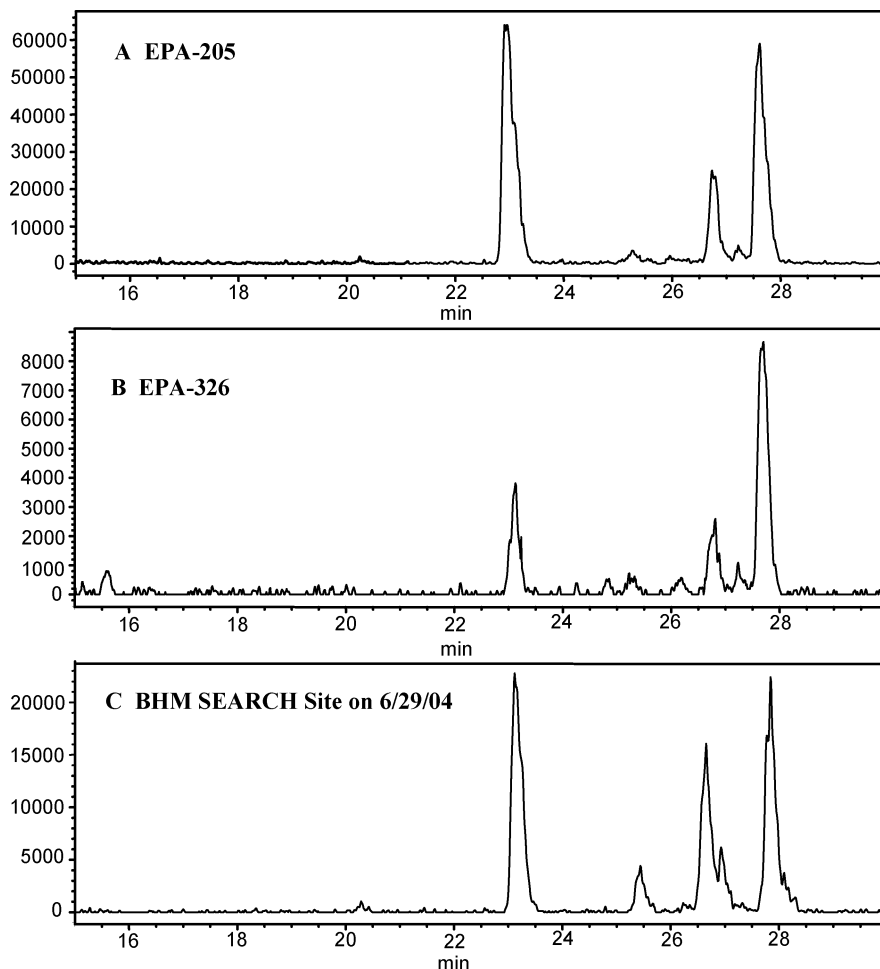
Last, a filter extract from an EPA  $\alpha$ -pinene experiment conducted without  $\text{SO}_2$  (thus no sulfate aerosol present) was spiked with pure  $\text{H}_2\text{SO}_4$ . Again, no sulfate esters were detected. These results strongly suggest the organosulfates (sulfate esters) were formed in the aerosol phase and are not an artifact of sampling or measurement.

## Discussion

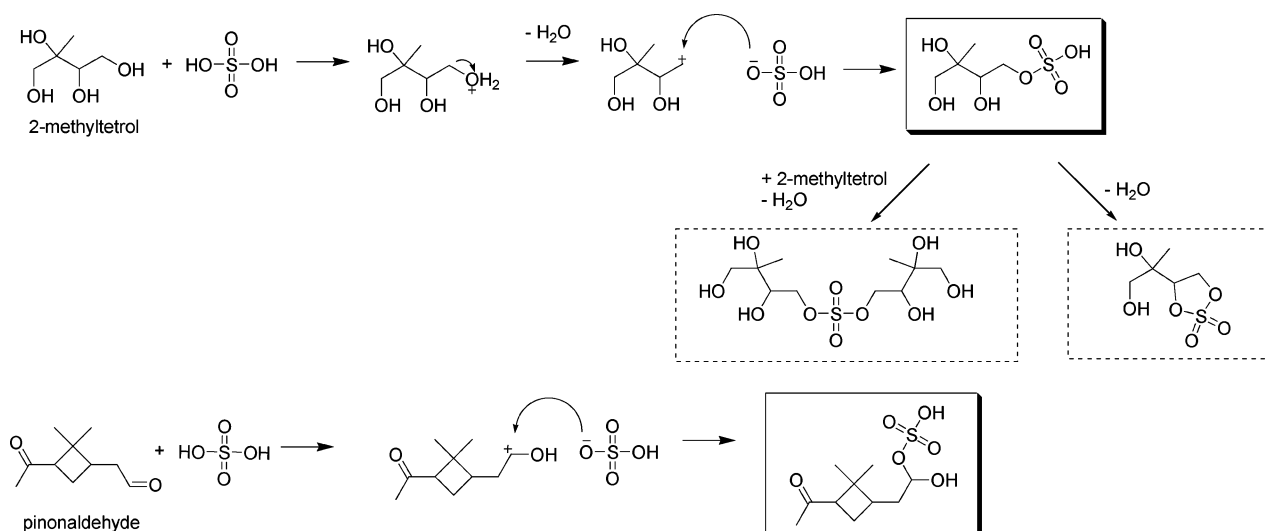
**Sulfate Esterification Reaction Mechanism.** Reactive uptake of gas-phase alcohols (e.g., methanol and ethanol) and

aldehydes (e.g., formaldehyde) in the upper troposphere and lower stratosphere have been suggested to occur in the presence of sulfate aerosols (35–37), where increased acidity was found to increase their uptake. Some of these studies proposed that the observed uptake of the alcohols and aldehydes likely occurred by sulfate ester formation, although no product studies were conducted. It has also been shown that reactive uptake of butanol and ethanol onto sulfate aerosols occurs at room temperature (38, 39). Esterification was recently shown to occur from the photooxidation of isoprene in the presence of  $\text{NO}_x$  from condensation reactions of organic acids with alcohols (9, 10). The large amounts of organic acids formed during the photooxidation were proposed to drive these reactions.

Figure 6 shows the general reactions proposed for the formation of sulfate esters from alcohols (2-methyltetrol used as model compound) and sulfate derivatives from carbonyl compounds (pinonaldehyde used as model compound). In the case of sulfate ester formation from alcohols, the proposed reactions likely involve nucleophilic substitution ( $\text{S}_\text{N}1$ ), where the sulfuric acid protonates the alcoholic group, making water the leaving group. The resulting carbocation becomes a nucleophilic site for the unshared pair of electrons on one of the oxygen atoms of the sulfate (40). Due to the low relative humidities of these experiments, this likely shifts the equilibrium in favor of sulfate ester formation. In the case of sulfate ester formation from aldehydes, the proposed reaction likely involves the electron pair of the carbonyl oxygen accepting a proton from sulfuric acid, producing the oxonium ion, and making it more susceptible to nucleophilic attack from an unshared pair of electrons from one of the oxygen atoms on sulfate. It should be stressed that other reaction



**FIGURE 5.** (–)LC/ESI–MS extracted ion chromatograms for  $m/z$  294. The retention times of the  $m/z$  294 compounds were the same as well as the mass spectra associated with each chromatographic peak; therefore, the comparison of these EICs suggests that the photooxidation of  $\alpha$ -pinene in the presence of  $\text{NO}_x$  and acid seed produces these sulfate esters in ambient aerosol. No  $m/z$  294 compounds were detected in experiments involving only isoprene and acid seed (or  $\text{SO}_2$ ).



**FIGURE 6.** Proposed reactions for the formation of sulfate esters from 2-methyltetrol and pinonaldehyde, a representative alcohol and aldehyde generated by the photooxidation of isoprene and  $\alpha$ -pinene, respectively. Solid boxes indicate (–)ESI–MS detected species. Dashed boxes indicate other proposed products possibly formed.

mechanisms are also possible, including: electrophilic addition of  $\text{H}_2\text{SO}_4$  to an aliphatic double bond, addition of  $\text{SO}_3$  through some radical process, or by some other unknown mechanism currently not understood. Sulfate diester ( $\text{ROSO}_3\text{R}$ ) formation and sulfate ester oligomerization could also take

place in the case of polyols; however, (–)ESI–MS is not sensitive to such neutral species, no such products have yet been identified. In prior work (9) we reported oligomeric signatures (14, 16, 18 Da differences) and compounds with masses up to  $\sim 620$  Da in matrix-assisted laser desorption

ionization (MALDI)–MS data collected for Caltech low-NO<sub>x</sub> seeded experiments; AAS seed cases produced the most prominent signals, possibly providing evidence for the sulfate diester or sulfate ester oligomerization reactions.

**Isoprene Sulfate Esters and the role of NO<sub>x</sub>.** Surratt et al. (9) observed a significant increase in the SOA yield in the low-NO<sub>x</sub> AAS seed aerosol experiments, whereas very little (if any) increase in the SOA yield was observed in the high-NO<sub>x</sub> AAS seed aerosol experiments. This difference likely occurs because of the large abundance of organic acids formed under high-NO<sub>x</sub> conditions competing with sulfuric acid (or sulfate) for esterification with alcohols. The low-NO<sub>x</sub> SOA was found to comprise largely of neutral polyols (e.g., 2-methyltetrols and hemiacetal dimers in Table 3) and hydroperoxides, which may react readily with sulfuric acid to produce sulfate esters. In previous work (9) we reported detecting no SOA components with (–)LC/ESI–MS for the low-NO<sub>x</sub> seeded cases; reanalysis of that data indicates that sulfate esters (*m/z* 215, 333, and 415) were in fact detected, but because they eluted very closely to inorganic sulfate (within 1–1.5 min), they were believed to be an artifact.

**Atmospheric Implications.** Sulfate esters identified previously in ambient aerosol (21, 22) appear to be secondary in nature, as demonstrated by the present study. Of particular significance is the detection of sulfate esters from isoprene and  $\alpha$ -pinene in ambient aerosols, which could be indicators for the acid induced reaction pathway. There is also the possibility that oxidation of other hydrocarbons emitted into the atmosphere in high abundances, including monoterpenes other than  $\alpha$ -pinene as well as sesquiterpenes, could lead to the formation of aerosol-bound sulfate esters. These esters could contribute significantly to the HULIS fraction of ambient aerosol due to their high water-solubility, acidity, thermally stability, and high molecular weights, all of which are common properties of HULIS (41). Strong chemical evidence is presented here for the substantial occurrence of sulfate esterification in both laboratory-generated and ambient aerosols. This evidence provides one concrete explanation for the observed increase in SOA yields in response to increasing aerosol acidity. Additional studies are needed to determine the mass fraction of sulfate esters in ambient aerosols and the factors that influence their formation, such as relative humidity, temperature, and initial sulfate aerosol mass concentrations, in order to better understand and model this chemistry.

## Acknowledgments

Research at Caltech was funded by the U.S. Environmental Protection Agency Science to Achieve Results (STAR) program grant no. RD-83107501-0, managed by EPA's Office of Research and Development (ORD), National Center for Environmental Research (NCER) and Cooperative Agreement CR-831194001, and by the U.S. Department of Energy, Biological, and Environmental Research Program DE-FG02-05ER63983. This article has been jointly developed and published by EPA and the California Institute of Technology. It was produced under Cooperative Agreement no. CR83194001 and is subject to 40 CFR 30.36. The article has been reviewed by EPA personnel under EPA scientific and technical peer review procedures and approved for joint publication based on its scientific merit, technical accuracy, or contribution to advancing public understanding of environmental protection. However, the Agency's decision to publish the article jointly with Caltech is intended to further the public purpose supported by Cooperative Agreement no. CR83194001 and not to establish an official EPA rule, regulation, guidance, or policy through the publication of this article. Further, EPA does not endorse any products or commercial services mentioned in this publication. J.D.S. was supported in part by the United States Environmental Protection Agency (EPA)

under the Science to Achieve Results (STAR) Graduate Fellowship Program. Research at the University of Antwerp was supported by the Belgian Federal Science Policy Office and the Research Foundation-Flanders (FWO). The Electric Power Research Institute provided support for the SEARCH network. We thank Rafal Szmigielski for his discussions on sulfation reactions.

## Literature Cited

- (1) Kanakidou, M.; Seinfeld, J. H.; Pandis, S. N.; Barnes, I.; Dentener, F. J.; Facchini, M. C.; van Dingenen, R.; Ervens, B.; Nenes, A.; Nielsen, C. J.; Swietlicki, E.; Putaud, J. P.; Balkanski, Y.; Fuzzi, S.; Horth, J.; Moortgat, G. K.; Winterhalter, R.; Myhre, C. E. L.; Tsigaridis, K.; Vignati, E.; Stephanou, E. G.; Wilson, J. Organic aerosol and global climate modeling: a review. *Atmos. Chem. Phys.* **2005**, *5*, 1053–1123.
- (2) Gao, S.; Keywood, M.; Ng, N. L.; Surratt, J. D.; Varutbangkul, V.; Bahreini, R.; Flagan, R. C.; Seinfeld, J. H. Low-molecular-weight and oligomeric components in secondary organic aerosol from the ozonolysis of cycloalkenes and  $\alpha$ -pinene. *J. Phys. Chem. A* **2004**, *108*, 10147–10164.
- (3) Gao, S.; Ng, N. L.; Keywood, M.; Varutbangkul, V.; Bahreini, R.; Nenes, A.; He, J.; Yoo, K. Y.; Beauchamp, J. L.; Hodys, R. P.; Flagan, R. C.; Seinfeld, J. H. Particle phase acidity and oligomer formation in secondary organic aerosol. *Environ. Sci. Technol.* **2004**, *38*, 6582–6589.
- (4) Tolocka, M. P.; Jang, M.; Ginter, J. M.; Cox, F. J.; Kamens, R. M.; Johnston, M. V. Formation of oligomers in secondary organic aerosol. *Environ. Sci. Technol.* **2004**, *38*, 1428–1434.
- (5) Tobias, H. J.; Ziemann, P. J. Thermal desorption mass spectrometric analysis of organic aerosol formed from reactions of 1-tetradecene and O<sub>3</sub> in the presence of alcohols and carboxylic acids. *Environ. Sci. Technol.* **2000**, *34*, 2105–2115.
- (6) Docherty, K. S.; Wu, W.; Lim, Y. B.; Ziemann, P. J. Contributions of organic peroxides to secondary aerosol formed from reactions of monoterpenes with O<sub>3</sub>. *Environ. Sci. Technol.* **2005**, *39*, 4049–4059.
- (7) Jang, M.; Kamens, R. M. Atmospheric secondary aerosol formation by heterogeneous reactions of aldehydes in the presence of sulfuric acid aerosol catalyst. *Environ. Sci. Technol.* **2001**, *35*, 4758–4766.
- (8) Jang, M.; Czoschke, N. M.; Lee, S.; Kamens, R. M. Heterogeneous atmospheric aerosol production by acid-catalyzed particle-phase reactions. *Science* **2002**, *298*, 814–817.
- (9) Surratt, J. D.; Murphy, S. M.; Kroll, J. H.; Ng, N. L.; Hildebrandt, L.; Sorooshian, A.; Szmigielski, R.; Vermeylen, R.; Maenhaut, W.; Claeys, M.; Flagan, R. C.; Seinfeld, J. H. Chemical composition of secondary organic aerosol formed from the photooxidation of isoprene. *J. Phys. Chem. A* **2006**, *110*, 9665–9690.
- (10) Szmigielski, R.; Surratt, J. D.; Vermeylen, R.; Szmigielska, K.; Kroll, J. H.; Ng, N. L.; Murphy, S. M.; Sorooshian, A.; Seinfeld, J. H.; Claeys, M. Characterization of 2-methylglyceric acid oligomers in secondary organic aerosol formed from the photooxidation of isoprene using trimethylsilylation and gas chromatography/ion trap mass spectrometry. *J. Mass. Spectrom.* **2006**, doi 10.1002/jms.1146.
- (11) Barsanti, K. C.; Pankow, J. F. Thermodynamics of the formation of atmospheric organic particulate matter by accretion reactions—part 1: aldehydes and ketones. *Atmos. Environ.* **2004**, *38*, 4371–4282.
- (12) Barsanti, K. C.; Pankow, J. F. Thermodynamics of the formation of atmospheric organic particulate matter by accretion reactions—part 2: dialdehydes, methylglyoxal, and diketones. *Atmos. Environ.* **2005**, *39*, 6597–6607.
- (13) Iinuma, Y.; Böge, O.; Gnauk, T.; Hermann, H. Aerosol-chamber study of the  $\alpha$ -pinene/O<sub>3</sub> reaction: influence of particle acidity on aerosol yields and products. *Atmos. Environ.* **2004**, *38*, 761–773.
- (14) Kleindienst, T. E.; Edney, E. O.; Lewandowski, M.; Offenberg, J. H.; Jaoui, M. Secondary organic carbon and aerosol yields from the irradiations of isoprene and  $\alpha$ -pinene in the presence of NO<sub>x</sub> and SO<sub>2</sub>. *Environ. Sci. Technol.* **2006**, *40*, 3807–3812.
- (15) Edney, E. O.; Kleindienst, T. E.; Jaoui, M.; Lewandowski, M.; Offenberg, J. H.; Wang, W.; Claeys, M. Formation of 2-methyltetrols and 2-methylglyceric acid in secondary organic aerosol from laboratory irradiated isoprene/NO<sub>x</sub>/SO<sub>2</sub>/air mixtures and their detection in ambient PM<sub>2.5</sub> samples collected in the eastern United States. *Atmos. Environ.* **2005**, *39*, 5281–5289.



- (16) Liggio, J.; Li, S.; McLaren, R. Heterogeneous reactions of glyoxal on particulate matter: identification of acetals and sulfate esters. *Environ. Sci. Technol.* **2005**, *39*, 1532–1541.
- (17) Liggio, J.; Li, S. Organosulfate formation during the uptake of pinonaldehyde on acidic sulfate aerosols. *Geophys. Res. Lett.* **2006**, *33*, L13808, doi:10.1029/2006GL026079.
- (18) Liggio, J.; Li, S. Reactive uptake of pinonaldehyde on acidic aerosols. *J. Geophys. Res.* **2006**, in press.
- (19) Blando, J. D.; Porcja, R. J.; Li, T.; Bowman, D.; Lioy, P. J.; Turpin, B. J. Secondary formation and the smoky mountain organic aerosol: an examination of aerosol polarity and functional group composition during SEAVS. *Environ. Sci. Technol.* **1998**, *32*, 604–613.
- (20) Maria, S. F.; Russell, L. M.; Turpin, B. J.; Porcja, R. J.; Campos, T. L.; Weber, R. J.; Huebert, B. J. Source signatures of carbon monoxide and organic functional groups in Asian Pacific Regional Characterization Experiment (ACE-Asia) submicron aerosol types. *J. Geophys. Res.* **2003**, *108*, 8637–8650.
- (21) Romero, F.; Oehme, M. Organosulfates—a new component of humic-like substances in atmospheric aerosols? *J. Atmos. Chem.* **2005**, *52*, 283–294.
- (22) Gao, S.; Surratt, J. D.; Knipping, E. M.; Edgerton, E. S.; Shahgholi, M.; Seinfeld, J. H. Characterization of polar organic components in fine aerosols in the southeastern United States: identity, origin, and evolution. *J. Geophys. Res.* **2006**, *111*, D14314, doi:10.1029/2005JD006601.
- (23) Murray, S.; Baillie, T. A. Direct derivatization of sulphate esters for analysis by gas chromatography mass spectrometry. *Biomed. Mass Spectrom.* **1979**, *6*, 81–89.
- (24) Boss, B.; Richling, E.; Herderich, M.; Schreier, P. HPLC-ESI-MS/MS analysis of sulfated flavor compounds in plants. *Phytochemistry* **1999**, *50*, 219–225.
- (25) Metzger, K.; Rehberger, P. A.; Erben, G.; Lehmann, W. D. Identification and quantification of lipid sulfate esters by electrospray ionization MS/MS techniques: cholesterol sulfate. *Anal. Chem.* **1995**, *67*, 4178–4183.
- (26) Cocker, D.; Flagan, R. C.; Seinfeld, J. H. State-of-the-art chamber facility for studying atmospheric aerosol chemistry. *Environ. Sci. Technol.* **2001**, *35*, 2594–2601.
- (27) Keywood, M.; Varutbangkul, V.; Bahreini, R.; Flagan, R. C.; Seinfeld, J. H. Secondary organic aerosol formation from the ozonolysis of cycloalkenes and related compounds. *Environ. Sci. Technol.* **2004**, *38*, 4157–4164.
- (28) Kroll, J. H.; Ng, N. L.; Murphy, S. M.; Flagan, R. C.; Seinfeld, J. H. Secondary organic aerosol formation from isoprene photooxidation under high-NO<sub>x</sub> conditions. *Geophys. Res. Lett.* **2005**, *32*, L18808, doi:10.1029/2005GL023637.
- (29) Kroll, J. H.; Ng, N. L.; Murphy, S. M.; Flagan, R. C.; Seinfeld, J. H. Secondary organic aerosol formation from isoprene photooxidation. *Environ. Sci. Technol.* **2006**, *40*, 1869–1877.
- (30) Hansen, D.; Edgerton, E. S.; Hartsell, B. E.; Jansen, J. J.; Kandasamy, N.; Hidy, G. M.; Blanchard, C. L. The southeastern aerosol research and characterization study: Part 1-overview. *J. Air Waste Manage.* **2003**, *53*, 1460–1471.
- (31) Sorooshian, A.; Brechtel, F. J.; Ma, Y.; Weber, R. J.; Corless, A.; Flagan, R. C.; Seinfeld, J. H. Modeling and characterization of a particle-into-liquid sampler (PILS). *Aerosol Sci. Technol.* **2006**, *40*, 396–409.
- (32) Matsunaga, S. N.; Wiedinmyer, C.; Guenther, A. B.; Orlando, J. J.; Karl, T.; Toohey, D. W.; Greenberg, J. P.; Kajii, Y. Isoprene oxidation products are significant atmospheric aerosol components. *Atmos. Chem. Phys. Discuss.* **2005**, *5*, 11143–11156.
- (33) Aschmann, S. M.; Reissell, A.; Atkinson, R.; Arey, J. Products of the gas phase reactions of the OH radical with  $\alpha$ - and  $\beta$ -pinene in the presence of NO. *J. Geophys. Res.* **1998**, *103*, 25553–25561.
- (34) Aschmann, S. M.; Atkinson, R.; Arey, J. Products of reaction of OH radicals with  $\alpha$ -pinene. *J. Geophys. Res.* **2002**, *107*, 4191–4197.
- (35) Iraci, L. T.; Tolbert, M. A. Heterogeneous interaction of formaldehyde with cold sulfuric acid: Implications for the upper troposphere and lower stratosphere. *J. Geophys. Res.* **1997**, *102*, 16099–16107.
- (36) Kane, S. M.; Leu, M. Uptake of methanol vapor in sulfuric acid solutions. *J. Phys. Chem. A* **2001**, *205*, 1411–1415.
- (37) Michelsen, R. R.; Staton, J. R.; Iraci, L. T. Uptake and dissolution of gaseous ethanol in sulfuric acid. *J. Phys. Chem. A* **2006**, *110*, 6711–6717.
- (38) Hanson, D. R.; Eisele, F. L.; Ball, S. M.; McMurry, P. M. Sizing small sulfuric acid particles with an ultrafine particle condensation nucleus counter. *Aerosol Sci. Technol.* **2002**, *36*, 554–559.
- (39) Joutsensaari, J.; Toivonen, T.; Vaattovaara, P.; Vesterinen, M.; Vepsäläinen, J.; Laaksonen, A. Time-resolved growth behavior of acid aerosols in ethanol vapor with a tandem-DMA technique. *J. Aerosol Sci.* **2004**, *35*, 851–867.
- (40) Deno, N. C.; Newman, M. S. Mechanism of sulfation of alcohols. *J. Am. Chem. Soc.* **1950**, *72*, 3852–3856.
- (41) Graber, E. R.; Rudich, Y. Atmospheric HULIS: how humic-like are they? A comprehensive and critical review. *Atmos. Chem. Phys.* **2006**, *6*, 729–753.

Received for review August 30, 2006. Revised manuscript received October 18, 2006. Accepted November 3, 2006.

ES062081Q

## Appendix C

# Characterization of 2-Methylglyceric Acid Oligomers in Secondary Organic Aerosol Formed from the Photooxidation of Isoprene Using Trimethylsilylation and Gas Chromatography/Ion Trap Mass Spectrometry\*

---

\*This chapter is reproduced by permission from “Characterization of 2-Methylglyceric Acid Oligomers in Secondary Organic Aerosol Formed from the Photooxidation of Isoprene Using Trimethylsilylation and Gas Chromatography/Ion Trap Mass Spectrometry” by R. Szmigielski, J. D. Surratt, R. Vermeylen, K. Szmigielska, J. H. Kroll, N. L. Ng, S. M. Murphy, A. Sorooshian, J. H. Seinfeld, and M. Claeys, *J. Mass. Spectrom.*, 42, 101-116, 2007. Copyright 2007. John Wiley & Sons, Ltd.

# Characterization of 2-methylglyceric acid oligomers in secondary organic aerosol formed from the photooxidation of isoprene using trimethylsilylation and gas chromatography/ion trap mass spectrometry

Rafal Szmigielski,<sup>1</sup> Jason D. Surratt,<sup>2</sup> Reinhilde Vermeylen,<sup>1</sup> Katarzyna Szmigielska,<sup>1</sup> Jesse H. Kroll,<sup>3,4</sup> Nga L. Ng,<sup>4</sup> Shane M. Murphy,<sup>4</sup> Armin Sorooshian,<sup>4</sup> John H. Seinfeld<sup>3,4</sup> and Magda Claeys<sup>1\*</sup>

<sup>1</sup> Department of Pharmaceutical Sciences, University of Antwerp (Campus Drie Eiken), Universiteitsplein 1, BE-2610 Antwerp, Belgium

<sup>2</sup> Department of Chemistry, California Institute of Technology, Pasadena, CA 91125, USA

<sup>3</sup> Department of Environmental Science and Engineering, California Institute of Technology, Pasadena, CA 91125, USA

<sup>4</sup> Department of Chemical Engineering, California Institute of Technology, Pasadena, CA 91125, USA

Received 12 July 2006; Accepted 24 October 2006

In the present work, we have characterized in detail the chemical structures of secondary organic aerosol (SOA) components that were generated in a smog chamber and result from the photooxidation of isoprene under high-NO<sub>x</sub> conditions typical for a polluted atmosphere. Isoprene high-NO<sub>x</sub> SOA contains 2-methylglyceric acid (2-MG) and oligoester derivatives thereof. Trimethylsilylation, in combination with capillary gas chromatography (GC)/ion trap mass spectrometry (MS) and detailed interpretation of the MS data, allowed structural characterization the polar oxygenated compounds present in isoprene SOA up to 2-MG trimers. GC separation was achieved between 2-MG linear and branched dimers or trimers, as well as between the 2-MG linear dimer and isomeric mono-acetate derivatives thereof. The electron ionization (EI) spectra of the trimethylsilyl derivatives contain a wealth of structural information, including information about the molecular weight (MW), oligoester linkages, terminal carboxylic and hydroxymethyl groups, and esterification sites. Only part of this information can be achieved with a soft ionization technique such as electrospray (ESI) in combination with collision-induced dissociation (CID). The methane chemical ionization (CI) data were used to obtain supporting MW information. Interesting EI spectral differences were observed between the trimethylsilyl derivatives of 2-MG linear and branched dimers or trimers and between 2-MG linear dimer mono-acetate isomers. Copyright © 2006 John Wiley & Sons, Ltd.

**KEYWORDS:** isoprene; 2-methylglyceric acid; oligomers; secondary organic aerosol; trimethylsilylation; gas chromatography / mass spectrometry; oligoesters

## INTRODUCTION

Isoprene (2-methyl-1,3-butadiene, C<sub>5</sub>H<sub>8</sub>) is a volatile organic compound (VOC) that is emitted in large amounts by terrestrial vegetation, estimated at about 500 Tg/year worldwide.<sup>1</sup> In the past, isoprene was assumed not to contribute significantly to secondary organic aerosol (SOA) formation because of the high volatility of its first-generation oxidation products (i.e. methacrolein, methyl vinyl ketone and formaldehyde).<sup>2</sup> However, during the past 3 years evidence from both field<sup>3–7</sup> and laboratory<sup>4,8–13</sup> studies has been obtained that isoprene is photooxidized to polar oxygenated products which are present in the aerosol phase. The aerosol yields from photooxidation of isoprene are rather

low (maximum about 3%),<sup>11,12</sup> a recent modeling study, however, shows that this aerosol source is quite significant on a global scale.<sup>14</sup> Knowledge of the detailed chemical structures of isoprene oxidation products is required in order to gain insights into the underlying photochemical oxidation mechanisms of isoprene, which so far are only partially understood.

In a recent work,<sup>10</sup> we characterized the chemical structures of SOA components that were produced in a smog chamber from photooxidation of isoprene under both high- and low-NO<sub>x</sub> conditions. A combination of several mass spectrometric techniques was used, including electrospray ionization (ESI), matrix-assisted laser desorption ionization (MALDI), aerosol mass spectrometry (MS), and derivatization gas chromatography (GC). It was shown in that study that isoprene high-NO<sub>x</sub> SOA contains 2-methylglyceric acid (2-MG), formed by further photooxidation of methacrolein, a

\*Correspondence to: Magda Claeys, Department of Pharmaceutical Sciences, University of Antwerp (Campus Drie Eiken), Universiteitsplein 1, BE-2610 Antwerp, Belgium.  
E-mail: magda.claeys@ua.ac.be

first-generation oxidation product of isoprene, and oligoester derivatives of 2-MG.

Soft ionization techniques such as ESI and MALDI are widely used currently in the analysis of oligomers and polymers, including oligomeric substances formed by photooxidation of biogenic and anthropogenic hydrocarbons such as isoprene,<sup>13</sup>  $\alpha$ -pinene,<sup>15–18</sup> cycloalkenes<sup>16</sup> and trimethylbenzene.<sup>19</sup> Combination of these techniques with collision-induced dissociation (CID) and tandem MS techniques generally only partially provide the structural information that is needed for elucidation of unknown multifunctional compounds. In the case of the oligomeric isoprene SOA compounds studied here, partial structural information was obtained by (–/+)-ESI-ion trap MS and by upfront CID mode of analysis on a LC/ESI-MS instrument.<sup>10</sup> The major fragmentation observed for 2-MG oligomers was loss of 102 Da 2-MG residue(s), likely corresponding to 2-hydroxy-2-methylpropiolactone and formed through a nucleophilic reaction directed by the negative charge on the terminal ionized carboxylic acid function. In the present study, we demonstrate that additional structural information can be achieved on oligomeric isoprene SOA compounds by trimethylsilylation in combination with GC/ion trap MS and detailed interpretation of the electron ionization (EI) spectra.

A derivatization protocol based on methylation of carboxylic acid functions prior to trimethylsilylation of neutral hydroxyl groups has been successfully applied in a previous work<sup>20</sup> to the analysis of polar oxygenated compounds present in organic aerosol. In the present work, preference was given to a one-step trimethylsilylation procedure that converts neutral and acidic hydroxyl functions to trimethylsilyl (TMS) ether or ester functions and allows the analysis of polar multifunctional compounds in the EI and/or chemical ionization (CI) mode. The EI mass spectra of trimethylsilylated compounds generally contain a wealth of structural information but often provide insufficient molecular weight (MW) information.<sup>6,20,21</sup> The latter shortcoming can however be overcome by recording spectra in the CI mode. In the EI mode, information can be obtained on functional groups and their locations owing to the fragmentation-directing effect of ionized trimethylsilylated hydroxyl groups. Rearrangement reactions of the trimethylsilyl group may occur, rendering EI mass spectra quite complex and difficult to interpret, but have the merit that they can yield structurally characteristic ions.

The isoprene high-NO<sub>x</sub> SOA examined in the present study contains 2-MG, 2-MG dimers, 2-MG dimer monoacetate derivatives, and 2-MG trimers. We will first discuss the EI fragmentation behaviors of the 2-MG monomer and its oligomeric derivatives. In addition, we will examine the fragmentation behaviors of the ethyl ester derivatives that are formed by subjecting isoprene high-NO<sub>x</sub> SOA to acidic hydrolysis in ethanol. Part of this work has been briefly presented in our previous study dealing with the overall chemical composition and mechanism of SOA formed from the photooxidation of isoprene under low- and high-NO<sub>x</sub> conditions.<sup>10</sup>

## EXPERIMENTAL

### Aerosol samples and workup

SOA was generated from isoprene (500 ppb) in Caltech's indoor 28 m<sup>3</sup> Teflon chambers using hydrogen peroxide as the OH radical precursor and 800 ppb NO; the oxidation reaction was initiated by UV irradiation,<sup>11,12</sup> and the SOA was collected on Teflon filters. Full details about SOA generation from isoprene are given in our previous study.<sup>10</sup> The SOA sample used in the present study was from a high-NO<sub>x</sub> isoprene nucleation (seed-free) experiment (Experiment 5). 2-MG and a branched and linear dimer thereof were prepared by reacting methacrylic acid (250  $\mu$ l; purity, 99%; Sigma, St. Louis, MI, USA) with hydrogen peroxide (250  $\mu$ l; 50% aqueous solution) in the presence of formic acid (125  $\mu$ l) for ten days at room temperature, following a procedure adapted from a previously reported one.<sup>4</sup> The yield of 2-MG, as determined by trimethylsilylation GC with flame ionization detection and using glyceric acid (Sigma) as an internal recovery standard, was 222 mg; the 2-MG linear and branched dimer were produced in small yield (combined yield estimated at about 3.3 mg assuming a similar EI response as 2-MG), and the ratio branched/linear 2-MG dimer was 1:10.

The sample workup of the isoprene SOA sample consisted of extraction of the filter with methanol under ultrasonic agitation and derivatization. The extract was divided into two parts; one part was trimethylsilylated, while the other part was subjected to a hydrolysis/ethylation procedure. For analysis of the methacrylic acid reaction products, 2  $\mu$ l of the 30 times diluted reaction mixture (with methanol) was dried and trimethylsilylated. Trimethylsilylation was performed by reacting the extract residue with 40  $\mu$ l of a mixture containing 1 ml *N*-methyl-*N*-trimethylsilyltrifluoroacetamide (+1% trimethylchlorosilane) (Pierce, Rockford, IL, USA) and 500  $\mu$ l of dry pyridine (Merck) for an hour at 70 °C. The reagent employed for deuterium labeling of the TMS methyl groups, *N,O*-bis(trimethyl-<sup>2</sup>H<sub>9</sub>-silyl)acetamide, was obtained from Cambridge Isotope Laboratories (Andover, MA, USA). The hydrolysis/ethylation procedure involved reaction of the extract residue with 40  $\mu$ l of analytical-grade ethanol and 8  $\mu$ l of trimethylchlorosilane (Supelco, Bellefonte, PA, USA) for 1 h at 60 °C. Aliquots of 1  $\mu$ l were used for GC/MS analysis and were injected in the splitless mode.

### GC/ion trap MS

GC/MS analyses were performed with a system comprising a TRACE GC2000 gas chromatograph, which was coupled to a Polaris Q ion trap mass spectrometer equipped with an external ionization source (ThermoElectron, San Jose, CA, USA). A Heliflex AT-5MS fused-silica capillary column (5% phenyl, 95% methylpolysiloxane, 0.25  $\mu$ m film thickness, 30 m  $\times$  0.25 mm i.d.) preceded by a deactivated fused-silica precolumn (2 m  $\times$  0.25 mm i.d.) (Alltech, Deerfield, IL, USA) was used to separate the derivatized extracts. Helium was used as the carrier gas at a flow rate of 1.2 ml/min. The temperature program was as follows: isothermal hold at 50 °C for 5 min, temperature ramp of 3 °C/min up to 200 °C, isothermal hold at 200 °C for 2 min, temperature ramp of

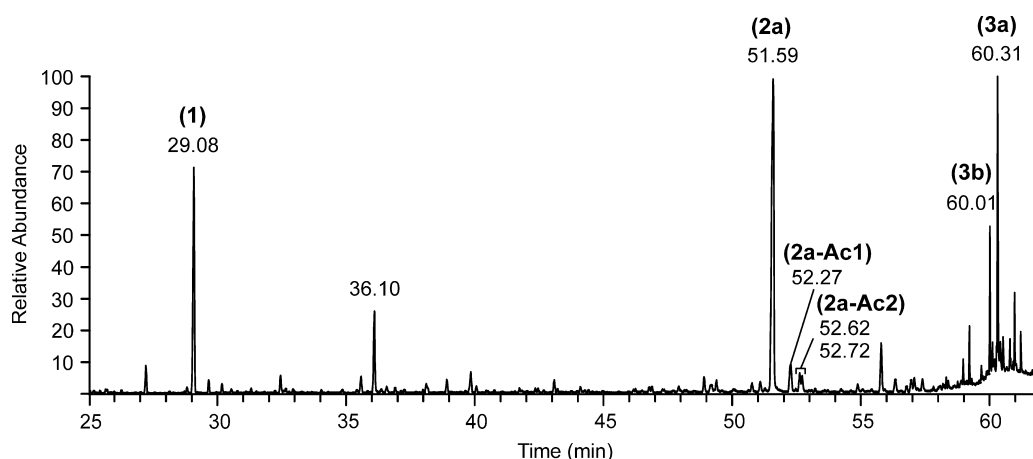
30°C/min up to 310°C; and isothermal hold at 310°C for 2 min. The analyses were performed in the full-scan mode (mass range:  $m/z$  50–800), and were first carried out in the EI mode and subsequently in the CI mode. The ion source was operated at an electron energy of 70 eV and temperatures of 200°C and 140°C in the EI and CI modes, respectively. The temperatures of the GC injector and the GC/MS transfer line were 250°C and 280°C, respectively. For CI, methane was introduced as the reagent gas at a flow rate of 1.8 ml/min. We present here mainly data collected in the EI mode; data collected in the CI mode was used to obtain supporting MW information.

For CID experiments, the ions of interest were activated by applying a percentage of a 5-V supplementary a.c. potential to the end-caps of the ion trap at the resonance frequency of the selected ion [referred to as *collision energy level* (CEL)]. The CEL was 16%, while the excitation time was 15 ms. Helium was introduced as damping and collision gas at a flow rate of 1.1 ml/min. In some cases, MS/MS experiments were performed on several mass-selected precursor ions sequentially during the same chromatographic run. For this purpose, the width of the isolation waveform at which the ion trap separation of the precursor ions turned out to be the best was determined; the optimized value ranged between 3.5 and 5 a.m.u. For each precursor ion, the excitation time was 12 ms.

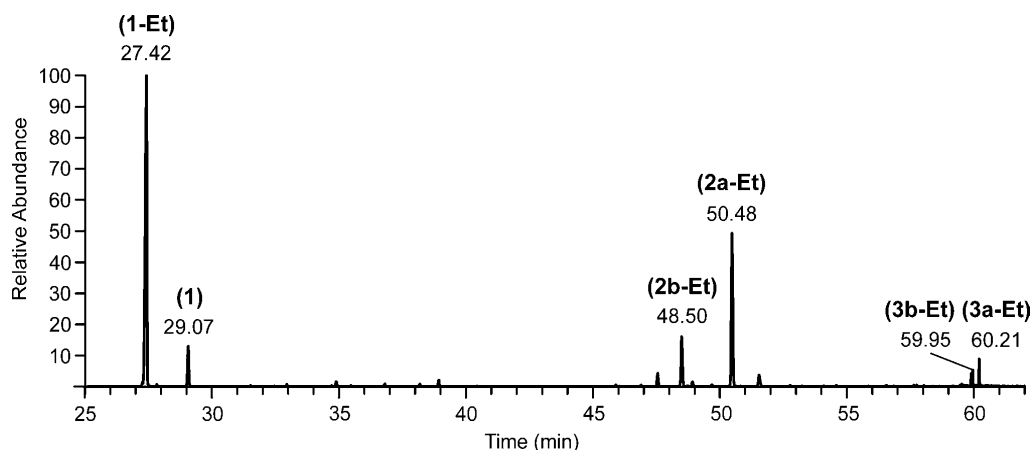
## RESULTS AND DISCUSSION

Figure 1 shows a GC/MS total ion current chromatogram (TIC) obtained for SOA produced from the photooxidation of isoprene under high-NO<sub>x</sub> conditions. Compound **1** was identified as the dihydroxymonocarboxylic acid, 2-MG (where 2-methylglyceric acid is its common name), which has retained part of the isoprene skeleton. This compound was reported for the first time in rural PM<sub>2.5</sub> aerosol collected at K-pusztá, Hungary, during a 2003 summer field campaign,<sup>4</sup>

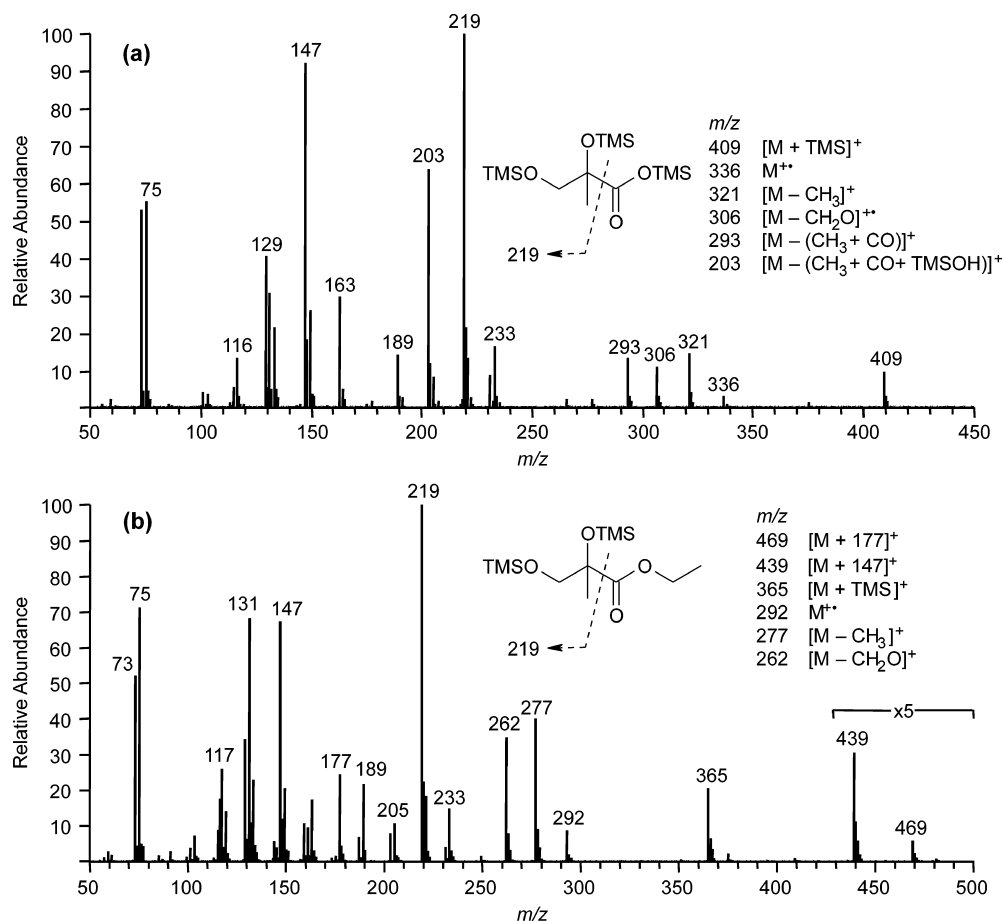
and has since been reported in several field studies.<sup>5,7,8</sup> In addition, it was shown in smog chamber studies that 2-MG is formed by photooxidation of isoprene<sup>8</sup> and, more specifically, by further oxidation of methacrolein, which is a first-generation photooxidation product of isoprene.<sup>10</sup> Compound **2a** was characterized in our previous laboratory study as a linear oligoester dimer of 2-MG (denoted as 2-MG linear dimer), using a combination of several MS techniques, including ESI-MS, MALDI-MS, aerosol-MS, and trimethylsilylation GC/MS.<sup>10</sup> In the present work, we discuss the EI behavior of the TMS derivative of the 2-MG linear dimer in more detail and compare it with that of the branched dimer (**2b**), which is not formed during photooxidation of isoprene under high-NO<sub>x</sub> conditions (and therefore is not shown in Fig. 1) but which together with the 2-MG linear dimer is produced as a minor reaction product during the acid-catalyzed oxidation of methacrylic acid with hydrogen peroxide. The 2-MG branched dimer was found to elute at an earlier retention time (RT = 50.37 min) compared to the linear dimer (RT = 51.59 min) (GC/MS TIC not shown). No conclusions can be drawn about the relative amounts of 2-MG and its oligoester derivatives in the samples since it is possible that 2-MG oligoester derivatives are partially degraded owing to hydrolysis during the trimethylsilylation procedure which uses an acidic catalyst (i.e. trimethylchlorosilane). Figure 2 shows the  $m/z$  219 mass chromatogram obtained after subjecting the isoprene high-NO<sub>x</sub> SOA extract to acidic hydrolysis in ethanol, an experiment that was performed to obtain evidence for ester linkages in the 2-MG oligomers. Compounds identified are the ethyl ester derivatives of 2-MG (**1-Et**), a branched (**2b-Et**) and linear 2-MG dimer (**2a-Et**), and a branched (**3b-Et**) and linear 2-MG trimer (**3a-Et**). In a following section, we will first discuss in detail the rather complex fragmentation behavior of the TMS derivatives of 2-MG (**1**) and its ethyl derivative (**1-Et**) and will limit the discussion to diagnostic ions with  $m/z$  values >140. In subsequent sections, we will then use this information to derive



**Figure 1.** GC/MS TIC obtained for a trimethylsilylated extract of isoprene high-NO<sub>x</sub> SOA. Peak identifications: **1**, 2-MG; **2a**, 2-MG linear dimer; **2a-Ac1** and **2a-Ac2**, 2-MG linear dimer mono-acetates; **3a**, 2-MG linear trimer; **3b**, 2-MG branched trimer. The peak eluting at 36.10 min is not discussed in the present work; it was found to correspond to an oxidation product of isoprene but not to be related to 2-MG, and was tentatively identified as 2-hydroxymethyl-3-ketopropanoic acid. Other peaks not marked were also found in a control filter and were identified as fatty acids and monoglycerides thereof. Reprinted from *J. Phys. Chem. A*, **110**, Surratt JD *et al.*, Chemical composition of secondary organic aerosol formed from the photooxidation of isoprene, 9665, Copyright (2006), with permission from American Chemical Society.



**Figure 2.** GC/MS extracted ion chromatogram ( $m/z$  219) obtained for an extract of isoprene high- $\text{NO}_x$  SOA subjected to a hydrolysis/ethylation procedure prior to trimethylsilylation. Reprinted from *J. Phys. Chem. A*, **110**, Surratt JD *et al.*, Chemical composition of secondary organic aerosol formed from the photooxidation of isoprene, 9665, Copyright (2006), with permission from American Chemical Society.

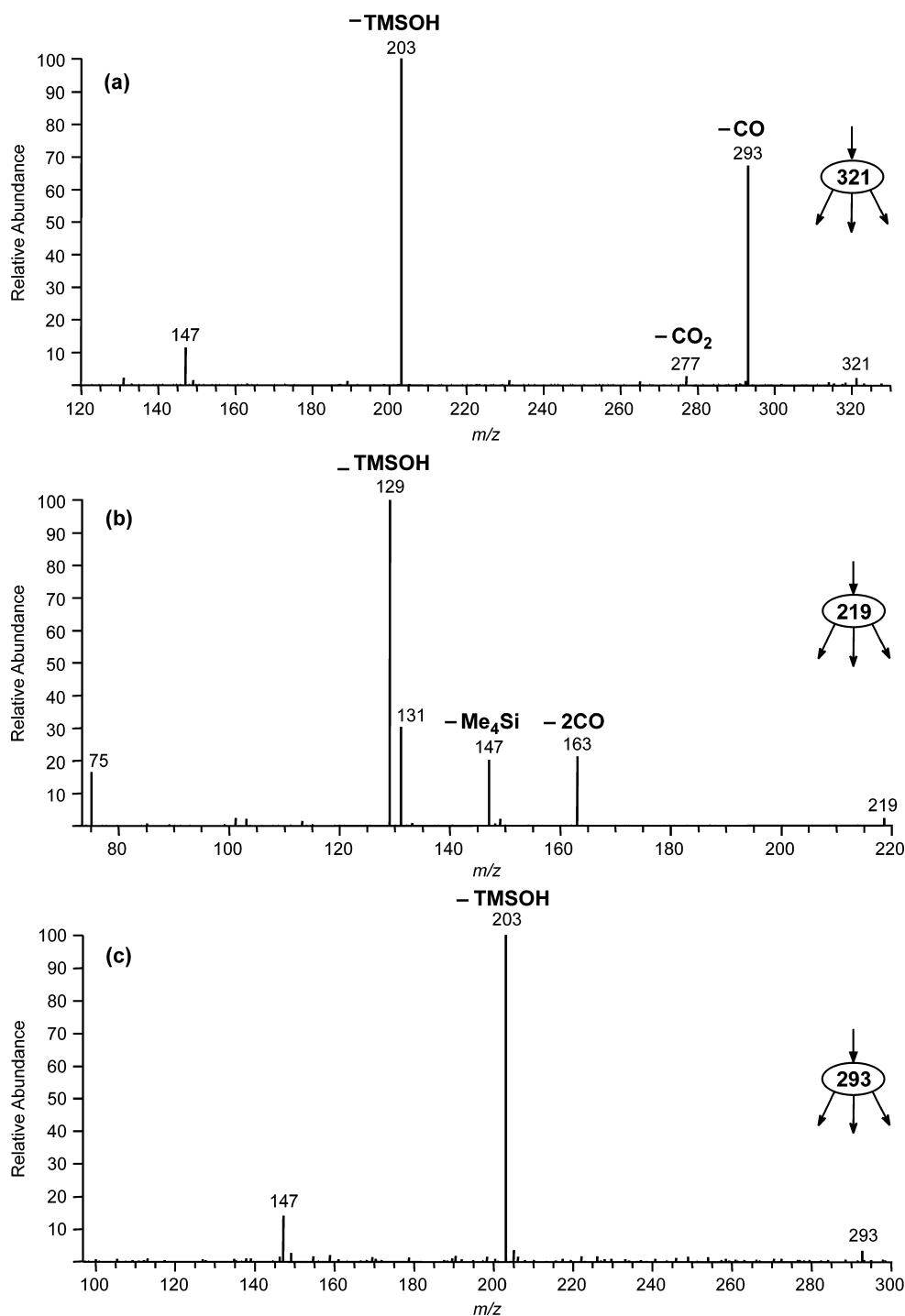


**Figure 3.** EI mass spectra for the TMS derivatives of (a) 2-MG (1) and (b) its ethyl ester derivative (1-Et). Part (a) reprinted from *J. Phys. Chem. A*, **110**, Surratt JD *et al.*, Chemical composition of secondary organic aerosol formed from the photooxidation of isoprene, 9665, Copyright (2006), with permission from American Chemical Society.

structural information for 2-MG dimers (2a,b), 2-MG trimers (3a,b), the ethyl derivatives of 2-MG dimers (2a,b-Et), as well as mono-acetate derivatives of the 2-MG linear dimer (2a-Ac1,2). In order to support fragmentation pathways, ion trap MS/MS experiments were used; only in the case of the 2-MG monomer was deuterium labeling of the TMS groups carried out.

### Fragmentation behavior of 2-methylglyceric acid and its ethyl ester derivative

Figure 3 shows the EI mass spectra of the TMS derivatives of (a) 2-MG (1) and (b) its ethyl ester derivative (1-Et). The fragmentation pathways of the TMS derivative of 2-MG are summarized in Schemes 1 and 2; all pathways supported by an  $\text{MS}^2$  ion trap experiment are indicated

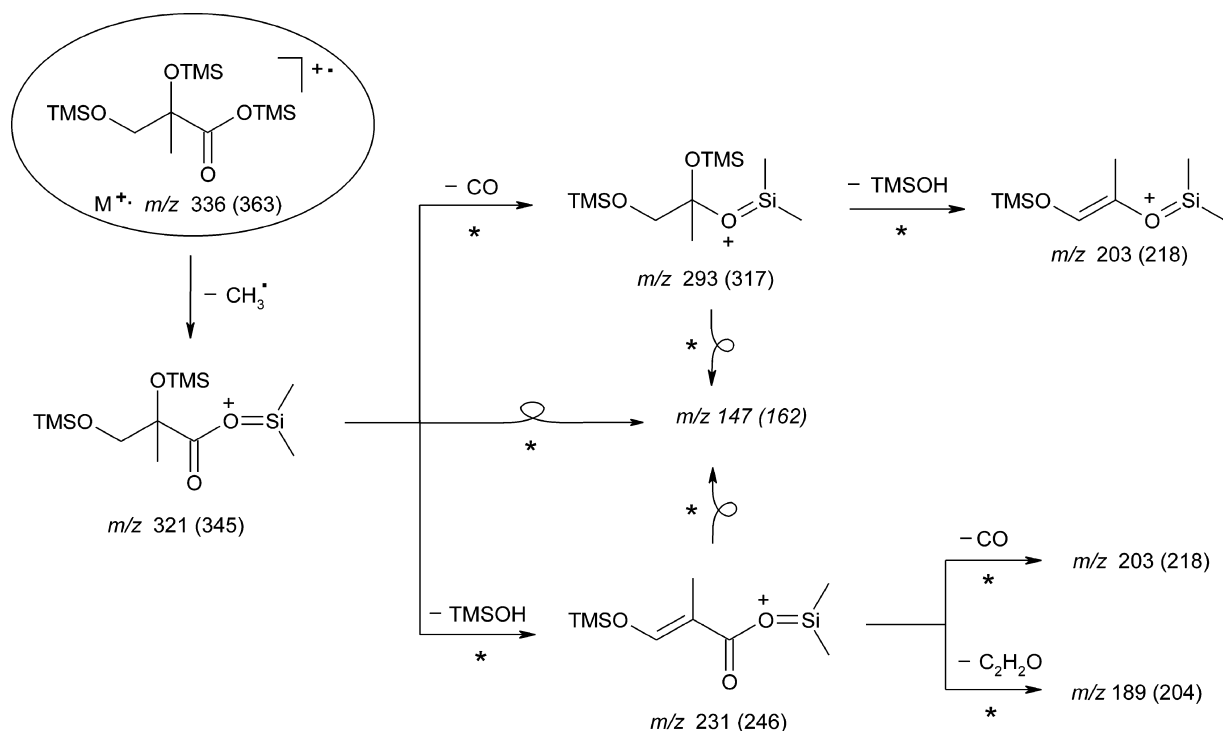


**Figure 4.** MS<sup>2</sup> ion trap spectra for selected ions of the TMS derivative of 2-MG: (a)  $m/z$  321, (b)  $m/z$  219 and (c)  $m/z$  293.

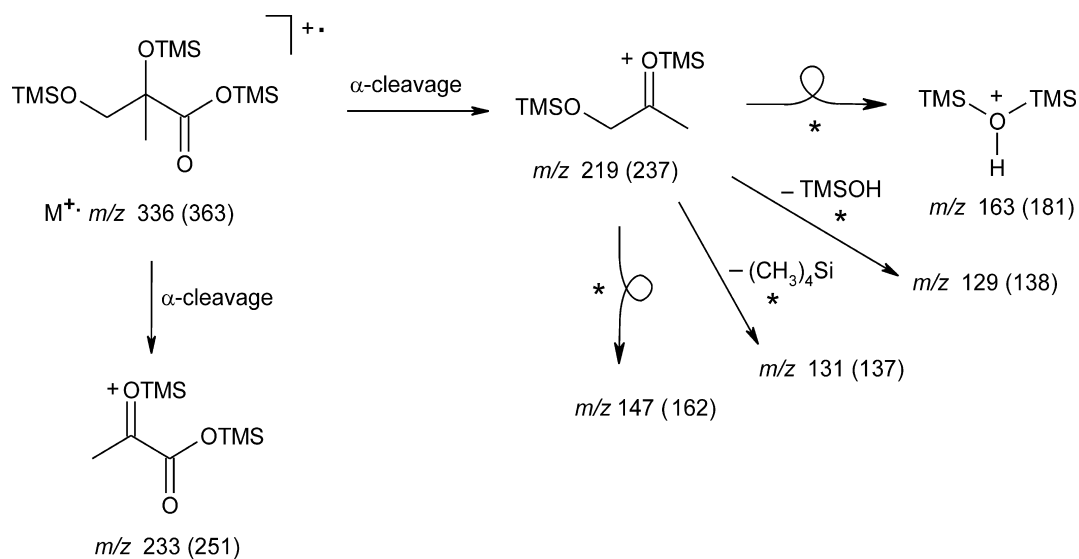
with an asterisk, while mass shifts obtained by introducing a deuterium labeled TMS group are given in parentheses. The molecular ion ( $M^{+\bullet}$ ;  $m/z$  336) of the TMS derivative of 2-MG is very weak, as is generally the case for TMS derivatives of compounds containing multiple hydroxyl groups.<sup>6,21</sup> The molecular ion region has a signature that is characteristic of a trimethylsilylated carboxylic acid, i.e. the  $[M - \text{CH}_3]^+$  ion ( $m/z$  321) and the  $[M - (\text{CH}_3 + \text{CO})]^+$  ion ( $m/z$  293). Proof that  $m/z$  321 is the precursor of  $m/z$  293 was obtained through an MS<sup>2</sup> ion trap experiment on  $m/z$  321 (Fig. 4(a)). Besides the  $M^{+\bullet}$  ion, other useful ions for inferring the MW

(336) are the  $[M - \text{CH}_3]^+$  ion ( $m/z$  321) and the  $[M + \text{TMS}]^+$  ion ( $m/z$  409). In addition, the molecular ion region contains a  $[M - \text{CH}_2\text{O}]^{+\bullet}$  ion ( $m/z$  306), which is indicative of a terminal trimethylsilylated hydroxymethyl function and can be explained via a rearrangement reaction of a TMS group to the ionized ester function as outlined in Scheme 3.

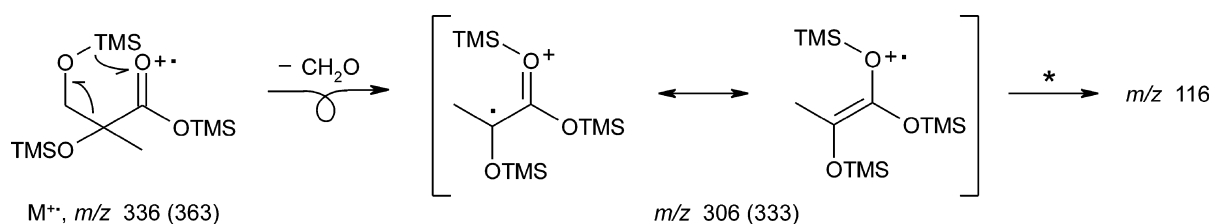
The ion at  $m/z$  219 is the base peak in the mass spectrum and can be explained by a homolytic  $\alpha$ -cleavage (Scheme 2). Fragmentation of  $m/z$  219 (Fig. 4(b)) yields the specific signature that was previously reported for the  $m/z$  219 ion of trimethylsilylated 2-methyltetrols,<sup>21</sup>



**Scheme 1.** Main fragmentation pathways for the TMS derivative of 2-methylglyceric acid. All pathways supported by an  $MS^2$  ion trap experiment are indicated with an asterisk.

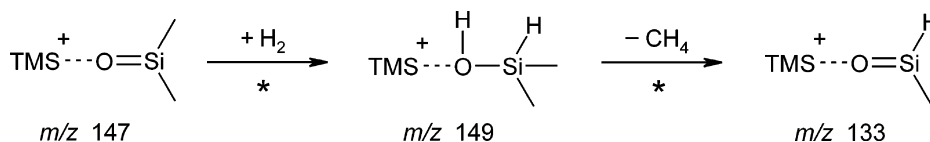


**Scheme 2.** Proposed pathways for  $m/z$  233 and 219 formed from the TMS derivative of 2-MG and pathways for formation of  $m/z$  219.

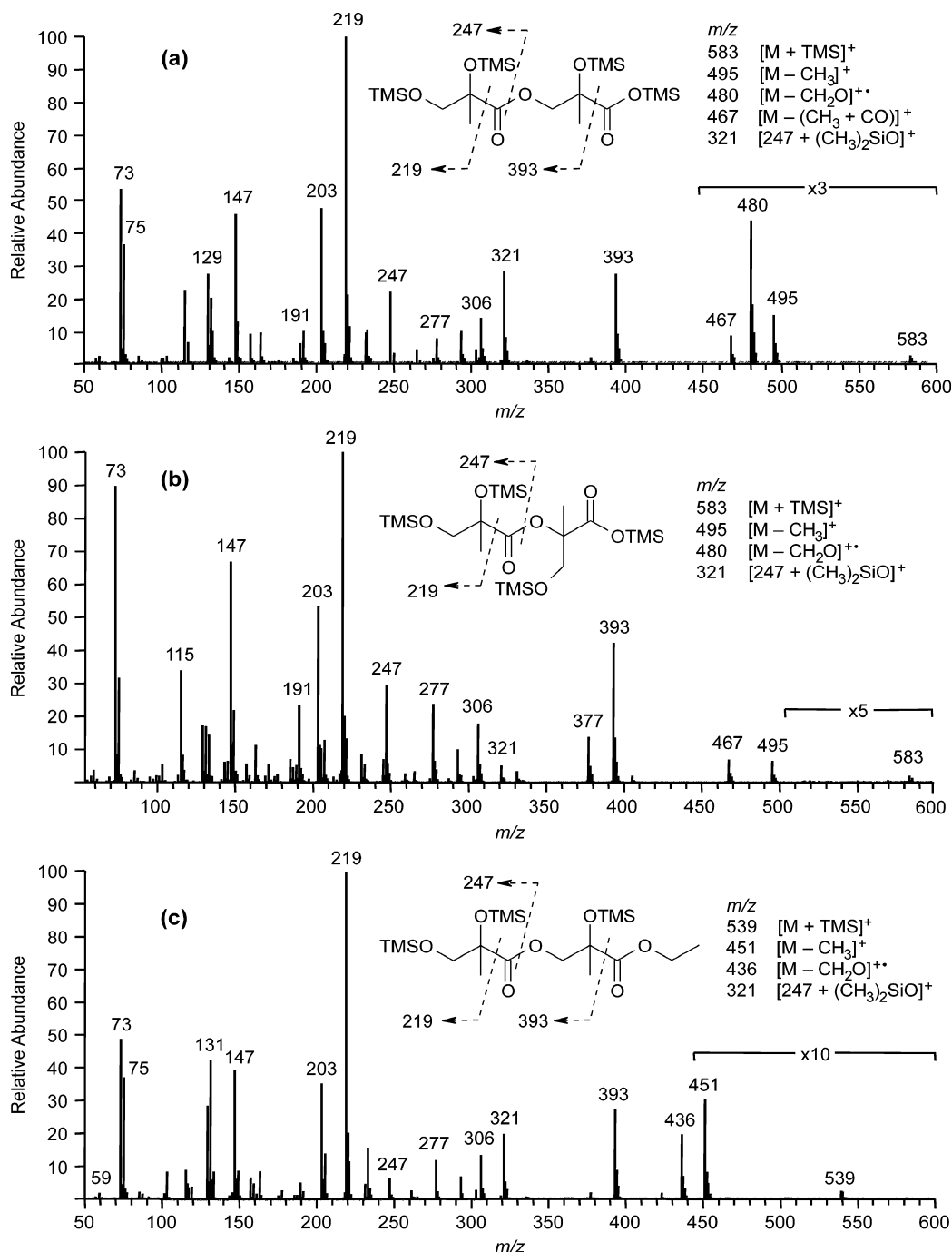


**Scheme 3.** Postulated gas-phase rearrangement process for the TMS derivative of 2-MG resulting in a resonance-stabilized  $m/z$  306 ion.





**Scheme 4.** Hydrogenation reaction of  $m/z$  147 occurring in the ion trap resulting in  $m/z$  149 and 133.



**Figure 5.** EI mass spectra of the TMS derivatives (a) 2-MG linear dimer (**2a**), (b) 2-MG branched dimer (**2b**), and (c) 2-MG linear dimer ethyl ester (**2a-Et**). Part (a) reprinted from *J. Phys. Chem. A*, **110**, Surratt JD *et al.*, Chemical composition of secondary organic aerosol formed from the photooxidation of isoprene, 9665, Copyright (2006), with permission from American Chemical Society.

and is therefore consistent with a trimethylsilylated 1,2-dihydroxy-2-methylethyl group in the molecule. The  $m/z$  203 ion can be explained by loss of TMSOH from  $m/z$  293 (Scheme 1; Fig. 4(c)), while the  $m/z$  147 ion corresponding to  $(\text{CH}_3)_2\text{Si} = \text{O}^+ - \text{TMS}$  is due to interaction between two TMSO groups<sup>22</sup> and indicates that the molecule contains at least two TMSO groups. The  $m/z$  147 ion is accompanied by a  $m/z$  149 ion which was shown to be formed from the  $m/z$  147 ion, and is explained by addition of hydrogen in the ion trap, and fragments to  $m/z$  133 through loss of methane (Scheme 4).

Comparison of the spectra of the TMS derivatives of 2-MG (Fig. 3(a)) and its ethyl ester (Fig. 3(b)) shows that ethylation results in the expected mass shifts but has little effect on the fragmentation pathways. MW information is provided by the  $\text{M}^{++}$  ion ( $m/z$  292), the  $[\text{M} - \text{CH}_3]^+$  ion ( $m/z$  277), and the  $[\text{M} + \text{TMS}]^+$  ion ( $m/z$  365). It is worth noting that the higher  $m/z$  region contains additional adduct ions at  $m/z$  439  $[\text{M} + 147]^+$  and  $m/z$  469  $[\text{M} + 177]^+$ . Of these ions,  $m/z$  439 can be explained by adduct formation of the 2-MG ethyl ester molecule with  $m/z$  147, which is an abundant ion in the spectrum. The formation of  $m/z$  177 likely involves the further addition of formaldehyde (30 Da), which is generated in the formation of  $m/z$  262  $[\text{M} - \text{CH}_2\text{O}]^+$ . The latter ion supports a terminal trimethylsilylated hydroxymethyl function, while the base peak at  $m/z$  219 is consistent with a trimethylsilylated 1,2-dihydroxy-2-methylethyl group.<sup>21</sup>

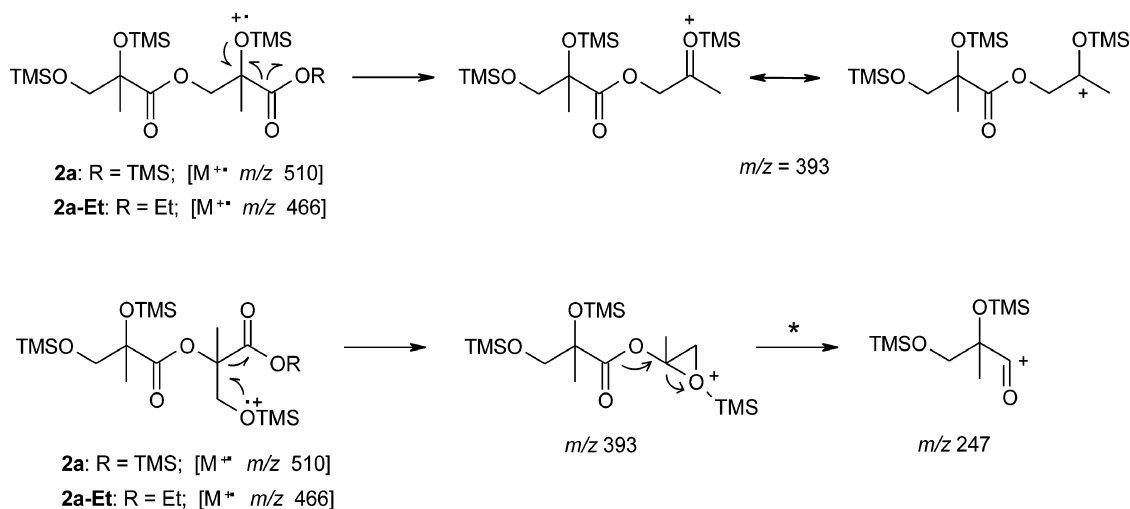
### Fragmentation behavior of 2-MG dimers and their ethyl ester derivatives

Figure 5 shows the EI mass spectra of the TMS derivatives of (a) the linear (**2a**) and (b) branched dimer of 2-MG (**2b**) and

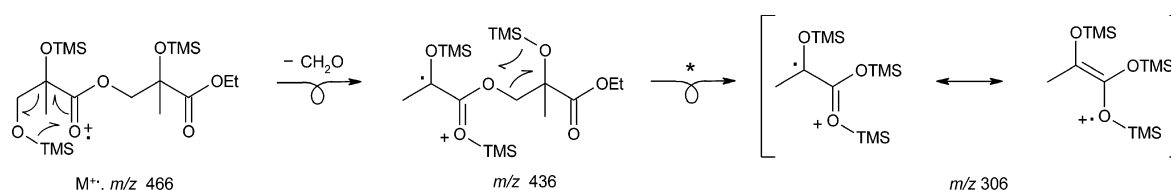
(c) the ethyl ester derivative of the 2-MG linear dimer (**2a-Et**). Examination of the  $m/z$  range 450–600 provides information about the MW. In the case of the 2-MG linear dimer (Fig. 5(a); MW 510), these ions include  $m/z$  583  $[\text{M} + \text{TMS}]^+$ ,  $m/z$  495  $[\text{M} - \text{CH}_3]^+$ , and  $m/z$  467  $[\text{M} - (\text{CH}_3 + \text{CO})]^+$ . The latter ion supports the presence of a terminal COOTMS group in the molecule as has been discussed above for 2-MG (Scheme 1). In the case of the 2-MG linear dimer ethyl ester (Fig. 5(c)), the MW (466) is supported by  $m/z$  539  $[\text{M} + \text{TMS}]^+$  and  $m/z$  451  $[\text{M} - \text{CH}_3]^+$ . The ion at  $m/z$  393 detected for both of the 2-MG linear and branched dimers and their ethyl esters can be readily explained by a homolytic  $\alpha$ -cleavage reaction as depicted in Scheme 5.

The mass spectra of the TMS derivatives of the 2-MG linear dimer as well as of its ethyl ester display an abundant  $[\text{M} - \text{CH}_2\text{O}]^{++}$  ion ( $m/z$  480 and  $m/z$  436, respectively), which is consistent with a terminal trimethylsilylated hydroxymethyl function as has been discussed above for the 2-MG monomer (Scheme 2). Subsequent elimination of a neutral (130 Da) through a rearrangement of a TMS group leads to  $m/z$  306, an ion that is also observed for the 2-MG monomer (Fig. 3(a)) and is stabilized by resonance (Scheme 6).

Comparison of the EI spectrum of the TMS derivative of the 2-MG linear dimer (Fig. 5(a)) with that of the branched dimer (Fig. 5(b)) reveals some interesting differences. It can be seen that the  $[\text{M} - \text{CH}_2\text{O}]^{++}$  ion ( $m/z$  480) is absent in the case of the 2-MG branched dimer. However, it is noted that a  $m/z$  306 ion is also present in the 2-MG branched dimer, suggesting that the internal TMS group rearrangement (shown for **2a** in Scheme 6) occurs prior to



**Scheme 5.** Formation of the  $m/z$  393 characteristic of the 2-MG linear and branched dimers and their ethyl esters via a homolytic  $\alpha$ -cleavage reaction.



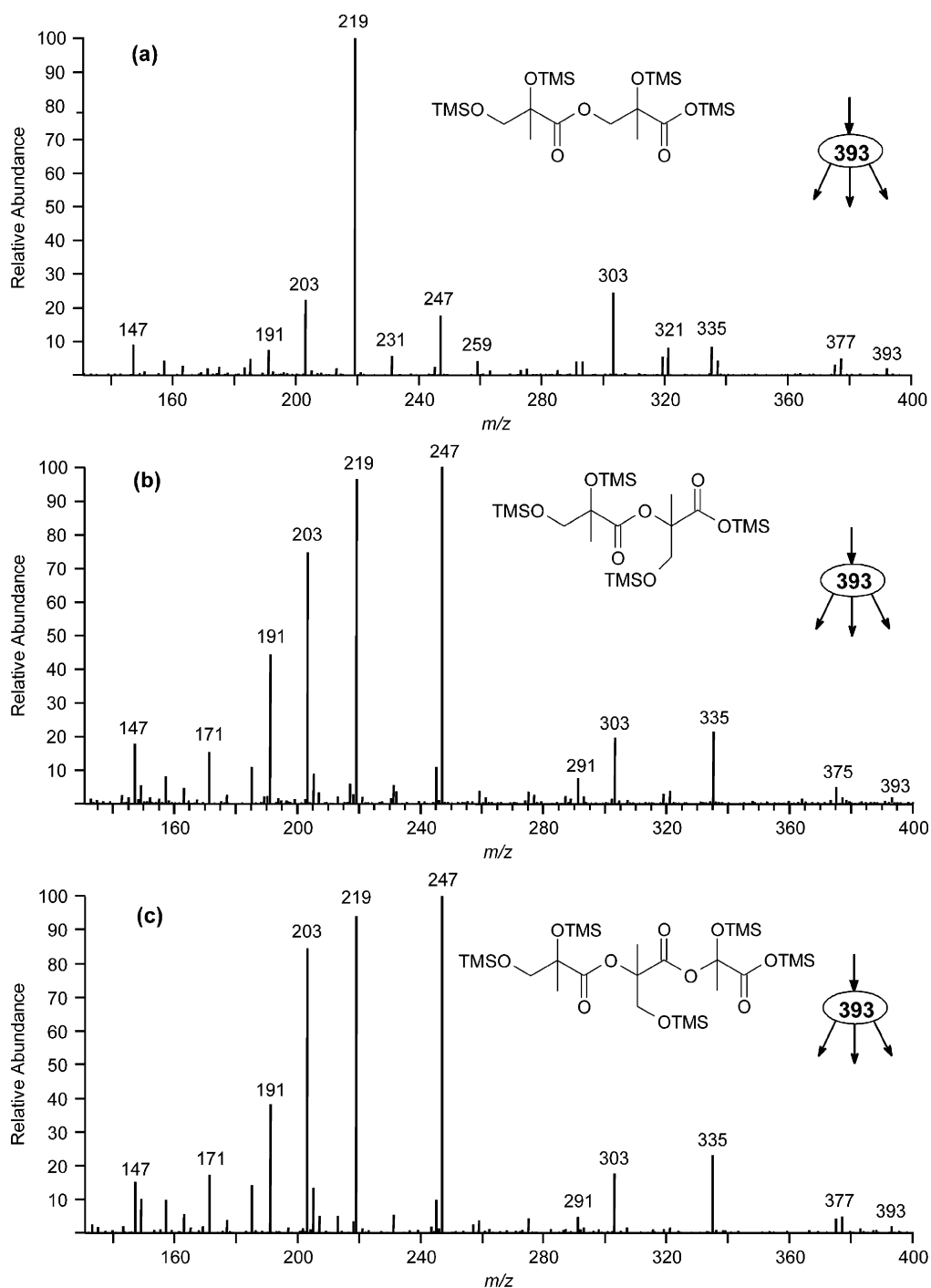
**Scheme 6.** Plausible mechanisms for the formation of  $m/z$  436 and 306 from the TMS derivative of 2-MG linear dimer ethyl ester.

$\text{CH}_2\text{O}$  loss. Furthermore, it can be seen that there is an additional ion at  $m/z$  377 in the latter case, which corresponds to  $[\text{M} - (\text{CH}_3 + \text{CO} + \text{TMSOH})]^+$ . An MS/MS experiment confirmed that  $m/z$  467 is the precursor for  $m/z$  377; a possible explanation is a favorable 1,3-elimination of TMSOH in the branched carboxylic acid-containing 2-MG residue.

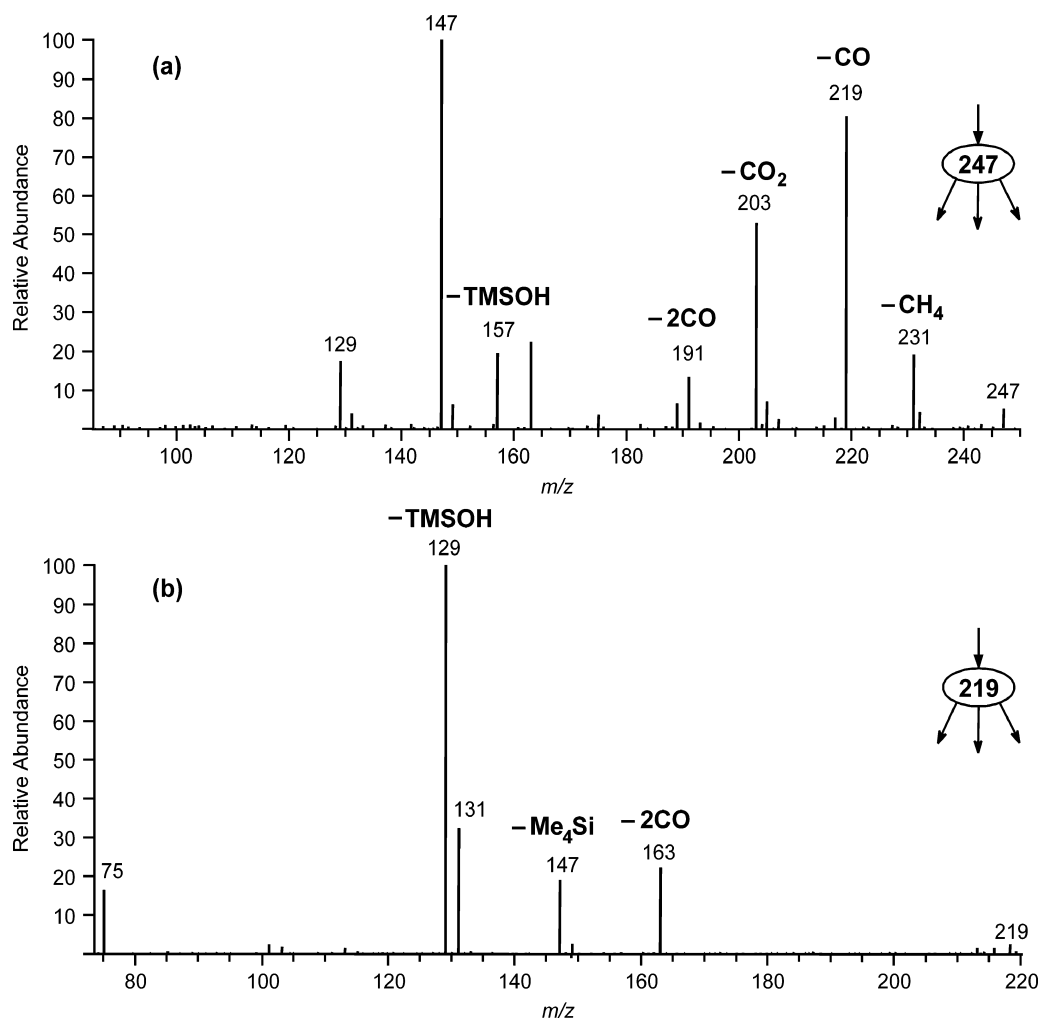
Figure 6 shows the  $m/z$  393 product ion spectra for the two isomeric 2-MG dimers. Interesting differences can be noted, with  $m/z$  247 being most abundant in the branched case; this information will be used in the following section to establish an esterification site in the 2-MG branched

trimer. In the case of the 2-MG branched dimer,  $m/z$  247 can be readily formulated through a charge-directed loss of trimethylsilylated hydroxyacetone (Scheme 5).

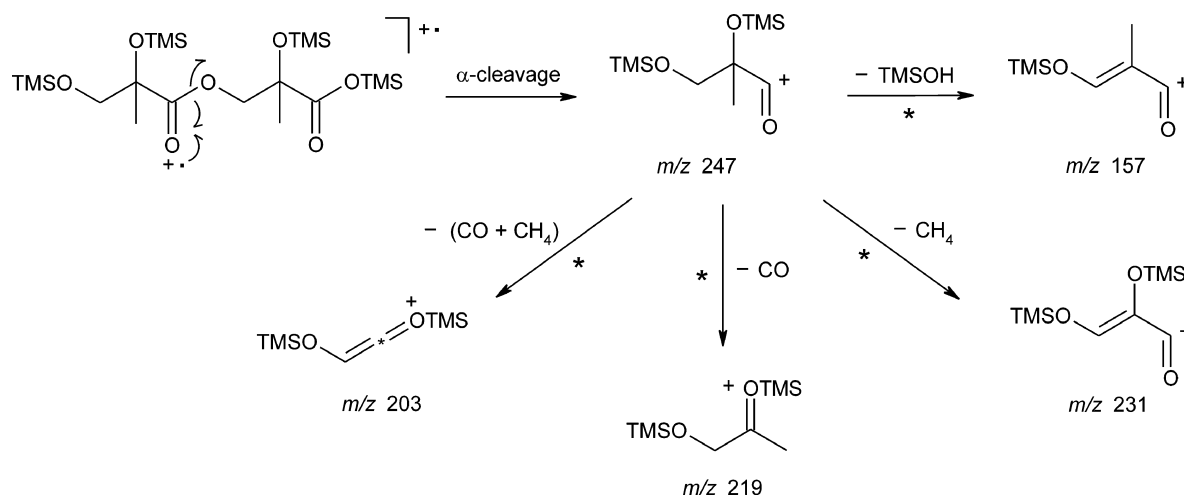
Other structurally informative ions in the EI spectra of the TMS derivatives of the 2-MG linear and branched dimers worth discussing are  $m/z$  247 and 321. The  $m/z$  247 ion is explained by an  $\alpha$ -cleavage relative to the ester  $\text{C}=\text{O}$  bond (Scheme 7) but can also be formed by other pathways (e.g. from  $m/z$  393; Scheme 5) and is characteristic for the presence of an ester linkage in the molecule. The ion at  $m/z$  247 fragments further to  $m/z$  231, 219, 203, and 157, as confirmed



**Figure 6.** MS<sup>2</sup> ion trap spectra for  $m/z$  393 of the TMS derivative of (a) the 2-MG linear dimer, (b) the 2-MG branched dimer and (c) the 2-MG branched trimer.



**Figure 7.** MS<sup>2</sup> ion trap spectra for selected ions of the TMS derivative of the 2-MG linear dimer: (a)  $m/z$  247 and (b)  $m/z$  219.

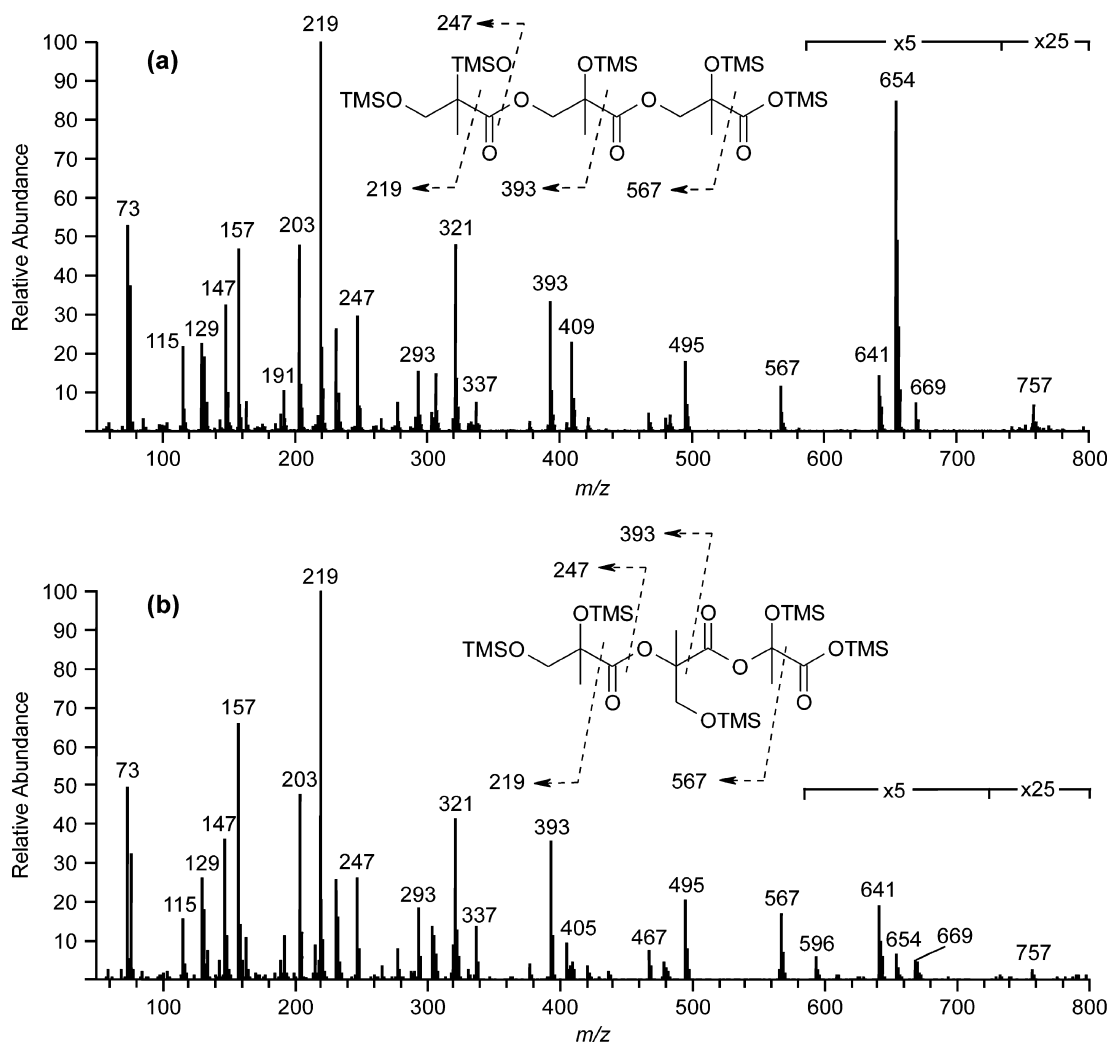


**Scheme 7.** A plausible formation mechanism for  $m/z$  247 and its further fragmentation as confirmed by MS<sup>2</sup> ion trap experiments.

by MS<sup>2</sup> experiments (Fig. 7(a); Scheme 7). The MS<sup>2</sup> ion trap spectrum of  $m/z$  219 (Fig. 7(b)) unambiguously proves that its structure is consistent with a trimethylsilylated 1,2-dihydroxy-2-methylethyl group,<sup>21</sup> which has already been discussed above in the case of 2-MG and its ethyl ester derivative.

### Fragmentation behavior of 2-MG trimers and their ethyl esters

Figure 8(a) and (b) shows the EI mass spectra of the TMS derivatives of the two isomeric trimers of 2-MG that were detected in the GC/MS TIC of high-NO<sub>x</sub> isoprene SOA (Fig. 1). Since both spectra display the same set of ions



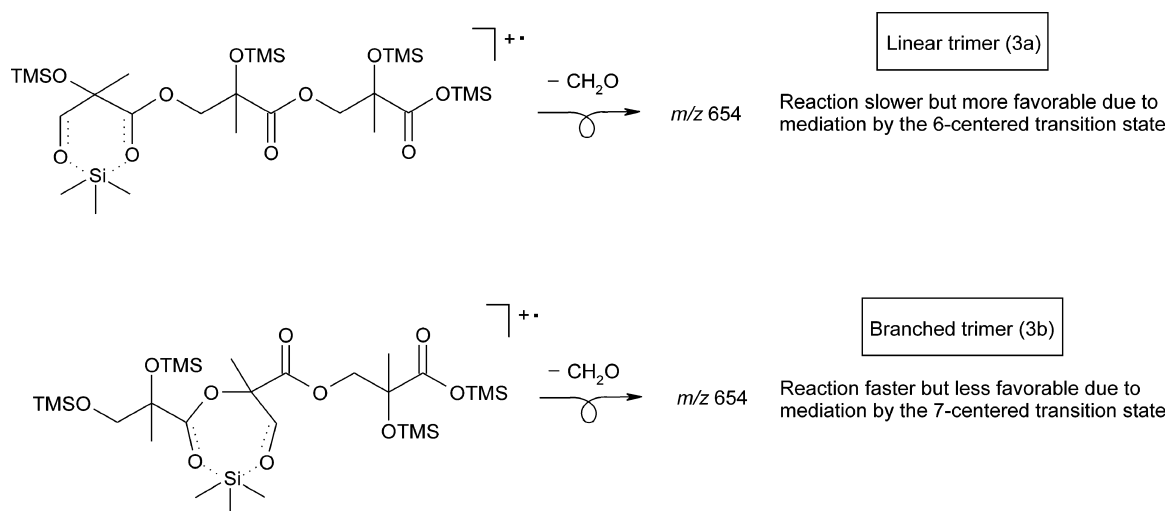
**Figure 8.** EI mass spectra of the TMS derivatives of 2-MG (a) linear (**3a**) and (b) branched trimer (**3b**).

differing only in terms of their relative abundances, one can conclude that they represent isomeric compounds. The most abundant compound which elutes at the latest retention time (RT = 60.31 min) is attributed to the linear trimer (**3a**), while the other one (RT = 60.01 min) is attributed to a branched trimer (**3b**), given that under the GC conditions employing a nonpolar stationary phase, branched isomers, which have a more compact structure than their linear forms, elute at an earlier retention time. As will be discussed below, evidence for a branched internal 2-MG residue was obtained. However, we have no evidence for the esterification site in the terminal carboxylic acid-containing 2-MG residue and assume that after dimer formation, esterification proceeds by reaction with a terminal hydroxymethyl group of a 2-MG molecule, thus resulting in a linear form, since the formation of linear forms is sterically less hindered.

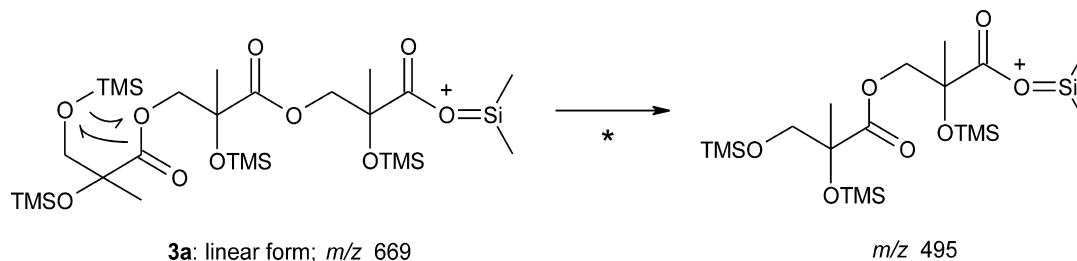
As in the case of the 2-MG dimers, examination of the high  $m/z$  range enables us to infer the MW (684). Both isomers reveal a very weak  $[M + \text{TMS}]^+$  adduct ion ( $m/z$  757) as well as  $[M - \text{CH}_3]^+$  ion ( $m/z$  669) and  $[M - (\text{CH}_3 + \text{CO})]^+$  ions ( $m/z$  641). The latter ion also supports a terminal carboxyl group in the underivatized molecules. It can be seen that the abundance of the  $[M - \text{CH}_2\text{O}]^{+\bullet}$  ion ( $m/z$  654) is strikingly different and is more abundant for the linear

system compared to the branched one. The same observation was made for the  $[M - \text{CH}_2\text{O}]^{+\bullet}$  ion ( $m/z$  610) in the mass spectra of the 2-MG dimers and the ethyl derivatives of 2-MG trimers (results not shown). A possible explanation for this phenomenon is given in Scheme 8. A TMS group transfer may not only proceed from the terminal  $\text{TMSOCH}_2$  group but also from an internal  $\text{TMSOCH}_2$  group, involve different geometries of the transition state, and take place at a different rate. The interaction between the terminal  $\text{TMSOCH}_2$  group and a neighboring ester function involves a 6-centered transition state, while that between the internal  $\text{TMSOCH}_2$  group of the branched isomer and a neighboring ester function involves a 7-centered state which is less favorable but may be formed faster.

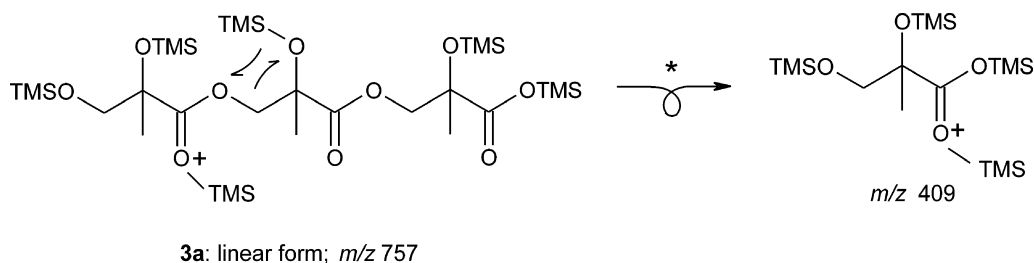
The  $m/z$  393 ion can be explained by an  $\alpha$ -cleavage directed by the ionized internal TMSO group of the inner 2-MG residue. Figure 6(c) shows that the  $m/z$  393 product ion profile of the branched trimer is very similar to that of the branched dimer (Fig. 6(b)), suggesting that the branched 2-MG trimer contains an inner branched 2-MG residue. In the following discussion, attention will be given to structurally informative ions, which were not present in the case of the 2-MG dimers. Both the linear and branched 2-MG trimer reveal an ion at  $m/z$  495 which can be explained



**Scheme 8.** Differences in the geometry of the transition state providing a rational explanation for the more favorable loss of formaldehyde from the  $M^{+\bullet}$  ion of the TMS derivative of the 2-MG linear trimer compared to that of the branched form.



**Scheme 9.** Formation of  $m/z$  495 in the case of the TMS derivative of the 2-MG linear trimer. The same mechanism can be proposed for the 2-MG branched trimer.



**Scheme 10.** Pathway leading to  $m/z$  409 in the TMS derivative of the 2-MG linear trimer.

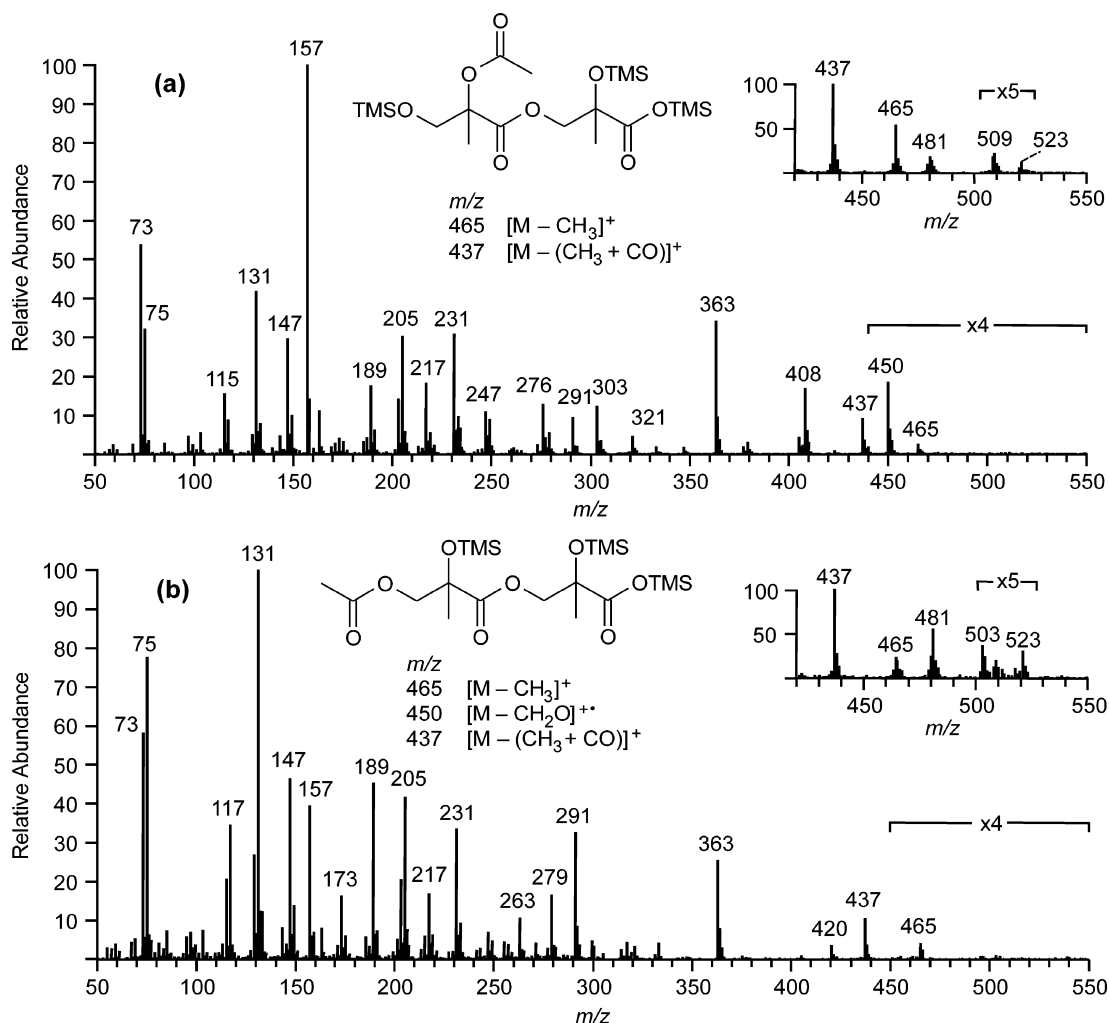
from the  $[M - \text{CH}_3]^+$  ion by loss of a neutral (174 Da) from the terminal 2-MG residue through a rearrangement of a TMS group (Scheme 9). In addition, ions are present, which are isomer-specific. In the case of the 2-MG linear trimer, an ion can be seen at  $m/z$  409, while the 2-MG branched trimer reveals an ion at  $m/z$  596. The  $m/z$  409 ion can be generated from the  $[M + \text{TMS}]^+$  adduct ion by an internal rearrangement of a TMS group resulting in the  $[2\text{-MG} + \text{TMS}]^+$  adduct ion (Scheme 10). The  $m/z$  596 ion characteristic of the 2-MG branched trimer is believed to result from a favorable interaction in the  $M^{+\bullet}$  ion between the trimethylsilylated hydroxymethyl group of the branched unit and a trimethylsilylated hydroxyl group, leading to loss of  $(\text{CH}_3)_4\text{Si}$  (88 Da).

#### Fragmentation behavior of 2-MG linear dimer mono-acetate derivatives

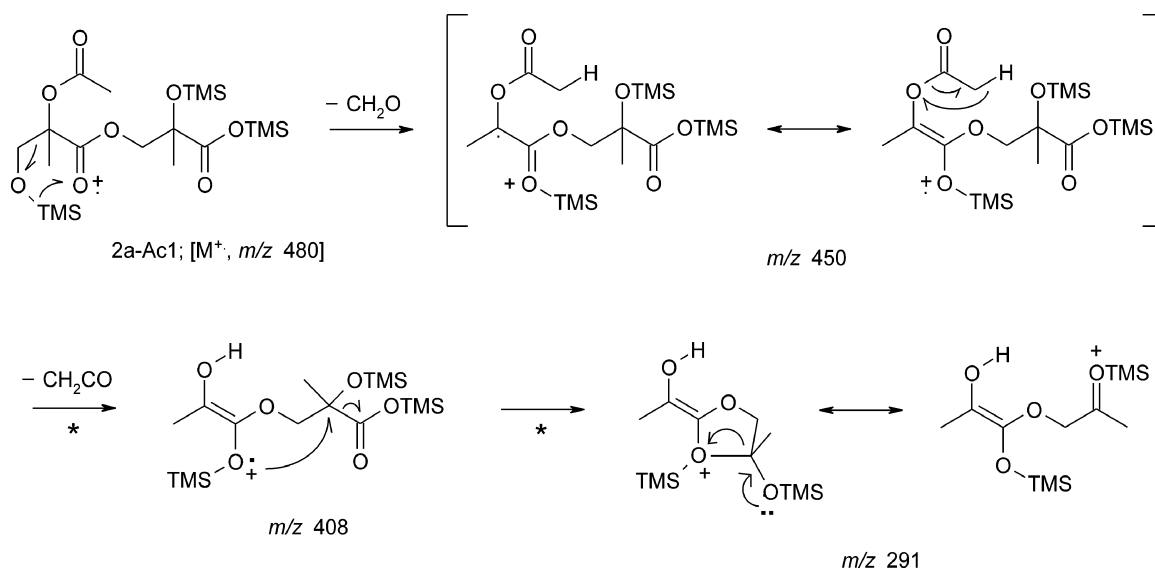
The two small peaks in the GC/MSTIC of high- $\text{NO}_x$  isoprene SOA (Fig. 1) eluting just after the 2-MG linear dimer (2a) were

identified as isomeric 2-MG linear dimer mono-acetates (2a-Ac1,2). These products were already partially characterized in our previous study using (–) ESI-MS, and are formed by esterification between the 2-MG linear dimer and acetic acid, which is also generated from isoprene in the smog chamber under high- $\text{NO}_x$  conditions.<sup>10</sup> As will be discussed below, a more complete characterization of the isomeric 2-MG linear dimer mono-acetates was possible by detailed interpretation of the EI mass spectral data. The EI spectra of the TMS derivatives of the isomeric 2-MG linear dimer mono-acetates are shown in Fig. 9. The peak eluting at a RT of 52.3 min was characterized as the isomer containing an internal acetate group (2a-Ac1), while the peak at a RT of 52.6 min was attributed to the isomer containing a terminal acetate group (2a-Ac2). The partial splitting noted in the latter chromatographic peak can be explained by diastereoisomerism.

Examination of the high  $m/z$  range enables us to infer the MW (480); the EI spectra of the TMS derivatives of both



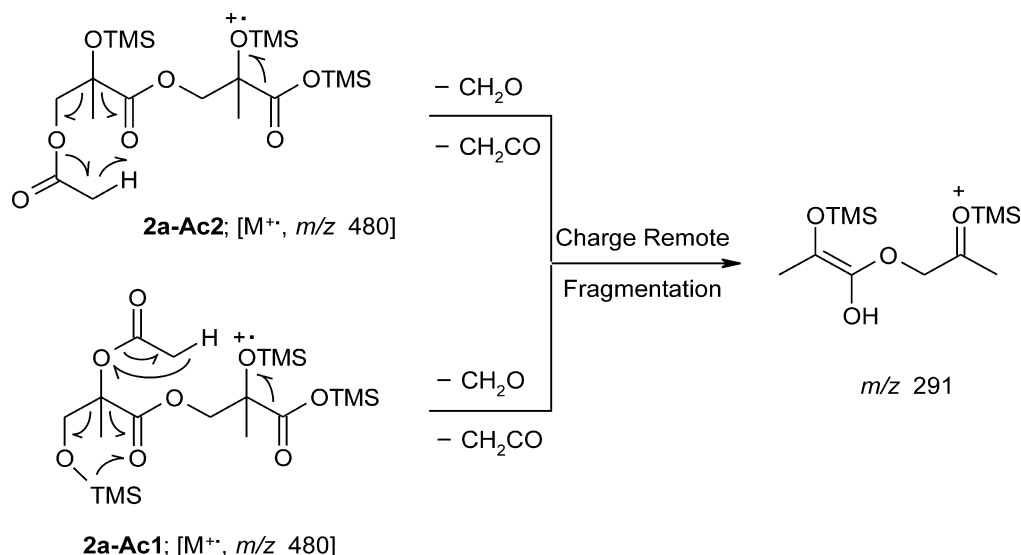
**Figure 9.** EI mass spectra of the TMS derivatives of 2-MG linear dimer mono-acetates bearing the acetate group at (a) the terminal hydroxymethyl group (**2a-Ac1**) and (b) an internal hydroxyl group (**2a-Ac2**). Insets: CI (methane) data.



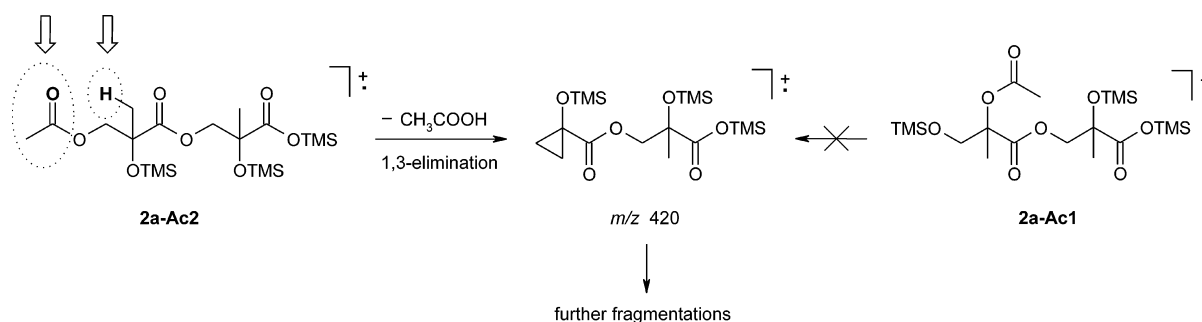
**Scheme 11.** Mechanisms proposed for the formation of  $m/z$  450, 408, and 291 present in the EI spectrum of the TMS derivative of the 2-MG dimer mono-acetate isomer eluting at RT 52.3 min (**2a-Ac1**).

2-MG linear dimer mono-acetates show  $[M - \text{CH}_3]^+$  ( $m/z$  465) and  $[M - (\text{CH}_3 + \text{CO})]^+$  ions ( $m/z$  437). Supporting MW information was derived from the CI (methane)

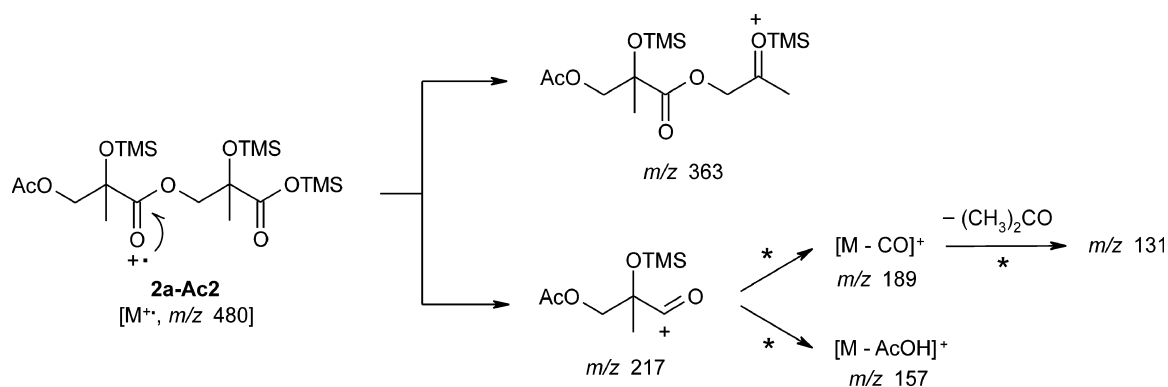
spectra (insets in Fig. 9), which reveal  $[M + \text{H}]^+$  ( $m/z$  481),  $[M + \text{C}_2\text{H}_5]^+$  ( $m/z$  509), and  $[M + \text{C}_3\text{H}_7]^+$  ( $m/z$  523) ions as well as  $[\text{MH} - \text{CH}_4]^+$  ions ( $m/z$  465). It can be



**Scheme 12.** Possible formation pathways for  $m/z$  291 in the TMS derivatives of both 2-MG dimer mono-acetate isomers through charge-remote fragmentation reactions.



**Scheme 13.** Mechanism proposed for the formation of  $m/z$  420, an ion characteristic of the TMS derivative of the 2-MG dimer mono-acetate bearing an acetyl group at the terminal hydroxymethyl group of the non-carboxylic acid-containing 2-MG residue (**2a-Ac2**). Parts of the molecule engaged in the elimination process are circled.



**Scheme 14.** Mechanisms proposed for formation of  $m/z$  363, 217, 189, 157, and 131 in the TMS derivative of an 2-MG linear dimer mono-acetate (**2a-Ac2**). The same mechanisms hold for the isomer **2a-Ac1**.

seen that the spectrum of the first-eluting isomer (**2a-Ac1**) contains an ion at  $m/z$  450, corresponding to the  $[M - CH_2O]^+$  ion formed through a rearrangement of a TMS group (Scheme 11). This ion firmly supports the presence of a terminal trimethylsilylated hydroxymethyl group in the non-carboxylic acid-containing 2-MG residue and is consistent with a nonbranched carboxylic acid-containing

2-MG residue. Following the loss of formaldehyde,  $m/z$  450 fragments by loss of ketene (42 Da) from the acetate group, resulting in  $m/z$  408. Further fragmentation of  $m/z$  408 through loss of a  $TMSO(CO)^\bullet$  radical leads to  $m/z$  291. It can be seen that  $m/z$  291 is also present in the case of the 2-MG dimer mono-acetate isomer eluting at a RT of 52.6 min (**2a-Ac2**); an alternative explanation for  $m/z$  291



in both 2-MG dimer mono-acetate isomers through charge-remote rearrangement reactions involving neutral loss of both ketene (42 Da) and formaldehyde (30 Da) is outlined in Scheme 12.

The EI spectrum of the compound corresponding to the 2-MG dimer mono-acetate isomer eluting at a RT of 52.6 min (**2a-Ac2**) (Fig. 9(b)) shows a unique ion at  $m/z$  420, which is explained by loss of acetic acid from the  $M^{+\bullet}$  ion (Scheme 13). This favorable elimination of acetic acid involves a hydrogen at a 3-position relative to the acetate group<sup>23</sup> and does not occur in the other isomer (RT 52.3 min) in which only hydrogen atoms at the 2-position are available.

Ions present in the spectra of the TMS derivatives of both isomeric 2-MG linear dimer mono-acetates worth discussing are  $m/z$  363, 217, 189, 157, and 131. Their formation mechanisms are given in Scheme 14. The formation of  $m/z$  217 and 189 in both isomers is consistent with the presence of an acetate group in the non-carboxylic acid-containing 2-MG residue. As expected,  $m/z$  157 is more prominent in the case of the 2-MG dimer mono-acetate bearing an acetyl group at the terminal hydroxymethyl group because of the favorable 1,3-elimination of acetic acid. On the other hand, the formation of  $m/z$  131 due to loss of acetone from  $m/z$  189 seems to be a favored pathway in the case of the 2-MG dimer mono-acetate bearing an internal acetyl group.

## CONCLUSIONS

Detailed interpretation of the EI mass spectral data of the TMS derivatives of 2-MG and oligoester derivatives thereof allows one to obtain key structural features of the molecules and as such to elucidate their chemical structures and differentiate isomeric compounds. The  $m/z$  219 ion containing the trimethylsilylated 1,2-dihydroxy-2-methylethyl group is a characteristic ion of 2-MG and its oligomers. Evidence for an ester function in the 2-MG dimers and trimers is indicated by the  $m/z$  247 ion formed by an  $\alpha$ -cleavage in the ester group linking the non-carboxylic acid-containing 2-MG residue to the remaining part of the molecules. In addition, evidence for an inner branched 2-MG residue in the case of the 2-MG branched trimer was obtained, while the 2-MG linear and branched dimers could be readily differentiated. Characteristic ions of the terminal carboxyl group are the  $[M - CH_3]^+$  and  $[M - (CH_3 + CO)]^+$  ions, while the terminal hydroxymethyl group was found to give rise to a  $[M - CH_2O]^{+\bullet}$  ion in linear 2-MG oligomers. Furthermore, it was possible to differentiate isomeric mono-acetates of the 2-MG linear dimer containing an acetyl group in the non-carboxylic acid-containing 2-MG residue and locate the position of the acetyl group. We can conclude that the EI spectra of the TMS derivatives contain a wealth of structural information, including information about the MW, ester linkages, terminal carboxylic and hydroxymethyl groups, and esterification sites.

## Acknowledgements

Research at the University of Antwerp was supported by the Belgian Federal Science Policy Office through the BIOSOL project (contract SD/AT/02A) and a visiting postdoctoral fellowship to Rafal Szmigielski, and by the Research Foundation – Flanders (FWO)

(grant number G.0091.06). Research at Caltech was funded by the U.S. Environmental Protection Agency under the Science to Achieve Results (STAR) Program grant number RD-83107501-0, managed by EPA's Office of Research and Development (ORD), National Center for Environmental Research (NCER), and by the U.S. Department of Energy, Biological, and Environmental Research Program DE-FG02-05ER63983; this work has not been subjected to the EPA's required peer and policy review and therefore does not necessarily reflect the views of the Agency and no official endorsement should be inferred. Jason Surratt was supported in part by the United States Environmental Protection Agency (EPA) under the STAR Graduate Fellowship Program.

## REFERENCES

- Guenther A, Hewitt CN, Erickson D, Fall R, Geron C, Graedel T, Harley P, Klinger L, Lerdau M, McKay WA, Pierce T, Scholes B, Steinbrecher R, Tallamraju R, Taylor J, Zimmerman P. A global model of natural volatile organic compound emissions. *J. Geophys. Res.* 1995; **100**: 8873.
- Pandis SN, Paulson SE, Seinfeld JH, Flagan RC. Aerosol formation in the photooxidation of isoprene and  $\beta$ -pinene. *Atmos. Environ.* 1991; **25A**: 997.
- Claeys M, Graham B, Vas G, Wang W, Vermeylen R, Pashynska V, Cafmeyer J, Guyon P, Andreae MO, Artaxo P, Maenhaut W. Formation of secondary organic aerosols through photooxidation of isoprene. *Science* 2004; **303**: 1173.
- Claeys M, Wang W, Ion AC, Kourtchev I, Gelencsér A, Maenhaut W. Formation of secondary organic aerosols from isoprene and its gas-phase oxidation products through reaction with hydrogen peroxide. *Atmos. Environ.* 2004; **38**: 4093.
- Ion AC, Vermeylen R, Kourtchev I, Cafmeyer J, Chi X, Gelencsér A, Maenhaut W, Claeys M. Polar organic compounds in rural PM<sub>2.5</sub> aerosols from K-puszt, Hungary, during a 2003 summer field campaign: sources and diel variations. *Atmos. Chem. Phys.* 2005; **5**: 1805.
- Wang W, Kourtchev I, Graham B, Cafmeyer J, Maenhaut W, Claeys M. Characterization of oxygenated derivatives of isoprene related to 2-methyltetrols in Amazonian aerosols using trimethylsilylation and gas chromatography/ion trap mass spectrometry. *Rapid Commun. Mass Spectrom.* 2005; **19**: 1343.
- Kourtchev I, Ruuskanen T, Maenhaut W, Kulmala M, Claeys M. Observation of 2-methyltetrols and related photo-oxidation products of isoprene in boreal forest aerosols from Hyytiälä, Finland. *Atmos. Chem. Phys.* 2005; **5**: 2761.
- Edney EO, Kleindienst TE, Jaoui M, Lewandowski M, Offenberg JH, Wang W, Claeys M. Formation of 2-methyl tetrols and 2-methylglyceric acid in secondary organic aerosol from laboratory irradiated isoprene/NO<sub>x</sub>/SO<sub>2</sub>/air mixtures and their detection in ambient PM<sub>2.5</sub> samples collected in the eastern United States. *Atmos. Environ.* 2005; **39**: 5281.
- Böge O, Miao Y, Plewka A, Herrmann H. Formation of secondary organic particle phase compounds from isoprene gas-phase oxidation products: an aerosol chamber and field study. *Atmos. Environ.* 2006; **40**: 2501.
- Surratt JD, Murphy SM, Kroll JH, Ng NL, Hildebrandt L, Sorooshian A, Szmigielski R, Vermeylen R, Maenhaut W, Claeys M, Flagan RC, Seinfeld JH. Chemical composition of secondary organic aerosol formed from the photooxidation of isoprene. *J. Phys. Chem. A* 2006; **110**: 9665.
- Kroll JH, Ng NL, Murphy SM, Flagan RC, Seinfeld JH. Secondary organic aerosol formation from isoprene photooxidation under high-NO<sub>x</sub> conditions. *Geophys. Res. Lett.* 2005; **32**: L18808, Doi:10.1029/2005GL023637.
- Kroll JH, Ng NL, Murphy SM, Flagan RC, Seinfeld JH. Secondary organic aerosol formation from isoprene photooxidation. *Environ. Sci. Technol.* 2006; **40**: 1867, Doi:10.1021/es054301.
- Dommen J, Metzger A, Duplissy J, Kalberer M, Alfarra MR, Gascho A, Weingartner E, Prevot ASH, Verheggen B, Baltensperger U. Laboratory observation of oligomers in the aerosol

- from isoprene/NO<sub>x</sub> photooxidation. *Geophys. Res. Lett.* 2006; **33**: L13805, Doi:10.1029/2006GL026523.
14. Henze DK, Seinfeld JH. Global secondary organic aerosol from isoprene oxidation. *Geophys. Res. Lett.* 2006; **33**: L09812, Doi:10.1029/2006GL025976.
  15. Iinuma Y, Böge O, Gnauk T, Herrmann H. Aerosol-chamber study of the  $\alpha$ -pinene/O<sub>3</sub> reaction: influence of particle acidity on aerosol yields and products. *Atmos. Environ.* 2004; **38**: 761.
  16. Gao S, Keywood M, Ng NL, Surratt JD, Varutbangkul V, Bahreini R, Flagan RC, Seinfeld JH. Low-molecular-weight and oligomeric components in secondary organic aerosol from the ozonolysis of cycloalkenes and  $\alpha$ -pinene. *J. Phys. Chem. A* 2004; **108**: 10147.
  17. Gao S, Ng NL, Keywood M, Varutbangkul V, Bahreini R, Nenes A, He J, Yoo KY, Beauchamp JL, Hodyss RP, Flagan RC, Seinfeld JH. Particle phase acidity and oligomer formation in secondary organic aerosol. *Environ. Sci. Technol.* 2004; **38**: 6582.
  18. Tolocka MP, Jang M, Ginter JM, Cox FJ, Kamens RM, Johnston MV. Formation of oligomers in secondary organic aerosol. *Environ. Sci. Technol.* 2004; **38**: 1428.
  19. Kalberer M, Paulsen D, Sax M, Steinbacher M, Dommen J, Prevot ASH, Fisseha R, Weingartner E, Frankevich V, Zenobi R, Baltensperger U. Identification of polymers as major compounds of atmospheric organic aerosols. *Science* 2004; **308**: 1659.
  20. Jaoui M, Kleindienst TE, Lewandowski M, Edney EO. Identification and quantification of aerosol polar oxygenated compounds bearing carboxylic acid or hydroxy groups. 1. Method development. *Anal. Chem.* 2004; **76**: 4765.
  21. Wang W, Vas G, Dommissie R, Loones K, Claeys M. Fragmentation study of diastereoisomeric 2-methyltetrols, oxidation products of isoprene, as their trimethylsilyl ethers, using gas chromatography/ion trap mass spectrometry. *Rapid Commun. Mass Spectrom.* 2004; **18**: 1787.
  22. Maenhaut-Claeys M, Vandewalle M. Studies in organic mass spectrometry XIX. The fragmentation of the trimethylsilyl derivatives of some 2,3-diakyl-1,4-cyclopentanediols. *Bull. Soc. Chim. Belges* 1974; **83**: 343.
  23. Liptak M, Heerma W. Fast atom bombardment mass spectrometric study of some *N*-glycosides and *S*-glycosides of acetylated hexose isomers. *Rapid Commun. Mass Spectrom.* 1993; **7**: 676.

## **Appendix D**

# **Aerosol-Cloud Drop Concentration Closure for Clouds Sampled during the International Consortium for Atmospheric Research on Transport and Transformation 2004 Campaign\***

---

\*This chapter is reproduced by permission from “Aerosol-Cloud Drop Concentration Closure for Clouds Sampled during the International Consortium for Atmospheric Research on Transport and Transformation 2004 Campaign” by C. Fountoukis, A. Nenes, N. Meskhidze, R. Bahreini, W. C. Conant, H. Jonsson, S. M. Murphy, A. Sorooshian, V. Varutbangkul, F. J. Brechtel, R. C. Flagan, and J. H. Seinfeld, *J. Geophys. Res.* **112**, D10S30, doi:10.1029/2006JD007272, 2007. Copyright 2007. American Geophysical Union.



## Aerosol–cloud drop concentration closure for clouds sampled during the International Consortium for Atmospheric Research on Transport and Transformation 2004 campaign

Christos Fountoukis,<sup>1</sup> Athanasios Nenes,<sup>1,2</sup> Nicholas Meskhidze,<sup>3,4</sup> Roya Bahreini,<sup>5,6</sup> William C. Conant,<sup>5,7</sup> Hafliði Jonsson,<sup>8</sup> Shane Murphy,<sup>9</sup> Armin Sorooshian,<sup>9</sup> Varuntida Varutbangkul,<sup>9</sup> Fred Brechtel,<sup>5</sup> Richard C. Flagan,<sup>5,10</sup> and John H. Seinfeld,<sup>5,10</sup>

Received 8 March 2006; revised 19 November 2006; accepted 21 February 2007; published 26 April 2007.

[1] This study analyzes 27 cumuliform and stratiform clouds sampled aboard the CIRPAS Twin Otter during the 2004 International Consortium for Atmospheric Research on Transport and Transformation (ICARTT) experiment. The data set was used to assess cloud droplet closure using (1) a detailed adiabatic cloud parcel model and (2) a state-of-the-art cloud droplet activation parameterization. A unique feature of the data set is the sampling of highly polluted clouds within the vicinity of power plant plumes. Remarkable closure was achieved (much less than the 20% measurement uncertainty) for both parcel model and parameterization. The highly variable aerosol did not complicate the cloud droplet closure, since the clouds had low maximum supersaturation and were not sensitive to aerosol variations (which took place at small particle sizes). The error in predicted cloud droplet concentration was mostly sensitive to updraft velocity. Optimal closure is obtained if the water vapor uptake coefficient is equal to 0.06, but can range between 0.03 and 1.0. The sensitivity of cloud droplet prediction error to changes in the uptake coefficient, organic solubility and surface tension depression suggest that organics exhibit limited solubility. These findings can serve as much needed constraints in modeling of aerosol–cloud interactions in the North America; future in situ studies will determine the robustness of our findings.

**Citation:** Fountoukis, C., et al. (2007), Aerosol–cloud drop concentration closure for clouds sampled during the International Consortium for Atmospheric Research on Transport and Transformation 2004 campaign, *J. Geophys. Res.*, 112, D10S30, doi:10.1029/2006JD007272.

### 1. Introduction

[2] Most of the uncertainty in anthropogenic climate change is associated with aerosol–cloud interactions [Lohmann and Feichter, 2004; Andreae et al., 2005].

Explicitly resolving cloud formation, microphysical evolution and aerosol–precipitation interactions in Global Climate Models (GCMs) is a challenging computational task [Khairoutdinov et al., 2005; Randall et al., 2003]; parameterizations are used instead. In terms of predicting droplet number, empirical correlations are often used [e.g., Jones et al., 1994; Gultepe and Isaac, 1996; Boucher and Lohmann, 1995; Lohmann and Feichter, 1997; Kiehl et al., 2000; Menon et al., 2002; Brasseur and Roeckner, 2005], which relate an aerosol property (usually total number or mass) to cloud droplet number concentration,  $N_d$ . The data is usually obtained from observations. Although simple and easy to implement, correlations are subject to substantial uncertainty [Kiehl et al., 2000]. Prognostic parameterizations of aerosol–cloud interactions have also been developed [Lohmann et al., 1999, 2000; Ghan et al., 2001a, 2001b; Rotstayn and Penner, 2001; Peng et al., 2002; Nenes and Seinfeld, 2003; Fountoukis and Nenes, 2005] in which  $N_d$  is calculated using cloud-scale updraft velocity, aerosol size distribution and composition. These approaches are based on the “parcel” concept of 1-D Lagrangian numerical cloud models [e.g., Jensen and Charlson, 1984; Considine and Curry, 1998; Nenes et al., 2001]. Although inherently

<sup>1</sup>School of Chemical and Biomolecular Engineering, Georgia Institute of Technology, Atlanta, Georgia, USA.

<sup>2</sup>Also at School of Earth and Atmospheric Sciences, Georgia Institute of Technology, Atlanta, Georgia, USA.

<sup>3</sup>School of Earth and Atmospheric Sciences, Georgia Institute of Technology, Atlanta, Georgia, USA.

<sup>4</sup>Now at School of Marine, Earth, and Atmospheric Sciences, North Carolina State University, Raleigh, North Carolina, USA.

<sup>5</sup>Environmental Science and Engineering, California Institute of Technology, Pasadena, California, USA.

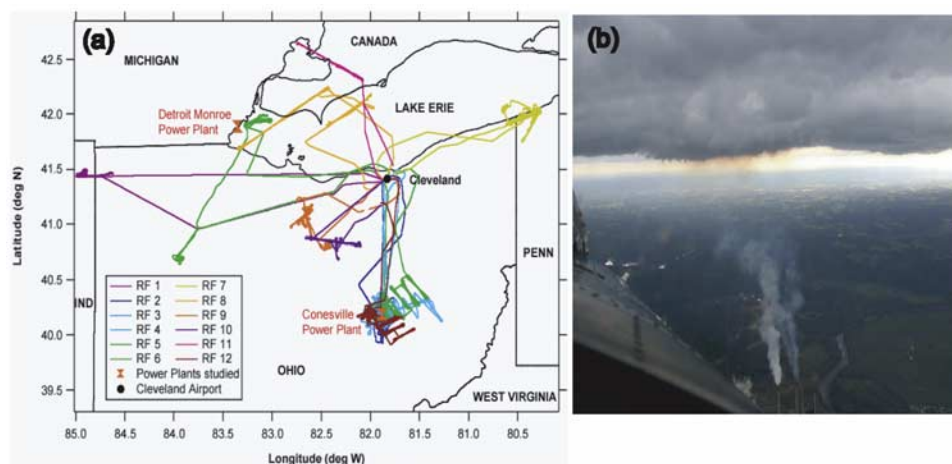
<sup>6</sup>Now at NOAA, Boulder, Colorado, USA.

<sup>7</sup>Now at Department of Atmospheric Sciences, University of Arizona, Tucson, Arizona, USA.

<sup>8</sup>Center for Interdisciplinary Remotely-Piloted Aircraft Studies, Naval Postgraduate School, Monterey, California, USA.

<sup>9</sup>Department of Chemical Engineering, California Institute of Technology, Pasadena, California, USA.

<sup>10</sup>Also at Department of Chemical Engineering, California Institute of Technology, Pasadena, California, USA.



**Figure 1.** (a) Map of the 12 Twin Otter research flight tracks during ICARTT. (b) Photograph of Conesville power plant plume affecting cloud depth (flight IC3; 6 August 2004).

better than correlations, prognostic parameterizations are still subject to uncertainties in the subgrid (i.e., cloud-scale) updraft velocity [e.g., Menon *et al.*, 2002], aerosol size distribution and composition [e.g., Rissman *et al.*, 2004], aerosol “chemical” effects and changes in droplet growth kinetics [e.g., Nenes *et al.*, 2002].

[3] The ultimate test for prognostic parameterizations and cloud models is the comparison of their predictions against comprehensive in situ data. When done for cloud droplet number, this procedure is termed “cloud droplet closure study,” in which a discrepancy between  $N_d$  predicted by models and measured in situ is usually determined. Hallberg *et al.* [1997] report  $\sim 50\%$  disagreement between predicted and observed  $N_d$  for continental stratocumulus clouds. Chuang *et al.* [2000] studied marine and continental stratus clouds sampled during the second Aerosol Characterization Experiment (ACE-2) and found a large discrepancy (about a factor of 3) between predictions and observations for updraft velocity range expected for stratocumulus clouds. Snider and Brenguier [2000] and Snider *et al.* [2003] found up to 50% discrepancy between predicted and measured droplet concentrations for ACE-2 and marine stratocumulus clouds. Part of this discrepancy was attributed to the usage of ground-based observations in the closure. Conant *et al.* [2004] achieved remarkable closure, to within 15%, for cumulus clouds of marine and continental origin sampled during the NASA Cirrus Regional Study of Tropical Anvils and Cirrus Layers–Florida Area Cirrus Experiment (CRYSTAL-FACE). Meskhidze *et al.* [2005] also found excellent agreement between predicted and measured  $N_d$  ( $\sim 30\%$ ) for the stratiform cloud data gathered during Coastal Stratocumulus Imposed Perturbation Experiment (CSTRIPE, Monterey, California, July 2003). In general, cloud droplet closure has been successful for clouds formed in clean air masses, and to a lesser degree for polluted clouds. It is however unclear if the latter results from limitations in the observations or in the theory used for predicting cloud droplet number.

[4] In this study we assess aerosol–cloud drop number closure using (1) a detailed cloud parcel model [Nenes *et al.*, 2001] and (2) the parameterization of Nenes and Seinfeld [2003] with recent extensions by Fountoukis and

Nenes [2005] (hereinafter referred to as “modified NS” parameterization). The observations used in this study were collected on board the Center for Interdisciplinary Remotely Piloted Aircraft Studies (CIRPAS) Twin Otter aircraft (<http://www.cirpas.org>) during the NASA International Consortium for Atmospheric Research on Transport and Transformation experiment (ICARTT). A unique feature of this data set is the sampling of highly polluted cloudy air within the vicinity of power plant plumes. Closure with the parcel model tests our predictive understanding of cloud droplet formation under extremely polluted conditions, while using the parameterization assesses its performance and quantifies the uncertainty arising from its simplified physics.

## 2. In Situ Observation Platform and Analysis Tools

[5] During ICARTT, the Twin Otter realized twelve research flights in the vicinity of Cleveland and Detroit (Figure 1), several of which sampled cumuliform and stratiform clouds. Seven flights are considered in this study. The cloud sampling strategy involves several under-cloud “passes” to characterize the aerosol size distribution and chemical composition, followed by in-cloud “legs” to sample the cloud microphysics, chemistry and turbulence.

### 2.1. Description of Airborne Platform

[6] Table 1 summarizes the instruments and measured quantities aboard the CIRPAS Twin Otter aircraft. A Dual Automatic Classifier Aerosol Detector (DACAD [Wang *et al.*, 2003]) was used to measure dry aerosol size between 10 and 800 nm. The DACAD consists of two scanning Differential Mobility Analyzers (DMAs) operating in parallel, one at a “dry” relative humidity (RH) less than 20%, and another at a “humid” RH of  $\sim 75\%$ . From the dry-wet size distributions, the size-resolved hygroscopicity is obtained. Aerosol chemical composition (sulfate, nitrate, ammonium and organics) was measured in real time by an Aerodyne Aerosol Mass Spectrometer (AMS [Bahreini *et al.*, 2003; Jayne *et al.*, 2000]). Concurrently, aerosol inorganics ( $\text{NO}_3^-$ ,  $\text{SO}_4^{2-}$ ,  $\text{NH}_4^+$ ) and some organics (oxalate)



**Table 1.** Instrumentation and Measurement Parameters During ICARTT

Instrument	Measurement	Measured Property	Measurement Principle
Forward scattering spectrometer probe (FSSP)	cloud droplet number distribution	geometric diameter: 1.5–37 $\mu\text{m}$	optical forward scattering
Cloud, aerosol, and precipitation spectrometer (CAS)	cloud droplet number distribution	geometric diameter: 0.5–50 $\mu\text{m}$	optical forward scattering and 2-D imaging
Condensation particle counter (CPC)	aerosol number concentration	geometric diameter > (3 nm, 7 nm, 13 nm)	varying supersaturations of butanol
Dual automated classifier aerosol detector (DACAD)	aerosol size distribution	geometric diameter: 10–800 nm	classification by electrical mobility
Passive cavity aerosol spectrometer probe (PCASP)	aerosol size distribution	geometric diameter: 100–2500 nm	optical scattering
Aerodynamic particle sizer (APS)	aerosol size distribution	aerodynamic diameter: 500–10,000 nm	aerodynamic classification
Three-column cloud condensation nuclei counter (CCN)	CCN concentration	three supersaturations	activation at constant supersaturation; optical detection of droplets
Aerodyne aerosol mass spectrometer (AMS)	aerosol chemical composition	mass concentration: $\text{SO}_4^{2-}$ , $\text{NH}_4^+$ , $\text{NO}_3^-$ , OC	Flash ionization; quadrupole mass spectrometer
Particle-into-liquid sampler (PILS)	aerosol chemical composition	mass concentration: $\text{SO}_4^{2-}$ , $\text{NH}_4^+$ , $\text{NO}_3^-$ , oxalate	ion chromatography
C-Navigational System and Novatel GPS	updraft velocity, wind speed	wind velocity; aircraft position and altitude	wind velocity = aircraft ground velocity (C-MIGITS INS/GPS) – aircraft air velocity (turbulence and Pitot-static probes)

were measured with a Particle-into-Liquid Sampler (PILS [Sorooshian *et al.*, 2006a]). Updraft velocities were obtained from a five-hole turbulence probe, a Pitot-static pressure tube, a C-MIGITS GPS/INS Tactical System, GPS/inertial navigational system (INS), and the Novatel GPS system.

[7] Droplet number concentrations were measured with a Cloud and Aerosol Spectrometer (CAS) optical probe [Baumgardner *et al.*, 2001], and the Forward Scattering Spectrometer Probe (FSSP [Brenguier *et al.*, 1998; Jaenicke and Hanusch, 1993]). The FSSP measures droplets ranging from 1.5 to 37  $\mu\text{m}$  diameter. As with any optical counter, the FSSP is subject to numerous uncertainties such as variations of the size calibration and of the instrument sampling section, nonuniformity in light intensity of the laser beam, probe dead time and coincidence errors [Baumgardner and Spowart, 1990; Brenguier, 1989]. The FSSP is most accurate for measurements of  $N_d$  below  $200 \text{ cm}^{-3}$  [Burnet and Brenguier, 2002]. At high droplet concentrations,  $N_d$  can be noticeably underestimated when measured with the Fast-FSSP [Burnet and Brenguier, 2002]. The CAS measures droplet sizes from 0.4 to 50  $\mu\text{m}$  in 20 size bins using a measurement principle similar to that of the FSSP, but improved electronics relaxes the requirement for dead time and coincidence corrections [Burnet and Brenguier, 2002]. A Passive Cavity Aerosol Spectrometer Probe (PCASP) was also flown, which is an optical probe that measures particles between 100 and 2500 nm.

## 2.2. Cloud Parcel Model

[8] The numerical cloud parcel model used in this study [Nenes *et al.*, 2001, 2002] simulates the dynamical balance between water vapor availability from cooling of an ascending air parcel and water vapor depletion from condensation onto a growing droplet population. The model has successfully been used to assess cloud droplet closure in cumulus during CRYSTAL-FACE [Conant *et al.*, 2004] and has been used in numerous model assessments of aerosol-cloud interactions [e.g., Nenes *et al.*, 2002; Rissman *et al.*, 2004; Lance *et al.*, 2004]. The model predicts cloud droplet number concentration and size distribution using as input the cloud updraft velocity, aerosol size distribution and chemical composition. “Chemical effects,” such as surface tension depression [Shulman *et al.*, 1996; Facchini *et al.*, 1999], partial solubility or the presence of film-forming compounds [Feingold and Chuang, 2002; Nenes *et al.*, 2002; Rissman *et al.*, 2004; Lance *et al.*, 2004] can also be easily considered; their effect on droplet closure will be assessed through sensitivity analysis.

## 2.3. Droplet Formation Parameterization

[9] The modified NS parameterization [Fountoukis and Nenes, 2005] is one of the most comprehensive, robust and flexible formulations available for global models. The calculation of droplet number is based on the computation of maximum supersaturation,  $s_{\text{max}}$ , within an ascending air parcel framework. The parameterization provides a computationally inexpensive algorithm for computing droplet number and size distribution and can treat externally mixed aerosol subject to complex chemical effects (e.g., surface tension effects, partial solubility, changes in water vapor uptake). The parameterization’s excellent performance has been evaluated with detailed numerical cloud parcel model

**Table 2.** ICARTT Cloud Characteristics for the Flights Considered in This Study

Flight (Cloud) Number	Flight Date	$w_{++}$ , $\text{ms}^{-1}$	$\sigma_{++}$ , $\text{ms}^{-1}$	Observed $N_d$ , $\text{cm}^{-3}$ ( $\pm$ st.dev%)	Predicted $N_d$ , $\text{cm}^{-3}$ Parcel Model (Parameterization)	Originating Air Mass <sup>a</sup> (Cloud Type)	Mission Description	Wind Direction
IC3 (1)	6 Aug	1.67	0.868	1086 (15.9)	1046 (1066)	clean (cumulus)	Conesville PP <sup>b</sup>	N
IC3 (2)	6 Aug	0.39	1.732	354 (45.6)	321 (356)	clean (stratocu)	Conesville PP <sup>b</sup>	N
IC3 (3)	6 Aug	1.89	0.750	825 (44.5)	1109 (1116)	clean (cumulus)	Conesville PP <sup>b</sup>	N
IC3 (4)	6 Aug	1.18	0.619	828 (27.0)	980 (943)	clean (cumulus)	Conesville PP <sup>b</sup>	N
IC5 (1)	9 Aug	0.69	0.407	1293 (9)	1607 (1420)	polluted (cumulus)	Conesville PP <sup>b</sup>	W-SW
IC5 (2)	9 Aug	0.28	0.209	1160 (17)	1147 (1224)	polluted (stratocu)	Conesville PP <sup>b</sup>	W-SW
IC5 (3)	9 Aug	0.59	0.528	1045 (37.8)	1223 (1281)	polluted (cumulus)	Conesville PP <sup>b</sup>	W-SW
IC6 (1)	10 Aug	0.69	0.430	695 (14.7)	744 (813)	polluted (stratocu)	Monroe PP <sup>b</sup>	W-SW
IC6 (2)	10 Aug	0.35	0.283	415 (50.1)	508 (577)	polluted (stratus)	Monroe PP <sup>b</sup>	NW-SW
IC6 (3)	10 Aug	0.44	0.303	668 (28.4)	555 (636)	polluted (stratus)	Monroe PP <sup>b</sup>	NW-SW
IC6 (4)	10 Aug	0.69	0.375	808 (25.6)	745 (809)	polluted (stratocu)	Monroe PP <sup>b</sup>	NW-SW
IC6 (5)	10 Aug	0.57	0.477	700 (47.8)	649 (730)	polluted (stratocu)	Monroe PP <sup>b</sup>	NW-SW
IC6 (6)	10 Aug	1.07	0.819	1075 (15.7)	1008 (1073)	polluted (stratocu)	Monroe PP <sup>b</sup>	NW-SW
IC9 (1)	16 Aug	0.59	0.360	1012 (31.9)	1000 (1089)	clean (stratocu)	SW of Cleveland	NW-SW
IC9 (2)	16 Aug	0.17	0.131	540 (36)	487 (455)	clean (stratus)	SW of Cleveland	NE-N
IC9 (3)	16 Aug	0.15	0.170	524 (48.5)	413 (392)	clean (stratus)	SW of Cleveland	NE-N
IC9 (4)	16 Aug	0.72	0.727	1229 (8.7)	1507 (1384)	clean (stratocu)	SW of Cleveland	NE-N
IC10 (1)	17 Aug	0.69	0.401	1258 (6)	1306 (1367)	polluted (cumulus)	SW of Cleveland	NE-N
IC10 (2)	17 Aug	0.47	0.228	1040 (19.6)	1309 (1060)	polluted (stratocu)	SW of Cleveland	S-SW
IC10 (3)	17 Aug	0.17	0.212	811 (20.4)	718 (495)	polluted (stratocu)	SW of Cleveland	S-SW
IC11 (1)	18 Aug	0.35	0.313	963 (14.1)	803 (780)	polluted (stratocu)	SW of Ontario	S-SW
IC11 (2)	18 Aug	0.54	0.621	954 (32.1)	1056 (1054)	polluted (stratocu)	SW of Ontario	S-SW
IC11 (3)	18 Aug	0.62	0.428	965 (13.1)	1145 (1153)	polluted (stratocu)	SW of Ontario	S-SW
IC11 (4)	18 Aug	0.56	0.239	1141 (18.6)	1060 (1080)	polluted (stratocu)	SW of Ontario	S-SW
IC12 (1)	21 Aug	0.55	0.823	1314 (24.3)	1269 (1265)	polluted (cumulus)	Conesville PP <sup>b</sup>	S-SW
IC12 (2)	21 Aug	0.38	0.250	1016 (32.1)	783 (766)	polluted (stratocu)	Conesville PP <sup>b</sup>	NW-SW
IC12 (3)	21 Aug	0.12	0.134	322 (11.1)	287 (296)	polluted (stratocu)	Conesville PP <sup>b</sup>	N

<sup>a</sup>See section 3.1 for characteristics of air mass types.<sup>b</sup>Read “PP” as “power plant.”

simulations [Nenes and Seinfeld, 2003; Fountoukis and Nenes, 2005] and in situ data for cumuliform and stratiform clouds of marine and continental origin [Meskhidze et al., 2005]. Formulations for sectional [Nenes and Seinfeld, 2003] or lognormal [Fountoukis and Nenes, 2005] aerosol have been developed. The latter (lognormal) formulation is used in this study.

### 3. Observations and Analysis

#### 3.1. Description of Research Flights

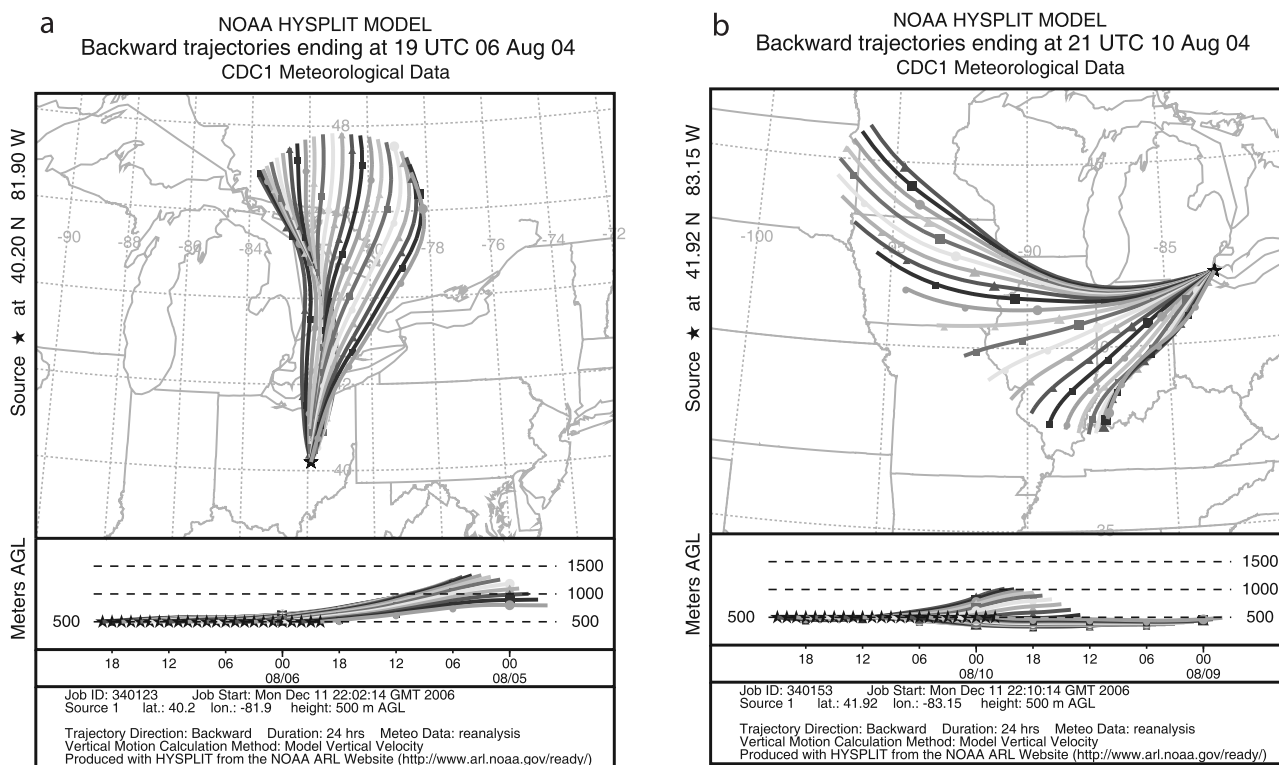
[10] Seven flights are analyzed in this study, in which 27 clouds are profiled (Table 2). The clouds formed downwind of power plants, Cleveland and Detroit. Three research flights (IC3, 5 and 12) sampled clouds downwind of the Conesville power plant (Figure 1a), one flight (IC6) sampled clouds downwind of the Monroe power plant (Figure 1a), two flights (IC 9, 10) sampled clouds southwest of Cleveland (Figure 1a) and one flight (IC11) sampled clouds southwest of Ontario (Figure 1a). Flight IC3 was the first to probe the Conesville power plant plume; its visible impact on local clouds (Figure 1b) motivated two more research flights (IC5 and 12) that fully characterized the plume and its influence on clouds. Backward Lagrangian trajectory analysis computed from the NOAA-HYSPLIT model (<http://www.arl.noaa.gov/ready/hysplit4.html>) suggests that during flights IC3 and IC9, the air mass sampled was transported by northerlies (Figure 2a). The air sampled in all other flights originated in the boundary layer and was transported by westerly winds (Figure 2b). Prevailing wind directions, cloud types and other characteristics for each cloud case are given in Table 2.

#### 3.2. Cloud Droplet Number and Updraft Velocity Measurements

[11] The observed cloud droplet spectra are carefully screened to eliminate biases in  $N_d$ . Dilution biases are avoided by considering only measurements with effective droplet diameter greater than  $2.4 \mu\text{m}$  and geometric standard deviation less than 1.5 [Conant et al., 2004]. A lack of a drizzle mode (liquid water) present, i.e., negligible concentrations of droplets larger than  $30 \mu\text{m}$  (typically  $0\text{--}0.2 \text{ cm}^{-3}$ ) suggest that collision-coalescence and drizzle formation were not important for the clouds sampled. Particles below  $1 \mu\text{m}$  are either evaporating or unactivated haze and not counted as droplets.

[12] For flights before 13 August, the CAS suffered from a saturation bias for concentrations above  $1500 \text{ cm}^{-3}$ . About 3% of the data set was subject to this bias and was disregarded from this study. The CAS was also found to overcount droplets smaller than  $6 \mu\text{m}$  but reliably counted droplet larger than  $6 \mu\text{m}$ . This problem is addressed by disregarding the  $1\text{--}6 \mu\text{m}$  CAS data and replacing them with FSSP data corrected for dead time and coincidence errors [Burnet and Brenguier, 2002]. Droplet concentration uncertainty was assessed by comparing FSSP and CAS concentrations in the  $6\text{--}10 \mu\text{m}$  range; the former was to be about 40% lower than the latter. As all known sources of bias are accounted for in the FSSP correction, we assume that the difference between the two probes (40%) expresses an unbiased uncertainty ( $\pm 20\%$ ) in observed droplet concentration for the whole data set and droplet size range.

[13] The observed cloud droplet concentrations for each flight are presented in Table 2. Average  $N_d$  varied from  $320 \text{ cm}^{-3}$  to  $1300 \text{ cm}^{-3}$  and as expected, correlated with



**Figure 2.** HYSPLIT backward trajectory analysis for (a) flight IC3 and (b) flight IC6.

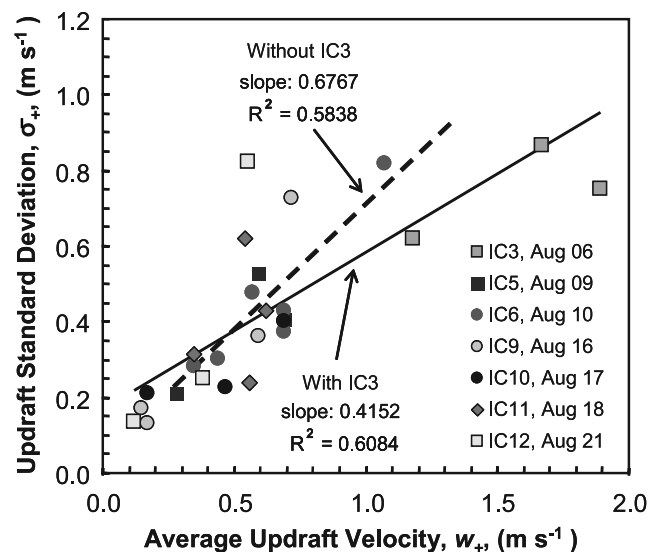
cloud updraft velocity,  $w$ ; clouds with  $N_d > 1000 \text{ cm}^{-3}$  typically had  $w > 1 \text{ m s}^{-1}$ ,  $N_d \sim 500\text{--}1000$  for  $w \sim 0.5 \text{ m s}^{-1}$  and  $N_d \sim 300\text{--}500$  for  $w \sim 0.25 \text{ m s}^{-1}$ . High droplet concentration (even for clouds with low updraft velocity) is indicative of the high aerosol loading in almost all clouds profiled.

[14] As expected, updraft velocity varied significantly in each cloud (even at cloud base); we chose to fit observations to a mass-flux-weighted Gaussian probability density function (pdf), as discussed by Meskhidze *et al.* [2005] and Conant *et al.* [2004]. Aircraft turns were eliminated from our analysis and the pdf in the measurements were shifted to have a mean of zero (consistent with the assumption of a slowly evolving boundary layer). Table 2 shows the values of average updraft velocity (closest to cloud base) and its standard deviation. Average cloud updraft velocity (at cloud base),  $w_+$ , varied between  $0.12 (\pm 0.13)$  and  $1.89 (\pm 0.73) \text{ m s}^{-1}$ .  $w_+$  and its standard deviation,  $\sigma_+$ , were highly correlated (Figure 3); typical of stratocumulus clouds,  $\sigma_+$  is significant and comparable to the mean updraft velocity.

### 3.3. Aerosol Size Distribution and Composition

[15] Flight legs were first conducted below cloud base to characterize aerosol composition and size distribution, followed by constant-altitude transects through the cloud; a final pass was done at the cloud top (at 300–1000 m). The vertical profiles and horizontal transects are used to deduce cloud spatial extent and height. The under-cloud aerosol size distributions are averaged and fit to three (or four) lognormal modes (depending on the observations) using least squares minimization. Average total aerosol concentration ranged from  $4200 \text{ cm}^{-3}$  to  $13300 \text{ cm}^{-3}$ ; the distribution information for each cloud case is summarized in Table 3.

[16] Whenever available (flights IC3, IC5, IC6), AMS measurements were used to describe the dry aerosol composition. The AMS always detected significant amounts of organics, constituting 35–85% of the total aerosol mass. Highest organic mass fractions were observed outside of power plant plumes (Table 3). The ammonium-sulfate molar ratio obtained both by the PILS and the AMS was larger than 2 for most flights (ranging from 2.0 to 3.7), except for IC5, where the ratio was 1.75. This suggests that the aerosol was



**Figure 3.** Correlation between average cloud base updraft velocity and velocity standard deviation. All clouds listed in Table 2 are used.



**Table 3.** Aerosol Size Distribution and Chemical Composition for ICARTT Clouds

Flight Number (Date)	Aerosol Mode	Modal $D_{pg}$ , $\mu\text{m}$	Modal $\sigma$	Modal $N_{ap}$ , $\text{cm}^{-3}$	$(\text{NH}_4)_2\text{SO}_4$ Mass Fraction, %
IC3 (8/6/2004)	nucleation	0.014	1.253	6667	40
IC3 (8/6/2004)	accumulation	0.024	1.222	2630	40
IC3 (8/6/2004)	coarse	0.064	1.720	1541	40
IC5-a (8/9/2004)	nucleation	0.027	1.477	2813	61
IC5-a (8/9/2004)	accumulation	0.112	1.638	3353	61
IC5-a (8/9/2004)	coarse	0.253	1.176	530	61
IC5-b (8/9/2004)	nucleation	0.030	1.330	2949	61
IC5-b (8/9/2004)	accumulation	0.051	1.121	486	61
IC5-b (8/9/2004)	coarse	0.124	1.712	3170	61
IC5-c (8/9/2004)	nucleation	0.013	1.066	163	66
IC5-c (8/9/2004)	accumulation	0.035	1.479	2578	66
IC5-c (8/9/2004)	coarse	0.138	1.708	2995	66
IC6-a (8/10/2004)	nucleation	0.015	1.336	2287	65
IC6-a (8/10/2004)	accumulation	0.042	1.400	3856	65
IC6-a (8/10/2004)	coarse	0.141	1.663	652	65
IC6-b (8/10/2004)	nucleation	0.014	1.230	1881	65
IC6-b (8/10/2004)	accumulation	0.040	1.496	4381	65
IC6-b (8/10/2004)	accumulation	0.163	1.534	533	65
IC6-b (8/10/2004)	coarse	0.738	1.027	0.1	65
IC9-a (8/16/2004)	nucleation	0.032	1.720	11890	15
IC9-a (8/16/2004)	accumulation	0.128	1.380	1310	15
IC9-a (8/16/2004)	coarse	0.274	1.150	420	15
IC9-b (8/16/2004)	nucleation	0.051	1.438	8491	70
IC9-b (8/16/2004)	accumulation	0.135	1.339	1365	70
IC9-b (8/16/2004)	coarse	0.249	1.161	289	70
IC9-c (8/16/2004)	nucleation	0.056	1.384	7959	50
IC9-c (8/16/2004)	accumulation	0.141	1.354	1300	50
IC9-c (8/16/2004)	coarse	0.260	1.140	244	50
IC10-a (8/17/2004)	nucleation	0.016	1.161	469	38
IC10-a (8/17/2004)	accumulation	0.037	1.360	4702	38
IC10-a (8/17/2004)	accumulation	0.077	1.060	243	38
IC10-a (8/17/2004)	coarse	0.143	1.581	1953	38
IC10-b (8/17/2004)	nucleation	0.024	1.269	3577	38
IC10-b (8/17/2004)	accumulation	0.042	1.123	355	38
IC10-b (8/17/2004)	coarse	0.112	1.841	2393	38
IC11 (8/18/2004)	nucleation	0.017	1.521	1322	15
IC11 (8/18/2004)	accumulation	0.098	1.676	2339	15
IC11 (8/18/2004)	coarse	0.237	1.289	587	15
IC12 (8/21/2004)	nucleation	0.013	1.117	133	36
IC12 (8/21/2004)	accumulation	0.096	1.296	206	36
IC12 (8/21/2004)	coarse	0.082	1.728	4336	36

neutralized in all flights except IC5. Lack of size-resolved composition precludes the detection of acidity changes throughout the aerosol distribution, but any gas phase ammonia (for all flights except IC5) would quickly condense and neutralize acidic particles formed from in-cloud production of sulfate. The PILS analysis showed small amounts of nitrate and oxalate, the latter being generated by in-cloud oxidation of organic precursors [Sorooshian *et al.*, 2006b]. It is unclear whether particulate nitrate is associated with aerosol phase organics. When combined, nitrates and oxalate did not exceed 2% of the total (soluble + insoluble) aerosol mass and were excluded from our analysis; a small change in the soluble fraction would not significantly impact droplet concentrations [Rissman *et al.*, 2004]. Table 3 presents the aerosol size distribution and composition for each cloud case considered in this study.

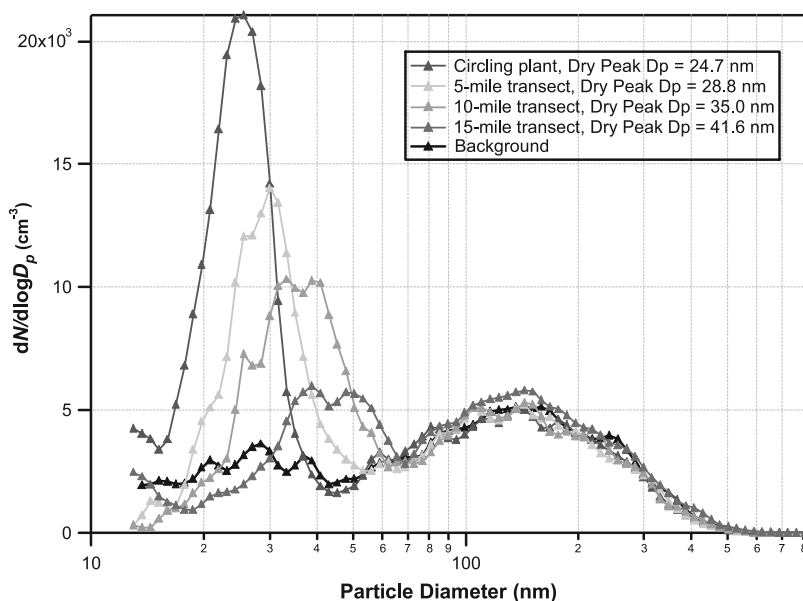
[17] Additional compositional insight (and its spatial variability) can be obtained from the DACAD; the hygroscopic growth factor (wet over dry aerosol diameter) during flight IC3 was  $\sim 1.17$ , (compared to 1.44 for pure ammonium sulfate at 77% relative humidity), characteristic of carbonaceous material with low sulfate content. Ageing of the plume downwind showed an increase in hygroscopicity,

consistent with condensation of sulfates on the aerosol. The influence of the power plant plume could be detected for more than 20 miles downwind of the plant (Figure 4). Representative examples of measured and fitted size distributions are shown in Figure 5; the discrepancy for CCN-relevant size range (larger than 30 nm) is generally small, less than 10%.

### 3.4. Cloud Droplet Closure: Parcel Model

[18] The average updraft velocity,  $w_+$ , is used to compute  $N_d$ ; this was shown by Meskhidze *et al.* [2005] to give optimal closure for cumulus and stratocumulus clouds.  $w_+$  is defined as,  $w_+ = \int_0^\infty wp(w)dw / \int_0^\infty p(w)dw$ , where  $p(w)$  is the vertical velocity probability density function (pdf). For a Gaussian pdf with standard deviation  $\psi_w$  and zero average velocity,  $p(w) = \frac{1}{(2\pi)^{1/2}\psi_w} \exp\left\{-\frac{w^2}{2\psi_w^2}\right\}$ , and

$$w_+ = \frac{-\frac{\psi_w}{(2\pi)^{1/2}} \int_0^\infty \exp(-x)d(-x)}{0.5} = \left(\frac{2}{\pi}\right)^{1/2} \psi_w \cong 0.8\psi_w \quad (1)$$



**Figure 4.** Dry aerosol size distributions for flight IC5 (Conesville power plant). Distributions are shown for plume transects downwind of the power plant.

$w_+$ , as calculated from equation (1), is identical to the “characteristic” velocity found by Peng *et al.* [2005] used for assessing cloud droplet closure for stratocumulus clouds sampled in the North Atlantic Ocean. Equation (1) is also reflected in the updraft velocity observations (Figure 3);  $\sigma_+$ , which is roughly half of  $\psi_w$ , yields after substitution into equation (1)  $\sigma_+ \cong 0.63w_+$ , which is consistent with the slope of Figure 3.

[19] The under-cloud temperature, pressure and relative humidity describe the precloud thermodynamic state of the atmosphere and are used as initial conditions for the parcel model. Aerosol observations and cloud updraft velocity are obtained from Tables 2 and 3.

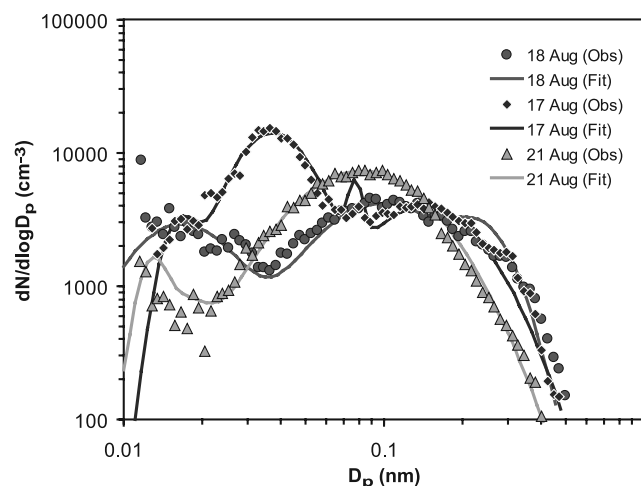
[20] It is assumed that the aerosol is internally mixed and composed of two compounds: ammonium sulfate (with density  $\rho_{sul} = 1760 \text{ kg m}^{-3}$ ) and organic (with density  $\rho_{org} = 1500 \text{ kg m}^{-3}$ ). The “organic” density is slightly larger than the 1200–1250  $\text{kg m}^{-3}$  value of Turpin and Lim [2001] proposed for Los Angeles to account for ageing and the presence of some crustal species. For flights which AMS data were not available (i.e., IC9, IC10, IC11, IC12), the “insoluble” volume fraction,  $V_{ins}$ , was inferred by subtracting the ammonium sulfate volume,  $V_{sul}$ , (obtained from PILS measurements) from the total aerosol volume,  $V_{total}$  (obtained from size distribution measurements). The mass fraction of the insoluble material,  $m_{ins}$ , is then calculated as,

$$m_{ins} = \frac{\rho_{org} V_{ins}}{\rho_{sul} V_{sul} + \rho_{org} V_{ins}} \quad (2)$$

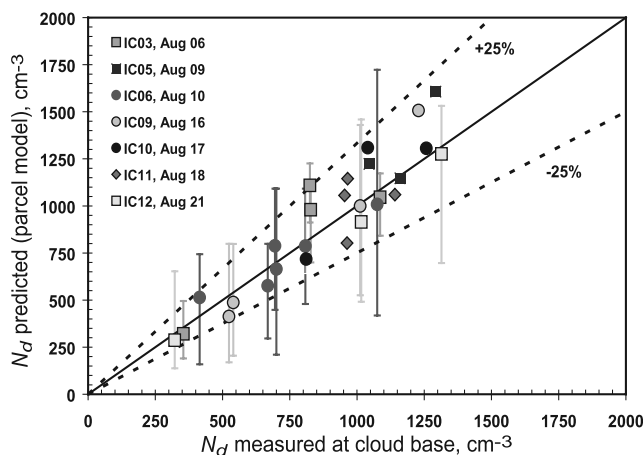
The assumption that only inorganics contribute soluble mass relevant for CCN activation appears to be reasonable in CCN closure studies conducted in North America [e.g., Medina *et al.*, 2007; Broekhuizen *et al.*, 2005]. Equation (2) assumes uniform composition with size; this can introduce a significant amount of uncertainty in predicting CCN

concentrations [e.g., Medina *et al.*, 2007; Broekhuizen *et al.*, 2005]. The importance of both assumptions in cloud droplet number prediction is discussed in section 3.5.

[21] The mass water vapor uptake (condensation) coefficient,  $a_c$ , needed for computing the water vapor mass transfer coefficient [Fountoukis and Nenes, 2005] is currently subject to considerable uncertainty. Li *et al.* [2001] have shown that if uptake is controlled by the accommodation of water vapor molecules onto droplets,  $a_c$  can range from 0.1 to 0.3 for pure water droplets, from 0.04 to 0.06 for aged atmospheric CCN [Shaw and Lamb, 1999; Pruppacher and Klett, 2000; Chuang, 2003; Conant *et al.*, 2004], while a recent work suggests that it should be close to unity for dilute droplets and pure water [Laaksonen *et al.*, 2004]. However, ambient CCN at the point of activation are concentrated solutions composed of electrolytes and (potentially) organic surfactants,



**Figure 5.** Examples of observed size distributions and corresponding lognormal fits.



**Figure 6.** Cloud droplet number closure using the parcel model. The conditions for predicting  $N_d$  are summarized in Tables 2 and 3.

which, together with other kinetic processes (e.g., solute dissolution [Asa-Awuku and Nenes, 2007]), can slow water uptake and growth kinetics; this would give an apparent uptake coefficient much less than unity (even if  $a_c$  were unity). Because of this, and following the suggestions of Shaw and Lamb [1999] and Conant *et al.* [2004], we consider a “base case” value of  $a_c$  equal to 0.06. The data set (Tables 2 and 3) is used to determine a “best fit” value for  $a_c$  and constrain its uncertainty (section 3.5).

[22] Figure 6 shows the cloud droplet number closure for all 27 clouds analyzed in this study. The parcel model predictions of  $N_d$  are close to the 1:1 line of perfect agreement with observations. In most cases, predictions are within 25% of the observations (average error  $3.0 \pm 15.4\%$ ; average absolute error  $12.8 \pm 8.7\%$ ), which is considerably less than the estimated  $N_d$  uncertainty of  $\sim 20\%$ .

### 3.5. Cloud Droplet Closure: Modified NS Parameterization

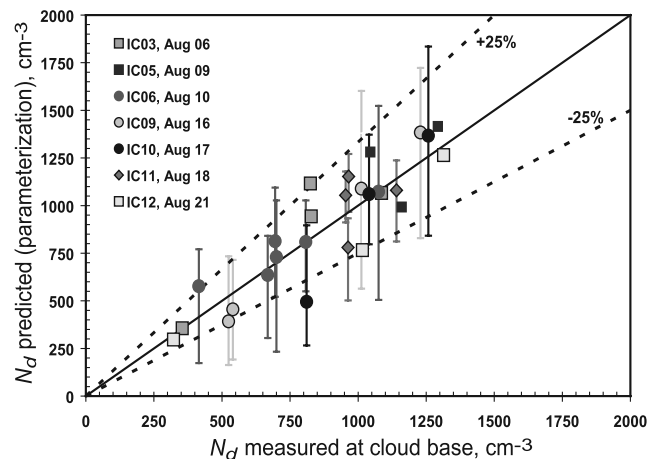
[23] Evaluation of the modified NS parameterization is carried out via a closure study, using the procedure outlined in section 3.3. The results are shown in Figure 7; on average, the modified NS parameterization was found to reproduce observed  $N_d$  with the same accuracy as the parcel model (average error  $1.5 \pm 17.9\%$ ; average absolute error  $13.5 \pm 11.5\%$ ). There is no systematic bias between the modeled and the observed  $N_d$ . This is remarkable, given that highly polluted clouds formed from CCN containing large amounts of organics have long been considered a challenge for any parameterization and parcel model [e.g., Conant *et al.*, 2004]. This study, combined with the work of Meskhidze *et al.* [2005] clearly show that the modified NS parameterization can accurately and robustly predict the process of cloud droplet activation and reliably be used in GCM assessments of the aerosol indirect effect.

### 3.6. Sources of Uncertainty and Sensitivity Analyses

[24] Despite the excellent closure, it is important to identify key contributors to  $N_d$  error (defined as the difference between predicted and measured  $N_d$  normalized to measured  $N_d$ ). This is done by examining the correlation of  $N_d$  error with key parameters affecting  $N_d$ , being (1) total aerosol

number, (2) accumulation mode aerosol number, (3) average cloud base updraft velocity, (4) cloud base updraft velocity variance, (5) observed cloud droplet number, and (6) aerosol sulfate mass fraction. The first two parameters are used as a proxy for pollution. The next two parameters are used as a proxy for cloud dynamics, which strongly impact cloud droplet number and its sensitivity to “chemical effects” [e.g., Nenes *et al.*, 2002; Rissman *et al.*, 2004]. Sulfate mass fraction itself is a proxy for “chemical effects,” as low sulfate is usually correlated with high organic content, which in turn may be water-soluble and contain surfactants. Finally, observed cloud droplet number is used to explore whether the  $N_d$  observations are subject to some concentration-dependant bias (section 3.2). Table 4 presents the results of the correlation analysis. When the whole data set is considered,  $N_d$  error only correlates significantly with  $w_+$  ( $R^2$  in Table 4 is for  $w_+ < 1 \text{ m s}^{-1}$ ) and its variance. There is practically no correlation of droplet error with  $w_+$  when it is above  $1.0 \text{ m s}^{-1}$  (roughly 50% of the data set). The correlation of error with updraft is stronger as the  $w_+$  decreases; this is expected as vertical velocity uncertainty becomes substantial for low updrafts. Lack of droplet error correlation with chemical composition variations is consistent with Rissman *et al.* [2004], who show droplet number is most sensitive to variations in updraft velocity under conditions of low supersaturation (i.e., strong competition for water vapor from high aerosol concentration and low updraft velocity). When considering subsets of data, updraft velocity still correlates with droplet error (Table 4), more weakly ( $R^2 = 0.2$ ) for power plant flights alone (IC3,5,6,12) and more strongly ( $R^2 = 0.5$ ) for non-power-plant plume flights (IC9,10,11). The strength of correlation is expected, as power plant clouds are more vigorous (56% have  $w_+ > 1.0$ , and only 6% with  $w_+ < 0.25$ ), than non-power-plant clouds (55% have  $w_+ > 1.0$ , and 27% with  $w_+ < 0.25$ ).

[25] For power plant flights alone, droplet error also correlates with aerosol number. This is likely from the temporal averaging of the aerosol size distribution; an averaged distribution cannot account for the spatial heterogeneity of the aerosol (hence droplet number) in the vicinity of power plant plumes. Therefore droplet error does not arise



**Figure 7.** Same as Figure 3 but using the modified NS parameterization for predicting  $N_d$ .

**Table 4.** Correlation of Droplet Number Error With Important Aerosol-Cloud Interaction Properties<sup>a</sup>

Observed Property	Correlation Coefficient ( $R^2$ )		
	Whole Data Set	Non-Power-Plant	Power Plant Only
Total aerosol number	0.002	0.018	<b>0.111</b>
Accumulation mode aerosol number	0.002	0.043	<b>0.198</b>
Cloud updraft velocity	<b>0.358</b>	<b>0.500</b>	<b>0.209</b>
Updraft velocity standard deviation	<b>0.150</b>	<b>0.383</b>	0.066
Cloud droplet number	0.067	<b>0.343</b>	0.014
Aerosol sulfate mass fraction	0.025	0.036	0.014

<sup>a</sup>The parcel model was used for computing cloud droplet number. Strongest correlations are shown in bold.

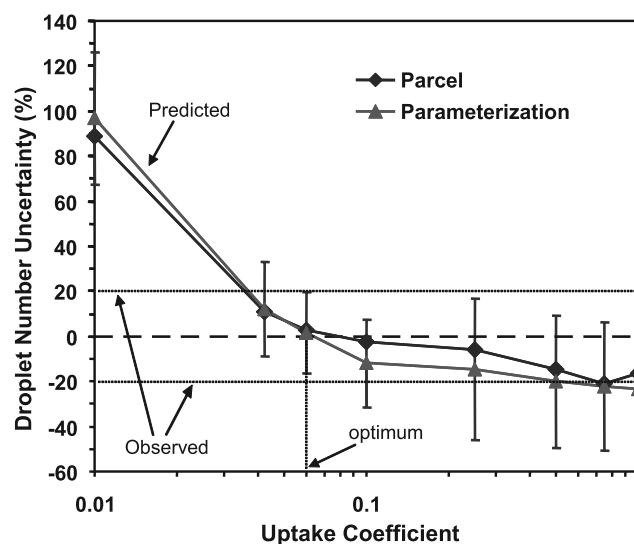
from the presence of very high aerosol concentrations at cloud base, but variations thereof. The observations support this hypothesis;  $N_d$  error decreases as the plume ages and dilutes to the polluted (but homogeneous) background aerosol. Despite the correlation, the droplet number variability is still small compared to the highly variable aerosol near the vicinity of a power plant plume (Figure 4) for two reasons: droplet number variability is inherently less than the CCN variability [Sotiropoulou *et al.*, 2006], and clouds may not respond to aerosol variations when they take place at small particle sizes and  $s_{max}$  is not sufficiently high to activate them. The latter can be seen in Figure 4; most of the aerosol variability is seen in small diameters (<60 nm), while droplets formed upon CCN with diameter greater than 70 nm (simulations suggest that  $s_{max} \sim 0.085\%$ ). For non-power-plant plume flights (IC9,10,11), cloud droplet error correlates with cloud droplet number (but not sulfate fraction or aerosol number), which suggests the presence of minor biases in the  $N_d$  observations, which however are not significant enough to affect closure.

[26] Droplet number error also arises by assuming that aerosol chemical composition is invariant with particle size (section 3.3). Broekhuizen *et al.* [2005], Medina *et al.* [2007] and Sotiropoulou *et al.* [2006] have shown that this assumption for polluted areas can result in up to 50% error in CCN predictions. If our data set is subject to similar uncertainty, the resulting  $N_d$  error should range between 10 and 25% [Sotiropoulou *et al.*, 2006], well within the observational uncertainty. If organics partially dissolve and depress droplet surface tension,  $N_d$  can become less sensitive to variations in chemical composition [Rissman *et al.*, 2004].

[27] Figure 8 presents the sensitivity of droplet number prediction error, averaged over the data set, to the uptake coefficient,  $a_c$ . Figure 8 displays the  $N_d$  standard deviation only for the parcel model, as the parameterization exhibits roughly the same behavior. The sensitivity analysis was done using the parcel model and activation parameterization, and assuming that the organic fraction is insoluble. Assuming that the droplet number prediction error is random, our simulations indicate that the “best fit” value of  $a_c$  (i.e., the value which the average  $N_d$  error is minimal and its standard deviation lies between the measured droplet uncertainty range) is 0.06, which is in agreement with values obtained from the Conant *et al.* [2004] and Meskhidze *et al.* [2005] closure studies. Assuming a 20% uncertainty in observed  $N_d$  (and neglecting the  $N_d$  error standard deviation) constrains  $a_c$  between 0.03 and 1.0 (Figure 8). Peng *et al.* [2005] also obtain good closure using a much different  $a_c$  (=1) in their analysis; this does not suggest

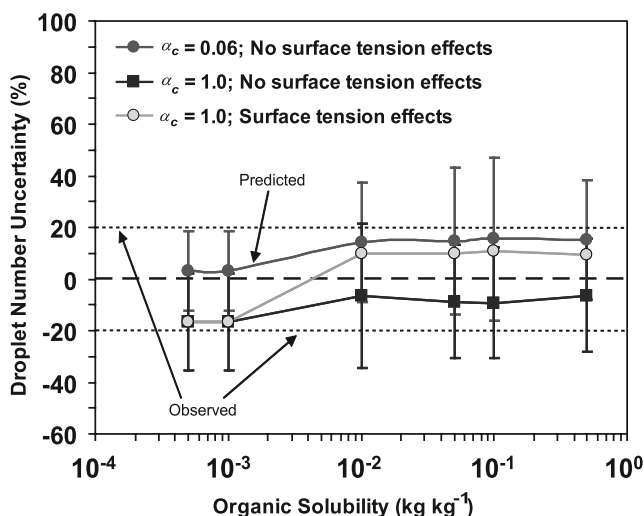
that the closure is insensitive to  $a_c$ , but rather that updraft velocity and droplet number measurements require reduction in their uncertainty (Figure 8) to further constrain  $a_c$ .

[28] Finally, we assess the sensitivity of droplet closure to “chemical effects” (i.e., solubility of the organic fraction and depression of surface tension); the focus is to assess whether different values of the uptake coefficient and organic solubility (compared with the “base case” simulations for  $a_c = 0.06$ ) can yield good closure. In the sensitivity analysis, the dissolved organic was assumed to have a molar volume of  $66 \text{ cm}^3 \text{ mol}^{-1}$  and a Van’t Hoff factor of 1, which is consistent with a lower limit of properties derived from the activation of water-soluble organic carbon extracted from biomass burning samples (A. Asa-Awuku, Georgia Institute of Technology, personal communication, 2006). Organic solubility varied from  $10^{-4}$  to  $1 \text{ kg kg}^{-1}$ ; when surface tension is allowed to decrease, we use the correlation of Facchini *et al.* [1999], assuming 8 mols of carbon per mol of dissolved organic [Nenes *et al.*, 2002]. We also consider two values of the uptake coefficient, 0.06 and 1.0. Simulations indicate (Figure 9) that organic solubility less than  $10^{-3} \text{ kg kg}^{-1}$  is not enough to affect CCN (thus droplet number) concentrations. All the organic dissolves during activation when its solubility is larger than  $10^{-2} \text{ kg kg}^{-1}$ ; this leads to an average increase



**Figure 8.** Sensitivity of droplet number error (between model and observations) to the value of the water vapor uptake coefficient.





**Figure 9.** Sensitivity of droplet number error (between model and observations) to the solubility of the aerosol organic mass. The dissolved organic was assumed to have a molar volume of  $66 \text{ g mol}^{-1}$  and a Van't Hoff factor of 1.

in droplet number (error) by 10–15%, accompanied with a substantial increase in droplet error variability. If surface tension depression is included, droplet number (error) is on average increased by about 30% compared to the “base case” simulation. Surface tension depression is considered only for simulations with  $\alpha_c = 1.0$ , as a lower value would yield droplet error outside of the uncertainty range. Using a larger organic molar volume (i.e., molecular weight) would just decrease their effect on CCN activation; a lower molar volume is unlikely, given that a lower estimate was already used. The simulations suggest that combinations of organic solubility, degree of surface tension depression and uptake coefficient can give cloud droplet closure within experimental uncertainty. However, the “base case” conditions give by far the best closure since average droplet error and its variability are within measurement uncertainty (Figure 9). This suggests that “chemical effects” do not considerably influence aerosol activation. The sensitivity analysis above illustrates the importance of reducing the droplet number measurement uncertainty. On the basis of Figure 9, a 10% uncertainty would further constrain the extent of “chemical effects” on cloud droplet formation.

#### 4. Summary

[29] This study analyzes 27 cumuliform and stratiform clouds sampled aboard the CIRPAS Twin Otter during the 2004 ICARTT (International Consortium for Atmospheric Research on Transport and Transformation). A unique feature of the data set is the sampling of highly polluted clouds within the vicinity of power plant plumes. In situ observations of aerosol size distribution, chemical composition and updraft velocity were input to (1) a detailed adiabatic cloud parcel model [Nenes *et al.*, 2001, 2002] and (2) the modified NS parameterization [Fountoukis and Nenes, 2005; Nenes and Seinfeld, 2003]; predicted droplet number is then compared with the observations. Remark-

able closure was achieved (on average to within 10%) for parcel model and parameterization. The error in predicted cloud droplet concentration was found to correlate mostly with updraft velocity. Aerosol number also correlated with droplet error for clouds affected by power plant plumes (which is thought to stem from spatial variability of the aerosol not considered in the closure). Finally, we assess the sensitivity of droplet closure to “chemical effects.” A number of important conclusions arise from this study:

[30] 1. Cloud droplet number closure is excellent even for the highly polluted clouds downwind of power plant plumes. Droplet number error does not correlate with background pollution level, only with updraft velocity and aerosol mixing state.

[31] 2. A highly variable aerosol does not necessarily imply a highly variable  $N_d$  concentration. The clouds in this study often do not respond to aerosol variations because they take place primarily at small particle sizes, and cloud  $s_{max}$  is not high enough to activate them. Any droplet variability that does arise is inherently less than the CCN variability it originated from [Sotiropoulou *et al.*, 2006].

[32] 3. Usage of average updraft velocity is appropriate for calculating cloud droplet number.

[33] 4. The water vapor uptake coefficient ranges between 0.03 and 1.0. Optimum closure (for which average  $N_d$  error is minimal and its standard deviation is within droplet measurement uncertainty) is obtained when the water vapor uptake coefficient is about 0.06. This agrees with values obtained from previous closure studies for polluted strato-cumulus [Meskhidze *et al.*, 2005] and marine cumulus clouds [Conant *et al.*, 2004].

[34] 5. On average, organic species do not seem to influence activation through contribution of solute and surface tension depression. Optimal cloud droplet closure is obtained if the CCN are approximated by a combination of soluble inorganics and partially soluble organics (less than  $1 \text{ g kg}^{-1}$  water assuming a molar volume of  $66 \text{ cm}^3 \text{ mol}^{-1}$  and a Van't Hoff factor of 1).

[35] 6. The cloud droplet activation parameterization used in this study [Nenes and Seinfeld, 2003; Fountoukis and Nenes, 2005] has performed as well as the detailed cloud parcel model. Excellent performance has also been reported by Meskhidze *et al.* [2005]. Together, both studies suggest that the parameterization can robustly be used in GCM assessments of the aerosol indirect effect.

[36] 7. Distinguishing the “chemical effects” on the cloud droplet spectrum requires the observational uncertainty to be of order 10%.

[37] The above conclusions can serve as much needed constraints for the parameterization of aerosol-cloud interactions in the North America. Future in situ studies will determine the robustness of our findings.

[38] **Acknowledgments.** We acknowledge the support of the National Science Foundation under award ATM-0340832. C.F., A.N. and N.M. acknowledge support from an NSF CAREER award, a NASA EOS-IDS and a NASA NIP. C.F. acknowledges support from a Gerondelis Foundation Fellowship.

#### References

Andreae, O. M., C. D. Jones, and P. M. Cox (2005), Strong present-day aerosol cooling implies a hot future, *Nature*, **435**, 1187–1190.

- Asa-Awuku, A., and A. Nenes (2007), Effect of solute dissolution kinetics on cloud droplet formation: 1. Extended Köhler theory, *J. Geophys. Res.*, doi:10.1029/2005JD006934, in press.
- Bahreini, R., J. L. Jimenez, J. Wang, R. C. Flagan, J. H. Seinfeld, J. T. Jayne, and D. R. Worsnop (2003), Aircraft-based aerosol size and composition measurements during ACE-Asia using an Aerodyne aerosol mass spectrometer, *J. Geophys. Res.*, 108(D23), 8645, doi:10.1029/2002JD003226.
- Baumgardner, D., and M. Spowart (1990), Evaluation of the Forward Scattering Spectrometer Probe. Part III: Time response and laser inhomogeneity limitations, *J. Atmos. Oceanic Technol.*, 7, 666–672.
- Baumgardner, D., H. Jonsson, W. Dawson, D. O'Connor, and R. Newton (2001), Cloud, aerosol and precipitation spectrometer: A new instrument for cloud investigations, *Atmos. Res.*, 59–60, 251–264.
- Boucher, O., and U. Lohmann (1995), The sulfate-CCN-cloud albedo effect: A sensitivity study with two general circulation models, *Tellus, Ser. B*, 47, 281–300.
- Brasseur, G. P., and E. Roeckner (2005), Impact of improved air quality on the future evolution of climate, *Geophys. Res. Lett.*, 32, L23704, doi:10.1029/2005GL023902.
- Brenguier, J.-L. (1989), Coincidence and deadtime corrections for particle counters. Part II: High concentration measurements with an FSSP, *J. Atmos. Oceanic Technol.*, 6, 575–584.
- Brenguier, J.-L., T. Bourrianne, A. Coelho, J. Isbert, R. Peytavi, D. Trevarin, and P. Weschler (1998), Improvements of droplet size distribution measurements with the Fast-FSSP (Forward Scattering Spectrometer Probe), *J. Atmos. Oceanic Technol.*, 15, 1077–1090.
- Broekhuizen, K., R. Y.-W. Chang, W. R. Leitch, S.-M. Li, and J. P. D. Abbatt (2005), Closure between measured and modeled cloud condensation nuclei (CCN) using size-resolved aerosol compositions in downtown Toronto, *Atmos. Chem. Phys. Disc.*, 5, 6263–6293.
- Burnet, F., and J.-L. Brenguier (2002), Comparison between standard and modified forward scattering spectrometer probes during the small cumulus microphysics study, *J. Atmos. Oceanic Technol.*, 19, 1516–1531.
- Chuang, P. (2003), Measurement of the timescale of hygroscopic growth for atmospheric aerosols, *J. Geophys. Res.*, 108(D9), 4282, doi:10.1029/2002JD002757.
- Chuang, P. Y., D. R. Collins, H. Pawlowska, J. R. Snider, H. H. Jonsson, J. L. Brenguier, R. C. Flagan, and J. H. Seinfeld (2000), CCN measurements during ACE-2 and their relationship to cloud microphysical properties, *Tellus, Ser. B*, 52, 843–867.
- Conant, W. C., et al. (2004), Aerosol–cloud drop concentration closure in warm cumulus, *J. Geophys. Res.*, 109, D13204, doi:10.1029/2003JD004324.
- Considine, G., and J. A. Curry (1998), Effects of entrainment and droplet sedimentation on the microphysical structure of stratus and stratocumulus clouds, *Q. J. R. Meteorol. Soc.*, 124, 123–150.
- Facchini, M., M. Mircea, S. Fuzzi, and R. Charlson (1999), Cloud albedo enhancement by surface-active organic solutes in growing droplets, *Nature*, 401, 257–259.
- Feingold, G., and P. Y. Chuang (2002), Analysis of the influence of film-forming compounds on droplet growth: Implications for cloud microphysical processes and climate, *J. Atmos. Sci.*, 59, 2006–2018.
- Fountoukis, C., and A. Nenes (2005), Continued development of a cloud droplet formation parameterization for global climate models, *J. Geophys. Res.*, 110, D11212, doi:10.1029/2004JD005591.
- Ghan, S. J., R. Easter, E. Chapman, H. Abdul-Razzak, Y. Zhang, L. Leung, N. Laulainen, R. Saylor, and R. Zaveri (2001a), A physically-based estimate of radiative forcing by anthropogenic sulfate aerosol, *J. Geophys. Res.*, 106, 5279–5293.
- Ghan, S. J., N. Laulainen, R. Easter, R. Wagoner, S. Nemesure, E. Chapman, Y. Zhang, and R. Leung (2001b), Evaluation of aerosol indirect forcing in MIRAGE, *J. Geophys. Res.*, 106, 5317–5334.
- Gultepe, I., and G. Isaac (1996), The relationship between cloud droplet and aerosol number concentrations for climate models, *Int. J. Climatol.*, 16, 941–946.
- Hallberg, A., et al. (1997), Microphysics of clouds: Model versus measurements, *Atmos. Environ.*, 31, 2453–2462.
- Jaenicke, R., and T. H. Hanusch (1993), Simulation of the optical-particle counter forward scattering spectrometer probe-100 (FSSP-100)—Consequences for size distribution measurements, *Aerosol Sci. Technol.*, 18(4), 309–322.
- Jayne, J. T., D. C. Leard, X. Zhang, P. Davidovits, K. A. Smith, C. E. Kolb, and D. Worsnop (2000), Development of an aerosol mass spectrometer for size and composition analysis of submicron particles, *Aerosol Sci. Technol.*, 33, 49–70.
- Jensen, J. B., and R. J. Charlson (1984), On the efficiency of nucleation scavenging, *Tellus, Ser. B*, 36, 367–375.
- Jones, A., D. L. Roberts, and A. Slingo (1994), A climate model study of indirect radiative forcing by anthropogenic sulphate aerosols, *Nature*, 370, 450–453.
- Khairoutdinov, M., D. Randall, and C. DeMott (2005), Simulations of the atmospheric general circulation using a cloud-resolving model as a superparameterization of physical processes, *J. Atmos. Sci.*, 62(7), 2136–2154.
- Kiehl, J. T., T. L. Schneider, P. J. Rasch, M. C. Barth, and J. Wong (2000), Radiative forcing due to sulfate aerosols from simulations with the NCAR Community Climate Model, *J. Geophys. Res.*, 105, 1441–1457.
- Laaksonen, A., T. Vesala, M. Kulmala, P. M. Winkler, and P. E. Wagner (2004), On cloud modeling and the mass accommodation coefficient of water, *Atmos. Chem. Phys. Disc.*, 4, 7281–7290.
- Lance, S., A. Nenes, and T. Rissman (2004), Chemical and dynamical effects on cloud droplet number: Implications for estimates of the aerosol indirect effect, *J. Geophys. Res.*, 109, D22208, doi:10.1029/2004JD004596.
- Li, Y. Q., P. Davidovits, Q. Shi, J. T. Jayne, and D. R. Worsnop (2001), Mass and thermal accommodation coefficients of  $H_2O_{(g)}$  on liquid water as a function of temperature, *J. Phys. Chem. A*, 105, 10,627–10,634.
- Lohmann, U., and J. Feichter (1997), Impact of sulfate aerosols on albedo and lifetime of clouds: A sensitivity study with the ECHAM4 GCM, *J. Geophys. Res.*, 102, 13,685–13,700.
- Lohmann, U., and J. Feichter (2004), Global indirect aerosol effects: A review, *Atmos. Chem. Phys. Disc.*, 4, 7561–7614.
- Lohmann, U., J. Feichter, C. C. Chuang, and J. E. Penner (1999), Predicting the number of cloud droplets in the ECHAM GCM, *J. Geophys. Res.*, 104, 9169–9198.
- Lohmann, U., J. Feichter, J. E. Penner, and R. Leitch (2000), Indirect effect of sulfate and carbonaceous aerosols: A mechanistic treatment, *J. Geophys. Res.*, 105, 12,193–12,206.
- Medina, J., A. Nenes, R.-E. P. Sotiropoulou, L. D. Cottrell, L. D. Ziemba, P. J. Beckman, and R. J. Griffin (2007), Cloud condensation nuclei closure during the International Consortium for Atmospheric Research on Transport and Transformation 2004 campaign: Effects of size-resolved composition, *J. Geophys. Res.*, 112, D10S31, doi:10.1029/2006JD007588.
- Menon, S., A. D. DelGenio, D. Koch, and G. Tselioudis (2002), GCM simulations of the aerosol indirect effect: Sensitivity to cloud parameterization and aerosol burden, *J. Atmos. Sci.*, 59, 692–713.
- Meskhidze, N., A. Nenes, W. C. Conant, and J. H. Seinfeld (2005), Evaluation of a new cloud droplet activation parameterization with in situ data from CRYSTAL-FACE and CSTRIP, *J. Geophys. Res.*, 110, D16202, doi:10.1029/2004JD005703.
- Nenes, A., and J. H. Seinfeld (2003), Parameterization of cloud droplet formation in global climate models, *J. Geophys. Res.*, 108(D14), 4415, doi:10.1029/2002JD002911.
- Nenes, A., S. Ghan, H. Abdul-Razzak, P. Chuang, and J. Seinfeld (2001), Kinetic limitations on cloud droplet formation and impact on cloud albedo, *Tellus, Ser. B*, 53, 133–149.
- Nenes, A., R. J. Charlson, M. C. Facchini, M. Kulmala, A. Laaksonen, and J. H. Seinfeld (2002), Can chemical effects on cloud droplet number rival the first indirect effect?, *Geophys. Res. Lett.*, 29(17), 1848, doi:10.1029/2002GL015295.
- Peng, Y., U. Lohmann, R. Leitch, C. Banic, and M. Couture (2002), The cloud albedo-cloud droplet effective radius relationship for clean and polluted clouds from RACE and FIRE.ACE, *J. Geophys. Res.*, 107(D11), 4106, doi:10.1029/2000JD000281.
- Peng, Y., U. Lohmann, and R. Leitch (2005), Importance of vertical velocity variations in the cloud droplet nucleation process of marine stratus clouds, *J. Geophys. Res.*, 110, D21213, doi:10.1029/2004JD004922.
- Pruppacher, H. R., and J. D. Klett (2000), *Microphysics of Clouds and Precipitation*, Springer, New York.
- Randall, D., M. Khairoutdinov, A. Arakawa, and W. Grabowski (2003), Breaking the cloud parameterization deadlock, *Bull. Am. Meteorol. Soc.*, 84(11), 1547–1564.
- Rissman, T., A. Nenes, and J. H. Seinfeld (2004), Chemical amplification (or dampening) of the Twomey effect: Conditions derived from droplet activation theory, *J. Atmos. Sci.*, 61(8), 919–930.
- Rotstain, L. D., and J. E. Penner (2001), Indirect aerosol forcing, quasi-forcing, climate response, *J. Clim.*, 14, 2960–2975.
- Shaw, R. A., and D. Lamb (1999), Experimental determination of the thermal accommodation and condensation coefficients of water, *J. Chem. Phys.*, 111, 10,659–10,663.
- Shulman, M. L., M. C. Jacobson, R. J. Charlson, R. E. Synovec, and T. E. Young (1996), Dissolution behavior and surface tension effects of organic compounds in nucleating cloud droplets, *Geophys. Res. Lett.*, 23, 277–280.
- Snider, J. R., and J. L. Brenguier (2000), Cloud condensation nuclei and cloud droplet measurements during ACE-2, *Tellus, Ser. B*, 52, 827–841.

- Snider, J. R., S. Guibert, J.-L. Brenguier, and J.-P. Putaud (2003), Aerosol activation in marine stratocumulus clouds: 2. Köhler and parcel theory closure studies, *J. Geophys. Res.*, *108*(D15), 8629, doi:10.1029/2002JD002692.
- Sorooshian, A., F. J. Brechtel, Y. Ma, R. J. Weber, A. Corless, R. C. Flagan, and J. H. Seinfeld (2006a), Modeling and characterization of a particle-into-liquid sampler (PILS), *Aerosol Sci. Technol.*, *40*, 396–409.
- Sorooshian, A., et al. (2006b), Oxalic acid in clear and cloudy atmospheres: Analysis of data from International Consortium for Atmospheric Research on Transport and Transformation 2004, *J. Geophys. Res.*, *111*, D23S45, doi:10.1029/2005JD006880.
- Sotiropoulou, R. E. P., J. Medina, and A. Nenes (2006), CCN predictions: Is theory sufficient for assessments of the indirect effect?, *Geophys. Res. Lett.*, *33*, L05816, doi:10.1029/2005GL025148.
- Turpin, B. J., and H. Lim (2001), Species contributions to PM<sub>2.5</sub> mass concentrations: Revisiting common assumptions for estimating organic mass, *Aerosol Sci. Technol.*, *35*, 602–610.
- Wang, J., R. C. Flagan, and J. H. Seinfeld (2003), A differential mobility analyzer (DMA) system for submicron aerosol measurements at ambient relative humidity, *Aerosol Sci. Technol.*, *37*, 46–52.
- R. Bahreini, NOAA, Boulder, CO 80305, USA.
- F. Brechtel, R. C. Flagan, and J. H. Seinfeld, Environmental Science and Engineering, California Institute of Technology, Pasadena, CA 91125, USA.
- W. C. Conant, Department of Atmospheric Sciences, University of Arizona, Tucson, AZ 85721, USA.
- C. Fountoukis and A. Nenes, School of Chemical and Biomolecular Engineering, Georgia Institute of Technology, Atlanta, GA 30332, USA. (nenes@cas.gatech.edu)
- H. Jonsson, Center for Interdisciplinary Remotely-Piloted Aircraft Studies, Naval Postgraduate School, Monterey, CA 93933, USA.
- N. Meskhidze, School of Marine, Earth, and Atmospheric Sciences, North Carolina State University, Raleigh, NC 27695, USA.
- S. Murphy, A. Sorooshian, and V. Varutbangkul, Department of Chemical Engineering, California Institute of Technology, Pasadena, CA 91125, USA.

## Appendix E

# Secondary Aerosol Formation from Atmospheric Reactions of Aliphatic Amines\*

---

\*This chapter is reproduced by permission from “Secondary Aerosol Formation from Atmospheric Reactions of Aliphatic Amines” by S. M. Murphy, A. Sorooshian, J. H. Kroll, N. L. Ng, P. Chhabra, C. Tong, J. D. Surratt, E. Knipping, R. C. Flagan, and J. H. Seinfeld, *Atmos. Chem. Phys.*, 7(9), 2313–2337, 2007. © 2007 Author(s). This work is licensed under a Creative Commons License.



## Secondary aerosol formation from atmospheric reactions of aliphatic amines

S. M. Murphy<sup>1</sup>, A. Sorooshian<sup>1</sup>, J. H. Kroll<sup>2</sup>, N. L. Ng<sup>1</sup>, P. Chhabra<sup>1</sup>, C. Tong<sup>1</sup>, J. D. Surratt<sup>1</sup>, E. Knipping<sup>3</sup>, R. C. Flagan<sup>1</sup>, and J. H. Seinfeld<sup>1</sup>

<sup>1</sup>Division of Chemistry and Chemical Engineering, California Institute of Technology, Pasadena, CA 91125, USA

<sup>2</sup>Current Address: Aerodyne Research Inc., Billerica, MA, USA

<sup>3</sup>Electric Power Research Institute, Palo Alto, CA, USA

Received: 17 December 2006 – Published in Atmos. Chem. Phys. Discuss.: 10 January 2007

Revised: 13 April 2007 – Accepted: 13 April 2007 – Published: 8 May 2007

**Abstract.** Although aliphatic amines have been detected in both urban and rural atmospheric aerosols, little is known about the chemistry leading to particle formation or the potential aerosol yields from reactions of gas-phase amines. We present here the first systematic study of aerosol formation from the atmospheric reactions of amines. Based on laboratory chamber experiments and theoretical calculations, we evaluate aerosol formation from reaction of OH, ozone, and nitric acid with trimethylamine, methylamine, triethylamine, diethylamine, ethylamine, and ethanolamine. Entropies of formation for alkylammonium nitrate salts are estimated by molecular dynamics calculations enabling us to estimate equilibrium constants for the reactions of amines with nitric acid. Though subject to significant uncertainty, the calculated dissociation equilibrium constant for diethylammonium nitrate is found to be sufficiently small to allow for its atmospheric formation, even in the presence of ammonia which competes for available nitric acid. Experimental chamber studies indicate that the dissociation equilibrium constant for triethylammonium nitrate is of the same order of magnitude as that for ammonium nitrate. All amines studied form aerosol when photooxidized in the presence of NO<sub>x</sub> with the majority of the aerosol mass present at the peak of aerosol growth consisting of aminium (R<sub>3</sub>NH<sup>+</sup>) nitrate salts, which repartition back to the gas phase as the parent amine is consumed. Only the two tertiary amines studied, trimethylamine and triethylamine, are found to form significant non-salt organic aerosol when oxidized by OH or ozone; calculated organic mass yields for the experiments conducted are similar for ozonolysis (15% and 5% respectively) and photooxidation (23% and 8% respectively). The non-salt organic aerosol formed appears to be more stable than the nitrate salts and does not quickly repartition back to the gas phase.

### 1 Introduction

Amines are emitted into the atmosphere from a variety of sources including meat cooking, biomass burning, motor vehicle exhaust, industrial processes, and marine organisms. The dominant anthropogenic source is emissions from animal husbandry operations (Table 1). While amine emissions from animal husbandry are typically reported to be two to three orders of magnitude less than those of ammonia (Ngwabie and Hintz, 2005; Schade and Crutzen, 1995), at least one study has reported gas-phase concentrations of amines in the hundreds of ppb in areas of intense animal husbandry (Rabaud et al., 2003). Though emission estimates vary widely, amines have been detected in marine, rural, and urban atmospheres in the gas phase, particle phase and within aqueous fog and rain drops (Zhang and Anastasio, 2003). Mass spectrometric studies by both Murphy (1997) and Angelino (2001) have shown that molecular ions typically associated with amines are present in ambient particles, especially in air masses from agricultural regions. Tan et al. (2002) identified particle phase amines during multiple smog events in Toronto's winter atmosphere. Recent field studies suggest that organic nitrogen species could be an appreciable fraction of organic aerosol mass (Beddows et al., 2004; Mace et al., 2003; Makela et al., 2001; McGregor and Anastasio, 2001; Neff et al., 2002; Simoneit et al., 2003; Tan et al., 2002), although the relative importance of amines as a source of particulate organic nitrogen remains unclear.

During the 1970's, interest in the gas-phase atmospheric chemistry of amines focused on carcinogenic nitrosamines formed when amines are photooxidized (Pitts et al., 1978). It was subsequently determined that gas-phase nitrosamines photolyze rapidly in the troposphere and are believed to pose a minimal threat to human health. More recently, toxicology studies have demonstrated that particulate organic nitrogen species are associated with adverse health effects (Hamoir et

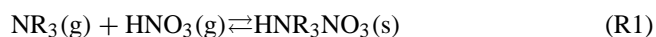
Correspondence to: J. H. Seinfeld  
(seinfeld@caltech.edu)

**Table 1.** Summary of structures of amines studied and estimated global emissions from animal husbandry.

Amine (abbrev)	Formula	Estimated Global Emissions, Gg N y <sup>-1</sup> (Schade and Crutzen, 1995)
Ammonia	NH <sub>3</sub>	23 300
Methylamine (MA)	CH <sub>3</sub> NH <sub>2</sub>	24±15
Trimethylamine (TMA)	(CH <sub>3</sub> ) <sub>3</sub> N	108±30
Diethylamine (DEA)	(CH <sub>3</sub> CH <sub>2</sub> ) <sub>2</sub> NH	–
Triethylamine (TEA)	(CH <sub>3</sub> CH <sub>2</sub> ) <sub>3</sub> N	–
Ethanolamine (MEA)	(CH <sub>2</sub> OH)CH <sub>2</sub> NH <sub>2</sub>	–

al., 2003). Nemmar (2002) found that particles coated with amines produced a significant increase in the rate of blood clots (by nearly 4 times) when installed in the trachea of hamsters; in contrast, the effects of particles coated with carboxylic acids and unmodified polystyrene particles were not statistically significant when compared to the control group of hamsters.

Amines are oxidized in the atmosphere by the hydroxyl radical (OH), ozone (O<sub>3</sub>), and possibly by the nitrate radical (NO<sub>3</sub>), with measured rate constants suggesting that the reaction rates of ozone and OH with amines are competitive during the day if ozone levels are in the tens to hundreds of ppb (Tuazon et al., 1994). The nitrate radical may play a significant role in amine oxidation at night, though very little is known about this pathway. While many of the gas-phase oxidation pathways involving OH and ozone have been elucidated, secondary aerosol formation resulting from the photooxidation of amines has received limited attention. Also, because amines are basic compounds, they can form particulate salts through reactions with gas-phase acids present in the atmosphere (HNO<sub>3</sub>, H<sub>2</sub>SO<sub>4</sub>),



Reactions (R1) and (R2) are analogous to those of ammonia to form ammonium sulfate and ammonium nitrate. While the equilibria between gas-phase ammonia and nitric or sulfuric acid to form particle-phase salts have been thoroughly investigated and the thermodynamic parameters governing these reactions are well known (Mozurkewich, 1993; Stelson and Seinfeld, 1982), similar thermodynamic parameters for amine systems were not available prior to this study.

There have been a limited number of laboratory chamber experiments in which aerosol resulting from amine photooxidation was observed (Angelino et al., 2001; Pitts et al., 1978). Aerosol yields, the relative importance of acid-base chemistry, and the oxidative pathways leading to particle formation remain poorly understood. The goal of the present work is to use controlled laboratory chamber studies to evaluate the aerosol forming potential, by acid-base reactions, photooxidation and ozonolysis, of aliphatic amines known to be

present in the atmosphere. The amines studied (with abbreviation used) are: trimethylamine (TMA), methylamine (MA), triethylamine (TEA), diethylamine (DEA), ethylamine (EA), and monoethanolamine (MEA), which will be referred to as ethanolamine in this paper.

## 2 Experimental

All experiments (Table 2) were carried out in the Caltech dual 28 m<sup>3</sup> FEP Teflon chambers (Cocker et al., 2001; Keywood et al., 2004). The chambers are surrounded by banks of black lights (276GE350BL) which output ultraviolet light predominantly between 300 and 400 nm, with a maximum at 354 nm. Ports allow for the introduction of clean, dry (<10% RH) air, gas-phase reagents, inorganic seed aerosol, and for measurement of NO, NO<sub>x</sub>, O<sub>3</sub>, RH, temperature, and particulate mass, size, number concentration, and chemistry. Temperature is held at 20°C, increasing to 25°C during photooxidation experiments using the black lights. Commercial monitors (Horiba) are used to measure O<sub>3</sub> (by UV absorption) and NO/NO<sub>x</sub> (NO<sub>x</sub> conversion to NO by activated carbon, followed by NO + O<sub>3</sub> chemiluminescence). Both amines and nitric acid (when added) were injected into the chamber by passing a stream of dry, clean air over a known volume of high purity liquid phase compound. The purity and source of the amines used in this study are: trimethylamine (45% solution in H<sub>2</sub>O, Fluka), methylamine (40 wt.% solution in H<sub>2</sub>O, Sigma-Aldrich), triethylamine (>99.5% purity, Sigma Aldrich), diethylamine (>99.5% purity, Sigma Aldrich), ethylamine (70 wt.% solution in H<sub>2</sub>O, Aldrich), ethanolamine, (≥99% purity, Sigma Aldrich). Gas-phase concentrations of amines and nitric acid were not directly measured and were instead estimated based on the volume of liquid phase amine injected; these concentrations represent the maximum possible within the chamber in the absence of wall loss.

“Seed” aerosol was generated by atomizing a solution of 0.015 M ammonium sulfate or 0.75 M ammonium nitrate. Particle-phase measurements were made by an Aerodyne Time of Flight Aerosol Mass Spectrometer (cToF-AMS), a Particle-Into-Liquid Sampler coupled to Ion

**Table 2.** Initial conditions of all experiments conducted.

Exp.	Amine	Estimated Initial (ppb) Mixing Ratios	Oxidant	Initial NO <sub>x</sub> Mixing Ratios (ppb)	HNO <sub>3</sub> Injected (ppb)	Atomized Seed Aerosol
1	Trimethylamine	100	NO <sub>x</sub> , Propene	100 (NO <sub>2</sub> )	–	–
2	Trimethylamine	100	NO <sub>x</sub> , Propene	100 (NO <sub>2</sub> )	10	–
3	Trimethylamine	100	H <sub>2</sub> O <sub>2</sub>	100 (NO <sub>2</sub> )	10	–
4	Trimethylamine	100	Ozone	–	18	–
5	Methylamine	100	NO <sub>x</sub>	100 (NO <sub>2</sub> )	10	–
6	Methylamine	100	H <sub>2</sub> O <sub>2</sub>	100 (NO)	10	–
7	Methylamine	100	Ozone	–	–	(NH <sub>4</sub> ) <sub>2</sub> SO <sub>4</sub>
8	Triethylamine	500	H <sub>2</sub> O <sub>2</sub>	–	–	–
9	Triethylamine	500	H <sub>2</sub> O <sub>2</sub>	400 (NO)	–	–
10	Triethylamine	100	NO <sub>x</sub>	100 (NO)	–	–
11	Triethylamine	100	NO <sub>x</sub>	100 (NO) 100 (NO <sub>2</sub> )	–	–
12	Triethylamine	100	NO <sub>x</sub>	140 (NO <sub>2</sub> )	–	–
13	Triethylamine	100	NO <sub>x</sub>	100 (NO <sub>2</sub> )	–	–
14	Triethylamine	100	NO <sub>x</sub>	100 (NO <sub>2</sub> )	10	–
15	Triethylamine	50	NO <sub>x</sub> , Propene	100 (NO <sub>2</sub> )	100	–
16	Triethylamine	100	O <sub>3</sub>	–	8	–
17	Triethylamine	100	HNO <sub>3</sub>	–	100	–
18	Triethylamine	20 ppb TEA aliquots	–	–	–	NH <sub>4</sub> NO <sub>3</sub>
19	Triethylamine	100 ppb NH <sub>3</sub> inject TEA in aliquots	–	–	5 (twice)	–
20	Triethylamine	50 ppb TEA 50 ppb NH <sub>3</sub>	–	–	8	–
21	Diethylamine	100	H <sub>2</sub> O <sub>2</sub>	–	–	–
22	Diethylamine	100	H <sub>2</sub> O <sub>2</sub>	80 (NO)	–	–
23	Diethylamine	100	NO <sub>x</sub> , Propene	100 (NO)	–	–
24	Diethylamine	100	NO <sub>x</sub>	100 (NO)	–	–
25	Diethylamine	100	NO <sub>x</sub>	100 (NO <sub>2</sub> )	–	(NH <sub>4</sub> ) <sub>2</sub> SO <sub>4</sub>
26	Diethylamine	100	NO <sub>x</sub>	100 (NO <sub>2</sub> )	10	–
27	Ethylamine	100	NO <sub>x</sub>	100 (NO <sub>2</sub> )	10	–
28	Ethanolamine	100	NO <sub>x</sub> , Propene	140 NO 140 NO <sub>2</sub>	–	–
29	Ethanolamine	100	NO <sub>x</sub> , Propene	135 NO <sub>2</sub>	–	–
30	Ethanolamine	300	NO <sub>x</sub> , Propene	100 (NO <sub>2</sub> )	–	–
31	Ethanolamine	100	–	–	–	(NH <sub>4</sub> ) <sub>2</sub> SO <sub>4</sub> mixed with H <sub>2</sub> SO <sub>4</sub> (aq)
32	Ethanolamine	100	H <sub>2</sub> O <sub>2</sub>	100	100	–
33	Ethanolamine	100	O <sub>3</sub>	–	–	–
34	NH <sub>3</sub>	100	NO <sub>x</sub> , Propene	100 (NO <sub>2</sub> )	10	–

Chromatography (PILS-IC), and a differential mobility analyzer (DMA, TSI 3760). During experiment number 20 (Table 2), chamber particles were collected onto a Teflon (PALL Life Sciences, 47-mm diameter, 1.0- $\mu$ m pore size) filter for analysis by mass spectrometry using both Matrix Assisted Laser Desorption Ionization (MALDI) and electrospray ionization (ESI) to determine how spectra from these ionization techniques compared to the electron impact ionization spectra of the cToF-AMS. Details of the extraction and analysis methodology used for the Teflon filter are given in Surratt et al. (2006).

## 2.1 PILS-IC

The particle-into-liquid sampler coupled with ion chromatography is a quantitative technique for measuring water-soluble ions, including inorganic, organic acid, and amine ions in aerosol particles. The PILS-IC used in this study (Sorooshian et al., 2006) is based on the prototype design (Weber et al., 2001) with key modifications, including integration of a liquid sample fraction collector and real-time control of the steam injection tip temperature. Chamber air is sampled through a 1  $\mu$ m cut-size impactor and a set of three denuders (URG and Sunset Laboratories) to remove in-

organic (basic and acidic) and organic gases that would otherwise bias aerosol measurements. Sample air mixes with steam in a condensation chamber where rapid adiabatic mixing produces a high water supersaturation. Droplets grow sufficiently large to be collected by inertial impaction before being delivered to vials held on a rotating carousel. The contents of the vials are subsequently analyzed off-line using a dual IC system (ICS-2000 with 25  $\mu$ L sample loop, Dionex Inc.) for simultaneous anion and cation analysis.

Data for the following ions are reported: acetate, formate, nitrate, sulfate ammonium, methylammonium, dimethylammonium, trimethylammonium, ethylammonium, diethylammonium, and triethylammonium. The PILS-IC technique cannot be used to speciate many of the organic compounds that make up the total aerosol mass since these are not sufficiently ionic in water to have affinity for the IC columns used (anion: Dionex AS-11 column 2 $\times$ 250 mm, ASRS Ultra II 2-mm suppressor, potassium hydroxide eluent; cation: CS12A column 2 $\times$ 250 mm, CSRS Ultra II 2-mm suppressor, methanesulfonic acid eluent); nevertheless, all of the amine salts formed in the experiments reported here were successfully speciated. It should be noted that ammonium, methylammonium, and ethylammonium co-elute; additional co-eluting pairs are diethylammonium:trimethylammonium

and potassium:dimethylammonium. While potassium was never expected to be present and ammonium formation was not anticipated for many of the experiments, background levels of these species in the IC baseline noise did interfere with quantification of co-eluting species. The limit of detection (LOD) for each ion ( $\text{NH}_4^+$ ,  $\text{NO}_3^-$ , acetate, formate, and the six aforementioned amine species) is defined in this study as the air-equivalent concentration of the lowest concentration standard that is distinct from baseline noise in the IC plus three times the standard deviation ( $n=3$ ) of this measurement. The LOD's for the ions measured using the PILS-IC technique for this study are all below  $0.1 \mu\text{g m}^{-3}$ , with the exceptions of trimethylamine and triethylamine, which have LOD's of 0.60 and  $0.89 \mu\text{g m}^{-3}$ , respectively. In all experiments, chamber air containing gas-phase amine and nitric acid (when added) was run through a particle filter and sampled by the PILS-IC; none of the amines was ever detected in these filtered vials, confirming that the carbon denuder was able to completely remove gas-phase species and that the PILS-IC signal is entirely a result of aerosol-phase compounds.

## 2.2 Aerodyne cToF-AMS

The design parameters and capabilities of the cToF-AMS instrument are described in detail elsewhere (Drewnick et al., 2004a, b). Briefly, chamber air enters the instrument through a  $100 \mu\text{m}$  critical orifice at a flowrate of  $1.4 \text{ cm}^3 \text{ s}^{-1}$ . Particles with a vacuum aerodynamic diameter between roughly 50 and 800 nm are efficiently focused by an aerodynamic lens, passed through a 1% chopper, and then impacted onto a tungsten vaporizer. The chopper can be operated in three modes: (1) completely blocking the beam to gather background mass spectra; (2) out of the beam's path to collect ensemble average mass spectra over all particles sizes; (3) chopping the beam to create size-resolved mass spectra. The vaporizer is set at  $\sim 550^\circ\text{C}$  to ensure complete volatilization of the aerosol. Once vaporized, molecules undergo electron impact ionization at 70 eV and are orthogonally pulsed every  $19 \mu\text{s}$  into the time of flight mass analyzer. The resolution of the mass analyzer is  $\sim 800$  ( $M/\Delta M$ ). For all mass spectra shown in this work the ion signal is represented as sticks, the height of which represent the raw ion signal integrated over 1 amu bins. These stick mass spectra are divided into different chemical species based on the methodology of Allan et al. (2003), with exceptions noted in the text. The limits of detection, calculated as three times the standard deviation of the noise for particle filtered air are  $<0.05 \mu\text{g m}^{-3}$  for all species measured.

## 2.3 Effective density

Calculating the density of aerosol particles is important for two reasons. First, multiplying the aerosol volume measured by the DMA by the material density allows one to calculate aerosol mass yields. (The cToF-AMS cannot be used to di-

rectly quantify aerosol mass because the fraction of particles that bounce off of the vaporizer is unknown and the PILS-IC does not measure the mass of non-ionic species) Second, changes in the density give an indication of alterations in particle morphology during secondary aerosol formation.

The effective density ( $\rho_{\text{eff}}$ ) is a function of the vacuum aerodynamic diameter ( $d_{\text{va}}$ ) measured by the cToF-AMS and the mobility diameter ( $d_{\text{m}}$ ) measured by the DMA (DeCarlo et al., 2004),

$$\rho_{\text{eff}} = \frac{d_{\text{va}}}{d_{\text{m}}} \rho_o = \rho_m \frac{C_c(d_{\text{ve}})}{\delta^3 \chi_t \chi_v C_c(d_{\text{m}})} \quad (1)$$

where  $\rho_o$  is unit density ( $1 \text{ g cm}^{-3}$ ),  $\rho_m$  is the material density,  $C_c$  is the slip correction factor,  $d_{\text{ve}}$  is the volume equivalent diameter,  $\delta$  is a measure of the internal void space defined by  $\delta = (\rho_m/\rho_p)^{1/3}$  where  $\rho_p$  is the particle density,  $\chi_t$  is the dynamic shape factor in the transition regime, and  $\chi_v$  is the dynamic shape factor in the free molecular regime.

As described in Bahreini et al. (2005) and Decarlo et al. (2004), the effective density is equivalent to the material density if the shape factor and slip correction factor are unity and the internal void fraction is zero. These assumptions are probably slightly incorrect for amine salts and amine oxidation products, given that ammonium nitrate particles have an effective density 20 percent less than the material density of ammonium nitrate when  $\rho_{\text{eff}}$  is calculated using simultaneous cToF-AMS and DMA measurements (Jayne et al., 2000). Indeed the effective densities calculated in this way for the aminium nitrates are less than the literature values. While there is no need to use effective densities to calculate the mass of pure salts (the PILS-IC is able quantitatively measure these), it is necessary to use effective densities (as an approximation of the material density) to calculate the mass of aerosol formed during photooxidation and ozonolysis because non-ionic species are present.

To calculate the effective density, one represents the DMA volume distribution, normally expressed as  $dV/d\log(d_{\text{m}})$ , as  $dV/d\log(\rho_{\text{eff}}d_{\text{m}})$  and adjusts  $\rho_{\text{eff}}$  until this distribution (with peak height normalized to 1) aligns in diameter space with the mass distribution from the cToF-AMS,  $dM/d\log(d_{\text{va}})$  (peak height also normalized to 1). The two distributions align when the correct effective density is used because  $\rho_{\text{eff}}d_{\text{m}} = d_{\text{va}}\rho_o$  (if unity shape and slip correction factors and zero internal void fraction are assumed). Figure 1a shows the calculated effective density of triethylammonium nitrate (TEAN) is  $1.0 \pm 0.1 \text{ g cm}^{-3}$  while the effective density of the aerosol formed from photolysis of TEA (mixed TEAN and products from TEA oxidation) has a slightly increased effective density of  $1.1 \pm 0.1 \text{ g cm}^{-3}$ .

## 2.4 Oxidation experiments

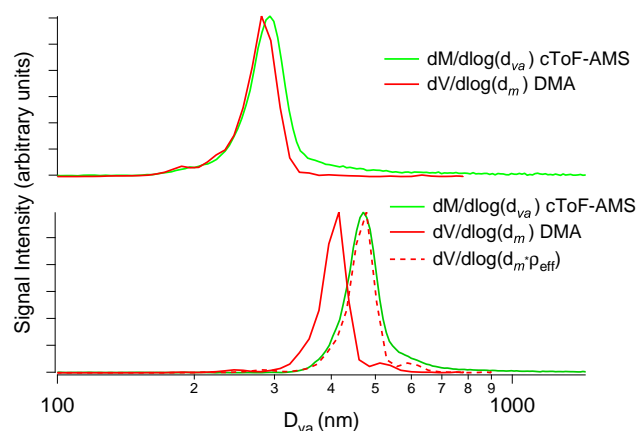
Three types of amine oxidation experiments were conducted in this study: (1) Photooxidation in the absence of  $\text{NO}_x$ , (2)

Photooxidation in the presence of  $\text{NO}_x$ , and (3) dark ozonolysis. Hydrogen peroxide ( $\text{H}_2\text{O}_2$ ) was used as the OH radical precursor for all of the  $\text{NO}_x$ -free photooxidation experiments and many of the high  $\text{NO}_x$  experiments (see Table 2 for details).  $\text{H}_2\text{O}_2$  is introduced by bubbling  $5 \text{ L min}^{-1}$  of humidified room-temperature air for 2.5 h through a 50%  $\text{H}_2\text{O}_2$  solution (Aldrich), through a particle filter to avoid the introduction of droplets, and finally into the chamber. The mixing ratio of  $\text{H}_2\text{O}_2$  achieved using this method has been previously estimated to be between 3 and 5 ppm (Kroll et al., 2006). To minimize potential uptake of  $\text{H}_2\text{O}_2$  by the aerosol, all experiments were carried out under dry ( $\text{RH} < 10\%$ ) conditions. To determine if the presence of hydrogen peroxide significantly affected the particle-phase chemistry, numerous high  $\text{NO}_x$  photooxidation experiments were conducted in the absence of  $\text{H}_2\text{O}_2$ , some with the gas-phase amine and  $\text{NO}_x$  alone, and others where propene was added to generate higher levels of OH in the chamber and increase the rate of oxidation (see Table 2 for details). For all photooxidation studies,  $\text{H}_2\text{O}_2$ ,  $\text{NO}_x$ , propene, or a combination of these was injected first. For many experiments using  $\text{NO}_x$ , this step was followed by the injection of nitric acid or, occasionally, ammonium sulfate (see Table 2 for details). After the  $\text{HNO}_3$  or ammonium sulfate had mixed throughout the chamber, the amine was added. When nitric acid is present, formation of aminium nitrate salt occurs once the amine is injected. By using a similar concentration of  $\text{HNO}_3$  in all experiments, we were able to roughly control the size distribution of the aerosol. Nucleating the aminium nitrate before the start of oxidation also allowed us to measure the chemistry of pure salt particles in situ with the cToF-AMS and PILS-IC. Photooxidation reactions were initiated by irradiation from the black lights surrounding the chamber. Ozonolysis experiments were conducted in the dark in the absence of an OH scavenger. The order of reactant introduction for ozonolysis experiments was: nitric acid, amine, and finally ozone. Between experiments, the chamber was continuously flushed with clean air and irradiated with UV light. Contamination from previous experiments was occasionally observed and has been accounted for in the analyses.

### 3 Atmospheric reaction pathways of amines

At the outset, it is useful to frame the results of this study by outlining a hypothesis for the atmospheric reaction pathways of amines. Direct or indirect evidence of most of these pathways has been observed during the chamber experiments in this study.

Because amines are one of relatively few basic atmospheric compounds, they have the potential to undergo rapid acid-base reactions to form salt particles in the presence of nitric or sulfuric acid. Formation of salt particles depends on temperature, the identity of the amine, and the concentrations and identities of acidic species present. Formation



**Fig. 1.** Calculation of the effective density (data from exp. 14, Table 2). Panel (a) Volume distribution from the DMA ( $dV/d\log(d_m)$ , solid red line) and mass distribution from the cToF-AMS ( $dM/d\log(d_{va})$ , solid green line) of triethylammonium nitrate (TEAN). The fact that the two distributions are aligned indicates the effective density of TEAN is  $\sim 1$ . The slight tailing of the cToF-AMS signal could be caused by slow vaporization or higher uncertainty in the size calibration for larger particles. Panel (b) The same distributions shown in (a) after products from TEA photooxidation have condensed onto the nitrate salt shown in (a) for 7 h. The particles have grown larger from the condensation process. The dashed red line ( $dV/d\log(\rho_{\text{eff}} d_m)$ ) is created by adjusting the effective density ( $\rho_{\text{eff}}$ ) until the dotted red line aligns with the solid green line ( $\rho_{\text{eff}} = 1.1 \text{ g cm}^{-3}$ ).

of aminium salts also depends indirectly on the concentration of ammonia, which will compete with amines for acidic molecules. Once aminium-salt particles are formed, they can revolatize, undergo particle-phase reactions (including oxidation), or serve as a site for condensation of other organic species. Condensation of organics onto the salts particles may form a barrier that prevents the salts from remaining at equilibrium with the gas phase.

Gas-phase amines can be oxidized by OH,  $\text{O}_3$  and possibly  $\text{NO}_3$  (OH and  $\text{O}_3$  are known to be competitive oxidation agents of amines at atmospherically relevant concentrations while the rate of  $\text{NO}_3$  oxidation remains unexplored). Specifics of the known oxidation pathways will be discussed thoroughly in Sect. 5. Briefly, the products formed depend on the oxidizing species and the  $\text{NO}_x$  level. Many of the oxidation products of amines are themselves basic and can undergo reactions with atmospheric acids to form additional salts. Other oxidation products are sufficiently non-volatile to condense directly onto particles without forming salts. Finally, it is possible that certain amines, or their oxidation products, that are too volatile to condense onto dry particles will condense into, and ionize within, aqueous aerosols. Once condensed, amines and their oxidation products may undergo particle-phase reactions to form high molecular weight compounds, or they may be further oxidized into volatile species.

**Table 3.** Theoretically calculated dissociation constants for different nitrate systems.  $K_{p,298}$  for ammonium nitrate =  $7.14 \times 10^{-7} \text{ Pa}^2$ .

Species	$K_{p,298} \text{ (Pa}^2\text{)}$	
	$\Delta H^\circ_f$ from Cottrell and Gill (1951)	$\Delta H^\circ_f$ from NBS (1982)
Methylammonium nitrate	7.90E-06	8.56E-09
Dimethylammonium nitrate	1.01E-05	3.95E-09
Trimethylammonium nitrate	2.27E+00	5.29E-07
Ethylammonium nitrate	3.29E-06	9.56E-07
Diethylammonium nitrate	3.11E-10	3.30E-11
Triethylammonium nitrate	1.37E-05	1.18E-12

The remainder of the paper is divided into two main sections. In the first section, we investigate salt aerosol formation from acid-base reactions of amines through both laboratory chamber experiments and theoretical estimates. In the second section, aerosol formation resulting from photooxidation and ozonolysis of amines under varying  $\text{NO}_x$  conditions is addressed.

#### 4 Salt aerosol formation from acid-base reactions of amines

##### 4.1 Detection of aminium nitrate salts

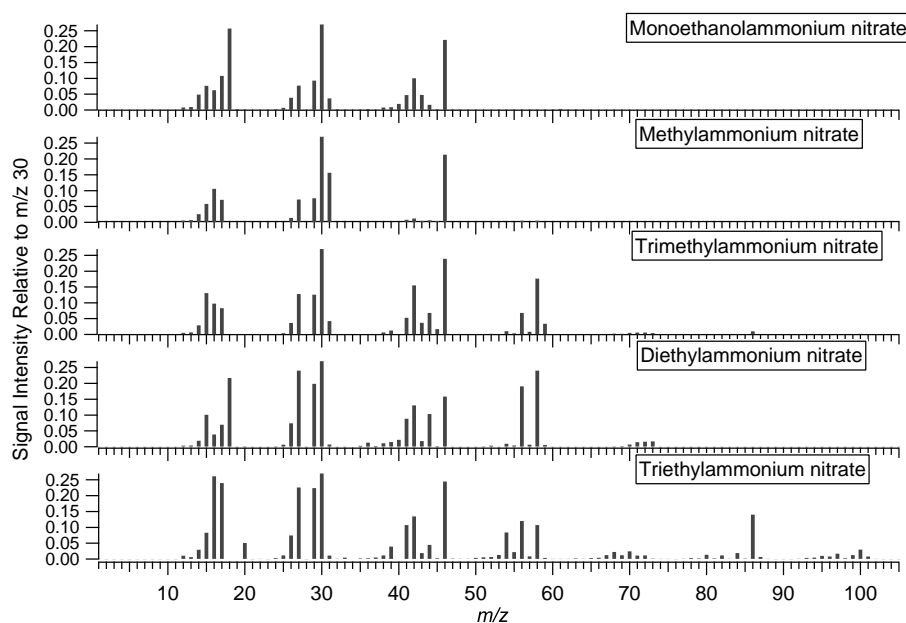
As described in the Experimental section, nitrate salts were formed by adding the amine of interest to a chamber containing gaseous nitric acid ( $\text{HNO}_3$ ). In all cases, particle nucleation occurred within a few minutes of amine injection. All of the aminium nitrate salts investigated were detected by the cToF-AMS, PILS-IC, and DMA instruments. The mass spectra for the nitrate salts of the amines studied are shown in Fig. 2. The spectra are similar to reference electron impact spectra in the NIST database for the gas-phase amines except for additional intensity at  $m/z$  30 and  $m/z$  46 caused by  $\text{NO}^+$  and  $\text{NO}_2^+$  ion fragments from nitrate (Stein, 2005). The only previous chamber study to focus on aerosol-phase amines was conducted by Angelino et al. (2001) using a laser desorption aerosol time of flight mass spectrometer (ATOFMS). In their study, the spectra of dialkyl ammonium salts exhibited prominent peaks  $(M+13)^+$ , attributed to ion-molecule reactions within the ionization region of the instrument. We do not observe peaks larger than the molecular ion for any of the salts, indicating that ion-molecule reactions do not occur in the ionization region of the Aerodyne cToF-AMS; this absence of ion-molecule reactions dramatically simplifies mass spectral interpretation.

Though we did not observe ion-molecule reactions, it is important to note that we did observe a dramatic increase in the number of ions detected by the cToF-AMS when the voltages that extract ions from the electron impact region into the flight chamber of the mass spectrometer were al-

tered by a few percent. When the voltages were in this altered state, we observed a further increase in both molecular and fragment amine ions with increasing vaporizer temperature above  $550^\circ\text{C}$ . No such correlation between increased vaporizer temperature and ion signal is observed when the extraction voltages are not in the altered state. Because altering the extraction voltages allows ions formed on the vaporizer surface to enter the mass spectrometer and because amines have low ionization potentials, we believe that the additional ions are formed on the high temperature tungsten surface of the vaporizer. The artificial signal enhancement (increased ion rate) caused by this proposed surface ionization indicates that there is a potential for overestimates of amine concentrations measured by the Aerodyne cToF-AMS if the instrument is not carefully calibrated and tuned. Similar effects caused by the unusually low ionization energy of amines may also occur in other aerosol mass spectrometry instruments. We observed enhancement of up to an order of magnitude by changing the voltages in the instrument a few percent. The  $m/z$  with the most prominent increase in ion rate was that corresponding to the molecular ion of the amine being studied. The fact that the molecular ion showed the most dramatic increase further supports the hypothesis that a non-electron impact surface ionization is occurring; 70 eV electron impact ionization typically induces alpha cleavage of amines and little, non-fragmented, molecular ion signal is observed. It should be noted that we have not observed an increase in detected ions when the extraction voltages are shifted when studying aerosol that does not contain amines. Though not investigated further, these observations raise the possibility that this type of tuning might be intentionally used to detect the presence of molecular amine ions.

##### 4.2 Atmospheric formation of aminium nitrate salts: theory

Having confirmed that aminium nitrate salts can be generated and detected, we wish to estimate the potential atmospheric importance of aminium nitrate salts relative to ammonium nitrate (typically assumed to be the dominant atmospheric nitrate salt in the fine mode). Based on theory, we estimate the dissociation constants ( $K_p = p_{\text{HNO}_3} p_{\text{amine}}$ )



**Fig. 2.** Mass spectra for the nitrate salts of the amines studied. On the  $\sim 550^{\circ}\text{C}$  surface of the vaporizer, all nitrate salts decompose into nitric acid and the parent amine. Signals at  $m/z$  30 and 46 are generated from the nitrate fragments  $\text{NO}^+$  and  $\text{NO}_2^+$  and are common to all spectra. Signal at  $m/z$  30 is a combination of signal from  $\text{NO}^+$  and from amine fragments resulting from rearrangements after electron impact ionization. For all spectra, molecular ions have significantly less signal intensity than the fragments resulting from the cleavage of the chemical group alpha to the nitrogen (alpha cleavage). For the ethyl amines, loss of methyl groups alpha to the nitrogen give fragments at  $[\text{M}-15]^+$  while for the methyl amines, loss of hydrogen atoms alpha to the nitrogen give fragments at  $[\text{M}-1]^+$ .

for the gas-particle equilibrium of all amines studied except for ethanolamine, while noting that the estimates have large uncertainties resulting from discrepancies in the literature values for the heats of formation of the aminium nitrate salts. If the required thermodynamic parameters are known, the dissociation constant for a given amine-nitric acid system can be obtained using the integrated form of the Van't Hoff equation,

$$\ln K_P = \frac{\Delta S_{\text{diss}}^{\circ} - \Delta C_{P,\text{diss}}}{R} - \frac{\Delta H_{\text{diss}}^{\circ} - T_0 \Delta C_{P,\text{diss}}}{RT} + \frac{\Delta C_{P,\text{diss}}}{R} \ln \left( \frac{T}{T_0} \right) \quad (2)$$

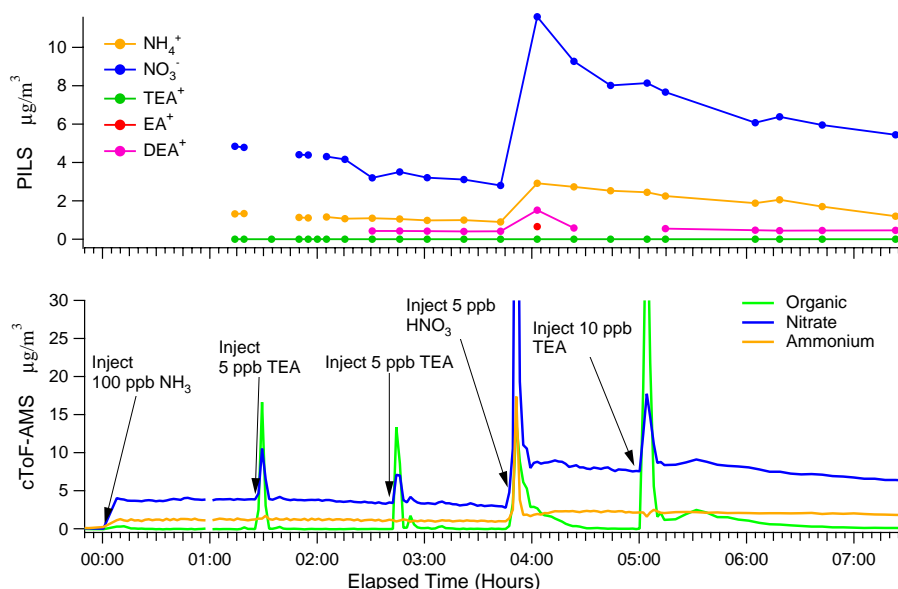
Entropies of formation for aminium nitrate salts have apparently not been reported in the literature; we estimate them using a molecular dynamics approach described in the Appendix. Also given in the Appendix are literature sources and values for the other thermodynamic parameters in Eq. (2). The calculated dissociation constants for all of the amines studied (except ethanolamine, for which the entropy was not estimated) are given in Table 3. Even if we assume that the estimated entropies are accurate, the results in Table 3 show that discrepancies in the literature values for the heats of formation lead to significant uncertainty in the calculated dissociation constants. While this uncertainty precludes us from gaining meaningful insight into how MA, DMA, or TEA might compete with ammonia for  $\text{HNO}_3$  in the atmosphere,

we are able to draw conclusions about the other salts. As mentioned earlier, most studies show that ambient ammonia concentrations tend to be an order of magnitude greater than amine concentrations, except perhaps in the immediate vicinity of an amine emissions source. Given this, and assuming that the calculated entropies are reasonable, it is improbable that nitrate salts of TMA or EA would form in the presence of typical ambient ammonia levels, because the  $K_P$  values for these two systems are greater than or equal to that of ammonium nitrate, independent of the precise value of the heat of formation. By contrast, the value of the dissociation constant for DEA is 2 to 3 orders of magnitude smaller than that of ammonium nitrate (independent of the uncertainty in the heat of formation), indicating that formation of DEAN particles under typical atmospheric mixing ratios is possible.

#### 4.3 Atmospheric formation of aminium nitrate salts; experimental

We conducted chamber experiments to evaluate and constrain the theoretical estimate for the dissociation constant of triethylammonium nitrate (TEAN), the highest molecular weight aminium nitrate studied.

The first experiment was carried out to study TEAN formation at atmospherically relevant ratios of ammonia:TEA (Fig. 3). Initially, 100 ppb of gas-phase ammonia was mixed in a chamber containing  $\sim 5$  ppb of nitric acid, leading to



**Fig. 3.** Time series from exp. 19 in Table 2 of the cToF-AMS (bottom) and the PILS-IC (top) showing rapid particle growth and evaporation after TEA and nitric acid were added in small aliquots to a chamber containing equilibrated ammonium nitrate particles. The transient spikes in particle loading do not appear in the PILS-IC data because of the relatively long averaging time (5 min) of measurements and because the PILS-IC inlet is not in the path of the highly concentrated injection plume.

nucleation of ammonium nitrate particles. Once the ammonium nitrate particle concentration and mass had stabilized, aliquots of TEA were injected into the chamber. As can be seen in Fig. 3, the concentration of TEAN salt, indicated by simultaneous shifts in the nitrate and organic signals, increased dramatically when TEA was added because the injection plume provided a high concentration region for particle formation. As the amine mixed throughout the chamber and became more dilute, the equilibrium shifted back to the gas phase, the salt returned to pure ammonium nitrate, and the organic signal = 0. This sequence of events occurred after each injection, including a second addition of 5 ppb of nitric acid to the chamber.

After concluding that TEA would be unable to form nitrate salts at ratios of TEA:NH<sub>3</sub> typically found in the atmosphere (except possibly near emissions sources), we developed an experimental technique to estimate the gas-particle equilibrium constant for TEAN. The procedure consists of adding an equimolar mixture of amine and ammonia to a chamber containing nitric acid (it is necessary to inject both ammonia and amine because we are unable to accurately measure gas-phase amine or nitric acid concentrations). Once ammonia, TEA, and nitric acid are injected, the following equilibria are established:

$$K_{P1} = p_{\text{HNO}_3} p_{\text{NH}_3} \quad (3)$$

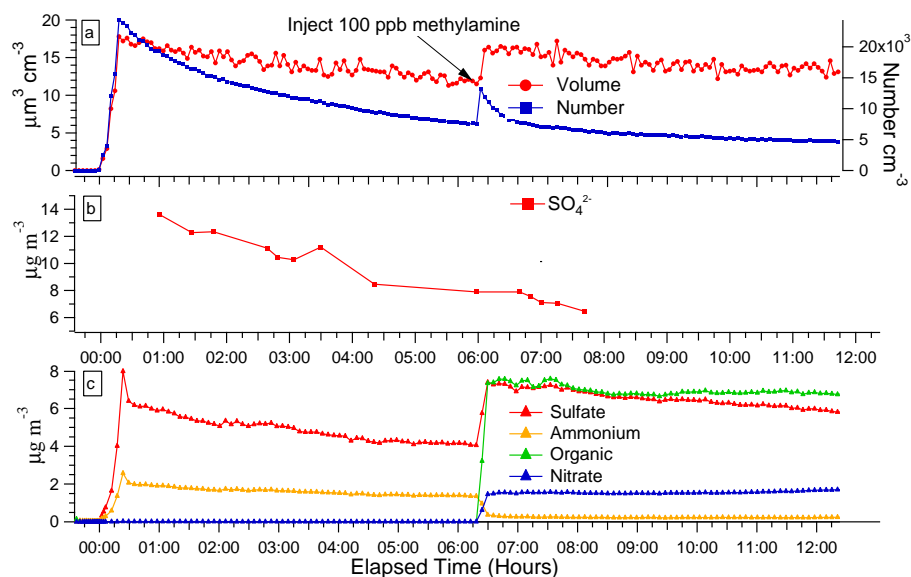
$$K_{P2} = p_{\text{HNO}_3} p_{\text{TEA}} \quad (4)$$

where  $p_{\text{HNO}_3}$ ,  $p_{\text{NH}_3}$ , and  $p_{\text{TEA}}$  are the partial pressures of nitric acid, ammonia, and triethylamine, and  $K_{P1}$  and  $K_{P2}$

are the dissociation constants for ammonium nitrate and triethylammonium nitrate, respectively. Using the values in Table A1 in Eq. (2),  $K_{P1}$  for the ammonium nitrate system is calculated to be  $1.916\text{E-}7 \text{ Pa}^2$  at 293 K. The partial pressures of NH<sub>3</sub> and TEA can be determined by subtracting the measured mass of each species in the aerosol phase from that which was injected, assuming negligible wall loss. Thus  $K_{P2}$  and  $p_{\text{HNO}_3}$  are the two unknown quantities to be determined. Although the PILS-IC can measure the amount of nitrate in the aerosol phase, this measurement was not used to calculate  $p_{\text{HNO}_3}$ , as nitric acid is subject to significant wall losses.

We report here an experiment in which 50 ppb of TEA and 50 ppb of ammonia were added simultaneously to a chamber containing 8 ppb of nitric acid. Upon injection of the amine/ammonia mixture, a rapid particle nucleation event was detected by the cToF-AMS (similar to those shown in Fig. 3). As the plume of ammonia and TEA mixed through the chamber, the mass loading of particles detected by the cToF-AMS decreased, and the other particle instruments (PILS-IC and DMA, which are not aligned with the injection port) began to detect particle loadings consistent with those of the cToF-AMS. After all of the instruments gave consistent readings and the particle concentration was stable (other than a slow decrease from wall loss), the triethylammonium and ammonium contents of the aerosol-phase were measured by the PILS-IC, which unambiguously and quantitatively detects these two species. The dissociation constant of triethylammonium nitrate determined from this experiment, using Eq. (4), is  $1.85\text{E-}7 \text{ Pa}^2$ . Although wall losses and slight





**Fig. 4.** Time Series of data from the DMA Panel (a), PILS-IC Panel (b), and cToF-AMS Panel (c) showing rapid replacement of ammonium sulfate by methylammonium sulfate during the injection of 100 ppb of methylamine into a chamber containing ammonium sulfate seed and ozone. The increase in the ratio of organic signal to sulfate signal near the end of the experiment results from the slow reaction of methylamine with ozone forming a small mass of organic aerosol.

contamination from other amine compounds from previous experiments influenced this result, the likely effect of these influences is judged to be too small to affect the conclusion that the dissociation constant for TEAN is close to that of ammonium nitrate. This conclusion is consistent with the previous experiment and the estimated dissociation constant falls within the large range of values predicted theoretically.

The two chamber experiments described above confirm that TEA does not form nitrate salts unless the ammonia concentration is roughly equivalent to that of TEA or there is a large excess of nitric acid. Experimental testing of all of the amines was beyond the scope of this study and further studies of this type are warranted, but these initial results indicate that the calculated dissociation constants, although subject to considerable uncertainty, are reasonable.

#### 4.4 Ammonium sulfate salts

Amines have the potential to form sulfate salts analogous to ammonium sulfate. Although nitrate salts are probably more relevant in agricultural settings, ammonium sulfate salts may form in the presence of high sulfate concentrations. Figure 4 shows results from the addition of 100 ppb methylamine (MA) to pure ammonium sulfate seed in a dry (less than 10% RH) chamber (the chamber also contained ozone because the experiment was designed for MA ozonolysis). The DMA data show a  $3 \mu\text{m}^3 \text{cm}^{-3}$  increase in particle volume and new particle formation when methylamine is injected. The new particles are formed from the reaction of methylamine with residual nitric acid in the chamber.

Intriguingly, the mass of methylammonium (labeled “organic” in Fig. 4) detected by the cToF-AMS is roughly 8 times the mass needed to neutralize the nitrate. Additionally, the time series from the cToF-AMS also shows a sharp decrease in the ammonium signal as the methylamine signal increases. The effective density of the particles decreases slightly ( $\sim 0.1 \pm 0.1 \text{ g cm}^{-3}$ ) as the organic signal increases. All of these trends indicate that the methylamine is displacing ammonia and forming methylammonium sulfate. One oddity is the apparent increase in sulfate observed by the cToF-AMS. The sulfate time series from the PILS-IC shows that there is no increase in sulfate loading after methylamine is injected (the growth of methylammonium cannot be followed by the PILS-IC because the IC column used is unable to distinguish between ammonium and methylammonium cations). The increase in sulfate signal from the cToF-AMS can most easily be explained as an artifact, often seen in chamber studies, resulting from an increase in collection efficiency as the physical properties of the aerosol change (Bahreini et al., 2005; Huffman et al., 2005). We hypothesize that replacement of the ammonium cation by methylammonium alters the physical characteristics of the particle which, in turn, causes fewer particles to bounce from the vaporizer surface, increasing collection efficiency. All of the signals from the cToF-AMS (sulfate, organic, nitrate and ammonium) have been scaled by a factor that causes the cToF-AMS sulfate mass to match the PILS-IC sulfate mass after the increase in collection efficiency. Accordingly, the masses shown for the cToF-AMS before the collection efficiency increase are low.

Though the gas-phase concentration of methylamine in this experiment is relatively large, a nearly complete conversion from ammonium sulfate to methylammonium sulfate was observed. The extent of this type of displacement at lower gas-phase amine concentrations, for other amines, and as a function of RH all warrant further study.

## 5 Aerosol formation from photooxidation and ozonolysis of amines

We begin this section by describing common trends observed during the oxidation experiments of all amines. The following subsections give the data and details for the oxidation of individual amines.

During all of the photooxidation experiments with  $\text{NO}_x$ , we observed aerosol growth resulting from a combination of aminium nitrate salt formation and condensation of non-volatile oxidized compounds (growth from the dissolution of water soluble amines was limited by the low, <10%, RH of the chamber). For all of the amines studied, some of the aminium nitrate salt that was initially formed during photooxidation partitioned back into the gas-phase as more of the parent amine was reacted away. The particle-phase salt repartitions back to the gas phase because the continued oxidation of the parent amine depletes its concentration in the gas phase and drives the equilibrium back towards gas-phase amine and nitric acid. For methylamine, ethylamine, ethanolamine, and diethylamine nearly 100 percent of the nitrate salt revolatilized while for trimethylamine and triethylamine the nitrate salts appeared to be more stable and did not return completely to the gas phase. All experiments were carried out until the mass of aerosol was stable, no further growth or decay other than a slow decay caused by particle loss to the walls. Based on estimates of the OH concentration in our chamber (Kroll et al., 2006) and measured ozone concentrations, the cessation of aerosol growth is not caused by a depletion of oxidant. Typically, one defines a mass yield of secondary organic aerosol (ratio of organic aerosol mass to the mass of hydrocarbon reacted), but for the amines the mass yield of aerosol depends on the concentration of nitric acid in the system. If ample nitric acid is formed during photooxidation, nearly all of the amine will form aminium nitrate salts, while in the absence of nitric acid, nitrate salts are not formed and the yield reflects the formation of non-volatile compounds from reaction of OH and  $\text{O}_3$  with the amine. Additional complexity arises because many of the oxidation products of amines are themselves basic and can form salts with nitric acid (e.g. amides and imines can all form salts with  $\text{HNO}_3$ ). These factors create a situation in which the yield of aerosol is related in a complex manner to the rate of formation of nitric acid in the system.

If all of the nitrate salts return to the gas phase as the parent amine is reacted away, the final aerosol mass yield would be relatively independent of the nitric acid concentra-

tion. Intriguingly, this is not the case for experiments involving TMA or TEA, as the PILS-IC detects significant loadings of salt at the end of these experiments. As described in detail later in this section, TMA and TEA are the only two amines that formed significant non-salt organic aerosol during oxidation. One explanation for the persistence of the aminium nitrate salts in these two systems is that the salt has been “trapped” inside an external layer of oxidized aerosol and is no longer in equilibrium with the gas phase. However, the timescale for diffusion through the organic layers formed in these experiments, which are less than 200 nm thick, is small and, unless the gas phase amine was completely insoluble in the organic layer, it is improbable that this layer could “trap” the salt for any significant amount of time. It is possible that mixing of organic material with the salt in the particle phase somehow lowers the volatility of the salt. Another possibility is that gas-phase concentrations of nitric acid are sufficiently high to force the equilibrium towards the particle phase even when the concentration of the parent amine is very low. Finally, given the large uncertainties in the calculated gas-particle equilibrium constants for the amines, it is possible that certain amines favor the particle phase even at very low gas-phase concentrations.

Regardless of the mechanism by which the salts persist, the formation of nitrate salts biases the calculated mass yields of the photooxidation experiments to be higher than they would be as a result of oxidation alone. In an attempt to estimate the purely oxidative yield in the absence of salt formation we conducted ozonolysis experiments and photooxidation experiments in the absence of  $\text{NO}_x$ . The aerosol mass yields for the different amines during photooxidation (with and without  $\text{NO}_x$ ) and ozonolysis are given in Table 4. It is important to note that these yields are derived from experiments run under a single set of conditions and are given to show relative differences in the behavior of the different amines; they are not quantitative yield estimates for the individual amines. Indeed, runs conducted with higher initial concentrations of amine give higher yields because of the increased particle-phase organic mass into which organics can condense (Seinfeld and Pankow, 2003). It is even possible that the mass of salt formed can affect the yield if the condensable organics formed are soluble in the nitrate salts. Because of the exploratory nature of this study and because of the complex behavior of amines forming aerosol both through salt formation and oxidation, we do not attempt to derive yield curves from these data.

The non-salt photooxidation yields given in Table 4 were obtained using the following method: first, the aerosol volume measured by the DMA was multiplied by the effective density; second, the salt fraction of the aerosol mass was determined as  $(\text{PILS-IC mass})/(\text{DMA volume} \times \text{effective density})$ . Finally, the wall-loss corrected DMA volume was multiplied by the effective density and then by the fraction of non-salt aerosol mass to give the mass of non-salt secondary organic aerosol (SOA). The yields were calculated using data

**Table 4.** Estimated percent mass yields<sup>a</sup> of non-salt aerosol during ozonolysis and photooxidation. All yields have an uncertainty of ~25% of their magnitude.

Amine	Ozonolysis Yield	High NO <sub>x</sub> Photooxidation Yield	Zero NO <sub>x</sub> Photooxidation Yield
Trimethylamine	15	23 <sup>b</sup>	–
Methylamine	<1	<1 <sup>b</sup>	–
Triethylamine	5	8 <sup>c</sup>	12 <sup>b</sup>
Diethylamine	<1	<1 <sup>b</sup>	<1 <sup>b</sup>
Ethylamine	–	<1 <sup>c</sup>	–
Ethanolamine	3	2 <sup>c</sup>	–

<sup>a</sup>All yields for high NO<sub>x</sub> and ozonolysis are derived from experiments using 100 ppb initial concentrations of amine (high NO<sub>x</sub> photooxidations were run with 100 ppb of NO<sub>x</sub>). The zero NO<sub>x</sub> yields are from experiments using 500 ppb initial amine concentrations. These yields are given to demonstrate trends in the aerosol forming potential of the different amines and are not meant to represent definitive yields for the systems shown.

<sup>b</sup>H<sub>2</sub>O<sub>2</sub> as OH precursor.

<sup>c</sup>Photooxidation without H<sub>2</sub>O<sub>2</sub>. Photooxidation of 500 ppb TEA using H<sub>2</sub>O<sub>2</sub> gave a mass yield of non-salt organic aerosol of > 20%.

<sup>d</sup>The effective densities used for the yield calculations are: TMA Ozonolysis: 1.4; TMA High NO<sub>x</sub> photox: 1.3; TEA Ozonolysis: 1.2; TEA High NO<sub>x</sub> photox: 1.1; TEA Low NO<sub>x</sub> photox: 1.1. All effective densities are given in g cm<sup>−3</sup> with uncertainties of ±0.1 g cm<sup>−3</sup>.

from the period after aerosol growth and decay appeared to have ceased other than from loss to the chamber walls. These yield results will be discussed in detail later, although it is immediately evident that while all of the amines can generate aerosol mass by forming nitrate salts, several do not form aerosol mass through oxidation.

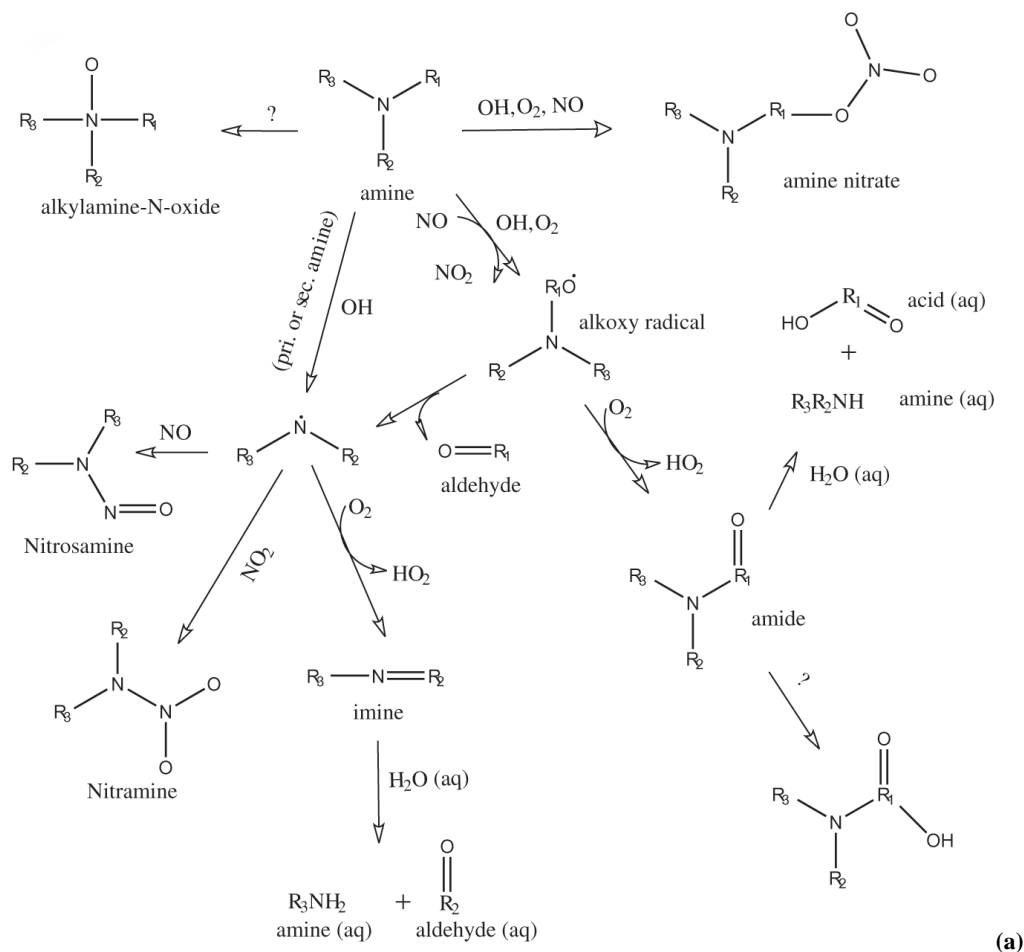
Before discussing results from individual photooxidation and ozonolysis experiments, it is useful to consider the general mechanisms by which OH and ozone oxidize aliphatic amines. The gas-phase chemistry of amine oxidation by OH (in the presence of NO<sub>x</sub>) and by ozone (without NO<sub>x</sub>) have been studied (Schade and Crutzen, 1995; Tuazon et al., 1994), and the major products formed by these reactions have been identified. For many of the oxidation pathways, the products of OH and ozone oxidation are similar, if not identical. The gas-phase products formed from oxidation of aliphatic amines by OH in low NO<sub>x</sub> environments are unknown.

Figure 5a shows the most common oxidation pathways for OH attack of an aliphatic amine in the presence of NO<sub>x</sub> (Angelino et al., 2001; Schade and Crutzen, 1995). Abstraction of hydrogen from the secondary carbon is believed to be the dominant pathway (Finlayson-Pitts and Pitts, 1986). Abstraction of a hydrogen atom bound directly to the nitrogen in a primary or secondary amine is also possible but is believed to play a less significant role (Schade and Crutzen, 1995). The gas-phase oxidation products formed are amides, nitramines, and imines. All of the products shown have the potential to partition to the aerosol phase, although amides are particularly water soluble and have the lowest vapor pressures. An unexpected product, alkylamine-N-oxide, was first detected by Angelino et al. (2001) in the aerosol phase and was again detected in the particle phase during the current study.

Figure 5b shows the pathways for ozone reaction with an aliphatic amine. While the loss of an alkyl group from the high energy amine oxide generates products distinct from those generated by reaction with OH, rearrangement of the amine oxide and subsequent loss of OH leads to alkoxy radicals similar to those generated from hydrogen abstraction by OH followed by loss of an oxygen atom to NO. Following this branch of the reaction diagram leads to similar, and in many cases identical, products as those formed by reaction with OH.

Figure 5c shows the beginning of the reaction pathways for amine oxidation by OH in the absence of NO<sub>x</sub>. Presumably, a number of the condensable species in this system consist of hydroperoxides and alkyl peroxides. Many of the same products formed in the high NO<sub>x</sub> and ozone systems are formed if, rather than forming peroxides, RO<sub>2</sub> + RO<sub>2</sub> and RO<sub>2</sub>+HO<sub>2</sub> reactions form alkoxy radicals.

Many of the photooxidation experiments reported here employed hydrogen peroxide (H<sub>2</sub>O<sub>2</sub>) as an OH source. As detailed in the Experimental section, a relatively large amount (3–5 ppm) of hydrogen peroxide must be introduced into the chamber to achieve sufficient levels of OH for rapid reaction. Because the reaction between OH and H<sub>2</sub>O<sub>2</sub> forms HO<sub>2</sub> and because hydrogen peroxide itself may affect the chemistry of the aerosol formed, we conducted additional photooxidation experiments using mixtures of propene and NO<sub>x</sub> as well as NO<sub>x</sub> alone. We found no major differences in chemistry between the systems with and without H<sub>2</sub>O<sub>2</sub>, although the reactions occurred much faster in the presence of hydrogen peroxide, as expected. All of the ozonolysis reactions were carried out in the absence of NO<sub>x</sub>.



**Fig. 5a.** Mechanism of amine oxidation by OH in the presence of  $\text{NO}_x$  (Schade and Crutzen, 1995).

### 5.1 Experimental protocol

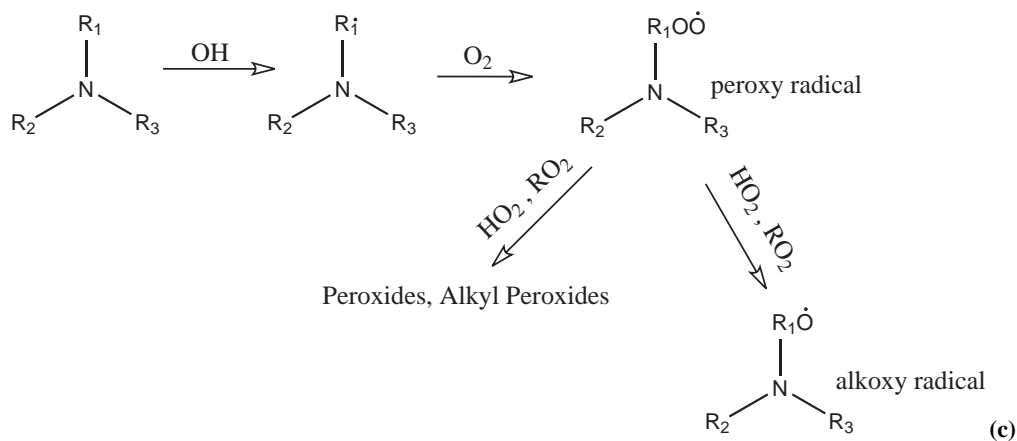
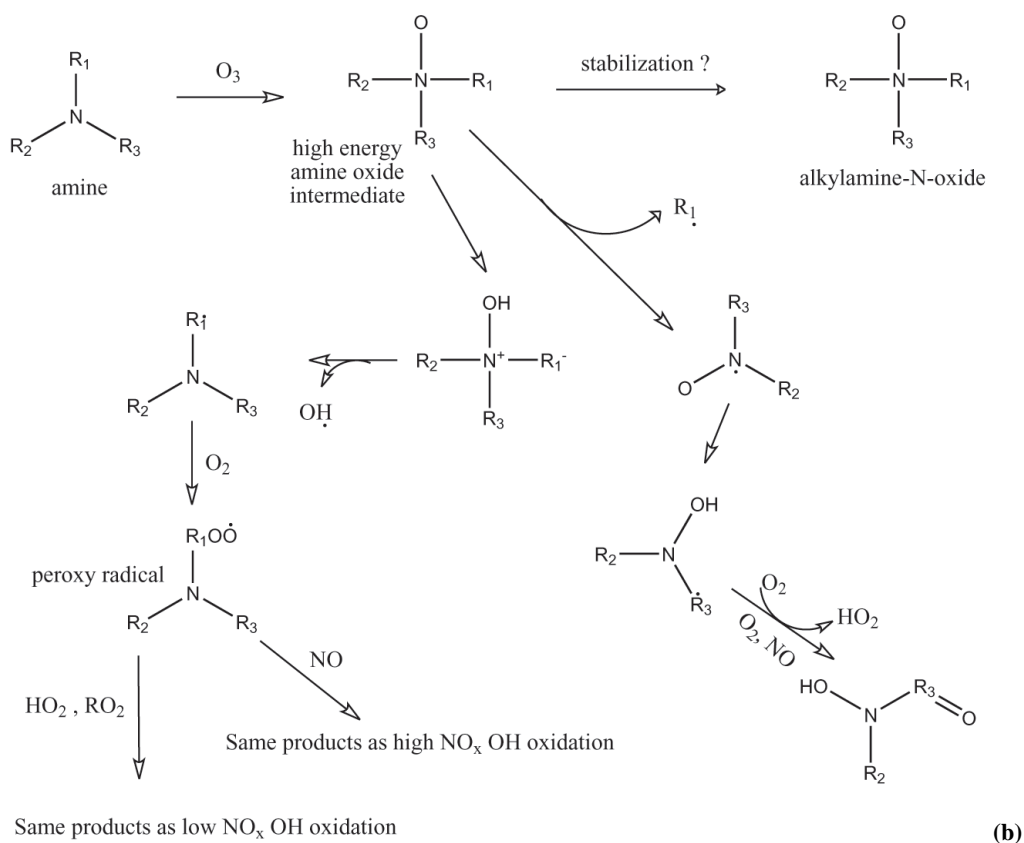
The same procedure was used for all photooxidation and ozonolysis experiments. For photooxidation experiments, the first step is the injection of either:  $\text{H}_2\text{O}_2$ , a  $\text{H}_2\text{O}_2$  and  $\text{NO}_x$  mixture, a  $\text{NO}_x$  and propene mixture, or  $\text{NO}_x$  alone. Table 2 gives the oxidant used and  $\text{NO}_x$  mixing ratio for each photooxidation experiment. For all types of experiments, except  $\text{NO}_x$ -free photooxidations, the next step was to add a small amount ( $\sim 10$  ppb) of  $\text{HNO}_3$ . Once the  $\text{HNO}_3$  had mixed, the amine was injected at a much higher concentration than the nitric acid (typically  $\sim 100$  ppb) causing nucleation of aminium nitrate salt while the vast majority of the amine remained in the gas phase. The concentration of nucleated salt particles was always observed to peak soon after the injection of the amine, followed by a sharp decrease in mass as mixing occurred and gas-particle equilibrium was established.

After the concentration of the nucleated particles became steady and sufficient time had elapsed to collect composition data with the cToF-AMS and the PILS-IC, oxidation was ini-

tiated. For photooxidation experiments, oxidation was initiated by turning on the black lights surrounding the chamber, while for ozonolysis ozone was injected into the chamber. All experiments were continued until there were no further changes in particle mass or volume, except for slow decay in mass and volume caused by particle loss to the chamber walls.

### 5.2 Trimethylamine (TMA) photooxidation

Trimethylamine (TMA) is one of the more abundant ambient alkyl amines near animal husbandry operations (Rabaud et al., 2003; Schade and Crutzen, 1995). Figure 6 shows the time profiles for  $\text{NO}_x$ ,  $\text{O}_3$ , particle volume (DMA), ionic particle mass (PILS-IC), and particle mass (cToF-AMS) during the photooxidation of TMA. For this experiment (number 3, Table 2), 300 ppb of  $\text{NO}_2$ , 10 ppb of  $\text{HNO}_3$  and 100 ppb of TMA were used. As expected, trimethylammonium nitrate (TMAN) salt began to nucleate soon after the injection of TMA. Approximately 30 min after the TMA injection the aerosol mass stabilized as the system reached gas-particle

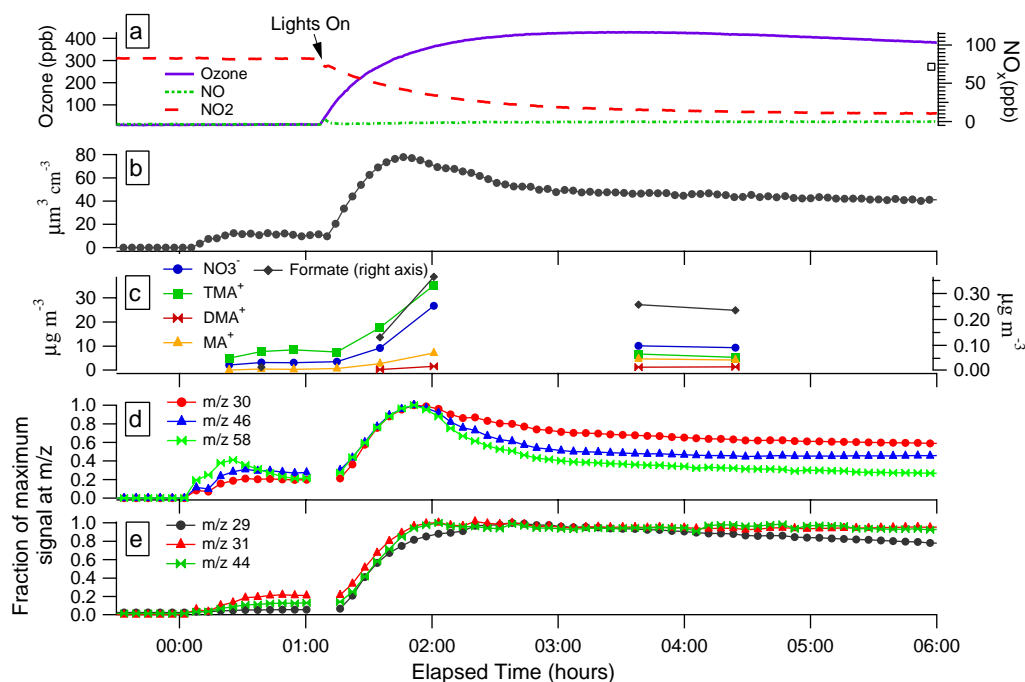


**Fig. 5b+c.** Mechanism of amine oxidation by (b) Ozone, in the absence of  $\text{NO}_x$  (Tuazon et al., 1994), (c) OH in the absence of  $\text{NO}_x$ . A ? indicates an unknown oxidation mechanism to form the product shown.

equilibrium. The composition of the TMAN particles was measured for an additional 30 min with the cToF-AMS and the PILS-IC before the black lights surrounding the chamber were turned on, initiating photooxidation.

When photooxidation begins, because of the large excess of TMA injected relative to  $\text{HNO}_3$ , much of the nitric acid has been converted into particle-phase nitrate. Assuming negligible wall loss,  $\sim 90$  ppb of TEA remains in the gas

phase at the time the lights are turned on. Upon irradiation, there is a brief spike in NO from the photolysis of  $\text{NO}_2$ ; as the TMA is oxidized by OH,  $\text{RO}_2$  radicals are formed that convert the NO back to  $\text{NO}_2$ , and ozone formation begins.  $\text{NO}_x$  gradually decreases throughout the course of the experiment as  $\text{NO}_2$  is converted to  $\text{HNO}_3$  by reaction with OH. Particle formation begins within  $\sim 10$  min of the start of irradiation.

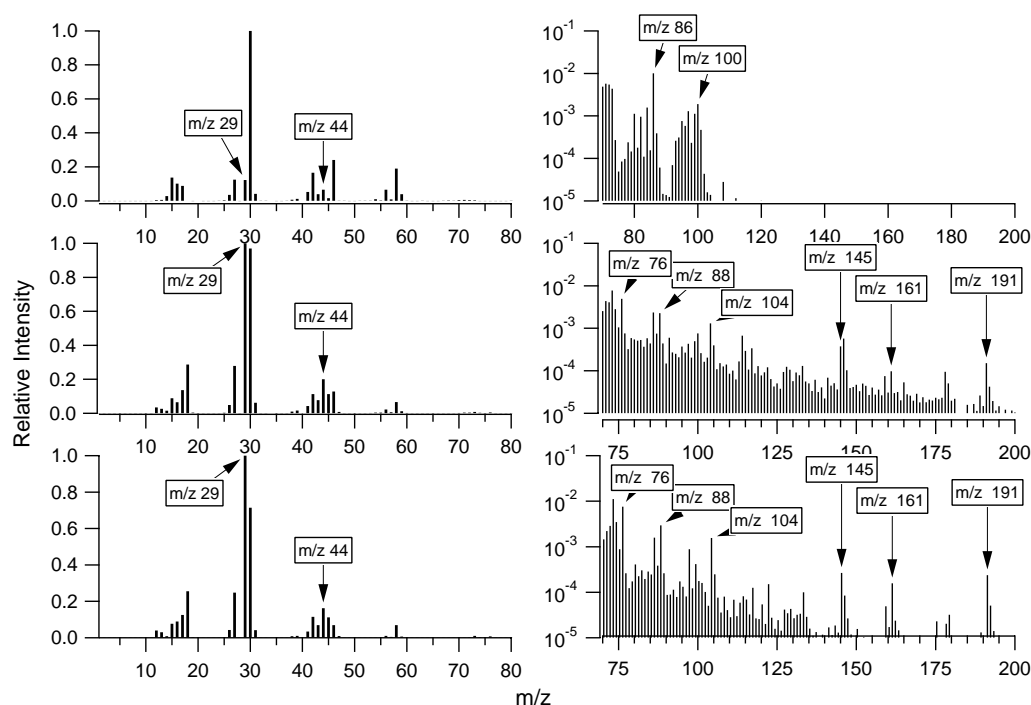


**Fig. 6.** Photooxidation of trimethylamine (experiment 3 from Table 2). Panel (a)  $\text{NO}_x$  and ozone concentrations. Panel (b) Particle volume measured by the DMA. Panel (c) Growth of ionic species measured by the PILS-IC. Panels (d) and (e) Fragment ions from the cToF-AMS. When injected, the TMA reacts with nitric acid in the chamber to form trimethylammonium nitrate. Upon activation of the black lights, there is an initial burst of particle growth followed by a rapid decay in particle mass and volume. The PILS-IC data show that much of the decay is a result of volatilization of the trimethylammonium nitrate salt. The cToF-AMS data show that while  $m/z$ 's corresponding to trimethylammonium nitrate salt fragments ( $30 \text{ NO}^+$ ,  $46 \text{ NO}_2^+$ ,  $58 ((\text{CH}_3)_2\text{NCH}_2^+)$ ) rapidly decrease after the peak in growth,  $m/z$ 's corresponding to methylammonium nitrate ( $31 \text{ CH}_3\text{NH}_2^+$ ) and oxidized fragments ( $29 \text{ HCO}^+$ ,  $44 \text{ CO}_2^+$ ) are level or decrease much more gradually.

Figure 6c–e shows the particle composition as measured by the cToF-AMS and the PILS-IC instruments. The PILS-IC data show that at the peak of particle growth,  $62 \mu\text{g m}^{-3}$  of the particle mass consists of TMAN salt. The volume measured by the DMA is  $78 \mu\text{m}^3 \text{ cm}^{-3}$  at the peak of particle growth. Based on a calculated effective density of  $(1.3 \pm 0.2)$ , nearly 80% of the particle mass is composed of the nitrate salt at the peak of particle growth. In addition to the salt present at the start of irradiation, additional salt is formed as TMA reacts with nitric acid formed as OH reacts with  $\text{NO}_2$ . After the peak of particle growth, both the mass and volume of aerosol drop dramatically. The drop in particle mass can be accounted for almost entirely by the volatilization of TMAN, and after 4.4 h of reaction TMAN salt accounts for less than 35% of the particle mass. Volatilization of TMAN is a direct consequence of the gas-particle equilibrium of the nitrate salt; as oxidation proceeds and gas-phase TMA is reacted away (and as nitric acid is lost to the walls of the chamber), the equilibrium for the salt shifts back towards the gas phase. Figure 6d–e shows time traces of signals from the cToF-AMS associated with trimethylammonium ( $m/z$  58  $(\text{CH}_3)_2\text{NCH}_2^+$ ), methylammonium ( $m/z$  31  $\text{CH}_3\text{NH}_2^+$ ), nitrate ( $m/z$  30  $\text{NO}^+$ ,  $m/z$  46  $\text{NO}_2^+$ ) and oxidized fragments

( $m/z$  44  $\text{CO}_2^+$ ,  $m/z$  29  $\text{CHO}^+$ ). The signals associated with trimethylammonium and nitrate all decrease quickly after the peak of particle growth while those associated with oxidized fragments and methylamine are relatively flat (some show slight decreases associated with the slow loss of particles to the chamber walls). The time trends of these fragments lend support to the hypothesis that TMAN salt is repartitioning to the gas phase while compounds formed from TMA oxidation are condensing.

Over the course of the reaction, both the cToF-AMS and the PILS-IC detected signals consistent with the presence of particle-phase methylammonium. Based on the PILS-IC data, nearly 10% of the particle mass at the peak of aerosol growth is methylammonium. The most plausible explanation for the detection of this species is that imines formed in the gas phase (see Fig. 5a) partition to the particle phase through either nitrate salt formation or direct condensation. Imines exposed to liquid water readily decompose into an amine and an aldehyde (Fig. 5a). It is possible that this reaction occurs in the particle phase, though it is unclear if sufficient particle-phase water existed to drive this reaction. The experiments are carried out at low RH ( $< 10\%$ ) but both the TEA and nitric acid were bubbled into the chamber from aqueous



**Fig. 7.** Aerosol mass spectra from the cToF-AMS during different stages of trimethylamine photooxidation (Fig. 6) and ozonolysis (Fig. 8). The top panel shows trimethylammonium nitrate before oxidation while the middle panel is from the end of the photooxidation experiment (8 h elapsed time). The bottom panel shows the spectra from aerosol formed from TMA after  $\sim 3$  h of ozone exposure. The right and left panels show different  $m/z$  ranges of the same spectra. The major peaks shift during the photooxidation from peaks corresponding to the trimethylammonium nitrate salt to more oxidized peaks ( $29 \text{ HCO}^+$ ,  $44 \text{ CO}_2^+$ ). There is also a significant increase in the fraction of higher molecular weight species.

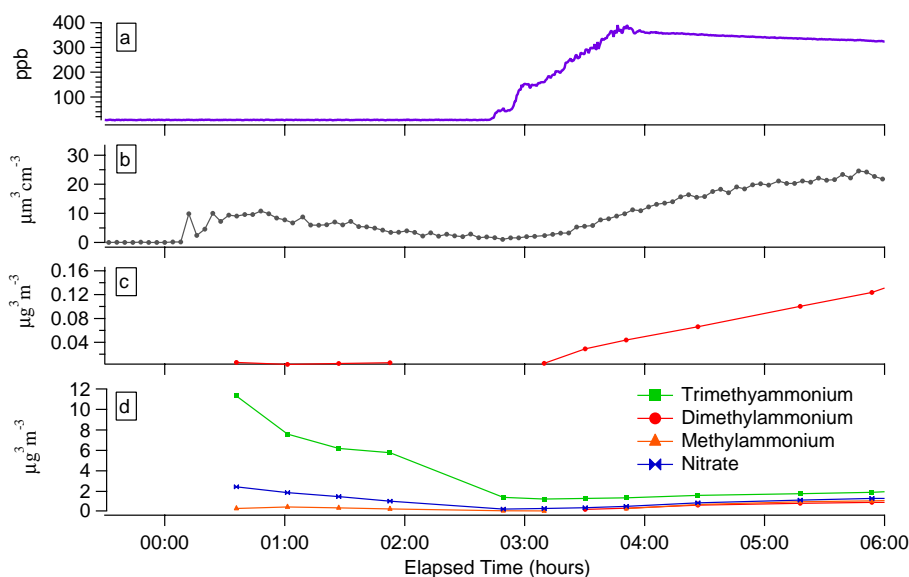
solutions and the efflorescence behavior of aminium nitrate particles is unknown (although if their behavior is similar to that of ammonium nitrate, the particles may retain water at low RH). Independent of the amount of particle water, because the PILS-IC dissolves collected aerosol particles into water droplets, the imines would almost certainly react with water inside of the instrument if this reaction had not already occurred in the chamber. The fact that more methylammonium nitrate is detected by the PILS-IC than dimethylammonium nitrate further supports the imine reaction pathway because this pathway does not lead to dimethylammonium nitrate. The PILS-IC data also show an increase in the abundance of formate, which is a byproduct of hydrolysis of imines. While the cToF-AMS peak at  $m/z$  31 could be a fragment from oxidized forms of TMA and not from methylammonium, it is improbable that this peak is a fragment from TMAN itself because it does not follow the same time profiles as  $m/z$  58 (the dominant peak for TMAN). It is improbable that this peak is a fragment from TMAN itself because it does not follow the same time profiles as  $m/z$  58 (the dominant peak for TMAN). The small amounts of dimethylammonium nitrate detected by the PILS-IC could be formed through hydrolysis of amides in the particle phase as shown in Fig. 5a.

Figure 7 shows the spectra from the cToF-AMS during different stages of the same photooxidation experiment discussed above (experiment 3, Table 2). As in Fig. 6, the growing importance of oxidized fragments relative to trimethylammonium nitrate fragments is evident. Of note is the relative prominence of  $m/z$  88, which is the expected dominant peak (resulting from  $\alpha$ -cleavage) of the carboxylic acid of TMA (shown in the bottom of Fig. 5a). Also of note is the increase in abundance of higher molecular weight species which could be the result of particle-phase reactions or multiple oxidations in the gas phase. The gas-phase route seems somewhat implausible for molecular weights above 150 ( $\text{RO}_2 + \text{RO}_2 = 148 \text{ amu}$  for TMA) because formation of these high molecular weight compounds would require multiple  $\text{RO}_2 + \text{RO}_2$  or  $\text{RO}_2 + \text{HO}_2$  reactions.

### 5.3 Trimethylamine (TMA) ozonolysis

During the photooxidation of trimethylamine a large amount of ozone is formed, and, based on reported rate constants (Atkinson et al., 1978; Tuazon et al., 1994), ozone and OH reactions with TMA are competitive under these conditions. To determine if the products of the ozone reaction form aerosol, we conducted a TMA ozonolysis experiment.





**Fig. 8.** Ozonolysis of trimethylamine (exp. 4, Table 2). Trimethylamine is injected into a chamber containing 18 ppb of nitric acid at time =0. The salt is allowed to decay away before 400 ppb of ozone is injected over  $\sim 1$  h. Panel (a) Ozone concentration. Panel (b) DMA volume showing significant aerosol growth as the TMA is oxidized. Panel (c) Formate concentration measured by the PILS-IC. Panel (d) Ions measured by the PILS-IC, showing that there is little increase in salt concentrations during the ozonolysis.

Figure 8 shows the time series of the DMA, cToF-AMS, and PILS-IC for this experiment. At time =0, 100 ppb of TMA was added to 16 ppb of  $\text{HNO}_3$  already in the chamber, forming trimethylammonium nitrate (TMAN). The TMAN salt remained in the chamber for  $\sim 3$  h during which time nearly all of it deposited on the chamber walls or volatilized. Oxidation was initiated by adding 200 ppb of ozone to the remaining gas-phase TMA in the system ( $\sim 85$  ppb assuming negligible wall loss of gas phase TMA and assuming all of the particulate TMAN was lost to the walls). During the ozonolysis, the vast majority ( $>90\%$ ) of the aerosol formed was non-ionic and accordingly was not detected by the PILS-IC. After 3 h of ozonolysis, aerosol growth had reached a peak. At this point, nitric acid was added (not shown in Fig. 8) to induce nitrate salt formation of gas-phase products too volatile to condense. The addition of nitric acid led to  $9 \mu\text{m}^3 \text{cm}^{-3}$  of aerosol growth, which was predominantly TMAN with a small contribution from methylammonium nitrate.

Though a large excess of ozone remained after the peak of aerosol growth, the aerosol formed appeared to be stable towards further oxidation and did not rapidly revolatilize. The mass yield of non-salt aerosol (before additional nitric acid was injected) was  $\sim 15\%$  (assuming 85 ppb as the starting concentration of amine). Interestingly, the yield from the ozonolysis is similar to the 23% yield of oxidized (non-salt) SOA formed during photooxidation with  $\text{NO}_x$ .

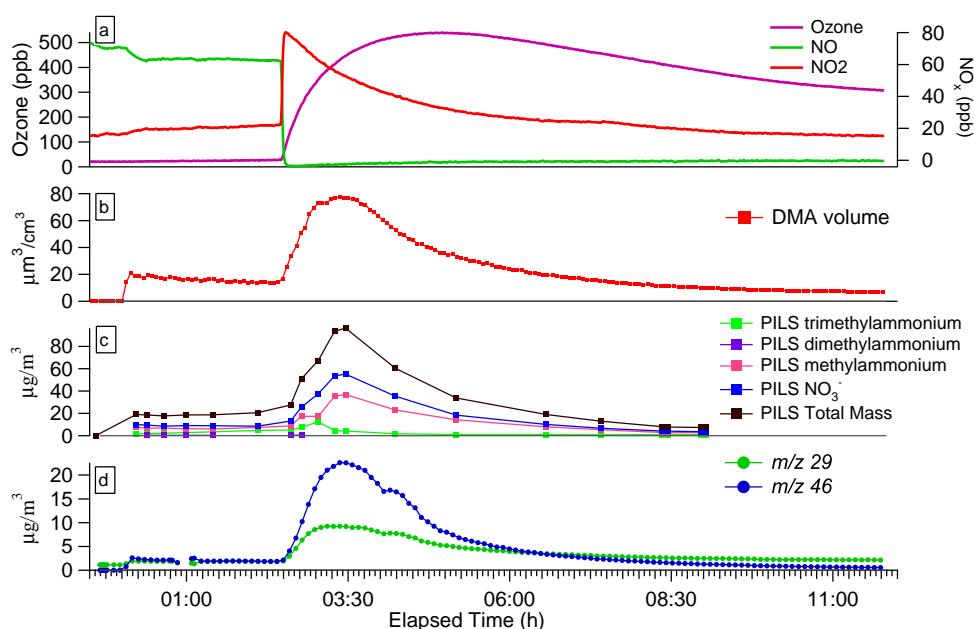
The bottom panel of Fig. 7 shows a spectrum from the cToF-AMS after three hours of ozone oxidation. The similarity between this spectrum and that in the middle panel of the figure (after photooxidation) is striking, with the one

obvious difference being that the nitrate fragments ( $m/z$  30 and 46) are less prominent because nitrate salts represent a smaller fraction of the particulate mass in the ozonolysis experiment. The similarity of the spectra indicates that ozonolysis generates similar condensable compounds to those from photooxidation. It should be noted that OH can be created during ozonolysis (see Fig. 5) and some of the compounds formed in ozonolysis could potentially be formed from amine reaction with OH.

#### 5.4 Methylamine (MA) photooxidation

In addition to being formed through oxidation and hydrolysis of TMA, methylamine (MA) is itself a major emission from animal husbandry operations. In the study of Schade and Crutzen (1995) methylamine and trimethylamine were the only two aliphatic amines detected near animal husbandry operations. Figure 9 shows the time series for the photooxidation of methylamine (experiment 6, Table 2) using  $\text{H}_2\text{O}_2$  as the OH precursor. Nitric acid, in the amount of 10 ppb, was added before methylamine was injected, and  $\text{NO}_x$  was added as 100 ppb of NO, instead of as  $\text{NO}_2$ . Injection of the methylamine caused the nucleation of methylammonium nitrate, which was allowed to equilibrate and mix for approximately two hours before the black lights were turned on 2.5 h after injection of the amine. When irradiation began, NO was quickly converted to  $\text{NO}_2$  through reactions with  $\text{RO}_2$  and  $\text{HO}_2$ . As NO was removed, ozone formation began,  $\text{NO}_2$  started to convert to  $\text{HNO}_3$ , and aerosol formation began. The aerosol volume shows the same behavior as that during





**Fig. 9.** Methylamine photooxidation (exp. 6, Table 2). Panel (a) Ozone and NO<sub>x</sub> concentrations. Panel (b) Time series for the DMA volume showing rapid decay after the peak of aerosol growth. Panel (c) Time series for the PILS-IC showing that most of the rapid mass decay is due to vaporization of the methylammonium nitrate salt. Panel (d) Fragment ions from the cToF-AMS. Signal from  $m/z$  29 which is a mix of oxidized organic fragments (CHO<sup>+</sup>) and salt fragments gradually grows more important than signal from from salt alone ( $m/z$  46 NO<sub>2</sub><sup>+</sup>).

the TMA photooxidation, growing to a peak as methylammonium nitrate is formed then rapidly decaying as gas-phase methylamine is oxidized. Subtracting the mass of all the ionic species detected by the PILS-IC from the aerosol mass calculated by multiplying the DMA volume by the effective density of  $1.1 \pm 0.2$ , one finds that nearly 100% of the aerosol formed at the peak of aerosol growth is methylammonium nitrate. There is a small signal in the PILS-IC from contaminant TMA which decreases as the experiment progresses. In contrast to the TMA photooxidation, there is little aerosol remaining after the rapid decay of the salt;  $< 1 \mu\text{g m}^{-3}$  of non-salt organic aerosol is present in the system after 4 h of photooxidation relative to more than  $20 \mu\text{g m}^{-3}$  remaining for the TMA with similar starting concentrations of amine. Though the mass of non-salt aerosol formed from the photooxidation was small, Panel (D) of Fig. 9 shows that the relative importance of non-salt organic aerosol increases throughout the experiment. Methanimine, one of the most abundant gas-phase products from methylamine photooxidation is known to polymerize on surfaces and may be a source of the non-ionic aerosol detected (Schade and Crutzen, 1995).

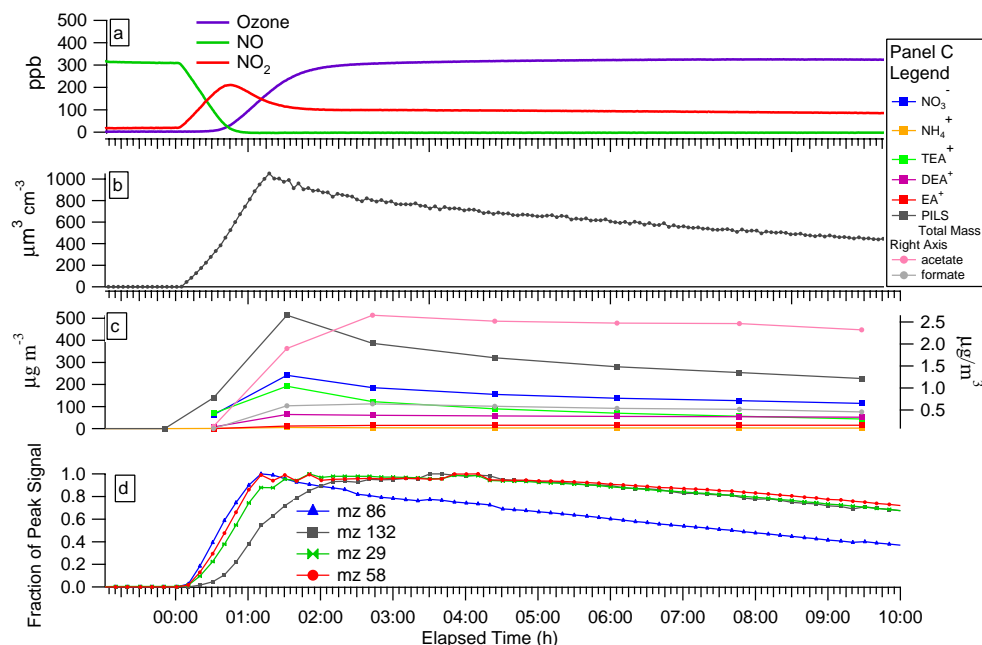
### 5.5 Methylamine (MA) ozonolysis

Because the vast majority of the aerosol formed during the photooxidation of methylamine is methylammonium nitrate, we performed an ozonolysis experiment to confirm that methylamine is unable to generate significant aerosol mass through oxidative routes. Time series from the ozonolysis

have already been shown, though in the context of sulfate salt formation, in Fig. 4. Ammonium sulfate seed was added to the methylamine-ozonolysis system to provide a surface for condensation if the system did not generate enough condensable products to induce nucleation. Ozone, in the amount of 200 ppb, was added to the chamber along with  $\sim 100$  ppb of methylamine. As discussed previously, the methylamine replaced the ammonium from the ammonium sulfate seed, but after this initial phase of growth by displacement, negligible further growth was observed, confirming the result of negligible non-salt organic mass yield observed during the photooxidation.

### 5.6 Triethylamine (TEA) photooxidation

Results from the photooxidation of 500 ppb of triethylamine with NO<sub>x</sub> using hydrogen peroxide as an OH precursor are shown in Fig. 10. For all TEA photooxidations, independent of OH source or starting concentration, rapid decay of aerosol mass after the peak growth was not observed. The reason for the observed stability of the salt formed is unclear. It probably indicates that TEAN has a smaller dissociation constant than the other amines studied. It could also indicate that there is interaction between the organic material and the salt lowering the volatility of the TEAN. Finally, it could be the result of salt formation by products of TEA oxidation. During all TEA photooxidations, diethylammonium and ethylammonium were detected by the PILS-IC with diethylammonium being formed at higher



**Fig. 10.** Photooxidation of 500 ppb triethylamine (TEA) (exp. 9, Table 2). Irradiation is initiated at  $t=0$ . Panel (a) Evolution of ozone and NO<sub>x</sub>. Panel (b) DMA volume. Panel (c) Time profile of species detected by the PILS-IC showing that diethylammonium and ethylammonium are formed during the photooxidation, with significantly more diethylammonium being formed. Panel (d) Fragments from the cToF-AMS. The most intense fragment of TEA ( $m/z$  86  $\text{N}(\text{CH}_2\text{CH}_3)_2\text{CH}_2^+$ ) grows in first followed by the major peak for DEA ( $m/z$  58  $\text{NH}(\text{CH}_2\text{CH}_3)\text{CH}_2^+$ ) and oxidized fragments ( $m/z$  29  $\text{CHO}^+$ ). Higher molecular weight fragments ( $m/z$  132) grow in more slowly.

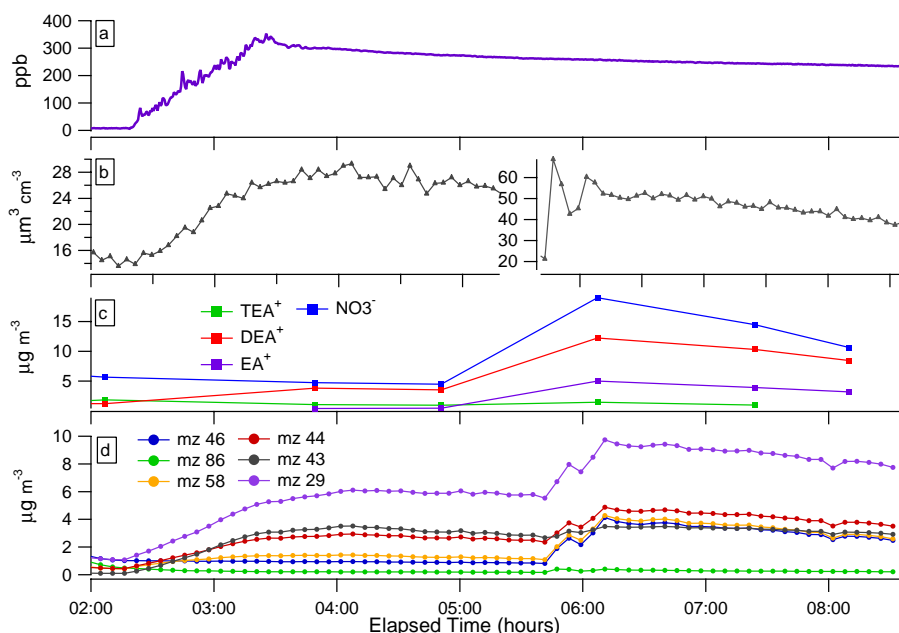
concentrations in the particle phase than ethylammonium. Based on our knowledge of the gas-phase oxidation reactions, it seems most plausible that the diethylammonium is formed by the particle-phase hydrolysis of N,N diethylacetamide (the amide shown in Fig. 5a if all R groups are ethyl groups. As mentioned earlier, it is possible that hydrolysis of the amide occurs in the PILS-IC instrument itself rather than in the chamber.) The detection of acetate by the PILS-IC during the experiment is consistent with the proposed mechanism of diethylammonium formation from hydrolysis of N,N diethylacetamide. The ethylammonium detected by the PILS-IC could be formed in two ways. First, it could result from aqueous reaction of the imine as shown in Fig. 5a (if all R groups being ethyl). Second, it could be the result of two successive amide hydrolysis reactions. The detection of higher levels of diethylammonium than ethylammonium contrasts with the results from the oxidation of trimethylamine for which higher levels of methylamine were detected than for dimethylamine. This difference suggests that more aerosol is formed through the imine route for trimethylamine whereas more aerosol is formed through the amide route for triethylamine.

During one photooxidation of TEA (experiment 20), a filter of the aerosol was collected and analyzed by LC/MS with electrospray ionization. All of the mass spectral peaks observed using LC/MS were consistent with the nitrate salt and

oxidation products already discussed, except for a peak at  $m/z$  118 detected in the positive mode. Peaks detected in the positive mode from electrospray ionization are typically  $[\text{M}+\text{H}]^+$  ions, making the molecular weight of the species detected 117 amu. This molecular weight is consistent with triethylamine-N-oxide (shown in Figs. 5a and b with R=ethyl group), a species that was previously detected by Angelino et al. (2001). There is not a significant peak in the spectrum from the cToF-AMS at  $m/z$  117 (or  $m/z$  116 which would be the expected largest fragment ion peak resulting from the alpha cleavage of a hydrogen from triethylamine-N-oxide); this is not particularly surprising because a high energy oxide of this type would be expected to fragment under electron impact ionization if it had not already thermally fragmented on the vaporizer. The extracted ion chromatogram (EIC) of  $m/z$  118 from the LC/MS system gives three distinct peaks with retention times of 1.38, 2.00, and 2.30 min, indicating the presence of three distinct isomers of this species. The structures of these isomers remain unknown.

### 5.7 Triethylamine (TEA) ozonolysis

Ozonolysis of TEA was conducted using the same procedure as for the ozonolysis of TMA and MA. First, nucleation of triethylammonium nitrate (TEAN) was initiated by adding 100 ppb of TEA to a chamber containing 8 ppb of nitric acid. After allowing the TEAN to equilibrate for 2 h,



**Fig. 11.** Ozonolysis of triethylamine (TEA) (exp. 16, Table 2). At  $t=0$  (not shown) 100 ppb of TEA is injected into a chamber containing 8 ppb of nitric acid, nucleating triethylammonium nitrate (TEAN) particles, which are still present when ozone is injected at  $t=2$  h 12 min. After growth of secondary aerosol formed through ozonolysis had ceased, an additional 8 ppb of nitric acid was injected at 5 h 31 min. Panel (a) Time series of ozone mixing ratio Panel (b) Aerosol volume as measured by the DMA (the time axis is coincident with all of the other panels, two y-axes have been used to show more precisely the growth resulting from ozonolysis). Panel (c) Ionic species measured by the PILS-IC showing an increase in DEA throughout the reaction and condensation of EA when additional  $\text{HNO}_3$  is added Panel (d) Ion fragments detected by the cToF-AMS:  $m/z$  46  $\text{NO}_2^+$ ,  $m/z$  86  $\text{N}(\text{CH}_2\text{CH}_3)_2\text{CH}_2^+$  (largest peak from triethylammonium),  $m/z$  58  $\text{NH}(\text{CH}_2\text{CH}_3)\text{CH}_2^+$  (largest peak from Diethylammonium),  $m/z$  44  $\text{CO}_2^+$ ,  $m/z$  43  $\text{C}_2\text{H}_3\text{O}^+$ ,  $m/z$  29  $\text{CHO}^+$ .

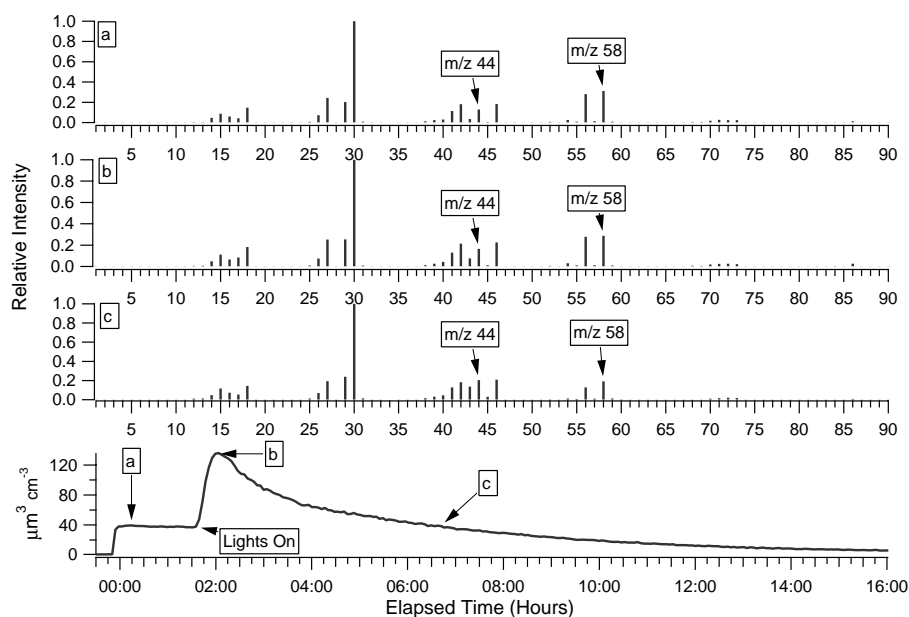
350 ppb of ozone was slowly added to the chamber causing further aerosol growth that peaked, after  $\sim 3$  h of ozone exposure, at a maximum of  $15 \mu\text{m}^3 \text{cm}^{-3}$ , or  $\sim 18 \mu\text{g}^3 \text{m}^{-3}$  (effective density  $= 1.2 \pm 0.2$ ) of additional growth. The mass yield from ozonolysis is 5%.

During ozonolysis, diethylammonium and ethylammonium were formed as they were during photooxidation, but there was no corresponding growth in the nitrate signal (either on the cToF-AMS or the PILS-IC) indicating that these compounds condensed in the particle phase in a form other than nitrate salts. At the peak of aerosol phase growth (3 h of oxidation), diethylammonium constituted 23% of the aerosol mass formed after ozone injection and ethylammonium accounted for 3% of the mass from ozonolysis. After the aerosol growth had peaked, an additional 8 ppb of nitric acid was added causing a further  $30 \mu\text{g} \text{m}^{-3}$  of aerosol growth. The aerosol generated by this second addition of nitric acid was a mix of diethylammonium ( $8.7 \mu\text{g} \text{m}^{-3}$ ), ethylammonium ( $4.5 \mu\text{g} \text{m}^{-3}$ ), triethylammonium ( $0.5 \mu\text{g} \text{m}^{-3}$ ), and nitrate ( $14.5 \mu\text{g} \text{m}^{-3}$ ). The near perfect ion balance between the positive amine ions and the negative nitrate ions (3% negative charge imbalance) substantiates that all of the additional growth was in the form of nitrate salts. The negligible increase in triethylammonium mass during the second

addition of nitric acid indicates that nearly all of the starting TEA had been oxidized. The final aerosol, composed of nitrate salts and oxidized SOA, did not rapidly decay. The PILS-IC data showed that nitrate decayed 7 percent faster than ethylammonium and 14 percent faster than diethylammonium further supporting the idea that these species are not entirely nitrate salts and that nitrate salts decay more rapidly than SOA formed through oxidation.

### 5.8 Diethylamine (DEA) photooxidation

Figure 12 shows the photooxidation of 100 ppb of diethylamine, conducted in the same manner as the previously discussed photooxidations using hydrogen peroxide as an OH precursor. Diethylammonium nitrate nucleates upon injection of DEA followed by a burst of aerosol mass when the lights are turned on that quickly decays away. The rapid decay is similar to the behavior of TMA and MA during photooxidation, with DEA being more similar to MA in that nearly all of the aerosol formed is nitrate salt. Experiments using different OH sources also yielded negligible non-salt aerosol. This is an intriguing result, because by molecular weight alone, DEA would be predicted to form more secondary organic aerosol when oxidized than TMA. Clearly, in this case, the chemical nature of the compound is more



**Fig. 12.** Photooxidation of diethylamine (exp. 22, Table 2). The volume trace from the DMA (bottom panel) shows that the aerosol formed decays quickly back to the volume present before the irradiation. The prominent peaks in the cToF-AMS spectra (Panels a–c) show little change throughout the course of the experiment, except for a slight increase in the relative intensity of oxidized peaks at  $m/z$  44 ( $\text{CO}_2^+$ ) and  $m/z$  43 ( $\text{C}_2\text{H}_3\text{O}^+$ ). There was also little change in the high  $m/z$  spectra indicating negligible growth of high molecular weight species.

important than molecular weight alone. Though the specific reactions that lead to the difference in yield between TEA and DEA remain unclear, Fig. 5 shows that there are several compounds that can be formed by tertiary amines through the loss of one of the alkyl groups, a reaction pathway that is not available for secondary or primary amines. Though believed to be a minor channel, OH can also extract a hydrogen atom directly from the nitrogen of primary and secondary amines; it is possible that this reaction pathway leads to more volatile compounds. Because photooxidation yielded no non-salt organic aerosol, an ozonolysis experiment was not conducted for DEA.

### 5.9 Ethylamine (EA) photooxidation

One photooxidation of ethylamine was conducted and yielded negligible non-salt aerosol mass. Though there was contamination from a previous DEA experiment, it is doubtful that this affected the amount of organic aerosol formed. Ethylamine ozonolysis was not pursued because of the negligible non-salt yield during photooxidation.

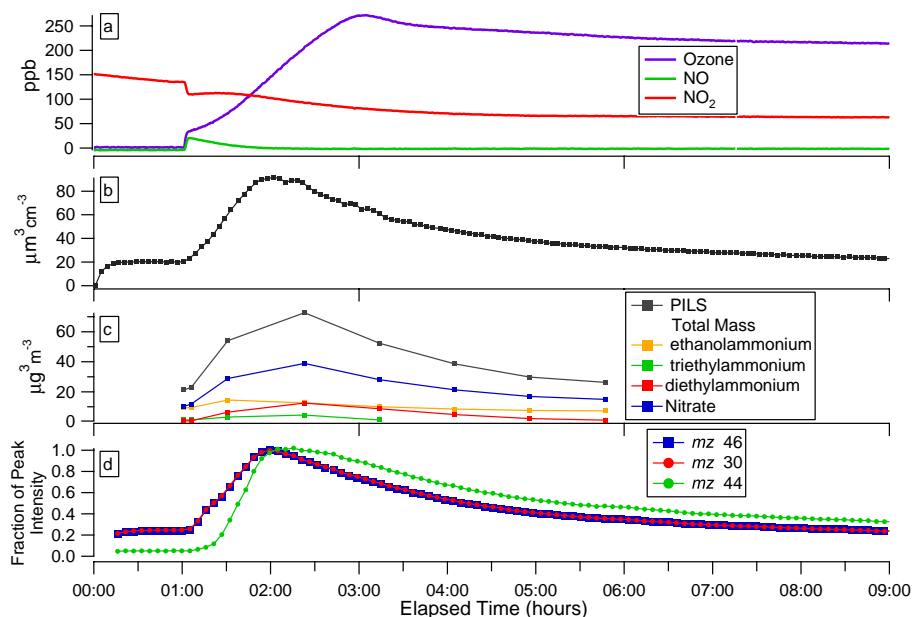
### 5.10 Ethanolamine (MEA) photooxidation and ozonolysis

Figure 13 shows the photooxidation of ethanolamine. Aerosol growth follows the same pattern as for the other amines with the majority of the initial growth being composed of nitrate salts that repartition back to the gas phase as the amine reacts away. Non-salt organic aerosol forms

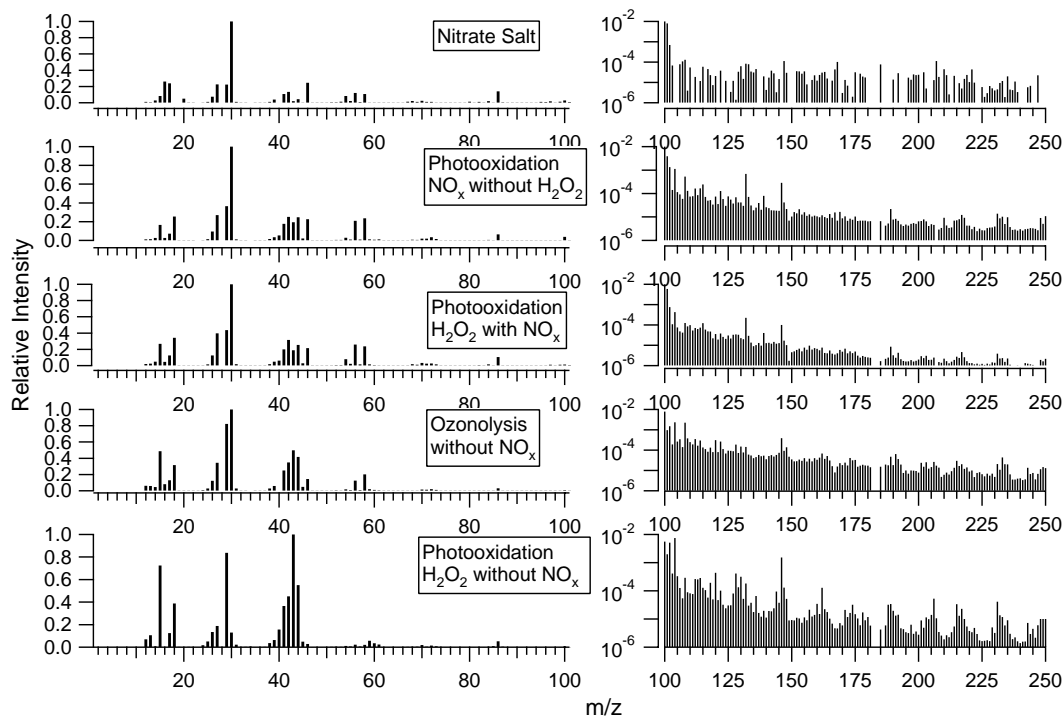
(~2% mass yield), but the yield is small as it is for the other non-tertiary amines studied. The cToF-AMS data show that oxidized fragments ( $m/z$  44,  $\text{CO}_2^+$ ) grow in more gradually and decay less than fragments associated with ethanolammonium nitrate ( $m/z$  46  $\text{NO}_2^+$  and  $m/z$  30  $\text{NO}^+$  and the major ion fragment from ethanolammonium itself). The PILS-IC shows growth of diethylammonium though this is probably a result of contamination because it is unclear how ethanolamine could react to form diethylammonium. The yield from ozonolysis of ethanolamine was small (~3%), as expected from the small yield observed during photooxidation.

### 5.11 Photooxidation in the absence of $\text{NO}_x$

$\text{NO}_x$ -free photooxidation experiments were conducted for both TEA and DEA. In both cases, negligible mass from nitrate salts was detected by the PILS-IC. Following the trends of the high  $\text{NO}_x$  photooxidation and ozonolysis results, 500 ppb of TEA formed  $260 \mu\text{g m}^{-3}$  of aerosol (mass yield of ~12%) while 500 ppb DEA formed less than  $2 \mu\text{g m}^{-3}$  (mass yield of ~0.1%). The cToF-AMS mass spectrum from the  $\text{NO}_x$ -free photooxidation of TEA is shown in Fig. 14. No dramatic changes in the mass spectrum occur during the course of the experiment.



**Fig. 13.** Photooxidation of 100 ppb of ethanolamine (MEA) (exp. 29, Table 2). Ethanolamine is injected at  $t=0$  forming ethanolammonium nitrate. Panel (a) Evolution of ozone and  $\text{NO}_x$  mixing ratios. Panel (b) DMA volume. Panel (c) PILS-IC data. Panel (d) Fragments from the cToF-AMS. Oxidized fragment ions ( $m/z$  44  $\text{CO}_2^+$ ) grow in slowly and decay less quickly than nitrate fragment ions ( $m/z$  46  $\text{NO}_2^+$  and  $m/z$  30  $\text{NO}^+$ ) or ethanolammonium fragment ions ( $m/z$  30 is the base peak for ethanolammonium in the cToF-AMS).



**Fig. 14.** cToF-AMS spectra (normalized to the largest peak) of aerosol generated from TEA oxidation under various conditions. In all cases, except for hydrogen peroxide without  $\text{NO}_x$ , the nitrate salt was intentionally formed by mixing TEA with nitric acid in the chamber before the start of oxidation. All spectra were collected after the peak of aerosol growth had been reached.

### 5.12 Effect of oxidation conditions on particle chemistry

Figure 14 shows cToF-AMS spectra from particles formed by oxidation of TEA using four different systems: (1) photooxidation with  $\text{NO}_x$  alone, (2) photooxidation with  $\text{NO}_x$  using  $\text{H}_2\text{O}_2$  as an OH precursor, (3) ozonolysis in the absence of  $\text{NO}_x$ , and (4) photooxidation in the absence of  $\text{NO}_x$  using  $\text{H}_2\text{O}_2$  as an OH precursor. Because the cToF-AMS uses electron impact ionization, differences in the peak height ratios can be used to assess chemical similarity between the systems even though the spectra are highly fragmented. Aerosol formed in the two different photooxidation systems containing  $\text{NO}_x$  have similar spectra with large peaks corresponding to fragments from the nitrate salt mixed with oxidized fragments ( $m/z$  29  $\text{HCO}^+$ ,  $m/z$  44  $\text{COO}^+$ ,  $m/z$  43  $\text{C}_2\text{H}_3\text{O}^+$ , etc.). The spectrum of aerosol generated by photooxidation (using hydrogen peroxide as an OH precursor) in the absence of  $\text{NO}_x$  is the most distinct from all other spectra, with dramatically different peak height ratios ( $m/z$  43 is the most intense signal) and more high molecular weight fragments than the other systems. The ozone spectrum shows characteristics of both the high and low  $\text{NO}_x$  spectra including a relatively large, yet not dominant,  $m/z$  43 peak.

The spectra from different oxidation systems show that in addition to affecting how much nitrate salt is formed, oxidant (OH,  $\text{O}_3$ ) and  $\text{NO}_x$  levels also affect the chemical composition of the oxidized aerosol. At the same time, the similarities between the spectra from high  $\text{NO}_x$  photooxidation systems with and without  $\text{H}_2\text{O}_2$  indicate that similar species condense independent of the OH source. All of the amines studied formed aerosol with similar spectra during photooxidation whether or not hydrogen peroxide was used as an OH precursor.

### 5.13 Effective density shifts

During the photooxidations of TEA and TMA the effective density of the aerosol continually increased as non-salt organic mass condensed. Figure 1 shows the increase observed during the photooxidation of TEA. The effective density of the aerosol formed during ozonolysis was higher than that of the salt for both TEA and TMA. Additionally, TEA formed aerosol with a higher effective density than TEAN when photooxidized in the absence of  $\text{NO}_x$ . The increases in effective densities observed in particles with a higher fraction of non-salt mass indicates that either: (1) the non-salt aerosol is more dense; or (2) the salt aerosol is either non-spherical or has void volumes, and the condensation of organic aerosol onto the salt alters these physical characteristics. In either case, it is evident that the physical morphology of the particles depends on the ratio of non-salt to salt mass.

## 6 Implications

Amines can undergo similar acid-base reactions as ammonia to form atmospheric nitrate and sulfate salts when in the presence of  $\text{HNO}_3$  or  $\text{H}_2\text{SO}_4$ . Whether amines, in fact, will form such aminium salts depends not only on the concentration of the amine and the acid, but also on the concentration of ammonia which competes for acidic molecules. Thermodynamic calculations using entropies estimated from quantum mechanics and molecular dynamics indicate that diethylammonium nitrate will be able to form when ammonia mixing ratios are greater than those of diethylamine. Triethylamine was shown experimentally to have a dissociation equilibrium constant similar to that of ammonia. Ethylammonium nitrate and trimethylammonium nitrate are predicted to be unable to form unless their mixing ratios are near to or greater than that of ammonia. We note that thermodynamic parameters for the aminium salts have large uncertainties that preclude us from making conclusions regarding the formation, in the presence of ammonia, of the other aminium salts studied.

Gas-phase amines are subject to atmospheric oxidation by the OH radical and ozone, leading to secondary organic aerosol formation. If nitric or sulfuric acid is present during the oxidation, aminium salts of the parent amine can form simultaneously with the SOA resulting from oxidation. The products of amine oxidation can also be basic and form additional aminium salts. Aminium salts will most often form in source-rich areas. As the parent amine is reacted away or as the air mass undergoes dilution, aminium salts can be expected to repartition back to the gas phase. SOA resulting from amine oxidation appears to be more stable in the particle phase than the aminium salts.

Table 4 gives the non-salt organic aerosol yields for all of the amines studied under a number of different oxidative conditions. While the yields shown are only applicable to the amine:oxidant and oxidant: $\text{NO}_x$  ratios of the particular experiments, we can draw the general conclusion that the tertiary amines (TMA and TEA) are able to form significant yields of non-salt SOA while the primary and secondary amines studied are not. Ethanolamine showed a small growth during ozonolysis which may be an indication that adding functional groups to the amines increases their organic (non-salt) aerosol yield.

## Appendix A

### Thermodynamic data for amine systems

Table A1 lists available thermodynamic data for common amine systems. Multiple heats of formation values of alkylammonium nitrates are listed to highlight their uncertainty. Data on entropy and heat capacities for alkylammonium nitrates, with the exception of ammonium nitrate, do not appear to be available.

**Table A1.** Thermodynamic data for various amine nitrate systems. Amines and nitric acid are in the gas phase and nitrates are solid.

Substance	$\Delta H_f^\circ$ (kJ/mol)	$S^\circ$ (J/mol K)	$C_p$ (J/mol K)
ammonia	−45.90 <sup>d</sup>	192.77 <sup>e</sup>	35.65 <sup>d</sup>
methylamine	−23.0 <sup>f</sup>	243 <sup>g</sup>	53 <sup>g</sup>
dimethylamine	−18.5 <sup>f</sup>	273 <sup>g</sup>	70.8 <sup>g</sup>
trimethylamine	−23.7 <sup>f</sup>	287 <sup>g</sup>	91.8 <sup>g</sup>
ethylamine	−47.5 <sup>f</sup>	285 <sup>g</sup>	72.7 <sup>g</sup>
diethylamine	−72.6 <sup>f</sup>	352 <sup>g</sup>	115.7 <sup>g</sup>
triethylamine	−92.4 <sup>f</sup>	405 <sup>g</sup>	160.9 <sup>g</sup>
ethanolamine	−210.2 <sup>j</sup>	321 <sup>j</sup>	85.3 <sup>j</sup>
ammonium nitrate	−365.61 <sup>a</sup>	146.44 <sup>b</sup>   141.56 <sup>*</sup>	140 <sup>c</sup>
methylammonium nitrate	−337 <sup>h</sup>   −354.4 <sup>k</sup>	194.7 <sup>*</sup>	
dimethylammonium nitrate	−331 <sup>h</sup>   −350.2 <sup>k</sup>	229.9 <sup>*</sup>	
trimethylammonium nitrate	−306 <sup>h</sup>   −343.9 <sup>k</sup>	243.5 <sup>*</sup>	
ethylammonium nitrate	−364 <sup>h</sup>   −366.9 <sup>k</sup>	237.2 <sup>*</sup>	206 <sup>i</sup>
diethylammonium nitrate	−413 <sup>h</sup>   −418.8 <sup>k</sup>	299.9 <sup>*</sup>	
triethylammonium nitrate	−407 <sup>h</sup>   −447.7 <sup>k</sup>	350.3 <sup>*</sup>	
ethanolammonium nitrate	−576 <sup>h</sup>   −577 <sup>k</sup>		
nitric acid	−134.31 <sup>d</sup>	266.39 <sup>d</sup>	53.31 <sup>d</sup>

\*values estimated from quantum mechanics/molecular dynamics

<sup>a</sup>Cox et al. (1979), <sup>b</sup>Eichenauer and Liebscher (1965), <sup>c</sup>Wagman et al. (1968), <sup>d</sup>Chase et al. (1998), <sup>e</sup>Haar (1968), <sup>f</sup>Schmitz et al. (2001),

<sup>g</sup>Perry et al. (1997), <sup>h</sup>Cottrell and Gill (1951), <sup>i</sup>Allen et al. (1985), <sup>j</sup>Yaws (2003), <sup>k</sup>Wagman et al. (1982)

One approach is to extract the entropy information from atomistic classical and quantum simulation. Lin et al. (2003) developed a 2-phase thermodynamic approach for calculating the thermodynamic properties of complex systems from single molecular dynamics simulation trajectories. In general the Fourier transform of the velocity autocorrelation function, obtained from a molecular dynamics trajectory is used to obtain the vibrational density of states, which is then used to calculate the thermodynamic properties by applying quantum statistics assuming each vibrational mode is a harmonic oscillator. This approach is quite accurate for solids, but leads to significant errors for liquids. Lin et al. (2003) extend this approach to fluids by applying the 2-phase model in which the density of states of the fluid systems are partitioned into gas and solid like components. However, for aminium nitrates that are solids in ambient conditions, the harmonic approximation is sufficiently accurate for entropy estimation.

Of the alkylammonium nitrates, crystal structures were only found for ammonium nitrate (Herrmann et al., 1994) and methylammonium nitrate (Mylrajan et al., 1985). For the compounds with experimental crystal structures, the periodic quantum mechanical (QM) Mulliken charge distribution were determined by the SeqQuest program (Feibelman, 1987; Verdozzi et al., 2002). For the compounds lacking experimental crystal structure, the solid structures were es-

timated by modifying the methylammonium nitrate crystal. For instance, methyl groups were replaced by ethyl groups in order to create the ethylammonium nitrate crystal structure. The QM charges were obtained using Density Functional Theory (DFT), B3LYP (Becke, 1993) functions as implemented in the Jaguar program (Jaguar, 2005) using basis sets aug-cc-pvtz (Kendall et al., 1992). Solid structures were built using this method for di and trimethylammonium nitrate, mono, di and triethylammonium nitrate in CERIUS2 (Cerius2, 1999). Molecular dynamic (MD) simulation at constant pressure, temperature and number of particles (NPT) were performed to equilibrate these solid structures. NVT simulations were then carried out for these experimental crystals or equilibrated solids for a total of 50 ps. Long-range interactions are included using the Ewald sum method and the Nose-Hoover thermostat. Using the MD trajectories, the density of states can be obtained, and the entropies can then be determined from quantum statistics (Lin et al., 2003).

The QM entropy is expected to be quite accurate for crystalline systems. Indeed, the QM entropy agrees rather well with the experimental values for ammonium nitrate (141.56 J/molK vs. 146.44 J/molK). Unfortunately, experimental entropy is available only for ammonium nitrate so further comparison cannot be done. Since crystal structure was also available for methylammonium nitrate, we expect

its QM entropy to be reasonably accurate. For other aminium nitrates, the accuracy of the calculated entropies remains undetermined although we observed a sensible correlation between the “flexibility” of the alkyl groups and the entropies.

**Acknowledgements.** This work was supported by the Electric Power Research Institute.

Edited by: A. Laaksonen

## References

- Allan, J. D., Jimenez, J. L., Williams, P. I., Alfarra, M. R., Bower, K. N., Jayne, J. T., Coe, H., and Worsnop, D. R.: Quantitative sampling using an Aerodyne aerosol mass spectrometer: 1. Techniques of data interpretation and error analysis, *J. Geophys. Res.*, 108(D3), 4090, doi:10.1029/2002JD002358, 2003.
- Allen, M., Evans, D. F., and Lumry, R.: Thermodynamic properties of the ethylammonium nitrate + water-system – partial molar volumes, heat-capacities, and expansivities, *J. Solution. Chem.*, 14(8), 549–560, 1985.
- Angelino, S., Suess, D. T., and Prather, K. A.: Formation of aerosol particles from reactions of secondary and tertiary alkylamines: Characterization by aerosol time-of-flight mass spectrometry, *Environ. Sci. Technol.*, 35(15), 3130–3138, 2001.
- Atkinson, R., Perry, R. A., and Pitts, J. N.: Rate constants for reactions of OH radical with (CH<sub>3</sub>)<sub>2</sub>NH, (CH<sub>3</sub>)<sub>3</sub>N, and C<sub>2</sub>H<sub>5</sub>NH<sub>2</sub> over temperature range 298–426 degrees K, *J. Chem. Phys.*, 68(4), 1850–1853, 1978.
- Bahreini, R., Keywood, M. D., Ng, N. L., Varutbangkul, V., Gao, S., Flagan, R. C., Seinfeld, J. H., Worsnop, D. R., and Jimenez, J. L.: Measurements of secondary organic aerosol from oxidation of cycloalkenes, terpenes, and m-xylene using an Aerodyne aerosol mass spectrometer, *Environ. Sci. Technol.*, 39(15), 5674–5688, 2005.
- Becke, A. D.: Density-functional thermochemistry III. The role of exact exchange, *J. Chem. Phys.*, 98(7), 5648–5652, 1993.
- Beddows, D. C. S., Donovan, R. J., Harrison, R. M., Heal, M. R., Kinnersley, R. P., King, M. D., Nicholson, D. H., and Thompson, K. C.: Correlations in the chemical composition of rural background atmospheric aerosol in the UK determined in real time using time-of-flight mass spectrometry, *J. Environ. Monit.*, 6(2), 124–133, 2004.
- Cerius2, v. 4.0, Accelrys, San Diego, CA, 1999.
- Chase, M. W.: NIST-JANAF thermochemical tables, fourth edition, *J. Phys. Chem. Ref. Data*, Monograph 9, 1343–1290, 1998.
- Cocker, D. R., Flagan, R. C., and Seinfeld, J. H.: State-of-the-art chamber facility for studying atmospheric aerosol chemistry, *Environ. Sci. Technol.*, 35(12), 2594–2601, 2001.
- Cottrell, T. L. and Gill, J. E.: The preparation and heats of combustion of some amine nitrates, *J. Chem. Soc.*, (Jul), 1798–1800, 1951.
- Cox, J. D., Harrop, D., and Head, A. J.: Standard enthalpy of formation of ammonium-nitrate and of the nitrate ion, *J. Chem. Thermodyn.*, 11(8), 811–814, 1979.
- DeCarlo, P. F., Slowik, J. G., Worsnop, D. R., Davidovits, P., and Jimenez, J. L.: Particle morphology and density characterization by combined mobility and aerodynamic diameter measurements. Part 1: Theory, *Aerosol Sci. Technol.*, 38(12), 1185–1205, 2004.
- Drewnick, F., Jayne, J. T., Canagaratna, M., Worsnop, D. R., and Demerjian, K. L.: Measurement of ambient aerosol composition during the PMTACS-NY 2001 using an aerosol mass spectrometer. Part II: Chemically speciated mass distributions, *Aerosol Sci. Technol.*, 38, 104–117, 2004a.
- Drewnick, F., Schwab, J. J., Jayne, J. T., Canagaratna, M., Worsnop, D. R., and Demerjian, K. L.: Measurement of ambient aerosol composition during the PMTACS-NY 2001 using an aerosol mass spectrometer. Part I: Mass concentrations, *Aerosol Sci. Technol.*, 38, 92–103, 2004b.
- Eichenau, W. and Liebsche, D.: Die molwärme des ammonium-nitrats zwischen 11 und 280 degrees K, *Zeitschrift für Naturforschung Part a-Astrophysik Physik und Physikalische Chemie*, A 20(1), 160, 1965.
- Feibelman, P. J.: Force and total-energy calculations for a spatially compact adsorbate on an extended, metallic crystal surface, *Phys. Rev. B*, 35(6), 2626–2646, 1987.
- Finlayson-Pitts, B. J. and Pitts, J. N. J.: *Atmospheric chemistry : Fundamentals and experimental techniques*, Wiley, New York, 1986.
- Haar, L.: Thermodynamic properties of ammonia as an ideal gas, *J. Res. Nbs. A. Phys. Ch.*, A 72(2), 207, 1968.
- Hamoir, J., Nemmar, A., Halloy, D., Wirth, D., Vincke, G., Vanderplasschen, A., Nemery, B., and Gustin, P.: Effect of polystyrene particles on lung microvascular permeability in isolated perfused rabbit lungs: Role of size and surface properties, *Toxicol. Appl. Pharmacol.*, 190(3), 278–285, 2003.
- Herrmann, M., Engel, W., Schneider, J., and Goebel, H.: Rietveld refinement of the phase of NH<sub>4</sub>NO<sub>3</sub> measured in-situ under different diffraction geometries, *Materials Science Forum*, 166, 489–494, 1994.
- Huffman, J. A., Jayne, J. T., Drewnick, F., Aiken, A. C., Onasch, T., Worsnop, D. R., and Jimenez, J. L.: Design, modeling, optimization, and experimental tests of a particle beam width probe for the Aerodyne aerosol mass spectrometer, *Aerosol Sci. Technol.*, 39(12), 1143–1163, 2005.
- Jaguar, v. 6.5, Schrodinger, LLC, New York, NY, 2005.
- Jayne, J. T., Leard, D. C., Zhang, X. F., Davidovits, P., Smith, K. A., Kolb, C. E., and Worsnop, D. R.: Development of an aerosol mass spectrometer for size and composition analysis of submicron particles, *Aerosol Sci. Technol.*, 33(1–2), 49–70, 2000.
- Kendall, R. A., Dunning Jr., T. H., and Harrison, R. J.: Electron affinities of the first-row atom revisited. Systematic basis sets and wave functions, *J. Chem. Phys.*, 96(9), 6796–6806, 1992.
- Keywood, M. D., Varutbangkul, V., Bahreini, R., Flagan, R. C., and Seinfeld, J. H.: Secondary organic aerosol formation from the ozonolysis of cycloalkenes and related compounds, *Environ. Sci. Technol.*, 38(15), 4157–4164, 2004.
- Kroll, J. H., Ng, N. L., Murphy, S. M., Flagan, R. C., and Seinfeld, J. H.: Secondary organic aerosol formation from isoprene photooxidation, *Environ. Sci. Technol.*, 40(6), 1869–1877, 2006.
- Lin, S.-T., Blanco, M., and Goddard III, W. A.: The two-phase model for calculating thermodynamic properties of liquids from molecular dynamics: Validation for the phase diagram of Lennard-Jones fluids, *J. Chem. Phys.*, 119(22), 11 792–11 805, 2003.
- Mace, K. A., Artaxo, P., and Duce, R. A.: Water-soluble organic nitrogen in Amazon basin aerosols during the dry (biomass burning) and wet seasons, *J. Geophys. Res.*, 108(D16), 4512,



- doi:10.1029/2003JD003557, 2003.
- Makela, J. M., Yli-Koivisto, S., Hiltunen, V., Seidl, W., Swietlicki, E., Teinila, K., Sillanpaa, M., Koponen, I. K., Paatero, J., Rosman, K., and Hameri, K.: Chemical composition of aerosol during particle formation events in boreal forest, *Tellus B*, 53(4), 380–393, 2001.
- McGregor, K. G. and Anastasio, C.: Chemistry of fog waters in California's central valley: 2. Photochemical transformations of amino acids and alkyl amines, *Atmos. Environ.*, 35(6), 1091–1104, 2001.
- Mozurkewich, M.: The dissociation-constant of ammonium-nitrate and its dependence on temperature, relative-humidity and particle-size, *Atmos. Environ. A-Gen.*, 27(2), 261–270, 1993.
- Murphy, D. M. and Thomson, D. S.: Chemical composition of single aerosol particles at Idaho hill: Positive ion measurements, *J. Geophys. Res.*, 102(D5), 6341–6352, 1997.
- Mylrajan, M., Srinivasan, T. K. K., and Sreenivasamurthy, G.: Crystal structure of monomethylammonium nitrate, *J. Cryst. Spectrosc.*, 15(5), 493–500, 1985.
- Neff, J. C., Holland, E. A., Dentener, F. J., McDowell, W. H., and Russell, K. M.: The origin, composition and rates of organic nitrogen deposition: A missing piece of the nitrogen cycle?, *Biogeochemistry*, 57(1), 99–136, 2002.
- Nemmar, A., Hoylaerts, M. F., Hoet, P. H. M., Dinsdale, D., Smith, T., Xu, H. Y., Vermeylen, J., Nemery, B., and Nemery, B.: Ultra-fine particles affect experimental thrombosis in an in vivo hamster model, *Am. J. Resp. Crit. Care.*, 166(7), 998–1004, 2002.
- Ngwabie, N. M. and Hintz, T.: Mxing ratio measurements and flux estimates of volatile organic compounds (voc) from a cowshed with conventional manure treatment indicate significant emissions to the atmosphere, *Geograph. Res. Abstr.*, 7(01175), 2005.
- Perry, R. H., Green, D. W., and Maloney, J. O.: Perry's chemical engineers' handbook, McGraw-Hill, New York, 1997.
- Pitts, J. N., Grosjean, D., Vancauwenberghe, K., Schmid, J. P., and Fitz, D. R.: Photo-oxidation of aliphatic-amines under simulated atmospheric conditions – formation of nitrosamines, nitramines, amides, and photo-chemical oxidant, *Environ. Sci. Technol.*, 12(8), 946–953, 1978.
- Rabaud, N. E., Ebeler, S. E., Ashbaugh, L. L., and Flocchini, R. G.: Characterization and quantification of odorous and non-odorous volatile organic compounds near a commercial dairy in California, *Atmos. Environ.*, 37(7), 933–940, 2003.
- Schade, G. W. and Crutzen, P. J.: Emission of aliphatic-amines from animal husbandry and their reactions – potential source of N<sub>2</sub>O and HCN, *J. Atmos. Chem.*, 22(3), 319–346, 1995.
- Schmitz, L. R., Chen, K. H., Labanowski, J., and Allinger, N. L.: Heats of formation of organic molecules calculated by density functional theory. III - amines, *J. Phys. Org. Chem.*, 14(2), 90–96, 2001.
- Seinfeld, J. H. and Pankow, J. F.: Organic atmospheric particulate material, *Annu. Rev. Phys. Chem.*, 54, 121–140, 2003.
- Simoneit, B. R. T., Rushdi, A. I., Bin Abas, M. R., and Didyk, B. M.: Alkyl amides and nitriles as novel tracers for biomass burning, *Environ. Sci. Technol.*, 37(1), 16–21, 2003.
- Sorooshian, A., Brechtel, F. J., Ma, Y. L., Weber, R. J., Corless, A., Flagan, R. C., and Seinfeld, J. H.: Modeling and characterization of a particle-into-liquid sampler (pils), *Aerosol Sci. Technol.*, 40(6), 396–409, 2006.
- Stein, S. E.: Mass spectra by NIST mass spec data center, NIST chemistry webbook, NIST standard reference database number 69, Eds. Linstrom PJ, Mallard WG, National Institute of Standards and Technology, Gaithersburg MD, (<http://webbook.nist.gov>), 2005.
- Stelson, A. W. and Seinfeld, J. H.: Relative-humidity and temperature-dependence of the ammonium-nitrate dissociation-constant, *Atmos. Environ.*, 16(5), 983–992, 1982.
- Surratt, J. D., Murphy, S. M., Kroll, J. H., Ng, N. L., Hildebrandt, L., Sorooshian, A., Szmigielski, R., Vermeylen, R., Maenhaut, W., Claeys, M., Flagan, R. C., and Seinfeld, J. H.: Chemical composition of secondary organic aerosol formed from the photooxidation of isoprene, *J. Phys. Chem. A*, 110(31), 9665–9690, 2006.
- Tan, P. V., Evans, G. J., Tsai, J., Owega, S., Fila, M. S., and Malpica, O.: On-line analysis of urban particulate matter focusing on elevated wintertime aerosol concentrations, *Environ. Sci. Technol.*, 36(16), 3512–3518, 2002.
- Tuazon, E. C., Atkinson, R., Aschmann, S. M., and Arey, J.: Kinetics and products of the gas-phase reactions of O<sub>3</sub> with amines and related-compounds, *Res. Chem. Intermed.*, 20(3–5), 303–320, 1994.
- Verdozzi, C., Schultz, P. A., Wu, R., Edwards, A. H., and Kiousis, N.: Layer intermixing during metal/metal oxide adsorption: Ti/sapphire(0001), *Phys. Rev. B*, 66, 125 408, 2002.
- Wagman, D. D., Evans, W. H., Parker, V. B., Halow, I., Bailey, S. M., and Schumm, R. H.: Selected values of chemical thermodynamic properties; tables for the first thirty-four elements in the standard order of arrangement, NBS Technical Note, 270(3), 1968.
- Wagman, D. D., Evans, W. H., Parker, V. B., Schumm, R. H., Halow, I., Bailey, S. M., Churney, K. L., and Nuttall, R. L.: The nbs tables of chemical thermodynamic properties – selected values for inorganic and C-1 and C-2 organic-substances in si units, *J. Phys. Chem. Ref. Data*, 11(2), 91–110, 1982.
- Weber, R. J., Orsini, D., Daun, Y., Lee, Y. N., Klotz, P. J., and Brechtel, F.: A particle-into-liquid collector for rapid measurement of aerosol bulk chemical composition, *Aerosol Sci. Technol.*, 35(3), 718–727, 2001.
- Yaws, C. L.: Yaws' handbook of thermodynamic and physical properties of chemical compounds, Knovel, 2003.
- Zhang, Q. and Anastasio, C.: Free and combined amino compounds in atmospheric fine particles (pm<sub>2.5</sub>) and fog waters from northern California, *Atmos. Environ.*, 37(16), 2247–2258, 2003.

## **Appendix F**

# **Regional Variation of Organic Functional Groups in Aerosol Particles on Four U.S. East Coast Platforms during ICARTT 2004\***

---

\*This chapter is reproduced by permission from “Regional Variation of Organic Functional Groups in Aerosol Particles on Four U.S. East Coast Platforms during ICARTT 2004” by S. Gilardoni, L. M. Russell, A. Sorooshian, R. C. Flagan, J. H. Seinfeld, T. S. Bates, P. K. Quinn, J. D. Allan, B. Williams, A. H. Goldstein, T. B. Onasch, and D.R. Worsnop, *J. Geophys. Res.*, *112*, D10S27, doi:10.1029/2006JD007737, 2007. Copyright 2007. American Geophysical Union.



## Regional variation of organic functional groups in aerosol particles on four U.S. east coast platforms during the International Consortium for Atmospheric Research on Transport and Transformation 2004 campaign

S. Gilardoni,<sup>1</sup> L. M. Russell,<sup>1</sup> A. Sorooshian,<sup>2</sup> R. C. Flagan,<sup>2</sup> J. H. Seinfeld,<sup>2</sup> T. S. Bates,<sup>3</sup> P. K. Quinn,<sup>3</sup> J. D. Allan,<sup>4</sup> B. Williams,<sup>5</sup> A. H. Goldstein,<sup>5</sup> T. B. Onasch,<sup>6</sup> and D. R. Worsnop<sup>6</sup>

Received 30 June 2006; revised 30 January 2007; accepted 2 April 2007; published 15 May 2007.

[1] Submicron atmospheric aerosol samples were collected during the International Consortium for Atmospheric Research on Transport and Transformation (ICARTT) 2004 campaign on four platforms: Chebogue Point (Nova Scotia, Canada), Appledore Island (Maine), the CIRPAS Twin Otter over Ohio, and the NOAA R/V *Ronald H. Brown* in the Gulf of Maine. Saturated aliphatic C-C-H, unsaturated aliphatic C=C-H, aromatic C=C-H, organosulfur C-O-S, carbonyl C=O, and organic hydroxyl C-OH functional groups were measured by calibrated Fourier Transform Infrared (FTIR) spectroscopy at all four sampling platforms. The ratio of molar concentrations of carbonyl C=O to saturated aliphatic C-C-H groups was nearly constant at each sampling platform, with the Twin Otter samples having the lowest ratio at 0.1 and the three more coastal platforms having ratios of 0.4 and 0.5. Organic mass (OM) to organic carbon (OC) ratios follow similar trends for the four platforms, with the Twin Otter having the lowest ratio of 1.4 and the coastal platforms having slightly higher values typically between 1.5 and 1.6. Organosulfur compounds were occasionally observed. Collocated organic aerosol sampling with two Aerodyne aerosol mass spectrometers for OM, a Sunset Laboratory thermo-optical analysis instrument for OC, and an ion chromatography-particle into liquid sampler (IC-PILS) for speciated carboxylic acids provided comparable results for most of the project, tracking the time series of FTIR OM, OC, and carbonyl groups, respectively, and showing simultaneous peaks of similar magnitude during most of the project. The FTIR/IC-PILS comparison suggests that about 9% of the carbonyl groups found in submicron organic particles on the Twin Otter are typically associated with low molecular weight carboxylic acids.

**Citation:** Gilardoni, S., et al. (2007), Regional variation of organic functional groups in aerosol particles on four U.S. east coast platforms during the International Consortium for Atmospheric Research on Transport and Transformation 2004 campaign, *J. Geophys. Res.*, 112, D10S27, doi:10.1029/2006JD007737.

### 1. Introduction

[2] Organic matter constitutes an important fraction of aerosol mass, both in remote and urban locations [Turpin

and Lim, 2001]. The presence of organic compounds in aerosol particles is due to primary emissions and secondary organic aerosol (SOA) formation. SOA can be formed by condensation of species produced by gas phase oxidation of volatile compounds. The chemical composition of the organic fraction affects the hygroscopicity of aerosol particles which in turn affects the aerosol size distribution, residence time in the atmosphere and optical properties [Markowicz *et al.*, 2003; Kim *et al.*, 2006].

[3] Although numerous studies have been performed to characterize polar and nonpolar components of organic aerosols, only a small percentage of the organic mass has been resolved by traditional analytical methods [Saxena and Hildemann, 1996; Turpin *et al.*, 2000]. Infrared spectroscopy has been used to investigate the organic functional group composition of atmospheric aerosol particles for more than 30 years [Blanco and McIntyre, 1972; Dangler *et al.*, 1987].

<sup>1</sup>Scripps Institution of Oceanography, University of California, San Diego, La Jolla, California, USA.

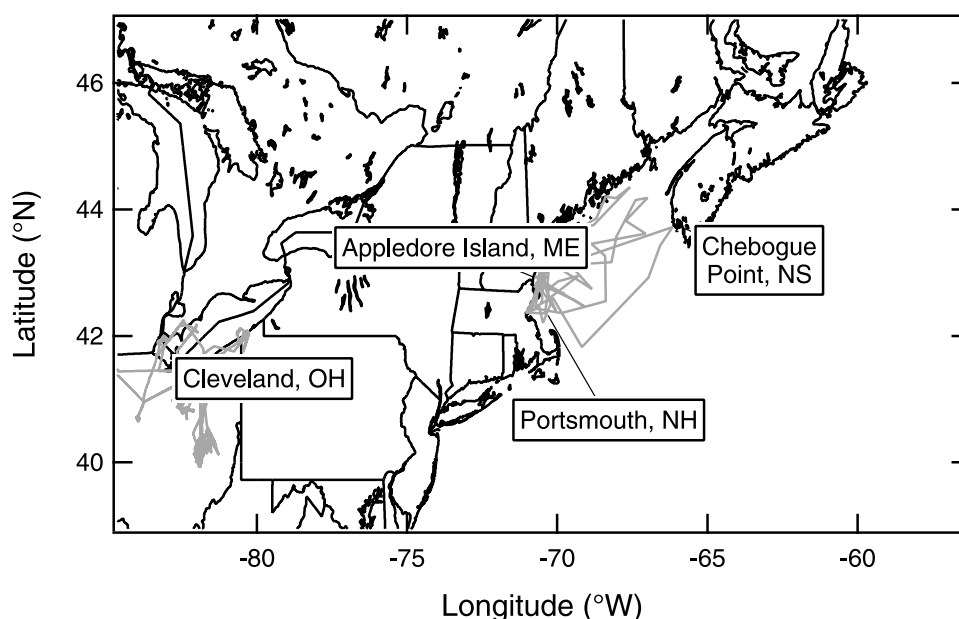
<sup>2</sup>Department of Chemical Engineering, California Institute of Technology, Pasadena, California, USA.

<sup>3</sup>Pacific Marine Environmental Laboratory, NOAA, Seattle, Washington, USA.

<sup>4</sup>School of Earth, Atmospheric and Environmental Science, University of Manchester, Manchester, UK.

<sup>5</sup>Department of Environmental Sciences, Policy and Management, University of California, Berkeley, California, USA.

<sup>6</sup>Aerodyne Research, Inc., Billerica, Massachusetts, USA.



**Figure 1.** Sampling platform locations, showing the Chebogue Point site (Nova Scotia, Canada), the Appledore Island site (Maine), the R/V *Ronald H. Brown* cruise track (started in Portsmouth, NH), and CIRPAS Twin Otter flight tracks (based in Cleveland, Ohio) in grey.

Recent work has provided a calibrated methodology for quantitative estimates of the functional group composition of organic aerosol [Maria *et al.*, 2002, 2003].

[4] The organic fraction of particles is composed of a large variety of compounds: alkanes, alkenes and aromatic compounds, monocarboxylic and dicarboxylic acids, alcohols and saccharides, organic sulfur compounds (sulfates and sulfonic acids), organic nitrogen compounds (organic nitrates, amines, imines, and amino acids), and polyfunctional oligomers. Some of these organic families are more hydrophobic and others show higher water solubility and uptake. Organic particles that are dominated by saturated and unsaturated carbon chains are less hygroscopic than an aerosol mass characterized by higher concentration of polar groups (hydroxyl and carboxylic acids, for example). The presence of heteroatoms in organic molecules may increase both their polarity and water solubility. Oxygenated functional groups are more common than sulfur and nitrogen in atmospheric particles.

[5] Oxygenated compounds are usually characteristic of SOA [Gao *et al.*, 2004; Lim and Ziemann, 2005] but may be found in primary aerosol particles as well (e.g., dicarboxylic acids have been identified in primary sea salt particles [Mochida *et al.*, 2002]). Carboxylic acids and saccharides have been detected in forest biogenic emissions [Graham *et al.*, 2003]. Ketones are components of plant waxes that contribute to atmospheric particles in rural areas [Simoneit and Mazurek, 1982]. The contribution of oxygenated compounds to total organic mass depends on both the aerosol sources and the chemical and physical processes that affect the atmospheric processing of the aerosol particles.

[6] During the ICARTT experiment in summer 2004, submicron particle samples were collected at four different platforms. Organic functional groups were quantified by Fourier Transform Infrared (FTIR) spectroscopy. This study

compares the similarities and differences in the measured unsaturated aliphatic C=C–H and saturated aliphatic C–C–H groups, oxygenated organic functional groups, organic mass to organic carbon ratios to illustrate the trends in organic composition at each platform, and the systematic differences between the upwind continental particles measured in Ohio and the downwind coastal particles on Chebogue Point, Appledore Island, and the R/V *Ronald H. Brown*. This study also affords the unique opportunity for a comprehensive intercomparison of four independent methods of quantifying organic composition.

## 2. Measurements

[7] Submicron aerosol samples have been collected in summer 2004, during the ICARTT experiment, at two ground stations (Chebogue Point, Nova Scotia, Canada, and Appledore Island, Maine) and on two mobile platforms (the CIRPAS Twin Otter and the NOAA R/V *Ronald H. Brown*) [Fehsenfeld *et al.*, 2006]. Measurements at Chebogue Point and Appledore Island included a suite of online gas and particle chemical and physical measurements [Williams *et al.*, 2007; Russell *et al.*, 2007; Fischer *et al.*, 2006]. The CIRPAS Twin Otter performed a total of 12 flights, investigating Ohio power plant emissions and regional aerosol background properties [Sorooshian *et al.*, 2006]. The R/V *Ronald H. Brown* collected particle samples in the Gulf of Maine, sampling urban plumes from Boston and New York, as well as aged industrial plumes from Midwestern regions [Quinn *et al.*, 2006]. Ground platform locations and flight and cruise tracks are illustrated in Figure 1.

[8] Aerosol particles were sampled on 37 mm Teflon filters for between 30 min and 24 hours, depending on aerosol loading. Samples collected during the Twin Otter flights are generally characterized by a shorter collection

**Table 1.** FTIR Absorption Characteristics for Organic Functional Groups

Functional Group	Absorption Frequencies, $\text{cm}^{-1}$	Quantified Peak, $\text{cm}^{-1}$	Absorptivity, $\text{abs}^{-1}\text{a}$	Detection Limit, $\mu\text{mol}$ of Bond
Saturated aliphatic C-C-H	1450, 2800–3000	2850–2920	0.895	0.013
Unsaturated aliphatic C=C-H	2900–3100	2980	3.8	0.122
Aromatic C=C-H	3000–3100	3050	8.7	0.035
Carbonyl C=O	1640–1850	1720	0.062	0.009
Organic hydroxyl C-OH	3100–3500	3350	0.057	0.006
Organosulfur C-O-S	876	876	0.031	0.002
Amines C-NH	3400, 1630	—	—	—

<sup>a</sup> Absorptivity is the micromole of functional group per unit of peak area (in absorbance). The calibration of absorptivity may be instrument-specific with values that differ slightly on the basis of the detector used [cf. *Maria et al.*, 2003].

interval in order to collect two or more samples during the 4 to 6 hour flights. Teflon filters were stored in polystyrene petri dishes, sealed with Teflon tape and kept at approximately  $-4^{\circ}\text{C}$  for later analysis. Identification and quantification of organic and inorganic functional groups were carried out by transmission FTIR spectroscopy. During the ICARTT 2004 campaign more than 250 samples and an equal number of field blanks were collected and analyzed on the four platforms. None of the blanks showed detectable quantities of organic functional groups.

## 2.1. FTIR Spectroscopy

[9] FTIR analyses were completed with a Bruker Tensor 27 FTIR Spectrometer with a DTGS detector. FTIR spectra were measured in transmission mode in the range between 400 and  $4000\text{ cm}^{-1}$ , with a spectral resolution of  $4\text{ cm}^{-1}$  and 32 scans for each spectrum. Blank filters were scanned before sampling and aerosol spectra were obtained by subtraction of the blank spectra from the corresponding sample spectra. Ambient aerosol spectra are usually characterized by broad double peaks in the absorption from 2800 to  $3400\text{ cm}^{-1}$  for ammonium. This interference was corrected by subtracting a reference spectrum of ammonium sulfate, normalized to the ammonium peak at  $3200\text{ cm}^{-1}$ . Table 1 lists the functional groups identified during the ICARTT experiment and the location of the associated peak in absorbance. Here the terms “saturated aliphatic C-C-H groups” and “unsaturated aliphatic C=C-H groups” indicate C-H bonds typical of alkane and alkene molecules, respectively. “Aromatic C=C-H groups” refer to C-H bonds from a benzenic ring structure. The identification of functional groups used multiple absorption peaks, while the quantification was based on an absorption peak with negligible interference. 1-docosanol, anthracene, sodium benzoate, 1-docosene, sodium ethyl-sulfate, citric acid and adipic acid have been employed as calibration standards [*Maria et al.*, 2002, 2003]. The absorbance for the detected species varies linearly with the number of moles of bonds and is independent of mixture composition [*Maria et al.*, 2002, 2003]. The error associated with the calibration of a single reference compound is typically 10% of the measured concentration for most functional groups, with the exception of organic hydroxyl C-OH groups for which interference from water, ammonia, and amines increases the error to 22%. The combined uncertainty of reference compounds, peak integration, and absorption artifacts is between 5% and 22% [*Russell*, 2003].

[10] Organic sulfur compounds have been identified in aerosol particles by an absorption peak at  $876\text{ cm}^{-1}$  [*Maria*

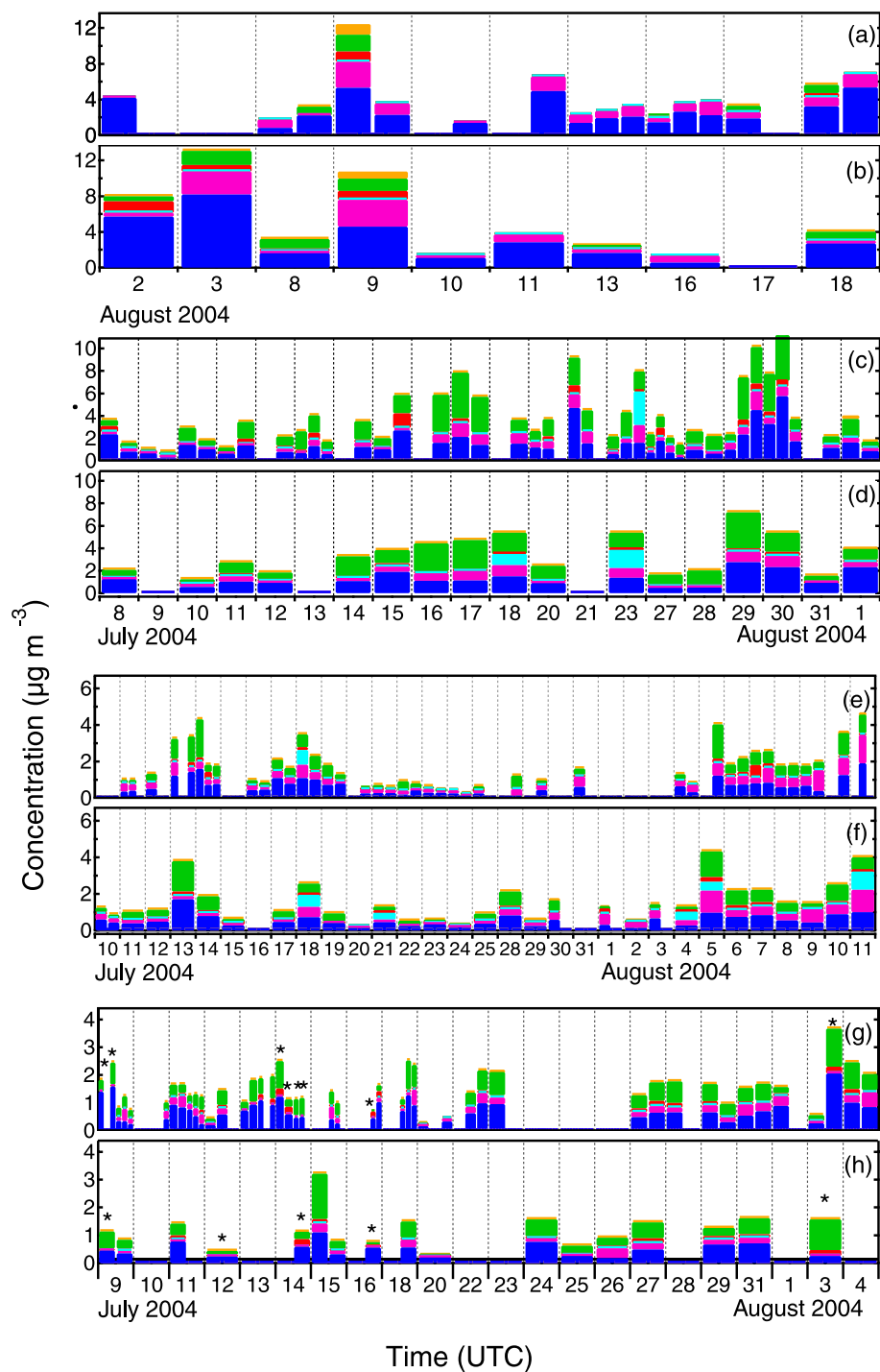
*et al.*, 2003; *Blando et al.*, 1998]. Carbonate and hydrogen sulfate ions also absorb in the region between 850 and  $890\text{ cm}^{-1}$  ([http://www.aist.go.jp/RIODB/SDBS/cgi-bin/cre\\_index.cgi](http://www.aist.go.jp/RIODB/SDBS/cgi-bin/cre_index.cgi)). Reference samples of carbonates, hydrogen sulfate, and sodium ethylsulfate were prepared using an atomizer (TSI Inc., model 3076) to collect deposits on Teflon filters, which were rinsed with hexane and acetone to separate the organic sulfur compounds by dissolving in organic solvents without removing the less soluble carbonate and hydrogen sulfate ions [*Maria et al.*, 2002]. This sequential rinsing with hexane and acetone was used for those samples with an absorption peak located in the region  $850\text{ cm}^{-1}$ – $890\text{ cm}^{-1}$  to distinguish organosulfur compounds from carbonate and hydrogen sulfate ions.

[11] Amines are characterized by two absorption peaks located at  $3400\text{ cm}^{-1}$  and  $1630\text{ cm}^{-1}$ . Amines were present below detectable amounts for all samples collected at Chebogue Point, on the Twin Otter, and on the R/V *Ronald H. Brown*. Significant amine absorption signals were observed in a few samples collected at Appledore Island. Identification of amines is noted in Figure 2, although their quantification was not possible during this project [*Maria et al.*, 2003].

[12] To convert calculated molar concentration to the mass concentration of equivalent organic carbon (OC), we assume that saturated carbon chains are present mainly as  $\text{CH}_2$  groups [*Maria et al.*, 2002]. The concentration of saturated carbon was obtained by multiplying the saturated aliphatic C-C-H bond molar concentration by 6 (corresponding to carbon molecular mass divided by 2 C-H bonds per  $\text{CH}_2$  unit). Contributions to organic carbon from unsaturated aliphatic C=C-H, aromatic C=C-H, and carbonyl C=O groups were calculated by multiplying the C=C-H and C=O molar concentrations by 12. To calculate organic mass (OM), the OC concentrations have been scaled to include the mass of associated hydrogen, sulfur, and oxygen atoms [*Maria et al.*, 2002]. Organic mass (OM) is the sum of both OC and associated heteroatoms in carbonyl C=O groups, saturated and unsaturated aliphatic C-H groups, aromatic C=C-H groups, organic hydroxyl C-OH groups, and sulfur from organosulfur C-O-S groups. OM values reported here neglect the contribution of organic nitrogen functional groups.

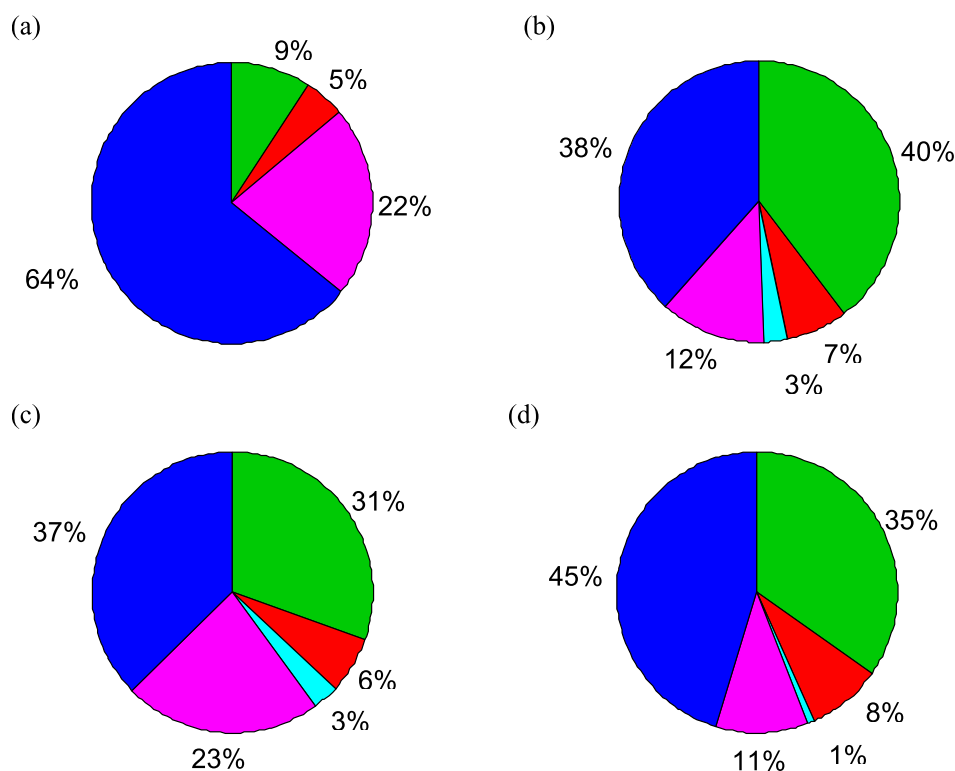
## 2.2. Air Mass Categorization

[13] Air masses sampled at Chebogue Point were categorized using the retroplume summaries calculated by FLEXPART (<http://www.esrl.noaa.gov/csd/metproducts/icartt2004/>). The FLEXPART model is run using two



**Figure 2.** Temporal trends of the measured functional group composition: (a and b) Twin Otter, (c and d) R/V *Ronald H. Brown*, (e and f) Chebogue Point, and (g and h) Appledore Island. For each platform, the lower plot (Figures 2b, 2d, 2f, and 2h) corresponds to functional group composition of cumulative samples (12 or 24 hour collection time), and the upper plot (Figures 2a, 2c, 2e, and 2g) reports simultaneous shorter time samples (3, 4, 6 or 8 hour collection time). All panels show saturated aliphatic C-C-H groups (blue), organic hydroxyl C-OH groups from alcohol and carboxylic acids (pink), aromatic C=C-H groups (light blue), unsaturated aliphatic C=C-H groups (red), carbonyl C=O groups (green), and organosulfur C-O-S groups (yellow) mass concentration. Samples marked by asterisks contained amine C-NH groups.





**Figure 3.** Project average composition of organic mass for (a) Twin Otter, (b) R/V *Ronald H. Brown*, (c) Chebogue Point, and (d) Appledore Island. The color assignments for the organic functional group mass fractions are the same as in Figure 2.

meteorological input data (Global Forecast System model and ECMWF model) with a global resolution of  $1 \times 1^\circ$  and a regional resolution of  $0.36 \times 0.36^\circ$ . FLEXPART is a particle dispersion model that uses the Frost and McKeene inventory for North America with a spatial resolution of 4 km. Air masses sampled at Chebogue Point and Appledore Island were categorized as “U.S.” or “Canada” on the basis of visual inspection of retrorplume calculations of the most important emission sources. We considered retrorplume trajectories over the 5 days before reaching the sampling platform and their evolution during the sampling interval, including 4 backward simulations during each 12 hour sample. If all simulations for a sampling interval showed the same source locations, the sample was assigned to one of the two source categories. Air mass categorizations for the R/V *Ronald H. Brown* showed that most of those samples were dominated by U.S. influenced air masses [Quinn *et al.*, 2006], whereas the coastal platforms sampled several days that could be characterized by two distinct types of air masses, those dominated by U.S. emissions and those dominated by Canada emissions.

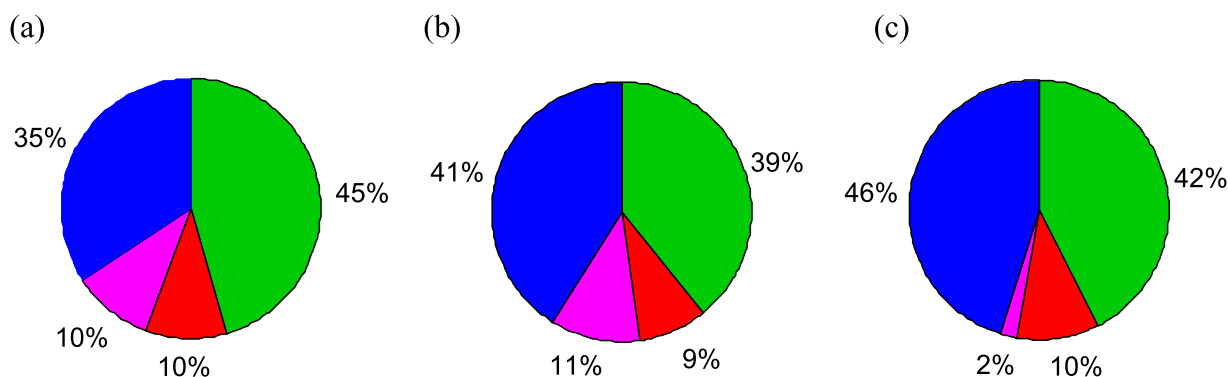
### 3. Results and Discussion

[14] Saturated aliphatic C-C-H groups, unsaturated aliphatic C=C-H groups, organic hydroxyl C-OH groups from alcohols and carboxylic acids, carbonyl C=O groups from carbonyl in ketones, aldehydes, and carboxylic acids, organosulfur C-O-S groups, ammonium, sulfate, and nitrate were detected during most of the ICARTT 2004 study on all sampling platforms. Figure 2 shows the temporal trend of OM

concentration. The average OM concentrations at Chebogue Point and Appledore Island were  $1.7$  and  $1.4 \mu\text{g m}^{-3}$ , respectively. Higher OM concentrations were observed during the R/V *Ronald H. Brown* cruise ( $3.6 \mu\text{g m}^{-3}$ ) and during the CIRPAS Twin Otter flights ( $4.6 \mu\text{g m}^{-3}$ ). The maximum OM concentration measured on board the Twin Otter was  $13 \mu\text{g m}^{-3}$ . This high OM concentration is probably a result of the proximity to large emission sources, such as coal burning power plants in Ohio [Sorooshian *et al.*, 2006].

[15] OM was dominated by saturated aliphatic C-C-H groups (as shown in Figure 3). The Chebogue Point and Appledore Island platforms show average saturated aliphatic C-C-H concentration of  $0.6 \mu\text{g m}^{-3}$ . R/V *Ronald H. Brown* and Twin Otter saturated aliphatic C-C-H concentrations were  $1.4$  and  $2.9 \mu\text{g m}^{-3}$ , respectively. The average carbonyl C=O group concentration ranged between  $0.4$  and  $0.5 \mu\text{g m}^{-3}$  on Chebogue Point, Appledore Island, and the Twin Otter and reached as high as  $1.4 \mu\text{g m}^{-3}$  for R/V *Ronald H. Brown*.

[16] Comparison of the time series of functional groups on the four sampling platforms in Figure 2 shows events that appear to be correlated at two or more different sampling platforms. At Chebogue Point from 12 July (during the biomass burning event reported by Duck *et al.* [2007]), the contribution of carbonyl C=O groups to organic mass started rising. Similar trends in oxygenated functional group composition occurred with a delay of about 12 hours at Appledore Island and on the R/V *Ronald H. Brown* (during the biomass burning event reported by Quinn *et al.* [2006]). During the time period between 12 July and



**Figure 4.** Project average OM composition on (a) the R/V *Ronald H. Brown*, (b) Chebogue Point, and (c) Appledore Island from 12 to 14 July. The color assignments for the organic functional group mass fractions is the same as in Figure 2.

noon on 13 July, Appledore Island was subject to northerly wind. The R/V *Ronald H. Brown* measured along the coast of New England and sampled air masses coming from the North, as indicated by retrorplume calculation. Figure 4 reports the average composition of the organic mass during the event occurred on 12 July, for R/V *Ronald H. Brown*, Chebogue Point and Appledore Island samples. At Chebogue Point, for the time period that goes from 12 to 13 July, 41% of organic mass is composed of saturated aliphatic C-C-H groups, 39% of carbonyl C=O groups, and 11% of organic hydroxyl C-OH groups. R/V *Ronald H. Brown* OM composition is characterized by a similar contribution of saturated aliphatic C-C-H groups (35%), organic hydroxyl C-OH groups (10%) and carbonyl C=O groups (45%). Appledore Island organic mass composition is similar to Chebogue Point, although a smaller contribution from organic hydroxyl C-OH groups was observed. The average functional group contribution to the total OM for 12–13 July differs from the project average reported in Figure 3 by its higher fraction of carbonyl C=O groups and lower fraction of organic hydroxyl C-OH groups.

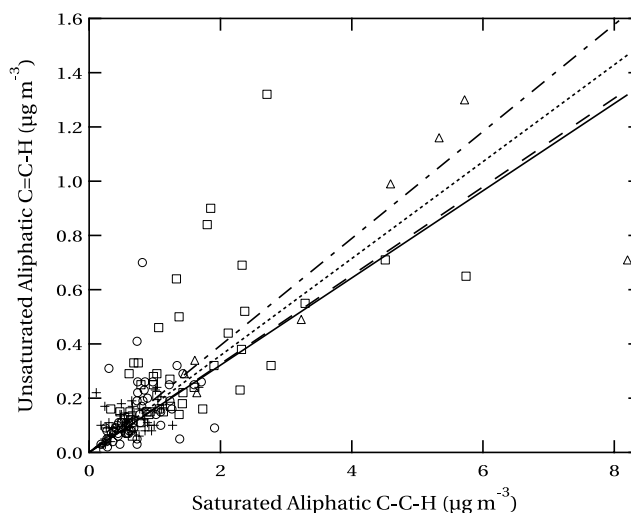
[17] A second event observed at multiple platforms in the ICARTT region took place from 17 to 18 July. On 18 July, R/V *Ronald H. Brown* and Chebogue Point measurements showed similar concentrations in carbonyl C=O groups and aromatic C=C-H groups. The maximum concentration of aromatic C=C-H groups measured during this event was  $1 \mu\text{g m}^{-3}$  on the R/V *Ronald H. Brown* (project average equal to  $0.1 \mu\text{g m}^{-3}$ ) and  $0.8 \mu\text{g m}^{-3}$  at Chebogue Point (project average equal to  $0.05 \mu\text{g m}^{-3}$ ). From 16 to 19 July Chebogue Point was influenced by southerly wind, with retrorplume calculations indicating air masses coming from the Gulf of Maine. The organic composition was similar to the project average during the sample taken during 17–18 July, with the single sample being insufficient to show any statistically significant differences.

### 3.1. Saturated and Unsaturated Aliphatic Organic Functional Groups

[18] During most of the sampling period, the organic mass is dominated by the contribution of saturated aliphatic C-C-H and unsaturated aliphatic C=C-H groups. Both saturated and unsaturated organic compounds are released as primary emissions from both fossil fuel combustion and

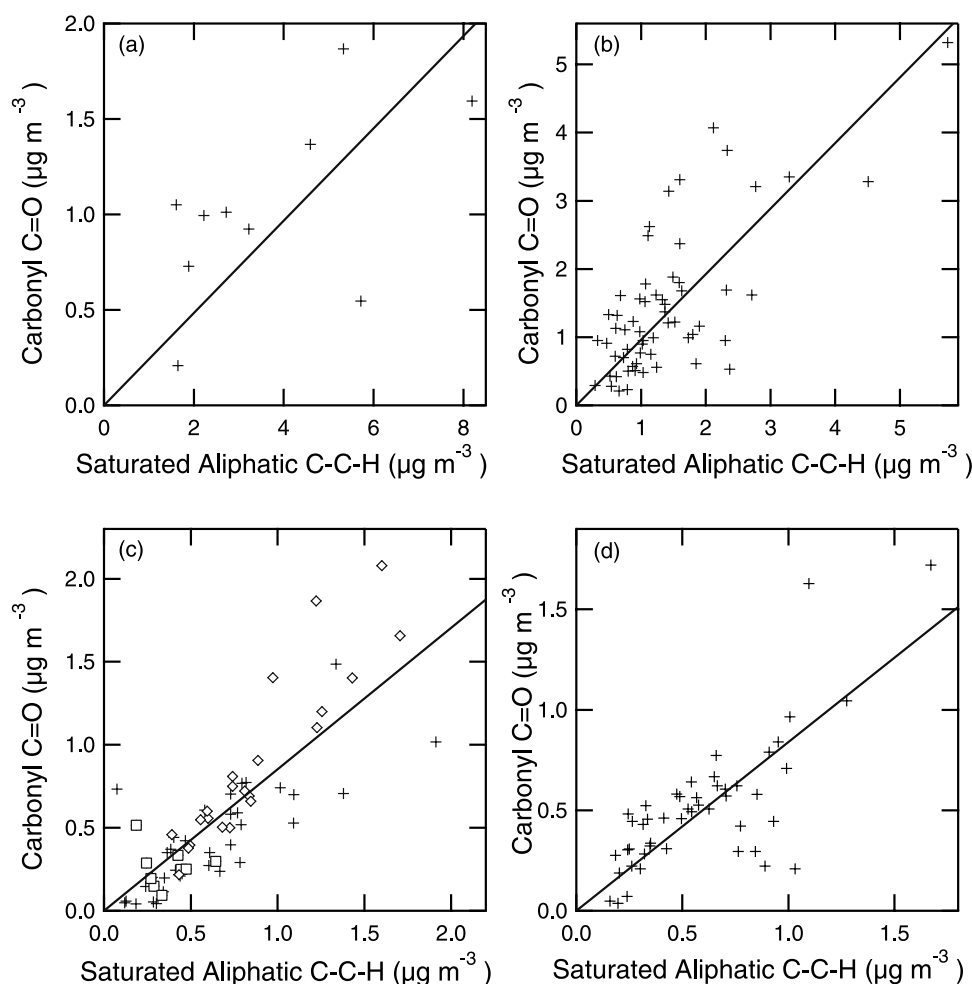
biogenic emissions. Unsaturated aliphatic C=C-H groups can be produced during the combustion processes by dehydration of alcohols or cracking of alkanes during incomplete combustion [Oros and Simoneit, 2000; Simoneit, 2002]. Unsaturated aliphatic C=C-H groups are also produced from oxidation of aromatic units [Johnson et al., 2005; Seinfeld and Pandis, 1998]. Figure 5 shows unsaturated aliphatic C=C-H relative to saturated aliphatic C-C-H concentration for the four sampling platforms.

[19] Figure 5 shows four weak linear relationships in the ratios of unsaturated to saturated organic compounds, indicating similar ratios during the sampling period with small average differences for each of the four platforms. Twin Otter samples are characterized by unsaturated aliphatic C=C-H to saturated aliphatic C-C-H group ratios equal to 0.10 ( $n = 25$ ); higher ratios were observed at the coastal platforms for Appledore Island (0.2,  $n = 65$ ), Chebogue



**Figure 5.** Ratios of saturated to unsaturated aliphatic C-H group concentration for Appledore Island (pluses), Chebogue Point (circles), R/V *Ronald H. Brown* (squares), and Twin Otter (triangles). Line fits for the different sampling sites are reported as solid line (Appledore Island), dotted line (Chebogue Point), dashed line (R/V *Ronald H. Brown*), and dot-dashed line (Twin Otter).





**Figure 6.** Ratios of carbonyl C=O to saturated aliphatic C-C-H group concentrations on (a) the Twin Otter, (b) the R/V *Ronald H. Brown*, (c) Chebogue Point, and (d) Appledore Island, indicated as pluses. For Chebogue Point, different symbols are used to indicate samples affected by Canada (diamond), U.S. (squares), and other (pluses) air masses.

Point (0.2,  $n = 43$ ), and the R/V *Ronald H. Brown* (0.2,  $n = 52$ ). These ratios are similar to the unsaturated to saturated C-H group concentration ratios of 0.2 to 0.5 which were measured by H-NMR of water soluble organic carbon (WSOC) from urban polluted areas [Fuzzi *et al.*, 2001; Decesari *et al.*, 2000]. The similarity of the average unsaturated to saturated aliphatic C-H group ratio observed at the three coastal sampling platforms suggests that those areas were often affected by air masses with similar sources. The higher average concentration of unsaturated compounds at the coastal platforms may indicate the larger contribution of biogenic sources or a lower contribution of saturated aliphatic C-C-H groups from unprocessed primary combustion emissions.

[20] Saturated aliphatic compounds dominate primary coal burning emissions [Oros and Simoneit, 2000]. For example, the bituminous coal combustion emission ratio of unsaturated to saturated aliphatic C-H is 0.02.

### 3.2. Oxygenated Organic Carbon

[21] Oxygenated functional groups (carbonyl C=O and organic hydroxyl C-OH) were observed on all platforms with concentrations that were often comparable to the

saturated aliphatic C-C-H group concentrations. Figure 6 shows carbonyl C=O group concentration relative to saturated aliphatic C-C-H concentration, for each platform. These molar ratios and correlation coefficients are reported in Table 2. The Twin Otter samples in Ohio were characterized by a lower molar ratio (0.1) compared to R/V *Ronald H. Brown* (0.5), Chebogue Point (0.5), and Appledore Island (0.4). The carbonyl C=O to saturated aliphatic C-C-H group molar ratios recorded on the R/V *Ronald H. Brown* and at the two coastal platforms are similar to the ratios measured by H-NMR on the WSOC of urban aerosol in the Po Valley, which ranged between 0.2 and 0.5 [Fuzzi *et al.*, 2001]. Overall the lower average carbonyl C=O group to saturated aliphatic C-C-H group ratio on the Twin Otter is consistent with the less aged emissions observed over Ohio [Sorooshian *et al.*, 2006] than those measured on the coastal platforms, as prior work indicated more carboxylic acids (containing more carbonyl groups) were typically associated with aged and secondary aerosol [Rogge *et al.*, 1993; Zhang *et al.*, 2005].

[22] The linear correlation between carbonyl C=O groups and saturated aliphatic C-C-H groups for each platform was significant at the 99% confidence level. The variability of

**Table 2.** Carbonyl C=O Group to Saturated Aliphatic C-C-H Group Molar and Average OM/OC Ratios for the Four Sampling Platforms and Air Mass Categories

Platform	C=O/C-H Molar Ratio <sup>a</sup>	OM/OC <sup>b</sup>
Twin Otter	0.1 (90)	1.4 (0.12) n = 25
R/V <i>Ronald H. Brown</i>	0.5 (99.9)	1.6 (0.14) n = 60
Appledore Island	0.4 (99.9)	1.5 (0.16) n = 79
Chebogue Point	0.5 (99.9) (Canada: 0.5 (99.9); United States: 0.3 (<75))	1.6 (0.14), n = 74 (Canada: 1.6 (0.11), n = 22; United States: 1.6 (0.18), n = 9)

<sup>a</sup>The significance of each linear regression was calculated by t-test and is reported in brackets.

<sup>b</sup>Standard deviation is reported between brackets, where “n” indicates number of samples for each platform and category.

the ratio of carbonyl C=O groups to saturated aliphatic C-C-H groups indicates a range of oxygenated organic aerosol compositions in the air masses sampled at each platform during the course of the project. To study the variability in the degree of oxidation of aerosol samples collected at Chebogue Point, the air masses measured have been separated according to the retroplume calculations. “Canada” and “U.S.” categories correspond to air masses affected mainly by Canadian or U.S. emissions. Samples at Chebogue Point associated with air masses from Canada are characterized by a carbonyl C=O to saturated aliphatic C-C-H groups molar ratio equal to 0.5. These samples also generally show a higher ratio of carbonyl C=O to saturated aliphatic C-C-H groups compared to air masses from the United States which had a ratio of 0.3. Figure 7 reports the temporal variation of carbonyl C=O to saturated aliphatic C-C-H groups molar ratio for Chebogue Point. Thermal desorption aerosol GCMS-FID (TAG) data show that compounds associated with biogenic emissions are often present in high concentrations in the air masses with retroplumes dominated by emission sources in Canada. For a detailed description of TAG measurements refer to Williams *et al.* [2007]. The FTIR functional group composition indicates that these aerosol particles associated with aged biogenic emissions are enriched in carbonyl C=O groups relative to saturated aliphatic C-C-H groups.

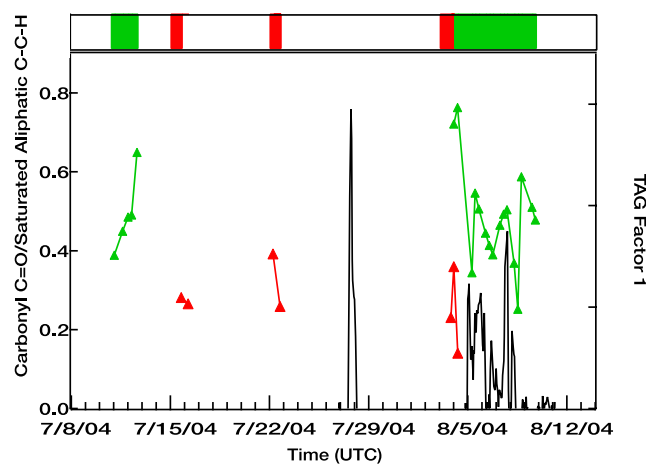
### 3.3. OM/OC Ratios

[23] The ratio of organic mass to organic carbon (OM/OC) describes the overall organic composition of aerosol particles, providing a distinction between organic compounds dominated by hydrocarbons with ratios ranging from 1 to 1.2 and OM containing a significant fraction of oxygen, sulfur and nitrogen which have OM/OC from 1.3 to more than 2 [Russell, 2003]. Ambient measurements of organic mass are still scarce. In addition to the FTIR technique used here, OM can be estimated from AMS measurements of organic fragments [Allan *et al.*, 2004; de Gouw *et al.*, 2005] or determined by elemental analysis of organic fraction after extraction with water or organic solvents [El-Zanan *et al.*, 2005]. For the 4 different platforms and 2 different air mass categories, Table 2 lists the OM/OC ratios calculated from FTIR functional group composition. Each sampling platform shows low variability in OM/OC, suggesting that organic composition during the ICARTT experiment was fairly constant at each platform. OM/OC measured on the R/V *Ronald H. Brown* in the Gulf of Maine agrees with other reports of OM/OC for urban and polluted continental locations, including a study performed

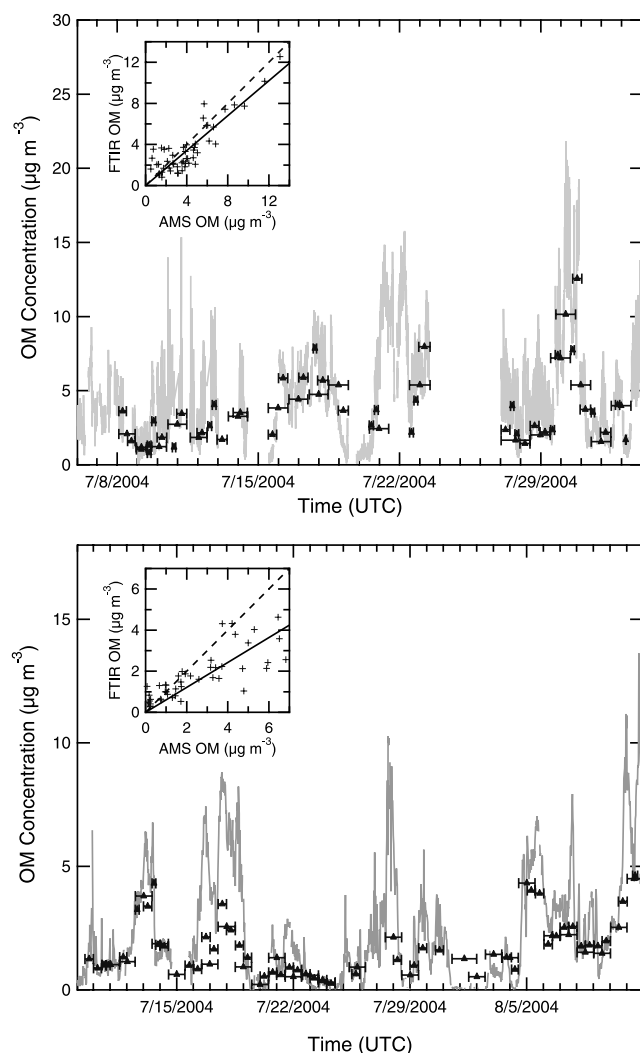
in the Gulf of Maine in 2002 in which OM/OC was equal to 1.8 [de Gouw *et al.*, 2005]. OM/OC reported for IMPROVE platforms ranges between 1.6 and 2.6 [El-Zanan *et al.*, 2005]. The lower OM/OC ratio recorded during the Twin Otter campaign can be explained by the observation that fresh emissions contain lower concentrations of oxidized functional groups which reduces the associated OM/OC ratio [Turpin and Lim, 2001]. Table 2 shows that OM/OC at Chebogue Point does not differ significantly for the two air mass retroplume emission categories.

### 3.4. Organosulfur Compounds

[24] Organosulfur compounds are a minor component of organic aerosol mass. Organosulfur compounds were detected at all four of the sampling platforms studied for ICARTT 2004, with a higher frequency at Chebogue Point. The organosulfur C-O-S functional group absorbance can be associated with either sulfuric or sulfonic esters. These classes of compounds may be produced by addition of sulfuric or sulfonic acid to alkenes or by esterification of hydroxyl group promoted by the same acids [Romero and Oehme, 2005]. In the aqueous aerosol particles, carbonyl



**Figure 7.** Time series of the ratio of carbonyl C=O groups to saturated aliphatic C-C-H group concentration ratio at Chebogue Point. The color of the symbols and the color bar at the top of the graph identify samples associated with air masses with emissions originating mostly from Canada (green) or the United States (red) (based on retroplume calculations). TAG factor 1 is a marker of biogenic emissions [Williams *et al.*, 2007] at Chebogue Point.



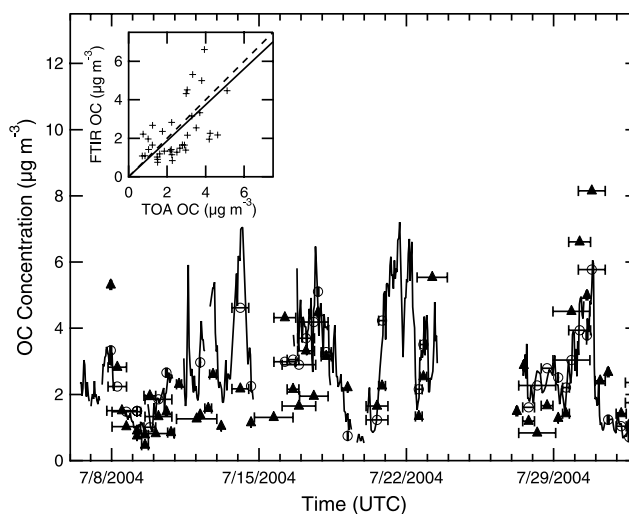
**Figure 8.** Comparison of AMS and FTIR OM on (a) the R/V *Ronald H. Brown* and (b) Chebogue Point. The time series of 5-min average AMS organic mass is shown as a grey line; FTIR organic mass is represented by black triangles. Horizontal error bars indicate the duration of the sampling time for each sample. Insets show scatterplots of AMS average OM versus FTIR OM for the times when sampling largely overlapped. The dashed line indicates the 1:1 ratio.

C=O functional groups may be converted into hydroxyl O-H group by several mechanisms including hydration and polymerization [Hastings *et al.*, 2005]. Reaction with sulfuric or sulfonic acid would produce sulfuric or sulfonic esters and would shift the partitioning of the original carbonyl compounds from the gas phase toward the particle phase. In this scenario, organosulfur compounds formation would explain the unusually high particle-to-gas phase distribution coefficient observed for some volatile carbonyl compounds [Hastings *et al.*, 2005]. Most of the samples in which organosulfur C-O-S groups were detected also had high organic mass loadings. Organosulfur C-O-S groups were detected only in samples that showed the simultaneous presence of sulfate and carbonyl species, with relative humidity higher than 80%.

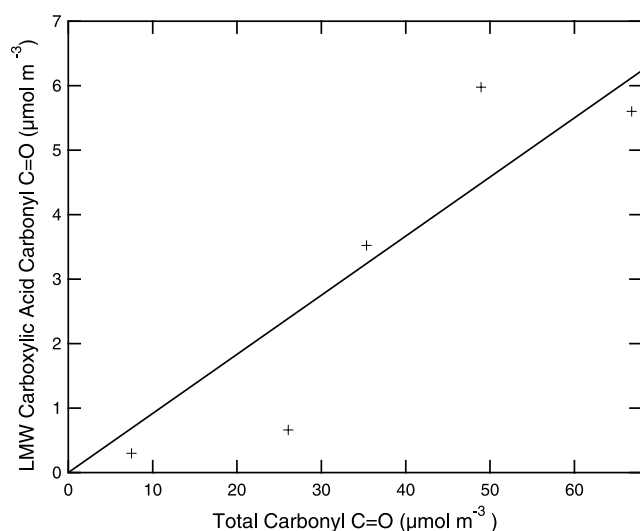
### 3.5. Intercomparison of FTIR With AMS OM and TOA OC

[25] During the ICARTT experiment AMS measurements were collected on Chebogue Point and the R/V *Ronald H. Brown*. AMS measurements were used to calculate OM of aerosol samples by summing contributions from mass fragments containing carbon atoms [Allan *et al.*, 2004; Quinn *et al.*, 2006]. The Aerodyne AMS measurements used quadrupole systems as described by Jayne *et al.* [2000] and Jimenez *et al.* [2003]. The instrument is capable of measuring the submicron, nonrefractory component of the aerosols, using the data analysis techniques described by Allan *et al.* [2003, 2004]. For the Chebogue Point OM concentration measurements, a collection efficiency of 0.5 and relative ionization efficiency of 1.4 were used. More details of the instruments and their results are published by Williams *et al.* [2007]. Figure 8 shows a comparison of the time series of AMS and FTIR organic mass concentrations for Chebogue Point and R/V *Ronald H. Brown*. The insets on Figures 8a and 8b show the quantitative correlation between the AMS and FTIR OM measurements, for which the AMS organic mass concentrations were integrated for the filter sampling period. At Chebogue Point the average FTIR to AMS ratio is  $0.6 \pm 0.1$  with a correlation coefficient equal to 0.80. The comparison of organic mass on the R/V *Ronald H. Brown* showed very similar trends in the time series in Figure 8a, and the inset shows that the ratio of the FTIR to AMS organic mass has a slope of  $0.9 \pm 0.1$  and a high correlation coefficient ( $r^2 = 0.87$ ).

[26] R/V *Ronald H. Brown* organic carbon (OC) was monitored by two Thermo-Optical Analysis (TOA) instruments with fast (45 to 105 min) and slow (4 to 8 hours)



**Figure 9.** Comparison of TOA and FTIR OC for R/V *Ronald H. Brown* measurements. Time series of high time resolution online TOA OC is shown as a grey line, low time resolution filter TOA OC is shown as circles, and FTIR organic carbon is shown as black triangles. Horizontal error bars indicate the duration of the sampling time for each sample. Inset shows scatterplots of low time resolution TOA filter sample OC versus simultaneous FTIR OC for the times when sampling largely overlapped. The dashed line indicates the 1:1 ratio.



**Figure 10.** Carbonyl C=O group molar concentration of PILS LMW carboxylic acids plotted as a function of total FTIR carbonyl C=O group molar concentration.

sampling times [Schauer *et al.*, 2003; Quinn *et al.*, 2006]. The FTIR is lower than AMS OM on average at both sites, which may result from underprediction of heteroatoms in the FTIR algorithm [Russell, 2003] or overprediction of mass fragments by the AMS calibration [Quinn *et al.*, 2006] for some organic compositions. Figure 9 shows the comparison of TOA OC with FTIR OC for samples collected simultaneously, with a slope of  $0.9 \pm 0.1$  and a correlation coefficient of 0.67. The higher scatter associated with the OC measurements may be a result of the uncertainty associated with inferring OC from measured functional groups [Russell, 2003].

### 3.6. LMW Carboxylic Acids and Carbonyl Groups on CIRPAS Twin Otter

[27] Low molecular weight (LMW) carboxylic acids were measured by PILS and IC during the Twin Otter flights over Ohio. The carboxylic acids measured were detected as oxalate, glyoxylate, glutarate, malonate, and pyruvate ions [Sorooshian *et al.*, 2006]. Oxalate concentration ranged between  $0.01 \mu\text{g m}^{-3}$  and  $0.3 \mu\text{g m}^{-3}$  during the sampling period overlapping to filter collection. Concentrations of glyoxylate, glutarate, malonate and pyruvate were generally one or two orders of magnitude lower than oxalate. The carbonyl C=O group fraction of the total measured LMW carboxylic acids was calculated for each FTIR sampling period and compared to the total carbonyl C=O group concentration determined by FTIR in Figure 10. Figure 10 reports carbonyl C=O group concentration from LMW carboxylic acid relative to total carbonyl C=O group concentration measured by FTIR. The number of points available for the comparison was limited but shows a linear correlation coefficient of 0.82 ( $n = 5$ ). The slope of the fit shows that the LMW carboxylic acids represent 9% of the total carbonyl C=O groups detected by FTIR.

## 4. Conclusions

[28] Analysis by FTIR spectroscopy of aerosol particle samples collected at four different locations in eastern North

America show high concentrations of saturated aliphatic C-C-H groups and carbonyl C=O groups. The functional group composition shows significant differences across the ICARTT region: The Twin Otter sampled near large sources of primary organic emissions (including several large regional power plants) and measured lower unsaturated to saturated aliphatic C-C-H groups and lower OM/OC ratios compared to the coastal platforms (Chebogue Point, Apple-dore Island, and the R/V *Ronald H. Brown*). The average OM/OC ranged between 1.4 (for Twin Otter in Ohio and Chebogue Point) and 1.6 (for R/V *Ronald H. Brown* and Chebogue Point). Organic particles collected during the Twin Otter flights over Ohio show a lower carbonyl C=O group concentration relative to saturated aliphatic C-C-H group concentration than samples collected at the coastal locations, suggesting that fresh emissions are predominant in those samples.

[29] Some of the variability within the samples at each platform can be attributed to changes in air masses, with those air masses associated with similar regional sources also having comparable functional group composition. Retroplume analysis for Chebogue Point samples suggested that air masses that reached this location from Canada and showed TAG factors that were indicative of biogenic emissions, were characterized by higher carbonyl C=O group concentration relative to saturated aliphatic C-C-H groups, compared to those air masses dominated by U.S. sources.

[30] Intercomparison of independent techniques for measuring the total OM and OC at two of the sampling locations (i.e., Chebogue Point and R/V *Ronald H. Brown*) showed that the two techniques generally track each other with time (with slopes of 0.6 and 0.9, respectively) but the linear correlations show a high variability in the data, as is typical for intercomparisons of organic measurements [Turpin and Lim, 2001]. Comparison of carbonyl C=O group concentration with LMW carboxylic acid concentration shows that LMW carboxylic acids represented approximately 9% of the total observed carbonyl C=O groups for samples collected near plumes associated with coal power plants.

[31] **Acknowledgments.** This multiplatform research effort was made possible by seed funding from the James S. McDonnell Foundation Award for 21st Century Science. Subsequent development, training, and analysis were supported by NOAA grant NA17RJ1231. Additional support and field measurement opportunities were provided by National Science Foundation grant ATM04-01611. We are grateful to Derek Coffman, Susanne Hering, Nathan Kreisberg, Roland von Glasow, Susanne Marquardt, Cynthia Randles, Kathryn Holderness, Alice Delia, Jennifer Ayers, Alex Pszenny, and William Keene for assistance in collecting samples and to Andreas Stohl for compiling the FLEXPART analyses. This paper is also contribution 138 to the Shoals Marine Laboratory.

## References

- Allan, J. D., J. L. Jimenez, P. I. Williams, M. R. Alfarra, K. N. Bower, J. T. Jayne, H. Coe, and D. R. Worsnop (2003), Quantitative sampling using an Aerodyne aerosol mass spectrometer: 1. Techniques of data interpretation and error analysis, *J. Geophys. Res.*, **108**(D3), 4090, doi:10.1029/2002JD002358.
- Allan, J. D., et al. (2004), A generalised method for the extraction of chemically resolved mass spectra from Aerodyne aerosol mass spectrometer data, *J. Aerosol Sci.*, **35**(7), 909–922.
- Blanco, A. J., and R. G. McIntyre (1972), Infrared spectroscopic view of atmospheric particulates over El Paso, Texas, *Atmos. Environ.*, **6**, 557–562.
- Blando, J. D., R. J. Porcja, T. H. Li, D. Bowman, P. J. Liroy, and B. J. Turpin (1998), Secondary formation and the Smoky Mountain organic aerosol:



- An examination of aerosol polarity and functional group composition during SEAVS, *Environ. Sci. Technol.*, **32**, 604–613.
- Dangler, M., S. Burke, S. V. Hering, and D. T. Allen (1987), A direct FTIR method for identifying functional-groups, in size segregated atmospheric aerosols, *Atmos. Environ.*, **21**, 1001–1004.
- Decesari, S., M. C. Facchini, and S. Fuzzi (2000), Characterization of water soluble organic compounds in atmospheric aerosol: A new approach, *J. Geophys. Res.*, **105**, 1481–1489.
- de Gouw, J. A., et al. (2005), Budget of organic carbon in a polluted atmosphere: Results from the New England Air Quality Study in 2002, *J. Geophys. Res.*, **110**, D16305, doi:10.1029/2004JD005623.
- Duck, T. J., et al. (2007), Transport of forest fire emissions from Alaska and the Yukon Territory to Nova Scotia during summer 2004, *J. Geophys. Res.*, doi:10.1029/2006JD007716, in press.
- El-Zanan, H. S., D. H. Lowenthal, B. Zielinska, J. C. Chow, and N. Kumar (2005), Determination of the organic aerosol mass to organic carbon ratio in IMPROVE samples, *Chemosphere*, **60**, 485–496.
- Fehsenfeld, F. C., et al. (2006), International Consortium for Atmospheric Research on Transport and Transformation (ICARTT): North America to Europe—Overview of the 2004 summer field study, *J. Geophys. Res.*, **111**, D23S01, doi:10.1029/2006JD007829.
- Fischer, E., A. Pszenny, W. Keene, J. Maben, A. Smith, A. Stohl, and R. Talbot (2006), Nitric acid phase partitioning and cycling in the New England coastal atmosphere, *J. Geophys. Res.*, **111**, D23S09, doi:10.1029/2006JD007328.
- Fuzzi, S., S. Decesari, M. C. Facchini, E. Matta, and M. Mircea (2001), A simplified model of the water soluble organic component of atmospheric aerosol, *Geophys. Res. Lett.*, **20**, 4079–4082.
- Gao, S., M. Keywood, N. L. Ng, J. Suratt, V. Varutbangkul, R. Bahreini, R. C. Flagan, and J. H. Seinfeld (2004), Low-molecular-weight and oligomeric components in secondary organic aerosol from the ozonolysis of cycloalkenes and  $\alpha$ -pinene, *J. Phys. Chem. A*, **108**, 10,147–10,164.
- Graham, B., et al. (2003), Composition and diurnal variability of the natural Amazonian aerosol, *J. Geophys. Res.*, **108**(D24), 4765, doi:10.1029/2003JD004049.
- Hastings, W. P., C. A. Koehler, E. L. Bailey, and D. O. De Hann (2005), Secondary organic aerosol formation by glyoxal hydration and oligomer formation: Humidity effects and equilibrium shifts during analysis, *Environ. Sci. Technol.*, **39**, 8728–8735.
- Jayne, J. T., D. C. Leard, X. F. Zhang, P. Davidovits, K. A. Smith, C. E. Kolb, and D. R. Worsnop (2000), Development of an aerosol mass spectrometer for size and composition analysis of submicron particles, *Aerosol Sci. Technol.*, **33**, 49–70.
- Jimenez, J. L., et al. (2003), Ambient aerosol sampling using the Aerodyne Aerosol Mass Spectrometer, *J. Geophys. Res.*, **108**(D7), 8425, doi:10.1029/2001JD001213.
- Johnson, D., M. C. Jenkin, K. Wirtz, and M. Martin-Reviejo (2005), Simulating the formation of secondary organic aerosol from the photo-oxidation of aromatic hydrocarbons, *Environ. Chem.*, **2**, 35–48.
- Kim, J., S.-C. Yoon, A. Jefferson, and S.-W. Kim (2006), Aerosol hygroscopic properties during Asian dust, pollution, and biomass burning episodes at Gosan, Korea in April 2001, *Atmos. Environ.*, **40**, 1550–1560.
- Lim, Y. B., and P. J. Ziemann (2005), Products and mechanism of secondary organic aerosol formation from reaction of n-alkanes with OH radicals in the presence of  $\text{NO}_x$ , *Environ. Sci. Technol.*, **39**, 9229–9236.
- Maria, S. F., L. M. Russell, B. J. Turpin, and R. J. Porcja (2002), FTIR measurements of functional groups and organic mass in aerosol samples over the Caribbean, *Atmos. Environ.*, **36**, 5185–5196.
- Maria, S. F., L. M. Russell, B. J. Turpin, R. J. Porcja, T. L. Campos, R. J. Weber, and B. J. Huebert (2003), Source signature of carbon monoxide and organic functional groups in Asian Pacific Regional Aerosol Characterization Experiment (ACE-Asia) submicron aerosol types, *J. Geophys. Res.*, **108**(D23), 8637, doi:10.1029/2003JD003703.
- Markowicz, K. M., P. J. Flatau, P. K. Quinn, C. M. Carrico, M. K. Flatau, A. M. Vogelmann, D. Bates, M. Liu, and M. J. Rood (2003), Influence of relative humidity on aerosol radiative forcing: An ACE-Asia experiment perspective, *J. Geophys. Res.*, **108**(D23), 8662, doi:10.1029/2002JD003066.
- Mochida, M., Y. Kitamori, K. Kawamura, Y. Nojiri, S. Yukihito, and K. Suzuki (2002), Fatty acids in the marine atmosphere: Factors governing their concentrations and evaluation or organic films on sea-salt particles, *J. Geophys. Res.*, **107**(D17), 4325, doi:10.1029/2001JD001278.
- Oros, D. R., and B. R. T. Simoneit (2000), Identification and emission rates of molecular tracers in coal smoke particulate matter, *Fuel*, **79**, 515–536.
- Quinn, P. K., et al. (2006), Impacts of sources and aging on submicrometer aerosol properties in the marine boundary layer across the Gulf of Maine, *J. Geophys. Res.*, **111**, D23S36, doi:10.1029/2006JD007582.
- Rogge, W. F., M. A. Mazurek, L. M. Hildemann, G. R. Cass, and B. R. T. Simoneit (1993), Quantification of urban organic aerosols at a molecular level: Identification, abundance and seasonal variation, *Atmos. Environ.*, **27**, 1309–1330.
- Romero, F., and M. Oehme (2005), Organosulfates—A new component of humic-like substances in atmospheric aerosols?, *J. Atmos. Chem.*, **52**, 283–294.
- Russell, L. M. (2003), Aerosol organic-mass-to-organic-carbon ratio measurements, *Environ. Sci. Technol.*, **37**, 2982–2987.
- Russell, L. M., A. A. Mensah, E. V. Fischer, B. C. Sive, R. K. Varner, W. C. Keene, J. Stutz, and A. A. P. Pszenny (2007), Nanoparticle growth following photochemical  $\alpha$ - and  $\beta$ -pinene oxidation at Appledore Island during ICARTT/CHAIOS 2004, *J. Geophys. Res.*, doi:10.1029/2006JD007736, in press.
- Saxena, P., and L. M. Hildemann (1996), Water-soluble organics in atmospheric particles: A critical review of the literature and application of thermodynamics to identify candidate compounds, *J. Atmos. Chem.*, **24**, 57–109.
- Schauer, J. J., et al. (2003), ACE-Asia intercomparison of a thermal-optical method for the determination of particle-phase organic and elemental carbon, *Environ. Sci. Technol.*, **37**, 993–1001.
- Seinfeld, J. H., and S. N. Pandis (1998), *Atmospheric Chemistry and Physics*, pp. 277–282, John Wiley, Hoboken, N. J.
- Simoneit, B. R. T. (2002), Biomass burning—A review of organic tracers for smoke from incomplete combustion, *Appl. Geochem.*, **17**, 129–162.
- Simoneit, B. R. T., and M. A. Mazurek (1982), Organic matter of the troposphere. II. Natural background of biogenic lipid matter in aerosols over the rural western United States, *Atmos. Environ.*, **16**, 1967–1989.
- Sorooshian, A., et al. (2006), Oxalic acid in clear and cloudy atmospheres: Analysis of data from International Consortium for Atmospheric Research on Transport and Transformation 2004, *J. Geophys. Res.*, **111**, D23S45, doi:10.1029/2005JD006880.
- Turpin, B. J., and H.-J. Lim (2001), Species contributions to PM<sub>2.5</sub> mass concentrations: Revisiting common assumptions for estimating organic mass, *Aerosol Sci. Technol.*, **35**, 602–610.
- Turpin, B. J., P. Saxena, and E. Andrews (2000), Measuring and simulating particulate organics in the atmosphere: Problems and prospects, *Atmos. Environ.*, **34**, 2983–3013.
- Williams, B. J., A. H. Goldstein, D. B. Millet, R. Holzinger, N. M. Kreisberg, S. V. Hering, A. B. White, D. R. Worsnop, J. D. Allan, and J. L. Jimenez (2007), Chemical speciation of organic aerosol during the International Consortium for Atmospheric Research on Transport and Transformation 2004: Results from in situ measurements, *J. Geophys. Res.*, **112**, D10S26, doi:10.1029/2006JD007601.
- Zhang, Q., D. R. Worsnop, M. R. Canagaratna, and J. L. Jimenez (2005), Hydrocarbon-like and oxygenated organic aerosol in Pittsburgh: Insights into sources and processes of organic aerosol, *Atmos. Chem. Phys.*, **5**, 3289–3311.

J. D. Allan, School of Earth, Atmospheric and Environmental Science, University of Manchester, Manchester M13 9PL, UK.

T. S. Bates and P. K. Quinn, Pacific Marine Environmental Laboratory, NOAA, Seattle, WA 98115, USA.

R. C. Flagan, J. H. Seinfeld, and A. Sorooshian, Department of Chemical Engineering, California Institute of Technology, Pasadena, CA 91125, USA.

S. Gilardoni and L. M. Russell, Scripps Institution of Oceanography, University of California, San Diego, La Jolla, CA 92093, USA. (lrmrussell@ucsd.edu)

A. H. Goldstein and B. Williams, Department of Environmental Sciences, Policy and Management, University of California, Berkeley, CA 94720, USA.

T. B. Onasch and D. R. Worsnop, Aerodyne Research, Inc., 45 Manning Road, Billerica, MA 01821-3976, USA.

## Appendix G

### Effect of NO<sub>x</sub> Level on Secondary Organic Aerosol (SOA) Formation from the Photooxidation of Terpenes\*

---

\*This chapter is reproduced by permission from “Effect of NO<sub>x</sub> Level on Secondary Organic Aerosol (SOA) Formation from the Photooxidation of Terpenes” by N. L. Ng, P. S. Chhabra, A. W. H. Chan, J. D. Surratt, J. H. Kroll, A. J. Kwan, D. C. McCabe, P. O. Wennberg, A. Sorooshian, S. M. Murphy, N. F. Dalleska, R. C. Flagan, and J. H. Seinfeld, *Atmos. Chem. Phys.*, 7, 5159-5174, 2007. © 2007 Author(s). This work is licensed under a Creative Commons License.

# Effect of $\text{NO}_x$ level on secondary organic aerosol (SOA) formation from the photooxidation of terpenes

N. L. Ng<sup>1</sup>, P. S. Chhabra<sup>1</sup>, A. W. H. Chan<sup>1</sup>, J. D. Surratt<sup>2</sup>, J. H. Kroll<sup>3</sup>, A. J. Kwan<sup>4</sup>, D. C. McCabe<sup>4</sup>, P. O. Wennberg<sup>4</sup>, A. Sorooshian<sup>1</sup>, S. M. Murphy<sup>1</sup>, N. F. Dalleska<sup>4</sup>, R. C. Flagan<sup>1,4</sup>, and J. H. Seinfeld<sup>1,4</sup>

<sup>1</sup>Department of Chemical Engineering, California Institute of Technology, Pasadena, CA 91125, USA

<sup>2</sup>Department of Chemistry, California Institute of Technology, Pasadena, CA 91125, USA

<sup>3</sup>Aerodyne Research, Inc., Billerica, MA 01821, USA

<sup>4</sup>Department of Environmental Science and Engineering, California Institute of Technology, Pasadena, CA 91125, USA

Received: 7 June 2007 – Published in Atmos. Chem. Phys. Discuss.: 12 July 2007

Revised: 14 September 2007 – Accepted: 29 September 2007 – Published: 8 October 2007

**Abstract.** Secondary organic aerosol (SOA) formation from the photooxidation of one monoterpene ( $\alpha$ -pinene) and two sesquiterpenes (longifolene and aromadendrene) is investigated in the Caltech environmental chambers. The effect of  $\text{NO}_x$  on SOA formation for these biogenic hydrocarbons is evaluated by performing photooxidation experiments under varying  $\text{NO}_x$  conditions. The  $\text{NO}_x$  dependence of  $\alpha$ -pinene SOA formation follows the same trend as that observed previously for a number of SOA precursors, including isoprene, in which SOA yield (defined as the ratio of the mass of organic aerosol formed to the mass of parent hydrocarbon reacted) decreases as  $\text{NO}_x$  level increases. The  $\text{NO}_x$  dependence of SOA yield for the sesquiterpenes, longifolene and aromadendrene, however, differs from that determined for isoprene and  $\alpha$ -pinene; the aerosol yield under high- $\text{NO}_x$  conditions substantially exceeds that under low- $\text{NO}_x$  conditions. The reversal of the  $\text{NO}_x$  dependence of SOA formation for the sesquiterpenes is consistent with formation of relatively low-volatility organic nitrates, and/or the isomerization of large alkoxy radicals leading to less volatile products. Analysis of the aerosol chemical composition for longifolene confirms the presence of organic nitrates under high- $\text{NO}_x$  conditions. Consequently the formation of SOA from certain biogenic hydrocarbons such as sesquiterpenes (and possibly large anthropogenic hydrocarbons as well) may be more efficient in polluted air.

## 1 Introduction

Atmospheric oxidation of certain volatile organic compounds (VOCs) leads to the formation of low volatility species that partition into the condensed phase and form secondary organic aerosol (SOA). Biogenic hydrocarbons, such as isoprene ( $\text{C}_5\text{H}_8$ ), monoterpenes ( $\text{C}_{10}\text{H}_{16}$ ), and sesquiterpenes ( $\text{C}_{15}\text{H}_{24}$ ), are important contributors to the total atmospheric burden of SOA owing to their large global emissions and high reactivity with hydroxyl radicals (OH), ozone ( $\text{O}_3$ ), and nitrate radicals ( $\text{NO}_3$ ) (Guenther et al., 1995; Griffin et al., 1999a; Geron et al., 2000; Owen et al., 2001; Atkinson and Arey, 2003; Seinfeld and Pankow, 2003; Kanakidou et al., 2005).

Over the last two decades, numerous laboratory chamber experiments have been conducted to study aerosol formation from biogenic hydrocarbons. Level of odd nitrogen ( $\text{NO}_x$ ) has been found to be highly influential in SOA production for a variety of compounds. Recent studies on isoprene photooxidation,  $\alpha$ -pinene ozonolysis, and benzene, toluene, and *m*-xylene photooxidation have demonstrated that aerosol yields are generally highest at low levels of  $\text{NO}_x$  (Hatakeyama et al., 1991; Kroll et al., 2006; Presto et al., 2005; Song et al., 2005; Ng et al., 2007). These observations are consistent with competitive chemistry of peroxy radicals between NO and  $\text{HO}_2$ , with the  $\text{RO}_2 + \text{HO}_2$  reaction producing products of lower volatility than the  $\text{RO}_2 + \text{NO}$  reaction (Hatakeyama et al., 1991; Johnson et al., 2004, 2005; Kroll et al., 2005, 2006; Presto et al., 2005; Ng et al., 2007). For example, in  $\alpha$ -pinene ozonolysis, Presto et al. (2005) observed relatively volatile organic nitrates under high- $\text{NO}_x$  conditions, while less volatile products, such as 10-hydroxypinonic acid, were more abundant under low- $\text{NO}_x$  conditions. Although a

Correspondence to: J. H. Seinfeld  
(seinfeld@caltech.edu)

decreasing SOA yield with increasing NO<sub>x</sub> level has been established for relatively small hydrocarbons (10 carbons or fewer), it is unknown whether larger molecules, such as sesquiterpenes, exhibit a similar NO<sub>x</sub> dependence of SOA yield.

In the present study, we focus on two sesquiterpenes, longifolene and aromadendrene, and compare the NO<sub>x</sub>-dependence of their SOA formation with that of  $\alpha$ -pinene. Longifolene reacts very slowly with ozone (Atkinson and Arey, 2003), making it ideal for the study of OH photooxidation. Moreover, both longifolene and aromadendrene have only one double bond, thus one can infer more easily the general mechanisms of SOA formation than when multiple double bonds are present (Ng et al., 2006). Experiments are conducted under limiting NO<sub>x</sub> conditions (high-NO<sub>x</sub> conditions in which HONO is used as the OH precursor, and low-NO<sub>x</sub> conditions in which H<sub>2</sub>O<sub>2</sub> is used as the OH precursor), as well as with intermediate levels of NO<sub>x</sub>.

## 2 Experimental section

Experiments are performed in Caltech's dual 28 m<sup>3</sup> Teflon environmental chambers. Details of the facilities are given elsewhere (Cocker et al., 2001; Keywood et al., 2004). Before each experiment, the chambers are flushed continuously with dry purified air for  $\sim$ 24 h. Each chamber has a dedicated Differential Mobility Analyzer (DMA, TSI model 3081) coupled with a condensation nucleus counter (TSI model 3760) for measuring aerosol size distribution, number concentration, and volume concentration. All aerosol growth data are corrected for wall loss, in which size-dependent coefficients determined from inert particle wall loss experiments are applied to the aerosol volume data (Keywood et al., 2004). Temperature, relative humidity (RH), O<sub>3</sub>, NO, and NO<sub>x</sub> are continuously monitored. The initial temperature of the chamber is  $\sim$ 20°C. Heating from the lights leads to a temperature increase of approximately 5°C inside the chamber over the course of the experiment. The analytical instruments are located outside the chamber enclosure and are at the temperature of the surrounding room ( $\sim$ 20–22°C). The air may cool slightly as it is sampled from the chamber into the instruments, and the measured aerosol likely corresponds to the gas-particle partitioning at the temperature of the surrounding room rather than the chamber enclosure. Such small temperature differences are unlikely to affect results significantly.

Seed particles are introduced into the chamber to act as substrates onto which the gas-phase semivolatile products may condense. Seed aerosols are generated from a 0.015 M aqueous ammonium sulfate solution with a constant-rate atomizer, producing initial particle number concentrations of  $\sim$ 25 000 particles cm<sup>-3</sup>, with a geometric mean diameter of  $\sim$ 50 nm, and an initial aerosol seed volume of  $\sim$ 10–15  $\mu$ m<sup>3</sup> cm<sup>-3</sup>. After introduction of the seed aerosol, a

known volume of the parent hydrocarbon is injected into a glass bulb, and then introduced into the chambers by an air stream. For experiments with  $\alpha$ -pinene and longifolene, the concentration (mixing ratio) of the parent hydrocarbon is monitored with a Hewlett Packard gas chromatograph (model 5890) with flame ionization detection (GC-FID). The concentration of longifolene in several experiments is also measured with a Proton Transfer Reaction Mass Spectrometer (PTR-MS), a custom-modified Varian 1200 system (see Appendix A). Owing to the difficulties in measuring aromadendrene with GC-FID, its concentration is measured solely with the PTR-MS. The PTR-MS is calibrated only for aromadendrene.

In the high-NO<sub>x</sub> experiments nitrous acid (HONO) serves as the OH precursor. HONO is prepared by dropwise addition of 15 mL of 1% NaNO<sub>2</sub> into 30 mL of 10% H<sub>2</sub>SO<sub>4</sub> in a glass bulb. After injection of the seed aerosol and parent hydrocarbon, the bulb is then attached to the chamber and a stream of dry air is passed through the bulb, sending HONO into the chamber. NO and NO<sub>2</sub>, formed as side products in the preparation of HONO, are also introduced into the chamber, and are measured by a commercial NO<sub>x</sub> monitor (Horiba APNA-360, Irvine, CA). Additional NO from a 500 ppm gas cylinder (Scott Marrin, Inc.) is introduced into the chamber after the addition of HONO to achieve a target NO<sub>x</sub> level in the chamber of about 1 ppm (upper limit of the NO<sub>x</sub> monitor).

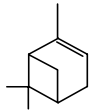
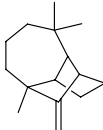
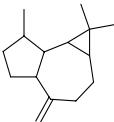
For low-NO<sub>x</sub> experiments, H<sub>2</sub>O<sub>2</sub> serves as the OH precursor. The background NO<sub>x</sub> level in the chamber during such experiments is  $\leq$ 2 ppb. H<sub>2</sub>O<sub>2</sub> is introduced into the chamber (prior to introduction of seed particles and parent hydrocarbon) by bubbling air through a 50% H<sub>2</sub>O<sub>2</sub> solution for 2.5 h at 5 L/min. The concentration of H<sub>2</sub>O<sub>2</sub> in the chamber is not measured; based on the rate of hydrocarbon decay and literature values of  $\sigma_{\text{H}_2\text{O}_2}$  and  $k_{\text{H}_2\text{O}_2}$ , we estimate [H<sub>2</sub>O<sub>2</sub>] to be  $\sim$ 3–5 ppm (Kroll et al., 2006). The air stream then passes through a particle filter to remove any droplets. Variable NO experiments are also carried out, in which a known concentration of NO is introduced into the chamber after the addition of H<sub>2</sub>O<sub>2</sub>. This allows for the study of SOA formation under intermediate NO<sub>x</sub> conditions. It is noted that for these intermediate NO<sub>x</sub> experiments, NO goes to zero during the experiment and so there is a switch from high- to low-NO<sub>x</sub> conditions over the course of the experiment.

Once the seed, parent hydrocarbon, and NO<sub>x</sub> concentrations stabilize, reaction is initiated by irradiating the chamber with blacklights. Output from the lights is between 300 and 400 nm, with a maximum at 354 nm. Half of the available black lights are used in the experiments. At these wavelengths HONO efficiently photolyzes to OH and NO. By contrast, H<sub>2</sub>O<sub>2</sub> absorbs only weakly in this wavelength range, requiring the use of ppm mixing ratios of H<sub>2</sub>O<sub>2</sub> to achieve target levels of OH.

A comprehensive range of measurements are employed to study the chemical composition of the SOA formed.



**Table 1.** Parent hydrocarbons used in this study.

Parent Hydrocarbon	Structure	Formula (MW)	$k_{OH}$ (cm <sup>3</sup> molec <sup>-1</sup> s <sup>-1</sup> )
$\alpha$ -pinene		C <sub>10</sub> H <sub>16</sub> (136)	$5.3 \times 10^{-11}$ <sup>a</sup>
longifolene		C <sub>15</sub> H <sub>24</sub> (204)	$4.8 \times 10^{-11}$ <sup>a</sup>
aromadendrene		C <sub>15</sub> H <sub>24</sub> (204)	$1.5 \times 10^{-10}$ <sup>b</sup>

<sup>a</sup> Rate constants were obtained from Atkinson et al. (2003).

<sup>b</sup> Rate constant was estimated from the rate of aromadendrene decay (experiment 1 in Table 4), assuming an OH concentration of  $3 \times 10^6$  molecule cm<sup>-3</sup> and that aromadendrene reacts with OH only.

Real-time particle mass spectra are obtained with an Aerodyne quadrupole Aerosol Mass Spectrometer (Q-AMS) (Jayne et al., 2000). A particle-into-liquid sampler (PILS, Brechtel Manufacturing, Inc.) coupled with ion chromatography is employed for quantitative measurements of water-soluble ions in the aerosol phase (Sorooshian et al., 2006). For offline chemical analysis, aerosol samples are collected on Teflon filters (PALL Life Sciences, 47-mm diameter, 1.0- $\mu$ m pore size, Teflo membrane) starting at the point when aerosol volume reaches its maximum value. Depending on the total chamber volume concentration of aerosol, the filter sampling time is 2–4 h, which results in  $\sim 1.5$ – $6$  m<sup>3</sup> of total chamber air sampled. Teflon filter extraction protocols in HPLC-grade methanol have been described previously (Surratt et al., 2006). The resultant filter extracts are then analyzed by high performance liquid chromatography/electrospray ionization-quadrupole mass spectrometry (HPLC/ESI-MS) and electrospray ionization-ion trap mass spectrometry (ESI-ITMS); details of the protocols are described elsewhere (Surratt et al., 2006). Filter extracts are also analyzed by a Waters ACQUITY ultra performance liquid chromatography (UPLC) system, coupled with a Waters LCT Premier time-of-flight (TOF) mass spectrometer (MS) equipped with an electrospray ionization (ESI) source (see Appendix B), allowing for exact mass and tandem MS measurements.

The parent hydrocarbons studied and their stated purities are as follows:  $\alpha$ -pinene (Aldrich, 99+%), longifolene (Aldrich, >99%), and aromadendrene (Aldrich, >97%). Ta-

ble 1 lists the structures of the parent hydrocarbons and the rate constants of the compounds for reaction with OH radicals ( $k_{OH}$ ). Experimental conditions and results for each of the parent hydrocarbons studied are given in Tables 2, 3, and 4. In calculating SOA yield, knowledge of the SOA density is required. By comparing volume distributions from the DMA and mass distributions from the Q-AMS, effective densities for the SOA formed can be estimated (Bahreini et al., 2005; Alfarra et al., 2006). The estimated densities of the SOA formed from different parent hydrocarbons are given in Table 5.

### 3 Aerosol yields

#### 3.1 $\alpha$ -pinene photooxidation

Under high-NO<sub>x</sub> conditions, the efficient photolysis of HONO generates relatively high concentrations of OH ( $\sim 2 \times 10^7$  molecules cm<sup>-3</sup> initially), leading to rapid  $\alpha$ -pinene decay. Aerosol growth occurs essentially immediately, even when [NO] is high (100's of ppb). With the high NO concentration throughout the entire experiment, formation of ozone and NO<sub>3</sub> is suppressed.

Under low-NO<sub>x</sub> conditions, aerosol growth is also observed immediately after initiation of irradiation. The  $\alpha$ -pinene decays at a slower rate than under high-NO<sub>x</sub> conditions, owing to the relatively slow production of OH radicals by H<sub>2</sub>O<sub>2</sub> photolysis. Ozone formation is observed at an increasing concentration over time ( $\sim 30$  ppb at the peak

**Table 2.** Initial conditions and results for  $\alpha$ -pinene experiments.

Expt. No.	NO <sub>x</sub> Condition	NO (ppb)	NO <sub>2</sub> (ppb)	T (K)	RH (%)	$\Delta$ HC (ppb) <sup>a</sup>	$\Delta$ M <sub>0</sub> ( $\mu$ g/m <sup>3</sup> ) <sup>b</sup>	SOA Yield (%) <sup>c</sup>
1	H <sub>2</sub> O <sub>2</sub>	0	0	298	5.3	13.8 $\pm$ 0.2	29.3 $\pm$ 2.4	37.9 $\pm$ 3.2
2	H <sub>2</sub> O <sub>2</sub>	0	1	298	6.2	47.5 $\pm$ 0.8	121.3 $\pm$ 9.4	45.8 $\pm$ 3.6
3	H <sub>2</sub> O <sub>2</sub> +NO	198	0	296	6.4	13.1 $\pm$ 0.2	15.6 $\pm$ 1.4	21.2 $\pm$ 2.0
4	HONO	475	463	299	3.3	12.6 $\pm$ 0.2	4.5 $\pm$ 0.9	6.6 $\pm$ 1.4
5	HONO	390	578	298	3.7	46.6 $\pm$ 0.8	40.8 $\pm$ 3.8	15.8 $\pm$ 1.5

<sup>a</sup> Stated uncertainties (1 $\sigma$ ) include scatter in GC measurements and GC calibration errors.<sup>b</sup> Stated uncertainties (1 $\sigma$ ) are from scatter in particle volume measurements.<sup>c</sup> Stated uncertainties are propagated from errors in  $\Delta$ HC and  $\Delta$ M<sub>0</sub>.**Table 3.** Initial conditions and results for longifolene experiments.

Expt. No.	NO <sub>x</sub> Condition	NO (ppb)	NO <sub>2</sub> (ppb)	T (K)	RH (%)	$\Delta$ HC (ppb) <sup>b</sup>	$\Delta$ M <sub>0</sub> ( $\mu$ g/m <sup>3</sup> ) <sup>c</sup>	SOA Yield (%) <sup>d</sup>
1	H <sub>2</sub> O <sub>2</sub>	0	0	298	5.8	4.5 $\pm$ 0.2	28.5 $\pm$ 2.4	75.7 $\pm$ 7.0
2	H <sub>2</sub> O <sub>2</sub>	0	2	297	6.0	8.4 $\pm$ 0.4	52.5 $\pm$ 4.2	74.4 $\pm$ 6.7
3	H <sub>2</sub> O <sub>2</sub>	0	2	297	6.3	19.4 $\pm$ 0.8	117.1 $\pm$ 9.3	72.1 $\pm$ 6.5
4	H <sub>2</sub> O <sub>2</sub>	0	2	299	5.7	24.8 $\pm$ 1.1	148.4 $\pm$ 11.6	71.8 $\pm$ 6.4
5	H <sub>2</sub> O <sub>2</sub> +NO	70	31 <sup>a</sup>	297	6.2	3.8 $\pm$ 0.2	35.8 $\pm$ 2.9	111.7 $\pm$ 10.2
6	H <sub>2</sub> O <sub>2</sub> +NO	209	26 <sup>a</sup>	297	8.0	4.7 $\pm$ 0.2	43.4 $\pm$ 3.5	110.2 $\pm$ 10.0
7	H <sub>2</sub> O <sub>2</sub> +NO	316	0	298	6.4	4.1 $\pm$ 0.2	43.4 $\pm$ 3.5	127.2 $\pm$ 1.5
8	H <sub>2</sub> O <sub>2</sub> +NO	394	0	297	6.1	4.8 $\pm$ 0.2	50.0 $\pm$ 4.1	124.9 $\pm$ 11.5
9	H <sub>2</sub> O <sub>2</sub> +NO	564	0	297	6.2	3.9 $\pm$ 0.2	51.6 $\pm$ 4.1	157.0 $\pm$ 14.1
10	HONO	428	550	298	3.7	9.7 $\pm$ 0.4	68.3 $\pm$ 5.1	84.0 $\pm$ 7.1
11	HONO	469	502	298	3.7	19.6 $\pm$ 0.9	141.9 $\pm$ 10.3	86.8 $\pm$ 7.3
12	HONO	394	577	299	3.2	26.6 $\pm$ 1.2	213.6 $\pm$ 15.3	96.3 $\pm$ 8.0

<sup>a</sup> NO<sub>2</sub> formed due to NO reacting with residual ozone in the chamber.<sup>b</sup> Stated uncertainties (1 $\sigma$ ) include scatter in GC measurements and GC calibration errors.<sup>c</sup> Stated uncertainties (1 $\sigma$ ) are from scatter in particle volume measurements.<sup>d</sup> Stated uncertainties are propagated from errors in  $\Delta$ HC and  $\Delta$ M<sub>0</sub>.

of aerosol growth), possibly from residual material released from the chamber walls. Based on the reaction rate constants of  $\alpha$ -pinene+O<sub>3</sub> ( $k_{\text{ozone}}=8.4\times 10^{-17}$  cm<sup>3</sup> molecule<sup>-1</sup> s<sup>-1</sup>, Atkinson et al., 2003) and  $\alpha$ -pinene+OH ( $k_{\text{OH}}=5.3\times 10^{-11}$  cm<sup>3</sup> molecule<sup>-1</sup> s<sup>-1</sup>, Atkinson et al., 2003), and an inferred OH concentration of  $3\times 10^6$  molecules cm<sup>-3</sup> (estimated from longifolene low-NO<sub>x</sub> experiments, see Sect. 3.2), it is estimated that an ozone source of  $\sim 0.1$  ppb/min would be required to produce the observed  $\alpha$ -pinene decay. It is estimated that only about 35% of the  $\alpha$ -pinene reacts by ozonolysis at the point of maximum growth. Therefore, while  $\alpha$ -pinene ozonolysis accounts for some of the SOA yield under low-NO<sub>x</sub> conditions, it is unlikely that the observed yield differences between high- and low-NO<sub>x</sub> conditions (described below) arise solely from the presence of ozone.

Figure 1 shows the time-dependent growth curves (organic aerosol generated, denoted as  $\Delta$ M<sub>0</sub>, as a function of hydrocarbon reacted,  $\Delta$ HC) for  $\alpha$ -pinene under different NO<sub>x</sub> conditions. The curves are referred to as “time-dependent growth curves” as each curve represents aerosol growth data for a single experiment over the course of the experiment (Ng et al., 2006). As hydrocarbon measurements are made with a lower frequency than those of particle volume, the  $\alpha$ -pinene concentrations shown are obtained by fitting the GC measurements to an exponential decay. In all cases, the initial mixing ratio of  $\alpha$ -pinene is about 15 ppb, all of which is consumed by the end of the experiment. It is clear that the aerosol growth under low-NO<sub>x</sub> (H<sub>2</sub>O<sub>2</sub>) conditions substantially exceeds that under high-NO<sub>x</sub> (HONO) conditions, while the intermediate NO<sub>x</sub> (“H<sub>2</sub>O<sub>2</sub>+NO”) experiment exhibits an aerosol yield between those of the two extremes. The time-dependent growth curve of the intermediate NO<sub>x</sub>

**Table 4.** Initial conditions and results for aromadendrene experiments.

Expt. No.	NO <sub>x</sub> Condition	NO (ppb)	NO <sub>2</sub> (ppb)	T (K)	RH (%)	ΔHC (ppb) <sup>a</sup>	ΔM <sub>0</sub> (μg/m <sup>3</sup> ) <sup>b</sup>	SOA Yield (%)
1	H <sub>2</sub> O <sub>2</sub>	0	0	299	5.5	5.7±1.2	19.7±2.0	41.7±10
2	H <sub>2</sub> O <sub>2</sub> +NO	120	0	298	9.3	5.3±1.2	23.1±2.2	52.0±12.4
3	H <sub>2</sub> O <sub>2</sub> +NO	195	0	298	7.7	6.0±1.4	29.3±2.6	58.8±14.4
4	H <sub>2</sub> O <sub>2</sub> +NO	517	0	299	7.4	3.2±0.7	22.6±2.2	84.7±20.0

<sup>a</sup> Stated uncertainties (1σ) include scatter in PTR-MS measurements and PTR-MS calibration errors.

<sup>b</sup> Stated uncertainties are derived from scatter in particle volume measurements.

**Table 5.** Estimated effective SOA densities.

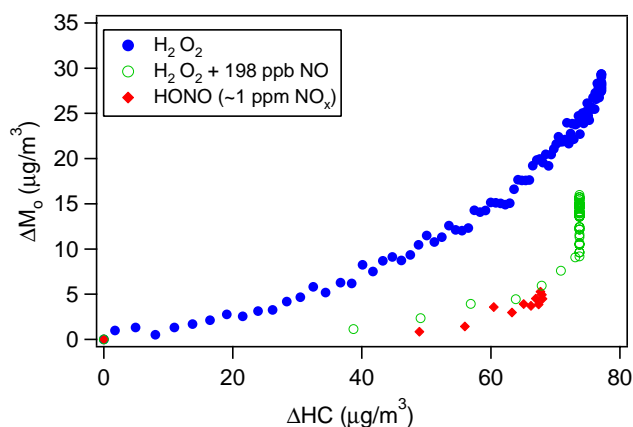
Parent Hydrocarbon	NO <sub>x</sub> Condition	Effective Density (g cm <sup>-3</sup> ) <sup>a</sup>
α-pinene	Low-NO <sub>x</sub>	1.32±0.10
α-pinene	Intermediate NO <sub>x</sub>	1.32±0.10
α-pinene	High-NO <sub>x</sub>	1.33±0.10
longifolene	Low-NO <sub>x</sub>	1.29±0.10
longifolene	Intermediate NO <sub>x</sub>	1.30±0.10
longifolene	High-NO <sub>x</sub>	1.40±0.10
aromadendrene	Low-NO <sub>x</sub>	1.20±0.10
aromadendrene	Intermediate NO <sub>x</sub>	1.35±0.10

<sup>a</sup> Stated uncertainties (1σ) are from repeated measurement of ammonium sulfate seed densities.

experiment exhibits a vertical section at the end, indicating that further reactions are contributing to aerosol growth after α-pinene is consumed. We return to this observation in Sect. 5.2.2.

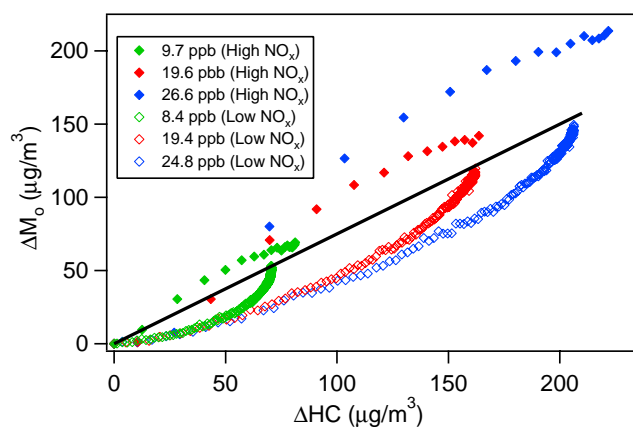
### 3.2 Longifolene photooxidation

For longifolene, a series of high-NO<sub>x</sub> (HONO) experiments and low-NO<sub>x</sub> (H<sub>2</sub>O<sub>2</sub>) experiments with varying initial hydrocarbon concentrations are carried out. The time-dependent growth curves for 3 high-NO<sub>x</sub> and 3 low-NO<sub>x</sub> experiments, with initial longifolene mixing ratios ranging from ~10 to 30 ppb, are shown in Fig. 2. In contrast to α-pinene photooxidation, longifolene aerosol yields under high-NO<sub>x</sub> conditions exceed those under low-NO<sub>x</sub> conditions. Under high-NO<sub>x</sub> conditions, the maximum SOA yield is about ~100–130% and is reached in ~10 min after initiation of the experiments, with the yield decreasing after that point. It is noted that SOA yield is defined on a mass basis so oxidation (addition of O or N atoms) can lead to yields larger than 100%. Under low-NO<sub>x</sub> conditions, SOA yield continues to increase over the course of the experiment, reaching a maximum when all the longifolene is consumed. The final SOA yields of each longifolene low-NO<sub>x</sub> experiment lie on a straight line that passes through the origin, indicating that under low-NO<sub>x</sub> conditions SOA yield is constant (~75%) under the range of ΔM<sub>0</sub> studied. It is possible that under lower SOA loadings the yields

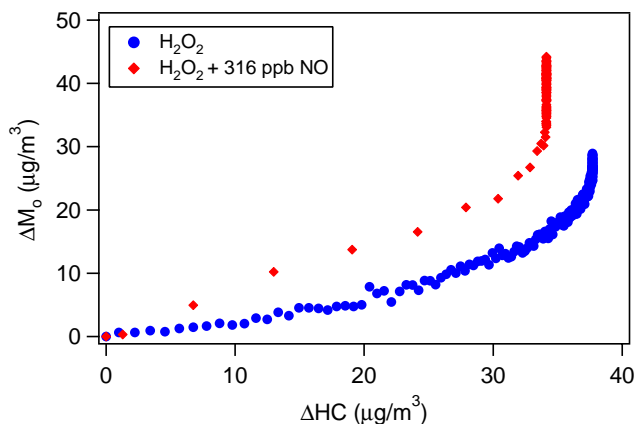
**Fig. 1.** Time-dependent growth curves for α-pinene photooxidation under different NO<sub>x</sub> conditions (Experiments 1, 3 and 4 in Table 2).

may decrease as some of the products partition back into the gas phase. Based on the observed longifolene decay and *k*<sub>OH</sub> for longifolene, the chamber OH concentration under low-NO<sub>x</sub> conditions is estimated to be ~3 × 10<sup>6</sup> molecules cm<sup>-3</sup>.

The effect of NO<sub>x</sub> on longifolene aerosol formation is further illustrated by the time-dependent growth curves in Fig. 3. In both experiments H<sub>2</sub>O<sub>2</sub> is used as the OH precursor and the initial longifolene mixing ratio is 4–5 ppb; in one experiment no extra NO is added, while in the other experiment about 300 ppb of NO is introduced into the chamber after the addition of H<sub>2</sub>O<sub>2</sub>. Aerosol growth in the presence of ~300 ppb NO is substantially higher. A series of experiments with the same initial longifolene concentration but different initial NO concentrations (~100–600 ppb) are also carried out. Figure 4 shows the final aerosol yield as a function of the initial NO<sub>x</sub> concentration. The amount of aerosol formed is highly dependent on the level of NO<sub>x</sub> present initially; with ~600 ppb NO, the ultimate aerosol yield is twice that at low-NO<sub>x</sub> conditions.



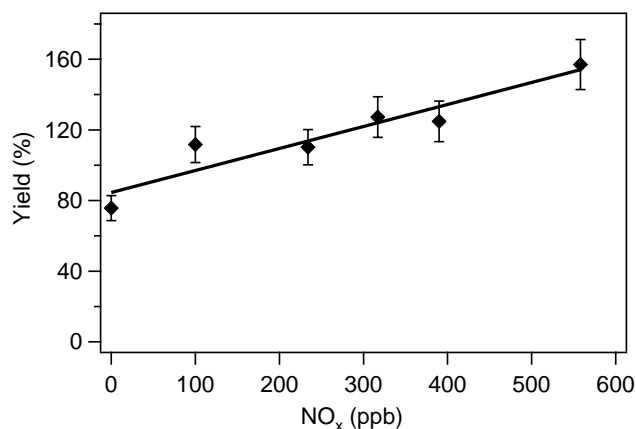
**Fig. 2.** Time-dependent growth curves for longifolene photooxidation under high- and low- $\text{NO}_x$  conditions (Experiments 2, 3, 4, 10, 11, and 12 in Table 3). The mixing ratios in the legend refer to the amount of longifolene reacted in each experiment. The final SOA yields of each low- $\text{NO}_x$  experiment lie on a straight line that passes through the origin, indicating that under low- $\text{NO}_x$  conditions SOA yield is constant, at  $\sim 75\%$ .



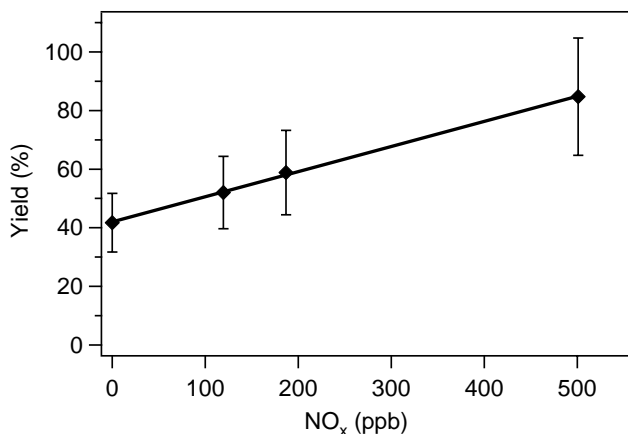
**Fig. 3.** Time-dependent growth curves for longifolene photooxidation with  $\text{H}_2\text{O}_2$  as the OH precursor. Aerosol growth in the presence of  $\sim 300$  ppb NO (Experiment 7 in Table 3) significantly exceeds that without NO (Experiment 1 in Table 3).

### 3.3 Aromadendrene photooxidation

Figure 5 shows the final aerosol yield as a function of initial  $\text{NO}_x$  concentration for aromadendrene photooxidation. The OH precursor used in these experiments is  $\text{H}_2\text{O}_2$  and the initial aromadendrene mixing ratio is  $\sim 5$  ppb. It is clear that aromadendrene aerosol yield also increases with  $\text{NO}_x$  concentration; as with longifolene, with  $\sim 500$  ppb NO, the aerosol yield is approximately double that at low- $\text{NO}_x$  conditions.



**Fig. 4.** SOA growth as a function of initial  $\text{NO}_x$  concentration, for a fixed longifolene concentration (4–5 ppb). Results shown are from Table 3.



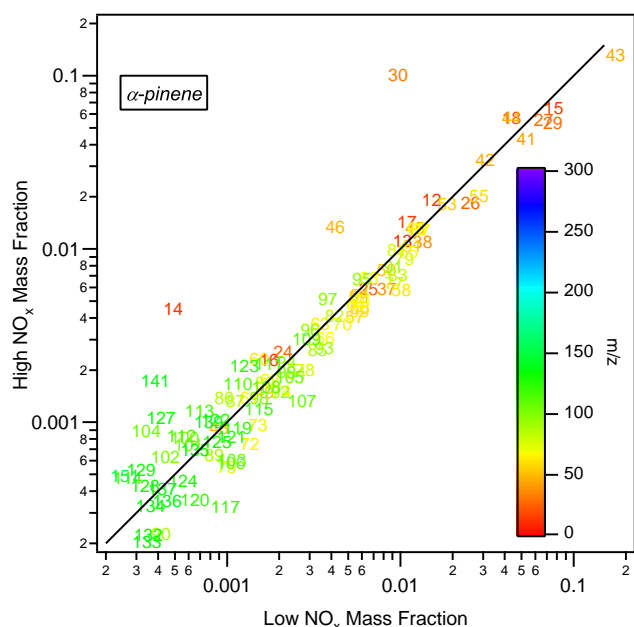
**Fig. 5.** SOA growth as a function of initial  $\text{NO}_x$  concentration, at a fixed initial aromadendrene concentration ( $\sim 5$  ppb). Results shown are given in Table 4.

## 4 Chemical composition of SOA

In this section, the measurements of the chemical composition of  $\alpha$ -pinene and longifolene SOA are presented. The aromadendrene experiments are performed mainly to verify the observed  $\text{NO}_x$  dependence for longifolene, in which SOA yield is higher under high- $\text{NO}_x$  conditions, and so detailed analysis of the chemical composition of aromadendrene SOA is not pursued.

### 4.1 Aerosol Mass Spectrometer (Q-AMS) measurements

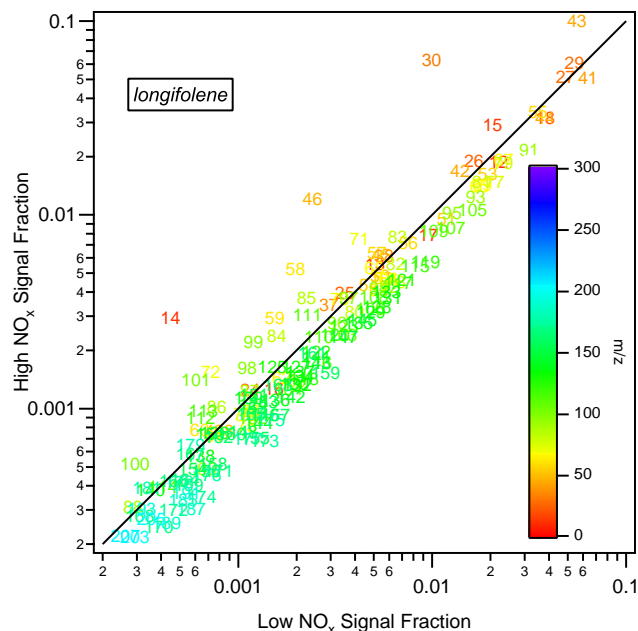
Figures 6 and 7 show the AMS high- $\text{NO}_x$  versus low- $\text{NO}_x$  spectrum signal for  $\alpha$ -pinene and longifolene photooxidation, respectively. Each mass fragment is normalized by the total signal. For both hydrocarbons, SOA at high  $\text{NO}_x$  conditions exhibit relatively strong signals at  $m/z$  30 and



**Fig. 6.** AMS high-NO<sub>x</sub> spectra signal versus low-NO<sub>x</sub> spectra signal for  $\alpha$ -pinene photooxidation. Each mass fragment is normalized by the total signal. The solid black line is the 1:1 line. The spectra are taken when all hydrocarbon has been consumed.

46, and to a much smaller extent  $m/z$  14. The signals at these mass to charge ratios likely correspond to NO<sub>2</sub><sup>+</sup> (46), NO<sup>+</sup> (30), and N<sup>+</sup> (14) fragments from nitrates in the aerosol. The significance of these fragments will be further discussed in Sect. 5.1.

Changes in AMS spectra over the course of the experiment for longifolene under high- and low-NO<sub>x</sub> conditions are shown in Figs. 8 and 9, respectively. The corresponding growth curves for these experiments are shown in Fig. 2 (the pair of experiments with  $\sim 30$  ppb of longifolene injected). The top panel shows the fractional contribution of each mass fragment to the total organic and nitrate signal during the growth phase of the experiment (the first  $\sim 100 \mu\text{g m}^{-3}$  longifolene reacted); the middle panel shows the fractional contributions at the point when all of the hydrocarbon is consumed ( $\Delta\text{HC} \sim 200 \mu\text{g m}^{-3}$ ); the bottom panel shows the percentage change of each mass fragment between these two phases. Under high-NO<sub>x</sub> conditions, changes in mass fractions of different fragments during aerosol growth are minimal, indicating that the aerosol composition is not changing significantly over time. Under low-NO<sub>x</sub> conditions, however, the mass fraction of  $m/z$  44 (corresponding to the CO<sub>2</sub><sup>+</sup> ion, indicative of highly oxidized organics) increases by 93% during the reaction, while those for higher mass to charge ratios are observed to decrease. The mass fractions of  $m/z$  44 and higher mass to charge ratios continue to change even after the aerosol growth levels off, suggesting the presence of further chemistry (either gas-phase or particle-phase) even after all the initial hydrocarbon is consumed.

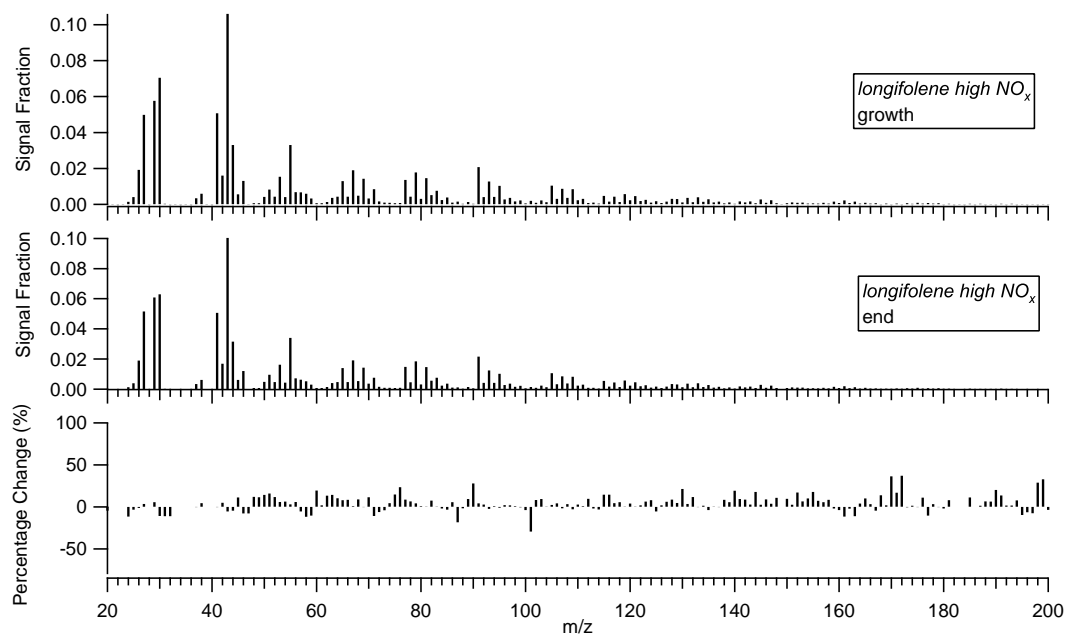


**Fig. 7.** AMS high-NO<sub>x</sub> spectra signal versus low-NO<sub>x</sub> spectra signal for longifolene photooxidation. Each mass fragment is normalized by the total signal. The solid black line is the 1:1 line. The spectra are taken when all hydrocarbon has been consumed.

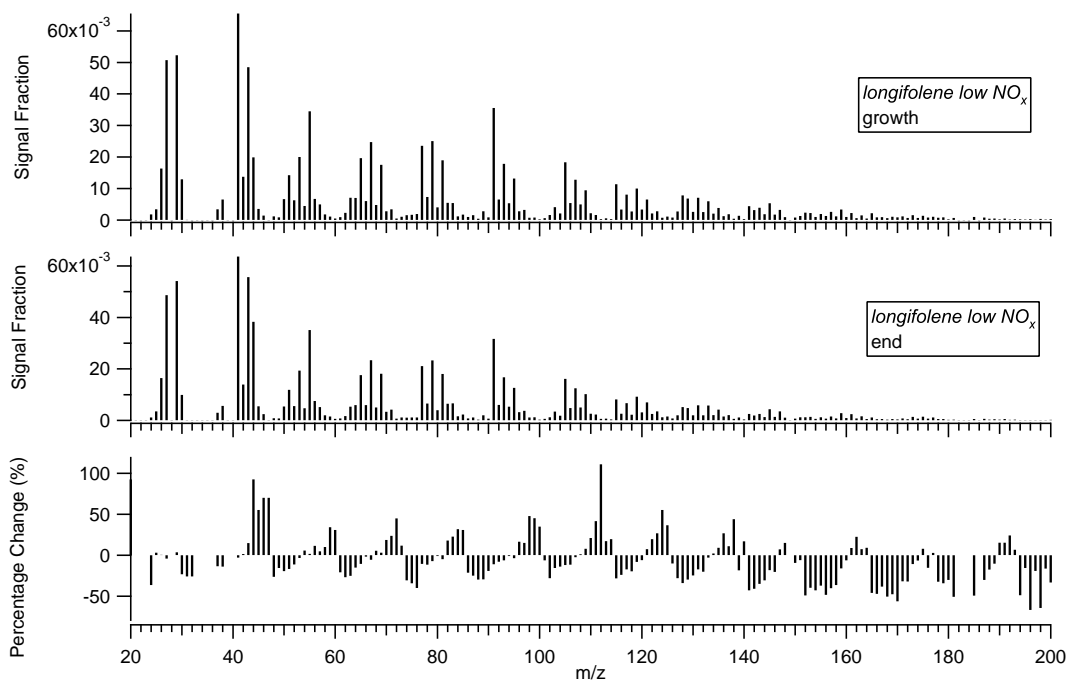
## 4.2 Offline chemical analysis

All ions detected by the UPLC/ESI-TOFMS instrument from  $\alpha$ -pinene and longifolene photooxidation are listed in Tables 6 and 7, respectively. The tables list the exact masses and their likely molecular formulas corresponding to each of the [M-H]<sup>−</sup> ions detected (in which M is the molecular weight of the compound). The error between the measured mass and theoretical mass is reported in two different ways, ppm and mDa. For most of the ions observed, the error between the measured and theoretical masses is less than  $\pm 2$  mDa and  $\pm 5$  ppm, allowing for generally unambiguous identification of molecular formulae. Solvent blanks and control filters are also run on the UPLC/ESI-TOFMS instrument; none of the listed ions is observed in these control samples. The ions listed in Tables 6 and 7 are also detected by HPLC/ESI-MS and ESI-ITMS, confirming that these compounds are not the result of artifact formation in a specific mass spectrometer.

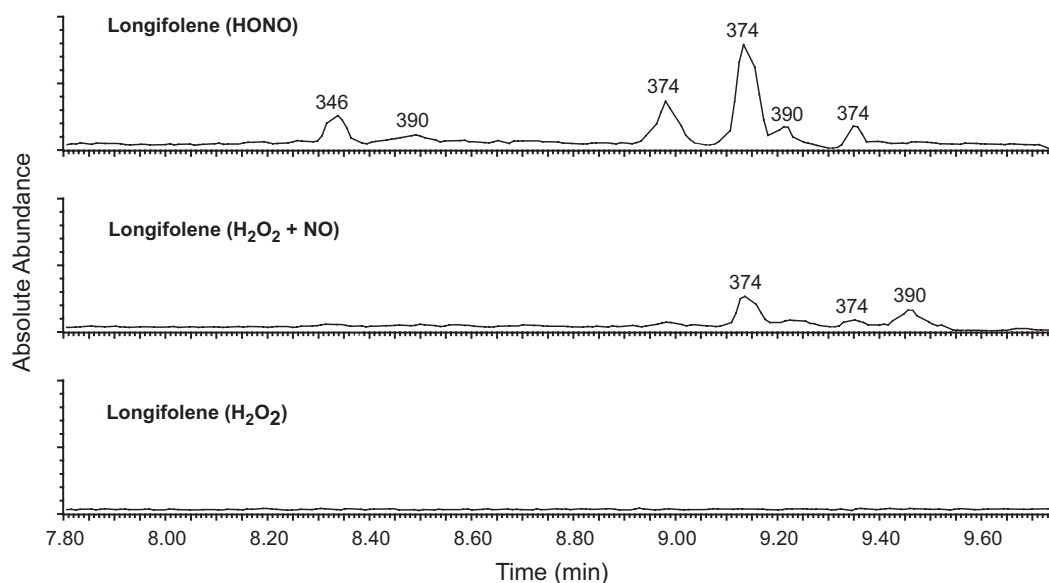
Acidic compounds, such as carboxylic acids and sulfate esters, readily ionize under (−)ESI-MS techniques (Gao et al., 2004; Surratt et al., 2006; Surratt et al., 2007). Hydroxylated compounds, as well as ketones and aldehydes, however, are generally not ionizable unless carboxylic acid and/or sulfate ester moieties are also present within the same molecule. Therefore, it is expected that all ions listed in Tables 6 and 7 are acidic compounds. For the SOA formed in the presence of NO<sub>x</sub> (HONO and “H<sub>2</sub>O<sub>2</sub>+NO” experiments), even-mass



**Fig. 8.** Change in AMS spectrum over the course of longifolene photooxidation under high- $\text{NO}_x$  conditions. Top panel: Fractional contribution of each mass fragment to the total organic and nitrate signal during the growth phase of the experiment. Middle panel: fractional contribution of each mass fragment to the total organic and nitrate signal when all hydrocarbon is consumed. Bottom panel: Percentage change of each mass fragment between the growth phase and the end of the experiment.



**Fig. 9.** Change in AMS spectrum over the course of longifolene photooxidation under low- $\text{NO}_x$  conditions. Top panel: Fractional contribution of each mass fragment to the total organic and nitrate signal during the growth phase of the experiment. Middle panel: fractional contribution of each mass fragment to the total organic and nitrate signal when all hydrocarbon is consumed. Bottom panel: Percentage change of each mass fragment between the growth phase and the end of the experiment.



**Fig. 10.** UPLC/ESI-TOFMS extracted ion chromatograms (EICs) ( $m/z$  346+374+390) for longifolene photooxidation. The even  $[M-H]^-$  ions listed above the chromatographic peaks correspond to organic nitrates detected in longifolene SOA. No organic nitrates are detected in the H<sub>2</sub>O<sub>2</sub> experiment (low-NO<sub>x</sub> condition). The HONO experiment (high-NO<sub>x</sub> condition) has the widest array of organic nitrates detected (as shown in Table 7), as well as the largest chromatographic peaks;  $m/z$  372 is the only exception, and is most abundant in the intermediate NO<sub>x</sub> experiment. These EICs are directly comparable as the volume of chamber air sampled is approximately the same (2 m<sup>3</sup>).

$[M-H]^-$  ions are observed in ESI mass spectra, indicating the compound has an odd number of nitrogen atoms, likely within organic nitrate functional groups. Nitrated organics were previously observed in isoprene SOA formed under high-NO<sub>x</sub> conditions (both HONO and H<sub>2</sub>O<sub>2</sub>+NO) (Surratt et al., 2006), and are further confirmed by the tandem MS data, which reveals a loss of 63 Da (HNO<sub>3</sub>). For  $\alpha$ -pinene, only one acidic organic nitrate ( $m/z$  322) is detected in the HONO experiment and none are detected in H<sub>2</sub>O<sub>2</sub> and intermediate NO<sub>x</sub> experiments. Masses of many ions detected in the  $\alpha$ -pinene experiments have been observed in previous laboratory work (Glasius et al., 1999, 2000; Larsen et al., 2001) and field studies (Gao et al., 2006). For longifolene, a much wider array of acidic organic nitrates is detected by the UPLC/ESI-TOFMS instrument in both HONO and intermediate NO<sub>x</sub> experiments. For both  $\alpha$ -pinene and longifolene, compounds with more carbons than the parent hydrocarbon are observed. Tandem MS data for these C<sub>12</sub>, C<sub>16</sub>, and C<sub>17</sub> acidic organic nitrates reveal a common neutral loss of 60 Da, which possibly corresponds to an acetic acid monomer. Surratt et al. (2006) and Szmigielski et al. (2007) recently showed that particle-phase esterification occurs in isoprene SOA formed under high-NO<sub>x</sub> conditions. The observed neutral loss of 60 Da for these acidic organic nitrates suggests that these compounds may be dimers formed by particle-phase esterification.

Figure 10 shows the extracted ion chromatograms (EICs) of  $m/z$  346, 374, and 390 from longifolene oxidation under different NO<sub>x</sub> conditions. These  $m/z$  values correspond to

acidic organic nitrates, as confirmed by the exact mass data (Table 7) as well as the loss of 63 Da in the tandem MS data. The chromatographic peaks are much larger in the highest NO<sub>x</sub> experiment than those in the intermediate NO<sub>x</sub> experiment (except  $m/z$  372, not shown); no chromatographic peaks are observed under low-NO<sub>x</sub> (H<sub>2</sub>O<sub>2</sub>) conditions. In addition, for several  $[M-H]^-$  ions (e.g.  $m/z$  374 and 390) there are several structural isomers present. Additionally, the intensity of non-nitrogen-containing ions (e.g.  $m/z$  223, 239, 253, 255, 267, 269, and 283), are generally larger under low-NO<sub>x</sub> conditions.

## 5 Discussion

### 5.1 Effect of hydrocarbon size on NO<sub>x</sub> dependence

It has been established that NO<sub>x</sub> levels exert a major influence on SOA formation (Hatakeyama et al., 1991; Pandis et al., 1991; Zhang et al., 1992, 2006; Hurley et al., 2001; Johnson et al., 2004, 2005; Song et al., 2005; Presto et al., 2005; Kroll et al., 2005, 2006; Ng et al., 2007). For photooxidation of isoprene, SOA yields increase as the NO<sub>x</sub> level decreases (Kroll et al., 2006). The proposed mechanism for this observed NO<sub>x</sub> dependence is the competitive chemistry of organic peroxy radicals between NO and HO<sub>2</sub>, in which the semivolatile products formed via the RO<sub>2</sub>+HO<sub>2</sub> path are less volatile than those formed via the RO<sub>2</sub>+NO route (Hatakeyama et al., 1991; Johnson et al., 2004, 2005;

**Table 6.**  $\alpha$ -Pinene acidic SOA components detected by UPLC/ESI-TOFMS.

Experiment	Measured [M - H] <sup>-</sup> ion ( <i>m/z</i> )	TOFMS suggested molecular formula	Error (mDa)	Error (ppm)	Retention Time (min)
H <sub>2</sub> O <sub>2</sub>	157.0497	C <sub>7</sub> H <sub>9</sub> O <sub>4</sub> <sup>-</sup>	-0.4	-2.5	5.09
	169.0873	C <sub>9</sub> H <sub>13</sub> O <sub>3</sub> <sup>-</sup>	0.8	4.7	6.89
	171.0654	C <sub>8</sub> H <sub>11</sub> O <sub>4</sub> <sup>-</sup>	-0.3	-1.8	5.61
	183.1027	C <sub>10</sub> H <sub>15</sub> O <sub>3</sub> <sup>-</sup>	0.6	3.3	7.50
	185.0821	C <sub>9</sub> H <sub>13</sub> O <sub>4</sub> <sup>-</sup>	0.7	3.8	6.85
	199.0983	C <sub>10</sub> H <sub>15</sub> O <sub>4</sub> <sup>-</sup>	1.3	6.5	6.17
	199.0982	C <sub>10</sub> H <sub>15</sub> O <sub>4</sub> <sup>-</sup>	1.2	6.0	6.29
	199.0976	C <sub>10</sub> H <sub>15</sub> O <sub>4</sub> <sup>-</sup>	0.6	3.0	6.34
	215.0923	C <sub>10</sub> H <sub>15</sub> O <sub>5</sub> <sup>-</sup>	0.4	1.9	5.99
	215.0930	C <sub>10</sub> H <sub>15</sub> O <sub>5</sub> <sup>-</sup>	1.1	5.1	7.18
H <sub>2</sub> O <sub>2</sub> + NO	231.0885	C <sub>10</sub> H <sub>15</sub> O <sub>6</sub> <sup>-</sup>	1.6	6.9	6.80
	157.0499	C <sub>7</sub> H <sub>9</sub> O <sub>4</sub> <sup>-</sup>	-0.2	-1.3	5.08
	171.0655	C <sub>8</sub> H <sub>11</sub> O <sub>4</sub> <sup>-</sup>	-0.2	-1.2	5.60
	183.1025	C <sub>10</sub> H <sub>15</sub> O <sub>3</sub> <sup>-</sup>	0.4	2.2	7.49
	185.0812	C <sub>9</sub> H <sub>13</sub> O <sub>4</sub> <sup>-</sup>	-0.2	-1.1	6.86
	197.0814	C <sub>10</sub> H <sub>15</sub> O <sub>4</sub> <sup>-</sup>	0.0	0.0	8.09
	199.0971	C <sub>10</sub> H <sub>15</sub> O <sub>4</sub> <sup>-</sup>	0.1	0.5	6.36
	203.0557	C <sub>8</sub> H <sub>11</sub> O <sub>6</sub> <sup>-</sup>	0.1	0.5	5.50
	215.0925	C <sub>10</sub> H <sub>15</sub> O <sub>5</sub> <sup>-</sup>	0.6	2.8	6.23
	229.0718	C <sub>10</sub> H <sub>13</sub> O <sub>6</sub> <sup>-</sup>	0.6	2.6	6.17
HONO	231.0856	C <sub>10</sub> H <sub>15</sub> O <sub>6</sub> <sup>-</sup>	-1.3	-5.6	6.79
	171.0649	C <sub>8</sub> H <sub>11</sub> O <sub>4</sub> <sup>-</sup>	-0.8	-4.7	5.60
	183.1022	C <sub>10</sub> H <sub>15</sub> O <sub>3</sub> <sup>-</sup>	0.1	0.5	7.49
	185.0457	C <sub>8</sub> H <sub>9</sub> O <sub>5</sub> <sup>-</sup>	0.7	3.8	6.63
	187.0606	C <sub>8</sub> H <sub>11</sub> O <sub>5</sub> <sup>-</sup>	0.0	0.0	5.65
	197.0819	C <sub>10</sub> H <sub>13</sub> O <sub>4</sub> <sup>-</sup>	0.5	2.5	8.09
	203.0546	C <sub>8</sub> H <sub>11</sub> O <sub>6</sub> <sup>-</sup>	-1.0	-4.9	5.50
	213.0781	C <sub>10</sub> H <sub>13</sub> O <sub>5</sub> <sup>-</sup>	1.8	8.4	5.26
	231.0883	C <sub>10</sub> H <sub>15</sub> O <sub>6</sub> <sup>-</sup>	1.4	6.1	6.80
	259.1182	C <sub>12</sub> H <sub>19</sub> O <sub>6</sub> <sup>-</sup>	0.0	0.0	5.85
	322.1148	C <sub>12</sub> H <sub>20</sub> NO <sub>9</sub> <sup>-</sup>	1.0	3.1	7.62

Presto et al., 2005; Kroll et al., 2006; Zhang et al., 2006; Ng et al., 2007). A similar yield dependence on NO<sub>x</sub> is observed here for photooxidation of  $\alpha$ -pinene (Fig. 1). For an initial  $\alpha$ -pinene concentration of  $\sim 15$  ppb, the SOA yield under low-NO<sub>x</sub> conditions is about a factor of 3 higher than that under high-NO<sub>x</sub> conditions. The observed NO<sub>x</sub> dependence is consistent with that of previous studies on  $\alpha$ -pinene photooxidation (Hatakeyama et al., 1991) and  $\alpha$ -pinene ozonolysis (Presto et al., 2005).

The observed NO<sub>x</sub> dependence of SOA yield for the sesquiterpenes, however, is different from that of isoprene and  $\alpha$ -pinene (as well as other hydrocarbons with 10 or fewer carbons, such as aromatic species). For longifolene and aromadendrene, aerosol yield increases with increasing NO<sub>x</sub> concentration (Figs. 2–5). This reversal of the NO<sub>x</sub> dependence of SOA formation could be the result of a number of factors. Figure 11 shows a simplified reaction mechanism involving peroxy radical chemistry. At the two limiting NO<sub>x</sub> conditions of this study, the peroxy radical chemistry is relatively well-defined; under high-NO<sub>x</sub> conditions, peroxy radicals react virtually entirely with NO, while under low-NO<sub>x</sub> conditions, RO<sub>2</sub> reacts predominantly with HO<sub>2</sub>. One of the possible explanations for the higher SOA yield under high-NO<sub>x</sub> conditions is the formation of large alkoxy radicals that isomerize rather than fragment. Isomerization is plausible if

**Table 7.** Longifolene acidic SOA components detected by UPLC/ESI-TOFMS.

Experiment	Measured [M - H] <sup>-</sup> ion ( <i>m/z</i> )	TOFMS suggested molecular formula	Error (mDa)	Error (ppm)	Retention Time (min)
H <sub>2</sub> O <sub>2</sub>	223.1344	C <sub>13</sub> H <sub>19</sub> O <sub>3</sub> <sup>-</sup>	1.0	4.5	8.92
	237.1500	C <sub>14</sub> H <sub>21</sub> O <sub>3</sub> <sup>-</sup>	0.9	3.8	9.06
	239.1651	C <sub>14</sub> H <sub>23</sub> O <sub>3</sub> <sup>-</sup>	0.4	1.7	10.50
	253.1445	C <sub>14</sub> H <sub>21</sub> O <sub>4</sub> <sup>-</sup>	0.5	2.0	9.36
	249.1499	C <sub>15</sub> H <sub>21</sub> O <sub>4</sub> <sup>-</sup>	0.8	3.2	9.25
	249.1501	C <sub>15</sub> H <sub>21</sub> O <sub>4</sub> <sup>-</sup>	1.0	4.0	10.14
	255.1611	C <sub>14</sub> H <sub>23</sub> O <sub>4</sub> <sup>-</sup>	1.5	5.9	9.88
	255.1622	C <sub>14</sub> H <sub>23</sub> O <sub>4</sub> <sup>-</sup>	2.6	10.2	8.99
	267.1602	C <sub>15</sub> H <sub>23</sub> O <sub>4</sub> <sup>-</sup>	0.6	2.2	8.88
	267.1606	C <sub>15</sub> H <sub>23</sub> O <sub>4</sub> <sup>-</sup>	1.0	3.7	9.01
	267.1611	C <sub>15</sub> H <sub>23</sub> O <sub>4</sub> <sup>-</sup>	1.5	5.6	9.28
	267.1601	C <sub>15</sub> H <sub>23</sub> O <sub>4</sub> <sup>-</sup>	0.5	1.9	9.70
	269.1392	C <sub>14</sub> H <sub>21</sub> O <sub>5</sub> <sup>-</sup>	0.3	1.1	7.71
	283.1561	C <sub>15</sub> H <sub>23</sub> O <sub>5</sub> <sup>-</sup>	1.6	5.7	7.35
	313.2018	C <sub>17</sub> H <sub>29</sub> O <sub>5</sub> <sup>-</sup>	0.3	1.0	9.20
H <sub>2</sub> O <sub>2</sub> + NO	223.1337	C <sub>13</sub> H <sub>19</sub> O <sub>3</sub> <sup>-</sup>	0.3	1.3	8.92
	239.1649	C <sub>14</sub> H <sub>23</sub> O <sub>3</sub> <sup>-</sup>	0.2	0.8	10.49
	265.1442	C <sub>15</sub> H <sub>21</sub> O <sub>4</sub> <sup>-</sup>	0.2	0.8	8.93
	269.1401	C <sub>14</sub> H <sub>21</sub> O <sub>5</sub> <sup>-</sup>	1.2	4.5	7.72
	316.1396	C <sub>14</sub> H <sub>22</sub> NO <sub>7</sub> <sup>-</sup>	0.0	0.0	9.88
	329.1972	C <sub>17</sub> H <sub>29</sub> O <sub>6</sub> <sup>-</sup>	0.8	2.4	9.35
	372.1664	C <sub>17</sub> H <sub>26</sub> NO <sub>8</sub> <sup>-</sup>	0.6	1.6	10.58
	374.1829	C <sub>17</sub> H <sub>28</sub> NO <sub>8</sub> <sup>-</sup>	1.4	3.7	9.14
	374.1829	C <sub>17</sub> H <sub>28</sub> NO <sub>8</sub> <sup>-</sup>	1.4	3.7	9.35
	390.1775	C <sub>17</sub> H <sub>28</sub> NO <sub>9</sub> <sup>-</sup>	1.1	2.8	9.46
HONO	223.1334	C <sub>13</sub> H <sub>19</sub> O <sub>3</sub> <sup>-</sup>	-0.1	-0.4	8.92
	241.1453	C <sub>13</sub> H <sub>21</sub> O <sub>4</sub> <sup>-</sup>	1.3	5.4	7.55
	253.1431	C <sub>14</sub> H <sub>21</sub> O <sub>4</sub> <sup>-</sup>	-0.9	-3.6	8.02
	269.1394	C <sub>14</sub> H <sub>21</sub> O <sub>5</sub> <sup>-</sup>	0.5	1.9	7.18
	269.1408	C <sub>14</sub> H <sub>21</sub> O <sub>5</sub> <sup>-</sup>	1.9	7.1	7.71
	342.1930	C <sub>17</sub> H <sub>28</sub> NO <sub>6</sub> <sup>-</sup>	1.3	3.8	9.65
	344.1348	C <sub>15</sub> H <sub>22</sub> NO <sub>8</sub> <sup>-</sup>	0.3	0.9	8.25
	346.1502	C <sub>15</sub> H <sub>24</sub> NO <sub>8</sub> <sup>-</sup>	0.2	0.6	8.34
	360.1674	C <sub>16</sub> H <sub>26</sub> NO <sub>8</sub> <sup>-</sup>	1.6	4.4	8.89
	372.1667	C <sub>17</sub> H <sub>26</sub> NO <sub>8</sub> <sup>-</sup>	-0.6	-1.6	10.61
	374.1809	C <sub>17</sub> H <sub>28</sub> NO <sub>8</sub> <sup>-</sup>	-0.6	-1.6	8.89
	374.1816	C <sub>17</sub> H <sub>28</sub> NO <sub>8</sub> <sup>-</sup>	0.1	0.3	9.13
	374.1808	C <sub>17</sub> H <sub>28</sub> NO <sub>8</sub> <sup>-</sup>	-0.7	-1.9	9.35
	390.1773	C <sub>17</sub> H <sub>28</sub> NO <sub>9</sub> <sup>-</sup>	0.9	2.3	8.49
	390.1778	C <sub>17</sub> H <sub>28</sub> NO <sub>9</sub> <sup>-</sup>	1.4	3.6	9.21
	435.1619	C <sub>17</sub> H <sub>27</sub> N <sub>2</sub> O <sub>11</sub> <sup>-</sup>	0.4	0.9	9.56

the alkoxy radical has four or more carbon atoms and can form a 6-membered transition state (Baldwin et al., 1977; Carter and Atkinson, 1985). The isomerization pathway leads to the formation of large hydroxycarbonyls, multifunctional products that are likely low in volatility. The relative importance of isomerization increases with the size of alkoxy radicals (Atkinson, 1994, 1997a, b; Atkinson et al., 1995, 1999), and larger compounds could exhibit increasing SOA yields under high-NO<sub>x</sub> conditions as a consequence of this mechanism. For example, Lim and Ziemann (2005) measured SOA yields up to  $\sim 50\%$  for C<sub>15</sub> alkanes in the presence of ppm levels of NO<sub>x</sub>. They proposed multiple isomerization steps leading to the formation of multifunctional compounds including nitrooxy, hydroxyl, and carbonyl groups, and it is suggested that the hydroxycarbonyls formed may isomerize to form furan species that can undergo further reactions (Lim and Ziemann, 2005). Gas-phase products that are consistent with the isomerization mechanism have been observed

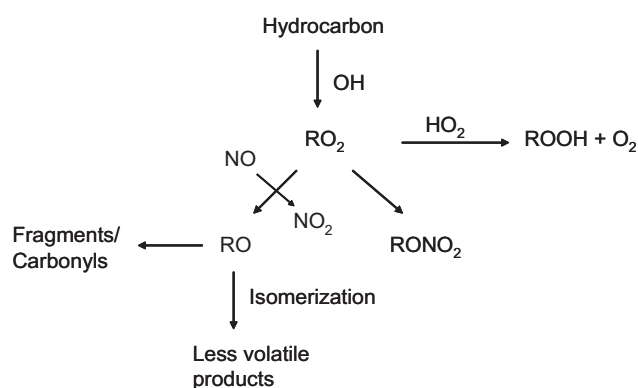


in  $\alpha$ -pinene photooxidation but this pathway does not appear to dominate SOA formation under high-NO<sub>x</sub> conditions (Aschmann et al., 1998, 2002), possibly due to the higher volatility of these species.

Higher SOA yields observed under high-NO<sub>x</sub> conditions for sesquiterpenes may, secondly, be a result of the formation of relatively nonvolatile organic nitrates, evidence for which appears in both Q-AMS data and filter sample data. In AMS data,  $m/z$  30 (NO<sup>+</sup>) and  $m/z$  46 (NO<sub>2</sub><sup>+</sup>) signals are commonly associated with nitrate species (organic and inorganic nitrates). For both  $\alpha$ -pinene and longifolene, the ratio of the sum of the intensities of ions at  $m/z$  30 and  $m/z$  46 to the total ion intensity is higher under high-NO<sub>x</sub> conditions: under low-NO<sub>x</sub> conditions, the ratio is very small (2%), under high-NO<sub>x</sub> conditions, the ratio is about 15–25%. The ratio of  $m/z$  30 to total mass and the ratio of  $m/z$  46 to total mass show the same trend, indicating  $m/z$  30 and  $m/z$  46 are correlated. It is possible that the signal at  $m/z$  30 could be the result of a non-nitrogen containing organic fragment ion; however, given the observed correlation between  $m/z$  30 and  $m/z$  46 and their small signals under low-NO<sub>x</sub> conditions, it appears that there is little interference from organics at these signals. Under high-NO<sub>x</sub> conditions,  $\sim 10 \mu\text{g m}^{-3}$  of inorganic nitrates, as measured by the PILS/IC, are present in the aerosol. Such nitrates may arise from the partitioning or reactive uptake of gas-phase HNO<sub>3</sub> into the aerosol phase. Assuming no non-nitrate contribution to  $m/z$  30 and  $m/z$  46, the total nitrate content of the SOA is estimated as the sum of the signals at each fragment. It is found that the calculated nitrate content ( $\sim 20 \mu\text{g m}^{-3}$ ) exceeds that measured by PILS/IC, suggesting the presence of organic nitrates.

The filter sample data provide a more direct comparison on the amount of organic nitrates formed in  $\alpha$ -pinene and longifolene photooxidation under different NO<sub>x</sub> conditions. For both  $\alpha$ -pinene and longifolene, no acidic nitrates are observed under low-NO<sub>x</sub> conditions, consistent with the lack of NO<sub>x</sub> and the prevailing RO<sub>2</sub>+HO<sub>2</sub> reaction in this case. Organic nitrate yield from the RO<sub>2</sub>+NO reaction increases with increasing carbon number (Atkinson et al., 1987; Carter and Atkinson, 1989; O'Brien et al., 1998; Arey et al., 2001; Aschmann et al., 2001; Zhang et al., 2004), and with the larger carbon skeleton the organic nitrates formed will be less volatile, this is consistent with the much wider array and larger quantities of acidic nitrates detected in longifolene photooxidation under high-NO<sub>x</sub> conditions compared to the  $\alpha$ -pinene experiments. Hence for photooxidation of larger compounds such as sesquiterpenes, the nitrate formation channel may play an important role in SOA formation under high-NO<sub>x</sub> conditions. With the formation of large molecular weight compounds with nitrate groups, mass-based SOA yields from longifolene photooxidation under high-NO<sub>x</sub> conditions actually exceed 100%.

Lacking appropriate analytical techniques for the detection of non-acidic nitrates, the contribution of these species under high-NO<sub>x</sub> conditions cannot be assessed. In  $\alpha$ -pinene



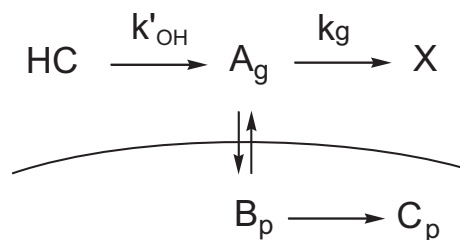
**Fig. 11.** General schematic of gas-phase peroxy radical chemistry in SOA formation.

photooxidation, hydroxynitrates have been identified in the gas phase using mass spectrometry (Aschmann et al., 1998, 2002). In SOA formation from alkanes under high-NO<sub>x</sub> conditions, Lim and Ziemann (2005) found that, while SOA from oxidation of C<sub>10</sub> alkane contains no  $\delta$ -hydroxynitrates, nitrates contribute  $\sim 40\%$  of the SOA mass for reactions of the C<sub>15</sub> alkane. It seems likely that higher levels of hydroxynitrates are present in longifolene SOA than in  $\alpha$ -pinene SOA.

## 5.2 General mechanisms of aerosol growth

### 5.2.1 Loss of semivolatiles

Substantial insight into the general mechanism of SOA formation and growth kinetics can be gained by examining “growth curves”, showing the amount of SOA formed per hydrocarbon reacted (Ng et al., 2006, 2007). Figure 2 shows the time-dependent growth curves from longifolene photooxidation under high- and low-NO<sub>x</sub> conditions. The high-NO<sub>x</sub> growth curves have a “convex” shape, indicating that aerosol growth slows down as longifolene approaches complete reaction. Similar behavior for longifolene growth was observed previously in our laboratory (Ng et al., 2006); the authors suggested that this atypical growth behavior may have been spurious, as a result of inaccuracies in PTR-MS measurements, owing to interference from product ions, or changes in the aerosol density over the course of the experiment. In this study, in those experiments in which the longifolene concentration is monitored by both GC-FID and PTR-MS, the shape of PTR-MS hydrocarbon decay agrees with that measured by GC-FID. The density of the aerosol is estimated during oxidation by comparing Q-AMS and DMA data. It is found that the SOA density decreases slightly ( $<5\%$ ) over the course of the experiment, however, such a small decrease in density is within experimental uncertainty and cannot account for the observed atypical growth behavior.



**Fig. 12.** A kinetic scheme depicting the competition between gas-particle partitioning and irreversible loss of the gas-phase semivolatiles. X represents the product of generic loss of semivolatile species  $A_g$  by chemical reaction, and/or loss to chamber walls.  $k'_{OH}$  is the pseudo-first-order rate constant ( $k'_{OH}=k_{OH}[OH]$ ) for photooxidation of the parent hydrocarbon;  $k_g$  is the first-order rate constant of loss of semivolatiles.

Deceleration in SOA growth can arise from the loss of semivolatiles by photolysis, further reaction with OH to form volatile products, or irreversible loss to chamber walls. Such processes reduce the amount of gas-phase semivolatiles species that partition into the aerosol phase. The effect on SOA growth of gas-phase reaction forming more volatile species has been examined in a recent modeling study (Chan et al., 2007). Figure 12 shows a kinetic scheme depicting the competition between gas-particle partitioning and irreversible loss of the gas-phase semivolatiles. X represents the product of generic loss of semivolatile species  $A_g$ ;  $k'_{OH}$  is the pseudo-first-order rate constant ( $k'_{OH}=k_{OH}[OH]$ ) for reaction of the parent hydrocarbon; and  $k_g$  is the first-order rate constant of loss of semivolatiles. When fitting the observed aerosol growth with this simple kinetic model, it is estimated that  $k_g$  is about 5 times larger than  $k'_{OH}$ . At the estimated OH concentration of  $\sim 2 \times 10^7$  molecules  $\text{cm}^{-3}$  under high-NO<sub>x</sub> conditions,  $k'_{OH}$  for longifolene is  $\sim 9.6 \times 10^{-4} \text{ s}^{-1}$ . A major difference in SOA composition under high- and low-NO<sub>x</sub> conditions is the presence of organic nitrates under high-NO<sub>x</sub> conditions. Thus the loss of organic nitrates (among other gas-phase species) may play a role in the observed deceleration in aerosol growth. The reaction rate constants of small alkyl nitrates with OH are generally of the order of  $10^{-13} \text{ cm}^3 \text{ molecule}^{-1} \text{ s}^{-1}$  (hence pseudo-first-order reaction rate of  $\sim 10^{-6} \text{ s}^{-1}$ ) and their photolysis rates have been measured to be  $\sim 1 \times 10^{-6} \text{ s}^{-1}$  (Talukdar et al., 1997; Finlayson-Pitts and Pitts, 2000). Although the OH reaction rate and photolysis rate of organic nitrates are much slower than the oxidation rate of longifolene, both rates are expected to increase with carbon number (Talukdar et al., 1997; Finlayson-Pitts and Pitts, 2000; Treves and Rudich, 2003). Hence, it is possible that gas-phase reaction of C<sub>15</sub> organic nitrates may be occurring at an appreciable rate. Further study on the OH reaction rate constant and photolysis rate of larger nitrates would be useful in evaluating the importance of gas-phase nitrate chemistry in aerosol formation.

Such a deceleration in SOA growth is not observed in longifolene low-NO<sub>x</sub> experiments. This is in contrast to the rapid decrease in aerosol volume observed in isoprene photooxidation under low-NO<sub>x</sub> conditions, in which photolysis and/or further reactions of organic hydroperoxides may be occurring (Kroll et al., 2006). There is evidence for further reactions with longifolene low-NO<sub>x</sub> SOA as well: the AMS  $m/z$  44 ( $\text{CO}_2^+$ ) mass fraction increases over the course of the experiment (Fig. 9), indicating the SOA is being further oxidized. Unlike with isoprene photooxidation, however, the compounds formed from the further oxidation of longifolene products are likely sufficiently nonvolatile to remain in the particle phase. The photochemistry of larger and more complex hydroperoxides merits further investigation.

### 5.2.2 SOA formation from higher generation products

In Figs. 1 and 3, the growth curves of  $\alpha$ -pinene and longifolene photooxidation exhibit a “hook” at the end of the intermediate NO<sub>x</sub> experiments, indicating that aerosol growth continues after the complete consumption of the parent hydrocarbon. Organic mass measured by the Q-AMS increases even after all the hydrocarbon is consumed, indicating that this additional aerosol growth is not a result of condensation of inorganic nitrate. Continued aerosol growth can arise from further gas-phase reactions of reactive oxidation products, such as aldehydes and furans, etc, or from further particle-phase reactions. In the intermediate NO<sub>x</sub> experiments, the NO concentration goes to zero within 20 min after the commencement of photooxidation, owing to the rapid reaction of NO and peroxy radicals ( $\text{HO}_2$  and other peroxy radicals). As a result, a transition from high-NO<sub>x</sub> to low-NO<sub>x</sub> conditions occurs over the course of the experiment, and the final aerosol formed is potentially a mixture of the products formed under both conditions. It is possible that particle-phase reactions, such as the formation of peroxyhemiacetals from hydroperoxides and aldehyde species, may be contributing to the further aerosol growth observed in the intermediate NO<sub>x</sub> experiments (Johnson et al., 2004, 2005).

## 6 Implications

A series of chamber experiments investigating the NO<sub>x</sub> dependence of SOA formation from the photooxidation of one monoterpene and two sesquiterpenes is reported here. SOA formation from monoterpenes such as  $\alpha$ -pinene is found to have a similar NO<sub>x</sub> dependence as isoprene (as well as other hydrocarbons with 10 or fewer carbons, such as aromatic species), in which the aerosol yields are substantially higher under low-NO<sub>x</sub> conditions. The NO<sub>x</sub> dependence of SOA formation from the two sesquiterpenes is, however, markedly different; for longifolene and aromadendrene, aerosol yields are at their maximum under high-NO<sub>x</sub> conditions. The reason for this reversal of the NO<sub>x</sub> dependence, while not

unequivocally established here, may be the result of production of highly nonvolatile organic nitrates, the existence of which is suggested by both Q-AMS and filter sample data, and/or isomerization of alkoxy radicals to form low-volatility multifunctional organics.

The increase in SOA yield from photooxidation of the larger biogenic hydrocarbons under high-NO<sub>x</sub> conditions could have implications in terms of the effect of anthropogenically influenced air masses on biogenic SOA formation. In the recent study of de Gouw et al. (2005), it is suggested that over the western Atlantic the majority of the measured organic aerosol is from secondary anthropogenic sources, a conclusion that is somewhat at odds with the radio-carbon measurements that indicate high fractions of “modern” (presumably biogenic) carbon (e.g. Klinedinst and Currie, 1999; Weber et al., 2007). If the production of SOA from biogenic hydrocarbons is enhanced in the presence of NO<sub>x</sub>, observations of enhanced SOA correlated with anthropogenic sources can occur, even for organic carbon of biogenic origin. Large anthropogenic hydrocarbons may exhibit a similar NO<sub>x</sub> behavior as that of the sesquiterpenes studied, as suggested by the substantial SOA yields from the OH-initiated reaction of large alkanes in the presence of ppm levels of NO<sub>x</sub> (Lim and Ziemann, 2005). If the NO<sub>x</sub> behavior observed for longifolene and aromadendrene extends to other sesquiterpenes as well as larger alkanes, the contribution to the total SOA from these compounds in polluted air may actually be higher than previously estimated (Griffin et al., 1999a, b; Carreras-Sospedra et al., 2005; de Gouw et al., 2005).

In this study, we have investigated the NO<sub>x</sub> dependence of SOA formation from photooxidation of only the monoterpene  $\alpha$ -pinene and two sesquiterpenes, each containing one double bond. SOA formation from compounds with two or more double bonds can exhibit characteristics that suggest significant contributions from multiple generation products (Ng et al., 2006) and this may have impacts on the NO<sub>x</sub> dependence. It is clear that the effect of NO<sub>x</sub> on SOA yields from the complete suite of atmospherically relevant aerosol-forming hydrocarbons should be evaluated thoroughly.

## Appendix A

### Description of PTR-MS technique

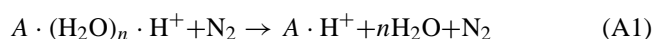
For PTR-MS sampling, a constant flow of  $\sim 2.5$  standard liters per minute (slm) is drawn from the chamber through PFA tubing. The residence time in the inlet tubing is roughly 1 s. A small portion of the flow, 93 standard cubic centimeters per minute (sccm), is pulled through a glass critical orifice into a 2.54-cm diameter glass flow tube, in which this sample flow is diluted with dry N<sub>2</sub> (1.6 slm) to maintain the flow tube pressure at 35 mbar. This dilution minimizes confounding effects owing to large concentrations of hydrogen

peroxide and other compounds typically used or produced in chamber experiments.

In the flow tube, analyte ionization occurs in a manner similar to that described by Crounse et al. (2006) for negative ionization. N<sub>2</sub> (400 sccm) flows through an ion source cup composed of a cylindrical silver foil lined with <sup>210</sup>Po and sealed with gold.  $\alpha$  bombardment from the <sup>210</sup>Po, coupled with trace water present in the N<sub>2</sub>, leads to the formation of positively charged clusters, e.g. (H<sub>2</sub>O)<sub>n</sub>H<sup>+</sup>. The electric potentials of the ion source components are set such that these positively charged clusters then pass through a 6.35 mm aperture into the 35 mbar flow tube, flowing perpendicular to the sample flow. The clusters then react via proton transfer with the analyte (e.g. aromadendrene) in the sample flow to form aromadendrene-H<sup>+</sup> and higher order water clusters.

Across the flow tube from the ion source, a pinhole aperture (diameter 0.34 mm) allows a portion of the ions and neutral gas ( $\sim 30$  sccm) to flow into the mass spectrometer, a Varian 1200 tandem mass spectrometer. The spectrometer was modified by removing the electron impact source and extending the hexapole ion guide that leads to the quadrupole mass analyzer to the pinhole aperture. For these measurements, the mass spectrometer was operated exclusively in one-dimensional mass spectrometry mode.

In order to simplify the mass spectra, a DC potential of  $-10$  V (relative to the pinhole aperture) is applied to the hexapole. This offset pulls ions into the hexapole, where the pressure is relatively high owing to the neutral gas flow (chiefly N<sub>2</sub>) through the pinhole. The ions therefore undergo high energy collisions with the neutral gas molecules which dissociate water clusters of analyte A:



Thus, species are predominantly observed at  $m/z = M+1$ , where  $M$  is the molecular mass of the species. Hydrates,  $A \cdot (H_2O)_m \cdot H^+$ , particularly  $m=1$ , are also observed for some species, though not for aromadendrene or longifolene.

Each day, the PTR-MS sensitivity towards aromadendrene was determined by sampling standard mixtures of aromadendrene in teflon bags filled with 50 L zero air. The sensitivity was determined to be linear from 0 ppb to at least 5 ppb. Also, because of the large amounts of H<sub>2</sub>O<sub>2</sub> utilized in the experiments, the sensitivity as a function of H<sub>2</sub>O<sub>2</sub> was determined, with [H<sub>2</sub>O<sub>2</sub>] measured by operating the Varian 1200 in negative ionization mode, exploiting the reaction of CF<sub>3</sub>O<sup>-</sup> with H<sub>2</sub>O<sub>2</sub> (Crounse et al., 2006). Thus, the sensitivity determined from H<sub>2</sub>O<sub>2</sub>-free standards was corrected for sampling from the chamber when H<sub>2</sub>O<sub>2</sub> was present.

The uncertainty of aromadendrene measurements using PTR-MS is estimated to be  $\sim \pm 22\%$ , based on the scatter of replicate data and background measurements and uncertainties in the H<sub>2</sub>O<sub>2</sub> correction.

## Appendix B

### Description of UPLC/ESI-TOFMS technique

Filter extracts (in 1:1 (v/v) solvent mixture of methanol and 0.1% aqueous acetic acid solution) are analyzed by a Waters ACQUITY ultra performance liquid chromatography (UPLC) system, coupled with a Waters LCT Premier time-of-flight (TOF) mass spectrometer (MS) equipped with an electrospray ionization (ESI) source. The ESI source on this instrument contains two individual sprays; one spray is for the eluent and the other is for the lock-mass correction. Optimum ESI conditions are found using a 2.5 kV capillary voltage, 40 V sample cone voltage, 350°C desolvation temperature, 130°C source temperature, 20 L h<sup>-1</sup> cone gas flow rate, and a 650 L h<sup>-1</sup> desolvation gas flow rate. Data are collected from *m/z* 50–1000 in the negative (–) ionization mode using the TOFMS operated in the W geometry reflectron mode. The W reflectron mode offers the highest mass resolution, which is approximately 12 000, and allows for exact mass measurements to be conducted on detected SOA components. The chromatographic separations are carried out on a Waters ACQUITY HPLC HSS (high strength silica) column (2.1 × 100 mm, 1.8 μm particle size) at 45°C using a gradient elution scheme. The eluent composition is (A) 0.1% acetic acid in water and (B) 0.1% acetic acid in methanol; both eluents are high purity solvents (LC-MS ChromaSolv Grade, Sigma-Aldrich). In the 12-min gradient elution program used, the concentration of eluent B is 0% for the first 2 min, increased to 90% from 2 to 10 min, held at 90% from 10 to 10.2 min; and then decreased back to 0% from 10.2 to 12 min. The flow rate of the eluent is 0.3 mL min<sup>-1</sup> and the sample injection volume is 2 μL. At the beginning of each analysis period, the TOFMS is calibrated using a 1:1 (v/v) solvent mixture of acetonitrile and 0.1% phosphoric acid aqueous solution. During each chromatographic run, 2 ng/μL of leucine enkephalin (MW=555) is used for the lock-mass spray for lock-mass correction to obtain accurate masses for each SOA component eluting from the column. The lock-mass syringe pump is operated at 20 μL min<sup>-1</sup>. In addition to the lock-mass spray, the dynamic range enhancement feature of this mass spectrometer is applied to prevent dead time, which affects mass accuracy, from occurring. As confirmation of the UPLC/ESI-TOFMS technique, a standard sample containing known isoprene and α-pinene sulfate esters previously characterized by Surratt et al. (2007) are analyzed. The known elemental compositions (i.e. molecular formulas) of the previously characterized sulfate esters (Surratt et al., 2007) are in excellent agreement with their measured exact masses (i.e. within ±2 mDa or ±2 ppm). In addition to exact mass measurements, further insights into the structures of the SOA components are obtained by generating tandem MS data, which are generated by increasing the first aperture voltage on the TOFMS from 10 V to 25 V.

**Acknowledgements.** This research was funded by U.S. Department of Energy Biological and Environmental Research Program grant DE-FG02-05ER63983. This material is based in part on work supported by the National Science Foundation (NSF) under grant ATM-0432377. The Waters LCT Premier XT time-of-flight mass spectrometer interfaced to a Waters UPLC system was purchased in 2006 with a grant from the National Science Foundation, Chemistry Research Instrumentation and Facilities Program (CHE-0541745). The LCQ Ion Trap mass spectrometer was purchased in 1997 with funds from the National Science Foundation through the CRIF program (CHE-9709233). J. D. Surratt is supported in part by the U.S. EPA under the STAR Graduate Fellowship Program. A. J. Kwan acknowledges the support of a NSF graduate research fellowship. The authors would like to thank M. Shahgohli of the Chemistry Department at Caltech for her useful communications regarding high-resolution mass spectrometry.

Edited by: A. Nenes

### References

- Alfarra, M. R., Paulsen, D., Gysel, M., Garforth, A. A., Dommen, J., Prevot, A. S. H., Worsnop, D. R., Baltensperger, U., and Coe, H.: A mass spectrometric study of secondary organic aerosols formed from the photooxidation of anthropogenic and biogenic precursors in a reaction chamber, *Atmos. Chem. Phys.*, 6, 5279–5293, 2006, <http://www.atmos-chem-phys.net/6/5279/2006/>.
- Arey, J., Aschmann, S. M., Kwok, E. S. C., and Atkinson, R.: Alkyl nitrates, hydroxyalkyl nitrates and hydroxycarbonyl formation from the NO<sub>x</sub> – air photooxidation of C<sub>5</sub>–C<sub>8</sub> n-alkanes, *J. Phys. Chem. A*, 105, 1020–1027, 2001.
- Aschmann, S. M., Arey, J., and Atkinson, R.: Atmospheric chemistry of three C<sub>10</sub> alkanes, *J. Phys. Chem. A*, 105, 7598–7606, 2001.
- Aschmann, S. M., Atkinson, R., and Arey, J.: Products of reaction of OH radicals with α-pinene, *J. Geophys. Res.*, 107(D14), 4191, doi:10.1029/2001JD001098, 2002.
- Aschmann, S. M., Reissell, A., Atkinson, R., and Arey, J.: Products of the gas phase reactions of the OH radical with α- and β-pinene in the presence of NO, *J. Geophys. Res.*, 103(D19), 4191, 25 553–25 561, 1998.
- Aschmann, S. M., Reissell, A., Atkinson, R., and Arey, J.: Products of the gas phase reactions of the OH radical with a- and b-pinene in the presence of NO, *J. Geophys. Res.*, 103(D19), 25 553–25 561, 1998.
- Atkinson, R., Kwok, E. S. C., Arey, J., and Aschmann, S. M.: Reactions of alkoxy radicals in the atmosphere, *Faraday Discuss.*, 100, 23–37, 1995.
- Atkinson, R. and Arey, J.: Gas-phase tropospheric chemistry of biogenic volatile organic compounds: a review, *Atmos. Environ.*, 37, S197–S219, 2003.
- Atkinson, R., Aschmann, S. M., and Winer, A. M.: Alkyl nitrate formation from the reaction of a series of branched RO<sub>2</sub> radicals with NO as a function of temperature and pressure, *J. Phys. Chem.*, 5, 91–102, 1987.
- Atkinson, R., Baulch, D. L., Cox, R. A., Hampson, R. F., Kerr, J. A., Rossi, M. J., and Troe, J.: Evaluated kinetic and photochemical

- data for atmospheric chemistry, organic species, supplement VII, *J. Phys. Chem. Ref. Data.*, 28, 2, 1999.
- Atkinson, R.: Atmospheric reactions of alkoxy and  $\beta$ -hydroxyalkoxy radicals, *Int. J. Chem. Kinet.*, 29, 99–111, 1997a.
- Atkinson, R.: Gas phase tropospheric chemistry of organic compounds, *J. Phys. Chem. Ref. Data, Monogr.*, 2, 11–216, 1994.
- Atkinson, R.: Gas phase tropospheric chemistry of volatile organic compounds: 1. Alkanes and Alkenes, *J. Phys. Chem. Ref. Data.*, 215–290, 1997b.
- Baldwin, A. C., Barker, J. R., Golden, D. M., and Hendry, D. G.: Photochemical smog – rate parameter estimates and computer simulations, *J. Phys. Chem.*, 81, 2483–2492, 1977.
- Bahreini, R., Keywood, M. D., Ng, N. L., Varutbangkul, V., Gao, S., Flagan, R. C., and Seinfeld, J. H.: Measurements of secondary organic aerosol (SOA) from oxidation of cycloalkenes, terpenes, and m-xylene using an Aerodyne aerosol mass spectrometer, *Environ. Sci. Technol.*, 39, 5674–5688, 2005.
- Carreras-Sospedra, M., Griffin, R. J., and Dabdub, D.: Calculations of incremental secondary organic aerosol reactivity, *Environ. Sci. Technol.*, 39, 1724–1730, 2005.
- Carter, W. P. L. and Atkinson, R.: Alkyl nitrate formation from the atmospheric photooxidation of alkanes; a revised estimation, *J. Phys. Chem.*, 8, 165–173, 1989.
- Carter, W. P. L. and Atkinson, R.: Atmospheric chemistry of alkanes, *J. Atmos. Chem.* 3, 377–405, 1985.
- Chan, A. W. H., Kroll, J. H., Ng, N. L., and Seinfeld, J. H.: Kinetic modeling of secondary organic aerosol formation: effect of particle- and gas-phase reactions of semivolatile products, *Atmos. Chem. Phys. Discuss.*, 7, 7051–7085, 2007, <http://www.atmos-chem-phys-discuss.net/7/7051/2007/>.
- Cocker III, D. R., Flagan, R. C., and Seinfeld, J. H.: State-of-the-art chamber facility for studying atmospheric aerosol chemistry, *Environ. Sci. Technol.*, 35, 2594–2601, 2001.
- Crounse, J. D., McKinney, K. A., Kwan, A. J., and Wennberg, P. O.: Measurements of gas-phase hydroperoxides by chemical ionization mass spectrometry, *Anal. Chem.*, 78, 6726–6732, 2006.
- de Gouw, J. A., Middlebrook, A. M., Warneke, C., Goldan, P. D., Kuster, W. C., Roberts, J. M., Fehsenfeld, F. C., Worsnop, D. R., Canagaratna, M. R., Pszenny, A. A. P., Keene, W. C., Marchewka, M., Bertman, S. B., and Bates, T. S.: Budget of organic carbon in a polluted atmosphere: Results from the New England Air Quality Study in 2002, *J. Geophys. Res.*, 110, D16305, doi:10.1029/2004JD005623, 2005.
- Finlayson-Pitts, B. J. and Pitts, J. N.: Chemistry of the upper and lower atmosphere: theory, experiments and applications, Academic Press, San Diego, 220–221, 2000.
- Gao, S., Keywood, M. D., Ng, N. L., Surratt, J. D., Varutbangkul, V., Bahreini, R., Flagan, R. C., and Seinfeld, J. H.: Low-molecular weight and oligomeric components in secondary organic aerosol from the ozonolysis of cycloalkenes and  $\alpha$ -pinene, *J. Phys. Chem. A*, 108, 10 147–10 164, 2004.
- Gao, S., Surratt, J. D., Knipping, E. M., Edgerton, E. S., Shahgholi, M., and Seinfeld, J. H.: Characterization of polar organic components in fine aerosols in the southeastern United States: Identity, origin, and evolution, *J. Geophys. Res.*, 111, D14314, doi:10.1029/2005JD006601, 2006.
- Geron, C., Rasmussen, R., Arnts, R. R., and Guenther, A.: A review and synthesis of monoterpene speciation from forests in the United States, *Atmos. Environ.*, 34, 1761–1781, 2000.
- Glasius, M., Duane, M., and Larsen, B. R.: Determination of polar terpene oxidation products in aerosols by liquid chromatography-ion trap mass spectrometry, *J. Chrom. A.*, 833, 121–135, 1999.
- Glasius, M., Lahaniati, M., Calogirou, A., Di Bella, D., Jensen, N. R., Hjorth, J., Kotzias, D., and Larsen, B. R.: Carboxylic acids in secondary aerosols from oxidation of cyclic monoterpenes by ozone, *Environ. Sci. Technol.*, 34, 1001–1010, 2000.
- Griffin, R. J., Cocker, D. R., Flagan, R. C., Seinfeld, J. H., and Dabdub, D.: Estimate of global atmospheric organic aerosol formation from the oxidation of biogenic hydrocarbons, *Geophys. Res. Lett.*, 26, 17, 2721–2724, 1999a.
- Griffin, R. J., Cocker, D. R., Flagan, R. C., and Seinfeld, J. H.: Organic aerosol formation from the oxidation of biogenic hydrocarbons, *J. Geophys. Res.*, 104(D3), 3555–3567, 1999b.
- Guenther, A., Hewitt, C. N., Erickson, D., Fall, R., Geron, C., Graedel, T., Harley, P., Klinger, L., Lerdau, M., McKay, W. A., Pierce, T., Scholes, B., Steinbrecher, R., Tallamraju, R., Taylor, T., and Zimmerman, P.: A global model of natural volatile organic compound emission, *J. Geophys. Res.*, 100, (D5), 8873–8892, 1995.
- Hatakeyama, S., Izumi, K., Fukuyama, T., Akimoto, H., and Washida, N.: Reactions of OH with  $\alpha$ -pinene and  $\beta$ -pinene in air: Estimates of global CO production from the atmospheric oxidation of terpenes, *J. Geophys. Res.*, 96(D1), 947–958, 1991.
- Hurley, M. D., Sokolov, O., Wallington, T. J., Takekawa, H., Karasawa, M., Klotz, B., Barnes, I., and Becker, K. H.: Organic aerosol formation during the atmospheric degradation of toluene, *Environ. Sci. Technol.*, 35, 1358–1366, 2001.
- Jayne, J. T., Leard, D. C., Zhang, X., Davidovits, P., Smith, K. A., Kolb, C. E., and Worsnop, D. W.: Development of an Aerosol Mass Spectrometer for size and composition analysis of submicron particles, *Aerosol Sci. Tech.*, 33, 49–70, 2000.
- Johnson, D., Jenkin, M. E., Wirtz, K., and Martín-Reviejo, M.: Simulating the formation of secondary organic aerosol from the photooxidation of aromatic hydrocarbons, *Environ. Chem.*, 2, 35–48, 2005.
- Johnson, D., Jenkin, M. E., Wirtz, K., and Martín-Reviejo, M.: Simulating the formation of secondary organic aerosol from the photooxidation of toluene, *Environ. Chem.*, 1, 150–165, 2004.
- Kanakidou, M., Seinfeld, J. H., Pandis, S. N., Barnes, I., Dentener, F. J., Facchini, M. C., Van Dingenen, R., Evers, B., Nenes, A., Swietlicki, E., Pautaud, J. P., Balkanski, Y., Fuzzi, S., Horth, J., Moortgat, G. K., Winterhalter, R., Myhre, C. E. L., Tsigaridis, K., Vignati, E., Stephanou, E. G., and Wilson, J.: Organic aerosol and global climate modeling: a review, *Atmos. Chem. Phys.*, 5, 1053–1123, 2005, <http://www.atmos-chem-phys.net/5/1053/2005/>.
- Keywood, M. D., Varutbangkul, V., Bahreini, R., Flagan, R. C., and Seinfeld, J. H.: Secondary organic aerosol formation from the ozonolysis of cycloalkenes and related compounds, *Environ. Sci. Technol.*, 38, 4157–4164, 2004.
- Klinedinst, D. B. and Currie, L. A.: Direct quantification of PM<sub>2.5</sub> fossil and biomass carbon within the northern front range air quality study's domain, *Environ. Sci. Technol.*, 33, 4146–4154, 1999.
- Kroll, J. H., Ng, N. L., Murphy, S. M., Flagan, R. C., and Seinfeld, J. H.: Secondary organic aerosol formation from isoprene photooxidation under high-NO<sub>x</sub> conditions, *J. Geophys. Res.*, 32,

- L18808, doi:10.1029/2005GL023637, 2005.
- Kroll, J. H., Ng, N. L., Murphy, S. M., Flagan, R. C., and Seinfeld, J. H.: Secondary organic aerosol formation from isoprene photooxidation, *Environ. Sci. Technol.*, 40, 1869–1877, 2006.
- Larsen, B. R., Di Bellla, D., Glasius, M., Winterhalter, R., Jensen, N. R., and Hjorth, J.: Gas-phase OH oxidation of monoterpenes: Gaseous and particulate products, *J. Atmos. Chem.*, 38, 231–276, 2001.
- Lim, Y. B. and Ziemann, P. J.: Products and mechanism of secondary organic aerosol formation from reactions of *n*-alkanes with OH radicals in the presence of NO<sub>x</sub>, *Environ. Sci. Technol.*, 39, 9229–9236, 2005.
- Ng, N. L., Kroll, J. H., Keywood, M. D., Bahreini, R., Varutbangkul, V., Flagan, R. C., Seinfeld, J. H., Lee, A., and Goldstein, A. H.: Contribution of first- versus second-generation products to secondary organic aerosols formed in the oxidation of biogenic hydrocarbons, *Environ. Sci. Technol.*, 40, 2283–2297, 2006.
- Ng, N. L., Kroll, J. H., Chan, A. W. H., Chhabra, P. S., Flagan, R. C., and Seinfeld, J. H.: Secondary organic aerosol formation from *m*-xylene, toluene, and benzene, *Atmos. Chem. Phys. Discuss.*, 7, 4085–4126, 2007, <http://www.atmos-chem-phys-discuss.net/7/4085/2007/>.
- O'Brien, J. M., Czuba, E., Hastie, D. R., Francisco, J. S., and Shepson, P. B.: Determination of the hydroxy nitrate yields from the reaction of C<sub>2</sub>–C<sub>6</sub> alkenes with OH in the presence of NO, *J. Phys. Chem.*, 102, 8903–8908, 1998.
- Odum, J. R., Hoffmann, T., Bowman, F., Collins, D., Flagan, R. C., and Seinfeld, J. H.: Gas/particle partitioning and secondary organic aerosol yields, *Environ. Sci. Technol.*, 30, 2580–2585, 1996.
- Odum, J. R., Jungkamp, T. P. W., Griffin, R. J., Forstner, H. J. L., Flagan, R. C., and Seinfeld, J. H.: Aromatics, reformulated gasoline and atmospheric organic aerosol formation, *Environ. Sci. Technol.*, 31, 1890–1897, 1997.
- Owen, S. M., Boissard, C., and Hewitt, C. N.: Volatile organic compounds (VOCs) emitted from 40 Mediterranean plant species: VOC speciation and extrapolation to habitat scale, *Atmos. Environ.*, 35, 5393–5409, 2001.
- Pandis, S. N., Paulson, S. E., Seinfeld, J. H., and Flagan, R. C.: Aerosol formation in the photooxidation of isoprene and  $\beta$ -pinene, *Atmos. Environ.*, 25A, 997–1008, 1991.
- Presto, A. A., Huff Hartz, K. E., and Donahue, N. M.: Secondary organic aerosol production from ozonolysis: 2. Effect of NO<sub>x</sub> concentration, *Environ. Sci. Technol.*, 39, 7046–7054, 2005.
- Seinfeld, J. and Pankow, J. F.: Organic atmospheric particulate material, *Annu. Rev. Phys. Chem.*, 54, 121–140, 2003.
- Song, C., Na, K., and Cocker III, D. R.: Impact of the hydrocarbon to NO<sub>x</sub> ratio on secondary organic aerosol formation, *Environ. Sci. Technol.*, 39, 3143–3149, 2005.
- Sorooshian, A., Brechtel F. J., Ma, Y. L., Weber R. J., Corless, A., Flagan, R. C., and Seinfeld, J. H.: Modeling and characterization of a particle-into-liquid sampler (PILS), *Aerosol Sci. Tech.*, 40, 396–409, 2006.
- Surratt, J. D., Kroll, J. H., Kleindienst, T. E., Edney, E. O., Claeys, M., Sorooshian, A., Ng, N. L., Offenberg, J. H., Lewandowski, M., Jaoui, M., Flagan, R. C., and Seinfeld, J. H.: Evidence for organosulfates in secondary organic aerosol, *Environ. Sci. Technol.*, 41, 517–527, 2007.
- Surratt, J. D., Murphy, S. M., Kroll, J. H., Ng, N. L., Hildebrandt, L., Sorooshian, A., Szmigielski, R., Vermeylen, R., Maenhaut, W., Claeys, M., Flagan, R. C., and Seinfeld, J. H.: Chemical composition of secondary organic aerosol formed from the photooxidation of isoprene, *J. Atmos. Chem.*, 31, 9665–9690, 2006.
- Szmigielski, R., Surratt, J. D., Vermeylen, R., Szmigielska, K., Kroll, J. H., Ng, N. L., Murphy, S. M., Sorooshian, A., Seinfeld, J. H., and Claeys, M.: Characterization of 2-methylglyceric acid oligomers in secondary organic aerosol formed from the photooxidation of isoprene using trimethylsilylation and gas chromatography/ion trap mass spectrometry, *J. Mass Spectrom.*, 42, 101–116, 2007.
- Talukdar, R. K., Herndon, S. C., Burkholder, J. B., Roberts, J. M., and Ravishankara, A. R.: Atmospheric fate of several alkyl nitrates, *J. Chem. Soc., Faraday Trans.*, 93, 2787–2796, 1997.
- Treves, K. and Rudich, Y.: The atmospheric fate of C<sub>3</sub>–C<sub>6</sub> hydroxylalkyl nitrates, *J. Phys. Chem. A*, 107, 7809–7817, 2003.
- Weber, R. J., Sullivan, A., Peltier, R. E., Russell, A., Yan, B., Zheng, M., de Gouw, J., Warneke, C., Brock, C., Holloway, J. S., Atlas, E. L., and Edgerton, E.: A study of secondary organic aerosol formation in the anthropogenic-influenced southeastern USA, *J. Geophys. Res.*, 112, D13302, doi:10.1029/2007JD008408, 2007.
- Zhang, J., Dransfield, T., and Donahue, N. M.: On the mechanism for nitrate formation via the peroxy radical + NO reaction, *J. Phys. Chem. A*, 108, 9082–9095, 2004.
- Zhang, J., Hartz, K. E. H., Pandis, S. N., and Donahue, N. M.: Secondary organic aerosol formation from limonene ozonolysis: Homogeneous and heterogeneous influences as a function of NO<sub>x</sub>, *J. Phys. Chem. A*, 110, 11 053–11 063, 2006.
- Zhang, S. H., Shaw, M., Seinfeld, J. H., and Flagan, R. C.: Photochemical aerosol formation from  $\alpha$ -pinene and  $\beta$ -pinene, *J. Geophys. Res.*, 97(D18), 20 717–20 729, 1992.

## Appendix H

### Secondary Organic Aerosol (SOA) Formation from Reaction of Isoprene with Nitrate Radicals ( $\text{NO}_3$ )\*

---

\*This chapter is reproduced by permission from “Secondary Organic Aerosol (SOA) Formation from Reaction of Isoprene with Nitrate Radicals ( $\text{NO}_3$ )” by N. L. Ng, A. J. Kwan, J. D. Surratt, A. W. H. Chan, P. S. Chhabra, A. Sorooshian, H. O. T. Pye, J. D. Crounse, P. O. Wennberg, R. C. Flagan, and J. H. Seinfeld, *Atmos. Chem. Phys. Disc.*, 8, 3163-3226, 2008. © 2008 Author(s). This work is distributed under the Creative Commons Attribution 3.0 License.

**Secondary organic aerosol (SOA) formation from reaction of isoprene with nitrate radicals (NO<sub>3</sub>)**

Nga L. Ng<sup>1</sup>, Alan J. Kwan<sup>2</sup>, Jason D. Surratt<sup>1</sup>, Arthur W. H. Chan<sup>1</sup>, Puneet S. Chhabra<sup>1</sup>, Armin Sorooshian<sup>1</sup>, Haval O. T. Pye<sup>1</sup>, John D. Crounse<sup>1</sup>, Paul O. Wennberg<sup>2,3</sup>, Richard C. Flagan<sup>1,2</sup>, and John H. Seinfeld<sup>1,2\*</sup>

<sup>1</sup>Divison of Chemistry and Chemical Engineering, California Institute of Technology, Pasadena, CA 91125

<sup>2</sup>Divison of Engineering and Applied Science, California Institute of Technology, Pasadena, CA 91125

<sup>3</sup>Divison of Geological and Planetary Sciences, California Institute of Technology, Pasadena, CA 91125

\* Author to whom correspondence should be addressed. Phone (626) 395-4635, fax (626) 796-2591, e-mail seinfeld@caltech.edu



## Abstract

Secondary organic aerosol (SOA) formation from the reaction of isoprene with nitrate radicals ( $\text{NO}_3$ ) is investigated in the Caltech indoor chambers. Experiments are performed in the dark and under dry conditions ( $\text{RH} < 10\%$ ) using  $\text{N}_2\text{O}_5$  as a source of  $\text{NO}_3$  radicals. For an initial isoprene concentration of 18.4 to 101.6 ppb, the SOA yield (defined as the ratio of the mass of organic aerosol formed to the mass of parent hydrocarbon reacted) ranges from 4.3% to 23.8%. By examining the time evolutions of gas-phase intermediate products and aerosol volume in real time, we are able to constrain the chemistry that leads to the formation of low-volatility products. Although the formation of ROOR from the reaction of two peroxy radicals ( $\text{RO}_2$ ) has generally been considered as a minor channel, based on the gas-phase and aerosol-phase data it appears that  $\text{RO}_2 + \text{RO}_2$  reaction (self reaction or cross-reaction) in the gas phase yielding ROOR products is a dominant SOA formation pathway. A wide array of organic nitrates and peroxides are identified in the aerosol formed and mechanisms for SOA formation are proposed. Using a uniform SOA yield of 10% (corresponding to  $M_o \approx 10 \mu\text{g m}^{-3}$ ), it is estimated that  $\sim 2$  to  $3 \text{ Tg yr}^{-1}$  of SOA results from isoprene +  $\text{NO}_3$ . The extent to which the results from this study can be applied to conditions in the atmosphere depends on the fate of peroxy radicals (i.e. the relative importance of  $\text{RO}_2 + \text{RO}_2$  versus  $\text{RO}_2 + \text{NO}_3$  reactions) in the nighttime troposphere.

## 1. Introduction

Isoprene is the most abundant non-methane hydrocarbon emitted into the atmosphere with a global emission of  $\sim 500 \text{ Tg yr}^{-1}$  (Guenther et al., 1995; Guenther et al., 2006). In the troposphere, isoprene reacts with hydroxyl radicals (OH), ozone ( $\text{O}_3$ ), and nitrate radicals ( $\text{NO}_3$ ). Owing to its high concentration and reactivity with OH radicals, isoprene plays an important role in the photochemistry occurring within the atmospheric boundary layer. Recently, it has been shown that the photooxidation of isoprene leads to the formation of low volatility species that condense to form SOA (Claeys et al., 2004; Edney et al., 2005; Kroll et al., 2005; Dommen et al., 2006; Kroll et al., 2006; Surratt et al., 2006); SOA yields as high as  $\sim 3\%$  have been observed (Kroll et al., 2005; Kroll et al., 2006). Global SOA production from isoprene photooxidation has been estimated to be about  $13 \text{ Tg yr}^{-1}$  (Henze et al., 2007).

Although emission of isoprene from vegetation is triggered by sunlight and increases with light intensity and temperature (e. g. Sharkey et al., 1996), the isoprene mixing ratio has been observed to peak in early evening in several field studies, with a measured mixing ratio up to a few ppb (Curren et al., 1998; Starn et al., 1998; Stroud et al., 2002; Steinbacher et al., 2005). After sunset, the isoprene mixing ratio drops rapidly, and it has been suggested that the reaction with nitrate radicals,  $\text{NO}_3$ , is a major contributor to isoprene decay at night (Curren et al., 1998; Starn et al., 1998; Stroud et al., 2002; Steinbacher et al., 2005). Typical  $\text{NO}_3$  radical mixing ratios in boundary layer continental air masses range between  $\sim 10$  to  $\sim 100 \text{ ppt}$  (Platt and Janssen, 1995; Smith et al., 1995; Heintz et al., 1996; Carslaw et al., 1997). However, concentrations as high as several hundred ppt have been observed over northeastern USA and Europe (Platt et al.,

1981; von Friedeburg et al., 2002; Brown et al., 2006; Penkett et al., 2007). Given the rapid reaction rate between isoprene and NO<sub>3</sub> radicals ( $k_{\text{NO}_3} = 7 \times 10^{-13} \text{ cm}^3 \text{ molecule}^{-1} \text{ s}^{-1}$  at  $T = 298 \text{ K}$ , IUPAC), it is likely that NO<sub>3</sub> radicals play a major role in the nighttime chemistry of isoprene.

The kinetics and gas-phase products of the isoprene-NO<sub>3</sub> reaction have been the subject of several laboratory and theoretical studies (Jay and Stieglitz, 1989; Barnes et al., 1990; Skov et al., 1992; Kwok et al., 1996; Berndt and Böge, 1997; Suh et al., 2001; Zhang et al., 2002; Fan et al., 2004). In many studies, C<sub>5</sub>-nitroxycarbonyl is identified as the major first-generation gas-phase reaction product (Jay and Stieglitz, 1989; Skov et al., 1992; Kwok et al., 1996; Berndt and Böge, 1997). Other compounds such as C<sub>5</sub>-hydroxynitrate, C<sub>5</sub>-nitroxyhydroperoxide, and C<sub>5</sub>-hydroxycarbonyl have also been identified (Kwok et al., 1996); C<sub>5</sub>-hydroxynitrate has also been measured in ambient air with concentrations in the lower ppt range at a few ng m<sup>-3</sup> (Werner et al., 1999). According to the experimental study by Barnes et al. (1990), the yield for nitrate-containing compounds from the reaction of isoprene and NO<sub>3</sub> radicals can be as high as 80%. A recent modeling study in conjunction with observations from the ICARTT field campaign suggests that ~50% of the total isoprene nitrates production occurs via reaction of isoprene and NO<sub>3</sub> radicals (Horowitz et al., 2007).

Little is known beyond the formation of the first-generation products of the reaction of NO<sub>3</sub> with isoprene. The isoprene nitrates and other first-generation products still contain a double bond, and it is likely that the further oxidation of these species will lead to low volatility products that can contribute to SOA formation at nighttime.

In this work, SOA formation from the reaction of isoprene with  $\text{NO}_3$  radicals is investigated. Laboratory chamber experiments are performed in the dark using  $\text{N}_2\text{O}_5$  as a source of  $\text{NO}_3$  radicals. Aerosol yields are obtained over a range of initial isoprene concentrations (mixing ratios). By examining the time evolutions of aerosol volume and different intermediate gas-phase products, we are able to constrain the chemistry that leads to the formation of low-volatility products. Mechanisms for SOA formation are proposed and chemical composition data of the SOA formed are also presented.

## 2. Experimental Section

Experiments are carried out in the Caltech dual  $28 \text{ m}^3$  teflon chambers. A detailed description of the facility is provided elsewhere (Cocker et al., 2001; Keywood et al., 2004). Before each experiment, the chambers are flushed continuously for over 24 h. Aerosol number concentration, size distribution, and volume concentration are measured by a Differential Mobility Analyzer (DMA, TSI model 3081) coupled with a condensation nucleus counter (TSI model 3760). All aerosol growth data are corrected for wall loss, in which size-dependent particle loss coefficients are determined from inert particle wall loss experiments (Keywood et al., 2004). Temperature, relative humidity (RH),  $\text{O}_3$ ,  $\text{NO}$ , and  $\text{NO}_x$  are continuously monitored. Experiments are performed in the dark at room temperature ( $20\text{-}21^\circ\text{C}$ ) and under dry conditions ( $\text{RH} < 10\%$ ).

In most experiments, seed aerosols are introduced into the chamber to act as a substrate onto which the gas-phase products may condense. Seed aerosols are generated by atomizing an aqueous solution with a constant-rate atomizer. The seed solution consists of  $0.015 \text{ M } (\text{NH}_4)_2\text{SO}_4$ . In a few experiments, acidic seed is used, consisting of

0.03 M MgSO<sub>4</sub> and 0.05 M H<sub>2</sub>SO<sub>4</sub>. The initial particle number concentration is ~20,000 particles cm<sup>-3</sup>, with a geometric mean diameter of ~50 nm. The initial seed volume is 10-12 μm<sup>3</sup> cm<sup>-3</sup>. In some experiments, no seed particles are added and aerosols are formed via nucleation. After introduction of the seed aerosol (in seeded experiments), a known volume of isoprene (Aldrich, 99%) is injected into a glass bulb and introduced into the chambers by an air stream. The mixing ratio of isoprene is monitored with a gas chromatograph equipped with a flame ionization detector (GC-FID, Agilent model 6890N). The column used is a bonded polystyrene-divinylbenzene based column (HP-PLOT Q, 15 m × 0.53 mm, 40 μm thickness, J&W Scientific). The oven temperature is held at 60°C for 0.5 min, ramped at 35°C min<sup>-1</sup> to 200°C, and held constant for 3.5 min.

The thermal decomposition of N<sub>2</sub>O<sub>5</sub> serves as a source of NO<sub>3</sub> radicals in these experiments. N<sub>2</sub>O<sub>5</sub> is prepared and collected offline by mixing a stream of nitric oxide (≥99.5%, Matheson Tri Gas) with a stream of ozone in a glass bulb (Davidson et al., 1978):



Ozone is generated by flowing oxygen through an ozonizer (OREC model V10-0, Phoenix, AZ) at ~1 L min<sup>-1</sup>. The mixing ratio of ozone is measured by a UV/VIS spectrometer (Hewlett Packard model 8453) to be ~2%. The flow rate of nitric oxide into the glass bulb is adjusted until the brown color in the bulb disappears. The N<sub>2</sub>O<sub>5</sub> is trapped for 2 h in an acetone-dry ice bath (approximately at -80°C; cold enough to trap N<sub>2</sub>O<sub>5</sub> but not O<sub>3</sub>, as condensed O<sub>3</sub> can explode upon warming and is extremely

dangerous) as a white solid, and stored between experiments under liquid nitrogen temperature. Once the seed and isoprene concentrations in the chamber stabilize, reaction is initiated by vaporizing  $\text{N}_2\text{O}_5$  into an evacuated 500 mL glass bulb and introduced into the chamber with an air stream of  $5 \text{ L min}^{-1}$ . The amount of  $\text{N}_2\text{O}_5$  injected is estimated based on the vapor pressure in the glass bulb, which is measured using a capacitance manometer (MKS); this amount corresponds to an initial mixing ratio of  $\sim 1$  ppm in the chamber. The thermal decomposition of  $\text{N}_2\text{O}_5$  forms  $\text{NO}_2$  and  $\text{NO}_3$  radicals. Impurities in the  $\text{N}_2\text{O}_5$  starting material are quantified by FTIR spectroscopy (Nicolet model Magna 550).  $\text{N}_2\text{O}_5$  is vaporized into an evacuated pyrex cell (18 cm in length and  $300 \text{ cm}^3$ ) with  $\text{CaF}_2$  windows. Spectra are collected immediately upon addition over the  $1000 \text{ cm}^{-1}$  to  $4000 \text{ cm}^{-1}$  window allowing for quantification of  $\text{NO}_2$  ( $1616 \text{ cm}^{-1}$  band) and  $\text{HNO}_3$  ( $3550 \text{ cm}^{-1}$  band) impurities.

A custom-modified Varian 1200 Chemical Ionization Mass Spectrometer (CIMS) is used to continuously monitor the concentrations of various gas-phase intermediates and products over the course of the experiments. The CIMS is operated in negative mode using  $\text{CF}_3\text{O}^-$  as a reagent ion, which selectively clusters with protonated compounds to form ions at  $m/z \text{ MW} + 85$ . Typically, we scan from  $m/z$  50 to 400. More details about the CIMS technique are given in Crounse et al. (2006) and Ng et al. (2007a). Because authentic standards are not available for most of the major products, sensitivities have been estimated from calibration of similar species (Crounse et al., 2006).

Aerosol physical and chemical properties are monitored by many instruments. Real-time particle mass spectra are obtained with an Aerodyne quadrupole Aerosol Mass Spectrometer (Q-AMS) (Jayne et al., 2000). A Particle-Into-Liquid Sampler (PILS,

Brechtel Manufacturing, Inc.) coupled with ion chromatography (IC) is employed for quantitative measurements of water-soluble ions in the aerosol phase (Sorooshian et al., 2006). Duplicate Teflon filters (PALL Life Sciences, 47-mm diameter, 1.0- $\mu$ m pore size, teflo membrane) are collected from a select number of experiments for offline chemical analysis. Filter sampling is initiated when the aerosol volume reaches its maximum value. Depending on the total volume concentration of aerosol in the chamber, the filter sampling time is 2-4 h, which results in  $\sim 2\text{-}5\text{ m}^3$  of total chamber air sampled. Teflon filters used for high-resolution electrospray ionization-time-of-flight mass spectrometry (ESI-TOFMS) analysis are extracted in 5 mL of high-purity methanol (LC-MS CHROMASOLV-Grade, Sigma-Aldrich) by 45 minutes of sonication. Methanol sample extracts are then blown dry under a gentle  $\text{N}_2$  stream (without added heat) once the filters are removed and archived at  $-20\text{ }^\circ\text{C}$ . Dried residues are then reconstituted with 500 mL of a 1:1 (v/v) solvent mixture of 0.1% acetic acid in water (LC-MS CHROMASOLV-Grade, Sigma-Aldrich) and 0.1% acetic acid in methanol (LC-MS CHROMASOLV-Grade, Sigma Aldrich). All resultant filter extracts are analyzed by a Waters ACQUITY ultra performance liquid chromatography (UPLC) system, coupled to a Waters LCT Premier XT time-of-flight mass spectrometer (TOFMS) equipped with an ESI source that is operated in the negative (–) ionization mode. Detailed operating conditions for the UPLC/(–)ESI-TOFMS instrument have been described previously (Ng et al., 2007a). A Waters ACQUITY UPLC HSS column is selected to separate the SOA components because of its increased retention of water-soluble polar organics; separation is achieved as a result of trifunctionally-bonded (T3)  $\text{C}_{18}$  alkyl residues on this column, which prevent stationary phase collapse when a 100% aqueous mobile phase is used and result

in better retention of water-soluble polar organic compounds. In addition to the UPLC/(–)ESI-TOFMS analysis, all remaining Teflon filters are extracted and analyzed for total peroxide content (sum of ROOR and ROOH) by using an iodometric-spectroscopic method previously described by Surratt et al. (2006).

To study the mechanism of SOA formation, in several experiments the experimental protocols are slightly modified: (1) An excess amount of isoprene (relative to  $\text{N}_2\text{O}_5$  concentration) is injected into the chamber to prevent the further reaction of first-generation gas-phase products, allowing these products to be detected more readily; (2) After the addition of isoprene, pulses of  $\text{N}_2\text{O}_5$  are introduced into the chamber to study the evolution of different intermediate gas-phase products; (3) With isoprene well mixed in the chamber,  $\text{N}_2\text{O}_5$  is introduced slowly to maximize the self-reaction of peroxy radicals (see Sect. 4.2). This is achieved by first injecting  $\text{N}_2\text{O}_5$  into a 65 L Teflon bag; then an air stream of  $1 \text{ L min}^{-1}$  is passed through the Teflon bag to introduce  $\text{N}_2\text{O}_5$  into the chamber over a 7-h period. We refer to this as the “slow  $\text{N}_2\text{O}_5$  injection experiment”; and (4) With  $\text{N}_2\text{O}_5$  well mixed in the chamber, isoprene is introduced slowly to maximize the reaction between peroxy radicals and nitrate radicals (see Sect. 4.2). This is achieved by first injecting isoprene into a 65 L Teflon bag, and then introduced into the chamber with an air stream of  $0.1 \text{ L min}^{-1}$  for 7 h. We refer to this as the “slow isoprene injection experiment”.

Experimental conditions and results are given in Table 1. In calculating SOA yield (defined as the ratio of the organic aerosol mass formed to the mass of parent hydrocarbon reacted), knowledge of the SOA density is required. By comparing volume



distributions from the DMA and mass distributions from the Q-AMS, the effective density for the SOA formed can be estimated (Bahreini et al., 2005; Alfarra et al., 2006).

### 3. Results

#### 3.1 Blank experiments

Blank experiments are performed to ensure that the aerosol growth observed is from the reaction of isoprene with  $\text{NO}_3$  radicals. In these experiments,  $\sim 1$  ppm  $\text{N}_2\text{O}_5$  is introduced into chamber after the addition of ammonium sulfate seed aerosol (with no isoprene present). As shown in Fig. 1, aerosol volume increases to  $\sim 2 \mu\text{m}^3 \text{ cm}^{-3}$  within an hour after the introduction of  $\text{N}_2\text{O}_5$ . About  $2.5 \mu\text{g m}^{-3}$  of inorganic nitrate is measured by PILS/IC, which agrees well with the amount of nitrates detected by Q-AMS. FTIR analysis indicates the presence of  $\sim 10\%$   $\text{HNO}_3$  and  $4\%$   $\text{NO}_2$  impurity in the  $\text{N}_2\text{O}_5$  prepared, thus the nitrates measured by PILS/IC and Q-AMS likely arise from the partitioning or reactive uptake of gas-phase  $\text{HNO}_3$  into the aerosol phase, or  $\text{HNO}_3$  produced from heterogeneous hydrolysis of  $\text{N}_2\text{O}_5$ . As for the Q-AMS analysis, no organic species are detected in the filter samples collected from these blank experiments.

#### 3.2 Aerosol yields

A series of experiments with different initial isoprene concentrations are carried out (these are referred to as “typical yield experiments” hereafter). The initial isoprene concentration ranged from 18.4 to 203.4 ppb. Figure 2 shows the reaction profile of the oxidation of an initial mixture containing 203.4 ppb isoprene. Since the chamber is  $\text{NO}_x$ -free at the beginning of the experiment, once  $\text{N}_2\text{O}_5$  is introduced into the chamber the

equilibrium in Reaction (3) favors the formation of  $\text{NO}_3$ . This generates a relatively high concentration of  $\text{NO}_3$  radicals and results in rapid isoprene decay. Aerosol growth is observed and aerosol volume continues to increase even after all the isoprene is consumed. Owing to the rapid isoprene decay and the relatively long time between each GC measurement (12 min), the isoprene decay over time is captured only in experiments in which the initial isoprene concentration is  $> 100$  ppb. Based on the observed isoprene decay in these experiments and the isoprene- $\text{NO}_3$  rate constant  $k_{\text{NO}_3}$ , the  $\text{NO}_3$  concentration in the chamber is estimated to be  $\sim 140$  ppt.

The SOA yield of each experiment (Table 1) is shown in Fig. 3. The density of the SOA is determined to be  $1.42 \text{ g cm}^{-3}$ . The amount of inorganic nitrate detected by PILS/IC in each experiment ranges from  $1.6$  to  $2.6 \text{ } \mu\text{g m}^{-3}$ , which is approximately equal to that measured in the blank experiments. In calculating SOA yield, the organic aerosol mass is corrected for the amount of inorganic nitrate measured in each experiment. For convenience, SOA yields can be parameterized by a semi-empirical model based on absorptive gas-particle partitioning of two semivolatile products (Odum et al., 1996, 1997ab):

$$Y = \Delta M_o \left[ \frac{\alpha_1 K_{om,1}}{1 + K_{om,1} M_o} + \frac{\alpha_2 K_{om,2}}{1 + K_{om,2} M_o} \right] \quad (4)$$

in which  $Y$  is the aerosol yield,  $\Delta M_o$  is the organic aerosol mass produced,  $M_o$  is the organic aerosol mass present (equal to  $\Delta M_o$  in chamber experiments with no absorbing organic mass present initially),  $\alpha_i$  is the mass-based gas-phase stoichiometric fraction for semivolatile species  $i$ , and  $K_{om,i}$  is the gas-particle partitioning coefficient for species  $i$ . With this two-product model, Eq. (4) is fit to the experimental yield data (data with  $\Delta M_o$

$< 100 \mu\text{g m}^{-3}$ ) and the yield parameters obtained are:  $\alpha_1 = 0.089$ ,  $\alpha_2 = 0.203$ ,  $K_{om,1} = 0.182 \text{ m}^3 \mu\text{g}^{-1}$ , and  $K_{om,2} = 0.046 \text{ m}^3 \mu\text{g}^{-1}$ . For an organic aerosol mass of  $\sim 10 \mu\text{g m}^{-3}$ , the aerosol yield is  $\sim 10\%$ .

Also shown in Fig. 3 are aerosol yields from the slow isoprene/ $\text{N}_2\text{O}_5$  injection experiments. Since the PILS/IC is not employed in these experiments, in calculating SOA yields it is assumed that the amount of inorganic nitrate formed in these slow injection experiments is roughly the same as that in other experiments. For the slow isoprene injection experiment, no isoprene is observed by the GC-FID, indicating that once the isoprene enters the chamber, it is quickly consumed by reaction with  $\text{NO}_3$ . The time profile of isoprene injection is obtained in a separate experiment, in which the same amount of isoprene is added into the chamber without  $\text{N}_2\text{O}_5$  present. Assuming the amount of isoprene injected into the chamber is the same as the isoprene reacted, the amount of isoprene reacted over the course of the slow isoprene experiment can be deduced. As seen in Fig. 3, the SOA yield from the slow  $\text{N}_2\text{O}_5$  injection experiment is roughly the same as those in the other yield experiments; the yield from the slow isoprene injection experiment, however, is lower.

The time-dependent “growth curves” (organic aerosol,  $\Delta M_o$ , as a function of hydrocarbon reacted,  $\Delta \text{HC}$ ) over the course of the slow  $\text{N}_2\text{O}_5$  injection experiment and the slow isoprene injection experiment are shown in Fig. 4. As hydrocarbon measurements are made with a lower frequency than particle volume, the isoprene concentrations shown are obtained by interpolating GC-FID measurements. In both experiments about 50 ppb of isoprene is consumed, the only difference being the order of isoprene/ $\text{N}_2\text{O}_5$  injection. From Fig. 4 it is clear that as the reaction proceeds, more aerosol

is formed in the slow isoprene injection experiment for the same amount of isoprene reacted. However, the final SOA yield under the slow  $\text{N}_2\text{O}_5$  injection conditions is higher due to continued aerosol formation even after the complete consumption of isoprene. The presence of a “hook” at the end of the growth curve for the slow  $\text{N}_2\text{O}_5$  injection experiment indicates that further reactions are contributing to aerosol growth after isoprene is consumed (Ng et al., 2006). This is further discussed in Sect. 4.3.

### 3.3 Gas-phase measurements

The CIMS measures the concentrations of different gas-phase products over the course of the experiments. A series of experiments is carried out to study the mechanisms of SOA formation by varying the relative amount of isoprene and  $\text{N}_2\text{O}_5$  injected and monitoring the time evolution of the intermediate products. Shown in Fig. 5 are the time profiles of three major gas-phase products and the corresponding aerosol growth from the excess isoprene experiment. In this experiment,  $\sim 120$  ppb of  $\text{N}_2\text{O}_5$  is first injected into the chamber, followed by the introduction of  $\sim 800$  ppb isoprene. The initial concentration of isoprene is estimated based on the volume of the isoprene injected and the chamber volume. Once isoprene is injected, a number of product ions are formed immediately, with  $m/z$  230, 232, and 248 being the most dominant ones. Several minor product ions at  $m/z$  185, 377, and 393 are also observed (not shown). With the presence of excess isoprene, it is expected that the three major products detected are first-generation products. Their further reaction is suppressed, as indicated by the relatively constant concentrations of the product ions once they are formed. At the end of the experiment, 725 ppb of isoprene is measured by GC-FID. A small amount of aerosol is formed

instantaneously, likely from the condensation of relatively nonvolatile first-generation products, or from further generation products that are formed at a very rapid rate.

To study further the evolution of the gas-phase products, an experiment is performed in which pulses of  $\text{N}_2\text{O}_5$  are introduced into the chamber (with isoprene present) (Fig. 6). The top panel shows the isoprene decay and aerosol formation; the middle panel shows the time profiles of the three major first-generation products ( $m/z$  230, 232, and 248); the bottom panel shows the time profiles of three minor products ( $m/z$  185, 377, and 393). In this experiment, 179 ppb of isoprene is first injected into the chamber, followed by the addition of 3 pulses of  $\text{N}_2\text{O}_5$  (~120, 50, 210 ppb). The observations after the addition of the first pulse of  $\text{N}_2\text{O}_5$  are similar to the excess isoprene experiment described above. With the addition of ~120 ppb  $\text{N}_2\text{O}_5$ , 97 ppb of isoprene is reacted away,  $m/z$  230, 232, and 248 are formed with concentrations of ~ 53 ppb, 25 ppb, and 21 ppb, respectively. Because of the lack of authentic standards, the concentrations are uncertain. Because the sum of the ion concentrations derived from our estimated sensitivities is equal to the reacted isoprene, our estimated sensitivity must represent a lower limit for the actual sensitivity of the CIMS to these compounds. Similar to the data in Fig. 5, the concentrations of these product ions stay relatively constant owing to the presence of excess isoprene. The minor products at  $m/z$  185, 377, and 393, are formed with the concentrations of ~1.5 ppb, 1 ppb, and 1ppb, respectively. It is noted that the  $m/z$  393 ion is formed with a relatively slower rate than all other product ions. A small amount of aerosol is observed. At  $t = 15:40$ , a second pulse of  $\text{N}_2\text{O}_5$  (~50 ppb) is introduced into the chamber and the remaining 82 ppb isoprene is completely consumed. As seen from Fig. 6, the concentrations of all intermediate products increase accordingly

and more aerosol is produced. The relative increase in the concentration of  $m/z$  232 ion is not as high as would be expected if we assume the ratio of  $m/z$  230 to 232 formed to be the same as in the first pulse of  $\text{N}_2\text{O}_5$  addition (i.e.  $\sim 2:1$ ). This indicates that some of  $m/z$  232 ion has reacted with  $\text{NO}_3$  radicals. The last pulse of  $\text{N}_2\text{O}_5$  ( $\sim 210$  ppb) is added at  $t = 19:00$ . Since all isoprene has been consumed, the additional  $\text{NO}_3$  radicals react mainly with the first-generation products, as indicated by the decay of  $m/z$  230, 232, and 248, 185, 377, and 393 ions. Of all of the observed products, it appears that  $m/z$  232 and 377 ions are the most reactive with  $\text{NO}_3$  radicals, and their decays in excess  $\text{NO}_3$  are strongly correlated with aerosol growth. The rest of the product ions display relatively slower decay kinetics. The decay of the major product ion at  $m/z$  230 does not appear to correlate with aerosol growth, as the concentration of the  $m/z$  230 ion continues to decrease throughout the experiment but there is no further aerosol growth. Although the CIMS instrument has only 0.5 AMU resolution and it cannot distinguish products of the similar or identical molecular weight, it is likely that many of observed masses comprise isomers formed from the  $\text{NO}_3$  attack at different positions. The fact that many of the observed product ions show two distinct decay time scales indicates that these isomers have substantially different reactivity towards  $\text{NO}_3$  radicals.

### 3.4 Chemical composition of SOA

#### 3.4.1 Aerosol Mass Spectrometer (Q-AMS) measurements

Figure 7 shows the AMS spectrum of SOA formed in the typical yield experiments. Each mass fragment is normalized by the total signal. The SOA exhibits relatively high signals at  $m/z$  30, 43, and 46. The signals at  $m/z$  30 and 46 likely

correspond to  $\text{NO}^+$  (30) and  $\text{NO}_2^+$  (46) fragments from the nitrates in the aerosol. The spectrum shown in Fig. 7 is obtained when aerosol volume reaches its maximum value; the spectrum obtained several hours after aerosol volume peaks shows minimal changes in the mass fractions of different fragments, indicating that the aerosol composition is not changing significantly over time.

Figure 8 shows the mass spectrum of the slow  $\text{N}_2\text{O}_5$  injection experiment versus a typical yield experiment; Figure 9 shows the mass spectrum of the slow isoprene injection experiment versus a typical yield experiment. As shown in both figures, the mass fragments fall on the 1:1 line, suggesting a similar SOA composition under the three different experimental conditions.

### 3.4.2. Offline chemical analysis

Figure 10 shows the representative UPLC/(-)ESI-TOFMS base peak ion chromatograms (BPCs) for different types of experiments conducted. The numbers denoted above the selected chromatographic peaks correspond to the most abundant negative ions observed in their respective mass spectra. Comparison of the BPCs shown in Fig. 10 indicates that the compositions of the SOA are quite similar for the typical yield experiment, slow isoprene injection experiment, and the acid seed experiment, suggesting a common SOA formation pathway. The SOA composition from the excess isoprene experiment, however, is different from these experiments. This will be discussed further in Sect. 4.4.

Accurate mass measurements for all ions observed by the UPLC/(-)ESI-TOFMS technique for a typical yield experiment are listed in Table 2. The error between the

measured mass and theoretical mass is reported in two different ways, ppm and mDa. Overall, the error between the measured and theoretical masses is found to be less than  $\pm 2$  mDa and  $\pm 5$  ppm, allowing for generally unambiguous identification of molecular formulae. None of the listed ions is observed in solvent blanks and control filters. By combining the elemental SOA composition (i.e. TOFMS suggested ion formula) data and the gas-phase data from CIMS, structures for each of the SOA components are also proposed. As shown in Table 2, the types of compounds formed included nitroxy-organic acids, hydroxynitrates, nitroxy-organic peroxides (e.g. nitroxy-hydroxyperoxides), and nitroxy-organosulfates. It should be noted that the data presented in Table 2 are also applicable to all other types of experiments conducted in this study; however, none of the organosulfates are observed in the nucleation experiments, consistent with previous work (Liggio et al., 2005; Liggio et al., 2006; Surratt et al., 2007ab; Iinuma et al., 2007ab). Surprisingly, previously characterized organosulfates of the 2-methyltetrols and the 2-methyltetrol mono-nitrates detected at  $m/z$  215 and  $m/z$  260 (not listed in Table 2), respectively, which are produced from the photooxidation of isoprene in the presence of acidified sulfate seed aerosol (Surratt et al., 2007ab; Gómez-González et al., 2007), are also observed in the acid seed experiment shown in Fig. 10, suggesting that nighttime oxidation of isoprene in the presence of acidic seed may also be a viable pathway for these known ambient tracer compounds.

Owing to the implementation of reverse-phase chromatography, the SOA components that are more hydrophilic elute from the column the earliest, while the more hydrophobic components elute the latest. It is clear from Table 2 that compounds with the same carbon number and general functionality (i.e. carboxylic acid, alcohol, or



organosulfate), but differing number of nitroxy groups, exhibit distinctly different chromatographic behaviors. The presence of more nitroxy groups appears to increase the retention time of the SOA compound. For example, it is found that  $m/z$  194 organic acid compound ( $C_5H_8NO_7^-$ ) containing one nitroxy group elutes earlier than that of the  $m/z$  239 organic acid compounds ( $C_5H_7N_2O_9^-$ ) containing two nitroxy groups. Similarly, the  $m/z$  305 organosulfate ( $C_5H_9N_2O_{11}S^-$ ) elutes earlier than that of the  $m/z$  349 organosulfate ( $C_5H_8N_3O_{13}S^-$ ).

SOA components that are either nitroxy-organic acids or nitroxy-organosulfates are detected strongly as the  $[M - H]^-$  ion, consistent with previous work (Surratt et al., 2006; Surratt et al., 2007ab; Gao et al., 2004ab; Gao et al., 2006), whereas the hydroxynitrates and nitroxy-hydroxyperoxides are detected as both the  $[M - H]^-$  and  $[M - H + C_2H_4O_2]^-$  ions, with the latter acetic acid adduct ion, in most cases, being the base peak ion (i.e. dominant ion). The acetic acid adduct ions for the hydroxynitrates and the nitroxy-hydroxyperoxides are formed owing to the presence of acetic acid in the UPLC mobile phase. Previous studies have shown that non-acidic hydroxylated species (such as the 2-methyltetrols) and organic peroxides formed from the photooxidation of isoprene (Claeys et al., 2004; Edney et al., 2005; Surratt et al., 2006) are either undetectable or yield weak negative ions when using  $(-)$ ESI-MS techniques. However, it appears that the co-presence of nitroxy groups in the hydroxylated SOA components allow for these compounds to become acidic enough to be detected by the UPLC/ $(-)$ ESI-TOFMS technique, or allow for adduction with acetic acid. Further confirmation for the presence of organic peroxides in the isoprene SOA produced from  $NO_3$  oxidation is provided by the iodometric-spectroscopic measurements shown in Table 3. Based upon the UPLC/ $(-)$

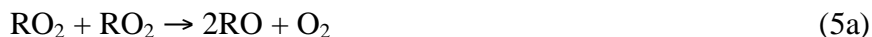
)ESI-TOFMS measurements shown in Table 2, an average molecular weight of 433 for the organic peroxides is assumed for the calculations shown in Table 3. The contribution of organic peroxides to the SOA mass concentration is found to be fairly reproducible for duplicate typical experiments (i.e. 8/22/07 and 10/24/07). The amount of organic peroxides in the excess isoprene experiment is below detection limits.

## 4. Gas-phase chemistry and SOA formation

### 4.1 Formation of various gas-phase products

As seen from Fig. 5 and Fig. 6, the three major first-generation products formed from isoprene-NO<sub>3</sub> reaction are the  $m/z$  230, 232, and 248 ions. Since CIMS uses CF<sub>3</sub>O<sup>-</sup> (MW 85) as the reagent ion, compounds are identified by their molecular weight (MW) plus 85. The product ions at  $m/z$  230, 232, and 248 likely correspond to C<sub>5</sub>-nitroxycarbonyl (MW 145), C<sub>5</sub>-hydroxynitrate (MW 147), and C<sub>5</sub>-nitroxyhydroperoxide (MW 163). These products have been observed in previous studies (Jay and Stieglitz, 1989; Skov et al., 1992; Kwok et al., 1996; Berndt and Böge, 1997) and their formation from the isoprene-NO<sub>3</sub> reaction is relatively straightforward (Fig. 11). The reaction proceeds by NO<sub>3</sub> addition to the C=C double bond, forming four possible nitroxyalkyl radicals depending the position of the NO<sub>3</sub> attack. Previous studies suggest that NO<sub>3</sub> radicals predominantly attack isoprene in the 1-position, with a branching ratio (C1-position/C4-position) varying between 3.5 and 7.4 (Skov et al., 1992; Berndt and Böge, 1997; Suh et al., 2001). In Fig. 11, only the nitroxyalkyl radical formed from the C1 attack is shown. The nitroxyalkyl radicals then react with O<sub>2</sub> to form RO<sub>2</sub> radicals, which react further with HO<sub>2</sub>, RO<sub>2</sub>, or NO<sub>3</sub> radicals under the experimental conditions in this

study. The reaction of RO<sub>2</sub> radicals and HO<sub>2</sub> radicals leads to the formation of C<sub>5</sub>-nitroxyhydroperoxide (*m/z* 248). The reaction of two RO<sub>2</sub> radicals (self reaction or cross reaction) has three different possible channels:



The second channel results in the formation of C<sub>5</sub>-nitroxycarbonyl (*m/z* 230) and C<sub>5</sub>-hydroxynitrate (*m/z* 232). According to channel (5b), these two products should be formed with a 1:1 ratio; however, C<sub>5</sub>-nitroxycarbonyl can also be formed from alkoxy radicals (either from RO<sub>2</sub> + RO<sub>2</sub> reaction or RO<sub>2</sub> + NO<sub>3</sub> reaction). In Fig. 6, about 53 ppb of C<sub>5</sub>-nitroxycarbonyl and 25 ppb of C<sub>5</sub>-hydroxynitrate are formed after the addition of the first pulse of N<sub>2</sub>O<sub>5</sub>, indicating ~28 ppb of C<sub>5</sub>-nitroxycarbonyl is formed from the fragmentation of alkoxy radicals. The branching ratios for the reaction of small peroxy radicals have been investigated in previous studies. It is found that the branching ratio for channel (5a) for methylperoxy and ethylperoxy radicals is ~0.3-0.4 and ~0.6, respectively (Lightfoot et al., 1992; Wallington et al., 1992; Tyndall et al., 1998). It is likely that the isoprene peroxy radicals react via this pathway to form alkoxy radicals and contribute to the “extra” 28ppb of C<sub>5</sub>-nitroxycarbonyl. Although the concentrations of the product ions measured by CIMS are only rough estimates, the above observation is indicative that most RO<sub>2</sub> radicals react with other RO<sub>2</sub> radicals instead with NO<sub>3</sub> or HO<sub>2</sub> radicals.

Other than C<sub>5</sub>-nitroxycarbonyl, C<sub>5</sub>-hydroxynitrate, and C<sub>5</sub>-nitroxyhydroperoxide, three other minor products (*m/z* 185, 377 and 393 ions) are also observed as intermediate products. The proposed mechanisms for the formation of these gas-phase products are

also shown in Fig. 11. Although channel (5c) in the  $\text{RO}_2 + \text{RO}_2$  reaction is found to be minor for small peroxy radicals such as methylperoxy and ethylperoxy radicals (Kan et al., 1980; Niki et al., 1981; Niki et al., 1982; Wallington et al., 1989; Tyndall et al., 1998; Tyndall et al., 2001), the product ion at  $m/z$  377 could be the corresponding ROOR product formed from the self reaction of isoprene peroxy radicals. The product ion at  $m/z$  185 likely corresponds to the  $\text{C}_5$ -hydroxycarbonyl. It has been observed in previous studies and it likely arises from the isomerization of nitroxyalkoxy radicals through a 6-member transition state to form a hydroxynitroxy alkyl radical, which then decomposes to form  $\text{NO}_2$  and  $\text{C}_5$ -hydroxycarbonyl (Kwok et al., 1996). Such isomerization has also been proposed to occur in the photooxidation of isoprene (Paulson and Seinfeld, 1992; Carter and Atkinson, 1996; Dibble, 2002). It is possible that the hydroxynitroxy alkyl radical formed proceeds to react with  $\text{O}_2$  to form a peroxy radical, which then reacts with the isoprene peroxy radical to form the product ion  $m/z$  at 393. The product ion at  $m/z$  393 shows a slower rate of formation (Fig. 6) compared to other product ions suggesting that it might also be formed from the further oxidation of a first-generation product. 2-methyl-2-vinyl-oxirane has been observed from isoprene- $\text{NO}_3$  reaction in previous studies at 20 mbar in helium (Berndt and Böge, 1997) and 20 Torr in argon (Skov et al., 1994), respectively. When operated in positive mode with  $\text{H}^+$  as the reagent ion (products are observed at  $m/z = \text{MW} + 1$ ), CIMS detects a product ion at  $m/z$  85. Although the epoxide yield is found to be  $<1\%$  of the total reacted isoprene at atmospheric pressure (Skov et al., 1994), the signal at  $m/z$  85 can arise in part from the epoxide. The further oxidation of the epoxide results in the formation of an epoxide peroxy radical, which can react with the isoprene peroxy radical to form the peroxide at  $m/z$  393. It is noted that a product ion at

$m/z$  246 is detected in the CIMS, which could arise from the corresponding carbonyl product formed from the reactions of two epoxide peroxy radicals, or from the fragmentation of the epoxide alkoxy radicals. Unlike  $m/z$  393 which decays after the addition of the last pulse of  $N_2O_5$ ,  $m/z$  246 stays relatively constant suggesting that it is not being further oxidized by  $NO_3$  radicals. To examine further the possibility of peroxide formation ( $m/z$  377 and 393) in the gas phase, an experiment is conducted using 1,3-butadiene as the parent hydrocarbon. The analogous product ions for the 1,3-butadiene system, i.e.  $m/z$  349 and 365, are observed in the CIMS, providing further indication that the formation of ROOR products from two  $RO_2$  radicals is occurring in the gas phase. Further details of the gas-phase chemistry of isoprene and 1,3-butadiene will be forthcoming in a future manuscript.

## 4.2 Effect of peroxy radical chemistry on SOA yield

The SOA yield ranges from 4.3% to 23.8% for an initial isoprene concentration of 18.4 to 101.6 ppb in the typical yield experiments. While the SOA yield from the slow  $N_2O_5$  injection experiment is roughly the same as that in the typical yield experiments, the SOA yield from the slow isoprene injection experiment is lower (Fig. 3). In both cases, ~40 ppb of isoprene is consumed, the main difference being the relative importance of  $RO_2 + RO_2$  reaction versus  $RO_2 + NO_3$  reaction in each system. In the slow  $N_2O_5$  injection experiment, a relatively small amount of  $NO_3$  is available in the chamber. Once  $RO_2$  radicals are formed, it is expected that they would react primarily with other  $RO_2$  radicals instead of  $NO_3$  radicals owing to the presence of a relatively higher isoprene concentration in the chamber. On the other hand, the slow isoprene injection experiment

favors  $\text{RO}_2 + \text{NO}_3$  reaction owing to the presence of excess  $\text{N}_2\text{O}_5$  in the chamber. Thus the higher SOA yield observed in the slow  $\text{N}_2\text{O}_5$  injection experiment suggests the products formed via  $\text{RO}_2 + \text{RO}_2$  reaction partition more readily into the aerosol phase, or the  $\text{RO}_2 + \text{RO}_2$  reaction forms products that further react and contribute significantly to aerosol growth. The fact that the SOA yield from the slow  $\text{N}_2\text{O}_5$  injection experiment is roughly the same as in the typical yield experiments implies that  $\text{RO}_2 + \text{RO}_2$  reaction dominates in typical yield experiments.

The time profile for the three major first-generation gas phase products and SOA growth from the slow  $\text{N}_2\text{O}_5$  injection experiment and slow isoprene injection experiment are shown in Fig. 12 and Fig. 13, respectively. In both cases, once the first-generation products are formed they can react further with  $\text{NO}_3$  radicals, making it difficult to estimate the formation yields of these products based on the measured concentrations. The extent to which these products react further is expected to be higher in the slow isoprene injection experiment owing to the presence of excess  $\text{NO}_3$  in chamber; this is consistent with the relatively lower concentrations of first-generation products observed. As mentioned before, it is possible that the CIMS signal at the observed  $m/z$  comprises isomers formed from the  $\text{NO}_3$  attack at positions other than the C1 carbon. Such isomers have slightly different structures but they could exhibit a very different reaction rate towards  $\text{NO}_3$  radicals. For instance, studies have shown that the reaction rates of  $\text{NO}_3$  radicals with unsaturated alcohols and unsaturated carbonyl compounds can vary by several orders of magnitude depending on the position of the substituted methyl group (Noda et al., 2002; Canosa-Mas et al., 2005). It is possible that the minor products formed from  $\text{NO}_3$  attack at other positions react much slower with  $\text{NO}_3$  radicals, hence the

concentrations of the observed product ions do not decay to zero towards the end of the experiment. At the end of the experiment, about 8 ppb and 3 ppb of C<sub>5</sub>-hydroxynitrate is left in the slow N<sub>2</sub>O<sub>5</sub> injection experiment and slow isoprene injection experiment, respectively. Assuming the amount of reactive isomers and unreactive (or relatively slow reacting) isomers are formed in the same ratio in the slow N<sub>2</sub>O<sub>5</sub> injection experiment and the slow isoprene injection experiment, we can deduce that a relatively higher concentration of reactive C<sub>5</sub>-hydroxynitrate (as well as the two other first-generation products) is formed in the slow N<sub>2</sub>O<sub>5</sub> injection experiment. This is consistent with the larger extent of RO<sub>2</sub> + RO<sub>2</sub> reaction (which forms C<sub>5</sub>-hydroxynitrate) and the higher SOA yield observed in the slow N<sub>2</sub>O<sub>5</sub> injection experiment, as it appears that C<sub>5</sub>-hydroxynitrate is an effective SOA precursor (Fig. 6).

### 4.3 Growth curves: multiple steps in SOA formation

By examining the time-dependent growth curves (organic aerosol,  $\Delta M_o$ , as a function of hydrocarbon reacted,  $\Delta HC$ ) we can gain insights into the general mechanisms of SOA formation (Ng et al., 2006, 2007ab). Fig. 4 shows the time-dependent growth curves for the slow N<sub>2</sub>O<sub>5</sub> injection experiment and the slow isoprene injection experiment, respectively. For the slow N<sub>2</sub>O<sub>5</sub> injection experiment, the initial aerosol growth likely arises from the condensation of first-generation products as the presence of excess isoprene in the chamber suppresses their further oxidation. If higher generation products do contribute to SOA formation, they would have to be formed at very rapid rates. After isoprene is consumed, aerosol mass continues to increase and results in a “hook” in the growth curve. This indicates that secondary products (or higher generation

products) also contribute significantly to SOA formation. The same observation can be made if we examine the reaction profile of a typical yield experiment (Fig. 2): there is further SOA growth after all isoprene is reacted away, indicating that the further oxidation of first generation products are contributing to SOA formed. These observations are consistent with the fact that the decay of first-generation products observed in the CIMS (especially the  $m/z$  232 and  $m/z$  377 ions) is strongly anticorrelated with further SOA growth (Fig. 6). On the other hand, the slow isoprene injection experiment does not allow us to differentiate the contribution of first- and second-generation products to SOA formation. With the presence of excess  $\text{NO}_3$  radicals in the chamber, the first-generation products formed in the slow isoprene injection experiment would be further oxidized once they are formed. The SOA growth observed throughout this experiment is from the partitioning of these highly oxidized and nonvolatile products. Hence, at the beginning of the experiment, for the same amount of  $\Delta\text{HC}$ , the amount of SOA formed in this experiment is higher than that in the slow  $\text{N}_2\text{O}_5$  injection experiment, in which the aerosol growth is probably from the condensation of relatively more volatile first-generation products. Both the AMS data and filter sample data (Figs. 8, 9, and 10) show a very similar composition for the final SOA formed in slow  $\text{N}_2\text{O}_5$  injection experiment and the slow isoprene injection experiment, suggesting a common SOA forming channel. Based on the previous discussion on the effect of peroxy radical chemistry on SOA yields, it is likely that the  $\text{RO}_2 + \text{RO}_2$  reaction is the SOA-forming channel in both cases; such a reaction occurs to a large extent in the slow  $\text{N}_2\text{O}_5$  injection experiments and results in the formation of more SOA.



#### 4.4 Proposed mechanisms of SOA formation

The combination of CIMS gas-phase data and elemental SOA composition data provides substantial insights into the mechanisms of SOA formation. Shown in Fig. 14-17 are the proposed SOA formation mechanisms from the further oxidation of the various gas-phase products measured by CIMS. The compounds in the boxes are the SOA products detected by UPLC/(-)ESI-TOFMS. Owing to multiple chromatographic peaks observed in the UPLC/(-)ESI-TOFMS extracted ion chromatograms (EICs) for the negative ions of the proposed SOA products, structural isomers are likely; however, for simplicity we show only one possible isomer for each product formed from a particular reaction pathway. Many of the SOA products detected are formed from the further oxidation of first- or higher-generation products, which is consistent with the observation of continual SOA growth after the complete consumption of isoprene (hence a “hook” in the growth curve). With the large number of nitrate-substituted compounds detected by UPLC/(-)ESI-TOFMS technique, it is also not surprising that the AMS shows strong signals at  $m/z$  30 ( $\text{NO}^+$ ) and  $m/z$  46 ( $\text{NO}_2^+$ ).

Shown in Fig. 14 and 15 are the proposed SOA formation pathways from the further oxidation of the  $m/z$  232 (i.e.  $\text{C}_5$ -hydroxynitrate) and 377 gas-phase product ions (as detected by the CIMS). The decay of these two products has been found to be strongly correlated with aerosol growth (Fig. 6), which is consistent with the large number of SOA products formed from their further oxidation. The further oxidation of these two gas-phase products also yields SOA compounds of the same molecular weight (compounds of MW 371 and 450). Although  $m/z$  393 is a minor gas-phase product, the further oxidation of this compound leads to formation of several SOA products (Fig. 16).

As mentioned before, there are two possible formation routes for  $m/z$  393, and the further oxidation of both products is shown in Fig. 16. The further oxidation of the  $m/z$  393 ion appears to yield SOA products that are specific only to this gas-phase product: these include the SOA products of MW 387 and 467.

Figure 17 shows the proposed SOA formation mechanisms from three other gas-phase products ( $m/z$  185,  $m/z$  230, and  $m/z$  277); the further oxidation of these product ions leads to relatively minor SOA products. Although C<sub>5</sub>-nitroxycarbonyl ( $m/z$  230) is the most abundant gas-phase product detected by CIMS, its further oxidation is not well correlated with aerosol growth (Fig. 6). The further oxidation of  $m/z$  230 yields an SOA product at MW 240. This organic acid product is found to be quite minor when examining the peak area in its corresponding extracted ion chromatogram (EIC). It is noted that no SOA products are detected from the further oxidation of the C<sub>5</sub>-nitroxyhydroperoxide ( $m/z$  248) (also a major gas-phase product); it is possible that these hydroperoxide products are not acidic enough to be detected by the UPLC/(–)ESI-TOFMS technique, or degrade during sample workup and/or analysis procedures. It has been shown that hydroxycarbonyl plays a key role in SOA formation from the reaction of linear alkenes with NO<sub>3</sub> radicals (Gong et al., 2005), however, in the isoprene-NO<sub>3</sub> system, the further oxidation of the minor gas-phase product C<sub>5</sub>-hydroxycarbonyl ( $m/z$  185) leads to the formation of only one minor aerosol product at MW 195. Some evidence for the formation of a C<sub>5</sub>-dinitrate first-generation gas-phase product is indicated from the CIMS and UPLC/(–)ESI-TOFMS data. This first-generation gas-phase product has been observed previously by Werner et al. (1997). The CIMS detects a weak signal at  $m/z$  277, which could be associated to the dinitrate product; we do not know,

however, whether the negative ion efficiently clusters with such compounds. Further evidence for the dinitrate gas-phase product is provided by the UPLC/(-)ESI-TOFMS detection of an SOA product at MW 495, which could result from the further oxidation of a C<sub>5</sub>-dinitrate precursor. The precursor compound before the last oxidation step shown in this mechanism in Fig. 17 may exist in the particle phase; however, this compound is not likely to be detected by the UPLC/(-)ESI-TOFMS technique owing to the lack of acidic hydrogens from neighboring hydroxyl and/or carboxyl groups.

The SOA products highlighted in Fig. 14-17 are observed in all major experiments conducted; however, not all of these products are strongly detected in the excess isoprene experiment (Fig. 10c). With the presence of excess isoprene, further oxidations of first-generation products should be minimal and no significant SOA formation is expected. However, SOA growth is observed and it appears from the UPLC/(-)ESI-TOFMS data that enough RO<sub>2</sub> + RO<sub>2</sub> chemistry is occurring to yield many of the products shown in Fig. 14-17. When comparing the UPLC/(-)ESI-TOFMS BPCs (Fig. 10) of all experiments, it is clear that the *m/z* 430 and *m/z* 446 are the dominant ions in the excess isoprene experiment, while *m/z* 333 is the dominant chromatographic peak in other experiments. The chromatographic peak at *m/z* 430 corresponds to the acetic acid cluster ion for the compound at MW 371, which can be formed from the further oxidation of CIMS *m/z* 232 and 377 ions (Fig. 14 and 15). The chromatographic peak at *m/z* 446 corresponds to the acetic acid cluster ion for the compound at MW 387, which is formed from the further oxidation of CIMS *m/z* 393 (Fig. 16). The detection of these two SOA products (MW 371 and MW 387) suggests that further oxidation of *m/z* 232, 377, and 393 is occurring in the excess isoprene experiment and contributing to SOA growth. It is

also possible that CIMS  $m/z$  393 (a first-generation product according to one of the formation routes) is nonvolatile enough that it partitions into the aerosol phase and its further oxidation proceeds heterogeneously. Chromatographic peaks such as  $m/z$  333 (associated with MW 271 compound), 449 (MW 450 compound) and 554 (MW 495 compound) are not as strong in the excess isoprene experiment owing to the fact there is not enough  $\text{NO}_3$  in the system to allow for the formation of these highly oxidized compounds.

As discussed earlier, the formation yields of ROOR from the reaction of two peroxy radicals is very low for small peroxy radicals (Kan et al., 1980; Niki et al., 1981; Niki et al., 1982; Wallington et al., 1989; Tyndall et al., 1998; Tyndall et al., 2001). However, according to both gas-phase and aerosol-phase data in this study, it appears that  $\text{RO}_2 + \text{RO}_2$  reaction (self reaction or cross-reaction) in the gas phase yielding ROOR products is a dominant SOA formation pathway. In the case of self-reaction of peroxy radicals, the molecular weight of the product is essentially doubled, providing an efficient way to form products of low volatility. Owing to the lack of authentic standards, we cannot accurately quantify how much each of the peroxide products contributes to the SOA mass. Nevertheless, the total peroxide measurement (Table 3) indicates that they contribute significantly to the total SOA formed.

From the UPLC/(-)ESI-TOFMS (Table 2) and PILS/IC measurements, it appears that organic acids are not a major contributor to SOA formation from the oxidation of isoprene by  $\text{NO}_3$  radicals. The UPLC/(-)ESI-TOFMS technique detects only two minor organic acids at MW 195 and 240. Additionally, the PILS/IC technique does not detect large quantities of any small organic acids. The sum of formate, acetate, glycolate,

lactate, oxalate, and pyruvate are usually between  $0.01 - 0.50 \mu\text{g m}^{-3}$ . These observations are different from the SOA produced in the photooxidation of isoprene (under high- and low- $\text{NO}_x$  conditions), in which a large number of organic acids, such as 2-methylglyceric, formic, and acetic acid, are observed (Surratt et al., 2006; Szmigielski et al., 2007). In the photooxidation experiments, the level of organic acids detected under low- $\text{NO}_x$  conditions is lower than under high- $\text{NO}_x$  conditions. The low- $\text{NO}_x$  isoprene SOA was previously found to also have a significant amount of organic peroxides, as detected in the current study (Table 3); however, organic peroxides detected previously in low- $\text{NO}_x$  isoprene SOA were not structurally elucidated through MS techniques performed in the present study (Table 2, Fig. 14-17), possibly owing to the lack of nitroxy groups which seem to induce acidity and/or increase the adductive abilities of organic peroxides with acetic acid during the ESI-MS analysis. Overall, it appears that the isoprene- $\text{NO}_3$  SOA is much more similar to the previously studied low- $\text{NO}_x$  isoprene SOA. More specifically, it appears that both contain a large amount of organic peroxides, organosulfates (if conducted in the presence of sulfate seed aerosol), and neutral hydroxylated compounds, such as the hydroxynitrates observed in Fig. 14 (e.g. MW 226 and 271 products).

## 5. Approximate estimate of global production of SOA from isoprene + $\text{NO}_3$

The global chemical transport model GEOS-Chem (v. 7-04-11) (<http://www.as.harvard.edu:16080/chemistry/trop/geos/>) is used to estimate, roughly, global SOA formation from the isoprene +  $\text{NO}_3$  reaction. The current version of GEOS-Chem treats mechanistically SOA formation from isoprene + OH, monoterpenes and sesquiterpenes, and aromatics; here we will estimate SOA formation from isoprene +

NO<sub>3</sub> by using an approximate, uniform SOA yield of 10% (corresponding to  $M_o \approx 10 \mu\text{g m}^{-3}$  in Fig. 3). It is noted that this yield is quite uncertain and the importance of peroxy radical self reactions in this study suggest that the SOA yield in the atmosphere will be highly sensitive to the nature of the nighttime peroxy radical chemistry. Here, we seek to obtain only a “back-of-the-envelope” estimate.

Two global isoprene emissions are available in GEOS-Chem: GEIA (Global Emission Inventory Activity) (Guenther et al., 1995) and MEGAN (Model of Emissions and Gases from Nature) (Guenther et al., 2006). Both models require, as input, meteorological data such as temperature to calculate the amount isoprene emitted. For the present estimate, the meteorological fields employed by Wu et al. (2007), generated by the Goddard Institute for Space Studies (GISS) General Circulation Model III, are used. Meteorological conditions correspond approximately to those of year 2000.

Table 4 presents the annual emissions of isoprene as predicted by each of the emission models, together with the amount of isoprene predicted to react via OH, O<sub>3</sub>, and NO<sub>3</sub>, the global burden, and lifetime. We note that there is a significant difference between the annual isoprene emissions predicted by the earlier and newer emission models. Isoprene + OH accounts for 300 to 400 Tg yr<sup>-1</sup> of isoprene consumption. Henze et al. (2007) predict that annual SOA production from isoprene + OH is about 13 Tg yr<sup>-1</sup> (based on the MEGAN inventory and GEOS-4 meteorological fields, which are assimilated fields from actual year 2004). Note that SOA production from isoprene + OH, or any other pathway for that matter, is sensitive to the production of SOA from other hydrocarbon precursors since gas-aerosol partitioning depends on the total organic aerosol mass.

If we take as a rough estimate a 10% SOA yield from the isoprene + NO<sub>3</sub> pathway from the results in Table 4, 2 to 3 Tg yr<sup>-1</sup> of SOA results from isoprene + NO<sub>3</sub>. This rate of production would make SOA from isoprene + NO<sub>3</sub> as significant as that from sesquiterpenes, biogenic alcohols, and aromatics, each of which produces about 2 to 4 Tg yr<sup>-1</sup> of SOA (Henze et al., 2007). Owing to efficient photodissociation, NO<sub>3</sub> achieves its highest concentrations at night. By contrast, isoprene emissions are assumed to be zero at night in both emission models. Consequently, the isoprene + NO<sub>3</sub> reaction occurs only at night, involving isoprene that remains unreacted after each daytime period.

We caution that the estimates above are obtained at the crudest level of approximation, in which a globally uniform SOA yield of 10% from isoprene + NO<sub>3</sub> is applied. As we note from Table 4, there is also a substantial difference between predictions of the two available isoprene emission models; the more recent MEGAN model represents an improved level of understanding over the earlier GEIA model. Predictions of SOA formation from the isoprene + NO<sub>3</sub> pathway are, of course, highly dependent on ambient NO<sub>3</sub> radical concentrations. Nitrate radical concentrations predicted in the current simulations vary from about 0.1 ppt in remote regions of South America to 20 ppt or more in the southeastern USA (in August). Future work will address the simulation of SOA formation from isoprene + NO<sub>3</sub> following the microphysical treatment in GEOS-Chem.

## 6. Implications

We report a series of chamber experiments investigating the formation of secondary organic aerosols from the reaction of isoprene with nitrate radicals. For an

initial isoprene concentration of 18.4 to 101.6 ppb, the SOA yield ranges from 4.3% to 23.8% (typical yield experiments). The SOA yield from the slow  $\text{N}_2\text{O}_5$  injection experiment ( $\text{RO}_2 + \text{RO}_2$  reaction dominates) is much higher than that from the slow isoprene injection experiment ( $\text{RO}_2 + \text{NO}_3$  dominates), implying that  $\text{RO}_2 + \text{RO}_2$  is a more effective channel of forming SOA. The SOA yield from the slow  $\text{N}_2\text{O}_5$  experiment is roughly the same as that in the typical yield experiments, suggesting that SOA yields obtained in this study likely represent conditions in which peroxy-peroxy radical reactions are favored. Using a uniform SOA yield of 10% (corresponding to  $M_0 \approx 10 \mu\text{g m}^{-3}$ ),  $\sim 2$  to  $3 \text{ Tg yr}^{-1}$  of SOA results from isoprene +  $\text{NO}_3$ , which is about  $\frac{1}{4}$  of the amount of SOA estimated to be formed from isoprene + OH ( $\sim 13 \text{ Tg yr}^{-1}$ ) (Henze et al., 2007).

The extent to which the results from this study can be applied to conditions in the atmosphere depends on the relative importance of  $\text{RO}_2 + \text{RO}_2$  versus  $\text{RO}_2 + \text{NO}_3$  reactions in the nighttime troposphere. However, the fate of peroxy radicals in the atmosphere is uncertain owing to the large uncertainties in the reaction rate constants and ambient concentration of both  $\text{RO}_2$  and  $\text{NO}_3$  radicals (Skov et al., 1992; Kirchner and Stockwell, 1996; Bey et al., 2001ab; Vaughan et al., 2006). A modeling study by Kirchner and Stockwell et al. (1996) suggests that  $\text{RO}_2 + \text{NO}_3$  reaction is important at night; for a moderately polluted site,  $\sim 77$ -90% of the total  $\text{RO}_2$  at night is predicted to react with  $\text{NO}_3$ . These results are at odds with the study by Bey et al. (2001ab), which suggests that  $\text{NO}_3$  radicals are not involved significantly in the propagation of  $\text{RO}_2$  radicals. Currently, only the reaction rate constants for small, relatively simple  $\text{RO}_2$  radicals with  $\text{NO}_3$  radicals have been reported (e.g. Biggs et al., 1994; Daele et al., 1995; Canosa-Mas et al., 1996; Vaughan et al., 2006) and they are roughly in the range of (1-3)



$\times 10^{-12} \text{ cm}^3 \text{ molecule}^{-1} \text{ s}^{-1}$ . With the oxidation of various volatile organic compounds by  $\text{O}_3$  and  $\text{NO}_3$  under nighttime conditions, it is expected that multi-functional peroxy radicals would be prevalent; the reaction rates of these complex peroxy radicals warrants future study. Furthermore, more field measurements on the concentrations of peroxy radicals and nitrate radicals would also help to constrain the relative importance of  $\text{RO}_2 + \text{RO}_2$  versus  $\text{RO}_2 + \text{NO}_3$  reaction.

In this study, we have shown that the formation of ROOR from the reaction of two peroxy radicals is an effective SOA-forming channel based on gas-phase data and elemental SOA composition data. This reaction has generally been considered as a minor channel and has not been widely studied. If the results from this study can be applied to other systems (i.e. the reaction of  $\text{NO}_3$  radicals with other volatile organic compounds), the organic peroxides could possibly be very important SOA components in all systems; they may not have been identified previously owing to the lack of suitable analytical techniques (such as accurate mass measurements from high resolution MS) and clearly more study is needed.

**Acknowledgements**

This research was funded by U.S. Department of Energy Biological and Environmental Research Program DE-FG02-05ER63983. This material is based in part on work supported by the National Science Foundation (NSF) under grant ATM-0432377. The Waters LCT Premier XT time-of-flight mass spectrometer interfaced to a Waters UPLC system was purchased in 2006 with a grant from the National Science Foundation, Chemistry Research Instrumentation and Facilities Program (CHE-0541745). The LCQ Ion Trap mass spectrometer was purchased in 1997 with funds from the National Science Foundation through the CRIF program (CHE-9709233). Jason D. Surratt is supported in part by the U.S. EPA under the STAR Graduate Fellowship Program. Alan J. Kwan acknowledges the support of a NSF graduate research fellowship. The authors would like to thank Chad D. Vecitis, Jie Cheng, and Michael R. Hoffmann for use of and aid with their ozonizer and UV-VIS spectrometer; and to Kana Takematsu and Mitchio Okumura for helpful advice on preparing N<sub>2</sub>O<sub>5</sub>. The authors also thank Jesse H. Kroll for helpful discussions.

## References:

- Alfarra, M. R., Paulsen, D., Gysel, M., Garforth, A. A., Dommen, J., Prevot, A. S. H., Worsnop, D. R., Baltensperger, U., and Coe, H.: A mass spectrometric study of secondary organic aerosols formed from the photooxidation of anthropogenic and biogenic precursors in a reaction chamber, *Atmos. Chem. Phys.*, 6, 5279-5293, 2006.
- Bahreini, R., Keywood, M. D., Ng, N. L., Varutbangkul, V., Gao, S., Flagan, R. C., and Seinfeld, J. H. Measurements of secondary organic aerosol (SOA) from oxidation of cycloalkenes, terpenes, and m-xylene using an Aerodyne aerosol mass spectrometer. *Environ. Sci. Technol.*, 39, 5674-5688, 2005.
- Barnes, I., Bastian, V., Becker, K. H. and Tong, Z.: Kinetics and products of the reactions of  $\text{NO}_3$  with monoalkenes, dialkenes, and monoterpenes, *J. Phys. Chem.*, 94, 2413-2419, 1990.
- Berndt, T. and Böge, O.: Gas-Phase reaction of  $\text{NO}_3$  radicals with isoprene: A kinetic and mechanistic study, *Inter. J. Chem. Kinet.*, 29, 755-765, 1997.
- Bey, I., Aumont, B. and Toupance, G.: A modeling study of the nighttime radical chemistry in the lower continental troposphere. 1. Development of a detailed chemical mechanism including nighttime chemistry, *J. Geophys. Res.*, 106, D9, 9959-9990, 2001a.
- Bey, I., Aumont, B. and Toupance, G.: A modeling study of the nighttime radical chemistry in the lower continental troposphere. 2. Origin and evolution of  $\text{HO}_x$ , *J. Geophys. Res.*, 106, D9, 9991-10001, 2001b.
- Bey, I., Jacob, D. J., Yantosca, R. M., Logan, J. A., Field, B. D., Fiore, A. M., Li, Q. B., Liu, H. G. Y., Mickley, L. J. and Schultz, M. G.: Global modeling of tropospheric chemistry with assimilated meteorology: Model description and evaluation, *J. Geophys. Res.*, 106, D19, 23073-23095, 2001c .
- Biggs, P., Canosa-Mas, C. E., Fracheboud, J. M., Shallcross, D. E. and Wayne, R. P.: Investigation into the kinetics and mechanisms of the reaction of  $\text{NO}_3$  with  $\text{CH}_3$  and  $\text{CH}_3\text{O}$  at 298K between 0.6 Torr and 8.5 Torr – is there a chain decomposition mechanism in operation, *J. Chem. Soc., Faraday Trans.*, 90, 1197-1204, 1994.
- Brown, S. S., Ryerson, T. B., Wollny, A. G., Brock, C. A., Peltier, R., Sullivan, A. P., Weber, R. J., Dube, W. P., Trainer, M., Meagher, J. F., Fehsenfeld, F. C. and Ravishankara, A. R.: Variability in nocturnal nitrogen oxide processing and its role in regional air quality, *Science*, 311, 5757, 67-70, 2006.
- Canosa-Mas, C. E., Flugge, M. L., King, M. D. and Wayne, R. P.: An experimental study of the gas-phase reaction of the  $\text{NO}_3$  radical with  $\alpha,\beta$ -unsaturated carbonyl compounds, *Phys. Chem. Chem. Phys.*, 7, 643-650, 2005.

- Canosa-Mas, C. E., King, M. D., Lopez, R., Percival, C. J., Wayne, R. P., Shallcross, D. E., Pyle, J. A. and Daele, V.: Is the reaction  $\text{CH}_3\text{C}(\text{O})\text{O}_2$  and  $\text{NO}_3$  important in the night-time troposphere? *J. Chem. Soc., Faraday Trans.*, 92, 2211-2222, 1996.
- Carslaw, N., Carpenter, L. J., Plane, J. M. C., Allan, B. J., Burgess, R. A., Clemitshaw, K. C., Coe, H. and Penkett, S. A.: Simultaneous measurements of nitrate and peroxy radicals in the marine boundary layer, *J. Geophys. Res.*, 102, 18917-18933, 1997.
- Carter, W. P. L. and Atkinson, R.: Development and evaluation of a detailed mechanism for the atmospheric reactions of isoprene and  $\text{NO}_x$ , *Int. J. Chem. Kinet.*, 28, 497-530, 1996.
- Claeys, M., Graham, B., Vas, G., Wang, W., Vermeylen, R., Pashynska, V., Cafmeyer, J., Guyon, P., Andreae, M.O., Artaxo, P. and Maenhaut, W.: Formation of secondary organic aerosols through photooxidation of isoprene, *Science*, 303, 1173-1176, 2004.
- Cocker III, D. R., Flagan, R. C., and Seinfeld, J. H.: State-of-the-art chamber facility for studying atmospheric aerosol chemistry, *Environ. Sci. Technol.*, 35, 2594-2601, 2001.
- Crounse, J. D., McKinney, K. A., Kwan, A. J. and Wennberg, P. O.: Measurements of gas-phase hydroperoxides by chemical ionization mass spectrometry, *Anal. Chem.*, 78, 6726-6732, 2006.
- Curren, K., Gillespie, T., Steyn, D., Dann, T. and Wang, D.: Biogenic isoprene in the Lower Fraser Valley, British Columbia, *J. Geophys. Res.*, 103, D19, 25467-25477, 1998.
- Daele, V., Laverdet, G., Lebras, G. and Poulet, G.: Kinetics of the reactions of  $\text{CH}_3\text{O}+\text{NO}$ ,  $\text{CH}_3\text{O}+\text{NO}_3$ , and  $\text{CH}_3\text{O}_2+\text{NO}_3$ , *J. Phys. Chem.*, 99, 1470-1477, 1995.
- Davidson, J. A., Viggiano, A. A., Howard, C. J., Fehsenfeld, F. C., Albritton, D. L. and Ferguson, E. E.: Rate constants for the reaction of  $\text{O}_2^+$ ,  $\text{NO}_2^+$ ,  $\text{NO}^+$ ,  $\text{H}_3\text{O}^+$ ,  $\text{CO}_3^+$ ,  $\text{NO}_2^-$ , and halide ions with  $\text{N}_2\text{O}_5$  at 300K, *J. Chem. Phys.*, 68, 2085-2087, 1978.
- Dibble, T. S.: Isomerization of OH-isoprene adducts and hydroxyalkoxy isoprene radicals, *J. Phys. Chem.*, 106, 28, 6643-6650, 2002.
- Dommen, J., Metzger, A., Duplissy, J., Kalberer, M., Alfarra, M. R., Gascho, A., Weingartner, E., Prevot, A. S. H., Verheggen, B. and Baltensperger, U.: Laboratory observation of oligomers in the aerosol from isoprene/ $\text{NO}_x$  photooxidation, *Geophys. Res. Lett.*, 33, L13805, 2006.
- Edney, E. O., Kleindienst, T. E., Jaoui, M., Lewandowski, M., Offenberg, J. H., Wang, W. and Claeys, M.: Formation of 2-methyl tetrols and 2-methylglyceric acid in

- secondary organic aerosol from laboratory irradiated isoprene/NO<sub>x</sub>/SO<sub>2</sub>/air mixtures and their detection in ambient PM<sub>2.5</sub> samples collected in the eastern United States, *Atmos. Environ.*, 39, 5281-5289, 2005.
- Fan, J. and Zhang, R.: Atmospheric oxidation mechanism of isoprene, *Environ. Chem.*, 1, 140-149, doi:10.1071/EN04045, 2004.
- Gao, S., Keywood, M. D., Ng, N. L., Surratt, J. D., Varutbangkul, V., Bahreini, R., Flagan, R. C., and Seinfeld, J. H.: Low molecular weight and oligomeric components in secondary organic aerosol from the ozonolysis of cycloalkenes and  $\alpha$ -pinene, *J. Phys. Chem. A*, 108, 10147-10164, 2004a.
- Gao, S., Ng, N. L., Keywood, M. D., Varutbangkul, V., Bahreini, R., Nenes, A., He, J., Yoo, K. Y., Beauchamp, J. L., Hodyss, R. P., Flagan, R. C., and Seinfeld, J. H.: Particle phase acidity and oligomer formation in secondary organic aerosol, *Environ. Sci. Technol.*, 38, 6582-6589, 2004b.
- Gao, S., Surratt, J. D., Knipping, E. M., Edgerton, E. S., Shahgholi, M., and Seinfeld, J. H.: Characterization of polar organic components in fine aerosols in the southeastern United States: Identity, origin, and evolution, *J. Geophys. Res.*, 111, D14314, doi:10.1029/2005JD006601, 2006.
- Gong, H., Matsunaga, A. and Ziemann, P.: Products and mechanism of secondary organic aerosol formation from reactions of linear alkenes with NO<sub>3</sub> radicals, *J. Phys. Chem.*, 109, 4312-4324, 2005.
- Gómez-González, Y., Surratt, J. D., Cuyckens, F., Szmigielski, R., Vermeylen, R., Jaoui, M., Lewandowski, M., Offenberg, J. H., Kleindienst, T. E., Edney, E. O., Blockhuys, F., Van Alsenoy, C., Maenhaut, W. and Claeys, M.: Characterization of organosulfates from the photooxidation of isoprene and unsaturated fatty acids in ambient aerosol using liquid chromatography/(-) electrospray ionization mass spectrometry, *J. Mass Spectrom.*, 2007, doi:10.1002/jms.1329, 2007.
- Guenther, A., Hewitt, C. N., Erickson, D., Fall, R., Geron, C., Graedel, T., Harley, P., Klinger, L., Lerdau, M., Mckay, W. A., Pierce, T., Scholes, B., Steinbrecher, R., Tallamraju, R., Taylor, J. and Zimmerman, P.: A global-model of natural volatile organic compound emissions, *J. Geophys. Res.*, 100 (D5), 8873-8892, 1995.
- Guenther, A., Karl, T., Harley, P., Wiedinmyer, C., Palmer, P. I. and Geron, C.: Estimates of global terrestrial isoprene emissions using MEGAN (Model of Emissions of Gases and Aerosols from Nature), *Atmos. Chem. Phys.*, 6, 3181-3210, 2006.
- Heintz, F., Platt, U., Flentje, H. and Dubois, R.: Long-term observation of nitrate radicals at the tor station, Kap Arkona (Rugen), *J. Geophys. Res.*, 101, D17, 22891-22910, 1996.

- Henze, D. K., Seinfeld, J. H., Ng, N. L., Kroll, J. H., Fu, T. M., Jacob, D. J. and Heald, C. L.: Global modeling of secondary organic aerosol formation from aromatic hydrocarbons: High- vs low-yield pathways, *Atmos. Chem. Phys. Discuss.*, 7, 14569-14601, 2007.
- Horowitz, L. W., Fiore, A. M., Milly, G. P., Cohen, R. C., Perring, A., Wooldridge, P. J., Hess, P.G., Emmons, L. K. and Lamarque, J.: Observational constraints on the chemistry of isoprene nitrates over the eastern United States, *J. Geophys. Res.*, 112, D12S08, doi:10.1029/2006JD007747, 2007.
- Iinuma, Y., Müller, C., Berndt, T., Böge, O., Claeys, M. and Herrmann, H.: Evidence for the existence of organosulfates from  $\beta$ -pinene ozonolysis in ambient secondary organic aerosol, *Environ. Sci. Technol.*, 41, 6678-6683, 2007b.
- Iinuma, Y., Müller, C., Böge, O., Gnauk, T. and Herrmann, H.: The formation of organic sulfate esters in the limonene ozonolysis secondary organic aerosol (SOA) under acidic conditions, *Atmos. Environ.*, 41, 5571-5583, 2007a.
- Jay, K. and Stieglitz, L.: The gas phase addition of  $\text{NO}_x$  to olefins, *Chemosphere*, 19, 1939-1950, 1989.
- Jayne, J. T., Leard, D. C., Zhang, X., Davidovits, P., Smith, K. A., Kolb, C. E., and Worsnop, D. W.: Development of an Aerosol Mass Spectrometer for size and composition analysis of submicron particles, *Aerosol Sci. Technol.*, 33, 49-70, 2000.
- Kan, C. S., Calvert, J. G. and Shaw, J. H.: Reactive channels of the  $\text{CH}_3\text{O}_2\text{-CH}_3\text{O}_2$  reaction, *J. Phys. Chem.*, 84, 3411-3417, 1980.
- Keywood, M. D., Varutbangkul, V., Bahreini, R., Flagan, R. C., and Seinfeld, J. H.: Secondary organic aerosol formation from the ozonolysis of cycloalkenes and related compounds, *Environ. Sci. Technol.*, 38, 4157-4164, 2004.
- Kirchner, F. and Stockwell, W. R.: Effect of peroxy radical reactions on the predicted concentrations of ozone, nitrogenous compounds, and radicals, *J. Geophys. Res.*, 101, D15, 21007-21022, 1996.
- Kroll, J. H., Ng, N. L., Murphy, S. M., Flagan, R. C., and Seinfeld, J. H.: Secondary organic aerosol formation from isoprene photooxidation under high- $\text{NO}_x$  conditions, *J. Geophys. Res.*, 32, L18808, doi: 10.1029/2005GL023637, 2005.
- Kroll, J. H., Ng, N. L., Murphy, S. M., Flagan, R. C., and Seinfeld, J. H.: Secondary organic aerosol formation from isoprene photooxidation, *Environ. Sci. Technol.*, 40, 1869-1877, 2006.
- Kwok, E. S. C., Aschmann, S. M., Arey, J. and Atkinson, R.: Product formation from the

- reaction of the  $\text{NO}_3$  radical with isoprene and rate constants for the reactions of methacrolein and methyl vinyl ketone with the  $\text{NO}_3$  radical, *Inter. J. Chem. Kinet.* 28, 925-934, 1996.
- Liggio, J. and Li, S. M.: Organosulfate formation during the uptake of pinonaldehyde on acidic sulfate aerosols, *Geophys. Res. Lett.*, 33, L13808, 2006.
- Liggio, J., Li, S. M. and McLaren, R.: Heterogeneous reactions of glyoxal on particulate matter: Identification of acetals and sulfate esters, *Environ. Sci. Technol.*, 39, 1532-1541, 2005.
- Lightfoot, P. D., Cox, R. A., Crowley, J. N., Destriau, M. Hayman, G. D., Jenkin, M. E., Moortgat G. K. and Zabel, F.: Organic peroxy radicals – kinetics, spectroscopy and tropospheric chemistry, *Atmos. Environ.*, 26, 1805-1961, 1992.
- Ng, N. L., Chhabra, P. S., Chan, A. W. H., Surratt, J. D., Kroll, J. H., Kwan, A. J., McCabe, D. C., Wennberg, P. O., Sorooshian, A., Murphy, S. M., Dalleska, N. F., Flagan, R. C. and Seinfeld, J. H.: Effect of  $\text{NO}_x$  level on secondary organic aerosol (SOA) formation from the photooxidation of terpenes, *Atmos. Chem. Phys.*, 7, 5159-5174, 2007a.
- Ng, N. L., Kroll, J. H., Chan, A. W. H., Chhabra, P. S., Flagan, R. C. and Seinfeld, J. H.: Secondary organic aerosol formation from *m*-xylene, toluene, and benzene, *Atmos. Chem. Phys.*, 7, 3909-3922, 2007b.
- Ng, N. L., Kroll, J. H., Keywood, M. D., Bahreini, R., Varutbangkul, V., Flagan, R. C., Seinfeld, J. H., Lee, A. and Goldstein, A. H.: Contribution of first- versus second-generation products to secondary organic aerosols formed in the oxidation of biogenic hydrocarbons, *Environ. Sci. Technol.*, 40, 2283-2297, 2006.
- Niki, H., Maker, P. D., Savage, C. M. and Breitenbach L.P.: Fourier Transform Infrared studies of the self-reaction of  $\text{CH}_3\text{O}_2$  radicals, *J. Phys. Chem.*, 85, 877-881, 1981.
- Niki, H., Maker, P. D., Savage, C. M. and Breitenbach L.P.: Fourier Transform Infrared studies of the self-reaction of  $\text{C}_2\text{H}_5\text{O}_2$  radicals, *J. Phys. Chem.*, 86, 3825-3829, 1982.
- Noda, J., Nyman, G. and Langer S.: Kinetics of the gas-phase reaction of some unsaturated alcohols with the nitrate radical, *J. Phys. Chem.*, 106, 945-951, 2002.
- Odum, J. R., Hoffmann, T., Bowman, F., Collins, D., R. C. Flagan, R. C., and Seinfeld, J. H.: Gas/particle partitioning and secondary organic aerosol yields, *Environ. Sci. Technol.*, 30, 2580-2585, 1996.
- Odum, J. R., Jungkamp, T. P. W., Griffin, R. J., Flagan, R. C., and Seinfeld, J. H.: The atmospheric aerosol-forming potential of whole gasoline vapor, *Science*, 276, 96-99, 1997a.

- Odum, J. R., Jungkamp, T. P. W., Griffin, R. J., Forstner, H. J. L., Flagan, R. C., and Seinfeld, J. H.: Aromatics, reformulated gasoline and atmospheric organic aerosol formation, *Environ. Sci. Technol.*, 31, 1890-1897, 1997b.
- Paulson, S. E. and Seinfeld, J. H.: Development and evaluation of a photooxidation mechanism for isoprene, *J. Geophys. Res.*, 97, D18, 20703-20715, 1992.
- Penkett, S.A., Burgess, R.A., Coe, H., Coll, I., Hov, Ø., Lindskog, A., Schmidbauer, N., Solberg, S., Roemer, M., Thijssse, T., Beck, J. and Reeves C.E.: Evidence for large average concentrations of the nitrate radical ( $\text{NO}_3$ ) in Western Europe from the HANSA hydrocarbon database, *Atmos. Environ.*, 41, 3465-3478, 2007.
- Platt, U. and Janssen, C.: Observation and role of the free radicals  $\text{NO}_3$ , ClO, BrO and IO in the troposphere, *Faraday Discuss.*, 100, 175-198, 1995.
- Platt, U., Perner, D., Schroder, J., Kessler, C. and Toennissen, A.: The diurnal variation of  $\text{NO}_3$ , *J. Geophys. Res.*, 86, 11965-11970, 1981.
- Sharkey, T. D., Singsaas, E. L., Vanderveer, P. J. and Geron, C.: Field measurements of isoprene emission from trees in response to temperature and light, *Tree Physiol.*, 16, 649-654, 1996.
- Skov, H., Benter, Th., Schindler, R. N., Hjorth, J. and Restelli, G.: Epoxide formation in the reactions of the nitrate radical with 2,3-dimethyl-2-butene, cis- and trans-2-butene and isoprene, *Atmos. Environ.*, 28, 1583-1592, 1994.
- Skov, H., Hjorth, J., Lohse, C., Jensen, N. R. and Restelli, G.: Products and mechanisms of the reactions of the nitrate radical ( $\text{NO}_3$ ) with isoprene, 1,3-butadiene and 2,3-dimethyl-1,3-butadiene in air, *Atmos. Environ.*, 26A, 15, 2771-2783, 1992.
- Smith, N., Plane, J. M. C., Nien, C. F. and Solomon, P. A.: Nighttime radical chemistry in the San-Joaquin Valley, *Atmos. Environ.*, 29, 2887-2897, 1995.
- Sorooshian, A., Brechtel F. J., Ma, Y. L., Weber R. J., Corless, A., Flagan, R. C., and Seinfeld, J. H.: Modeling and characterization of a particle-into-liquid sampler (PILS), *Aerosol Sci. Technol.*, 40, 396-409, 2006.
- Starn, T. K., Shepson, P. B., Bertman, S. B., Riemer, D. D., Zika, R. G. and Olszyna, K.: Nighttime isoprene chemistry at an urban-impacted forest site, *J. Geophys. Res.*, 103, D17, 22437-22447, 1998.
- Steinbacher, M., Dommen, J. Ordonez, C., Reimann, S., Gruebler, F. C., Staehelin, J., Andreani-Aksoyoglu, S. and Prevot, A. S. H.: Volatile organic compounds in the Po Bason. Part B: Biogenic VOCs, *J. Atmos. Chem.*, 51, 293-315, 2005.



- Stroud, C. A., Roberts, J. M., Williams E. J., Hereid, D., Angevine, W. M., Fehsenfeld, F. C., Wisthaler, A., Hansel, A., Martinez-Harder, M., Harder, H., Brune, W. H., Hoenninger, G., Stutz, J. and White, A. B.: Nighttime isoprene trends at an urban forested site during the 1999 Southern Oxidant Study, *J. Geophys. Res.*, 107, D16, 4291, 10.1029/2001JD000959, 2002.
- Suh, I., Lei, W. and Zhang, R.: Experimental and theoretical studies of isoprene reaction with  $\text{NO}_3$ , *J. Phys. Chem.*, 105, 6471-6478, 2001.
- Surratt, J. D., Kroll, J. H., Kleindienst, T. E., Edney, E. O., Claeys, M., Sorooshian, A., Ng, N. L., Offenberg, J. H., Lewandowski, M., Jaoui, M., Flagan, R. C. and Seinfeld, J. H.: Evidence for organosulfates in secondary organic aerosol, *Environ. Sci. Technol.*, 41, 517-527, 2007a.
- Surratt, J. D., Lewandowski, M., Offenberg, J. H., Jaoui, M., Kleindienst, T. E., Edney, E. O. and Seinfeld, J. H.: Effect of acidity on secondary organic aerosol formation from isoprene, *Environ. Sci. Technol.*, 41, 5363-5369, 2007b.
- Surratt, J. D., Murphy, S. M., Kroll, J. H., Ng, N. L., Hildebrandt, L., Sorooshian, A., Szmigielski, R., Vermeylen, R., Maenhaut, W., Claeys, M., Flagan, R. C. and Seinfeld, J. H.: Chemical composition of secondary organic aerosol formed from the photooxidation of isoprene, *J. Phys. Chem. A*, 110, 9665-9690, 2006.
- Szmigielski, R., Surratt, J. D., Vermeylen, R., Szmigielska, K., Kroll, J. H., Ng, N. L., Murphy, S. M., Sorooshian, A., Seinfeld, J. H. and Claeys, M.: Characterization of 2-methylglyceric acid oligomers in secondary organic aerosol formed from the photooxidation of isoprene using trimethylsilylation and gas chromatography/ion trap mass spectrometry, *J. Mass Spectrom.*, 42, 101-116, 2007.
- Tyndall, G. S., Cox, R. A., Granier, C., Lesclaux, R., Moortgat, G. K., Pilling, M. J., Ravishankara, A. R. and Wallington, T. J.: Atmospheric chemistry of small peroxy radicals, *J. Geophys. Res.*, 106, D11, 12157-12182, 2001.
- Tyndall, G. S., Wallington, T. J. and Ball, J. C.: FTIR product study of the reactions of  $\text{CH}_3\text{O}_2 + \text{CH}_3\text{O}_2$  and  $\text{CH}_3\text{O}_2 + \text{O}_3$ , *J. Phys. Chem.*, 102, 2547-2554, 1998.
- Vaughan, S. Canosa-Mas, C. E., Pfrang, C., Shallcross, D. E., Watson, L. and Wayne, R. P.: Kinetic studies of reactions of the nitrate radical ( $\text{NO}_3$ ) with peroxy radicals ( $\text{RO}_2$ ): an indirect source of OH at night? *Phys. Chem. Chem. Phys.*, 8, 3749-3760, 2006.
- von Friedeburg, C., Wagner, T., Geyer, A., Kaiser, N., Platt, U., Vogel, B. and Vogel, H.: Derivation of tropospheric  $\text{NO}_3$  profiles using off-axis differential optical absorption spectroscopy measurements during sunrise and comparison with simulations, *J. Geophys. Res.*, 107, D13, doi:10.1029/2001JD000481, 2002.

- Wallington, T. J., Dagaut, P. and Kurylo, M. J.: Ultraviolet absorption cross-sections and reaction kinetics and mechanisms for peroxy radicals in the gas phase, *Chem. Rev.*, 92, 667-710, 1992.
- Wallington, T. J., Gierczak, C. A., Ball, J. C. and Japar, S. M.: Fourier Transform Infrared studies of the self-reaction of  $C_2H_5O_2$  radicals in air at 295K, *Int. J. Chem. Kinet.*, 21, 1077-1089, 1989.
- Werner, G., Kastler, J., Looser, R. and Ballschmiter, K.: Organic nitrates of isoprene as atmospheric trace compounds, *Angew. Chem. Int. Ed.*, 38, 11, 1634-1637, 1999.
- Wu, S. L., Mickley, L. J., Jacob, D. J. Logan, J. A., Yantosca, R. M. and Rind, D.: Why are there large differences between models in global budgets of tropospheric ozone? *J. Geophys. Res.*, 112, D5, D05302, 2007.
- Zhang, D. and Zhang, R.: Unimolecular decomposition of nitroxyalkyl radicals from  $NO_3$ -isoprene reaction, *J. Chem. Phys.*, 116, 22, 9721-9728, 2002.

Table 1. Initial conditions and results for yield experiments

Date	T (K)	RH (%)	$\Delta\text{HC}$ (ppb) <sup>a</sup>	$\Delta M_o$ ( $\mu\text{g}/\text{m}^3$ ) <sup>b</sup>	SOA Yield (%)
8/9/07	294	5.1	$101.6 \pm 0.6$	$68.1 \pm 1.1$	$23.8 \pm 0.5$
8/10/07	293	4.7	$30.2 \pm 0.1$	$11.5 \pm 0.4$	$13.5 \pm 0.5$
8/11/07	294	5.4	$67.1 \pm 0.1$	$39.3 \pm 1.2$	$20.8 \pm 0.7$
8/12/07	293	6.0	$51.7 \pm 0.2$	$26.7 \pm 0.6$	$18.2 \pm 0.5$
8/13/07	294	5.7	$18.4 \pm 0.1$	$2.2 \pm 0.2$	$4.3 \pm 0.5$
8/14/07	294	5.5	$21.8 \pm 0.1$	$4.8 \pm 0.4$	$7.8 \pm 0.6$
10/4/2007 <sup>c</sup>	293	5.5	$39.5 \pm 0.1^d$	$7.9 \pm 0.3$	$7.1 \pm 0.6$
10/25/2007 <sup>e</sup>	294	6.4	$42.0 \pm 0.1$	$16.6 \pm 0.6$	$14.1 \pm 0.7$

<sup>a</sup> Stated uncertainties ( $1\sigma$ ) are from scatter in isoprene measurements.

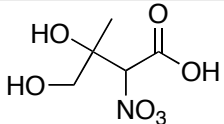
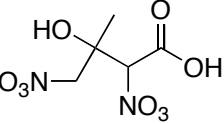
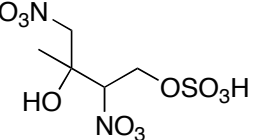
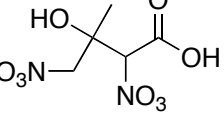
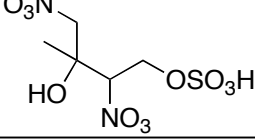
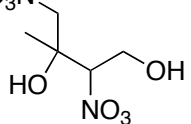
<sup>b</sup> Stated uncertainties ( $1\sigma$ ) are from scatter in particle volume measurements.

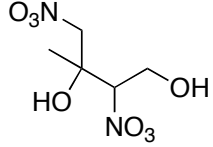
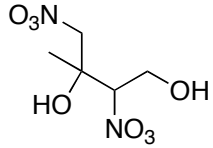
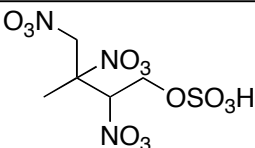
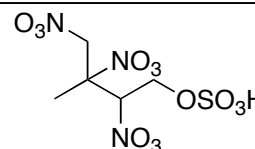
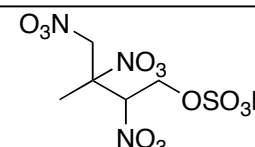
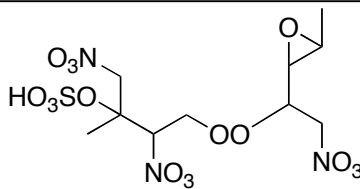
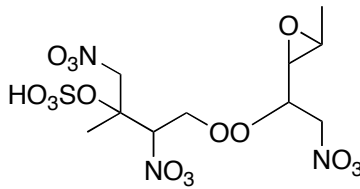
<sup>c</sup> Slow isoprene injection experiment

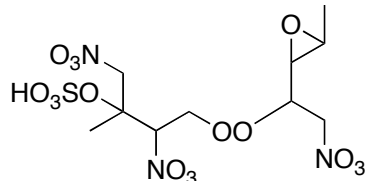
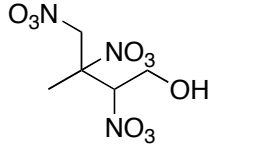
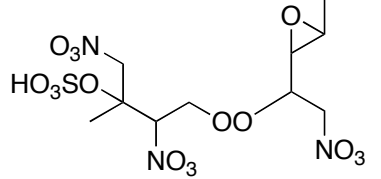
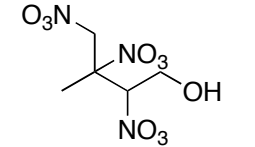
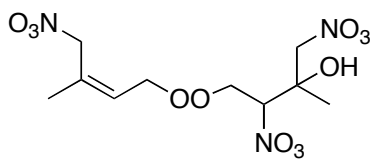
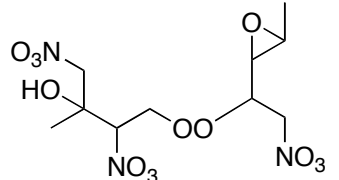
<sup>d</sup> Concentration estimated based on a separate calibration experiment (see Sect. 3.2); the uncertainty in the measured isoprene concentration is assumed to be the same as in the slow  $\text{N}_2\text{O}_5$  experiment.

<sup>e</sup> Slow  $\text{N}_2\text{O}_5$  injection experiment

Table 2. SOA products identified using UPLC/(-)ESI-TOFMS.

Retention Time (min)	Measured [M - H] <sup>-</sup> Ion (m/z)	TOFMS Suggested [M - H] <sup>-</sup> Ion Formula	Error (mDa, ppm)	Measured [M - H + C <sub>2</sub> H <sub>4</sub> O <sub>2</sub> ] <sup>-</sup> Ion (m/z)	TOFMS Suggested [M - H + C <sub>2</sub> H <sub>4</sub> O <sub>2</sub> ] <sup>-</sup> Ion Formula	Error (mDa, ppm)	Proposed Structure <sup>a</sup>
3.68 <sup>b</sup>	194.0310	C <sub>5</sub> H <sub>8</sub> NO <sub>7</sub> <sup>-</sup>	0.9, 4.6	c			
4.52 <sup>b</sup>	239.0137	C <sub>5</sub> H <sub>7</sub> N <sub>2</sub> O <sub>9</sub> <sup>-</sup>	-1.5, -6.3				
5.09 <sup>d</sup>	304.9946	C <sub>5</sub> H <sub>9</sub> N <sub>2</sub> O <sub>11</sub> S <sup>-</sup>	1.9, 6.2				
5.24 <sup>b</sup>	239.0152	C <sub>5</sub> H <sub>7</sub> N <sub>2</sub> O <sub>9</sub> <sup>-</sup>	0.0, 0.0				
5.43 <sup>d</sup>	304.9944	C <sub>5</sub> H <sub>9</sub> N <sub>2</sub> O <sub>11</sub> S <sup>-</sup>	1.7, 5.6				
6.07	225.0350	C <sub>5</sub> H <sub>9</sub> N <sub>2</sub> O <sub>8</sub> <sup>-</sup>	-0.9, -4.0				

6.12	225.0342	$\text{C}_5\text{H}_9\text{N}_2\text{O}_8^-$	-1.7, -7.6				
6.60	225.0375	$\text{C}_5\text{H}_9\text{N}_2\text{O}_8^-$	1.6, 7.1	285.0676	$\text{C}_7\text{H}_{13}\text{N}_2\text{O}_{10}^-$	0.6, 2.1	
7.75 <sup>d</sup>	349.9775	$\text{C}_5\text{H}_8\text{N}_3\text{O}_{13}\text{S}^-$	-0.3, -0.9				
7.85 <sup>d</sup>	349.9764	$\text{C}_5\text{H}_8\text{N}_3\text{O}_{13}\text{S}^-$	0.2, 0.6				
8.00 <sup>d</sup>	349.9784	$\text{C}_5\text{H}_8\text{N}_3\text{O}_{13}\text{S}^-$	-0.4, -1.1				
8.48 <sup>d</sup>	466.0268	$\text{C}_{10}\text{H}_{16}\text{N}_3\text{O}_{16}\text{S}^-$	1.7, 3.6				
8.54 <sup>d</sup>	466.0264	$\text{C}_{10}\text{H}_{16}\text{N}_3\text{O}_{16}\text{S}^-$	1.3, 2.8				

8.72 <sup>d</sup>	466.0237	$\text{C}_{10}\text{H}_{16}\text{N}_3\text{O}_{16}\text{S}^-$	-1.4, -3.0				
8.76 <sup>e</sup>	270.0199	$\text{C}_5\text{H}_8\text{N}_3\text{O}_{10}^-$	-1.1, -4.1	330.0393	$\text{C}_7\text{H}_{12}\text{N}_3\text{O}_{12}^-$	-2.8, -8.5	
8.81 <sup>d</sup>	466.0237	$\text{C}_{10}\text{H}_{16}\text{N}_3\text{O}_{16}\text{S}^-$	-1.4, -3.0				
8.85 <sup>e</sup>	270.0204	$\text{C}_5\text{H}_8\text{N}_3\text{O}_{10}^-$	-0.6, -2.2	330.0379	$\text{C}_7\text{H}_{12}\text{N}_3\text{O}_{12}^-$	-4.2, -12.7	
9.15	370.0734	$\text{C}_{10}\text{H}_{16}\text{N}_3\text{O}_{12}^-$	0.9, 2.4	430.0940	$\text{C}_{12}\text{H}_{20}\text{N}_3\text{O}_{14}^-$	-0.5, -1.2	
9.19	386.0678	$\text{C}_{10}\text{H}_{16}\text{N}_3\text{O}_{13}^-$	-0.5, -1.3	446.0888	$\text{C}_{12}\text{H}_{20}\text{N}_3\text{O}_{15}^-$	-0.6, -1.3	

9.24	370.0732	$C_{10}H_{16}N_3O_{12}^-$	-0.2, -0.5	430.0937	$C_{12}H_{20}N_3O_{14}^-$	-0.8, -1.9	
9.25	386.0683	$C_{10}H_{16}N_3O_{13}^-$	-0.2, -0.5	446.0893	$C_{12}H_{20}N_3O_{15}^-$	-0.1, -0.2	
9.37	449.0637	$C_{10}H_{17}N_4O_{16}^-$	-0.3, -0.7	509.0854	$C_{12}H_{21}N_4O_{18}^-$	0.3, 0.6	
9.41	386.0684	$C_{10}H_{16}N_3O_{13}^-$	0.1, 0.3	446.0903	$C_{12}H_{20}N_3O_{15}^-$	0.9, 2.0	
9.45	449.0653	$C_{10}H_{17}N_4O_{16}^-$	1.3, 2.9	509.0853	$C_{12}H_{21}N_4O_{18}^-$	0.2, 0.4	
9.90 <sup>f</sup>	494.0537	$C_{10}H_{16}N_5O_{18}^-$	4.7, 9.5	554.0669	$C_{12}H_{20}N_5O_{20}^-$	-3.3, -6.0	

---

9.98 <sup>f</sup>	494.0518	C <sub>10</sub> H <sub>16</sub> N <sub>5</sub> O <sub>18</sub> <sup>-</sup>	2.8, 5.7	554.0676	C <sub>12</sub> H <sub>20</sub> N <sub>5</sub> O <sub>20</sub> <sup>-</sup>	-2.6, -4.7	
-------------------	----------	---	----------	----------	---	------------	--

---

<sup>a</sup> Structural isomers containing nitrate, sulfate, or hydroxyl groups at other positions are likely; for simplicity, only one isomer is shown.

<sup>b</sup> These compounds appear to be very minor SOA products due to very small chromatographic peak areas, confirming that the further oxidation of the nitroxycarbonyl and hydroxycarbonyl first-generation gas-phase products do not yield significant quantities of SOA.

<sup>c</sup> A blank cell indicates that the detected SOA product had no observable acetic acid adduct ion (i.e. [M - H + C<sub>2</sub>H<sub>4</sub>O<sub>2</sub>]<sup>-</sup>).

<sup>d</sup> These organosulfate SOA products were observed only in experiments employing either (NH<sub>4</sub>)<sub>2</sub>SO<sub>4</sub> (i.e. neutral) or MgSO<sub>4</sub> + H<sub>2</sub>SO<sub>4</sub> (i.e. acidic) seed aerosol. These organosulfate SOA products were also observed in the excess isoprene experiments.

<sup>e</sup> In addition to the acetic acid adduct ion, these compounds also had a significant adduct ion at [M - H + HNO<sub>3</sub>]<sup>-</sup> (*m/z* 333), indicating that these compounds are likely not very stable due to the fragmentation of one of the NO<sub>3</sub> groups during the MS analysis.

<sup>f</sup> These compounds were only weakly detected in the excess isoprene experiments.



Table 3. Peroxide content of SOA formed by NO<sub>3</sub> oxidation of isoprene.

Experiment Date	Seeded <sup>a</sup> / Nucleation	[Isoprene] (ppb)	[N <sub>2</sub> O <sub>5</sub> ] (ppm)	SOA Volume Growth Observed <sup>b</sup> ( $\mu\text{m}^3/\text{cm}^3$ )	Total SOA Mass Concentration <sup>c</sup> ( $\mu\text{g}/\text{m}^3$ )	Peroxide Aerosol Mass Concentration ( $\mu\text{g}/\text{m}^3$ )	Contribution of Peroxides to the SOA Mass Concentration Observed (%)
8/22/07	AS	200	1	102	145	46	32
8/30/07	AMS	200	1	123	174	40	23
10/22/07 <sup>d</sup>	AS	1200	0.7	70	100	b.d.l. <sup>e</sup>	<sup>f</sup>
10/23/07	nucleation	200	1	125	177	31	17
10/24/07	AS	200	1	111	158	47	30
10/27/07 <sup>g</sup>	AS	300	1	110	156	47	30

<sup>a</sup> AS = ammonium sulfate seed, AMS = acidified magnesium sulfate seed.

<sup>b</sup> Averaged over the course of filter sampling.

<sup>c</sup> Assuming a SOA density of 1.42 g/cm<sup>3</sup>. This was based on DMA and Q-AMS measurements.

<sup>d</sup> Excess isoprene experiment.

<sup>e</sup> Below detection limits.

<sup>f</sup> No observable contribution of organic peroxides to the SOA mass concentration.

<sup>g</sup> Slow injection of isoprene in this experiment to enhance the RO<sub>2</sub> + NO<sub>3</sub> reaction pathway.

Table 4. Global estimation of isoprene using GEOS-Chem

	Emission Model	
	GEIA <sup>a</sup>	MEGAN <sup>b</sup>
Isoprene emission (Tg/y)	507	389
Global isoprene burden (Tg)	1.7	1.7
Isoprene lifetime (days)	1.2	1.6
Isoprene reacted (Tg/y) by		
Isoprene + OH	407	304
Isoprene + O <sub>3</sub>	69	62
Isoprene + NO <sub>3</sub>	29	21

<sup>a</sup> Modification of GEIA for GEOS-Chem are described at Bey et al. (2001c).

Original GEIA reference is Guenther et al. (1995).

<sup>b</sup> Guenther et al. (2006)

**Figure captions:**

Figure 1. Time profiles of aerosol volume, inorganic nitrate measured by PILS/IC, and nitrate signals from Q-AMS in a blank experiment ( $\sim 1$  ppm  $\text{N}_2\text{O}_5$ , ammonium sulfate seed, no isoprene).

Figure 2. Reaction profile of the oxidation of an initial mixture containing 203.4 ppb isoprene.

Figure 3. SOA yield data and yield curve for isoprene- $\text{NO}_3$  reaction. Also shown are SOA yields from the slow  $\text{N}_2\text{O}_5$  injection experiment and slow isoprene injection experiment.

Figure 4. Time-dependent growth curves for the slow  $\text{N}_2\text{O}_5$  injection experiment and slow isoprene injection experiment.

Figure 5. Time profiles of the major gas-phase products ( $m/z$  230, 232, and 248) and the corresponding aerosol growth from the excess isoprene experiment.

Figure 6. Time evolutions of various gas-phase products in the staggered  $\text{N}_2\text{O}_5$  injection experiment (Isoprene is first injected into the chamber, followed by the addition of 3 pulses of  $\text{N}_2\text{O}_5$ :  $\sim 120$ , 50, and 210 ppb). The top panel shows the isoprene decay and aerosol formation; the middle panel shows the time profiles of the three major first-generation products ( $m/z$  230, 232, and 248); the bottom panel shows the time profiles of three minor products ( $m/z$  377 and 393).

Figure 7. A typical AMS spectrum for SOA formed in typical yield experiments.

Figure 8. AMS spectra signal from the slow  $\text{N}_2\text{O}_5$  injection experiment versus a typical yield experiment. Each mass fragment is normalized by the total signal. The solid red line is the 1:1 line.

Figure 9. AMS spectra signal from the slow isoprene injection experiment versus a typical yield experiment. Each mass fragment is normalized by the total signal. The solid red line is the 1:1 line.

Figure 10. UPLC/(-)ESI-TOFMS base peak ion chromatograms (BPCs) for the following isoprene-NO<sub>3</sub> oxidation experiments: (a) 200 ppb isoprene + 1 ppm N<sub>2</sub>O<sub>5</sub> + seed aerosol generated from 15 mM (NH<sub>4</sub>)<sub>2</sub>SO<sub>4</sub> atomizing solution; (b) 300 ppb isoprene + 1 ppm N<sub>2</sub>O<sub>5</sub> + seed aerosol generated from 15 mM (NH<sub>4</sub>)<sub>2</sub>SO<sub>4</sub> atomizing solution; (c) 1.2 ppm isoprene + 700 ppb N<sub>2</sub>O<sub>5</sub> + seed aerosol generated from 15 mM (NH<sub>4</sub>)<sub>2</sub>SO<sub>4</sub> atomizing solution; (d) 200 ppb isoprene + 1 ppm N<sub>2</sub>O<sub>5</sub> + seed aerosol generated from 30 mM MgSO<sub>4</sub> + 50 mM H<sub>2</sub>SO<sub>4</sub> atomizing solution. The numbers indicated above the selected chromatographic peaks correspond to the most abundant negative ion, and is either the [M - H]<sup>-</sup> or [M - H + C<sub>2</sub>H<sub>4</sub>O<sub>2</sub>]<sup>-</sup> ions.

Figure 11. Proposed mechanisms for the formation of various gas-phase intermediate product ions observed by CIMS. Multiple structural isomers are possible. In this figure, RO<sub>2</sub>' refers to the isoprene peroxy radical (nitroxyperoxy radical), RO<sub>2</sub> refer to a generic peroxy radical.

Figure 12. Time profiles of the major gas-phase products (*m/z* 230, 232, and 248) and the corresponding aerosol growth from the slow N<sub>2</sub>O<sub>5</sub> injection experiment.

Figure 13. Time profiles of the major gas-phase products (*m/z* 230, 232, and 248) and the corresponding aerosol growth from the slow isoprene injection experiment.

Figure 14. Proposed mechanism for SOA formation from the formation and decay of the C<sub>5</sub>-hydroxynitrate gas-phase product formed from the isoprene + NO<sub>3</sub> reaction. Boxes

indicate UPLC/(-)ESI-TOFMS detected SOA products; molecular formulas were confirmed by the accurate mass data provided by the UPLC/(-)ESI-TOFMS. Multiple structural isomers are possible, consistent with the multiple chromatographic peaks observed in the extracted ion chromatograms; however, only one structural isomer is shown for simplicity. <sup>a</sup> This first-generation gas-phase product was previously observed by Jay and Stieglitz (1989), Skov et al. (1992), Kwok et al. (1996), and Berndt and Böge (1997); this gas-phase product was detected as the  $[M + CF_3O]^-$  ion by the CIMS instrument. <sup>b</sup> These particle-phase compounds were detected as both their  $[M - H]^-$  and  $[M - H + C_2H_4O_2]^-$  ions; the acetic acid adduct ( $[M - H + C_2H_4O_2]^-$ ) ion was, in most cases, the molecular ion (i.e. dominant ion). <sup>c</sup> These organosulfate compounds were detected as their  $[M - H]^-$  ions and were observed only in ammonium sulfate and acidified magnesium sulfate seeded experiments.

Figure 15. Proposed mechanism for SOA formation from the formation and decay of the CIMS  $m/z$  377 gas-phase product formed from the isoprene +  $NO_3$  reaction. Boxes indicate UPLC/(-)ESI-TOFMS detected SOA products; molecular formulas were confirmed by the accurate mass data provided by the UPLC/(-)ESI-TOFMS. Multiple structural isomers are possible, consistent with the multiple chromatographic peaks observed in the extracted ion chromatograms; however, only one structural isomer is shown for simplicity. <sup>a</sup> This first-generation gas-phase product was detected as the  $[M + CF_3O]^-$  ion by the CIMS instrument. <sup>b</sup> These particle-phase compounds were detected as both their  $[M - H]^-$  and  $[M - H + C_2H_4O_2]^-$  ions; the acetic acid adduct ( $[M - H + C_2H_4O_2]^-$ ) ion was, in most cases, the molecular ion (i.e. dominant ion).

Figure 16. Proposed mechanism for SOA formation from the formation and decay of the CIMS  $m/z$  393 gas-phase product formed from the isoprene +  $\text{NO}_3$  reaction. Boxes indicate UPLC/(-)ESI-TOFMS detected SOA products; molecular formulas were confirmed by the accurate mass data provided by the UPLC/(-)ESI-TOFMS. Multiple structural isomers are possible, consistent with the multiple chromatographic peaks observed in the extracted ion chromatograms; however, only one structural isomer is shown for simplicity. <sup>a</sup> This first-generation gas-phase product was detected as the  $[\text{M} + \text{H}]^+$  ion by the CIMS instrument; this gas-phase product was previously observed by Berndt and Böge (1997) and could also be 2-(1-methyl-vinyl)oxirane. <sup>b</sup> This gas-phase product was detected as the  $[\text{M} + \text{CF}_3\text{O}]^-$  ion. <sup>c</sup> These particle-phase compounds were detected as both their  $[\text{M} - \text{H}]^-$  and  $[\text{M} - \text{H} + \text{C}_2\text{H}_4\text{O}_2]^-$  ions; the acetic acid adduct ( $[\text{M} - \text{H} + \text{C}_2\text{H}_4\text{O}_2]^-$ ) ion was, in most cases, the molecular ion (i.e. dominant ion). <sup>d</sup> This organosulfate compound was detected as its  $[\text{M} - \text{H}]^-$  ion and was observed only in the ammonium sulfate and acidified magnesium sulfate seeded experiments.

Figure 17. Proposed mechanism for SOA formation from the formation and decay of the  $\text{C}_5$ -nitrooxycarbonyl,  $\text{C}_5$ -hydroxycarbonyl, and  $\text{C}_5$ -dinitrate first-generation products formed from the isoprene +  $\text{NO}_3$  reaction. Boxes indicate UPLC/(-)ESI-TOFMS detected SOA products; molecular formulas were confirmed by the accurate mass data provided by the UPLC/(-)ESI-TOFMS. Multiple structural isomers are possible, consistent with the multiple chromatographic peaks observed in the extracted ion chromatograms; however, only one structural isomer is shown for simplicity. <sup>a</sup> These first-generation gas-phase products were previously observed by Skov et al. (1994) and Kwok et al. (1996); these

gas-phase products were detected as the  $[M + CF_3O]^-$  ion by the CIMS instrument.<sup>b</sup> These are minor SOA products, confirming that the further oxidation of the C<sub>5</sub>-nitrooxycarbonyl and C<sub>5</sub>-hydroxycarbonyl first-generation products do not yield significant amounts of SOA.<sup>c</sup> This first-generation gas-phase product was previously observed by Werner et al. (1999); this gas-phase product was also detected as the  $[M + CF_3O]^-$  ion by the CIMS instrument.<sup>d</sup> This particle-phase compound was detected as both its  $[M - H]^-$  and  $[M - H + C_2H_4O_2]^-$  ions; the acetic acid adduct ( $[M - H + C_2H_4O_2]^-$ ) ion was the molecular ion (i.e. dominant ion).

Figure 1.

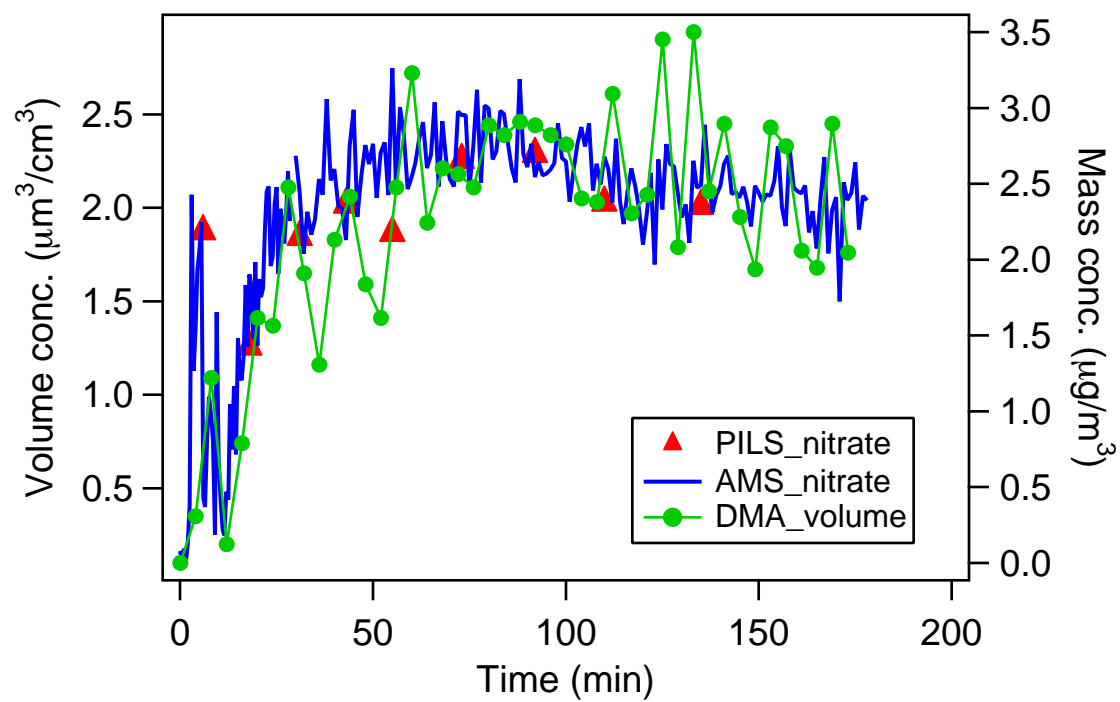




Figure 2.

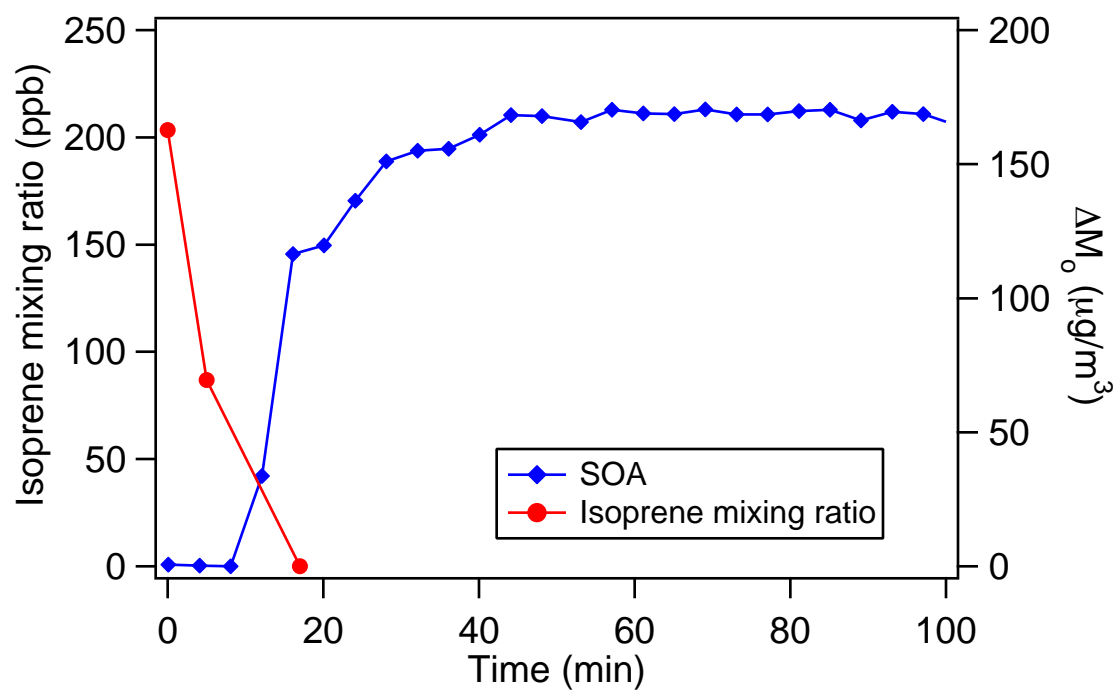


Figure 3.

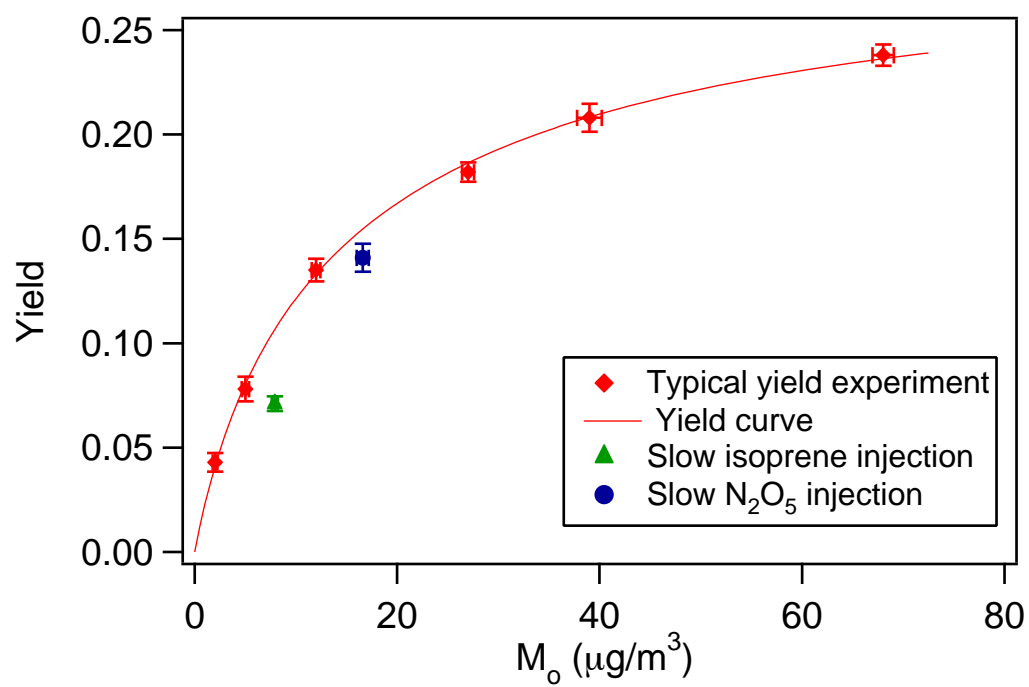


Figure 4.

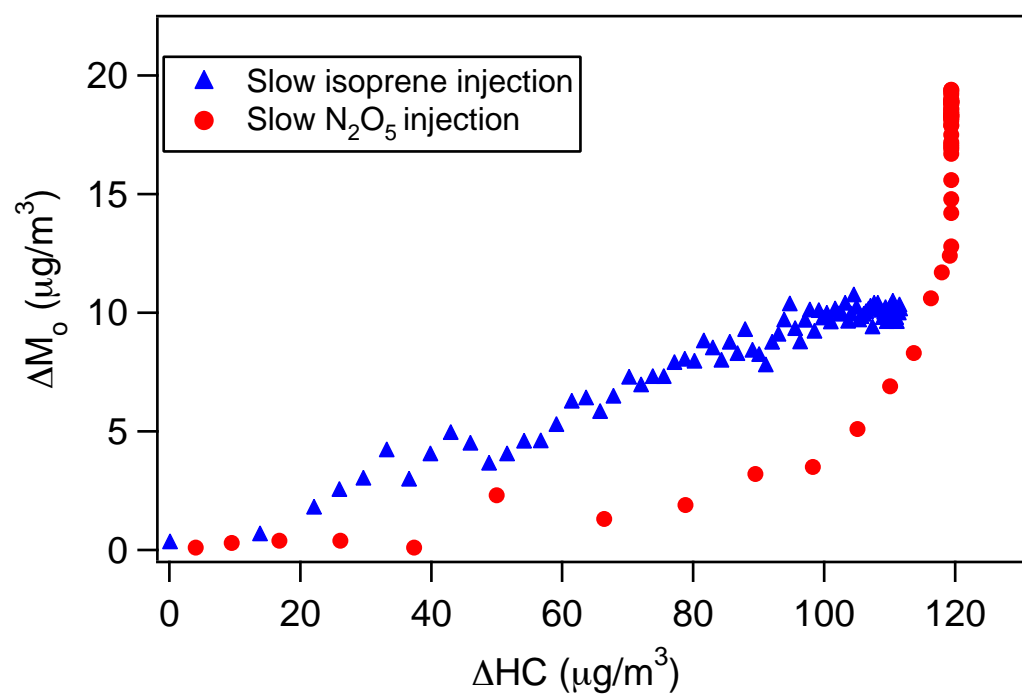


Figure 5.

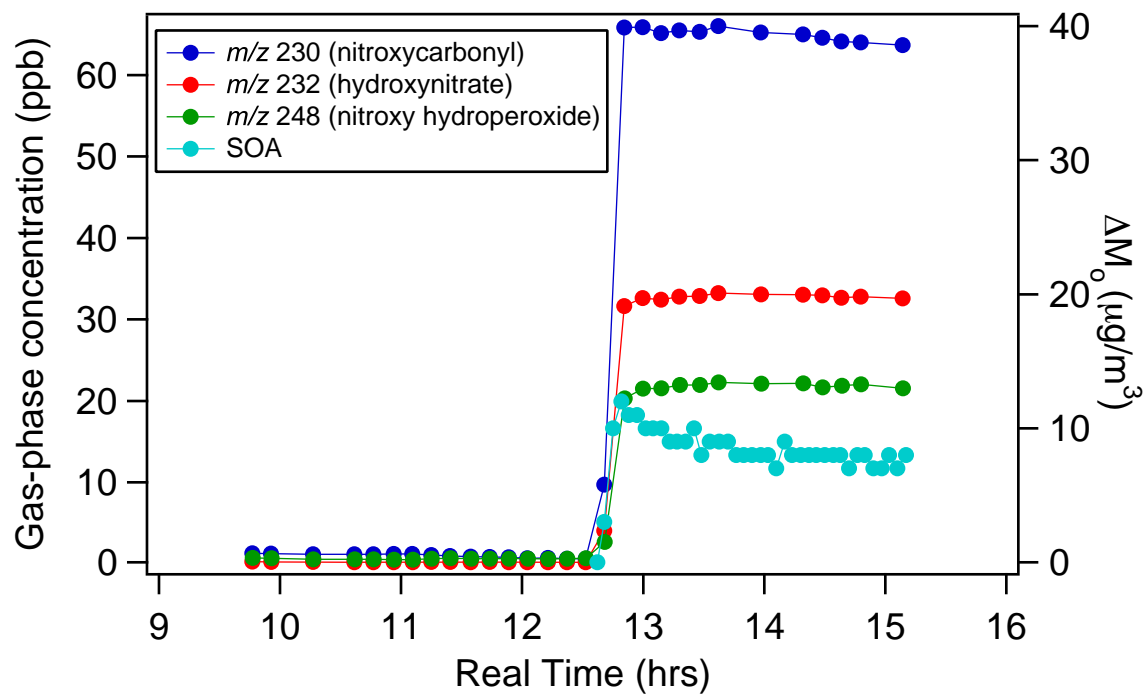


Figure 6.

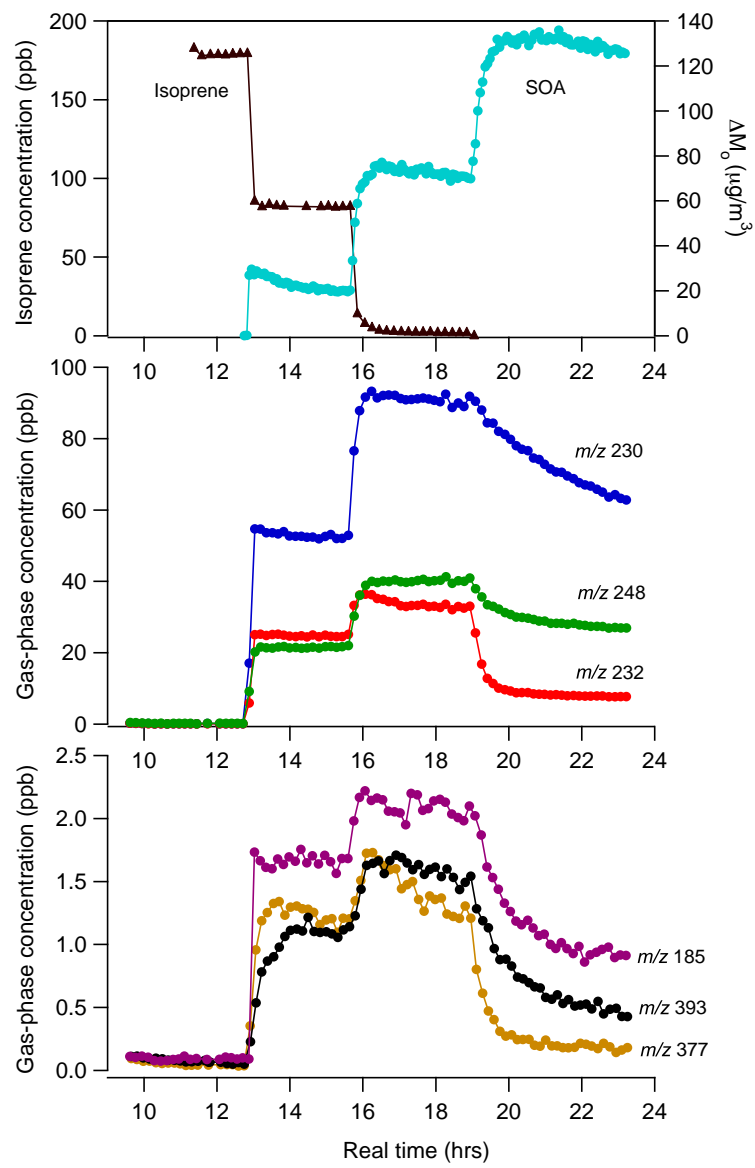


Figure 7.

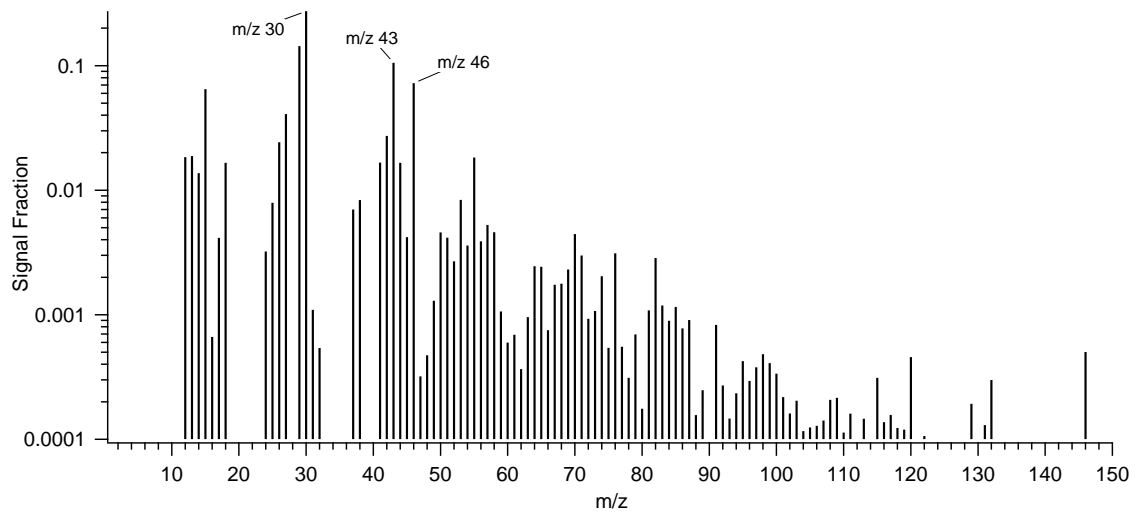


Figure 8.

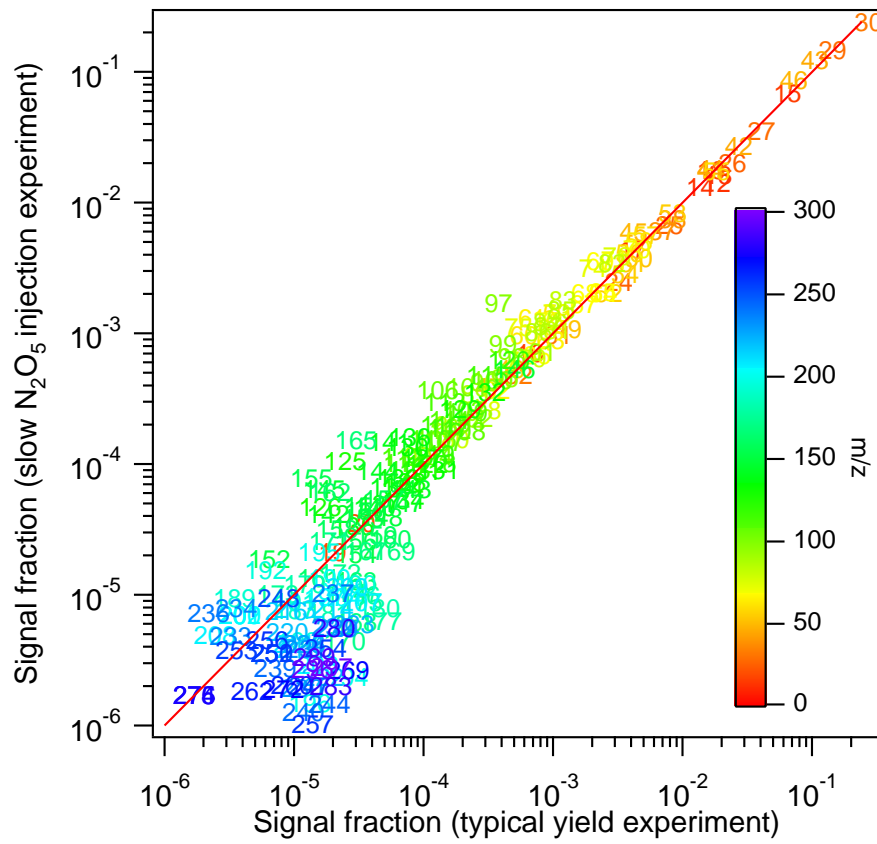


Figure 9.

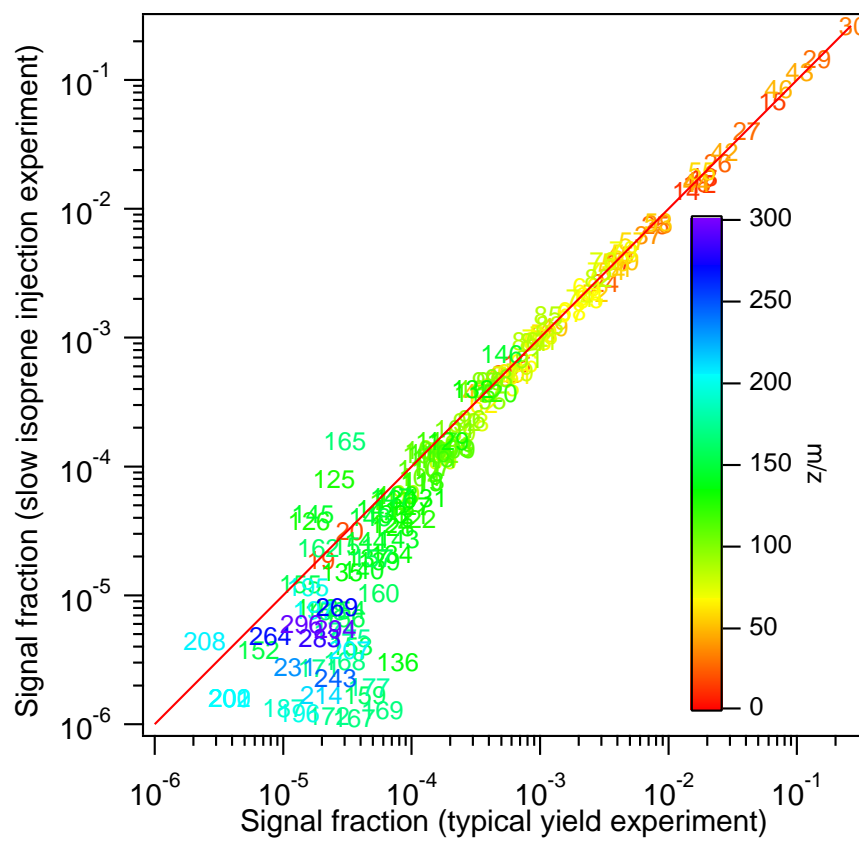




Figure 10.

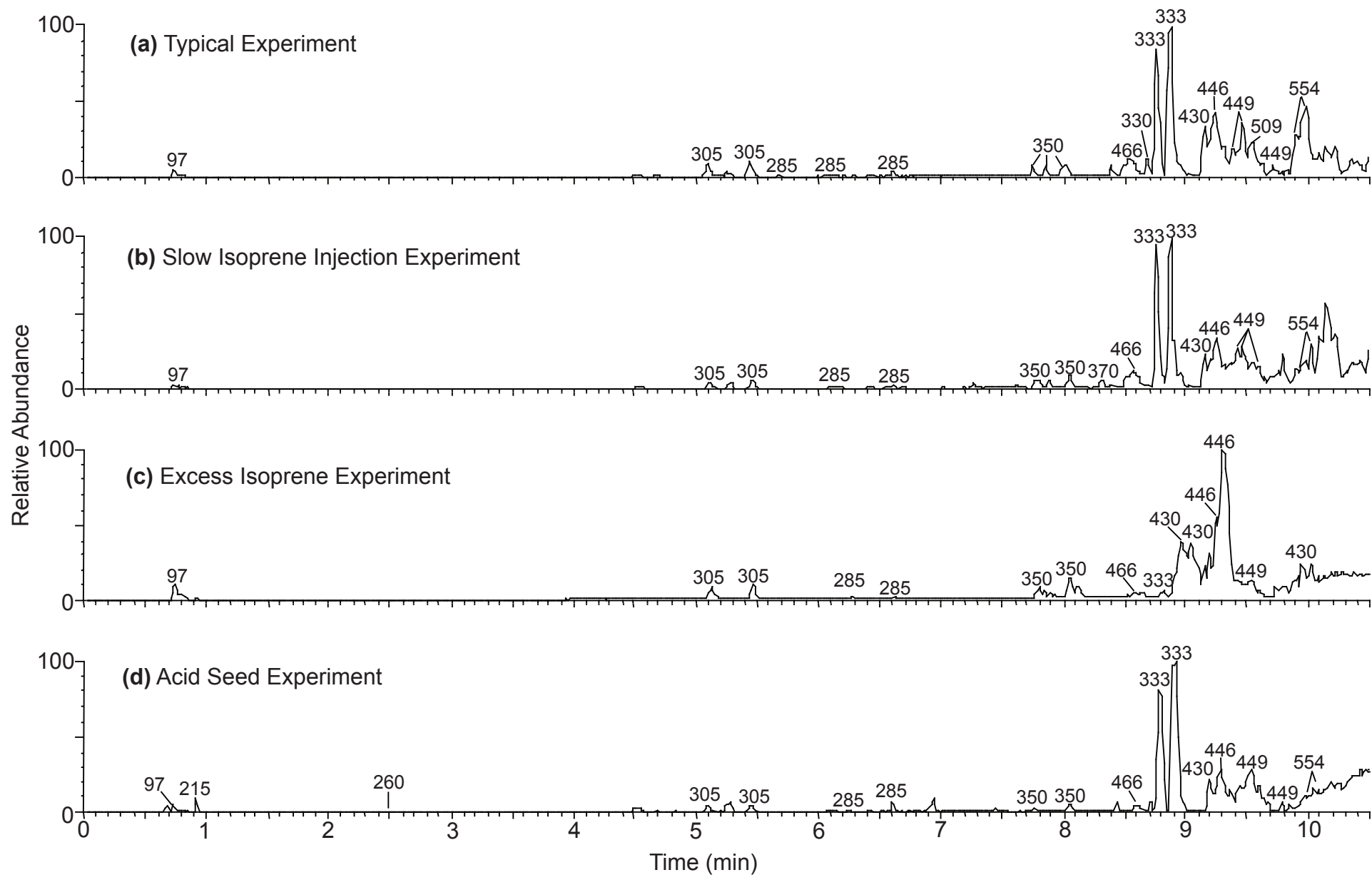


Figure 11.

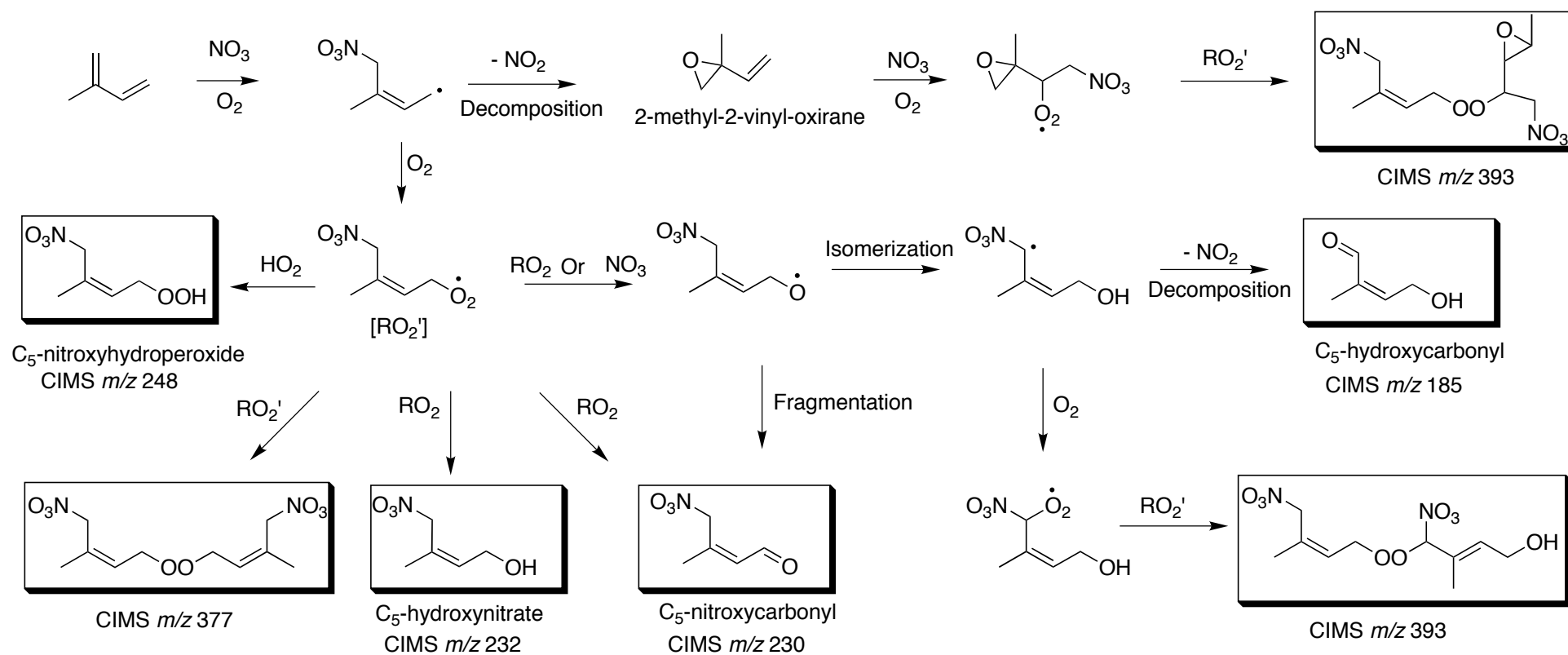


Figure 12.

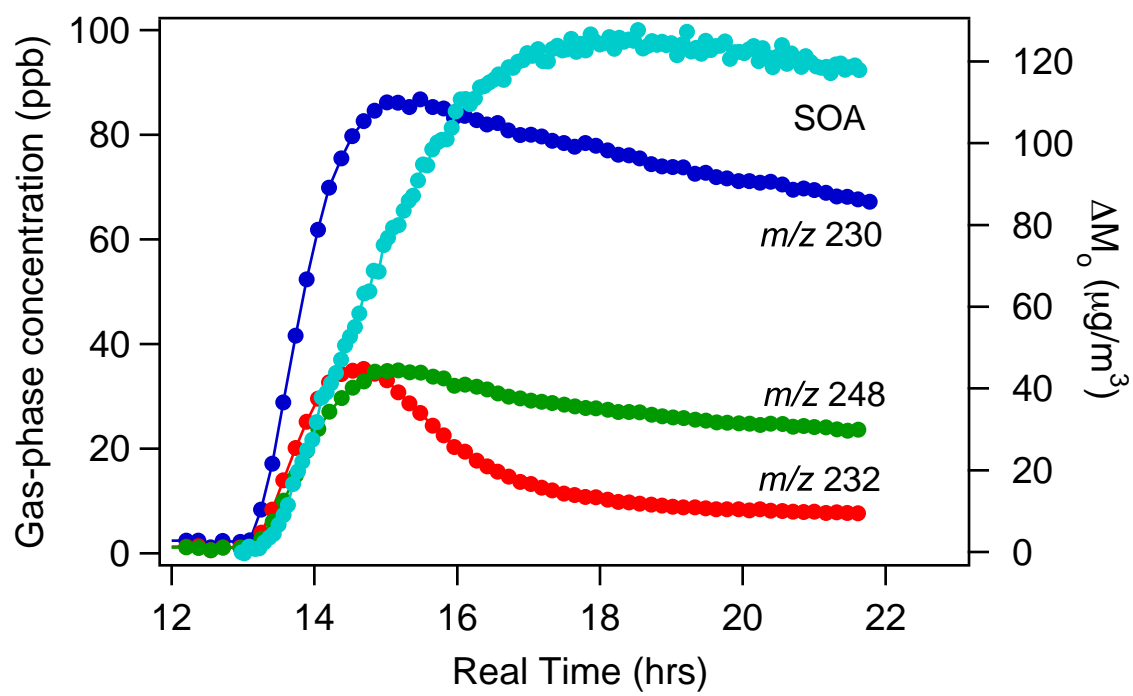


Figure 13.

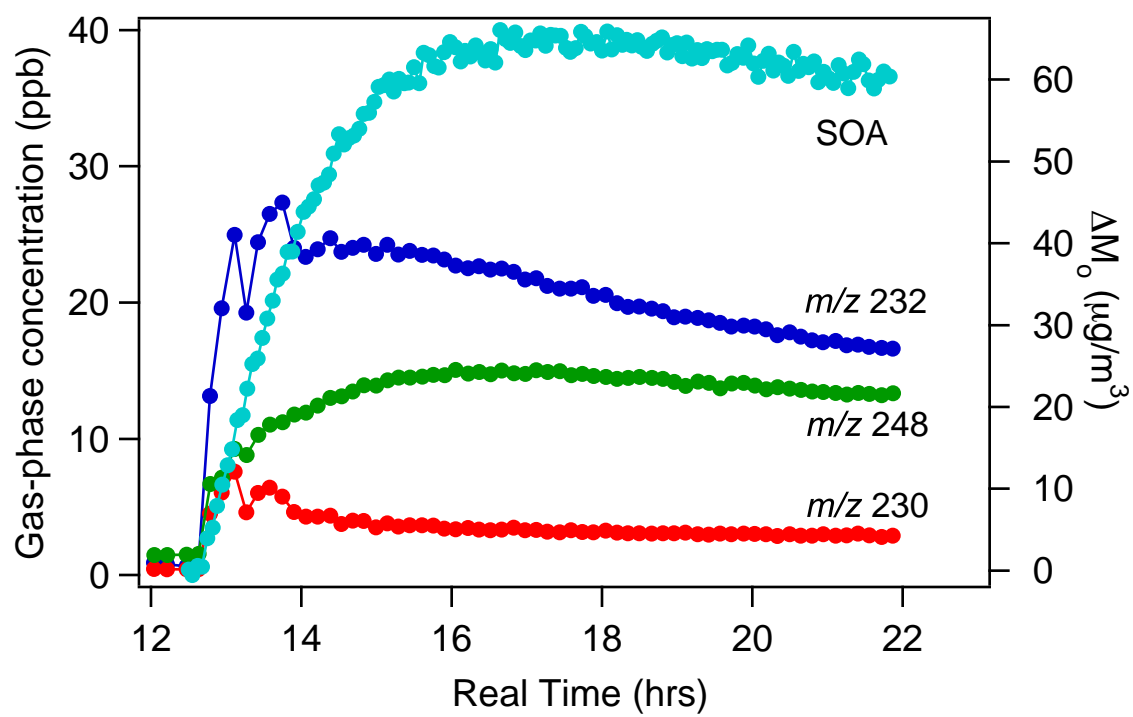


Figure 14.

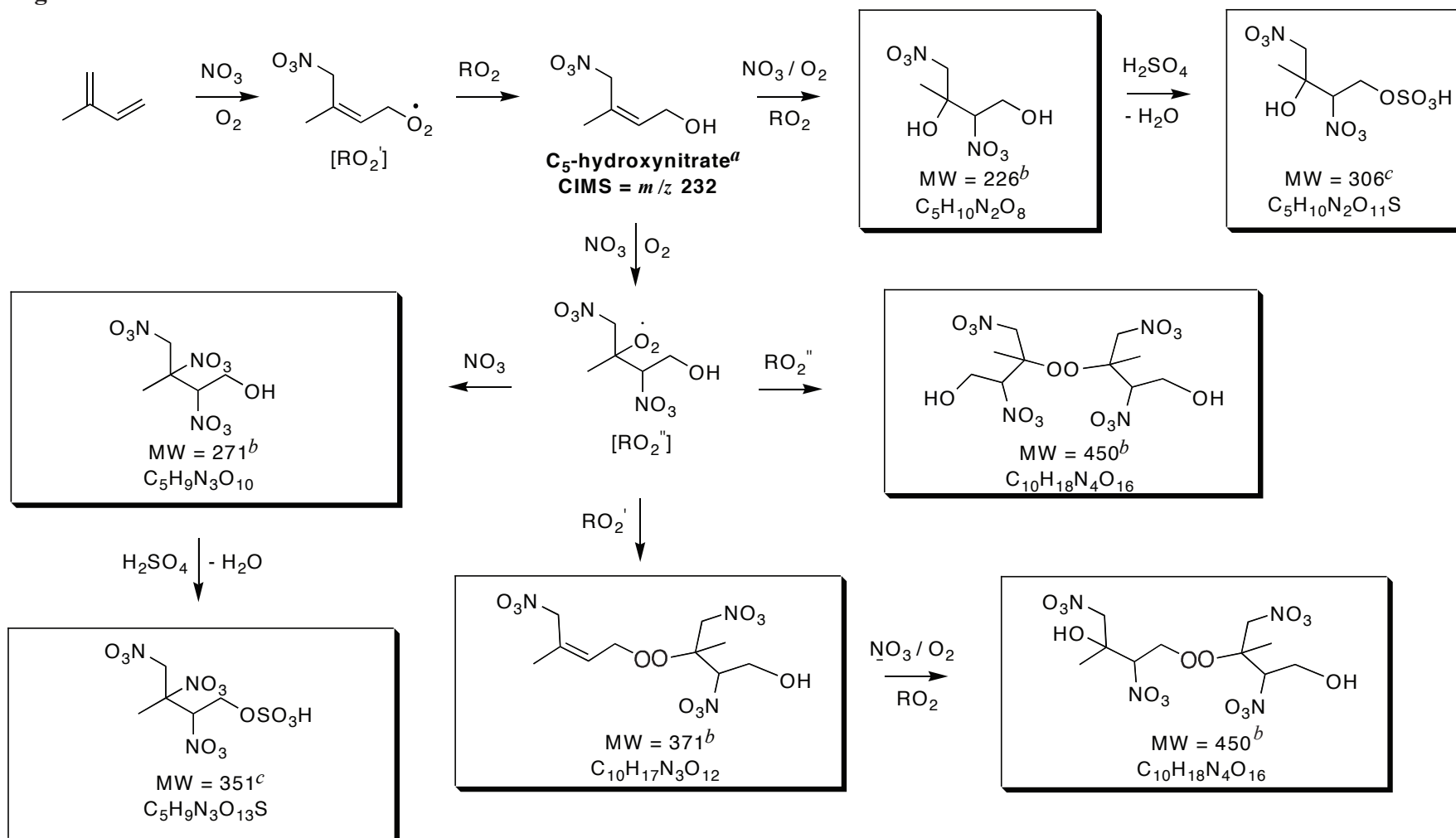


Figure 15.

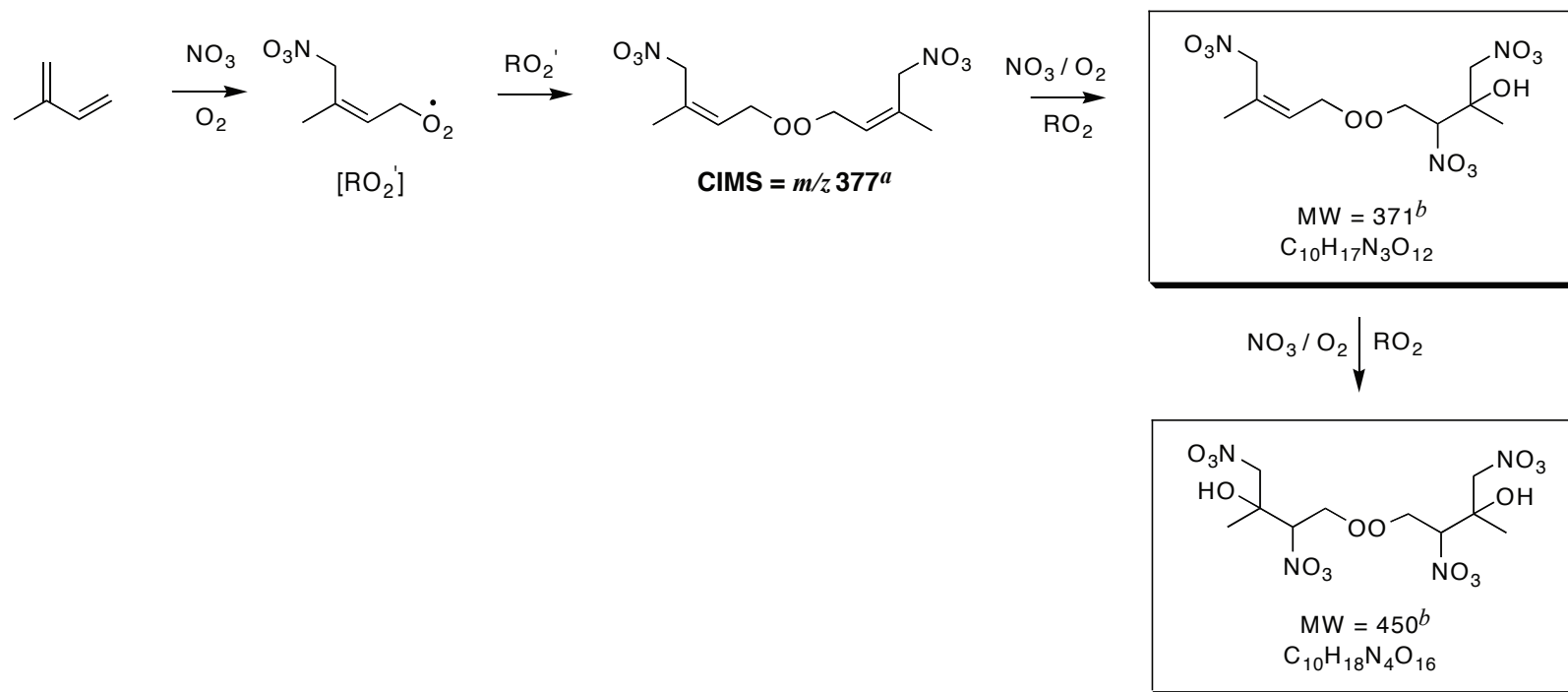


Figure 16.

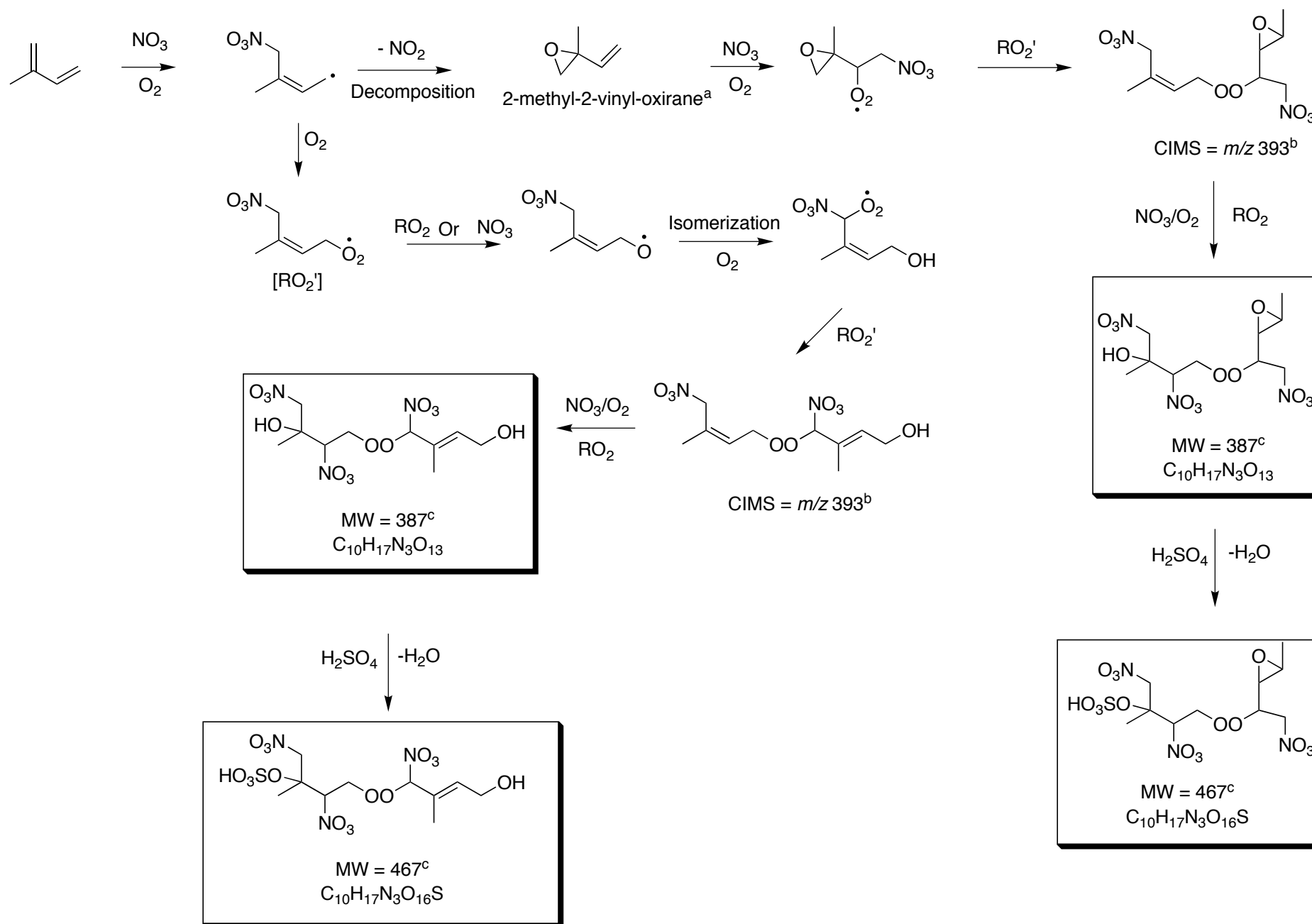
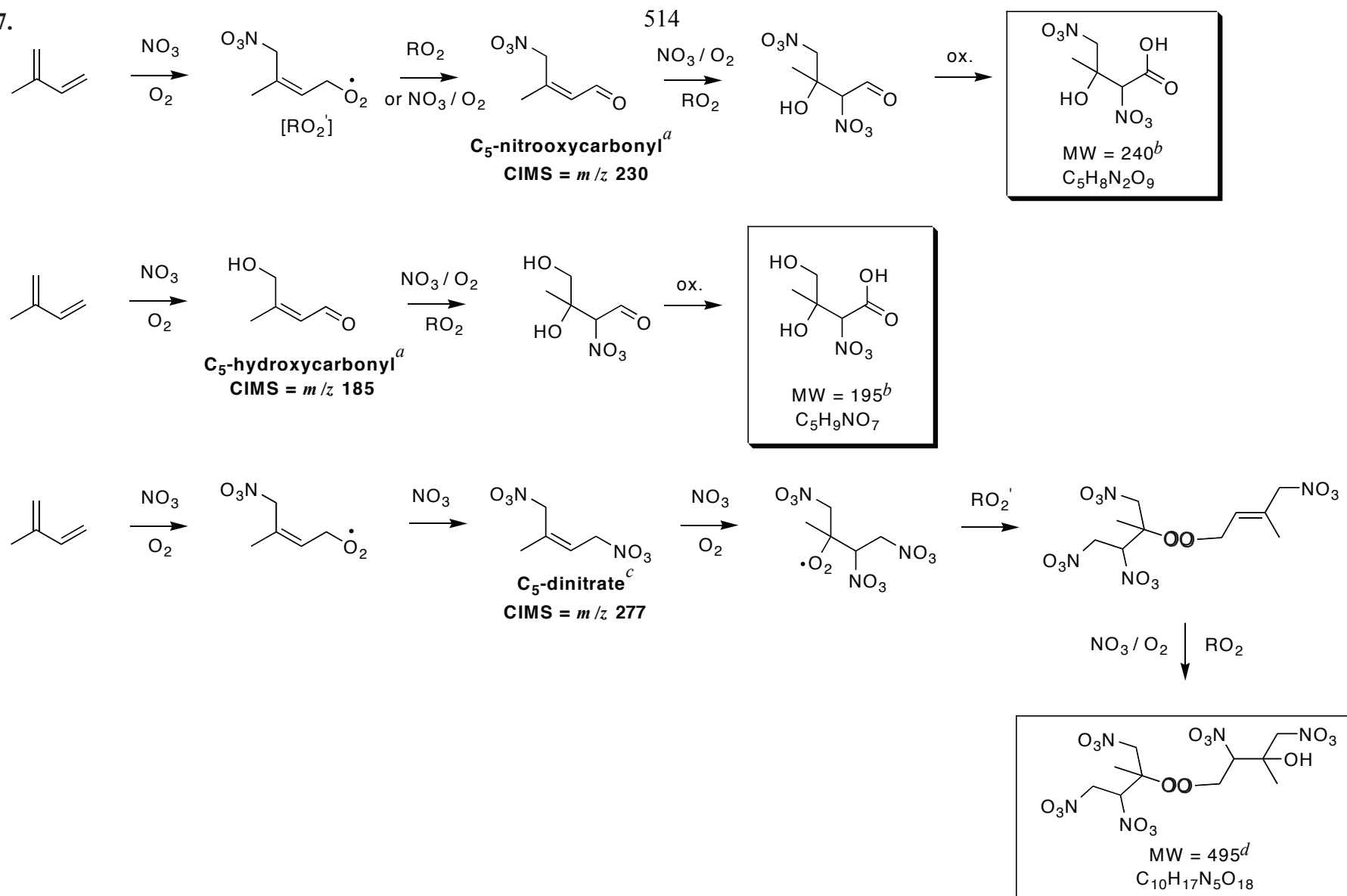


Figure 17.





## Appendix I

# **Molar Mass, Surface Tension, and Droplet Growth Kinetics of Marine Organics from Measurements of CCN Activity\***

---

\*This chapter is reproduced by permission from “Molar Mass, Surface Tension, and Droplet Growth Kinetics of Marine Organics from Measurements of CCN Activity” by R. H. Moore, E. Ingall, A. Sorooshian, and A. Nenes, *Geophys. Res. Lett.*, 35, L07801, doi:10.1029/2008GL033350, 2008. Copyright 2008. American Geophysical Union.



## Molar mass, surface tension, and droplet growth kinetics of marine organics from measurements of CCN activity

R. H. Moore,<sup>1</sup> E. D. Ingall,<sup>2</sup> A. Sorooshian,<sup>3</sup> and A. Nenes<sup>1,2</sup>

Received 23 January 2008; accepted 25 February 2008; published 1 April 2008.

[1] The CCN-relevant properties and droplet growth kinetics are determined for marine organic matter isolated from seawater collected near the Georgia coast. The organic matter is substantially less CCN active than  $(\text{NH}_4)_2\text{SO}_4$ , but droplet growth kinetics are similar. Köhler Theory Analysis (KTA) is used to determine the average organic molar masses of two samples, which are  $4370 \pm 24\%$  and  $4340 \pm 18\%$   $\text{kg kmol}^{-1}$ . KTA is used to infer surface tension depression, which is in excellent agreement with direct measurements. For the first time it is shown that direct measurements of surface tension are relevant for CCN activation, and this study highlights the power of KTA.

**Citation:** Moore, R. H., E. D. Ingall, A. Sorooshian, and A. Nenes (2008), Molar mass, surface tension, and droplet growth kinetics of marine organics from measurements of CCN activity, *Geophys. Res. Lett.*, 35, L07801, doi:10.1029/2008GL033350.

### 1. Introduction

[2] Oceanic surface waters contain a substantial amount of dissolved organic matter (DOM) that is transferred to the aerosol phase during the process of sea spray generation. The ocean surface layer contains large amounts of surfactants [Cavalli *et al.*, 2004], which can influence the ability of marine aerosol to act as cloud condensation nuclei (CCN). Measurements of primary marine aerosol composition have shown a size-dependent enrichment of organics (particularly water-insoluble species) in submicron aerosol [O'Dowd *et al.*, 2004; Oppo *et al.*, 1999]. Despite their potential importance, the CCN-relevant properties of marine organics are largely unknown. This is because DOM is difficult to isolate, as its concentration in bulk seawater is orders of magnitude lower than inorganic salts [Ogawa and Tanoue, 2003]. Recently, Vetter *et al.* [2007] developed a method to remove most of the salt in seawater samples via a combination of electrodialysis and reverse osmosis, thus enabling direct characterization of marine DOM.

[3] Köhler Theory Analysis (KTA) [Padró *et al.*, 2007] is a technique to infer the molar volume, surfactant characteristics, and droplet growth kinetics of organic aerosol constituents, all of which are important for linking organic aerosol with cloud formation. KTA has been previously evaluated for aerosol composed of  $\text{C}_3$ – $\text{C}_9$  organics mixed with  $(\text{NH}_4)_2\text{SO}_4$  [Padró *et al.*, 2007], for water-soluble

organics in biomass burning aerosol [Asa-Awuku *et al.*, 2008], and for secondary organic aerosol formed from the ozonolysis of biogenic volatile organic carbon [Asa-Awuku *et al.*, 2007]. Asa-Awuku *et al.* [2007] first extended KTA to infer surface tension as well, which is useful when sample size prohibits direct measurement of surface tension; this aspect of KTA is further developed here.

[4] In this study, we measure the CCN-relevant properties of marine DOM and then use KTA to infer its average molar mass and surface tension depression characteristics. The potential impact of marine surfactants on droplet growth kinetics is also explored. Inferred values of surface tension are compared against direct measurements using the pendant drop technique.

### 2. Experiment

#### 2.1. Sample Collection

[5] Seawater samples were collected near the Georgia Coast on board the R/V Savannah during an October 2006 research cruise in the Atlantic Ocean. 200-l samples from the Gulfstream current ( $31^\circ 32.5'\text{N}$ ,  $79^\circ 13.8'\text{W}$ , 84 m depth) and the Ogeechee River estuary ( $31^\circ 56.6'\text{N}$ ,  $81^\circ 9.1'\text{W}$ , 2 m depth) were collected in Niskin bottles and filtered to remove suspended particulates greater than  $0.45 \mu\text{m}$  with a polypropylene filter. The estuarine sample was collected under tidal conditions. Inorganic salt concentrations were similar in both samples ( $3.7 \times 10^4$  ppm in the Gulfstream sample and  $3.1 \times 10^4$  ppm in the estuarine sample); however, more organics were initially present in the estuarine sample than the Gulfstream sample (4.36 ppm and 0.95 ppm, respectively).

[6] The DOM in each sample was subsequently concentrated using the electrodialysis/reverse osmosis (ED/RO) technique of Vetter *et al.* [2007]. In this method, ED is first used to remove the majority of the inorganic salts and is followed by RO to remove excess water. This cycle is repeated until a desired concentration of DOM is attained, after which the sample is freeze-dried. Typical DOM recoveries range from 64–93% [Vetter *et al.*, 2007] and water conductivities were reduced by over 99.98%. During the process, all  $\text{Cl}^-$  is depleted, and the remaining inorganic fraction is primarily  $\text{Na}_2\text{SO}_4$  and  $(\text{NH}_4)_2\text{SO}_4$ .

#### 2.2. Chemical Composition of Samples

[7] The water-soluble organic carbon (WSOC) content of both samples was measured with a total organic carbon (TOC) analyzer (Sievers Model 800 Turbo). Additionally, inorganic ions ( $\text{SO}_4^{2-}$ ,  $\text{Cl}^-$ ,  $\text{NO}_3^-$ ,  $\text{Na}^+$ ,  $\text{NH}_4^+$ ,  $\text{Ca}^{2+}$ ,  $\text{Mg}^{2+}$ , and  $\text{K}^+$ ) were measured using a dual ion chromatography (IC) system (Dionex ICS-2000). TOC concentrations of the Gulfstream and estuarine dry samples are  $0.111 \text{ kgC kg}^{-1}$  and  $0.249 \text{ kgC kg}^{-1}$ , respectively. From the IC measurements, the

<sup>1</sup>School of Chemical and Biomolecular Engineering, Georgia Institute of Technology, Atlanta, Georgia, USA.

<sup>2</sup>School of Earth and Atmospheric Sciences, Georgia Institute of Technology, Atlanta, Georgia, USA.

<sup>3</sup>Department of Chemical Engineering, California Institute of Technology, Pasadena, California, USA.

major inorganic species present in the DOM extract are  $\text{Na}_2\text{SO}_4$  and  $(\text{NH}_4)_2\text{SO}_4$ . The solution pH is neutral, suggesting that the organics do not substantially dissociate.

### 2.3. Surface Tension Measurements

[8] Surface tension measurements were performed using the pendant drop method with a KSV CAM 200 goniometer. Each droplet was allowed to equilibrate for 20–30 seconds, allowing sufficient time for organics to partition between the bulk and surface layers [Taraniuk *et al.*, 2007]. The droplet shape was fit to the Young-Laplace equation to obtain the surface tension,  $\sigma$ , at the liquid-air interface. The temperature (approximately 297 K) was monitored throughout each set of measurements using a 50 k $\Omega$  thermistor (Digikey ERT-D2FHL503S). Seven pendant drops were photographed at ten frames per second for each surface tension measurement.

[9] Multiple solutions of each sample (done by preparing  $\sim 2000$  ppm samples, which are successively diluted down to 100 ppm) were prepared to determine  $\sigma$  as a function of dissolved carbon concentration,  $C$ . The data are fit to the Szyskowski-Langmuir (SL) adsorption isotherm [Langmuir, 1917]:

$$\sigma = \sigma_w - \alpha T \ln(1 + \beta C) \quad (1)$$

where  $\sigma_w$  is the surface tension of water (i.e., an “infinite dilution” sample),  $T$  is the absolute temperature, and  $\alpha$  and  $\beta$  are empirical constants obtained from least-squares fits to the data. While the SL isotherm is an adsorption model for one compound, it is able to model the complex DOM/salt system reasonably well (Figure 2).  $\alpha$  and  $\beta$  were determined to be 2.952 mN m $^{-1}$  K $^{-1}$  and  $2 \times 10^{-6}$  l mg $^{-1}$ , respectively.

### 2.4. CCN Activity and Droplet Growth Kinetics Measurements

[10] The experimental setup used for CCN activity measurements is described in detail elsewhere [e.g., Asa-Awuku *et al.*, 2008; Padró *et al.*, 2007]. Aerosol is generated by atomizing an aqueous solution of each of the seawater samples. The particles are dried and introduced into a scanning mobility CCN analyzer (SMCA) (A. Nenes and J. Medina, Scanning mobility CCN analysis: A method for fast measurements of size-resolved CCN activity and growth kinetics, submitted to Aerosol Science and Technology, 2007), for characterization of size-resolved CCN activity and growth kinetics. SMCA uses a differential mobility analyzer (DMA, TSI 3081), operating in voltage-scanning mode, to classify the aerosol. The monodisperse stream is then introduced simultaneously into a Droplet Measurement Technologies Continuous-Flow Streamwise Thermal Gradient CCN Counter (DMT-STGC) [Roberts and Nenes, 2005] and a condensation particle counter (CPC, TSI 3022). The time series of the DMT-STGC and CPC counts are inverted to obtain curves of CCN/CN as a function of mobility diameter (while maintaining instrument supersaturation at a constant value). The dry diameter,  $d_p$ , for which 50% of particles are activated (neglecting multiply-charged particles) represents the aerosol that activates at the instrument supersaturation,  $s_c$ . The DMT-STGC uses an optical particle counter (OPC) to obtain the size distribution of activated droplets exiting the instrument column.

[11] The CCN activity of aerosol containing the estuarine sample and a known amount of added  $(\text{NH}_4)_2\text{SO}_4$  was also measured in order to see if a “salting out” of the organic could be observed. The effect occurs at relatively high electrolyte concentrations ( $\sim 50$  wt%, dry concentration), when the salts enhance surfactant partitioning to the droplet surface, dramatically reducing the surface tension and increasing the CCN activity [Asa-Awuku *et al.*, 2007]. Two samples were prepared to total salt concentrations of approximately 60 and 90 wt%. The 60 wt% salt sample was also used as an independent mixture to infer molar mass and surface tension depression.

[12] For all CCN measurements, the flow rate of air through the column was maintained at 0.5 l min $^{-1}$  (10:1 sheath-to-aerosol ratio), which corresponds to a residence time of 15 seconds. The DMT-STGC instrument supersaturation was varied from 0.2% to 1.4%.

## 3. Results and Discussion

### 3.1. CCN Activity

[13] The CCN activation curves for both samples and pure  $(\text{NH}_4)_2\text{SO}_4$  are shown in Figure 1. For a CCN composed of soluble non-surfactant compounds, Köhler theory suggests that the “critical supersaturation”,  $s_c$ , scales with  $d_p$  to the  $-3/2$  power [Köhler, 1936]. However, for aerosol containing surfactants, this scaling will change, tending to be lower at smaller  $d$  and approaching  $-3/2$  at larger  $d$ . This is because at smaller particle diameters, the high concentration of WSOC depresses  $\sigma$ , which lowers  $s_c$  more than would be expected from the solute effect alone; at larger  $d$ , the WSOC concentration is insufficient to induce this effect [Padró *et al.*, 2007].

[14] The activation curve of the Gulfstream sample aerosol (blue circles) is almost identical to  $(\text{NH}_4)_2\text{SO}_4$  (yellow triangles), despite the presence of  $\sim 40$  wt% surface-active DOM. It is likely that the surface tension depression from the organic fraction compensates for the decreased soluble mole fraction. The estuarine sample aerosol contains  $\sim 85$  wt% organic matter and is much less CCN active than  $(\text{NH}_4)_2\text{SO}_4$  (red circles in Figure 1). Additionally, the activation curve deviates from the  $-3/2$  exponential power law fit (as indicated by the dotted line) at low dry particle diameters and high  $s_c$ , where the concentration of organic matter is high enough to significantly affect the droplet surface tension ( $C > 1000$  mg l $^{-1}$ , from Figure 2).

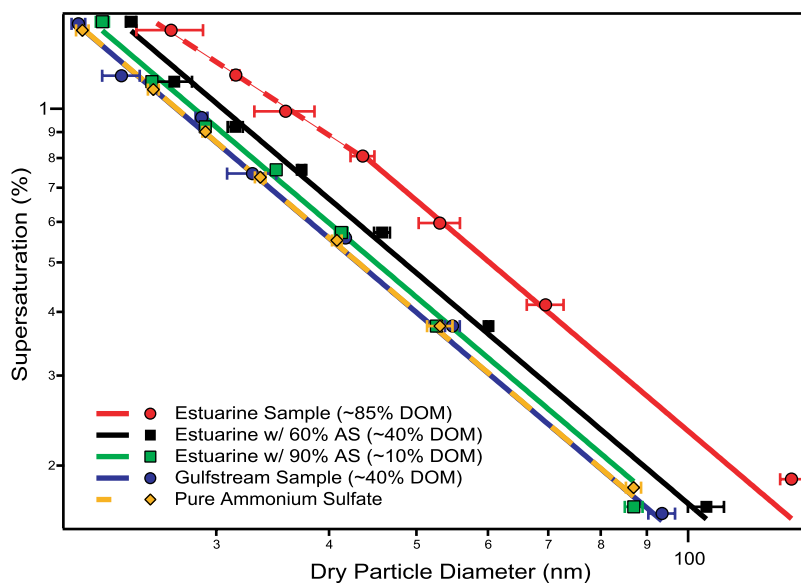
### 3.2. Köhler Theory Analysis

[15] The organic molar mass and surface tension depression were inferred from the CCN activity measurements using KTA, method b $_2$  [Padró *et al.*, 2007; Asa-Awuku *et al.*, 2008, 2007]. For each  $s_c/d_p$  measurement, the fitted CCN activity (FCA) parameter,  $\omega$ , is calculated from

$$\omega = s_c d_p^3 / 2 \quad (2)$$

KTA entails expressing FCA in terms of its constituents; assuming the aerosol is composed of  $N$  components [Padró *et al.*, 2007]:

$$\omega = 2 \left( \frac{4M_w \sigma}{3RT \rho_w} \right)^{3/2} \left[ \sum_{i=1}^N \left( \frac{\rho_w}{M_w} \right) \left( \frac{M_i}{\rho_i} \right) \frac{1}{\varepsilon_i \nu_i} \right]^{1/2} \quad (3)$$



**Figure 1.** Critical supersaturation versus dry particle diameter for all samples considered.

where  $M_w$ ,  $\rho_w$  are the molar mass and density of water, respectively,  $R$  is the universal gas constant, and  $M_i$ ,  $\rho_i$ ,  $\varepsilon_i$ ,  $v_i$  are the molar mass, density, volume fraction, and effective van't Hoff factor of component  $i$ , respectively. Denoting the organic fraction as component “ $j$ ” and rearranging Equation 3 to solve explicitly for  $M_j$  and  $\sigma$  yields

$$M_j = \frac{\rho_j \varepsilon_j v_j}{\frac{256}{27} \left( \frac{M_w}{\rho_w} \right)^2 \left( \frac{1}{RT} \right)^3 \sigma^3 \omega^{-2} - \sum_{i \neq j}^N \frac{\rho_i}{M_i} \varepsilon_i v_i} \quad (4)$$

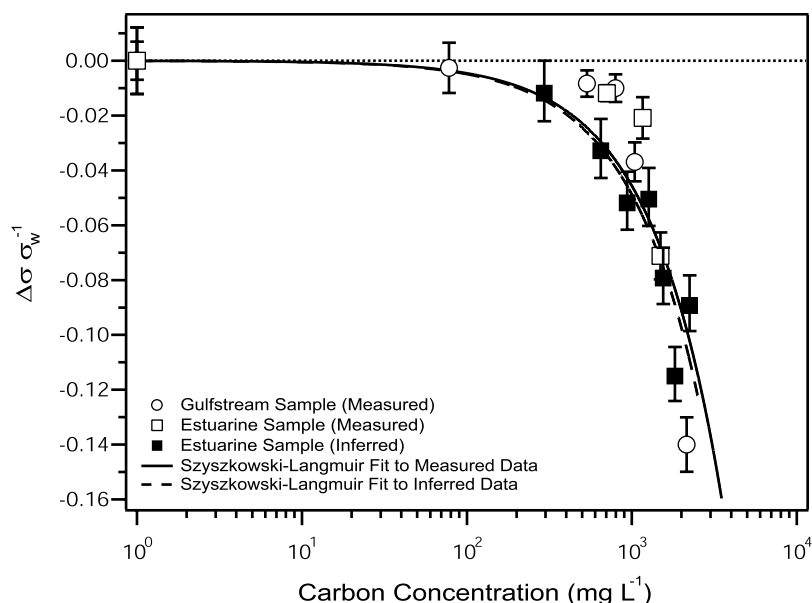
$$\sigma = \left[ \frac{\left( \frac{\rho_j}{M_j} \right) \varepsilon_j v_j + \sum_{i \neq j}^N \frac{\rho_i}{M_i} \varepsilon_i v_i}{\frac{256}{27} \left( \frac{M_w}{\rho_w} \right)^2 \left( \frac{1}{RT} \right)^3 \omega^{-2}} \right]^{1/3} \quad (5)$$

$\sigma$  corresponds to the value at activation for a dissolved carbon concentration, of  $C_{act}$ , of [Padró et al., 2007],

$$C_{act} = \frac{27}{8} x_{c,j} \varepsilon_j \rho_j \frac{d_p^3 s_c^3}{A^3} \quad (6)$$

where  $A = \frac{4M_w \sigma}{RT \rho_w}$  and  $x_{c,j} = 0.29$  is the mass fraction of carbon in the DOM, estimated from the Redfield ratio (C:N:P = 106:16:1) [Schulz and Zabel, 2006; Redfield et al., 1963]. In applying equations (4)–(6), we assume an organic density,  $\rho_j$ , of  $1400 \text{ kg m}^{-3}$  [Schulz and Zabel, 2006], an effective van't Hoff factor of 1 for the organics [Dinar et al., 2007], and 2.5 for  $(\text{NH}_4)_2\text{SO}_4$  and  $\text{Na}_2\text{SO}_4$  [Padró et al., 2007].

[16] To compute  $M_j$  and  $\sigma$  from KTA, the following procedure is used: First, the average organic molar mass,  $M_j^*$ , is estimated for each  $s_c/d_p$  pair (equation (4)), initially



**Figure 2.** Fractional surface tension depression with respect to pure water. Shown are direct measurements (open symbols) and values inferred from KTA (solid symbols).

**Table 1.** Molar Mass Uncertainty,  $\Delta M_j$ , From Parameter Uncertainty,  $\Delta x$ , for the Estuarine (Gulfstream) Samples

	$\omega \text{ m}^{3/2}$	$\rho_p \text{ kg m}^{-3}$	$v_j$	$x_{c,p} \%$
Base $x$ Value		1400	1	0.29
$\Delta x$	$1.47(2.16) \times 10^{-15a}$	$400^b$	$0.2^c$	$0.044^b$
$\Delta M_j \%$	3.7 (6.9)	10 (17)	0.2 (0.1)	15 (16)
Total molar mass uncertainty, %				18 (24)

<sup>a</sup>One standard deviation from the mean FCA value.

<sup>b</sup>From Schulz and Zabel [2006].

<sup>c</sup>From Dinar *et al.* [2007].

assuming the surface tension of pure water.  $M_j$  is introduced in equations (5) and (6) to estimate  $\sigma$  for the  $s_c/d_p$  data of the sample plus 60%  $(\text{NH}_4)_2\text{SO}_4$ . The updated  $\sigma$  values are used to reevaluate  $M_j^*$  and this process is iterated until the  $\sigma$  and  $M_j^*$  values converge. This procedure allows the concurrent inference of  $M_j$  and  $\sigma$  (as a function of WSOC concentration) from the CCN activity data alone.

[17]  $M_j$  is estimated to be  $4370 \pm 26\% \text{ kg kmol}^{-1}$  and  $4340 \pm 6\% \text{ kg kmol}^{-1}$  for the Gulfstream and estuarine samples, respectively, (the reported uncertainty is one standard deviation from the mean  $M_j$  over all  $s_c/d_p$  pairs). The sensitivities of  $M_j$  to each of the independent parameters is computed with the method of Padró *et al.* [2007] (Table 1). Using this method, the total estimated uncertainties of  $M_j$  for the estuarine and Gulfstream samples are 18% and 24%, respectively. As expected, the Gulfstream sample uncertainty exceeds the estuarine sample uncertainty, since the lower organic mass increases the  $M_j$  sensitivity to most of the independent parameters [Padró *et al.*, 2007].

[18] Both molar masses are consistent with each other and fall in the mid-range of the high molar-mass fraction that comprises 30–35% of the marine surface DOM [Ogawa and Tanoue, 2003]. The inferred  $M_j$  is also consistent with that of a theoretical Redfield-based molecule,  $(\text{CH}_2\text{O})_{106}(\text{NH}_3)_{16}\text{H}_3\text{PO}_4$  [Schulz and Zabel, 2006]. While most of the DOM is recovered, it is expected that the

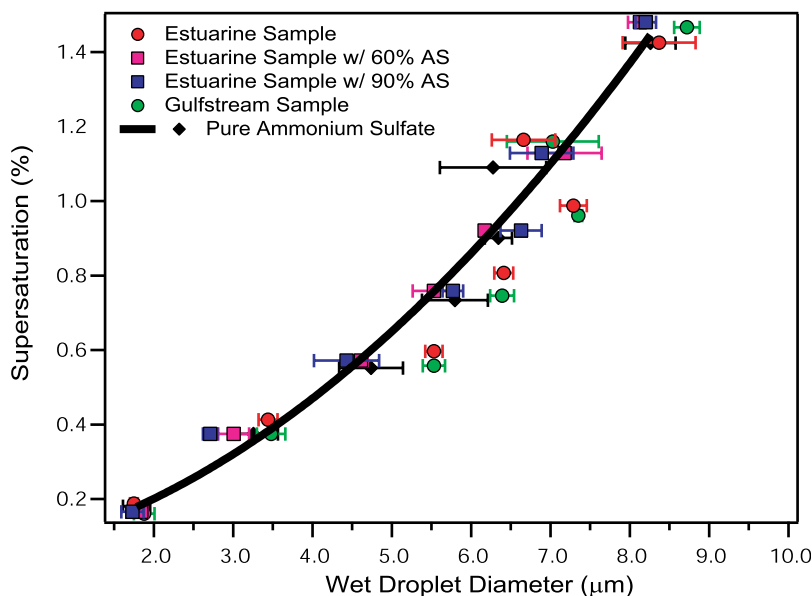
small amount of DOM not recovered during the ED/RO process would be low-molar-mass species that can permeate the ED membranes easiest; therefore, higher molar-mass DOM in the sample may be enriched in the process and the  $M_j$  of the sample (and hence, that inferred using KTA) may be greater than the  $M_j$  of in-situ marine DOM.

[19] The inferred  $\sigma$  is in excellent agreement with the SL fit to direct measurements (Figure 2). The agreement is still excellent if other functions for fitting the data are used; the variability in inferred  $M_j$  remains within the reported uncertainty (not shown). Since the inferred values are derived independently of the direct measurements, their agreement shows conclusively that diffusion of surface-active molecules to the droplet surface is sufficiently rapid to achieve equilibrium surface tension depression. Taraniuk *et al.* [2007] and Asa-Awuku and Nenes [2007] showed that humic-like organic species ( $\sim 500 \text{ kg kmol}^{-1}$ ) in growing droplets are in equilibrium; we find this to apply for marine DOM with a tenfold higher molar mass (hence,  $\sim \sqrt{10}$  times lower diffusivity). The latter finding is consistent with the analysis of Asa-Awuku and Nenes [2007], as a diffusivity of  $2 \times 10^{-10} \text{ m}^2 \text{ s}^{-1}$  ( $= \frac{6 \times 10^{10}}{10^{1/2}}$ , with  $6 \times 10^{-10}$  being the diffusivity of HULIS) [Taraniuk *et al.*, 2007] implies that the organic concentration at the droplet surface is more than 90% of its equilibrium value for the supersaturation range considered here.

[20] While the inferred and measured surface tensions agree, the surfactants require tenfold higher concentrations to give the same effect as organics isolated from marine aerosol [Cavalli *et al.*, 2004]. This difference reflects the enrichment of marine aerosol in organic surfactants from the process of bubble bursting. Hence, the samples investigated here are representative of natural marine DOM, but should be interpreted as the lower limit of CCN activity of primary marine organic aerosol.

### 3.3. Droplet Growth Kinetics

[21] The mean droplet sizes for each sample measured by the DMT-STGC OPC at varying values of  $s_c$  are shown in Figure 3. All samples studied exhibit growth similar to that

**Figure 3.** Activated droplet sizes for CCN with  $s_c = s_{\text{instrument}}$



of pure  $(\text{NH}_4)_2\text{SO}_4$  for most supersaturations. For the three intermediate supersaturations (0.6%, 0.8%, and 1.0%), both seawater samples appear to grow to larger droplet sizes than for pure  $(\text{NH}_4)_2\text{SO}_4$ . Since it is not expected that organics would enhance droplet growth, the observed discrepancy may be caused by slight shifts in the laser scattering during the sizing measurement, resulting from the presence of a compressed film.  $(\text{NH}_4)_2\text{SO}_4$  growth could also be depressed because of water vapor depletion in the column during the calibrations; however, this is unlikely since the total CCN concentrations were relatively low ( $\sim 500 \text{ cm}^{-3}$ ) and constant for all supersaturations. Laser shifts over long time periods are unlikely, as the results are reproducible. The data suggest that the dissolved organics, compared to pure  $(\text{NH}_4)_2\text{SO}_4$ , do not significantly alter the droplet growth kinetics (i.e., the water vapor mass transfer coefficient).

#### 4. Summary and Conclusions

[22] In this study, measurements of CCN activity, droplet growth kinetics, and WSOC/ionic composition of marine DOM were used to infer its CCN-relevant properties. Köhler Theory Analysis (KTA) determined the molar masses of the organic matter in the Gulfstream sample and estuarine sample to be  $4370 \pm 24\%$  and  $4340 \pm 18\%$ , respectively. This is consistent with the high-molar-mass marine DOM typically found in surface ocean waters. KTA was used to infer the organic surface tension depression, and was found to be in excellent agreement with direct measurements using the pendant drop technique. This shows that very large organic molecules are able to diffuse to the surface of a growing droplet and establish an equilibrium surface tension depression; in fact, direct equilibrium surface tension measurements adequately describe droplet surface tension at activation. Furthermore, KTA is proven to be a powerful technique that can be used to infer organic surface tension depression using small amounts of aerosol generated from a dilute solution. Finally, while the dissolved organics form compressed surface films that can substantially change surface tension, they exhibited similar growth to pure  $(\text{NH}_4)_2\text{SO}_4$ . This suggests that the primary chemical effect of marine DOM on CCN activity is through its impact on surface tension.

[23] **Acknowledgments.** We acknowledge support from an NSF CAREER Award, NSF grants OCE0425624 and OCE0526178, and a DOE GCEP GRE Fellowship. The authors gratefully acknowledge the crew of the R/V Savannah, C. Hennigan, R. Weber, S. Balachandran,

A. Russell, C. Jackson, E. M. Perdue, and P. Pfromm for assistance with this work.

#### References

- Asa-Awuku, A., and A. Nenes (2007), The effect of solute dissolution kinetics on cloud droplet formation, *J. Geophys. Res.*, **112**, D22201, doi:10.1029/2005JD006934.
- Asa-Awuku, A., A. Nenes, S. Gao, R. Flagan, and J. Seinfeld (2007), Alkene ozonolysis SOA: Inferences of composition and droplet growth kinetics from Köhler theory analysis, *Atmos. Chem. Phys. Discuss.*, **7**, 8983–9011.
- Asa-Awuku, A., A. Nenes, A. Sullivan, C. Hennigan, and R. Weber (2008), Investigation of molar volume and surfactant characteristics of water-soluble organic compounds in biomass burning aerosol, *Atmos. Chem. Phys.*, **8**, 1–14.
- Cavalli, F., et al. (2004), Advances in characterization of size-resolved organic matter in marine aerosol over the North Atlantic, *J. Geophys. Res.*, **109**, D24215, doi:10.1029/2004JD005137.
- Dinar, E., I. Taraniuk, E. R. Graber, T. Anttila, T. F. Mentel, and Y. Rudich (2007), Hygroscopic growth of atmospheric and model humic-like substances, *J. Geophys. Res.*, **112**, D05211, doi:10.1029/2006JD007442.
- Köhler, H. (1936), The nucleus in and growth of hygroscopic droplets, *Trans. Faraday Soc.*, **32**, 1152–1161.
- Langmuir, I. (1917), The constitution and fundamental properties of solids and liquids. II. Liquids, *Am. Chem. Soc.*, **39**, 1848–1906.
- O'Dowd, C., M. C. Facchini, F. Cavalli, D. Ceburnis, M. Mircea, S. Decesari, S. Fuzzi, Y. J. Yoon, and J. P. Putaud (2004), Biogenically driven organic contribution to marine aerosol, *Nature*, **431**, 676–680.
- Ogawa, H., and E. Tanoue (2003), Dissolved organic matter in oceanic waters, *J. Oceanogr.*, **59**, 129–147.
- Oppo, C., S. Bellandi, N. D. Innocenti, A. Stortini, G. Loglio, E. Schiavuta, and R. Cini (1999), Surfactant components of marine organic matter as agents for biogeochemical fractionation and pollutant transport via marine aerosols, *Mar. Chem.*, **63**, 235–253.
- Padró, L., A. Asa-Awuku, R. Morrison, and A. Nenes (2007), Inferring thermodynamic properties from CCN activation experiments: Single-component and binary aerosols, *Atmos. Chem. Phys.*, **7**, 5263–5274.
- Redfield, A., B. Ketchum, and F. Richards (1963), The influence of organisms on the composition of sea water, in *The Sea*, vol. 2, edited by M. N. Hill, pp. 26–77, Wiley Intersci., New York.
- Roberts, G., and A. Nenes (2005), A continuous-flow streamwise thermal-gradient CCN chamber for atmospheric measurements, *Aerosol Sci. Technol.*, **39**, 206–221.
- Schulz, H. D., and M. Zabel (Eds.) (2006), *Marine Geochemistry*, 2nd ed., Springer, Heidelberg.
- Taraniuk, I., E. R. Graber, A. Kostinski, and Y. Rudich (2007), Surfactant properties of atmospheric and model humic-like substances (HULIS), *Geophys. Res. Lett.*, **34**, L16807, doi:10.1029/2007GL029576.
- Vetter, T. A., E. M. Perdue, E. Ingall, J. F. Koprivnjak, and P. H. Pfromm (2007), Combining reverse osmosis and electrodialysis for more complete recovery of dissolved organic matter from seawater, *Sep. Purif. Technol.*, **56**, 383–387.
- E. D. Ingall, School of Earth and Atmospheric Sciences, Georgia Institute of Technology, Atlanta, GA 30332–0340, USA.
- R. H. Moore and A. Nenes, School of Chemical and Biomolecular Engineering, Georgia Institute of Technology, Atlanta, GA 30332–0340, USA. (nenes@eas.gatech.edu)
- A. Sorooshian, Department of Chemical Engineering, California Institute of Technology, Mail Code 210-41, Pasadena, CA 91125, USA.